The Development of Nanoparticle Formulations for NAD+ Delivery Towards the Prevention of Age-Related Ocular Diseases

By

Saoirse Casey-Power

A dissertation submitted to South East Technological University in fulfilment of the requirements for the award of Doctor of Philosophy (PhD).

Prepared under the supervision of Professor Peter McLoughlin, Dr. Gautam Behl, Dr. Richie Ryan, Professor Mark Byrne, and Dr. Laurence Fitzhenry.

Ocular Therapeutics Research Group, Pharmaceutical Molecular Biotechnology Research Centre, Department of Science, South East Technological University.

DECLARATION

I hereby certify that this material, which I now submit for assessment is entirely my own work and has not been taken from the work of others, save to the extent that such work has been cited and acknowledged within the text of my work.

Signed:

ID No.: 20071259

Date: 02/05/2024

ACKNOWLEDGEMENTS

"In science, you endeavour to control every variable of your experiment. The temperature in your lab, the number of contaminants, and the correct calibration for each piece of equipment. Sometimes, you can't count on a formula. Sometimes you can't control each variable. Sometimes, many times, things just turn out messy. Sometimes you will burn the lasagna" – Lessons in Chemistry.

I would like to take this opportunity to both acknowledge and express my profound gratitude to those who have helped me on this incredible journey. First and foremost, I would like to thank my principal supervisor, Dr Laurence Fitzhenry, and my co-supervisors, Professor Mark Byrne, Dr Richie Ryan, Dr Gautam Behl and Professor Peter McLoughlin for their continuous guidance, support, and in-depth expertise throughout this project. Undertaking a research project amid a global pandemic presented many challenges and the team's understanding, constructive recommendations and patience created a research environment where I felt continually motivated to express my ideas, be creative and bring my research to a higher standard.

I would also like to express my gratitude to the staff within the Pharmaceutical and Molecular Biotechnology Research Centre and the Department of Science at SETU, and our extended network of colleagues within the ORBITAL ITN network. Not only did they facilitate numerous, fantastic workshops and training opportunities, but their technical support and advice allowed me to both enhance and gain a number of analytical and transferrable skills.

A huge thank you is extended to my colleagues within the Ocular Therapeutics Research Group. Our chats and laughs over coffee, PhD memes and hilarious memories from our trips abroad were a great source of comfort during times of stress and panic. I would also like to give special thanks to my colleagues within the Department of Biomedical Engineering at Rowan University. Moving to New Jersey for three months was incredibly daunting but I came back to Ireland, not only with a variety of new analytical skills, but lifelong friendships and some incredible memories.

Lastly, I would like to express my most heartfelt appreciation for my incredible parents: Lorraine Casey Power and Tony Power, my brothers: Eamon and Daire Casey-Power, my beloved grandparents: Breda and Eamon Casey and Frances and Richard Power, my trusty research assistant: Bailey the Retriever-Doodle, and last, but certainly not least, my amazing fiancé: Liam Lanigan. Without you all, completing a PhD would not have been attainable and your endless love, support and advice mean more to me than you will ever know. I dedicate this thesis to you.

ABSTRACT

The decline in intracellular nicotinamide adenine dinucleotide (NAD+) is a critical risk factor for numerous neurodegenerative ocular diseases such as age-related macular degeneration, glaucoma, diabetic retinopathy, and dry eye. Such loss results in mitochondrial dysfunction, irreversible cellular damage and increased visual impairment. Ocular diseases are typically treated at the mid to late stages of their pathogeneses, which typically coincides with the development of debilitating visual conditions. As the eye itself contains numerous static and dynamic anatomical barriers, the efficacy of conventional ocular drug delivery systems (ODDs), such as eye drops and ointments, is limited by low therapeutic bioavailability at the target site, primarily attributed to poor ocular retention and intraocular clearance mechanisms. Such treatments are often administered frequently, presenting further challenges such as poor patient compliance and sporadic dosing, which can result in increased delocalised therapeutic absorption. Treatment options such as intravitreal injections offer enhanced bioavailability at the intraocular target site. However, continuous subjection to invasive surgical procedures poses the risk of adverse complications, such as vitritis, increased intraocular pressure, and retinal haemorrhaging . This research aims to develop and characterise a non-invasive nanomaterial formulation composed of polyelectrolyte biomaterials for the intraocular delivery of NAD+, as a means of upregulating cellular longevity and minimising deleterious ageing effects on ocular health.

NAD+-associated hyaluronic acid (HA) and poly(L-lysine) (PLL) polyelectrolyte complexes (PECs), and chitosan and NAD+ complexes (CH-NAD+) were formulated via polyelectrolyte complexation/ ionotropic gelation in aqueous medium. The biopolymers were chosen based on their inherent biocompatibility, tunable charge densities, mucoadhesive capabilities and biodegradation profiles. Critical evaluations of the physicochemical attributes of the formulations for suitability for ocular application were conducted, with formulations exhibiting optimal sizes, surface charges, and NAD+ association efficiencies (AE) being selected for further *in vitro* release and stability studies. Under microfluidic conditions, NAD+ is released in a sustained manner from the respective formulations over 24 hours, thus indicating their suitability as a depot for NAD+ ocular delivery on a once or twice-daily basis. Assessment of their physiochemical behaviour in solutions mimicking that of the ocular environment *in vivo* highlighted the susceptibility of the formulations to changes in environmental stimuli, confirming that the final form of the nanomaterials would be a governing factor of long-term formulation stability.*In vitro* and *ex vivo* safety and efficacy assessments using porcine ocular tissues and immortalised human corneal epithelial cells confirmed that the association of NAD+, particularly to the PECs, resulted in formulations with high cytocompatibility that could attenuate oxidative stress-mediated damage upon successful internalisation into the intracellular environment over 24 hours.

The screening of poly (lactic-co-glycolic acid (PLGA) and lipid-based nanoformulations, initially investigated as depots for the more targeted delivery of NAD+ to the posterior segment, highlighted the suitability of NAD+-laden liposomes for the intended application, primarily based on their physiochemical attributes. However, due to the high degree of variability observed in the *in vitro* release profile of this formulation under microfluidic conditions, this formulation will be subject to further investigations to improve the lipid later stability and NAD+ retention during release.

Ultimately, this research project details, for the first time, the development of an NAD+-laden nanoformulation for supplementary treatment of the ocular surface. Outcomes from this research provide justification to conduct future work on extensive *in vitro* efficacy trials to assess the ability of the formulations to prevent mitochondrial damage and promote cellular respiration, with more emphasis being placed on the pharmacokinetic and cellular internalisation mechanisms.

TABLE OF CONTENTS

DECLARATION i

ACKNOWLEDGEMENTS ii

ABSTRACT iii

TABLE OF CONTENTS iv

LIST OF FIGURES xiii

LIST OF TABLES xix

LIST OF ABBREVIATIONS xxi

CHAPTER 1: 1

INTRODUCTION 1

1. INTRODUCTION 2

1.1 Ocular Disease 2

1.1.1 Anatomy of the Eye 2

1.1.2 A Snapshot of Recent Global Trends in Ocular Disease 3

1.1.3 Ocular Disease Pathogeneses 6

1.1.3.1 Age-Related Macular Degeneration 6

1.1.3.2 Glaucoma 10

1.1.3.3 Diabetic Retinopathy 13

1.1.3.4 Dry Eye Disease 14

1.2 Ageing – The Protagonist of Ocular Disease 16

1.2.1 Oxidant Accumulation in Ageing Cells 17

1.2.1.1 Redox Homeostasis under Physiological Conditions 17

1.2.1.2 An Imbalance in Oxidant/Antioxidant Equilibrium 20

1.2.1.3 Antioxidant Supplementation in Ocular Cells 21

1.2.2 Intracellular Decline in Nicotinamide Adenine Dinucleotide (NAD+) Concentration . 22

1.2.2.1 Biosynthetic and Salvage Pathways of NAD+ 22

1.2.2.2 NAD+ Consumption and Mitochondrial Dysfunction 23
1.2.2.3 Cellular Restoration via NAD+ Supplementation in Ocular Disease 24
1.3 Barriers to Effective NAD+ Ocular Delivery 26
1.3.1 Conventional Routes of Administration 26
1.3.2 Primary Barriers to Effective Anterior Segment Delivery 28
1.3.2.1 Tear Film 29
1.3.2.2 Selective Inhibition by Corneal Layers 31
1.3.2.3 Barriers within the Conjunctival-Scleral Pathway 34
1.3.2.4 The Blood-Aqueous Barrier 36
1.3.3 Primary Barriers to Effective Posterior Segment Delivery 37
1.3.3.1 The Suprachoroid 37
1.3.3.2 Choriocapillaris and Bruch's Membrane 37
1.3.3.3 Melanin Binding 38
1.3.3.4 The Blood-Retinal Barriers 39
1.3.3.5 Vitreous Humour 39
1.4 Polyelectrolyte Complex Nanoparticles – Potential Candidates for NAD+ Ocular Delivery 40
1.4.1 Nanoparticle Characteristics for Ocular Drug Delivery 41
1.4.2 Pitfalls of Nanoparticle Preparation Methods 45
1.4.3 Polyelectrolyte Complexation - A Greener Approach 47
1.4.3.1 Polyelectrolyte Complex (PEC) Assembly Mechanism 48
1.4.3.2 Polysaccharide-Based PEC Systems 51
1.5 Research Project Goals and Scope 56
1.6 THESIS OUTLINE 57
CHAPTER 2: 58
OPTIMISATION OF CRITICAL FORMULATION ATTRIBUTES FOR POLYELECTROLYTE COMPLEX FORMATION 58

2. OPTIMISATION OF CRITICAL FORMULATION ATTRIBUTES FOR POLYELECTROLYTE COMPLEX FORMATION 59
2.1 Introduction 59
2.2 Experimental Methodology 62
2.2.1 Materials 62
2.2.2 Potentiometric Titration for Determination of Optimal Complexation pH 63
2.2.3 Preparation of Blank PLL Polyelectrolyte Complexes 63
2.2.4 Purification of Polyelectrolyte Complexes 64
2.2.4.1 Ultracentrifugation 64
2.2.4.2 Dialysis 65
2.2.4.3 Lyophilisation 65
2.2.5 Physicochemical Characterisation Methods 65
2.2.5.1 Fourier-Transform Infrared Spectroscopy (FT-IR) 65
2.2.5.2 Dynamic Light Scattering Analysis (DLS) 65
2.2.5.3 Percentage Transmittance Analysis (UV-Vis) 66
2.2.5.4 Isothermal Titration Calorimetry (ITC) 66
2.2.6 Statistical Analysis 67
2.3 Results & Discussion 68
2.3.1 Potentiometric Titrations for Complexation pH Determination 68
2.3.2 Optimisation of Polyelectrolyte Addition: Dropwise Titration or One-Shot Addition 70
2.3.3 Complexation Time 71
2.3.3.1 Dynamic Light Scattering Analysis 71
2.3.3.2 Fourier-Transform Infrared Spectroscopy (FT-IR) Analysis 73
2.3.4 Effect of Ultracentrifugation Speed on Complex Formation 75
2.3.5 Charge Ratio – A Critical Quality Attribute 77
2.3.5.1 Effect of Charge Ratio on Physicochemical Size Parameters 78

2.3.5.2 Loss of Turbidity with Decreasing Charge Ratio 81
2.3.6 Stoichiometry Analysis via Isothermal Titration Calorimetry 82
2.3.7 Effects of Lyophilisation on Complex Size 86
2.4 Conclusions 87
CHAPTER 3: 89
PREPARATION OF NAD+-ASSOCIATED PEC FORMULATIONS 89
3. PREPARATION OF NAD+-ASSOCIATED PEC FORMULATIONS 90
3.1 Introduction 90
3.2 Experimental Methodology 92
3.2.1 Materials 92
3.2.2 Preparation of NAD+-Associated HA and PLL Polyelectrolyte Complexes 93
3.2.3 Polyelectrolyte Complex Physicochemical Characterisation 93
3.2.3.1 Isothermal Titration Calorimetry (ITC) 93
3.2.3.2 DLS Analysis of Polyelectrolyte Complexes 94
3.2.3.3 Fourier-Transform Infrared Spectroscopy (FT-IR) 94
3.2.3.4 Scanning Electron Microscopy with Energy Dispersive X-Ray Spectroscopy (SEM-EDX) 94
3.2.3.5 NAD+ Chromatographic Conditions 95
3.2.3.6 Quantification of NAD+ Association Efficiency 96
3.2.3.7 NAD+ Stability in Sample Media 96
3.2.3.8 In Vitro NAD+ Release under Microfluidic Conditions 96
3.2.3.9 Kinetic Modelling of In Vitro NAD+ Release 98
3.2.3.10 Changes in PEC Stability in Response to Environmental Stimuli 99
3.2.3.11 Storage Stability of PECs 100
3.2.4 Statistical Analysis 101
3.3 Results & Discussion 101

3.3.1 NAD+-Polyelectrolyte Binding via ITC Analysis 101
3.3.2 Qualitative Analysis of NAD+ Association 103
3.3.2.1 Fourier-Transform Infrared Spectroscopy Analysis 103
3.3.2.2 Scanning Electron Microscopy with Energy Dispersive Spectroscopy 104
3.3.3 Quantification of NAD+ Association Efficiency 106
3.3.3.1 Validation of NAD+ HPLC Method 106
3.3.3.2 NAD+ Association Efficiency 108
3.3.4 Effect of Polyelectrolyte and NAD+ Loading Concentration on Size Parameters 112
3.3.5 Stability of PECs under Various Conditions 114
3.3.5.1 NAD+ Stability in Sample Media 114
3.3.5.2 PEC Matrix Stability in Response to Environmental Stimuli 116
3.3.5.3 PEC Stability under Storage Conditions 122
3.3.6 Dynamic *In Vitro* NAD+ Release 125
3.3.6.1 In Vitro NAD+ Release Profile 125
3.3.6.2 Mathematical Modelling of NAD+ Release Kinetics from PECs 128
3.5 Conclusions 129
CHAPTER 4: 132
PREPARATION OF CHITOSAN-NAD+ COMPLEXES 132
4. PREPARATION OF CHITOSAN-NAD+ COMPLEXES 133
4.1 Introduction 133
4.2 Experimental Methodology 134
4.2.1 Materials 134
4.2.2 CH-NAD+ Complex Preparation 135
4.2.3 Characterisation of the CH-NAD+ Complexes. 135
4.2.3.1 ITC Analysis of CH-NAD+ 135
4.2.3.2 CH-NAD+ Complex Stability as a Function of pH 136

4.2.3.3 Storage Stability of CH-NAD+ Formulations 136
4.2.4 Statistical Analysis 136
4.3 Results and Discussion 136
4.3.1 Screening of Chitosan-NAD+ Complexes 136
4.3.2 Association via Changes in Infrared Absorption Peaks 140
4.3.3 NAD+ Binding via Isothermal Titration Calorimetry 143
4.3.4 pH-Mediated Stability of Chitosan-NAD+ Complexes 145
4.3.5 Dynamic *In Vitro* NAD+ Release 148
4.3.5.1 In Vitro NAD+ Release 148
4.3.5.2 Mathematical Modelling of NAD+ Release Kinetics from PECs 150
4.3.6 Chitosan-NAD+ Complex Stability under Storage Conditions 151
4.4 Conclusions 154
CHAPTER 5: 156
IN VITRO SAFETY AND EFFICACY AND *EX VIVO* PERFORMANCE STUDIES ON COMPLEX FORMULATIONS 156
5. *IN VITRO* SAFETY AND EFFICACY AND *EX VIVO* PERFORMANCE STUDIES OF COMPLEX SYSTEMS 157
5.1 Introduction 157
5.2 Experimental Methodology 160
5.2.1 Materials 160
5.2.2 Mucoadhesion Analysis of PECs and Chitosan-NAD+ Complex Formulations 161
5.2.2.1 Quartz Crystal Microbalance with Dissipation (QCM-D) 161
5.2.2.2 Zeta Potential Analysis 161
5.2.3 *In Vitro* Cell Studies 162
5.2.3.1 Human Corneal Epithelial Cell Culture 162
5.2.3.2 In Vitro Cytotoxicity via Acid Phosphatase Assay 162
5.2.3.3 In Vitro Efficacy in an Oxidative Stress Model via Acid Phosphatase Assay 163

5.2.3.4 Quantification of NAD+ Cellular Uptake 164
5.2.3.5 Preparation of Fluorescent PECs and Chitosan-NAD+ Complex Formulations. 165
5.2.3.6 Qualitative Analysis of Cellular Uptake via Fluorescent Microscopy 165
5.2.4 *Ex Vivo* Studies using Porcine Corneal and Scleral Tissues 165
5.2.4.1 Tissue Dissection and Maintenance 165
5.2.4.2 Quantification of NAD+ Permeation 166
5.2.4.3 Visualisation of Complex Permeation via Fluorescence Microscopy 167
5.2.5 Statistical Analysis 167
5.3 Results and Discussion 168
5.3.1 Mucoadhesive Capabilities of Complex Formulations 168
5.3.2 Cytotoxic Assessment of NAD+ on Corneal Epithelial Cells 172
5.3.3 Analysis of Protective Effects of NAD+ in Response to Oxidative Stress 175
5.3.4 Complex Formulation Permeation via Fluorescence Microscopy 180
5.3.5 Quantification of NAD+ Cellular Uptake 183
5.3.6 Corneal vs. Scleral Permeation of Complex Formulations 186
5.4 Conclusions 192
CHAPTER 6: 195
PRELIMINARY TRIALS – NAD+-LADEN NANOFORMULATIONS FOR POSTERIOR SEGMENT DELIVERY 195
6. PRELIMINARY TRIALS – NAD+-LADEN NANOFORMULATIONS FOR POSTERIOR SEGMENT DELIVERY 196
6.1 Experimental Methodology 197
6.1.1 Materials 197
6.1.2 NAD+ Stability in Lipid Extraction Solvents 198
6.1.3 Preparation of NAD+-Laden PLGA Nanoparticles. 198
6.1.4 PEC Coating via Diethyl Ether Injection 200
6.1.5 PEC Coating via Mixing-Solvent Evaporation 201

6.1.6 Preparation of Liposomal Formulations via Thin Film Hydration 201
6.1.7 Physicochemical Characterisation of the PLGA- and Lipid-Based NAD+ Formulations 202
6.2 Results and Discussion 202
6.2.1 Discrepancy between Indirect and Direct NAD+ Encapsulation Efficiency in PLGA Nanoparticles 202
6.2.2 Selection of Lipid Extraction Solvent for NAD+ 208
6.2.3 PEC Coating with Lipid Material 209
6.2.4 NAD+-Laden Liposomes– Suitable Attributes but Irreproducible Release 211
6.3 CONCLUSIONS 215
CHAPTER 7: 217
FUTURE WORK AND CONCLUDING REMARKS 217
7. FUTURE WORK AND CONCLUDING REMARKS 218
7.1 FUTURE PERSPECTIVES 218
7.2 PROPOSED EXPERIMENTAL WORK 219
7.2.1 Addressing the Limitations of the Study 219
7.2.2 Soft X-Ray Microscopy for Complex Internalisation 220
7.2.2.1 Visualisation of Mitochondrial Dysfunction 220
7.2.2.2 Restoration of Mitochondrial Homeostasis Following Complex Uptake 221
7.2.3 Restoration of Basal Respiration via Seahorse Mito Stress Assay 221
7.2.4 Etheno-NAD+ Assay for Sirtuin Function Analysis 222
7.2.5 CD44 Receptor-Mediated Uptake of HA and PLL PECs 223
7.2.6 Investigation of Chitosan-Mediated Tight Junction Opening 223
RESEARCH DISSEMINATION 225
REFERENCES 227
APPENDIX I 301
SUPPLEMENTARY DATA 301

APPENDIX 1.1 QCM-D DATA 302
APPENDIX 1.2 *EX VIVO* PERMEATION – HPLC CHROMATOGRAMS 306
APPENDIX 2 308
RESEARCH DISSEMINATION 308
Appendix 2.1: REVIEW ARTICLE 309
Appendix 2.2: RESEARCH ARTICLE 349
Appendix 2.3: ARVO POSTER PRSENTATION 366

LIST OF FIGURES

Figure 1.1: A detailed, cross-sectional diagram of the human eye. (Figure generated using templates available on Servier Medical Art [3]). 2
Figure 1.2: Infographic map representing the percentage spread of AMD (a), glaucoma (b) and diabetic retinopathy (c) cases in people over 50 in each global region in 2020. (Infographic map created using data generated by the VLEG/GBD 2020 model and Adelson *et al.* [17]). 5
Figure 1.3: Schematic of the accumulation of drusen at the interface of the RPE layer and Bruch's membrane at the onset of atrophic AMD. (Figure generated using templates available on Servier Medical Art [3]) 7
Figure 1.4: Photo simulating the loss of peripheral vision in glaucoma patients in comparison to an individual with normal vision (a) (Picture sourced from National Eye Institute website [43]). Comparative schematic diagram of a glaucomic and healthy eye (b) (Picture insert sourced from All About Vision website [44]). 10
Figure 1.5: The migration of the electrons through the electron transport chain within the inner membrane of the mitochondria (Q = *ubiquinone and Cyt C = cytochrome C).* 18
Figure 1.6: The synthesis of NAD+ via the intracellular salvage pathway [102], [129]. 23
Figure 1.7: The various routes of ocular therapeutic administration [146]. 27
Figure 1.8: Schematic of the mucoaqueous layers of tear film (Figure generated using templates available on Biorender.com [164]. Information used to draw the resulting diagram was sourced from [144], [159], [163]) 30
Figure 1.9: The distinct layers of the cornea [153]. (Figure generated using templates available on Biorender.com [164]). 31
Figure 1.10: A schematic diagram of a typical migration pathway for drug molecules intended for transcorneal permeation. 33
Figure 1.11: Schematic of the conjunctival epithelial cell layer. 35
Figure 1.12: Confocal microscopy images of the migration of red fluorescent labelled PEI (a), HA (b) and HSA (c) nanoparticles within the retinal tissues 72 hours post-injection. (Blue – DAPI stained retinal cell nuclei [239].) 42
Figure 1.13: Confocal micrographs of ARPE-19 cells incubated for 4 hours with fluorescent-labelled uncoated HSA nanoparticles (a) and HA-coated HSA nanoparticles (b). ARPE-19 cells pre-incubated with HA for 1 hour prior to incubation with HA-coated HAS nanoparticles are shown in (c) [262]. .. 45
Figure 1.14: A double emulsion process that is typically used in nanoparticle formulations. 47

Figure 1.15: The potential, attribute-dependent, complex morphologies arising from the complexation of an anionic and cationic polyelectrolyte. 50
Figure 1.16: A schematic of the molecular structure of HA (a) and chitosan (b). The functional groups primarily involved in polyelectrolyte complexation are highlighted in green. 52
Figure 2.1: The initial formation of HA and PLL PECs, driven by Coulombs forces of attraction. (Blue anions – HA, green cations – PLL, red counterions – sodium cations, yellow counterions – chloride anions). 60
Figure 2.2: First derivative pH titration curves of (a) HA and (b) PLL. The fractional composition diagram, showing the percentage ionisation of each species at each pH value from pH 1 to pH 10, is shown in (c). (HA protonated fraction (COOH), – HA deprotonated fraction (COO^-), – PLL protonated fraction (NH_3^+), – PLL deprotonated fraction (NH_2)..... 69
Figure 2.3: Mechanism of PEC formation, beginning with instantaneous nucleation of primary PECs, followed by the formation of ordered, charge-stabilised secondary PEC structures. 73
Figure 2.4: Comparative FT-IR spectra of a HA and PLL PEC sample, withdrawn at 30 minutes and 24 hours. 74
Figure 2.5: (a) A photograph of the PEC formulations with the specified molar charge ratios. (b) The influence of charge ratio on the size and zeta potential (ZP) of the PEC formulations. Data is expressed as mean ± S.D (n = 3). 78
Figure 2.6: The electrical double layer surrounding a polyelectrolyte with residual surface charge in an ionic environment. 80
Figure 2.7: The change in % transmittance as a function of molar charge ratio at 500 nm. Data is expressed as mean ± S.D (n = 3). 81
Figure 2.8: Theoretical binding isotherms for both PLL vs. HA (a) and HA vs. PLL (b) ITC titrations upon optimisation of the sigmoidal factor value. (K_D – equilibrium dissociation constant, n – reaction stoichiometry, ΔH – change in enthalpy, ΔS – change in entropy). 83
Figure 3.1: A schematic of the potential interactions of NAD+ with the charged functional groups of both HA (blue) and PLL (red). 91
Figure 3.2: A schematic (a) and photograph (b) of the microfluidic release set-up. A close-up of the microfluidic device mould is shown in part (b). 97
Figure 3.3: Representative ITC binding isotherms obtained upon titration of PLL with NAD+ (a) and HA with NAD+ (b). 102
Figure 3.4: FT-IR spectra generated upon analysis of the individual starting materials and the HA:PLL PECs. (Resolution – 2 cm^{-1}). 103

Figure 3.5: Representative SEM micrographs of the PEC (a). Images were taken under the following conditions: Mixed image (backscattered and secondary electrons), 10 kV accelerating voltage, 6.5 mm x 2.00 k, scale – 20 μM). The correlogram (b) and the particle size distribution plot (c) of the sample are also shown for information purposes..... 105
Figure 3.6: EDX elemental spectrum profiles, generated using the SEM micrographs of F9 shown in Figure 3.5. 106
Figure 3.7: A schematic representing the proposed trends in AE values calculated for the F8, F9 and F10 formulations. 111
Figure 3.8: Size distribution plots of the F8 (a), F9 (b) and F10 (c) formulations, by intensity (after lyophilisation with 1% (w/w) trehalose). (n = 9 – 3 samples of each formulation with 3 runs each)..112
Figure 3.9: Representative HPLC chromatograms generated upon analysis of NAD+ at t_0 (blue) and after 168 hours post-incubation in 0.01 M PBS (pH 7.4) (red). 115
Figure 3.10: The change in size (a), ZP (b) and % NAD+ association (c) values for the NAD+ - associated PECs as a function of time in each of the sample media analysed. Data is expressed as mean ± S.D (n = 3). (* - statistically significant at a 5% confidence interval. Colour of the statistical significance bar: blue – between time points, green – between conditions and orange – from first to last time point). 119
Figure 3.11: Changes in size (a), zeta potential (b) and NAD+ concentration (c) upon storage of NAD+-associated PECs formulations at 4 and 25 °C over one month (Data is expressed as mean ± S.D (n = 3). 123
Figure 3.12: Cumulative *in vitro* NAD+ release profiles from the F9 formulation (circle) and an NAD+ bolus control (triangle) in 0.01 M PBS (pH 7.4) under microfluidic conditions. (Data is expressed as mean % Mt/Minf ± S.D (n = 3). 126
Figure 4.1: The size values recorded for chitosan and NAD+ complexes with 120 and 140% (w/w) of NAD+ after 24 hours, after lyophilisation and after lyophilisation with 1% (w/v) trehalose cryoprotectant. Data is expressed as the mean size ± S.D (n = 2)). 139
Figure 4.2: The FT-IR spectra of chitosan and NAD+. For comparative purposes, the FT-IR spectra of the chitosan-NAD+ complex with 120% (w/w) NAD+ are shown. (64 scans at a resolution of 2 cm^{-1}). 141
Figure 4.3: Schematic of the binding of TPP to chitosan (a) and NAD+ to chitosan (b) via phosphate-to-amine group electrostatic binding. The asymmetric stretching of the pyrophosphate bridge is represented in the 3D molecular structure of NAD+..... 142
Figure 4.4: The sequential titration of chitosan with NAD+ in ultrapure water at 25 °C (pH 4.5).... 143

Figure 4.5: The change in size and ZP following dispersal of the lyophilised CH-NAD+ complexes in ultrapure water at pH 7.4, as compared to those dispersed in ultrapure water at pH 4.5. Data is expressed as mean size/ZP ± S.D (n = 3). 145
Figure 4.6: Change in NAD+ association upon storage of CH-NAD+ complexes in ultrapure water at pH 4.5 and pH 7.4 for 4 hours. Data is expressed as mean residual NAD+ association ± S.D (n = 3). 147
Figure 4.7: Cumulative *in vitro* NAD+ release profiles from the 120% (w/w) (large, dashed diamonds) and 140% (w/w) (small, dashed circles) CH-NAD+ complexes in 0.01 M PBS (pH 7.4) under microfluidic conditions over 36 hours. The PECs (circles) and NAD+ bolus control (triangles) are shown for comparative purposes. (Data is expressed as mean % Mt/Minf ± S.D (n = 3). 149
Figure 4.8: A plot of the log of cumulative NAD+ release vs. the log of time, in minutes, showing a high correlation to the Korsmeyer-Peppas mathematical model. Data is expressed as mean log(% cumulative release) ± S.D (n = 3)..... 150
Figure 4.9: Changes size (a), zeta potential (b) and NAD+ concentration (c) upon storage of CH-NAD+ complexes at 4 (dark blue – 120% (w/w), light blue (140% (w/w)) and 25 °C (dark orange – 120% (w/w), light orange (140% (w/w)) over one month (Data is expressed as mean ± S.D (n = 3). 153
Figure 5.1: Diagram showing (a) the incision point (red) on the porcine cornea and (b) the resulting tissue segments following surgical removal. 166
Figure 5.2: Changes in ZP observed upon incubation of the individual reagents, PECs, and chitosan-NAD+ formulations with porcine mucin (Type II) for 2 hours at 37°C. (**Dark blue** – without mucin, **light blue** – with mucin). Data is expressed as mean zeta potential ± S.D. (n = 3). (Green * - statistically different from mucin alone)..... 171
Figure 5.3: Cell viabilities of IMHCE cells with each NAD+ concentration/NAD+ complex for 24 hours at 37°C under 5% CO_2. (Dark blue – NAD+ control, yellow – blank PECs, orange – blank CH-NAD+ (120% (w/w)), grey – blank CH-NAD+ (140% (w/w)), green – NAD+-associated PECs, red – CH-NAD+ (120% (w/w)), purple – CH-NAD+ (140% (w/w)). Data is expressed as mean % cell viability ± S.D (n = 3). (* = statistically significant difference between cell viability of the sample and that of the control (100 ± 3.7%) at a 5% confidence interval). (The cell viability categories are shown on the graph). 172
Figure 5.4: Percentage cell viabilities upon incubation of IMHCE cells with varying concentrations of H_2O_2 (200 to 1200 µM) (a) and H_2O_2 concentrations of 400, 800, and 1200 µM + NAD+ concentrations of 20 µM to 200 µM for 24 hours (b). * - significant difference between a sample and an H_2O_2-treated sample..... 176

Figure 5.5: Percentage cell viabilities upon incubation of IMHCE cells with 20 µM and 200 µM NAD+/NAD+-associated formulations over set supplementation times before exposure to 200 µM of H_2O_2 for 24 hours. * - significant difference between a sample and H_2O_2-treated sample, □ - significant difference between NAD+ alone and NAD+-associated formulation, * (with bridge) - significant difference between supplementation timepoint. (Data is expressed as mean % cell viability ± S.D (n = 3)..... 177
Figure 5.6: Morphology of IMHCE cells incubated with culture media (a), 20 µM NAD+ (b), 200 µM NAD+ (c), and 200 µM H_2O_2 (d). (Magnification – 20x). 178
Figure 5.7: Fluorescent microscopy images of FITC-PECs (0.1% (w/v) FITC) (a), FITC-CH-NAD+ (120% (w/w)) (b), FITC-CH-NAD+ (140% (w/w)) (c), a 0.1% (w/v) FITC solution (d), and negative control (incubation with 0.01 M PBS (pH 7.4)) (e), taken after incubation of porcine corneal tissues at 37 °C for 6 hours. (20 x magnification with scale – 50 µm) (Representative images of n = 3)..... 181
Figure 5.8: Fluorescent microscopy images of FITC-PECs (a), FITC-CH-NAD+ (120% (w/w)) (b), FITC-CH-NAD+ (140% (w/w)) (c), and FITC solution of equivalent concentration to that of the formulations (d) taken after incubation of IMHCE cells at 37 °C for 24 hours. (40 x magnification with scale – 20 µm – SAMPLES, 20 x magnification with scale – 50 µm -CONTROL) (Representative images of n = 3)..... 182
Figure 5.9: Representative HPLC chromatogram of cell lysate isolated from control IMHCE cells incubated with corneal epithelial culture medium alone for 24 hours. The peak representing typical NAD+ elution, as shown in the insert, is not present. 184
Figure 5.10: Representative HPLC chromatogram of cell lysate isolated from IMHCE cells incubated with CH-NAD+ (140% (w/w)) for 24 hours. The NAD+ peak at 260 nm is not present (4 minutes). 186
Figure 5.11: Cumulative mass of NAD+ permeated from NAD+ alone and NAD+-associated PECs per cm^2 of excised porcine corneal and scleral tissue isolates. Data is expressed as mean ± S.D (n = 3). 187
Figure 5.12: Representative HPLC chromatogram taken from the receptor chambers of the porcine cornea (a) following incubation with NAD+/NAD+-associated PECs. The donor chambers from the corneal sample (b) show preservation of the NAD+ peak at 4 minutes. 192
Figure 6.1: Schematic of the preparation and purification of NAD+-laden PLGA nanoparticles via ultracentrifugation. (Figure generated using templates available on Biorender.com). 200
Figure 6.2: The HPLC chromatogram generated for NAD+ in 1% (w/v) Triton™ X-100 in (a) 95:5 (deionised water:methanol) and (b) 50:50 (deionised water:methanol) extraction solvent. 209
Figure 6.3: The cholesterol (a) and lecithin (b)-coated PEC formulations prepared via mixing-solvent evaporation. 210

Figure 7.1: A reduction in ZO-1 fluorescence observed in human corneal epithelial cells after pre-incubation with CCH for 2 hours [640]..... 224

LIST OF TABLES

Table 1.1: A description of the more commonly used anti-VEGF therapeutics, administered via intravitreal injection (IVI), in the treatment of neovascular AMD [25], [27]–[30]. 8
Table 1.2: A description of the commonly used therapeutics in the treatment of IOP hypertension and glaucoma [30]. 12
Table 2.1: The formulation parameters of the PEC formulations (F1-F7). 64
Table 2.2: Optimised experimental parameters utilised for ITC titrations of PLL (titrant syringe) vs. HA (sample cell) and HA (sample cell) vs. HA (titrant syringe). 67
Table 2.3: The physicochemical size parameters obtained upon analysis of a reference PEC (HA:PLL mass ratio of 1:1) at set time points between 30 minutes and 24 hours. Data is expressed as the mean size or polydispersity index (PDI) ± S.D (n = 2). 72
Table 2.4: The characteristic IR absorption bands identified from the FT-IR spectra of both HA and PLL. 73
Table 2.5: Thermodynamic properties obtained upon fitting the ITC titration data from the PLL vs. HA titration to the independent site-binding model. Data is expressed as mean ± S.D (n = 3). The titration PLL with HA was conducted as a screening study (n = 1) to highlight changes in binding stoichiometry when the low MW polyelectrolyte is in excess. 83
Table 2.6: Thermodynamic properties obtained upon fitting the ITC titration data from the PLL vs. HA titrations, conducted in 0.01 M PBS (pH 5.5) to the independent site-binding model. 85
Table 3.1: The formulation parameters of the formulations (F8-F10) referenced throughout the chapter. 93
Table 3.2: Optimised experimental parameters utilised for ITC titrations of NAD+ (titrant syringe) vs. HA (sample cell) and NAD+ (titrant syringe) vs. PLL (sample cell). 94
Table 3.3: The correlation coefficient (R^2), limit of detection (LOD) and limit of quantification (LOQ) values generated upon analysis of twelve NAD+ analytical standard solutions using the Agilent 1200 HPLC system. Intra-assay precision is also represented by the coefficient of variation (CV) values obtained for each analytical standard. Data is expressed as mean ± S.D (conducted in duplicate). ... 107
Table 3.4: The extraction of NAD+ from the F8 formulation using various extraction solvent systems. 108
Table 3.5: The quantification of NAD+ AE and loading capacities (LC) in the F8 to F10 PECs. Data is expressed as mean % ± S.D (n = 3). 110

Table 3.6: Percentage NAD+ recoveries in each sample medium over a weeklong period. Data is expressed as mean % recovery ± S.D (n = 3). 115
Table 3.7: The mean percentage transmittance (%T) values of the F9 stability solutions in 0.01 M PBS buffer, compared to that of the control F9 solution diluted with ultrapure water at pH 5.5. Data is expressed as % mean transmittance at 500 nm ± S.D (n = 3). 118
Table 3.8: Kinetic analysis of NAD+ release from the F9 formulation using various mathematic models. 128
Table 4.1 Formulation parameters of the CH:NAD+ formulations prepared. 135
Table 4.2: The size, zeta potential (ZP) and polydispersity index (PDI) values recorded for crude CH-NAD+ complexes ranging from 20 to 180% (w/w) of NAD+. 137
Table 4.3: Percentage association efficiencies (AE) (indirect and direct) recorded for CH-NAD+ complexes with 120 to 140% (w/w) NAD+. Data is expressed as mean ± S.D (n = 6). 139
Table 5.1 Order of addition of each sample/media analysed via QCM-D. 161
Table 5.2: Details of the *in vitro* efficacy studies conducted on IMHCE cells via an acid phosphatase assay (APA). 163
Table 5.3: Changes in Δf and ΔD recorded upon deposition of the individual reagent/ formulations onto the respective quartz sensors at the 5th overtone. 169
Table 5.4: Quantification of both NAD+ internalisation in IMHCE cells and retention in cell culture media following 24-hour incubation. Data is expressed as mean ± S.D (n = 3). (LOD – 4.76 µM)... 185
Table 5.5: Mass balance analysis of NAD+ quantified at each step during ex vivo corneal and scleral permeation and retention analysis. Data is expressed as mean ± S.D (n = 3). 189
Table 6.1: Mass balance and %EE values obtained upon analysis of the lyophilisates (pellets and supernatants) isolated during centrifugation of the NAD+-PLGA nanoparticles..... 203
Table 6.2: Particle sizes of NAD+-PLGA nanoparticles prepared with various emulsifier stabilising agents. Data is expressed as mean size ± S.D (n=3). 207
Table 6.3: Physicochemical attributes of LPHNP formulations prepared via diethyl ether injection. Data is expressed as mean ± S.D (n=3). 210
Table 6.4: Summary of the physicochemical attributes of the PEC-Lipo and NAD+-Lipo formulations investigated. Data is expressed as mean ± S.D (n = 3)..... 212

LIST OF ABBREVIATIONS

%EE	Encapsulation efficiency
AA	Ascorbic acid
ACG	Angle-closure glaucoma
AE	Association efficiency
AH	Aqueous humour
AMD	Age-related macular degeneration
ANOVA	One-way analysis of variance
APA	Acid phosphatase assay
AQ1:O	Inner aqueous:organic ratio
AR-14034	Axitinib
ARPE-19	Spontaneously arising retinal pigment epithelium cells
AT	Artificial tears
ATP	Dianionic adenosine 5′-triphosphate
AUC	Area under the curve
BAB	Blood aqueous barrier
CCH	Chitosan conjugate eye drop formulation
CCK-8	Cell counting kit-8
CD	Cyclodextrin
CD38	ADP-ribosyl cyclase
CH-NAD+	Chitosan and NAD+ complexes
CO_2	Carbon dioxide
CV	Coefficient of variation
Da	Dalton

DAPI	2-(4-amidinophenyl)-1H-indole-6-carboxamide
DCM	Dichloromethane
DDI	Double-distilled
DDS	Drug delivery systems
DH	Dehydroascorbate
DLS	Dynamic light scattering
DLVO	Derjaguin, Landau, Verwey and Overbeek
DMSO	Dimethyl sulfoxide
DNA	Deoxyribonucleic acid
DR	Diabetic retinopathy
EDC	1-ethyl-3-(3-dimethylaminopropyl) carbodiimide
EDL	Electrical double layer
EDTA	Ethylenediaminetetraacetic acid
EGCG	Epigallocatechin-3-gallate
EpiCGS	Epithelial cell growth supplement
EPR	Enhanced permeation and retention
$FADH_2$	Flavin adenine dinucleotide
FBS	Fetal bovine serum
FCCP	Phenylhydrazone
FITC	Fluorescein isothiocyanate
FT-IR	Fourier transform-infrared spectroscopy
GC	Gas chromatography
GPx	Glutathione peroxidase
GRx	Glutathione reductase

GSH	Reduced glutathione
H_2O_2	Hydrogen peroxide
HA	Hyaluronic acid
HCECs	Human corneal epithelial cells
HCl	Hydrochloric acid
HEPES	4-(2-hydroxyethyl)-1-piperazineethanesulfonic acid
HIF-1	Hypoxia-induced factor – 1
HMWHA	High molecular weight hyaluronic acid
HPLC	High-performance liquid chromatography
HSA	Human serum albumin
IBRB	Inner blood-retinal barrier
IMHCE	Immortalised human corneal epithelial cells
IOP	Intraocular pressure
ITC	Isothermal titration calorimetry
IVI	Intravitreal injection
KCl	Potassium chloride
K_D	Equilibrium dissociation constants
kDa	Kilodalton
KH_2PO_4	Potassium dihydrogen phosphate
LAC	Linear absorption coefficient
LC	Loading capacity
LMWHA	Low molecular weight hyaluronic acid
LOD	Limit of detection
LOQ	Limit of quantification

LPHNP	Lipid-PEC hybrid nanoparticles
MAPK	Mitogen-activated protein kinase
MSVI	Moderate/severe visual impairment
MTT	3-(4,5-dimethylthiazol-2-yl)-2,5-diphenyltetrazolium bromide
MW	Molecular weight
MWCO	Molecular weight cut-off
Na_2HPO_4	Disodium hydrogen phosphate
NaCl	Sodium chloride
NAD+	Nicotinamide adenine dinucleotide
NADH	Nicotinamide adenine dinucleotide (reduced)
NAD+-Lipo	NAD+-laden liposomes
NAD+-PLGA	NAD+-laden PLGA
NAM	Nicotinamide
NAMPT	Nicotinamide phosphoribosyltransferase
NaOH	Sodium hydroxide
NHS	*N*-hydroxysuccinimide
NMN	Nicotinamide mononucleotide
NMNAT	Nicotinamide mononucleotide adenylyltransferase
NR	Nicotinamide riboside
Nrf2	Nuclear factor erythroid-related factor 2
OA	Oleic acid
OAG	Open-angle glaucoma
OBRB	Outer blood-retinal barrier
OCR	Oxygen consumption rate

ODDS	Ocular drug delivery systems
PAA	Polyacrylic acid
PARP-1	Poly (ADP- ribose) polymerase 1
PBS	Phosphate buffer saline
PDADMAC	Poly(diallyldimethylammonium chloride
PDI	Polydispersity index
PDS	Port delivery system
PEC	Polyelectrolyte complexes
PEI	Polyethylenemine
PHCECs	Primary human corneal epithelial cells
PLL	poly(L-lysine)
PLGA	Poly (lactic-co-glycolic acid)
PNPP	*Para*-nitrophenylphosphate
PTM	Pentamidine
PVA	Poly(vinyl) alcohol
QCM-D	Quartz crystal microbalance with dissipation
RGC	Retinal ganglion cells
ROS	Reactive oxygen species
RPE	Retinal pigment epithelium
RP-HPLC	Reverse-phase HPLC
SASPs	Senescence-associated secretory phenotypes
SEM-EDX	Scanning electron microscopy with energy-dispersive X-ray spectroscopy
siRNA	Small interfering RNA
SIRTs	Sirtuins

SQSTM-1	Sequestosome-1
SXM	Soft x-ray microscopy
TFH	Thin-film hydration
TM	Timolol maleate
TNF- α	Tumour necrosis factor α
TPP	Tripolyphosphate
UV-Vis	Ultraviolet-visible
VEGF	Vascular endothelial growth factor
ZO-1	Zona occludens
ZP	Zeta potential
ΛD	Debye length

CHAPTER 1:

INTRODUCTION

1. INTRODUCTION

1.1 OCULAR DISEASE

1.1.1 Anatomy of the Eye

The eye is a globular, sensory organ that transmits light from our external surroundings, in the form of electrical impulses, to the brain. Rod and cone photoreceptors within the neural retina initiate the transduction of the photons of light into signalling neurotransmitters [1]. The optic nerve transfers the electrical impulses to the occipital lobe. Located in the cerebrum cortex, the occipital lobe converts such stimuli into an image [2]. Under physiological conditions, this process results in sharp, clear vision. As shown in Figure 1.1, the eye can be divided into two sections, the anterior segment, and the posterior segment.

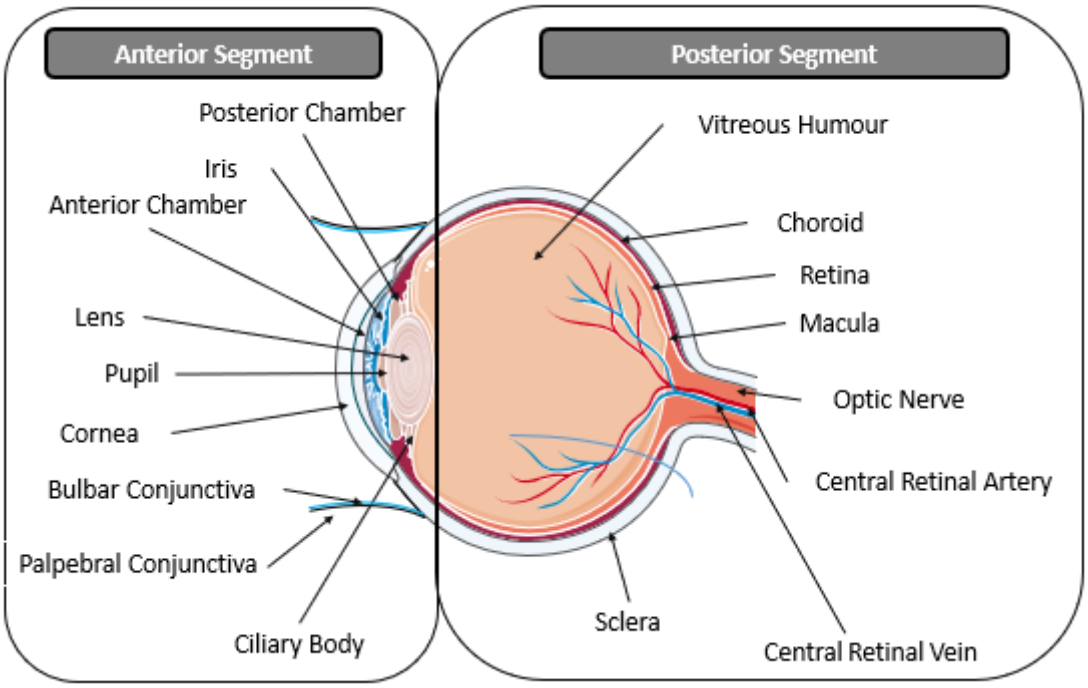

Figure 1.1: A detailed, cross-sectional diagram of the human eye. (Figure generated using templates available on Servier Medical Art [3]).

The anterior segment comprises the cornea, iris, lens, and ciliary body. Aqueous humour (AH), a thin, clear fluid, is secreted from the ciliary epithelium within the ciliary body and flows out

of the anterior chamber via both the trabecular and uveoscleral pathways. The continuous outflow of AH at a rate of approximately 600 µL/min into venous blood circulation exerts an intraocular pressure of approximately 21 mmHg. This allows for both the maintenance and removal of excretory cellular debris and a consistent supply of nutrients to the anterior avascular tissues [4]. The posterior segment encompasses the choroid, retina, Bruch's membrane, the optic nerve, and retinal vasculature. Vitreous humour, a clear gelatinous fluid consisting of approximately 99% water, is contained within the vitreous cavity between the segments [5], [6]. In contrast to aqueous humour, vitreous humour cannot flow nor be replenished. The remaining 1% is comprised of a complex mesh network of collagen Type II fibrils, interwoven with hyaluronic acid chains and structural proteins, such as fibrillin and opticin, exhibiting average pore sizes of 550 nm [7]–[10]. Hyaluronic acid, however, is not uniformly distributed throughout the vitreous humour. Higher concentrations of hyaluronic acid tend to accumulate within the posterior segment (1200 µg/cm^3) thus establishing a concentration gradient that results in lower concentrations accumulating towards the anterior region of the vitreous humour (250 µg/cm^3). Its primary function is the attainment of both sufficient intraocular pressure on the retina and the overall spherical shape of the eye.

1.1.2 A Snapshot of Recent Global Trends in Ocular Disease

According to the latest World Health Organisation data related to the prevalence of moderate/severe visual impairment (MSVI) and blindness in the global population, 2.2 billion people worldwide have some form of visual impairment. Of these 2.2 billion, approximately 1 billion are suffering from a visual impairment that is either preventable or is yet to be addressed [11]. A study conducted by the International Agency for the Prevention of Blindness estimated that over 295 million people were suffering from an MSVI in 2020. [12]. A further 43 million people are estimated to be completely blind. This equates to a 19.4% and 35.9% increase in blindness and MSVI cases, respectively, since 2015 [13].

Ageing is the primary risk factor of MSVI, with the increase in MSVI cases directly correlating to an increase in longevity of the global population [14]. By 2050, the global population of people over the age of 60 is projected to reach approximately 2.1 billion [14], [15]. As such, a concurrent, exponential increase in MSVI cases is also expected. In accordance with the data

collected by Fighting Blindness in 2022, approximately 272,000 people are either blind or visually impaired in Ireland [16]. On a global scale, by 2050, it is estimated that over 474 million people will be suffering from some form of MSVI, a percentage increase of almost 60.5% from 2020 [15].

With an increase in longevity comes a corresponding increase in the prevalence of ocular disease, due to the progressive decline in physiological homeostasis. However, ocular disease pathogeneses are also greatly influenced by lifestyle, diet, and environmental conditions. Therefore, it has also been predicted that ocular disease will become increasingly prevalent in developed countries worldwide. As an example of this, the global prevalence of age-related macular degeneration (AMD), glaucoma and diabetic retinopathy, specifically, is further illustrated in Figure 1.2.

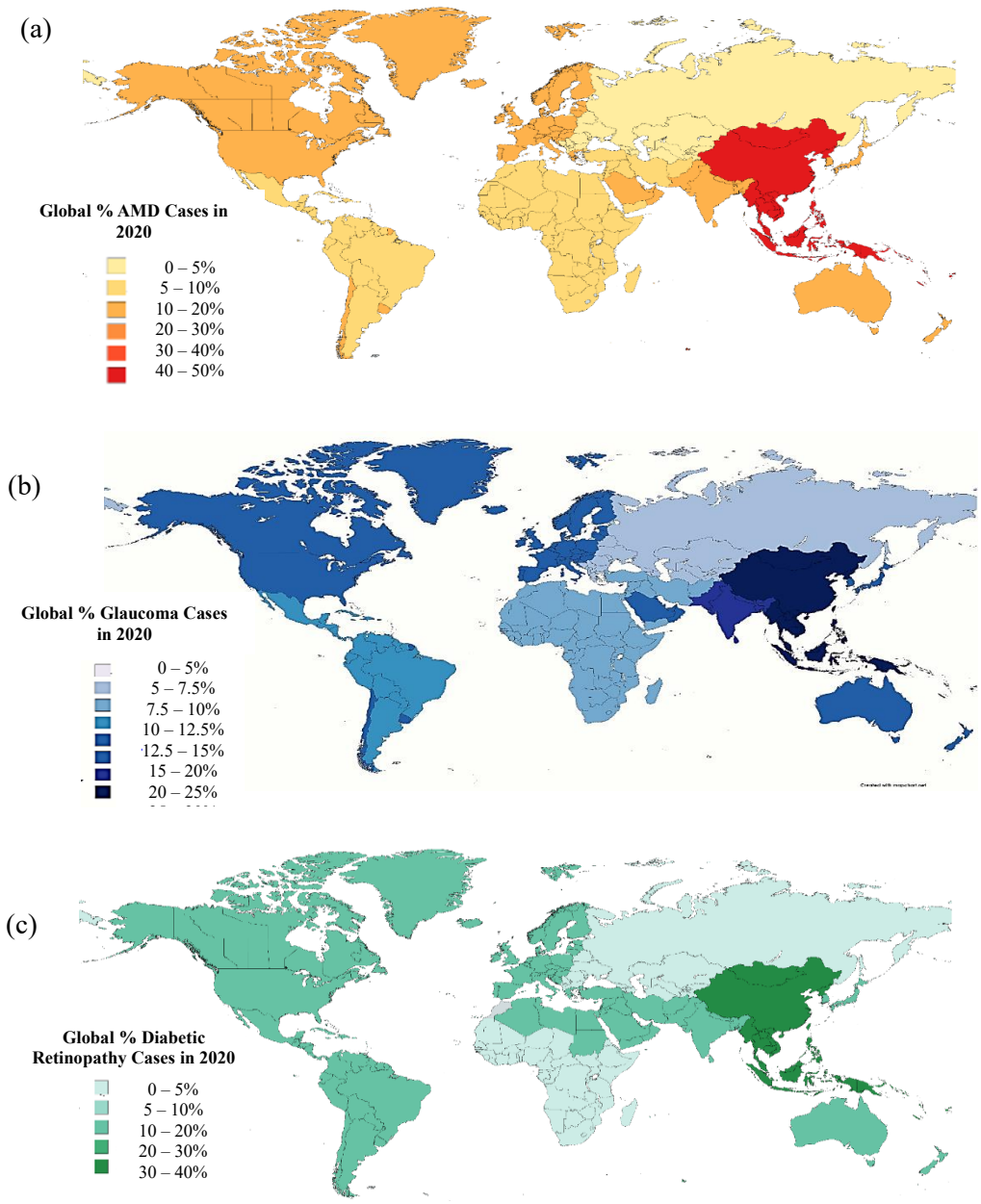

Figure 1.2: Infographic map representing the percentage spread of AMD (a), glaucoma (b) and diabetic retinopathy (c) cases in people over 50 in each global region in 2020. (Infographic map created using data generated by the VLEG/GBD 2020 model and Adelson *et al.* [17]).

1.1.3 Ocular Disease Pathogeneses

The most common examples of uncorrected refractive errors are myopia and hyperopia, typically referred to as short-sightedness and far-sightedness, respectively [18]. Cataracts occur as a result of the degeneration and aggregation of zonular fibres within the lens. Normally, the zonular fibres contract and relax, altering both the curvature and focal length of the lens, to allow us to focus on objects at varying distances. Degeneration of such fibres results in the opacification of small areas on the lens surface [19]. For the purpose of this literature review, AMD, glaucoma, diabetic retinopathy, and dry eye will be discussed in further detail. These diseases are among the primary causes of MSVI worldwide [20]. Although typically not associated with severe visual impairment, dry eye disease will also be discussed as its associated symptoms can significantly impact the quality of life of those who suffer from it.

Treatments for the aforementioned diseases vary in terms of their site of administration and administration method. Due to the complexity of their pathogenesis and the anatomy of the ocular sites that they affect, the efficacy of the currently available treatment options for such diseases is limited. Treatments are often administered over a long period of time to attain adequate treatment efficacy, which can prove problematic in terms of both patient compliance and discomfort. Also, the majority of the treatment options that guarantee the delivery of a high concentration of therapeutic to a specific ocular tissue are often invasive. Several surgical procedures are required throughout the treatment duration. Conversely, although safer, the bioavailability of therapeutics administered by the patient using non-invasive methods is severely limited. Therefore, the development of novel, targeted, yet user-friendly treatment methods is greatly sought after and has become one of the primary focuses of current ocular therapeutics research.

1.1.3.1 Age-Related Macular Degeneration

Age-related macular degeneration (AMD) is the predominant cause of both MSVI and vision loss in the ageing population, with over 8 million reported cases in people over 50 worldwide in 2020 [21], [22].

AMD is characterised by localised dysfunction of the macula, a highly pigmented region within the centre of the retina that is densely packed with both cone sensory neurons and ganglion cells, in response to the multifactorial interaction between metabolic, genetic, and environmental factors [4]. The pathogenesis of AMD can be broadly divided into two forms: atrophic and neovascular AMD. Atrophic, or dry, AMD is the most prevalent form of AMD, accounting for approximately 90% of all reported AMD cases. However, no viable treatment for atrophic AMD currently exists, primarily because its precise pathophysiologic progression is difficult to interpret [23]. As shown in Figure 1.3, atrophic AMD is characterised by the accumulation of drusen, a brown/yellow, degradation-resistant metabolite of lipid peroxidation, at the interface of the RPE monolayer and Bruch's membrane, the basement membrane separating the RPE cell layer and choroidal vasculature [23].

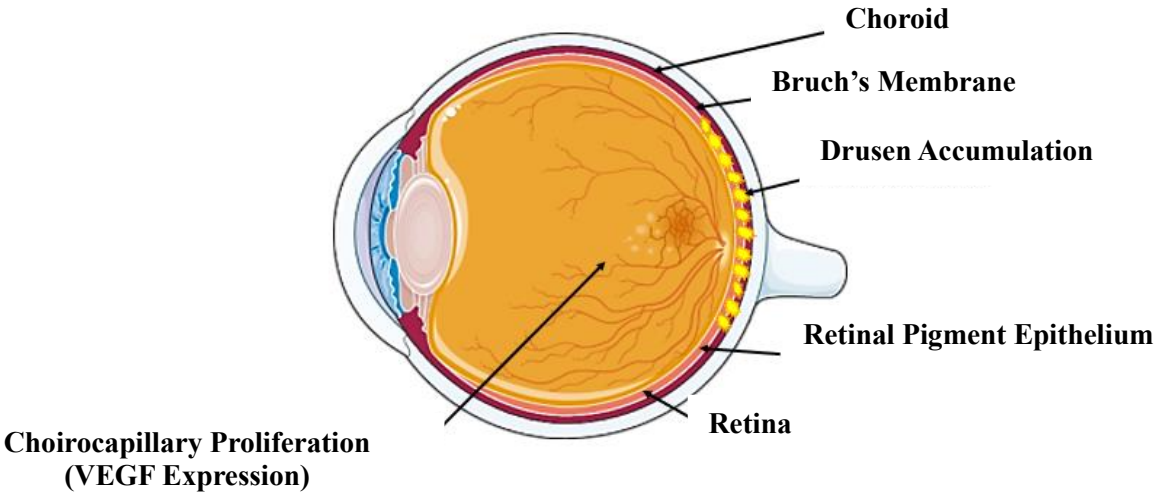

Figure 1.3: Schematic of the accumulation of drusen at the interface of the RPE layer and Bruch's membrane at the onset of atrophic AMD. (Figure generated using templates available on Servier Medical Art [3]).

With age, lipoproteins, typically degraded via lysosome activity within the RPE, begin to accumulate within Bruch's membrane. In an aged retina, the rate of reactive oxygen species (ROS) formation can easily exceed the antioxidant capabilities of the eye, due to both the high metabolic demands of the RPE, and the photo-oxidative stress from sunlight and environmental factors [24]. ROS induce the peroxidation of the accumulated lipoproteins and begin to generate highly reactive, oxidised lipoproteins. These lipoproteins can accumulate within lysosomes and

hinder degradation activity or react with neutral molecules to induce a pro-inflammatory immune response. Proinflammatory mediators enhance inflammation by increasing blood flow to the inflamed area via vasodilation and activate proinflammatory signalling cascades [25]. This ultimately results in the dysfunction and atrophy of the RPE.

The atrophic form of AMD often develops into neovascular AMD. Due to its fragility, Bruch's membrane can be easily, and often irreversibly, damaged by choroidal neovascularisation [1]. Inflammation and disruptions in retinal blood flow dysregulate retinal cell metabolism. The metabolic activity of the cells increases, thus also increasing oxygen consumption. This metabolic stress can induce hypoxia-inducible factor 1 (HIF-1), which in turn, induces excessive vascular endothelial growth factor (VEGF) expression, predominantly within the inner neural layer and ganglion cell layer of the retina [24]. VEGF binds to VEGFR-1 and VEGFR-2 receptor sites on the RPE cells and subsequently activates the signalling pathway for choroidal neovascularisation. These fragile choriocapillaries proliferate through the neural retina and are highly susceptible to leakage and haemorrhaging, which results in loss of clear vision and, in severe cases, retinal detachment [26]. As shown in Table 1.1, neovascular AMD is currently treated via the intravitreal administration of VEGF inhibitors, designed to inhibit the excessive expression of VEGF molecules responsible for choroidal neovascularisation under pathological conditions.

Table 1.1: A description of the more commonly used anti-VEGF therapeutics, administered via intravitreal injection (IVI), in the treatment of neovascular AMD [25], [27]–[30].

Therapeutic/ Commercial Brand Name	Company	Typical Dosage Concentration	Mode of Action
Ranibizumab Lucentis®	Genentech, a subsidiary of Roche	A single dose of 0.05 mL of a 10 mg/mL suspension	Inhibition of the binding of VEGF-A to its complimentary VEGF receptors on RPE cells.
Bevacizumab Avastin®	Roche	"Off-label" use for chorioretinal vascular diseases. Typically administered via a single injection of 0.05 mL Avastin ® solution.	Inhibition of the binding of all isoforms of VEGF-A to the target receptors.

		(Solution contains 25 mg/mL of bevacizumab).	
Aflibercept Eylea®	Bayer/ Regeneron	2 mg administered every 4 weeks for the first three injections. Followed by the administration of 2 mg every 8 weeks.	Dual inhibition of VEGF-A and VEGF-B binding. The affinity for VEGF-A binding is 94 and 120 times stronger than ranibizumab and bevacizumab, respectively.
Brolucizumab Beovu®	Novartis	6 mg administered once a month for three months. Followed by administration of 6 mg every 8 to 12 weeks.	Inhibition of all VEGF-A isoform binding

The AMD global therapeutic market is set to increase significantly within the next decade, reaching 18.7 billion dollars in 2028, an increase of 10.1 billion dollars from the 2018 market value [31]. Sustained anti-angiogenic therapeutic release is predicted to be of pivotal focus, primarily due to the increased financial burden and invasive nature of IVI treatments. Such therapies will significantly reduce the frequency of intravitreal administration [32]. A ranibizumab-laden, permanent, refillable port delivery system (PDS), developed by Roche/Genentech, has proven effective in increasing the best-corrected visual acuity score in patients with neovascular AMD during a Phase III clinical study [33]. Furthermore, the PDS implant, laden with 100 mg/mL of ranibizumab with fixed refills every 24 weeks, exhibited comparable efficacy to the monthly injections of 0.5 mg/mL ranibizumab over a two-year period. Aerie Pharmaceuticals has developed a bioerodible implant for the sustained release of axitinib (AR-14034) for neovascular AMD and diabetic macular edema treatment. Preclinical studies, conducted using *in vivo* rabbit and porcine models, highlighted the efficacy of the implant, loaded with various axitinib dosages, in significantly reducing retinal vessel leakage over 12 months [34]. Phase I and Phase II safety and efficacy clinical trials began on the 6th of December 2023, with an estimated completion date of May 2025 [35]. Two therapeutics are currently in the pipeline for atrophic AMD in the next decade [36]. A 0.1% topical formulation of MC-1101, a vasodilator therapeutic, is set to launch in the US by the end of 2028. It exhibited sufficient efficacy in enhancing choroidal blood flow in a Phase II/III safety and efficacy clinical study held in 2014. [37], [38]. However, this study was due for completion in 2016 and there has been no recent report of the findings. Ethamsylate, a fibroblast growth inhibitor, is

currently under development by Dobecure as a treatment for both atrophic and neovascular AMD and is set to launch in Germany, Spain, France, Italy, and the United Kingdom in the next decade [36].

1.1.3.2 Glaucoma

Glaucoma is the fourth highest cause of vision loss worldwide, equating to approximately 4 million of the 206 million reported cases of MSVI worldwide in people over 50 [39]. Glaucoma is caused by the accumulation of an excess volume of aqueous humour within the anterior chamber. Excessive production of aqueous humour, or a decrease in the outflow rate of aqueous humour from the anterior chamber results in an increase in the intraocular pressure (IOP) exerted on the optic nerve [40]. An IOP of more than 22 mmHg is said to be elevated [41]. However, IOP levels of up to 40 mmHg have been reported [42]. As illustrated in Figure 1.4, subjection to such persistent intraocular strain for long periods can irreversibly damage the optic nerve.

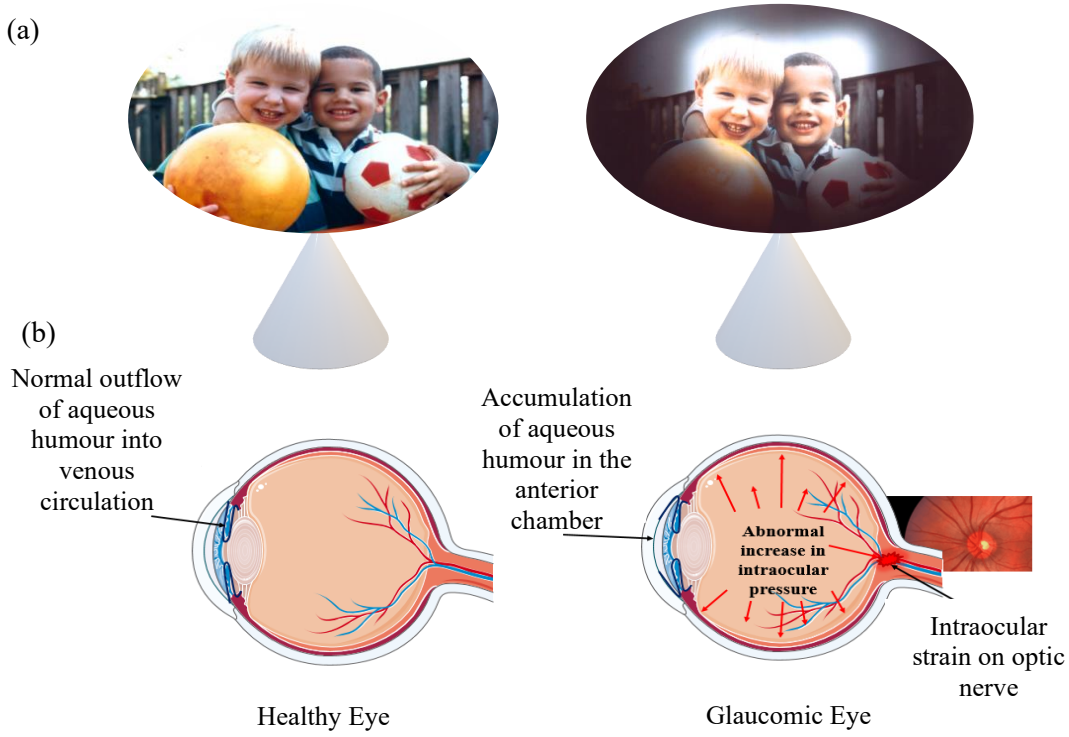

Figure 1.4: Photo simulating the loss of peripheral vision in glaucoma patients in comparison to an individual with normal vision (a) (Picture sourced from National Eye Institute website

[43]). Comparative schematic diagram of a glaucomic and healthy eye (b) (Picture insert sourced from All About Vision website [44]).

Although there are over several types of glaucoma, there are two widely known forms: angle-closure glaucoma (ACG) and open-angle glaucoma (OAG) [45]. ACG is characterised by the blockage of the canal of Schlemm, a drainage canal that transports aqueous humour to venous circulation, resulting in a sudden increase in IOP [46]. OAG, the more prominent form of glaucoma, progresses at a slower rate than ACG. Drainage canals become blocked over time, resulting in the slow accumulation of aqueous humour within the anterior chamber. This ultimately results in a gradual increase in IOP. Individuals with OAG do not typically exhibit symptoms and are not aware that they have developed OAG until it has reached an advanced stage in its pathogenesis. Common therapeutics indicated in the treatment of glaucoma and its secondary effects, primarily elevated IOP, are described in Table 1.2.

Table 1.2: A description of the commonly used therapeutics in the treatment of IOP hypertension and glaucoma [30].

Therapeutic	Commercial Brand Name	Dosage Form	Typical Dosage Concentration	Therapeutic Classification	Mechanism of Action
Latanoprost	Xelpros ®	Eye drop suspension	One drop of the 50 µg/mL suspension, once daily	Prostaglandin derivative (Anti-glaucoma)	Relaxation of ciliary body muscle enhances aqueous humour outflow.
Carbachol	Miostat ®	Intravitreal injection	A single injection of 0.5 mL of a 0.01% Miostat ® solution	Dual action parasympathomimetic (Anti-glaucoma)	Acts as both an acetylcholine agonist and a cholinesterase inhibitor. (Acetylcholine stimulates pupil contraction, thus reducing intraocular pressure. Acetylcholine is enzymatically degraded by cholinesterase).
Timolol	Betimol ®	Eye drop suspension	One drop of 0.25% Betimol ® solution twice a day (1 mL contains 2.5 mg of timolol).	Non-selective beta-adrenergic blocker	Binds to both β1 and β2 adrenergic receptors in the ciliary muscle, thus preventing aqueous humour production via norepinephrine and epinephrine stimulation.
Fluocinolone acetonide	Yutiq ®	Intravitreal implant	0.18 mg (0.25 µg a day for 36 months)	Anti-inflammatory corticosteroid	Modification of subsequent protein synthesis to inhibit proinflammatory mediator activity.
	Retisert ®	Intravitreal implant	0.59 mg (0.3 – 0.4 µg a day for up to 30 months).		
Brimonide	Alphagan ®	Eye drop suspension	One drop of 0.2% Alphagan ® solution twice daily (1 mL contains 1.3 mg of bromidine).	Selective α2 agonist	Binds to and activates a2 receptors, thus decreasing aqueous humour production and enhancing uveoscleral drainage.

The global market for glaucoma is projected to reach $11.05 billion by 2027, a 67.7% increase in market size from 2019 [48]. Many novel anti-glaucoma treatments are in the pipeline and are set to be released by 2027. Allergan, acquired by AbbVie Pharmaceuticals, received FDA approval for a bimatoprost-laden, bioerodible, intracameral implant for the treatment of open-angle glaucoma in 2020 [47]. This implant, designed to last between 4 to 6 months, is now commercially available under the brand name Durysta®. Kedalion Technologies is currently developing AcuStream™, a dispensing device for the topical delivery of IOP-lowering medication at a dose that is 80% less than what is required in a standard eye drop formulation. Following the completion of two successful Phase I clinical trials in 2017, Kedalion Technologies planned to conduct Phase II clinical trials in 2019, followed by the submission of marketing applications in 2022. However, Kedallion Technologies was acquired by Novartis in 2022. Bausch and Lomb now own the rights to the AcuStream™ technology as they acquired an ophthalmology subdivision of Novartis in 2023. Phase II dose-ranging clinical trials for a sustained release intracameral implant, capable of sustaining a therapeutic dose of latanoprost over 6 months are currently being conducted by PolyActiva Pty Ltd. Mati Technologies have developed a latanoprost-laden punctum plug, exhibiting sustained release of latanoprost into the tear film over 14 weeks. The results obtained from two multi-centre Phase II clinical trials suggest that the punctum plug exhibits retention rates of over 90% in the lower punctum over 12 weeks [48].

1.1.3.3 Diabetic Retinopathy

Diabetic retinopathy (DR) is an ocular disease closely associated with both Type 1 and Type 2 diabetes mellitus [49]. Just under 3 million of the MSVI cases reported in people over 50 in 2020 resulted from the deleterious effects of DR, with equal prevalence in Latin America, East Asia, North Africa and the Middle East and High-Income regions in 2020 [17]. Non-proliferative DR typically occurs first but slowly progresses into proliferative DR. Hyperglycaemia in intraretinal capillaries results in inflammation of the RPE layer [50]. Chronic inflammation results in enhanced vascular permeability and subsequent degeneration of the blood-retinal barrier. The accumulation of excess fluid and blood, coupled with intraretinal capillary microaneurysms and haemorrhaging, results in macular edema and

distorted vision. Similar to the pathogenesis of AMD, disruptions to retinal blood flow and increasing pressure cause degradation and closure of the capillary network, resulting in retinal ischemia. Induction of HIF-1 and subsequent expression of VEGF stimulates neovascularisation [51]. These abnormal blood vessels proliferate and haemorrhage into the vitreous humour. Vitreal haemorrhage is indicated by the appearance of dark, blurred areas in the field of vision. Continuous blockage of intraretinal capillaries leads to the formation of an epiretinal membrane [49], a layer of scar tissue that continuously pulls on the macular surface, increasing the risk of macular detachment.

Pan-retinal photocoagulation has been the primary treatment for proliferative DR for many years [52]. Vitrectomy surgery is also conducted in severe cases of proliferative DR where retinal haemorrhaging has resulted in vitreal blood pooling [53]. However, due to similarities in the pathogeneses of neovascular AMD and proliferative DR, treatment of DR has advanced to include the use of the anti-VEGF antibodies highlighted in Table 1.1 to target retinal neovascularisation [54].

Due to the significant increase in reported Type 2 diabetes cases, many pharmaceutical companies are investing in the development of novel methods for the treatment of DR. Roche/Genentech are currently investigating faricimab, a bispecific monoclonal antibody, for the treatment of diabetic macular edema. A 6 mg/mL IVI of faricimab, administered via a 16-week interval dosing regime, exhibited comparable efficacy, in terms of improved visual acuity, to aflibercept, administered every 8 weeks [55]. The RHONE-X Phase III clinical trial, assessing the long-term safety and tolerability of the faricimab injection, was completed in October 2023 [56]. Roche/Genentech have also received FDA approval for the repurposing of their ranibizumab-laden port delivery system for DR treatment in Q4 of 2021. The PAVILION study, comprising the long-term assessment of the efficacy, safety, and pharmacokinetics of the PDS, is due for completion in Q2 of 2024 [57].

1.1.3.4 Dry Eye Disease

Dry eye disease, or keratoconjunctivitis sicca, is a highly prevalent, multifactorial ocular surface disease within the global adult and elderly populations [58], [59]. Postmenopausal women are disproportionately affected by dry eye disease in comparison to men, primarily due

to the decrease in estrogen levels with ageing and a higher prevalence of inflammation-mediated autoimmune diseases [60], [61]. However, due to exposure to increased amounts of artificial light from electronics, the prevalence of dry eye disease in teenagers and young adults is also rapidly increasing.

Eyelid laxity, coupled with the dysfunction of the meibomian glands, results in the decreased secretion of poor quality, unstable tear film that is prone to rapid evaporation [[62]. Meibomian glands secrete meibum, an oily substance that comprises one of the primary components of tear film. Dysregulation of tear film production can result in corneal hyperosmolarity, which evokes an irritated, burning sensation. Damage to the corneal surface stimulates dysregulation of the immune system and the initiation of inflammatory cascades, which ultimately leads to excessive inflammatory insult and ocular irritation [63], [64]. Corneal surface abnormalities drastically hinder the stimulation of the lacrimal nerve, which in turn impairs fluid secretion from the lacrimal glands. Increased tear evaporation, caused by tear instability or exposure to environmental factors such as allergens, smoke and cold weather, can also result in ocular irritation and dryness [58], [62].

Dry eye is typically treated using over-the-counter or prescription eye drop formulations that exhibit lubricating and/or anti-inflammatory properties. Restasis®, a topical eye drop formulation comprised of the immunosuppressive drug, cyclosporine, is typically prescribed to inhibit pro-inflammatory cytokine release from T cells, thus preventing the suppression of tear film production via inflammation [65]. Artificial tear (AT) solutions are one of the primary treatment options to alleviate the discomfort and burning sensation caused by dry eye disease [66]–[68]. Blink® Tears and Hyalein® contain hyaluronic acid which is capable of binding up to 1000 times its mass in an aqueous solution [69], [70]. Bausch and Lomb Advanced Eye Relief® lubricant eye drops contain glycerin, a natural humectant agent. Other common active ingredients in artificial tears include polyethylene glycol (Visine ®) and carmellose sodium (Celluvisc®). EvoTears®, composed of perfluorohexyloctane, exhibits a dual mode of action by lubricating the corneal surface and stabilising the meibum layer [71], [72].

In October 2021, Oyster Point Pharma received FDA approval for Tyrvaya®, the first nasal spray approved for use in dry eye disease treatment and was officially launched onto the market

on the 1st of July 2022. Varenicline is said to increase basal tear film production by activating a parasympathetic pathway in the nose, thus avoiding the application of drops to an already irritated corneal surface [73]. NOV03 is a water and preservative-free eye drop solution based on the proprietary technology used in EvoTears® and developed by Novaliq [71]. 4 doses of NOV03 per day were found to be well tolerated and led to a reduction in corneal fluorescein staining (indicative of corneal abrasions) and symptom severity during the MOJAVE saline controlled efficacy and safety Phase III trial [74]. The KALAHARI Phase III trial also demonstrated the safety and efficacy of NOV03 over 12 months [75]. The outcome of such studies led to Bausch and Lomb receiving FDA approval for Miebo™ (formerly NOV03) in June 2023 [76]. tSkQ1-based eye drops are currently being developed by Mitotech. SkQ1 is an antioxidant capable of neutralising mitochondrial reactive oxygen species, thus preventing tissue degeneration resulting from chronic corneal inflammation [77]. The VISTA-2 Phase III trials, designed to assess the efficacy of SkQ1 for the treatment of dry eye symptoms in comparison to a vehicle placebo, are currently ongoing [78].

1.2 AGEING – THE PROTAGONIST OF OCULAR DISEASE

Ocular therapeutic development has been primarily centred on the creation of novel drug formulations or treatment strategies for diseases that have already reached an advanced stage of their pathogeneses [79]–[82]. Although their prevalence is widespread, the repercussions of such ocular diseases can be severely debilitating for the elderly. Ageing, characterised by the progressive loss of physiological cellular homeostasis over time, is the primary risk factor for several ocular diseases. Imbalances in cellular redox homeostasis, mitochondrial dysfunction and a decline in essential enzymatic co-factors result in cell senescence and an acceleration of the ageing process, rendering ageing cells more susceptible to disease-mediated damage. Increased discomfort, severe pain, vision impairment and vision loss can particularly impact the ability of an elderly person to live independently. Therefore, there is potential to proactively treat ocular disease, i.e., by re-establishing cellular homeostasis, promoting cellular longevity, and decreasing the risk of patients becoming predisposed to ocular disease. This can be achieved by administering molecules that are typically endogenously produced but whose production is downregulated during the ageing process. Such molecules, such as antioxidants,

vitamins, amino acids etc. exhibit the additional advantage of being inherently biocompatible in comparison to some of the synthetic therapeutic molecules.

1.2.1 Oxidant Accumulation in Ageing Cells

1.2.1.1 Redox Homeostasis under Physiological Conditions

Minimal oxidant production is an inevitable result of normal cellular respiration, innate immunity, and metabolism. [83], [84]. As shown in Figure 1.5, electrons can leak from the transport chain during the oxidation of the electron carriers, flavin adenine dinucleotide ($FADH_2$) and nicotinamide adenine dinucleotide (NADH), and prematurely react with molecular oxygen during transport, thus generating superoxide radicals [85]. Excessive reduction of Coenzyme Q, or ubiquinone, the carrier enzyme that shuttles electrons from Complex I and II to Complex III, to ubiquinol can also result in reverse electron transfer, resulting in the accumulation of electrons for superoxide generation in the mitochondrial matrix [86]. ROS are also released during the activation of phagocytic cells via pathological stimuli. Pro-inflammatory cytokines and growth factors, such as interleukin-1β and tumour necrosis factor α (TNF-α), stimulate an oxidative burst, resulting in the production of large concentrations of oxidants [87], [88].

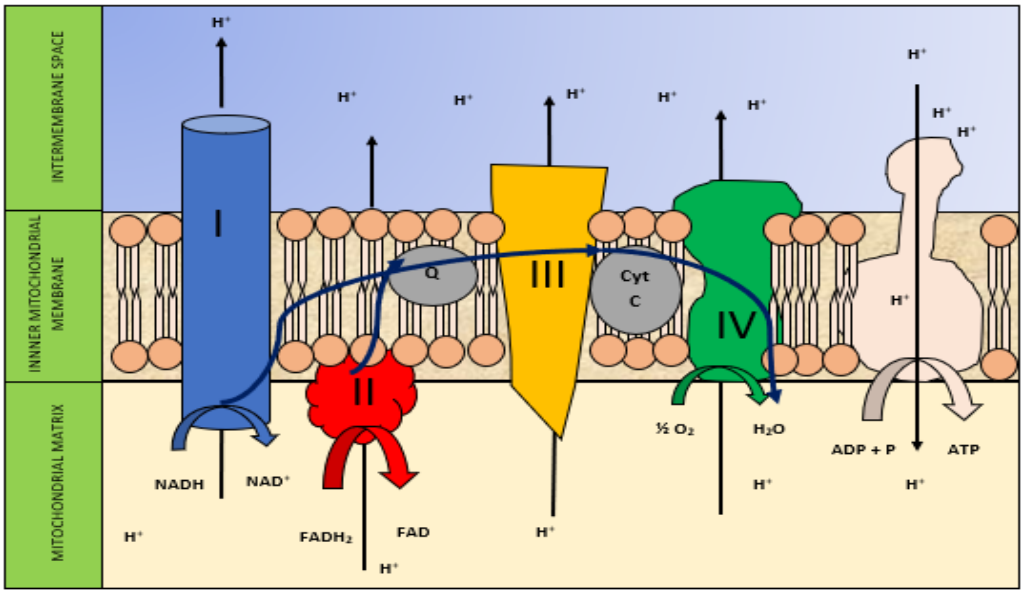

Figure 1.5: The migration of the electrons through the electron transport chain within the inner membrane of the mitochondria (Q = *ubiquinone and Cyt C = cytochrome C).*

Basal concentrations of ROS such as superoxide radicals are involved in the regulation of a variety of cellular processes, including proliferation, redox homeostasis, and survival [89]–[91]. They behave as secondary signalling messengers and transduce the signal originating from an extracellular stimulus within the intracellular environment [87]. Two examples of such signalling cascades include the mitogen-activated protein kinase pathway (MAPK) and the KEAP 1-Nrf2-ARE pathway. Downstream signalling and extensive phosphorylation of MAPKs results in the activation of nuclear transcription factors that regulate the expression of genes responsible for a range of cellular processes, including development, proliferation, and apoptosis [90], [92]–[94]. ROS are also linked to the upregulation of the KEAP 1-Nrf2-ARE pathway, the signalling cascade primarily responsible for endogenous cytoprotective and antioxidant response regulation [95], [96]. Nuclear factor erythroid-related factor 2 (Nrf2) is a crucial element of the cellular antioxidant response as, upon detachment from KEAP-1, it is translocated to the nucleus to bind to antioxidant response elements within the promoter regions of the Nrf2 target genes. This ultimately induces the expression of genes that encode a variety of detoxifying and metabolic enzymes [97].

Physiologically, ROS are regulated by the endogenous antioxidant defence system, thus minimising cellular damage caused by extensive free radical production. Antioxidants can be broadly divided into two sub-groups, depending on their mode of action [98], [99]. Enzymatic antioxidants catalyse the degradation of oxidants via redox reactions. Conversely, non-enzymatic antioxidants behave as free radical scavengers, donating electrons to stabilise free radicals. Superoxide radicals undergo instantaneous dismutation into hydrogen peroxide (H_2O_2) under physiological conditions via superoxide dismutase enzymatic action. H_2O_2 is further degraded to water and molecular oxygen via catalase enzymatic degradation [89]. This degradation is vital as H_2O_2 has a molecular mass of 0.034 kilodaltons (kDa) and can readily permeate through the corneal and conjunctival epithelial layers as they only hinder the migration of molecules with masses above 0.5 kDa and 10 kDa, respectively [100]. Glutathione peroxidase (GPx) and glutathione reductase (GRx) work symbiotically with one another. GPx utilises reduced glutathione (GSH), to catalyse the reduction of lipid hydroperoxides to alcohol. GRx catalyses the reduction of oxidised glutathione to reform GSH. Glutathione itself behaves as a non-enzymatic antioxidant. GSH is present within aqueous humour at a concentration of 2 μM and present in high concentrations in the lens and vitreous humour. Glutathione can scavenge free radicals directly or be used in the recycling of secondary antioxidants, such as ascorbic acid (AA), more commonly known as Vitamin C. AA cannot be endogenously produced and is delivered via dietary nutrients [98]. AA is oxidised to ascorbate free radicals during the detoxification of hydroxyl and superoxide anions before being extensively oxidised to form dehydroascorbate (DH) [89]. DH is reduced back to AA by glutathione-dependent enzymes or GSH. Without GSH, dehydroascorbate degrades to form diketoguloinic acid, which can irreversibly modify lens proteins, thus resulting in cataract formation. Similar to AA, α-tocopherol, or Vitamin E, is exogenously produced. As it is fat-soluble, α-tocopherol disrupts the peroxyl radical chain involved in lipid peroxidation, which is critical in the prevention of lipofuscin accumulation at the onset of atrophic AMD [24], [99], [101]. The actions of AA and α-tocopherol are also interrelated as AA recycles the oxidised α-tocopherol radical back to α-tocopherol.

1.2.1.2 An Imbalance in Oxidant/Antioxidant Equilibrium

As we age, there is a substantial shift in the oxidant/antioxidant equilibrium in favour of oxidant production, primarily resulting from increased mitochondrial dysfunction. However, secondary risk factors, such as smoking and poor dietary habits, can also contribute to the oxidant/antioxidant imbalance. Increased oxidant concentrations can induce lipid peroxidation of the fatty acid chains of cell membrane phospholipids, resulting in a loss of membrane integrity and a substantial increase in cell permeability [102], [103]. Mitochondrial DNA is highly susceptible to damage as it is not protected by histone moieties [104]. An influx of oxidant species through the dysfunctional cell membrane results in mitochondrial DNA damage, primarily through the premature shortening of telomeres on the mitochondrial chromosomes [102]. When exposed to oxidative stress, telomeres, which protect the ends of chromosomes from aggregation and damage, begin to shorten, resulting in chromosomes reaching a critical length at which they can no longer replicate. Cellular senescence is induced as a result. Although they cannot replicate, senescent cells remain metabolically active. The accumulation of such cells in ageing tissues can create a vicious cycle between pro-oxidant production and chronic inflammation [103]. Senescent cells release senescence-associated secretory phenotypes (SASPs), including several pro-inflammatory cytokines, such as TNF-α, growth factors and chemokines. The release of such cytokines results in the expression of several pro-inflammatory genes via activation of the NF-κB signalling pathway. Mistaking the senescent cells for exogenous antigens, phagocytic immune cells, such as neutrophils, migrate to the inflamed area and generate large concentrations of oxidants [98]. Once released, the oxidants induce the expression of inflammatory cytokines via the activation of signalling cascades, thus repeating the cycle. Such consistent exposure to chronic inflammation results in increased cellular necrosis and is regarded as the starting point of several age-related ocular diseases. In ageing cells, the concentration of free Nrf2 is increased in response to increasing intracellular oxidant concentrations [105]. However, due to accelerated ageing and chronic inflammatory conditions, KEAP 1-Nrf2 signalling becomes impaired over time. The expression of Nrf2 also decreases as a function of age, primarily due to the transcriptional dysregulation of genes such as NFE2L2 [106].

High concentrations of oxidants can also impact cellular respiration. Excessive oxidant accumulation within the inner mitochondrial membranes results in the collapse of the mitochondrial membrane potential and a significant decrease in ATP production [107].

The difference between basal respiration, the minimum limit that cells must meet to produce sufficient ATP for cellular metabolic functions, and the upper respiratory limit known as maximal respiration is the reserve respiratory capacity. A depletion of the reserve respiratory capacity below basal respiration occurs in the presence of ROS, thus triggering cellular apoptosis. Premature apoptosis can be severely debilitating for tissues with high metabolic demands, such as the retinal pigment epithelium.

1.2.1.3 Antioxidant Supplementation in Ocular Cells

Recent studies have demonstrated the efficacy of exogenous antioxidant supplementation against the deleterious effects of ageing in ocular cell models. In particular, compounds such as omega-3 and omega-6 polyunsaturated fatty acids, vitamins and polyphenols have been identified as potent Nrf2 activators [106]–[119]. Johansson *et al.* [120] demonstrated the correlation between docosahexaenoic acid administration and an increase in both NFE2L2/Nrf2 activation and the autophagy of oxidative stress-damaged misfolded proteins within the retinal pigment epithelium. NFE2L2 regulates the encoding of Nrf2. Upon carrying out immunoblotting analysis on APRE-19 cells treated with 70 μM and 140 μM of DHA, sequestosome-1 (SQSTM-1), a protein that selectively targets ubiquitinated protein aggregates for degradation during autophagy, expression and turnover, were significantly upregulated. This, in turn, led to an increase in NFE2L2/Nrf2 activation. However, to elicit an antioxidant response, DHA causes a transient increase in reactive oxygen species (ROS) concentration. Pre-treatment with 5mM of N-acetyl cysteine and 150 μM of Vitamin E was required to protect the APRE-19 cells from excessive ROS damage during the study. This seems like a counterintuitive outcome, particularly when the retinal tissues are under such high metabolic stress at the onset of AMD. Epigallocatechin-3-gallate (EGCG), has demonstrated great efficacy in the inhibition of proinflammatory cytokines and Nrf2 activation in various ocular diseases [121]. For example, Miyagawa *et al.* [122] significantly reduced corneal vascularisation in a corneal burn model via the daily administration of an EGCG-laden

nanoparticle eye drop formulation over one week. EGCG administration successfully decreased *in vivo* vascular endothelial growth factor receptor phosphorylation and subsequent activation. Huang *et al.* [123] encapsulated EGCG within gelatin nanoparticles via self-assembly of opposing ionic charges. The EGCG-laden gelatin nanoparticles administered twice daily for three weeks, re-established physiological tear secretion, minimised corneal damage and thinning post dry eye induction and significantly reduced the occurrence of premature corneal apoptosis.

1.2.2 Intracellular Decline in Nicotinamide Adenine Dinucleotide (NAD+) Concentration

The ageing process is also accelerated by a decline in intracellular nicotinamide adenine dinucleotide (NAD+) concentration [124], [125]. NAD+ is a redox coenzyme, found in abundance in all cellular organelles, that plays a pivotal role in the intracellular metabolism of glucose to ATP [126]. However, it also behaves as an essential co-substrate, initiating the enzymatic reactions carried out by a number of endogenous enzymes, including Sirtuins (SIRTs), ADP-ribosyl cyclase (CD38) and poly (ADP- ribose) polymerase 1 (PARP-1) [102].

1.2.2.1 Biosynthetic and Salvage Pathways of NAD+

De novo synthesis of NAD+ occurs via the enzymatic conversion of dietary tryptophan, or nicotinic acid, in the Kynurenine and Preiss-Handler pathways, respectively [127], [128]. Tryptophan is converted to nicotinic acid mononucleotide, which is subsequently converted to nicotinic acid dinucleotide (NaAD+) via nicotinamide mononucleotide adenylyltransferase (NMNAT) action. Amidation of NaAD+ results in the formation of NAD+. Similarly, NaAD+ is also formed via the three-step conversion of nicotinic acid, or niacin, in the Preiss Handler pathway.

Intracellular NAD+ concentration is also maintained by the salvage pathway. As shown in Figure 1.6, through the enzymatic action of nicotinamide phosphoribosyltransferase (NAMPT), nicotinamide (NAM) is converted to nicotinamide mononucleotide (NMN), which is subsequently converted to NAD+ [129]. NAM is a by-product of NAD+ consumption,

formed upon degradation of the glycosidic bond between NAM and ADP-ribose. NMNAT catalyses the binding of the adenylyl group of ATP to NMN, thus forming NAD+ [130], [131].

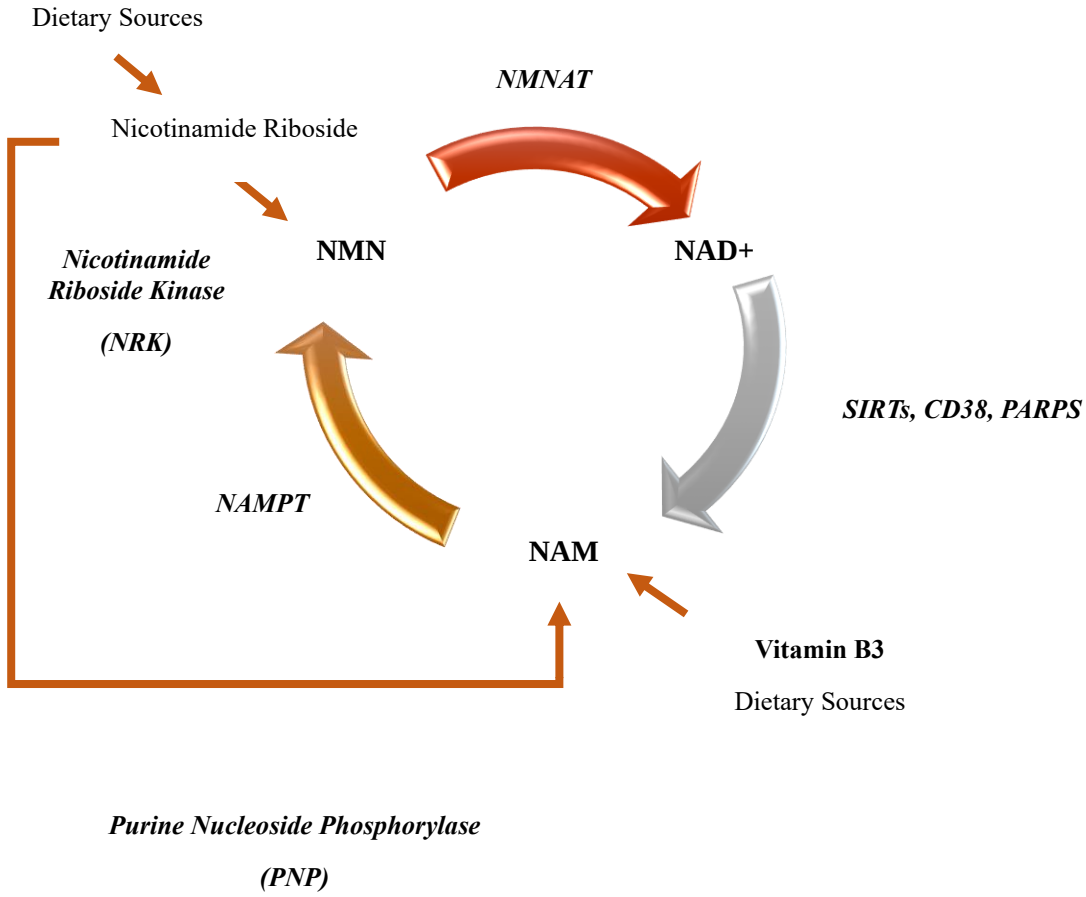

Figure 1.6: The synthesis of NAD+ via the intracellular salvage pathway [102], [129].

1.2.2.2 NAD+ Consumption and Mitochondrial Dysfunction

The intracellular NAD+ pool is attained by a balance between the activities of cellular NAD+-synthesising and NAD+-consuming enzymes. CD38 enzymes regulate several cellular functions under physiological conditions, including cell proliferation, inflammatory responses, and the synthesis of NAD+ precursors. However, hyperexpression of CD38 can lead to the rampant activation of several proinflammatory pathways and a severe decline in the reformation of NAD+ precursors such as nicotinamide mononucleotide (NMN) [125]. The expression of key NAD+ salvage pathway enzymes, such as NAMPT, is also downregulated under these conditions. PARP-1, a secondary NADase, is also upregulated in response to

cellular DNA damage caused by oxidant action [102], [124]. PARP-1 cleaves ADP-ribose from NAD+, forming nicotinamide, and catalyses the polymerisation of poly (ADP-ribose), a signalling molecule used in DNA repair mechanisms. PARP-1 and SIRTs compete for intracellular NAD+ pools. Increased PARP-1 activation with age results in increased NAD+ depletion, which ultimately results in significant inhibition of sirtuin function. SIRTs are a family of histone deacetylates that maintain cellular longevity through the mediation of mitochondrial biogenesis (SIRT-1, SIRT-3), chromosome stability (SIRT-6) and transcription regulation (SIRT-1) [132], [124], [133]. Regarding ocular tissues, SIRT-1 has been primarily detected in the nuclei of cells such as the retinal ganglion cell layer, the corneal and conjunctival epithelial layer, and fibrous lens cells. SIRTs deacetylate histones after sensing intracellular NAD+, thus enhancing the enzymatic activity of the deacylated target protein. ADP ribose from NAD+ binds to the acyl group, liberating nicotinamide. For example, SIRT-1 regulates the deacylation of BMAL1, the transcription factor responsible for the formation of circadian CLOCK:BMAL1 complex [130]. SIRT-3 regulates the permeability of the mitochondrial membrane transition pore, therefore hindering the migration of cellular organelles into the cytoplasm. If the intracellular NAD+ levels decline, SIRTs will not remove the acyl groups from the target mitochondrial proteins, resulting in augmented mitochondrial dysfunction, reduced NAD+ regeneration and impaired cellular metabolism, all of which are the hallmarks of age-related disease progression [134].

1.2.2.3 Cellular Restoration via NAD+ Supplementation in Ocular Disease

The replenishment of intracellular NAD+ pools with exogenous NAD+ supplements, or NAD+ precursors, could potentially minimise the deleterious effects that occur at the early onset of several ocular diseases, such as glaucoma, dry eye, and AMD [135]. In 2017, Williams *et al.* [136] demonstrated the protective effects of the NAD+ precursor, vitamin B_3, or nicotinamide (NAM), during the pathogenesis of glaucoma. By administering 550 mg/kg/day of NAM via drinking water, mice at various stages of glaucoma were all protected against deleterious effects such as mitochondrial dysfunction, retinal ganglion cell (RGC) loss, retinal nerve layer thinning and optic nerve degeneration. NAM also protected RGCs from damage caused by localised inflammation, induced upon injection of a TNF-α solution into the eyes of the murine

model. A higher dose (2000 mg/kg/day) exhibited superior neuroprotective effects and successfully alleviated high IOP in the eyes of mice with late-stage glaucoma. However, although endogenously produced, large concentrations of intracellular NAM have been known to cause increased vasodilation, leading to skin flushing [134], [137]. High doses of alternative NAD+ precursors, such as NAMPT and NMN, have been known to cause augmented proinflammatory cytokine and SASP release and axon degeneration [138]. Also, as the rate of NAD+ synthesising enzymes decreases as we age, the intracellular concentration of such enzymes may not be sufficient to effectively recycle high concentrations of NAD+ precursors. By inverting schedules in groups of Sprague-Dawley albino rats, Bai *et al.* [139] demonstrated that day-fed rats possessed higher levels of NAD+ at the onset of light exposure in comparison to those fed at night, and were less susceptible to light-induced retinal damage as a result. Retinal damage following light exposure was attributed to the accumulation of zinc within RPE and photoreceptor cells. The protective effects of higher levels of NAD+ in day-fed rats were attributed to the preservation of NAD+ intracellular concentration pools as opposed to a decrease in zinc accumulations. Intraperitoneal injection of 500 mg/kg of NAM immediately before light-induced retinal damage or H_2O_2-mediated oxidative stress also restored retinal NAD+ levels and prevented retinal cell death. Similarly, following analysis of RPE cells exposed to 300 μM of H_2O_2 via a cell counting kit-8 (CCK-8) assay, Zhu *et al.* [140] demonstrated the efficacy of a 0.1 mM NAD+ solution in preventing RPE cell death. Treatment with 0.1 mM of NAD+ also inhibited PARP-1 activation in H_2O_2-stressed RPE cells, thus preventing oxidative stress-induced necrosis, one of the primary pathological factors in AMD. Hui *et al.* [141] demonstrated that, compared to patients receiving a placebo, oral supplementation of 1.5 and 3 g of NAM over 12 weeks in patients receiving treatment for glaucoma led to a concurrent improvement in visual function and attainment in inner retinal function. Ren *et al.* [142] utilised an *in vitro* cell model to highlight the significant reduction in the expression of three senescence biomarkers following incubation of ARPE-19 cells with 1000 μM of NMN. 300 mg/kg/day of NMN, administered via intraperitoneal injection, successfully prevented sodium iodate-induced retinal pigment epithelial cell senescence in a murine model. NMN supplementation was found to restore basal intra-RPE NAD+

concentrations and quench the migration of immune cells and subsequent activation of inflammatory pathways in RPE cells.

1.3 BARRIERS TO EFFECTIVE NAD+ OCULAR DELIVERY

Due to the complexity of both its structure and physiology, the eye is quite well protected and difficult to penetrate [41]. The multifactorial interaction between several dynamic and static anatomical barriers within the eye protects against the intraocular permeation of exogenous debris and microbes. However, the restrictive nature of such barriers is non-selective. The physicochemical attributes of the therapeutic have a significant impact on its pharmacokinetic profile following administration. This, in turn, may limit bioavailability and therapeutic efficacy at the desired target area [143]. NAD+ is inherently biocompatible and possesses a molecular weight of 0.663 kDa and as such, may exhibit enhanced permeation upon ocular administration. However, as discussed in the following sections, its physicochemical attributes, such as surface charge and hydrophilicity, may not be suitable for overcoming the barriers associated with certain routes of administration.

1.3.1 Conventional Routes of Administration

As shown in Figure 1.7, there are a number of routes in which a therapeutic can be transported to the desired intraocular target site [144], [145]. The chosen route and method of administration is not only dependent on the locality and the severity of the ocular disease, but also on the specific needs of the end user.

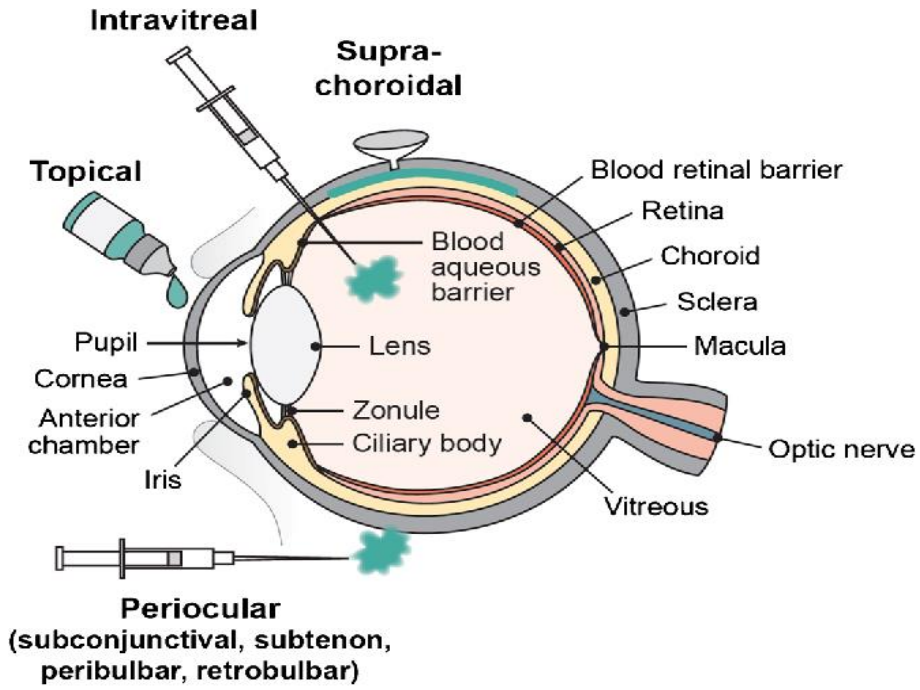

Figure 1.7: The various routes of ocular therapeutic administration [146].

The transcorneal absorption route, primarily intended for topical drug delivery to the anterior chamber, begins with either the paracellular or transcellular [147]. Upon reaching the aqueous humour within the anterior chamber, the drug can be readily distributed to the anterior uvea or be eliminated via trabecular and uveoscleral outflow.

Migration through the second pathway, the conjunctiva–sclera route, involves the permeation of the therapeutic through the conjunctiva via the precorneal tear film. The therapeutic then diffuses through the sclera before migrating further into the posterior segment via the choroid to reach the retinal pigment epithelium, the neural retina, the vitreous humour and surrounding intraocular tissues. Targeted absorption through the conjunctiva–sclera route is a suitable route for drugs that are both intended for posterior segment delivery and that exhibit poor corneal permeability [144].

When a therapeutic is administered via intravitreal administration, it is directly distributed into the vitreous humour for further diffusion into the neural retina. Regarding periocular administration, therapeutics are administered onto the external surface of the sclera, typically

via subconjunctival (beneath the conjunctiva), peribulbar (space on the periphery of the eyeball), retrobulbar (space directly behind the eyeball) and posterior juxtascleral (near-scleral) administration. Therapeutics can then migrate towards the posterior retinal tissues through the sclera, choroid, and retinal pigment epithelium cell layer [148]. Conversely, suprachoroidal administration involves the administration of the therapeutic in the space between the scleral endothelium layer and the choroid, providing more direct access to the posterior tissues [132].

Therapeutics can also reach the intended intraocular target site using a more delocalised approach. The administration of therapeutics into systemic circulation via gastrointestinal absorption or intravenous/subcutaneous injection has been previously utilised for ocular drug delivery [149]–[152]. However, only 2% of the concentration of the drug typically arrives at the target site, particularly within the posterior segment, predominantly due to the retinal blood barriers that will be discussed in Section 1.3.3.4 [144], [153]. However, as many ocular therapeutics exhibit a non-selective mode of action, the total concentration at the target site is also decreased by the delocalised absorption and use of the drug in other body tissues [154]. Such non-selective absorption can have several moderate to severe side effects. The administration of ocular therapeutics via intranasal routes, such as Tyrvaya®, has also been investigated due to the proximity of the olfactory region and the cribriform plate separating the nasal and ocular cavities [155].

1.3.2 Primary Barriers to Effective Anterior Segment Delivery

Topical administration has been the cornerstone treatment option for diseases affecting the anterior segment in recent decades [156], [157]. Ease of administration, user convenience and safety are the primary advantages of topical administration. As highlighted in Table 1.2 and Section 1.1.3.4, there are a wide variety of commercially available topical formulations for anterior segment diseases such as glaucoma and dry eye, 90% of which are in the form of eye drop solutions [100]. Alternative formulations include ointments, gel and ocular inserts [144], [153]. Despite its advantages, the efficacy of topical administration, particularly regarding drug bioavailability, is limited, predominantly due to the anatomical barriers within the anterior segment. Reduced bioavailability often leads to an increase in dosing frequency to illicit a therapeutic effect. Patient compliance is often challenged, thus leading to the sporadic dosing

of fluctuating therapeutic concentrations and an increased risk of disease progression and adverse effects.

1.3.2.1 Tear Film

Tear homeostasis is achieved by the regulation of the lacrimal functional unit, encompassing the lacrimal and meibomian glands, conjunctival goblet cells and the corneal and conjunctival surface [158]. Tear film turnover and precorneal drainage are the first and most prominent physiological barriers to ocular drug delivery, particularly when administered via the topical route. Stimulation of the corneal surface by exogenous particles, such as drug molecules, activates a sensory pathway that induces lacrimal fluid secretion from cells within the lacrimal glands. Lacrimal fluid then drains to the palpebral conjunctiva where it combines with mucin excreted from conjunctival goblet cells before migrating across the corneal surface into the nasolacrimal duct. This mechanism provides adequate clearance of corneal irritants via nasolacrimal drainage at a rate of 1.2 µL/min and allows for the attainment of an approximately constant volume of 7-10 µL of precorneal tear film in the conjunctival sac [144], [145], [159]. One drop of an eye drop solution typically equates to a volume of 50 µL [144], [145], [100], [160]. Therefore, upon administration of an eye drop, blinking, tear turnover and nasolacrimal drainage are all upregulated to re-establish the equilibrium volume. This ultimately results in the loss of approximately 75-90% of the administered volume of therapeutic solution [161], [162]. Also, tear film has a high turnover rate of approximately 3 µL/min with a restoration time of between 2 to 3 minutes [159], [163], thus severely limiting the residence time of the therapeutic molecules on the corneal surface and increasing the need for frequent application to achieve a therapeutic dose. Based on its inherent hydrophilicity, it is likely that NAD+ would be rapidly cleared via tear turnover. As such, a depot with mucoadhesive, cell-penetrating, or controlled release capabilities may be required to ensure sufficient retention on the corneal surface. The three distinct layers of tear film are depicted in Figure 1.8.

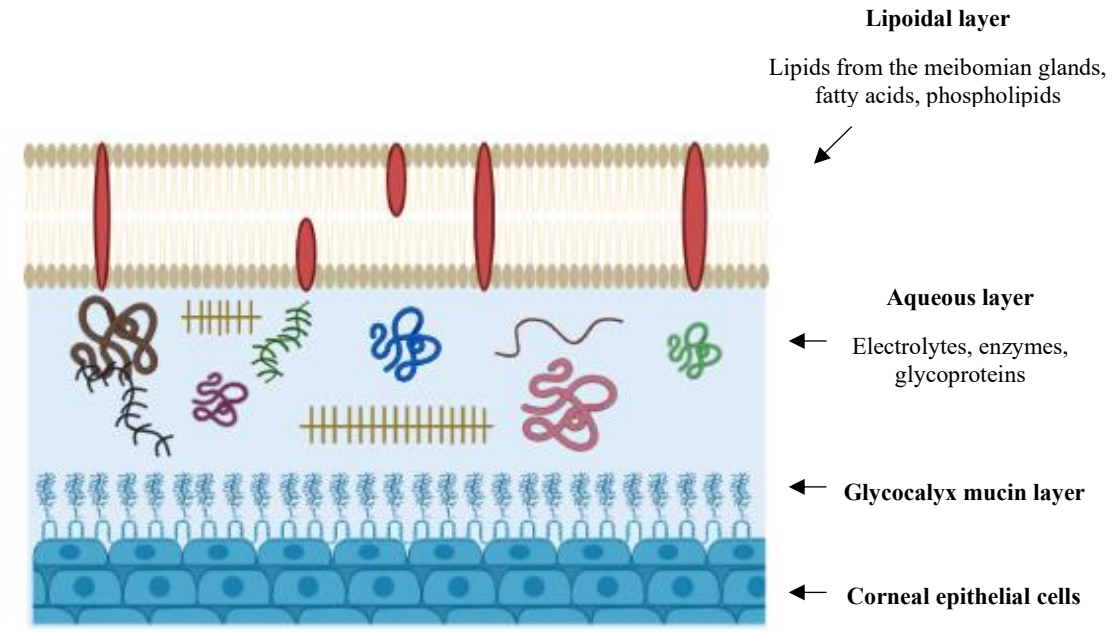

Figure 1.8: Schematic of the mucoaqueous layers of tear film (Figure generated using templates available on Biorender.com [164]. Information used to draw the resulting diagram was sourced from [144], [159], [163]).

The outermost lipid layer, composed of free phospholipids, triglycerides, and fatty acid molecules from the meibomian glands, prevents tear evaporation upon migration. Lacrimal fluid, an 8 μm thick layer in the centre of tear film secreted from the lacrimal glands, is primarily responsible for the hydration and supplementation of the avascular corneal surface and removal of extracellular debris. Electrolytes such as K^+ and Na^+, intercellular proteins such as glycoproteins and albumin, and enzymes such as lysozyme, are secreted in conjunction with lacrimal fluid [144], [161], [163]. Lastly, the transmembrane mucins secreted from the conjunctival goblet cells form the innermost layer and interact with the corneal epithelium to stabilise the tear film during spreading and prevent microbial contamination [165]. Mucins are negatively charged macromolecules and can hinder the migration of positively charged therapeutic molecules, such as the nicotinamide moiety of NAD+, via electrostatic binding. Carbonic acid within the aqueous layer and dispersed electrolytes may also modify the extent of ionisation of the therapeutic via electrostatic binding [100], [159], [160], [166]. Also, proteins and enzymes within the tear film may partially hydrolyse and bind to therapeutic molecules on

the corneal surface [167]. Such reactions will ultimately decrease the available concentration of free drug [168]. For example, a study conducted by Sebbag *et al.* [169] in 2020 demonstrated the impact of albumin binding on tropicamide activity in a canine model. The administration of 30 µL of a 0.4% or 1.5% canine albumin solution directly before the administration of 30 µL of 1% tropicamide reduced the extent of pupillary dilation, or mydriasis, by 1 mm (11.8 mm) in comparison to those treated with artificial tears and tropicamide (12.75 mm). Conversely, a small yet non-significant decrease in the extent of pupil constriction was found between eyes instilled with 0.005% latanoprost and canine albumin and those treated with artificial tears and latanoprost at any time post-instillation. Although some competitive inhibition of albumin binding via ligand-receptor interactions was evident, preservation of pupil constriction was attributed to the administration of a dose of latanoprost that was six orders of magnitude higher than the dose needed to illicit a therapeutic response (10^{-10} M) within the iris sphincter.

1.3.2.2 Selective Inhibition by Corneal Layers

As depicted in Figure 1.9, the cornea, a transparent, avascular tissue within the anterior segment, can be divided into five distinct layers: an epithelial cell layer, Bowman's layer, stroma, Descemet's membrane, and an endothelial cell layer [4], [165]. The thickness of the cornea increases from 500 µm in the centre to approximately 700 µm towards the periphery.

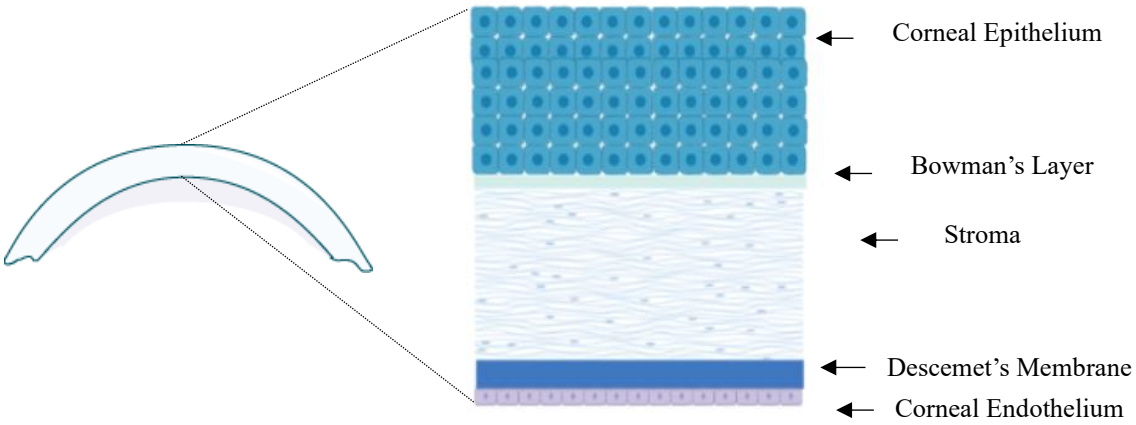

Figure 1.9: The distinct layers of the cornea [153]. (Figure generated using templates available on Biorender.com [164]).

Due to the amphiphilicity and varying thicknesses of these layers, the trans-corneal ingression of microbes, exogenous debris and therapeutic molecules alike is highly dependent on their physicochemical properties [165]. The epithelium cell layer, composed of 90% epithelial cells organised into layers, is naturally lipophilic and is considered the rate-limiting barrier to effective transcorneal permeation. Mucin is secreted from the apical epithelial layer, resulting in the epithelium layer being negatively charged at physiological pH (pH 7.3-7.4), above its isoelectric point of 3.2 [170]. As such, cationic molecules exhibit enhanced retention on the corneal epithelium whereas anionic molecule migration is hindered due to electrostatic repulsion [171]. Liaw *et al.* [172] demonstrated the ten-fold increase in *in vitro* corneal permeation of cationic lysine in comparison to anionic L-glutamic acid at physiological pH using excised New Zealand white rabbit cornea. Similarly, the permeability coefficient of salicylic acid, a negatively charged beta hydroxy acid, was 3 times less than that of positively charged benzylamine. Liu *et al.* [173] also demonstrated that penetratin, a cell-penetrating peptide, exhibited a permeability through excised rabbit cornea that was 87.5 times higher than its anionic counterpart, poly(serine)$_8$. *In vivo* distribution of 5-carboxyfluorescein-penetratin within the corneal and retinal tissues of a murine model was also visible for up to 6 hours post-administration. Fluorescent decay in the anterior and posterior segment was visible in the poly(serine)$_8$ treated group within 2 hours post-instillation.

The transcellular diffusion of lipophilic drug molecules across the lipoidal cellular membrane is favoured with compounds with a log P value of between 2 and 4 exhibiting enhanced transcellular permeation [174]. Toropainen *et al.* [175] demonstrated the enhanced apical to basolateral corneal epithelial cell permeation of β-blockers with high log P values in comparison to those with low log P values. The rate of transcellular permeation of bextaxolol (log P = 3.44) was approximately 13 times higher than that of sotalol, a hydrophilic β-blocker with a log P value of – 0.62. However, therapeutics exhibiting lipophilicity above log P values of 4 will exhibit poor desorption into the hydrophilic stroma layer [176]. The molecular weight of the therapeutic can also affect its extent of transcorneal permeation [177]. Epithelial cells limit the transmembrane diffusion of molecules with molecular weights above 400 Dalton (Da) [178]. A schematic diagram of transcorneal drug permeation, via transcellular and paracellular pathways, is shown in Figure 1.10.

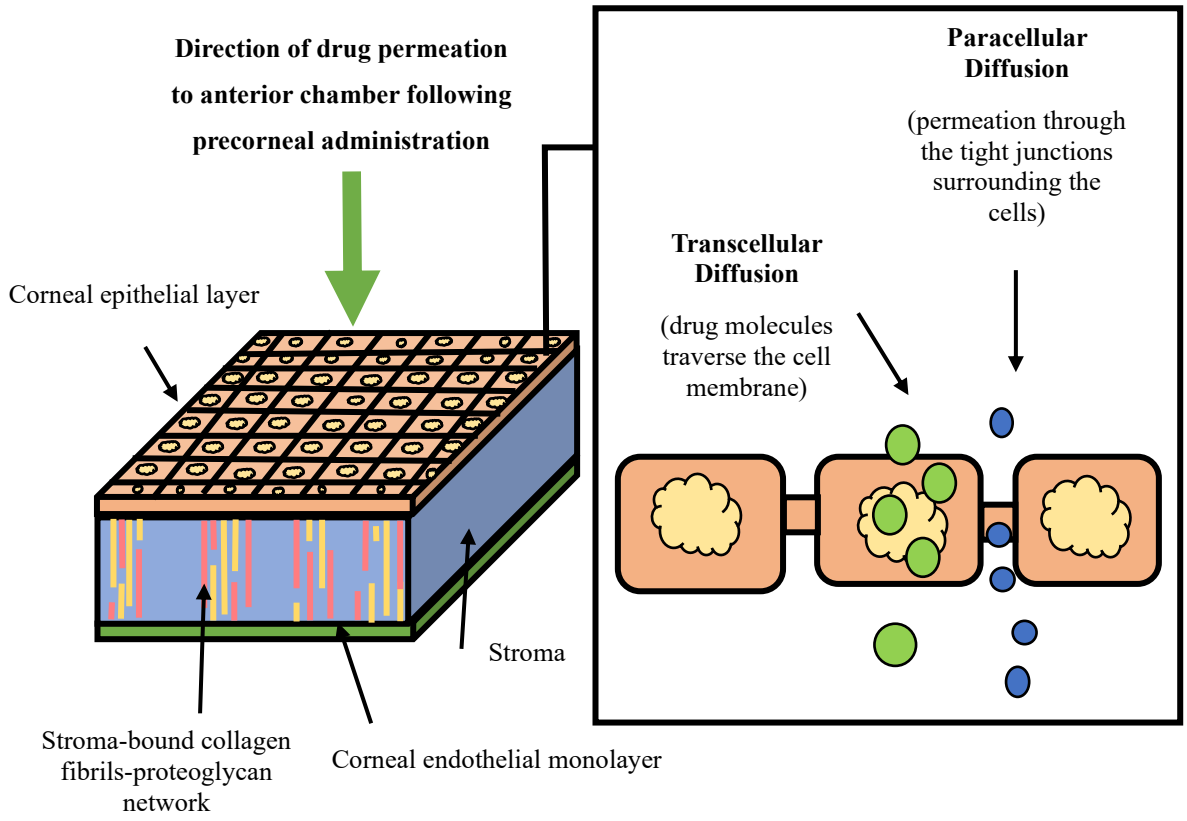

Figure 1.10: A schematic diagram of a typical migration pathway for drug molecules intended for transcorneal permeation.

Superficial corneal cells are joined to one another by junctional complexes to prevent the intraocular ingression of tear film and exogenous debris [167]. These tight junctional complexes are composed of assemblies of transmembrane proteins that create a seal around the junctions and dynamically regulate their structural integrity [179], [180]. Lipophilic drugs with physicochemical properties exceeding those required for transcellular diffusion, and hydrophilic drug molecules, can more readily undergo paracellular diffusion through the tight junctions. The paracellular pores have an average diameter of approximately 2 nm rendering the tight junctions impermeable to drug molecules with molecular weights of above 500 Da [100], [181]. Edwards *et al.* [182] demonstrated the molecular radius-dependent paracellular diffusion of molecules of inherently low lipophilicity. Molecules with a molecular weight of 100 Da exhibited increased transcellular diffusion compared to 500 Da molecules of similar distribution coefficient values. Ultimately, the bioavailability of lipophilic and hydrophilic drug

molecules within the aqueous humour, post transcorneal permeation, is estimated to be approximately 5% and 0.5% respectively [144], [183]–[185].

The stroma is a transparent layer composed of approximately 200 to 250 lamellar arrangements of Type I collagen fibrils and accounts for approximately 80% of the total thickness of the cornea [165]. Due to its inherent hydrophilicity, the stroma acts as a rate-limiting barrier for highly lipophilic molecules. Due to its biphasic nature, a drug must demonstrate dual amphiphilicity to achieve adequate transcorneal diffusion [186].

The endothelium, a 5 μm thick monolayer of cells residing at the interface of the cornea and the anterior chamber, regulates the hydration of the corneal membranes with aqueous humour [165]. Tight junctions between the endothelial cells limit the flow of aqueous humour into the stroma and, through the use of ionic fluid pumps, expel excess fluid back into the anterior chamber [187], [188]. The endothelium behaves as a reservoir, allowing for the gradual release of drug molecules into the aqueous humour. However, the diffusion of lipophilic molecules through the endothelium layer is also favoured.

If NAD+ were to successfully penetrate the corneal layer, the continuous turnover of aqueous humour at an approximate rate of 180 μL/h, coupled with the high vascularisation of the anterior uvea, may limit its total concentration available for subsequent diffusion [162], [167]. Therapeutics exhibit high clearance rates of between 1200 – 1800 μL/h via uveal blood flow due to permeation through the endothelial cells of uveal blood vessels [189].

1.3.2.3 Barriers within the Conjunctival-Scleral Pathway

Topically applied drugs that exhibit poor corneal permeability should be preferentially administered via the conjunctiva-sclera route [190]. As shown in Figure 1.11, intercellular tight junctions exist only at the apical layer of the conjunctival epithelial layer, thus increasing the likelihood of paracellular diffusion due to the absence of a permeation barrier [181], [191].

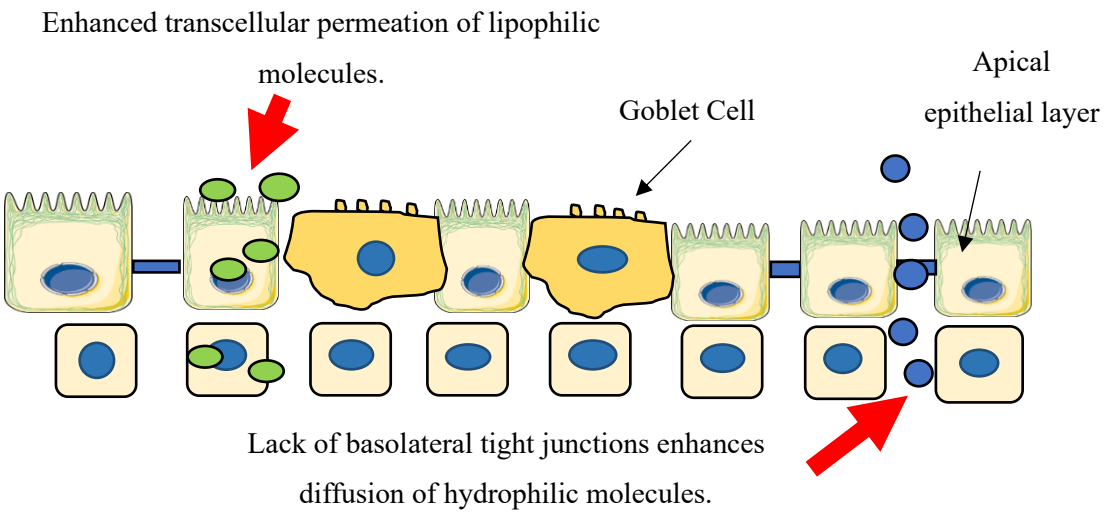

Figure 1.11: Schematic of the conjunctival epithelial cell layer.

The permeability of the conjunctiva is also 230 times greater than that of the cornea, primarily due to the 16% increase in paracellular pore density and the increased available epithelial surface area for absorption (16-18 cm^2) [100], [148], [192]. On average, the diameter of the intercellular pores of the bulbar and palpebral conjunctival cells is 3 nm and 5 nm, respectively. The pores allow for the enhanced permeation of hydrophilic drug molecules and drugs of a higher molecular weight, typically within the range of 5 to 10 kDa [100]. For example, Ramsay *et al.* [193] compared the *ex vivo* corneal and conjunctival permeability of 25 various therapeutic molecules in porcine eyes. In particular, pilocarpine (molecular weight (MW): 208.3 Da, log P: - 0.39) and aztreonam (MW: 435.4 Da, log P: -4.32) exhibited conjunctival permeation rates of 7.73 x 10^{-6} and 1.19 x 10^{-6} cm/s, respectively, approximately one order of magnitude higher than the corneal permeabilities recorded (1.79 x 10^{-6} and 1.02 x 10^{-7} cm/s). In a similar study, the paracellular conjunctival permeability of mannitol (MW: 182 Da) was found to be 55 times higher than its paracellular corneal permeability. The molecular size-selective permeability of the conjunctiva was also demonstrated, with 20 kDa fluorescein isothiocyanate (FITC)-dextran exhibiting adequate conjunctival permeability whereas the permeability of 40 kDa FITC-dextran was inhibited completely [194]. However, due to the vascularisation of the conjunctival sac, drug molecules may also be rapidly absorbed into systemic circulation and subsequently removed from the target area [162]. Approximately 34

to 79% of the administered therapeutics dose is removed to systemic circulation via conjunctival vasculature clearance [148].

Primarily consisting of a 0.5 to 1 mm thick extracellular matrix containing collagen fibrils interwoven with negatively charged proteoglycans, the sclera is highly impermeable to lipophilic drug molecules [159], [195], [196]. Although hydrophilicity is not a limiting factor, the surface charge and molecular radius of the drug can also significantly impact its trans-scleral permeation. Positively charged molecules may bind to the negatively charged glycosaminoglycan chains of the proteoglycans via electrostatic complexation, thus hindering deeper intraocular permeation [197]. Scleral pores are estimated to be between 10 and 40 nm in diameter [198]. Although the pores are larger than those of the conjunctiva and the cornea, the trans-scleral permeation of some macromolecules, such as anti-VEGF agents, dextrans and proteins can be hindered, depending on their molecular weight [85], [199]. An inversely proportional correlation exists between trans-scleral permeation and molecular weight [133]. The ability of a molecule to effectively permeate through the sclera is also dependent on its morphology [85]. Flexible molecules, such as polysaccharides, that can alter their molecular radii exhibit enhanced trans-scleral permeation in comparison to compact, rigid molecules [200].

Based on its characteristics, the conjunctival-scleral route may be more suitable for NAD+ ocular administration. However, its hydrophilicity will render it more susceptible to rapid systemic clearance via conjunctival vascularisation. This provides further justification for the encapsulation or association of NAD+ with a depot that can limit its exposure to physiological conditions following administration. Secondly, therapeutics are often administered via injection to the sub-conjunctival area to deliver a high concentration directly to the target site. Based on its supplementary nature, administration of NAD+ via injection may not be favourable in terms of patient compliance due to the fragility of the ocular tissues and the potential risks of severe adverse effects.

1.3.2.4 The Blood-Aqueous Barrier

The blood-aqueous barrier (BAB) presents another static, anatomical barrier to successful anterior segment drug delivery. The tight junctions between the non-pigmented ciliary

epithelium cells are the primary constituents of the BAB [201]. Selective inhibition of macromolecule migration from the circulatory system through the anterior segment of the eye occurs at the BAB. Tight junctions between the vascular endothelial cells of the iris and ciliary processes also limit macromolecule paracellular diffusion [202]. Selective paracellular diffusion of ions and fluids across the gap junctions between the pigmented and non-pigmented ciliary epithelium layers occurs [203]. These ionic gradients pull fluid through the extracellular space surrounding the ciliary epithelium from the ciliary stroma, thus producing aqueous humour [202]. The BAB also prevents the backflow of aqueous humour from the anterior chamber.

1.3.3 Primary Barriers to Effective Posterior Segment Delivery

1.3.3.1 The Suprachoroid

If successful trans-scleral permeation of NAD+ is achieved, it would then have to permeate through the barriers within the retina. The suprachoroid, the external 35 μm thick layer of the choroid bound to the outer sclera via lamellar fibres [132], behaves as a static barrier regulating both the diffusion of nutrients from the choroid to the RPE and outflow of metabolic degradants via osmosis. Facilitated by the energy supplied by the pumping activity of Na, K-ATPase ionic gradients, the RPE pumps water out of the subretinal space and into systemic circulation via the choriocapillaris [204].

1.3.3.2 Choriocapillaris and Bruch's Membrane

The vascularisation of the choriocapillaris layer facilitates the influx of high volumes of oxygen and nutrients into the retina via the outer blood-retinal barrier (OBRB). This poses a significant dynamic barrier to retinal bioavailability due to high blood flow within the choriocapillaris (~ 43 mL/h), coupled with the presence of 70-80 nm-sized pores within the choriocapillaris endothelium results in a high percentage of therapeutic clearance from the retinal tissues [205]. Successful intraretinal permeation is therefore highly dependent on the extent of therapeutic permeation through the OBRB. The transcellular diffusion of lipophilic compounds of small molecular radii across the retinal pigment epithelial (RPE) layer is favoured in comparison to hydrophilic compounds and macromolecules. As demonstrated by Pitkänen *et al.* [206], the permeation of small lipophilic molecules was highly dependent on the molecular radius as a

376 Da carboxyfluorescein exhibited enhanced intra-RPE permeation in comparison to an 80 kDa dextran molecule. Similarly, lipophilic molecules exhibited a permeation rate that was 8 times faster than that of a hydrophilic molecule of similar size. However, although retinal permeation of small molecules is favoured, such molecules will also be more susceptible to vasculature uptake.

1.3.3.3 Melanin Binding

Aside from the anatomical retinal barriers, retinal bioavailability can also be influenced by melanin, the polyanionic polymer present in granules within the peripheral regions of the RPE cell layer and the choroid [141]. Melanin is known to complex and sequester both free radicals and cationic, lipophilic molecules, thus decreasing the total free drug concentration available for subsequent intraretinal diffusion yet simultaneously prolonging the ocular residence time of the therapeutic [186], [208]. In 2016, Rimpela *et al.* [207] demonstrated the superior ability of the basic compounds, timolol and chloroquine, to bind to melanin isolated from porcine RPE and choroid samples. Acidic compounds, such as methotrexate, exhibited decreased melanin binding, highlighting that electrostatic interaction is the predominant binding force. Chloroquine exhibited superior uptake into porcine RPE cells (~99%) as a result of melanin binding in particular, equating to an intracellular concentration (μM):medium concentration (μM) ratio of over 22,000:1. This is an order of magnitude larger than the ratio calculated for chloroquine in non-pigmented cells. Cheruvu *et al.* [209] also highlighted the significance of melanin binding in effective retinal therapeutic delivery upon demonstrating the *ex vivo* accumulation of celecoxib, a lipophilic non-steroidal anti-inflammatory drug, in various ocular tissues of albino Sprague-Dawley and pigmented Brown-Norway rats. The area under the curve (AUC) obtained post periocular injection of 3 mg of celecoxib in the retina and vitreous humour (55.5 and 35.3 μg/g) in pigmented rats was significantly lower than that obtained for the same tissue samples in the non-pigmented rats (159.8 and 116.3 3 μg/g). This was attributed to the sequestration of celecoxib via binding to melanin in the pigmented tissues, thus hindering deeper intraretinal permeation.

1.3.3.4 The Blood-Retinal Barriers

The OBRB and IBRB within the retina are the most prominent barriers to effective posterior segment drug delivery, particularly via systemic or intravitreal administration [186]. Retinal pigment epithelial cells are the primary components of the OBRB whereas the IBRB is composed of retinal capillary endothelial cells [4]. The OBRB, behaving as both a regulator and a filter, facilitates the two-way transport of nutrients and waste between the choroid and the photoreceptor cell layer to attain retinal homeostasis [4], [179]. Tight junctions, existing between neighbouring endothelial cells and epithelial cells within the IBRB and OBRB, restrict the paracellular diffusion of macromolecules from both the vitreous humour and the highly permeable choriocapillaris vasculature, respectively, to the inner retina [179]. Similar to the limitations of transcorneal diffusion, the paracellular diffusion of hydrophilic and large molecular weight drug molecules is also hindered by the tight cellular junctions of the blood-retinal barrier (BRB) [186]. Intraretinal diffusion of highly lipophilic drug molecules, administered into systemic circulation, is favoured. However, this is also problematic due to delocalised absorption into other tissues, resulting in a substantial decrease in localised retinal bioavailability [210].

1.3.3.5 Vitreous Humour

Although relatively stagnant within the posterior chamber, vitreous humour poses a significant barrier to therapeutic diffusivity following IVI. The establishment of a concentration gradient within the posterior chamber results in therapeutic diffusion from the injection site. However, the rate of vitreal diffusion and subsequent absorption into the neural retina is highly dependent on the interplay between the physicochemical attributes of the therapeutic and the vitreal network. As demonstrated by Rattanakijsuntorn *et al.* [211] using a bovine vitreous humour model, anionic molecules exhibited a much larger diffusivity coefficient in comparison to a neutral counterpart of similar molecular weight, primarily due to electrostatic repulsion from the anionic glycosaminoglycan vitreal meshwork. Upon comparing an anionic molecule of a much larger molecular weight (74 kDa) to the aforementioned anionic molecule (0.938 kDa), a significant decrease in diffusivity coefficient from 2.739 x 10^{-6} cm^2/s to 2.271 x 10^{-7} cm^2/s was observed. Penkova *et al.* [212] also summarised the diffusivity coefficients of various

therapeutic molecules in *ex vivo* vitreal models and observed an inverse correlation between molecular weight and diffusivity. This further highlights that the viscosity of vitreous humour hinders the diffusion of larger molecules whereas smaller molecules can successfully interpenetrate the meshwork with pore sizes of approximately 550 nm. Due to its small size, and the presence of two anionic phosphate groups on the pyrophosphate bridge moiety, NAD+ may be a suitable candidate for intravitreal delivery. Although this administration technique would bypass both the metabolic and anatomical intraocular barriers, enhance localised NAD+ bioavailability within the posterior segment and minimise premature clearance, frequent injections over a prolonged period can increase the risk of adverse effects. With IVIs being associated with an increased risk of endophthalmitis, retinal detachment and haemorrhaging, and intraocular pressure fluctuations, the benefit does not outweigh the risk in regards to the delivery of a supplementary molecule.

1.4 POLYELECTROLYTE COMPLEX NANOPARTICLES – POTENTIAL CANDIDATES FOR NAD+ OCULAR DELIVERY

The development of novel drug delivery systems (DDS), and alteration of the physicochemical attributes of existing delivery systems, have been at the forefront of ophthalmic research in recent years. DDS for ocular drug delivery are typically designed with one purpose; to ameliorate the known pitfalls of conventional dosage forms, such as poor anterior and posterior bioavailability, decreased barrier permeation, decreased therapeutic stability, short ocular residence times and the invasiveness of the treatment method itself. Such developments include but are not limited to; the addition of viscosity and permeation enhancers to eye drops and *in situ* gel formulations [213]–[216], bioerodible implants for long-term administration [217]–[219], therapeutic and nanoparticle-laden contact lenses, formulated via film embedment, soak and release methodologies and molecular imprinting [220]–[224], and the formulation of therapeutic-laden nanoformulations such as nanoparticles, nanowafers and nanogels [225]–[229]. For the purpose of this literature review, nanoparticles, particularly those synthesised via the self-assembly of natural polymers, will be discussed in greater detail.

1.4.1 Nanoparticle Characteristics for Ocular Drug Delivery

Nanoparticle formulations offer a versatile and reliable approach to ocular drug delivery. With mean particle sizes between 1 and 1000 nm, the physicochemical properties and functionality of such formulations can be easily tailored to *in vivo* environmental conditions to improve the pharmacokinetic profile of conventional therapeutic solutions [230], [231]. As such, enhanced therapeutic bioavailability and solubility, increased ligand-mediated adhesion and retention, prolonged stability, and stimuli-triggered therapeutic release, can be achieved [232]–[235]. Nanoformulations with sizes ranging from 20 to 250 nm have exhibited enhanced permeability and retention (EPR) effects through various ocular tissues within both the anterior and posterior segments [236]–[238]. Koo *et al.* [239] observed that the biodistribution of polymeric nanoparticles within the vitreous humour was not only dependent on size but also the surface charge. Cationic polyethyleneimine (PEI) based nanoparticles (zeta potential: +33.4 ± 5.1 mV) accumulated within the vitreous humour and were retained even up to 72 hours post-IVI, primarily due to ionic interaction with the negatively charged glycosaminoglycan moieties in the vitreous meshwork. Size-selective retinal permeation was observed following confocal microscopy analysis of the glycol chitosan nanoparticle-treated retinal tissues. With a mean size of 229.1 ±18.7 nm, the migration of these nanoparticles through the 10 to 25 nm pores of the inner limiting retinal membrane was severely hindered. Conversely, as shown in Figure 1.12, anionic hyaluronic acid (HA) and human serum albumin nanoparticles (HSA) (zeta potential: -26.2 ± 4.0 mV and -20.9 ± 2.0 mV) exhibited enhanced retinal permeation 72 hours post-injection, despite their size (213.4 ± 10.3 and 326.3 ± 9.7 nm, respectively). However, although nanoparticles do not elicit increased ocular irritability upon administration due to their size, they may illicit a cytotoxic or inflammatory response over time due to their prolonged intraocular residence time in comparison to larger particles [240]–[242].

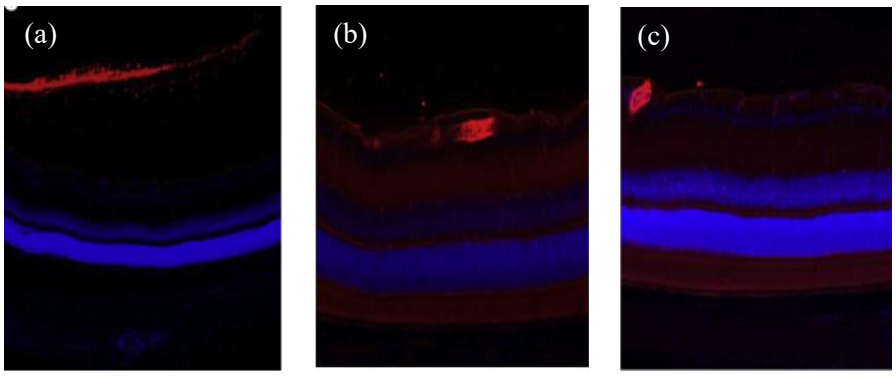

Figure 1.12: Confocal microscopy images of the migration of red fluorescent labelled PEI (a), HA (b) and HSA (c) nanoparticles within the retinal tissues 72 hours post-injection. (Blue – DAPI stained retinal cell nuclei [239].)

Controlled and sustained release of the drug at the intraocular target site can also be achieved via nanomaterial encapsulation. This is particularly important in cases where patient compliance with the dosing regimen may be low or where frequent administration can be invasive. The percentage cumulative release of bromidine from chitosan and alginate nanoparticles, incorporated into three different topical formulations (eye drops, *in-situ* gelling system composed of hydroxymethyl cellulose and preformed gel composed of methylcellulose) was significantly lower in all cases than bromidine release from Alphagan ® commercial eye drops [243]. Almost 100% of the theoretical bromidine concentration in Alphagan ® eye drops was released after 8 hours. Conversely, the nanoparticle-laden formulations minimised burst release kinetics. The *in situ* gelling systems exhibited the lowest *in vitro* bromidine release, reaching 47.9 and 54.5% release from the alginate and chitosan nanoparticle-laden systems over 24 hours, respectively. The alginate and chitosan nanoparticle-laden eye drops exhibited a higher rate of bromidine release, equating to 66.4 and 71.2% within the same timeframe, respectively. The *in situ* gel systems provided an additional polymeric matrix, which the bromidine molecules must diffuse through upon release from the nanoparticulate systems. Natarajan *et al.* [244] developed a latanoprost-laden egg-phosphatidylcholine liposomal formulation, demonstrating a sustained *in vitro* latanoprost release of 60% over a two-week period. A single subconjunctival injection (100 µL), equating to a dose of 100 µg of latanoprost, exhibited statistically equivalent therapeutic efficacy over 120 days to 50 µg/mL Xalatan ® eye

drops, administered once daily. Therapeutic efficacy was quantified by the reduction in intraocular pressure in a non-human primate model. Timolol maleate (TM)-laden glycerol monoolein and poloxamer 407 cubosomes, with an average size of 142 nm and a zeta potential value of -6.27 mV exhibited significant *ex vivo* corneal penetration compared to commercial TM eye drops [245]. Cubosomes are liquid crystalline nanoparticles, comprised of bicontinuous lipid bilayers organised into a three-dimensional structure, which exhibit higher physiological stability than conventional liposomes due to the larger lipid bilayer ratio [246]. 542 µg of TM was detected within the cornea 6 hours after cubosome application. A cumulative *ex vivo* penetration of just 154 µg of TM had penetrated through the rabbit cornea 6 hours post-eye drop administration.

Several nanomaterial formulations also exhibit mucoadhesive and bioadhesive properties, particularly if the primary constituent is electrostatically charged or capable of hydrogen bond formation. Mucoadhesive nanoparticles can reversibly bind to the mucin secreted by the corneal and conjunctival epithelium cells, thus prolonging the intraocular residence time of the drug, without causing a loss in visual acuity during administration [247]. Alternative mucoadhesive formulations, such as ophthalmic gels, are macroscopic and highly viscous, which may cause blurred vision and temporary visual impairment post-application. Surface modifications, such as the attachment of surface-bound ligands or coatings, can also impart some degree of adhesive or release barrier functionality to the resulting nanoparticle formulation. Natural polymers have been used extensively in nanomaterial formulation as coating materials to enhance the intraocular absorption of nanomaterials with unfavourable absorption properties [248]–[251]. Mahaling *et al.* [252] evaluated the spatiotemporal intraocular distribution of poly (lactic-co-glycolic acid) (PLGA) nanoparticles coated with chitosan, gelatin or Pluronic F68 following instillation of fluorescent labelled nanoparticles via eye drop in a C57BL/6J murine model. The addition of a coating influenced the bioavailability of the nanoparticles in various ocular tissues, particularly within the posterior segment of the eye. Whilst all of the coatings increased the bioavailability of the nanoparticles in the conjunctiva – sclera – choroid – retina pathway, attributed to the increased hydrophilicity and mucoadhesive capabilities of the coatings, chitosan-coated particles exhibited superior

bioavailability. Exhibiting zeta potential values of between +35 to 40 mV, chitosan is positively charged and can therefore facilitate ionic interaction with the negatively charged phospholipid bilayers of the corneal and conjunctival cell membranes, thus increasing the likelihood of intraocular retention. However, it was noted that this biodistribution study was conducted using enucleated eyes and therefore, particle biodistribution was unaffected by dynamic flow barriers in the posterior segment, such as lymphatic flow and choroidal blood flow. As the uncoated and coated nanoformulations were all relatively small in size (< 200 nm), they may be subject to rapid elimination to systemic circulation. Therefore, it is inconclusive as to whether the polymeric coatings can effectively enhance the biodistribution of the nanoparticles under true physiological conditions. Cheng *et al.* [253] demonstrated the increased bioavailability of chitosan-coated triamcinolone acetonide-laden phosphatidylcholine liposomes within the posterior segment in comparison to uncoated liposomes. Using a model fluorescent drug (coumarin-6), a significant increase in cellular transduction into human corneal epithelial (HCECs) and spontaneously arising retinal pigment epithelium (ARPE-19) cells was observed in the chitosan-coated liposome group. Coating apatinib-laden bovine serum albumin nanoparticles with hyaluronic acid resulted in a significant reduction in *in vitro* apatinib release from 98% to 66.7% at the 24-hour time point [254]. HA possesses the unique ability to selectively bind to amino acid residues within the link module domain of the hyaladherin glycoprotein receptor, CD44 [255], [256]. As the expression of CD44 is significantly upregulated in tumour and cancer stem cells, HA has been used as the primary component of cancer-targeting nanocarriers to enhance the intracellular targeting and endocytosis of the oncology drug [257]–[259]. Moreover, the overexpression of CD44 has also been observed upon induction of oxidative stress within the RPE [260]. CD44 receptors are also expressed on the corneal and conjunctival cells under physiological conditions [261]. Therefore, coating nanoformulations with HA could enhance the receptor-mediated delivery of ocular therapeutics to dysfunctional RPE cells. Huang *et al.* [262] demonstrated the enhanced *in vitro* cellular uptake and *ex vivo* retinal permeation of HA-modified HSA nanoparticles in comparison to the uncoated formulation. As shown in Figure 1.13, a statistically significant increase in fluorescence intensity was observed upon incubation of fluorescent-labelled HA-modified HSA nanoparticles with ARPE-19 cells in comparison to the uncoated nanoparticles.

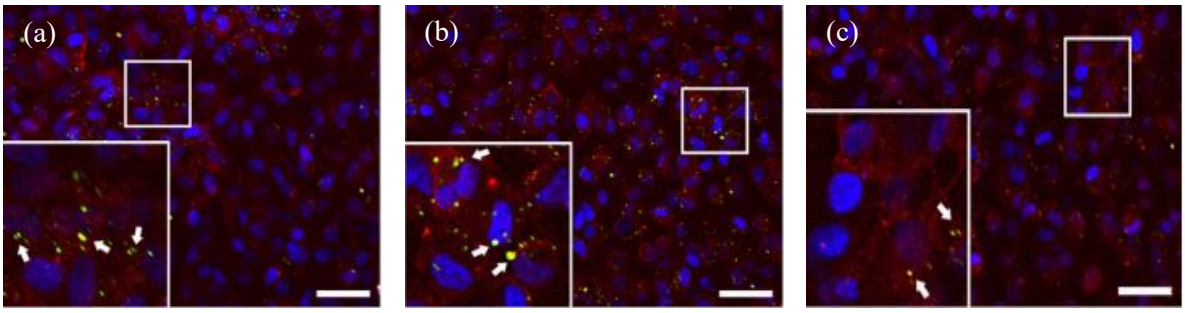

Figure 1.13: Confocal micrographs of ARPE-19 cells incubated for 4 hours with fluorescent-labelled uncoated HSA nanoparticles (a) and HA-coated HSA nanoparticles (b). ARPE-19 cells pre-incubated with HA for 1 hour prior to incubation with HA-coated HAS nanoparticles are shown in (c) [262].

Competitive binding analysis, conducted via the pre-treatment of ARPE-19 cells with free HA chains prior to incubation with HA-modified HSA nanoparticles, confirmed that endocytosis of such nanoparticles was mediated by HA-CD44 receptor interaction.

1.4.2 Pitfalls of Nanoparticle Preparation Methods

Numerous preparation methods, such as the top-down' or 'bottom-up' approach, have been utilised to formulate polymeric and lipoidal nanoparticles [263], [264], [265]. The bottom-up approach involves the self-assembly of monomeric units into nanoparticles via polymerisation. Such polymerisation techniques include emulsion polymerisation, interfacial polymerisation and atom transfer radical polymerisation [266], [267]. However, residual monomer aggregates, transition metal catalysts and free radical initiators from polymerisation reactions can cause significant toxicity issues. Conversely, top-down approaches involve the assembly of preformed polymers into nanoparticles [226]. Such methods include dialysis, solvent evaporation, nanoprecipitation, emulsion diffusion, etc. [263], [268]. These methods are typically based on the incompatibility and insolubility of the polymer within the solvent comprising the continuous phase during emulsification. Despite avoiding the issues associated with residual monomers, a number of the 'top-down' techniques require the use of large volumes of organic solvent [263]. The removal of such solvents from the final formulation, often via extensive dialysis, lyophilisation, or evaporation, is time-consuming and is not always

entirely effective in removing all of the residual solvents present. The addition of surfactant and stabilising molecules to reduce the surface tension and stabilise the nanoparticle formulation can also pose toxicity risks.

Although some of the preparation methods used to formulate lipoidal nanoparticles involve the use of organic solvents, alternative methods have been adapted to minimise the residual toxicity of the final formulation [263], [269]. For example, solid lipid nanoparticles are often prepared using hot homogenisation. Here, nanoparticles are formed by forcing a mixture composed of drug molecules dissolved within a molten lipid through a heated homogeniser under high pressure. However, despite the lack of residual, toxic substituents, hot homogenisation is not suitable for use when utilising thermolabile compounds. The high experimental temperatures required can result in temperature-induced degradation. Microemulsions can also be formulated [270], where the lipid phase is heated and subsequently mixed with a surfactant solution. The mixture is then dispersed in an excess volume of aqueous solution, thus resulting in the precipitation and solidification of the lipoidal nanoparticles. Although microemulsions are often produced at ambient temperatures to prevent a decrease in interfacial tension between respective emulsion droplets, exposure to temperatures above the phase transition temperature of the lipid renders this method unsuitable for the encapsulation of thermosensitive, lipophilic compounds. Also, high levels of surfactants are often required to produce stable microemulsions, thus posing a potential toxicity risk [271]. Finally, upon formation, the lipoidal nanoparticle formulations are heavily diluted, and several purification steps are often required to concentrate the formulation. Broadly speaking, several of the formulation methods used for lipid nanoparticles are not suitable for hydrophilic drug compounds. Although the encapsulation of hydrophilic compounds within the aqueous core encompassed within the phospholipid bilayer structure is possible, leakage can be an issue due to the fragility and fluidity of the bilayer [272]. As such, extensive trials involving the optimisation of a number of formulation parameters, such as the method itself, cholesterol content, lipid composition and lipid:drug ratios, are often required [273]–[275]. In most cases, hydrophilic drugs will accumulate on the surface of lipoidal nanoparticles and will readily diffuse into the aqueous medium, thus resulting in substantial drug loss during lipoidal nanoparticle formulation [276]. Double emulsion and inverse miniemulsion methods are often used to encapsulate sufficient

quantities of highly hydrophilic drug molecules [277]. A schematic diagram of a double emulsion is shown in Figure 1.14.

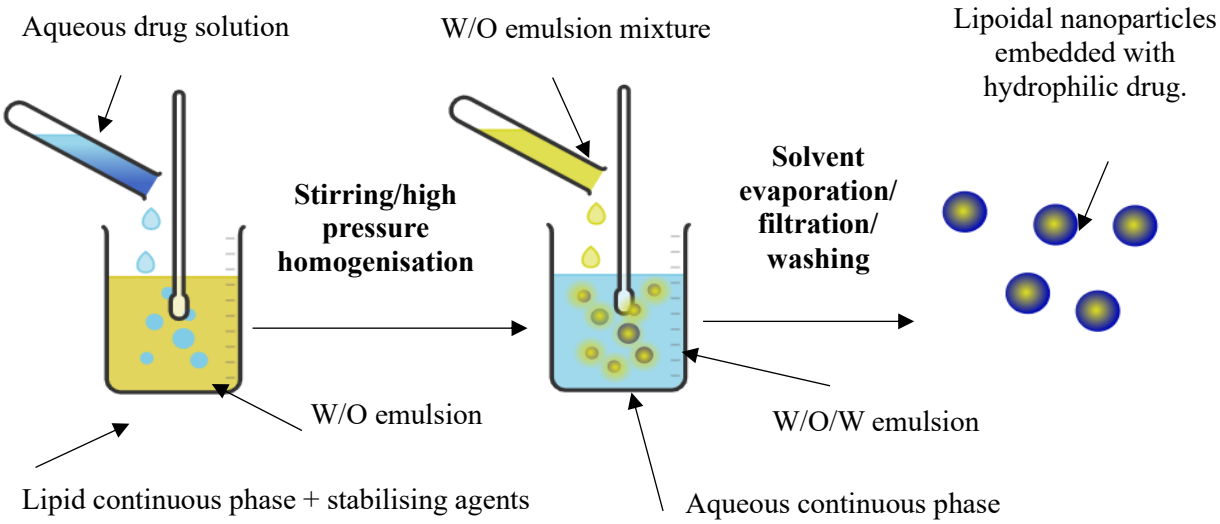

Figure 1.14: A double emulsion process that is typically used in nanoparticle formulations.

However, large volumes of organic solvents are required in both preparation methods to form the water in oil emulsions. This, in turn, both increases the number of purification steps required to remove the solvent and increases the risk of residual solvent toxicity.

1.4.3 Polyelectrolyte Complexation - A Greener Approach

The limitations associated with the preparation methods described in Section 1.4.2 have directed research in favour of the formulation of nanoparticles via self-assembly mechanisms [278]. Self-assembly occurs due to the association of polymers via non-covalent interactions such as Coulomb, or electrostatic, interactions, hydrogen bonding, van der Waals forces and hydrophobic interactions. Harsh organic solvents and surfactants are not required as self-assembled nanoparticles are produced under mild formulation conditions, with aqueous media typically being used as the reaction medium. Amphiphilic polymers will spontaneously self-assemble in aqueous medium via intramolecular and intermolecular interactions between the hydrophobic moieties that are in close proximity to one another [279]. To alleviate interfacial surface tension, the hydrophilic components will assemble around the hydrophobic aggregates at the polymer–medium interface. Both hydrophilic and hydrophobic polymers can be rendered

amphiphilic for self-assembly using chemical conjugation and graft chemistry [279]. Carbodiimide conjugation has often been used to graft a hydrophobic polymer to a hydrophilic polymer backbone by the formation of an amide bond between a carboxylic acid and primary amine functional group [259], [280], [281]. This reaction is typically carried out in the presence of 1-ethyl-3-(3-dimethylaminopropyl) carbodiimide (EDC) and *N*-hydroxysuccinimide (NHS). However, for this literature review, the self-assembly of natural polyelectrolytes via electrostatic complexation will be primarily discussed. Aside from the inherent biocompatibility and biodegradability of the polyelectrolytes themselves, electrostatic complexation does not typically require an extensive purification step post-formation, rendering this method a more cost-effective and environmentally friendly approach to nanoparticle preparation.

1.4.3.1 Polyelectrolyte Complex (PEC) Assembly Mechanism

Polyelectrolyte complexation is predominantly driven by two phenomena; the formation of Coulomb's interactions between oppositely charged polyelectrolytes and the increase in entropy resulting from counter ion and solvate displacement upon disruption of the respective electrical double layers (EDL) surrounding the individual polyelectrolyte chains [282], [283]. Both of these processes result in favourable enthalpic and entropic contributions, which ultimately lead to a reduction in the total Gibb's free energy of the system [284]. Polyelectrolyte complexation can be broadly summarised in three steps. Firstly, primary complexes are formed via mutual entanglement of the polyelectrolyte chains via Coulomb's interaction. Philips *et al.* [285] defined the mechanism of initial PEC formation as the combined effect of two countering processes:

- The supermolecular ordered packing of two oppositely charged polyelectrolytes, driven primarily by electrostatic charge compensation, followed by the conformational adaptation of such polyelectrolytes to favour charge compensation. (Follows the ladder-like structure model [286]).
- Chaotic interpolyelectrolyte aggregation with partial charge compensation and a significant number of free ionic sites (Follows the "scrambled egg model").

Correction of conformational distortions occurs via the establishment of secondary supramolecular or non-covalent interactions. Intercomplex aggregation of the structurally organised secondary complexes composes the final step in the complexation process.

Polyelectrolyte complexes, or PECs, are not thermodynamically stable and exhibit higher surface free energy in comparison to the bulk medium [287], [288]. A detailed description of PEC thermodynamics is summarised by Casey-Power *et al.* [289]. Briefly, dispersed polyelectrolyte complexes within the bulk will tend towards aggregation to decrease interfacial area, resulting in macroscopic thermodynamically stable phase separation and a further reduction in total Gibb's free energy. Kinetic stabilisation, typically imparted by the formation of polyelectrolyte complexes with residual opposing surface charges, is required to preserve the stability of the polyelectrolyte complex dispersed phase. Due to the dynamic and reversible nature of polyelectrolyte complexation, the resulting morphologies of the complexes formed are highly dependent on a number of formulation conditions, including pH, ionic strength, mixing order, polyelectrolyte molecular weight, molar charge ratio and polyelectrolyte concentration [290], [291]. A schematic of the more common morphologies of PECs is shown in Figure 1.15.

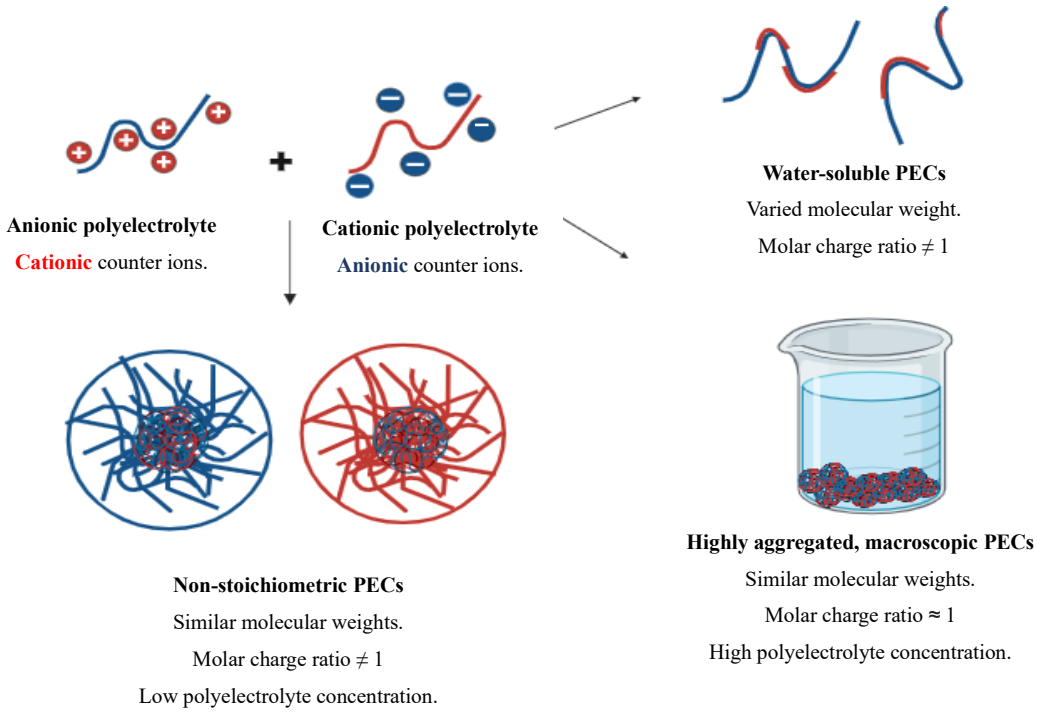

Figure 1.15: The potential, attribute-dependent, complex morphologies arising from the complexation of an anionic and cationic polyelectrolyte.

Water-soluble PECs tend to form when a large difference in molecular mass exists between two weak polyelectrolytes at a non-stoichiometric charge ratio (molar ratio between negative and positive polyionic charges ($n^-/n^+ < 1$ or > 1) [286], [292]. The respective polyelectrolytes tend to complex via a "zip mechanism", leading to the formation of a ladder-like structure, consisting of both unpaired hydrophilic, single-stranded blocks and neutralised, hydrophobic, double-stranded blocks. Populations of insoluble PECs can also co-exist with water-soluble PECs in solution under these reaction conditions. However, the formation of the latter is dependent on the charge ratio of the weak polyelectrolytes [293]. The complexation of highly concentrated, strong polyelectrolytes of similar molecular weights at stoichiometric charge ratios ($n^-/n^+ = 1$) results in high electroneutralisation [292], [294]. Under these conditions, macroscopic phase separation is favoured, stemming from the formation of charge-neutralised polyelectrolyte aggregates [295]. Such aggregates tend to form via the "scrambled egg" model of complexation, in which a large number of polyelectrolyte chains are incorporated into the resulting particles. Under dilute conditions and non-stoichiometric charge ratios, colloidally

stable PECs can form, which are kinetically stabilised by residual ionic charges imparted by the surface-bound polyelectrolyte in excess [287], [291], [296], [297]. Such electrostatic stabilisation is imperative to prevent aggregation *in vivo*, thus ultimately reducing size-exclusion during intraocular transport and subsequent delocalised, uncontrolled therapeutic release [195].

1.4.3.2 Polysaccharide-Based PEC Systems

To attain biocompatibility, many PEC systems for biomedical applications have been designed using polysaccharides as the primary component. Aside from having lower mechanical strength and variable molecular weights in comparison to their synthetic counterparts, polysaccharides exhibit enhanced biocompatibility, cell receptor recognition, site-specific enzymatic degradation and tunable mucoadhesive and viscoelastic capabilities [298]–[300]. Also, as they are found in abundance from a variety of plant, animal and microbial sources, polysaccharides are a sustainable and relatively cost-effective excipient in biomedical applications. Many polysaccharides have been investigated for use in PEC formulations, including chitosan, hyaluronic acid, dextran, alginate, xanthan gum, pectin etc. Of these, both chitosan and hyaluronic acid have gained significant traction.

HA is a linear, hydrophilic natural polysaccharide consisting of repeating β-1,4 glucuronic acid and β-1,3 acetylglucosamine disaccharide units that are joined by β-1,3- and β-1,4-glycosidic bonds [289], [301], [302]. Chitosan, a polysaccharide derived from the deacetylation of chitin, is composed of D-glucosamine and N-acetyl-D-glucosamine units that are also linked by β-1,4-glycosidic bonds [303]. The structures of both chitosan and HA are shown in Figure 1.16.

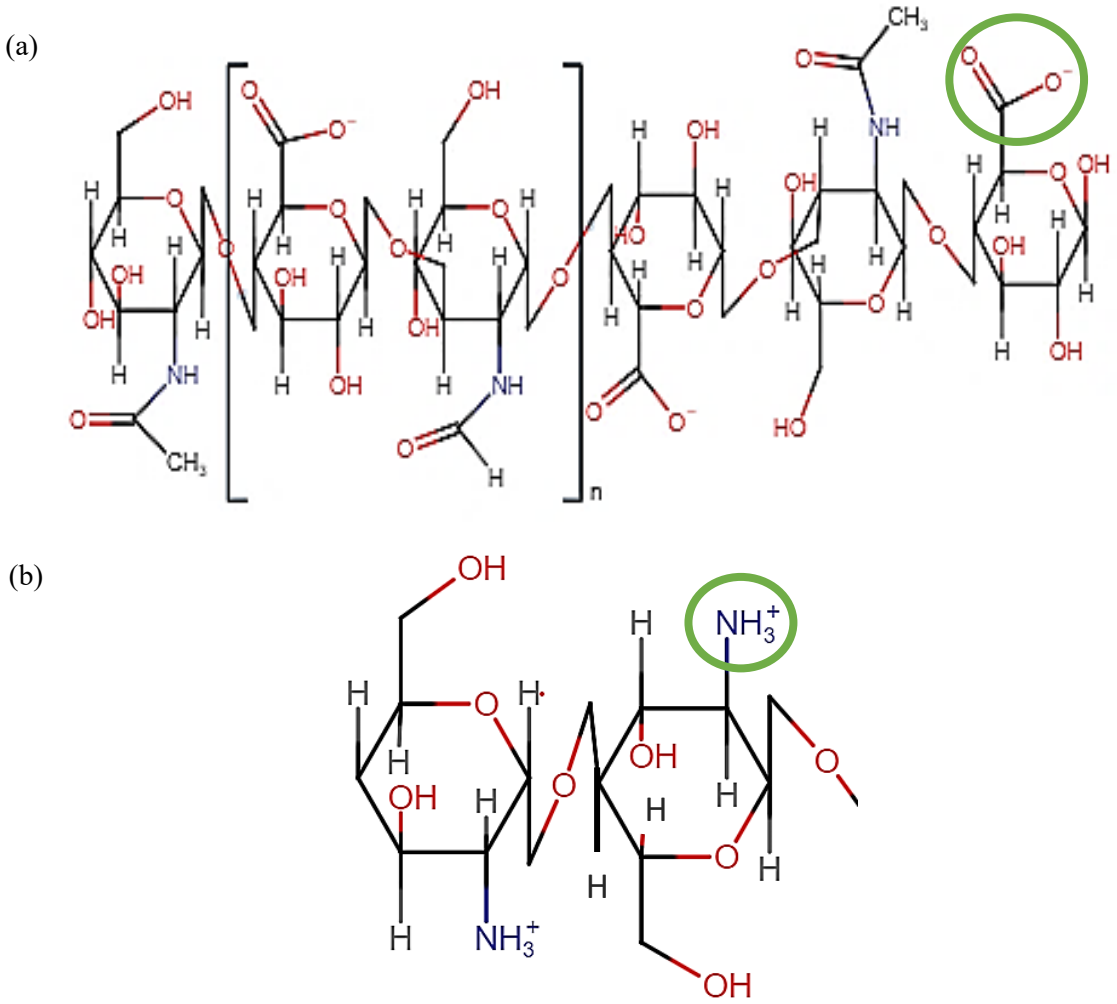

Figure 1.16: A schematic of the molecular structure of HA (a) and chitosan (b). The functional groups primarily involved in polyelectrolyte complexation are highlighted in green.

HA is inherently hydrophilic and is capable of increasing its initial solid volume by a thousand-fold upon hydration [304]. This, combined with its tunable viscoelasticity as a function of both molecular weight and concentration, renders hyaluronic acid an ideal ophthalmic lubrication and comfort agent, particularly in the formulation of artificial tears for the treatment of aqueous deficient dry eye [216], [305]–[307]. Also, as outlined in Section 1.4.1, receptor-mediated endocytosis is upregulated in formulations containing HA as an excipient due to an increase in HA to CD44 receptor binding. Mucoadhesion is enhanced via the electrostatic interaction between the anionic carboxyl groups of HA and the cationic amino moieties present and

hydrogen bond formation between the hydroxyl groups of HA and the glycosylated region of the mucin polypeptide backbones [308]. Chitosan also exhibits excellent mucoadhesive capabilities, primarily due to the electrostatic interaction between its cationic amino groups and both the anionic oligosaccharide-bound ester sulfate moieties and carboxyl groups within the sialic acid termini of mucin chains [309]. Paracellular permeation of chitosan-derived formulations through ocular epithelial cells is also enhanced in both a molecular weight and degree of deacetylation-dependent manner via the interaction between chitosan and the complex of transmembrane proteins within the tight junctions [310]. Namely, chitosan induces the redistribution and subsequent degradation of claudin-4, resulting in a loss in both transepithelial-electrical-resistance and tight junction integrity [311].

Due to the inherent lack of hydrophobic moieties, HA cannot spontaneously self-assemble in aqueous medium to form nano complexes [312]. However, as its carboxylic acid group is negatively charged at physiological pH, HA possesses a negative charge due to deprotonation of the carboxylate anion (pKa 3-4) and can readily complex with cationic species [313], [314]. Such polycations include chitosan and chitosan derivatives, polypeptides such as poly(L-lysine), poly(arginine) and colistin, [315]–[320]. The protonation of the primary amine groups of chitosan is highly dependent on both pH and the degree of deacetylation. The higher the percentage conversion of acetylamine groups to primary amine groups, the more positively charged the chitosan chains become. Possessing a pKa of approximately 6.5, the primary amine groups tend towards deprotonation at physiological pH and therefore need to be maintained under slightly acidic conditions to ensure sufficient electrostatic interaction with their anionic counterparts [321]. As its protonation and aqueous solubility are highly susceptible to the extrinsic attributes of the formulation medium, chitosan is often quaternised to yield more highly positive, aqueous soluble derivatives such as *N,N,N*-trimethyl chitosan [322]. Aside from its proven electrostatic crosslinking with tripolyphosphate via ionotropic gelation, chitosan has also been complexed to anionic polyelectrolytes such as hyaluronic acid, alginate, salecan, carboxymethylcellulose, okra gum, heparin, chondroitin sulfate etc. to yield PEC nanoformulations [294], [323]–[328].

Despite their favourable physicochemical attributes, and their proven ability to form PECs with suitable characteristics for drug delivery, limited research has been conducted into the use of chitosan and HA, both together and individually, in the design of PECs specifically for ophthalmic applications. Therefore, studies which evaluate the potential of chitosan and HA-based PECs for biomedical drug delivery applications will also be discussed.

Although exhibiting a lower percentage mucoadhesion in comparison to the cationic (chitosan:alginate – 2:1 - +12.4 ± 2 mV) and anionic formulations (chitosan:alginate – 1:2 - -7.4 ± 4 mV) Kimna *et al.* [329] demonstrated that a near stoichiometric chitosan and alginate PEC (+4.6 ± 1 mV), exhibited superior efficacy in prolonging the corneal retention of timolol maleate (TM) in an *ex vivo* porcine model. The PECs also facilitated the transportation of over 89% of the theoretical concentration of TM across the corneal barrier. Sustained *in vitro* release of approximately 70% of the loaded TM concentration was achieved from this formulation over 48 hours. However, although the *ex vivo* permeation of a free TM control solution was evaluated, the *in vitro* release profile of this control was not obtained. Therefore, it is difficult to interpret whether the PECs are providing a sufficient diffusion barrier to protect TM from ion-mediated exchange when exposed to a physiological buffer. For example, Battistini *et al.* [211] reported an approximate 10% increase in the cumulative release of TM from sodium hyaluronate-TM ionic complexes over 6 hours in 0.9% NaCl solution in comparison to that obtained when water was used as the receptor medium. A similar trend was observed by Dubashynskaya *et al.* [330] in which over 70% of the loaded colistin concentration complexed to HA was released in 0.01 M phosphate buffer saline (PBS) at pH 7.4 after one hour, whereas no release was detected from the same formulation when placed in deionised water. However, upon comparing the cumulative release of TM from the complexes to that of a TM reference solution, a decrease of approximately 40% was observed. This delayed effect was also evident in the *in vivo* pharmacokinetics study, with the complex achieving a longer time to peak concentration than a 0.5% TM commercial eye drop (Zopirol®). Increased TM bioavailability in rabbit aqueous humour over 4 hours, evidenced by a significantly higher area under the curve (607.7 ± 53.4 µg·h/mL) was also observed for the NaHA-TM formulation in comparison to Zopirol® (400.5 ± 12.2 µg·h/mL). Although a delayed therapeutic release was evident in this study, other studies have highlighted the burst release of charged therapeutics when associated

with PEC formulations, potentially arising from competitive binding between the therapeutic and the polyelectrolyte of equivalent charge. Although maximal complexation between two polyelectrolytes is necessary to form discreet sub-micron-sized particles, care must be taken to ensure there is a sufficient number of residual, charged groups remaining for both therapeutic association and kinetic electrostatic stabilisation. Carton *et al.* [331] highlighted this burst release phenomenon when investigating the potential of HA and poly(arginine) PECs for drug delivery applications. Due to its hydrophilicity and cationic nature at physiological pH, pentamidine (PTM) may have associated with the corona formed via the residual, anionic HA chains within the complexes with high HA:poly(arginine) molar charge ratios, thus resulting in a release of over 50% of the loaded PTM concentration in just 8 hours. Pilipenko *et al.* [332] also observed that anionic oligonucleotide release was faster from chitosan and heparin PECs in comparison to those synthesised from chitosan alone under *in vitro* physiological conditions. An *in vitro* burst release of erythropoietin, equating to approximately 70% of the loaded erythropoietin concentration, from chitosan and HA PECs was also observed by Silva *et al.* [333] within the first half-hour post-exposure to physiological buffer. When placed in a high ionic strength release medium, such as simulated tear fluid, released counter ions can effectively screen and disrupt the charge-to-charge interactions between respective polyelectrolytes [334]. As this study was conducted at a physiological pH in simulated tear fluid, the combined effect of chitosan deprotonation and interpolyelectrolyte charge screening may have facilitated ion-mediated destabilisation, thus resulting in rapid erythropoietin release. However, enhanced *ex vivo* erythropoietin permeation through porcine conjunctiva (0.71± 0.04%), sclera (0.52 ± 0.08%) and cornea (0.17 ± 0.04%), was achieved via HA-chitosan complex encapsulation when compared to the percentage *ex vivo* permeation values obtained for erythropoietin alone (0.52%, 0.35% and 0.07%), further highlighting the ability of chitosan to disrupt the integrity of protein complexes within the epithelial tight junctions [335]. The inherent hydrophilicity of HA explains the increased penetration through the hydrophilic collagen fibrils of the sclera. Chaharband *et al.* [318] also highlighted the complete retinal penetration of trimethyl chitosan and HA nanopolyplexes after one-hour post-IVI in an *in vivo* rabbit model. Retinal distribution of the nanopolyplexes was still detected 120 hours post-IVI. VEGFR-2 siRNA release from the nanopolyplexes was delayed until 24 hours post-

administration. This demonstrated the protective effects of nanopolyplexes against VEGFR-2 siRNA degradation, resulting in a significant reduction in the area of laser-induced corneal neovascularisation in the nanopolyplex-treated group as compared to the groups treated with hyaluronic acid and free VEGFR-2 siRNA. Enhanced TM corneal permeation via association with chitosan and sodium alginate PECs was also demonstrated by Ilka *et al.* [336]. Cumulative TM penetration through a rabbit cornea reached approximately 40 µg/mL after 6 hours, approximately double of what was achieved upon analysis of a TM eye drop solution. Interestingly, neither the charge ratio nor the zeta potential of the chosen chitosan-sodium alginate formulation was reported. Therefore, it was inconclusive as to whether the enhanced *ex vivo* corneal permeation observed was due to the presence of excess chitosan primary amine groups in the formulation.

1.5 RESEARCH PROJECT GOALS AND SCOPE

The aforementioned literature detailed in this section highlights the ever-growing need for ocular drug delivery systems (ODDs) that are capable of delivering a therapeutic with high bioavailability to the intraocular target site, whilst minimising ocular discomfort, reducing the need for frequent administration via invasive methods and maximises patient compliance. Nanoformulations, particularly those synthesised from natural, polymeric biomaterials, are advantageous due to their inherent biocompatibility, biodegradability, cell receptor recognition, and mucoadhesive capabilities. Nanoparticles may also exhibit enhanced permeation through the static anatomical ocular barriers in comparison to free therapeutic molecules due to their sub-micron size.

Many ODDs are developed for the treatment of age-related, neurodegenerative ocular diseases in the mid to late stages of their pathogeneses. Therefore, there is scope to develop ODDs for the preventative or supplementary treatment of such diseases. Such ODDs could provide a solution to the progressive, age-related decline in ocular cell viability by supplementing the intraocular tissues with endogenously produced co-factors that may potentially upregulate the processes involved in cellular longevity, thus prolonging cellular homeostasis, and protecting ocular cells from the deleterious effects of ageing.

This research project aims to develop nanomaterial formulations, formulated via the self-assembly of polyelectrolytes, either by polyelectrolyte complexation or ionotropic gelation, under mild, aqueous formulation conditions. Such polyelectrolyte complexes will be formulated to serve as a carrier for the ocular delivery of NAD+. The entrapment of NAD+ in a nanomaterial formulation intended for ocular administration provides a novel aspect to this project. These nanoformulations could provide a promising platform for the supplementary treatment of ocular cells before the onset of age-related ocular disease pathogenesis.

1.6 THESIS OUTLINE

The thesis is organised into six chapters outlined as follows:

- Chapter 1 includes an extensive literature review detailing current trends and advances in ocular drug delivery systems. A gap analysis, in which the novel aspect of the research project has been identified, has also been conducted.
- Chapter 2 is predominantly focused on the development of the hyaluronic acid (HA) and poly(L-lysine) (PLL) PEC formulation method. The selection of the optimal PEC prototype for NAD+ loading is also detailed.
- Extensive physicochemical characterisation of the NAD+-associated PECs, including an assessment of *in vitro* NAD+ release under microfluidic physiological conditions and formulation stability under set storage conditions, is outlined in Chapter 3.
- Chapter 4 is focused on the development of chitosan and NAD+ complexes via ionotropic gelation to investigate the physicochemical attributes of an alternative formulation in comparison to those of the PECs.
- *In vitro* and *ex vivo* safety and efficacy assessments of the HA and PLL PECs and the chitosan and NAD+ complexes, utilising both immortalised human corneal epithelial cells and porcine corneal and scleral tissues, are presented in Chapter 5.
- Chapter 6 details screening studies conducted for the development of both polymeric and lipoidal nanoparticle formulations intended for NAD+ delivery to the posterior segment.
- Chapter 7 includes a brief synopsis of future work for further investigation based on the completion of the studies conducted in previous chapters and final remarks.

CHAPTER 2:

OPTIMISATION OF CRITICAL FORMULATION ATTRIBUTES FOR POLYELECTROLYTE COMPLEX FORMATION

2. OPTIMISATION OF CRITICAL FORMULATION ATTRIBUTES FOR POLYELECTROLYTE COMPLEX FORMATION

2.1 INTRODUCTION

Supplementation of cells to ameliorate mitochondrial dysfunction and impaired cellular metabolism before the onset of ocular disease is a promising alternative to treating such diseases after the development of debilitating and painful symptoms. However, as discussed in Chapter 1, intravitreal or periocular administration of supplements is unfavourable, primarily due to the disparity between the invasiveness of the administration method and the potential benefit of the treatment itself. Additionally, topical supplementation is limited by poor therapeutic bioavailability at the target site, resulting from the multifactorial interaction between a number of anatomical, physiological, and biochemical intraocular barriers. Nanoparticles, particularly those synthesised from natural polysaccharidic biopolymers, have gained significant traction in the field of ophthalmology research due to their superior capabilities in comparison to conventional ocular drug delivery systems (ODDS) [230], [234], [337], [338]. Previous research on nanoparticles for ODDS has demonstrated an enhanced permeation and retention (EPR) effect through the static intraocular anatomical barriers within the anterior and posterior segments [339], [340]. Nanoparticles can also improve the residence time of therapeutics at an intracellular or extracellular target site by passive or ligand-mediated binding mechanisms [337], [341]–[343].

Many reviews have highlighted the increasing popularity of hyaluronic acid (HA), a hydrophilic glycosaminoglycan, for use as an excipient in nanoformulations intended for ocular applications, primarily due to its inherent hydrophilicity, mucoadhesion, biodegradability via hyaluronidase enzymatic action and wound healing capabilities [344]–[346]. Native HA, with a molecular weight of 1 x 10^6 Da, is present in abundance within the vitreous humour (250 µg/cm^3 – 1,200 µg/cm^3), rendering it highly biocompatible [9]. At physiological pH, carboxylate anions (pKa 3-4) present on the repeating subunits of HA can readily complex with cationic species [313], [314]. As discussed in Section 1.4.3.2, HA cannot form stable complexes via self-assembly due to its limited hydrophobicity. As such, many combinations of biocompatible cationic polyelectrolytes with HA have been studied for the production of stable

polyelectrolyte complexes, including chitosan, poly(arginine) and poly(L-lysine) [303], [319], [331], [333], [347], [348]. The complexation of poly(L-lysine) (PLL) with HA is of particular interest in the current study, as, not only is it a natural antimicrobial polypeptide but its inherent cationic nature allows for enhanced permeabilisation of the negatively charged phospholipid bilayer of cellular membranes [349]–[352]. At physiological pH, PLL adapts a positive charge due to protonation of the α amino group (pKa 11). This, combined with the ability of HA to undergo endocytosis by binding to the extracellular hyaluronic acid-binding domain of the CD44 receptor, could yield a nanoparticulate system capable of the targeted intracellular delivery following ocular administration [255], [259], [353].

Defined as the starting point for polyelectrolyte complexation, Coulombic forces of attraction should drive the association of the carboxylate anion of HA to the α amino group of PLL, followed by conformational adaptation to form PEC molecules [293], [354], [355]. This initial electrostatic interaction between HA and PLL is depicted in Figure 2.1.

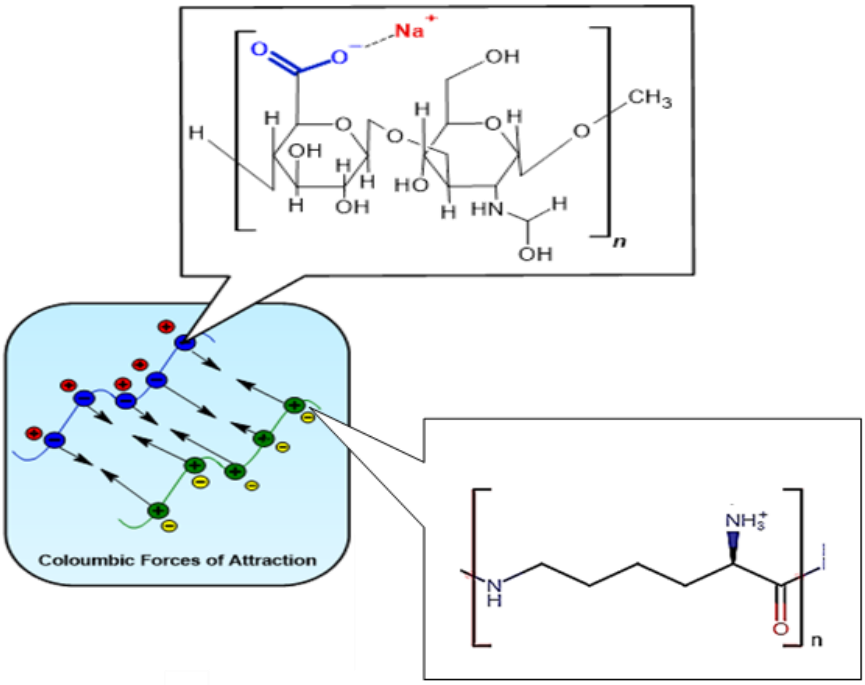

Figure 2.1: The initial formation of HA and PLL PECs, driven by Coulombs forces of attraction. (Blue anions – HA, green cations – PLL, red counterions – sodium cations, yellow counterions – chloride anions).

The complexation of HA and PLL, and the structure of the resulting polyelectrolyte complex, are highly dependent on a number of intrinsic and extrinsic formulation parameters. For example, as highlighted in Section 1.4.3.1, the complexation of polyelectrolytes with a large difference in molecular weight at a non-stoichiometric charge ratio results in the formation of water-soluble PECs [356]. Such PECs tend to be much larger in size in comparison to their colloidally stable counterpart, as the entrapment of water molecules via interaction with single-stranded, hydrophilic PEC segments prevents the formation of a densely packed polyelectrolyte meshwork. The formation of either highly aggregated gelatinous aggregates or turbid colloidal PECs is not only dependent on molecular weight but also the molar charge ratio and concentration of the polyelectrolytes in solution [357], [358]. In the absence of electrostatic stabilisation via residual surface charges, hydrophobic interactions between the charge-neutralised hydrophobic regions of the PECs can predominate, thus decreasing the surface-to-surface separation distance and increasing the formation of attractive Van der Waal's forces [359]–[361]. The higher the polyelectrolyte concentration in the bulk medium, the higher the likelihood of interparticle aggregation [362]. However, the molar charge ratio must also be fine-tuned to allow for maximal complexation without comprising stability via electrostatic repulsion. As HA and PLL are considered weak polyelectrolytes, the pH of the bulk medium must be carefully controlled to ensure that their respective charge densities, and the charge ratio of the resulting PECs, are maintained. The ionic strength of the medium can also significantly impact the electrostatic stabilisation of PECs [363]. Although a low concentration of counter ions can aid the thermodynamic rearrangement of the primary PEC structures during secondary complexation, higher counter ion concentrations can result in shrinkage of the counter ion cloud surrounding neighbouring PECs and screening of the interparticulate electrostatic repulsive forces, thus promoting aggregation via predominating forces of attraction. Loss of intrinsic ion pairs and subsequent dissociation of the charge-neutralised, insoluble PECs can occur above a critical ionic strength, resulting in the reformation of the polyelectrolytes [364], [365].

The primary aim of this body of work was to investigate and optimise the critical formulation parameters required for the formation of HA and PLL-based PECs. Complexation pH was determined using potentiometric titrations. The addition method was selected based on the

minimal formation of gel aggregates. PEC purification via both centrifugation and dialysis and the optimal method was chosen based on PEC stability and yield. Fourier transform infrared spectroscopy (FT-IR) and dynamic light scattering (DLS) analysis were utilised to determine the optimum complexation time. DLS analysis, in combination with ultraviolet-visible (UV-Vis) spectroscopy, was used to assess the effect of molar charge ratio on PEC size and turbidity. Complex stoichiometry and enthalpic and entropic changes, both in the presence and absence of ionic medium, were assessed via isothermal titration calorimetry (ITC). Finally, the effect of lyophilisation on PEC size was assessed by measuring physicochemical size parameters using DLS analysis following freezing and lyophilisation of PECs, with and without cryoprotectant moieties.

2.2 EXPERIMENTAL METHODOLOGY

2.2.1 Materials

Hyaluronic acid sodium salt (MW: 200 kDa – 500 kDa) (HMWHA), hyaluronic acid sodium salt (MW: 80 kDa to 100 kDa, purity > 91%) (LMWHA) and ε poly (L-lysine) (MW: 3.5 kDa – 4.5 kDa, purity > 98%) (PLL) were purchased from Carbosynth Ltd. (Berkshire, England). Additional quantities of LMWHA (80 kDa to 100 kDa) were later purchased from Cymit Quimica (Barcelona, Spain). HPLC grade methanol (purity ≥ 99.9%) and potassium dihydrogen phosphate (purity > 99%) were purchased from Fischer Scientific Ireland (Dublin, Ireland) and Sigma Aldrich Ireland Ltd. (Wicklow, Ireland), respectively. D-(+)-trehalose dihydrate (purity ≥ 99 %), was also purchased from Sigma Aldrich Ireland Ltd. (Wicklow, Ireland). SLS select 50 mL sterile polypropylene centrifuge tubes were purchased from Analab (Antrim, Northern Ireland). Ultra-pure water was prepared in-house using an Evoqua® Water Technologies purification system. Sodium hydroxide (NaOH) (purity ≥ 97%) and hydrochloric acid (HCl) (ACS reagent grade) were purchased from Merck KGaA (Darmstadt, Germany).

For the in-house preparation of phosphate buffer saline (PBS), the following materials were used: Sodium chloride (NaCl) (purity ≥ 99.5%), potassium chloride (KCl) (purity ≥ 99.0%), disodium hydrogen phosphate (Na_2HPO_4) (purity ≥ 99.0%) were purchased from Merck KGaA

(Darmstadt, Germany). Potassium dihydrogen phosphate (KH_2PO_4) (purity +98%) was purchased from Fisher Scientific Ireland (Dublin, Ireland). Pierce™ Buffer, PBS Solution Concentrate (20X) was also purchased from VWR International (Radnor, Pennsylvania, United States).

2.2.2 Potentiometric Titration for Determination of Optimal Complexation pH

The optimal complexation pH was calculated based on a method adapted from the study conducted by Kaur *et al.* [366]. pH adjustments were conducted using a pH meter and glass electrode (Eutech ®, Thermo Fisher Scientific, U.S.). Briefly, 20 mL aliquots of 0.1% (w/v) HA and PLL solutions were adjusted to pH values of 2 and 10, respectively (2 pH units either above or below the pKa of the functional group of interest) and titrated against 20 µL aliquots of either 0.1 M NaOH and 0.1 M HCl. Changes in pH were recorded after the addition of each aliquot. Using first derivative titration curves, the pKa of both HA and PLL were identified and used to plot pH-dependent fractional composition diagrams. The point of intersection on the resulting diagram highlighted the pH at which maximal ionisation of both HA and PLL was achieved. The ionised fractions of both HMWHA and PLL were calculated using Equation 2.1.

$$\frac{[H_3O^+]}{[H_3O^+] + \mathrm{Ka/Kb}} \text{ (Protonated)} \quad \frac{[\mathrm{Ka/Kb}]}{[H_3O^+] + \mathrm{Ka/Kb}} \text{ (Deprotonated)} \qquad \text{Equation 2.1}$$

where, $[H_3O^+]$ is the hydronium ion concentration at each respective pH value and Ka/Kb is the acid or base dissociation constant of HA and PLL, calculated using the antilog of the respective pKa and pKb values of HA and PLL.

2.2.3 Preparation of Blank PLL Polyelectrolyte Complexes

Solutions of HMWHA, LMWHA, and PLL were prepared in 50 mL polypropylene centrifuge tubes at final concentrations of 2% (w/v) in ultrapure water. The pH of each solution was adjusted to pH 5.5 using 0.1 M NaOH.

Under continuous stirring at 200 rpm, the polyelectrolyte in default was added to the polyelectrolyte in excess, either via a ‘one-shot’ or dropwise addition at a constant flow rate, to yield PECs with total concentrations of 2% (w/v) and molar charge ratios of between 0.5

and 2. If necessary, the pH of the resulting complexes was readjusted to pH 5.5. Complexation was monitored using dynamic light scattering and Fourier-Transform infrared spectroscopy at 30 minutes and 24 hours in an orbital shaker-incubator (ES-20, Grant Instruments, England), under a set temperature and shaking speed of 25 °C and 200 rpm, respectively. The molar charge ratio of each PEC formulation was calculated using Equation 2.2.

$$\frac{n^-}{n^+} = \frac{\text{Molar units of charge of HA } [COO^-]}{\text{Molar units of charge of PLL } [NH_3^+]} \qquad \text{Equation 2.2}$$

PECs prepared with excess of PLL exhibited an MCR of < 1 ($(COO^-)/(NH_3^+) < 1$). Conversely, PECs prepared in the presence of excess HA carboxylate anions possessed an MCR of > 1 ($(COO^-)/(NH_3^+) > 1$).

A list of the formulations mentioned throughout the chapter is highlighted in Table 2.1.

Table 2.1: The formulation parameters of the PEC formulations (F1-F7).

Sample Name	F1	F2	F3	F4	F5	F6	F7
Concentration (% (w/v))	2	2	2	2	2	2	2
HA:PLL Charge Ratio	0.96	0.96	2	0.5	0.75	1	1.5
HA Average Molecular Weight (kDa)	350	90	90	90	90	90	90

2.2.4 Purification of Polyelectrolyte Complexes

2.2.4.1 Ultracentrifugation

Following complexation, the PECs prepared were centrifuged at various speeds, ranging from 4804 to 16,000 rpm for 50 minutes at 4 °C using a refrigerated bench-top centrifuge (SIGMA 3-18KS, Focus Scientific, Ireland). The PECs retained were redispersed in a given volume of ultrapure water, adjusted to pH 5.5, and vortexed for 30 seconds using a vortex mixer (Fisherbrand™, Fisher Scientific, Ireland).

2.2.4.2 Dialysis

10 mL of crude complex was pipetted into 1000 kDa molecular weight cut-off (MWCO) dialysis tubing in 1 litre of ultrapure water, adjusted to pH 5.5. Dialysis proceeded for a total of 48 hours, during which, the dialysis medium was changed twice daily.

2.2.4.3 Lyophilisation

Following isolation, purified PECs were frozen at -20 °C for 4 hours. The frozen aliquots were then lyophilised for 48 hours in a freeze drier (Freezone 2.5 freeze drier, Labconco, United States), with and without the addition of 1% (w/v) trehalose dihydrate cryoprotectant solution, before further characterisation.

2.2.5 Physicochemical Characterisation Methods

2.2.5.1 Fourier-Transform Infrared Spectroscopy (FT-IR)

FT-IR analysis was conducted using a 660-IR & 610-IR Excalibur Series Biorad Elementec IR spectrometer (Agilent Technologies, Ireland). The resulting spectra were generated between the frequencies of 4000 cm^{-1} and 600 cm^{-1}, at a resolution of 2 cm^{-1} with a total of 32 overlay scans. Approximately 10 mg of each starting reagent or PEC lyophilisate was weighed and subsequently ground with potassium bromide (KBr) in a 1:5 ratio. Sample discs were prepared by pressing the resulting powder using an Atlas Power 25T pressure hydraulic press. A background spectrum of both the empty sample holder and a blank KBr disc was obtained to calibrate the IR spectrometer and correct for light scattering losses and absorption peaks arising from moisture absorbed by the KBr. Such spectra were subtracted from that of the sample to yield baseline-corrected spectra.

2.2.5.2 Dynamic Light Scattering Analysis (DLS)

Dynamic light scattering analysis was initially conducted using a Microtrac Nanotrac Wave II analyser and Microtrac Flex 11.1.0.8 software (Microtrac MRB, United States). Approximately 1 mL of each formulation was placed into the sample cell maintained at 25 °C. A 60 second set zero measurement was performed before each sample run. A runtime of 120 seconds for particle size measurement and 60 seconds for zeta potential measurement was selected for zeta-enabled sample runs.

A Malvern Zetasizer Ultra-Red analyser and ZS Xplorer software (Particular Sciences Ltd., Ireland) were also used for particle size analysis and the method used was as follows. Approximately 1 mL of each formulation was pipetted into 12 mm square, disposable polystyrene cuvettes (DTS0012). A separate 1 mL aliquot was placed into a U-shaped folded capillary zeta cell with gold-plated beryllium/copper electrodes for zeta potential (ZP) measurements. An equilibration time of 120 seconds for both particle size and ZP measurement was selected, with a set temperature of 25 °C, a backscattering angle of 173° and a refractive index of 1.39. Where appropriate, DLS analysis of the formulations was conducted in triplicate.

2.2.5.3 Percentage Transmittance Analysis (UV-Vis)

Approximately 2 mL of PEC samples with varying molar charge ratios were placed into a quartz cuvette. The percentage transmittance of the PEC solutions was recorded by running simple reads of the solution in transmittance mode at 500 nm using a UV/Vis spectrophotometer (Cary® 50, Agilent Technologies, Ireland). A blank run using ultrapure water at pH 5.5 was carried out after analysis of each sample.

2.2.5.4 Isothermal Titration Calorimetry (ITC)

HA and PLL solutions were prepared in accordance with the optimised characterisation parameters for ITC described in Table 2.2. The concentrations of polyelectrolytes for the respective titrations were chosen to yield molar charge ratios of 7.48 to 0.33 (PLL vs. HA) and molar charge ratios of 0.15 to 3.2 (HA vs. PLL). These molar charge ratio ranges were selected to investigate a highly negative (> 1) and highly positive (< 1) charge ratio that eventually would pass through the stoichiometric charge ratio (= 1) during the titration.

Table 2.2: Optimised experimental parameters utilised for ITC titrations of PLL (titrant syringe) vs. HA (sample cell) and HA (sample cell) vs. HA (titrant syringe).

Titration (titrant vs. titrand).	Sample Cell Volume (µL)	Conc. Sample Cell µM)	Total Syringe Volume (µL)	Conc. Syringe Volume (µM)	Injection Volume (µL)	Stirring Speed (rpm)	Injection Interval (s)
PLL vs. HA	300	0.5	50	71	2	200	180
HA vs. PLL	300	34.75	50	215.6	1	200	300

ITC analysis was conducted at 25 °C using a NanoITC Low Volume® isothermal titration calorimeter and Nanoanalyze software (Version 3.12.5) (TA Instruments, United States). Before use, the calorimeter was calibrated by conducting three titrations in accordance with the NanoITC test kit; a double-distilled (DDI) water-DDI water titration (minimal heat change – validates cleanliness of the instrument), a calcium chloride-ethylenediaminetetraacetic acid (EDTA) titration (validates accuracy of the binding affinity with a standard value), and a second DDI water-DDI water titration. Heats of dilution were corrected for by titration of the ligand into sample buffer alone under equivalent conditions. Briefly, the sample cell was flushed repeatedly with the solution in which the PEC reagents were prepared and then filled with either 300 µL of HA or PLL solution. The reference cell was filled with deionised water, followed by insertion of the reference needle. 50 µL of either HA or PLL solution was then loaded into the titrant syringe, followed by insertion of the syringe into the burette handle. The burette handle was then installed into the calorimeter. Following equilibration to a stable calorimeter heat reading, 20 injections of a set volume of titrant were slowly injected into the sample cell containing the titrand. Enthalpic fluctuations, indicated by changes in the heat intensity peaks, were continuously monitored throughout the titration, with all titrations conducted at 25 °C.

2.2.6 Statistical Analysis

Statistical analysis was conducted using Minitab® 17 Statistical Software (Penn State University, State College, PA, U.S.A). 2-sample t-tests were used throughout to determine

whether a statistically significant difference existed between the means of two sample populations when comparing the same variable. Ryan-Joiner normality tests and 2 Variances tests were also conducted to assess whether the experimental data was normally distributed and whether the standard deviations of two sample populations were equal to the hypothesised ratio, respectively. The generation of a p-value of < 0.05 was considered statistically significant.

2.3 RESULTS & DISCUSSION

2.3.1 Potentiometric Titrations for Complexation pH Determination

As shown in Figure 2.2, pKa values of 2.33 and 6.98 for the anionic carboxylate anion of HA and the α-amine group of PLL, respectively, were identified from the first derivative potentiometric titration curves. Such pKa values were then used to plot the fractional composition diagram.

(a)

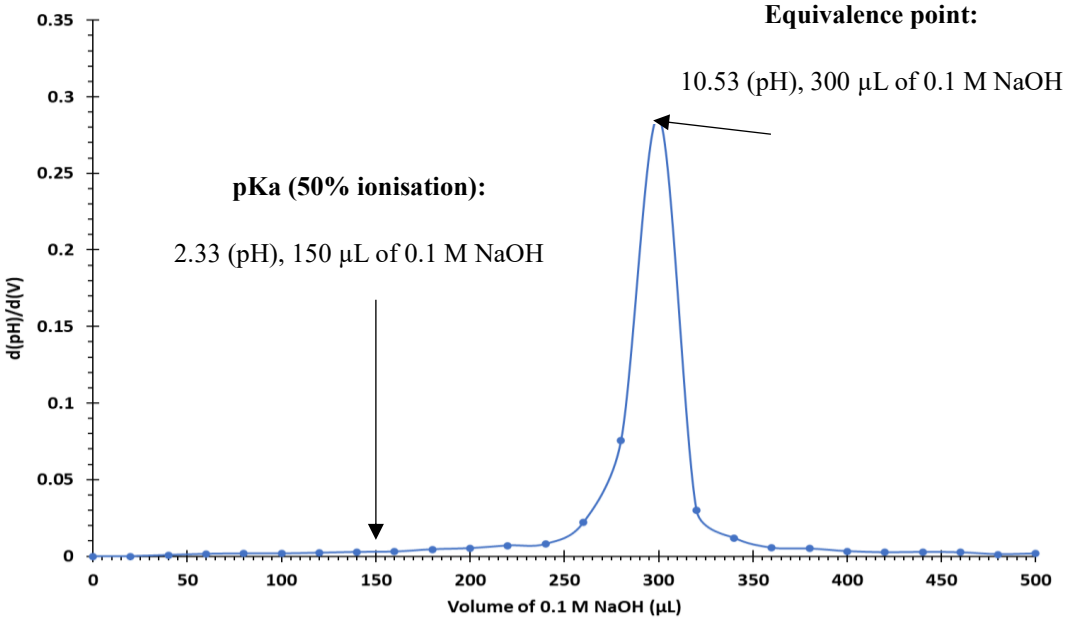

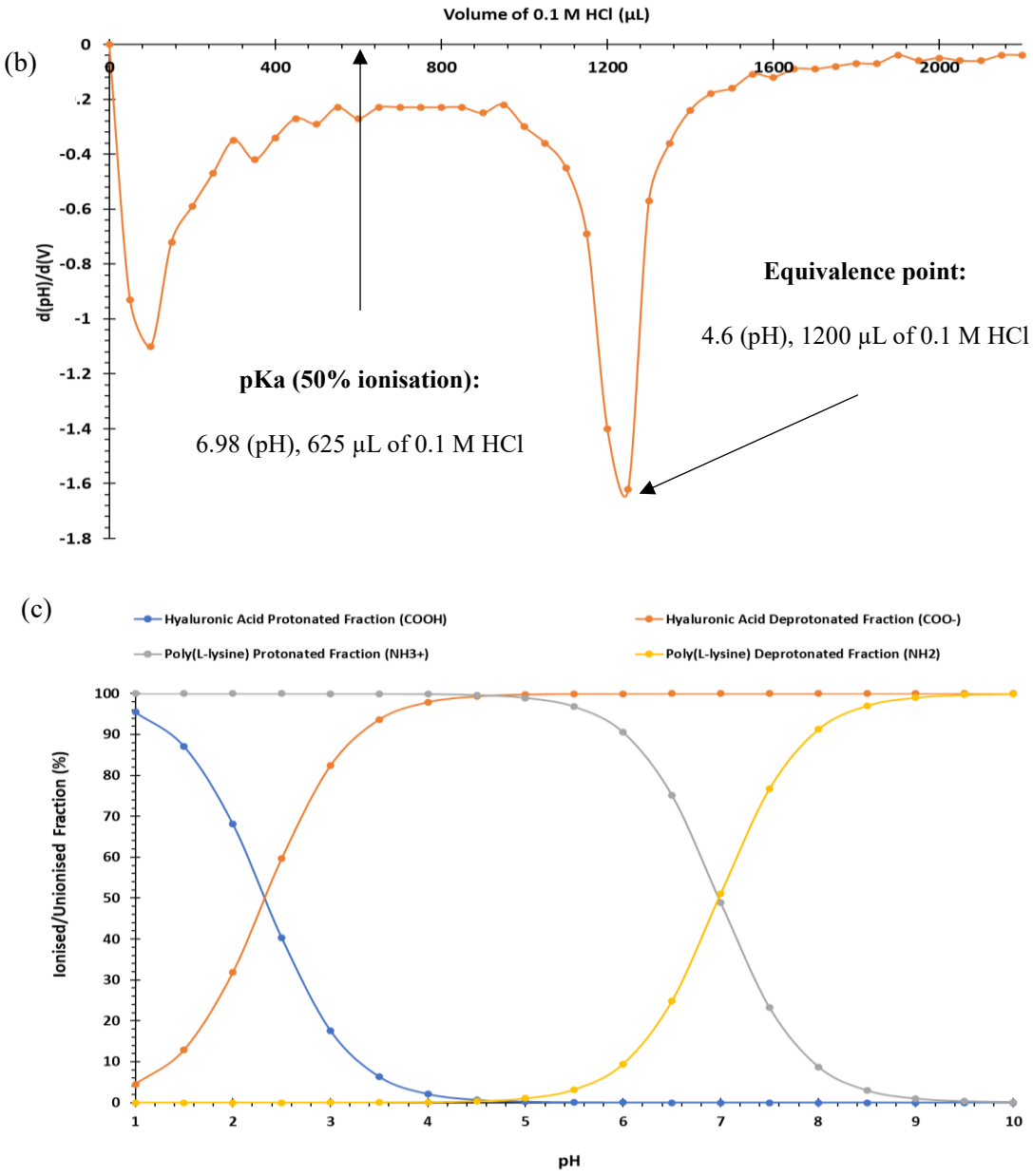

Figure 2.2: First derivative pH titration curves of (a) HA and (b) PLL. The fractional composition diagram, showing the percentage ionisation of each species at each pH value from pH 1 to pH 10, is shown in (c). (HA protonated fraction (COOH), – HA deprotonated fraction (COO^-), – PLL protonated fraction (NH_3^+), – PLL deprotonated fraction (NH_2).

HA and PLL are considered weak polyelectrolytes. Therefore, the pH of the formulation medium can significantly influence the charge density of the respective polyelectrolytes and

subsequent complexation [357], [367], [368]. Within the lower pH range of 1-2, the carboxylic acid groups of HA primarily exist in a neutral form (COOH – 68.1% to 95.5%) and are unlikely to undergo electrostatic interaction due to their weak charge density. Similarly, at a pH of above 9, the deprotonated state of the PLL α–amine group (NH_2) predominates (89.0 – 98.8 %), thus significantly decreasing the α–amine groups available for complexation with HA carboxylate anions. Between pH values of 5 to 6, 99.8% to 99.9% of HA carboxylate groups were deprotonated (COO^-). Similarly, 90.5% to 99.0% of the α–amine groups of PLL are protonated (NH_3^+). Complexation is likely to occur between pH values of 3 and 8. However, based on the reduction in HA carboxylic acid group deprotonation from 82.4% to 59.7% with a concurrent reduction in pH from 3 to 2.5 and a similar reduction in α–amine group protonation above a pH of 6.5, maximal complexation cannot be achieved. A pH range of 4.5 to 5 was chosen as the optimal pH for complexation due to the high percentage of HA and PLL ionisation, and the formation of negligible quantities of both protonated HA carboxylic acid groups (0.02–0.2%) and deprotonated PLL α–amine groups (1.0-9.5%). Similar pH values of 6 and 7 have been reported for the pH adjustment of ε-poly(L-lysine) and hyaluronic acid solutions before complexation [13,49].

2.3.2 Optimisation of Polyelectrolyte Addition: Dropwise Titration or One-Shot Addition

Two addition methods for the formation of 2% and 5% (w/v) PECs at varying charge ratios, using both HMWHA and LMWHA, were investigated as part of this study. The dropwise addition of the polyelectrolyte in default to the polyelectrolyte in excess during complexation produced homogenous, turbid PEC dispersions. By adding all of the polyelectrolyte in default to the polyelectrolyte in excess at once, large quantities of gelatinous aggregates were formed. Gel formation following one-shot polyelectrolyte addition was independent of HA molecular weight.

The rate of primary complexation is controlled by the rate of collision of the respective polyelectrolyte chains [50,51]. A one-shot addition of the polyelectrolyte solutions to one another may have resulted in an instantaneous collision and subsequent neutralisation of almost all of the available charges on the respective chains, leading to a reduction in intercomplex

repulsion and the formation of thermodynamically stable gel-like aggregates. Dropwise addition may allow for a more gradual formation of interpolyelectrolyte electrostatic interactions and the establishment of intercomplex repulsive forces during secondary complex reconfiguration, thus improving overall PEC stability. Similar to our study, Bravo *et al.* [369] observed that the use of a dropwise titration method minimised gel aggregate formation during the formation of calf-thymus DNA and elastin-like polypeptide complexes. Gel aggregate formation was also found to be independent of HA molecular weight. However, Van Le *et al.* [291] observed irreversible aggregate formation during the dropwise addition of HA to diethylaminoethyl dextran and vice versa. This was attributed to the polyelectrolytes reaching a stoichiometric charge ratio during complexation before adjustment to the final charge ratio. However, this only occurred when the polyelectrolyte in excess was added to the polyelectrolyte in default, highlighting the sensitivity of this addition method to the mixing order [370].

2.3.3 Complexation Time

2.3.3.1 Dynamic Light Scattering Analysis

The formation of complexes over time was initially investigated by observing changes in complex size from 30 minutes to 24 hours. As shown in Table 2.3, an increase in D50 value (601 ± 56 nm vs. 1237 ± 1105 nm (n = 2)) was observed between sample aliquots taken at 30 minutes and 24 hours. As a crude PEC was used to monitor changes in complexation as a function of time, the large variability in particle size and presence of bimodal size distributions may be attributed to the lack of work up and purification following PEC formation.

Table 2.3: The physicochemical size parameters obtained upon analysis of a reference PEC (HA:PLL mass ratio of 1:1) at set time points between 30 minutes and 24 hours. Data is expressed as the mean size or polydispersity index (PDI) ± S.D (n = 2).

Time (h)	Size (D50 value) (nm)	Polydispersity Index (PDI)	Size of Primary Peak in Particle Size Distribution (nm)	Size of Secondary Peak in Particle Size Distribution (nm)
0.5	601 ± 56	1.519 ± 0.169	546 (67.8%) (n =1) 475 (63.8%) (n = 2)	5920 (32.2%) (n = 1) 5840 (36.2%) (n = 2)
1	2369 ± 3396	1.203 ± 0.722	470 (46.3%) (n = 1) 439 (80.8%) (n = 2)	5900 (53.7%) (n = 1) 5920 (19.2%) (n = 2)
6	548 ± 51	0.936 ± 0.315	529 (69.1%) (n = 1) 485 (88.9%) (n = 2)	5960 (30.9%) (n = 1) 5580 (11.1%) (n = 2)
24	1237 ± 1105	0.208 ± 0.158	1446 (57.7%) (n = 1) 322 (48.5%) (n = 2)	5060 (42.3%) (n = 1) 1712 (45.6%) (n = 2)

Previous studies have utilized complexation times of between 10 minutes and 1 hour, based on the immediate formation of colloidal suspensions with increasing opacity [371]–[373]. Based on the principles of polyelectrolyte complexation proposed by Tsuchida *et al.* [374] and Veis *et al.* [375], primary complexation occurs almost immediately post addition (less than 5 μs) of two polyelectrolytes of opposing charge to one another due to the kinetically driven formation of Coulomb's interactions. As depicted in Figure 2.3, to attain thermodynamic stability, polyelectrolyte chains undergo secondary intracomplex reconfiguration to correct for any conformational changes or distortions that occurred during the initial primary complexation. It has been reported that this complexation proceeds within the order of an hour [376]. The trends observed suggest that secondary complexation has taken place at the 24-hour time point, with primary charged PECs tending towards aggregation into restructured, ordered, secondary PECs via subsequent Coulomb's interactions [354], [377].

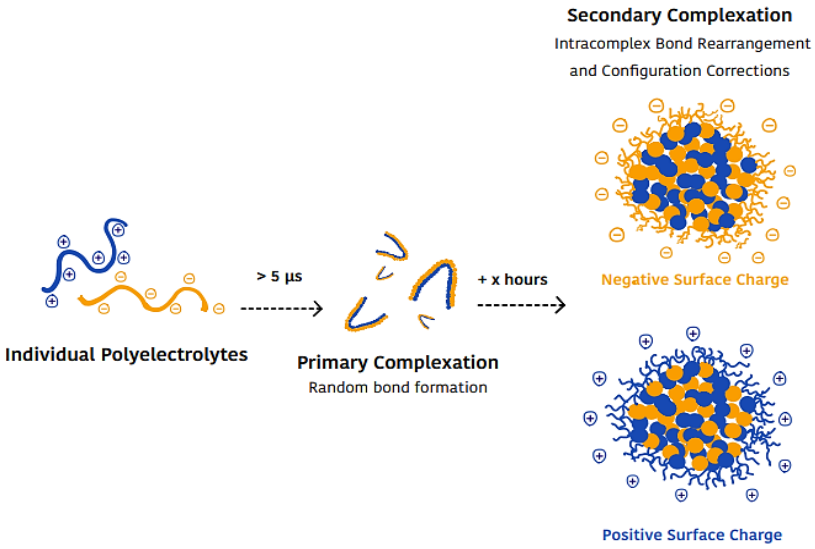

Figure 2.3: Mechanism of PEC formation, beginning with instantaneous nucleation of primary PECs, followed by the formation of ordered, charge-stabilised secondary PEC structures.

2.3.3.2 Fourier-Transform Infrared Spectroscopy (FT-IR) Analysis

The IR absorption bands specific to the stretching and bending vibrations of the functional groups of both HA and PLL are highlighted in Table 2.4.

Table 2.4: The characteristic IR absorption bands identified from the FT-IR spectra of both HA and PLL.

Polyelectrolyte	Wavenumber (cm^{-1})	Functional Group	Reference
HA	3372-3440	Overlap of polysaccharidic (O-H) and (N-H) stretching	[378]
	1670	Amide I (C=O) stretching	[378], [379]
	1616	Symmetric carboxylate (COO-) stretching	
	1565	Amide II (N-H) bending and (C-N) stretching	
	1411	Asymmetric carboxylate (COO-) stretching	
	1045 – 1077	Overlap of primary and secondary alcohol (C-O) stretching	[380]
PLL	3241 – 3442	Symmetric and asymmetric primary amine (N-H) stretching	[381]
	2921	Alkane (C-H) stretching	[378]
	1671	Amide I (C=O) stretching	[382]
	1560	Amide II (N-H) bending and (C-N) stretching	
	1540	Primary amine (N-H) in-plane scissor bend	[383]
	664	Primary amine (N-H) out-of-plane bend	

The change in the IR absorption bands from 30 minutes to 24 hours, shown in the spectra in Figure 2.4, supports the trends observed following the analysis of PEC size as a function of time. The immediate disappearance of the absorption bands representing the asymmetric stretching of the HA carboxylate (COO^-) functional group at 1411 cm^{-1}, followed by a reduction in the in-plane scissor bend of the primary amine N-H bonds of PLL at 1540 cm^{-1} from 30 minutes to 24 hours indicate the continual complexation of HA to PLL over time [380], [381].

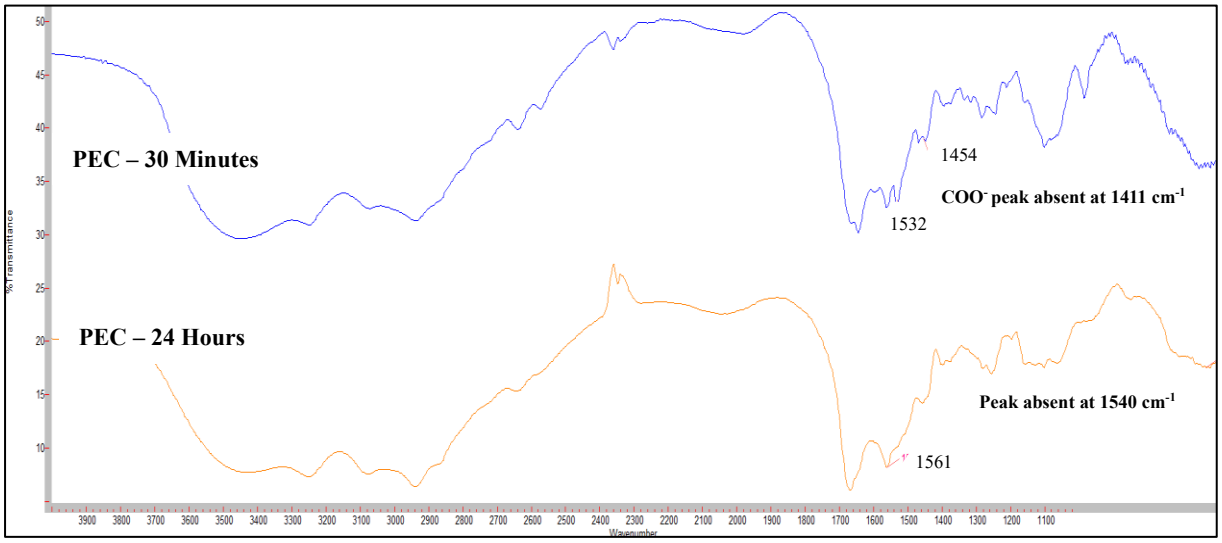

Figure 2.4: Comparative FT-IR spectra of a HA and PLL PEC sample, withdrawn at 30 minutes and 24 hours.

Broadening of the IR absorption bands representing the hydroxyl groups and amide and amine N-H groups of HA and PLL within the range of 3200 cm^{-1} to 3400 cm^{-1} suggests the development of hydrogen-bonded bridges between the electronegative atoms of HA and PLL [384]. The same trend was observed after 24 hours. However, the absorption peak broadened further and had become more intense at the 24-hour time point. This was presumably attributed to the formation of intercomplex hydrogen bonds, directly associated with hydrophobic aggregation following secondary complexation. The amide II absorption band within the PEC spectrum appeared at 1561 cm^{-1} at both time points, a downward shift of 4 cm^{-1} from that within the HA spectrum. As highlighted by Barroso *et al.* [379] when analysing chitosan and hyaluronic acid PECs via FT-IR analysis, a shift in the amide absorption bands may be

attributed to increased interaction between the respective polyelectrolytes. These interactions are primarily characterised by the formation of hydrogen bonds between the hydroxyl groups of HA and the lone pair of electrons on the nitrogen atoms of the amide groups of PLL and other HA chains [385], [386]. The peak corresponding to the stretching of the carbon to nitrogen bonds within the primary amine group of PLL also shifts from 1245 cm^{-1} to 1258 cm^{-1} over 24 hours. Due to complexation, the oxygen atoms of the carboxylate group of HA and the nitrogen atom of the primary amine of PLL become close in proximity to one another. As these atoms are highly electronegative, the length of the carbon to nitrogen bond of the primary amine will decrease, potentially causing the absorption peak to shift to a higher wavenumber, in this case, a shift from 1245 cm^{-1} to 1258 cm^{-1} in 24 hours.

2.3.4 Effect of Ultracentrifugation Speed on Complex Formation

The retention of a sufficient quantity of PECs following formation, work-up and purification for further characterisation was of critical importance. Purification of the PEC formulations via dialysis was initially carried out. The purification of nanomaterials via dialysis is advantageous as it allows for the physical separation of the nanomaterial from residual starting materials via diffusion without exposure to potentially destructive forces [387]. Dialysis has been used previously in the purification of self-assembled HA-based nanomaterial formulations [388]–[390]. However, PEC yields of below 1% were obtained following lyophilisation of the PECs purified via dialysis. This was attributed to the destabilisation of the PECs over 48 hours in the receptor medium. HA and PLL both exhibit inherent hydrophilicity [70], [391]. If destabilisation occurred over the dialysis period, both HA and PLL would have been displaced into the surrounding receptor medium. Therefore, PEC purification via centrifugation was investigated further.

Centrifugation of the F1 formulation at 16,000 rpm resulted in the retention of a PEC yield below 10% (8.1 ± 0.8% (n = 2)). Reducing the speed to 13,000 rpm over the same timeframe did not significantly improve complex yield (2.8 ± 1.9% (n = 2)) ($p = 0.069 > 0.05$). Also, no significant difference ($p = 0.866 > 0.05$) was found between the yields of the F1 and F2 (2.4 ± 2.0% (n = 2)) formulation following centrifugation at 13,000 rpm, suggesting that complex destabilisation under centrifugal force may be independent of HA MW. This contradicts the

observations made by Oyarzun-Ampuero *et al.* [392], in which PEC prepared with HMWHA (~165 kDa) and poly(arginine) (5-15 kDa), could be successfully isolated at high centrifugation speeds whereas those prepared with LMWHA (~29 kDa) could not be retained. This was primarily attributed to the larger number of consecutive associated residues between poly(arginine) and the longer HMWHA chains during complexation. The formation of such neutralised, hydrophobic regions leads to their entrapment within the core of the complexes formed, thus imparting considerable stability to the overall nanostructure. In comparison, the PLL utilised in this study has an average MW of 4.5 kDa. Therefore, being of higher MW, the poly(arginine) could undergo residue-to-residue interactions more readily with HMWHA than poly(L-lysine), allowing for enhanced interaction and intracomplex stability during centrifugation. Centrifugation of the F2 formulation at 7,000 rpm led to a slight improvement in complex yield of 8.5 ± 2.1% (n = 2). However, this was not statistically larger than the yield obtained after centrifugation at 13,000 rpm ($p = 0.10 > 0.05$).

F1 and F2 were prepared with a near stoichiometric molar charge ratio of 0.96. The pellets obtained following centrifugation of F2 at 7,000 rpm were hardened, gelatinous aggregates that could not be re-dispersed readily in ultrapure water following isolation. This provided the first indication of PEC instability at near-stoichiometric charge ratios. At a molar charge ratio of 0.96, there are fewer counter ions present in the electrical double layer (EDL) of such PECs as counter ions will not self-associate with complexes with low electrostatic surface potential. Therefore, if such PECs come into close proximity to one another, attractive van der Waals forces and intercomplex hydrophobic interactions will predominate over electrostatic repulsion, resulting in aggregation. As a starting point, PECs with a non-stoichiometric molar charge ratio of 2 were prepared, based on the upper limit for charge ratios used in previous studies [371], [393], [394]. No significant difference in yield was obtained following centrifugation of F2 (8.5 ± 2.1% (n = 2)) and F3 (3.7 ± 2.0 % (n = 2)) at 7,000 rpm ($p = 0.147 > 0.05$). However, pellets isolated from the latter PECs could be redispersed easily following centrifugation and lyophilisation. Theoretically, the non-stoichiometric PECs should exhibit enhanced electrostatic stabilisation in comparison to their stoichiometric counterpart, presumably attributed to the mutual repulsion of the free carboxylate anions of LMWHA on the surface.

As centrifugation would eventually be conducted in Amicon® ultracentrifuge tubes to isolate free NAD+ from the NAD+ that was associated with the PECs during formation, PEC yield was also investigated under these conditions. 4000g, equating to approximately 4804 rpm, is the maximal centrifugal force for such ultracentrifuge tubes. Centrifugation of the F3 formulation using this centrifugation programme led to an increase in yield for the F3 formulation of over 58.5 ± 7.3% (n = 3) ($p = 0.018 > 0.05$), rendering it the most suitable option for the recovery of a suitable PEC yield for further characterisation whilst attaining PEC stability upon dispersal following purification.

2.3.5 Charge Ratio – A Critical Quality Attribute

In accordance with the proposed "core-shell" model for colloidal polyelectrolyte complex formation as shown in Figure 1.15, electrostatically stable PECs are formed via the formation of a charge-neutralised, stoichiometric core, encompassed by a corona composed of excess polyelectrolyte chains bearing residual charges [282], [286], [370]. Meta-stabilisation of the colloidal dispersion is attained by the electrostatic repulsion of the like charges on the surface of the PECs [395]. The sign of the residual charge is dependent on the polyelectrolyte in excess. However, as previously reported by Drogoz *et al.* [396], if one polyion is added in high excess over the other (residual charges are present in great excess), large amounts of the excess polyion will remain dissolved in the reaction medium as there is an insufficient quantity of the other polyion present to initiate primary PEC nucleation. The ionisable groups of the excess polyion will presumably bond to the water molecules via the formation of ion-dipole interactions, resulting in enhanced solvation of the free polyelectrolyte chains. Such polyelectrolyte chains may be removed during the sublimation of the aqueous medium during lyophilisation, thus decreasing the yield of PEC retained after purification. Therefore, for maximal, electrostatically-stabilised PEC formation, a balance is required. Non-stoichiometric charge ratios must be used to prevent the formation of neutralised complexes that will flocculate due to the formation of van der Waals attraction forces [334]. However, the charge ratio must not be increased or decreased to such an extent that the PECs dissolve into the polyelectrolyte phase.

2.3.5.1 Effect of Charge Ratio on Physicochemical Size Parameters

The tendency of the HA and PLL PECs formulated to aggregate at near stoichiometric charge ratios, as evidenced by a drastic increase in particle size from sub-micron to micron-sized particles, is depicted in Figure 2.5.

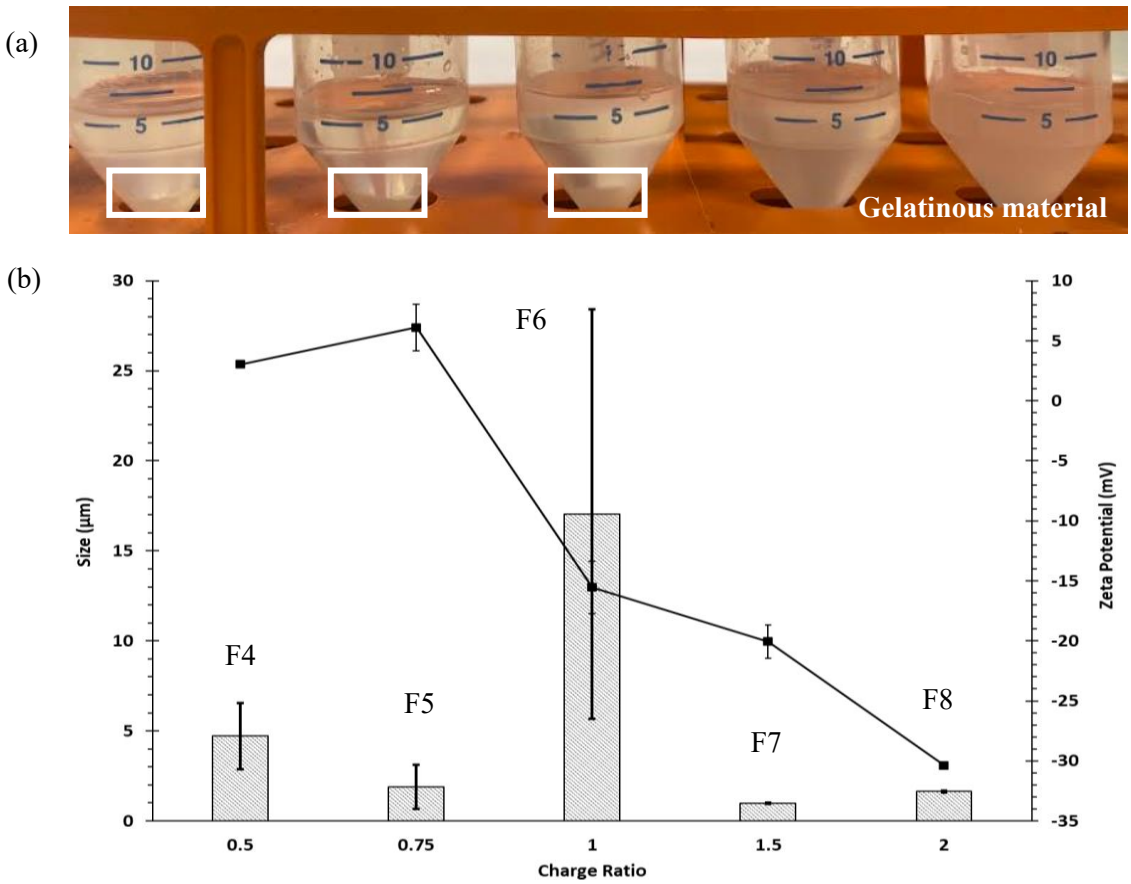

Figure 2.5: (a) A photograph of the PEC formulations with the specified molar charge ratios. (b) The influence of charge ratio on the size and zeta potential (ZP) of the PEC formulations. Data is expressed as mean ± S.D (n = 3).

Instantaneous aggregation, evidenced by the formation of a large quantity of gelatinous material, was visible in the F6 formulation, as highlighted in Figure 2.5 (b). Gelatinous aggregates were also visible in F4 and F5. The polydispersity index (PDI) value was also above 0.5. For pharmaceutical applications, a distribution width value, or PDI value, of less than 0.25 is deemed acceptable and is regarded as highly monodisperse. Values greater than 0.7 indicate that the formulation exists as a highly heterogeneous distribution [397]. Non-uniformity within

a particle size distribution may impact the reproducibility of the critical quality attributes of the formulation, such as therapeutic release and intraocular permeation.

As discussed in Section 1.4.3.1, without residual electrostatic stabilisation, PECs will tend towards aggregation to reduce the total Gibb's free energy of the system, thus resulting in macroscopic phase separation [288], [292], [398]. As expected, F4 and F5, both with molar charge ratios of less than 1, exhibited a positive ZP value, attributed to the presence of excess cationic amine groups. However, such PECs also aggregated, exhibiting sizes of over 2 μm and PDI values of over 0.7. This could be attributed to the molecular weight (MW) of PLL used. As observed by Schatz *et al.* [370] during an evaluation of the colloidal stability of 5 kDa dextran sulphate and 16 kDa chitosan PECs, both the molecular weight and flexibility of the polyelectrolyte in excess play a pivotal role in complex stability. The molecular backbone of PLL exhibits inherently high structural flexibility [399]. Upon titrating PLL with HA, an excess number of PLL amino acid chains of small MW may interact with a singular HA chain of a much larger MW, which behaves as a host molecule in this case. PLL may adapt its configuration to favour complete-ion pairing between the α-amine and carboxylate functional groups. This, combined with the absence of anionic carboxylate groups, opposes electrostatic PEC stabilisation, which may result in increased interpolyelectrolyte aggregation. Conversely, PECs containing HA in excess, such as F7 and F3, allow for the formation of an electrostatically stabilised, carboxylate anion-laden corona surrounding a charge-neutralised, stoichiometric polyelectrolyte core, formed via the sequential addition of a small number of small MW PLL chains to a larger number of large MW HA chains. This imparts kinetic meta-stabilisation to the system via electrostatic repulsive forces between the surface-bound charges of PECs in close proximity, thus preserving the PEC coacervate phase in solution [400], [401].

The inversion and decrease in ZP values with an increase in molar charge ratio also confirms the enhanced stability of the anionic PECs. ZP values provide an indication of both surface charge and electrostatic stability in a colloidal system and represent the electrokinetic potential at the edge of the slipping plane, the boundary that exists between the closely associated Stern layer and the more loosely associated diffuse layer shown in Figure 2.6.

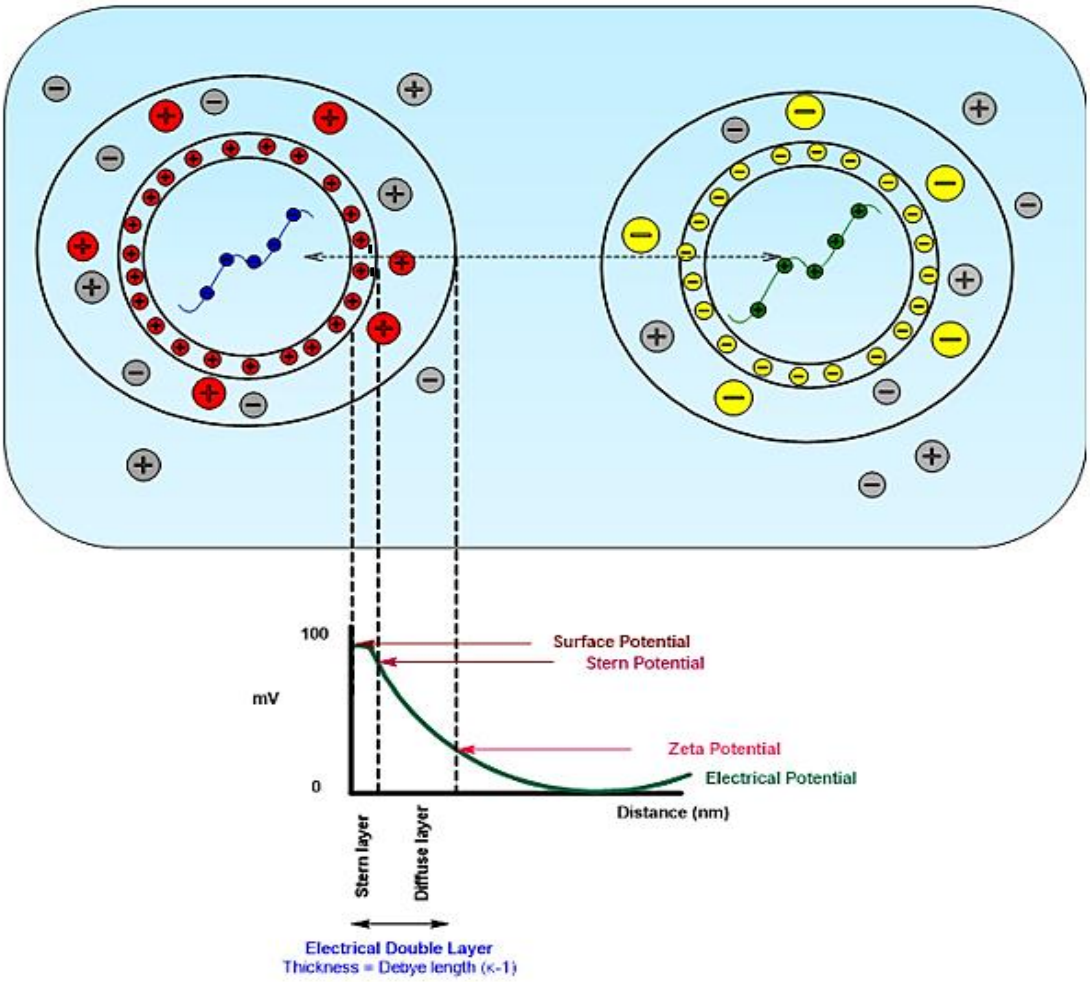

Figure 2.6: The electrical double layer surrounding a polyelectrolyte with residual surface charge in an ionic environment.

To ensure adequate colloidal stability, particles should exhibit ZP values of above +30 mV or below - 30 mV. ZP values of above + 60 mV or below - 60 mV indicate excellent stability [402]. Lower ZP values will result in particle aggregation due to the predominance of interparticle attractive forces resulting from hindered electrostatic repulsion, thus further highlighting the unsuitability of PECs with cationic charge ratios for further characterisation [403]. Based on both size and ZP, PECs with charge ratios of 2 were deemed suitable for further analysis.

2.3.5.2 Loss of Turbidity with Decreasing Charge Ratio

A sharp, significant decrease in percentage transmittance ($p \approx 0.000 \ll 0.05$) was observed upon analysis of the PECs with molar charge ratios above 1 (F7, F3) as shown in Figure 2.7. This suggests the formation of PECs that remain suspended in aqueous medium via mutual electrostatic repulsion between the residual HA carboxylate anions on adjacent PECs. Turbidity following complexation indicates the phase separation of the system into a polyelectrolyte-deficient phase and a PEC-rich colloidal phase [404]–[406]. The F4-F6 formulations were visually transparent and exhibited sedimentation of gelatinous aggregate material. The generation of percentage transmittance values above 70%, coupled with the DLS data obtained, supports this observation. An increase in percentage transmittance is indicative of irreversible aggregation and sedimentation of PECs, as fewer dispersed particles are restricting the transmission of light through the sample. The significant decrease in percentage transmittance from 85.68 ± 0.20% to 72.78 ± 0.41% between F4 and F6 ($p \approx 0.000 \ll 0.05$) may be attributed to the presence of both aggregated material and small populations of PECs within F6, which further supports the large error bars generated upon analysis of the size of F6.

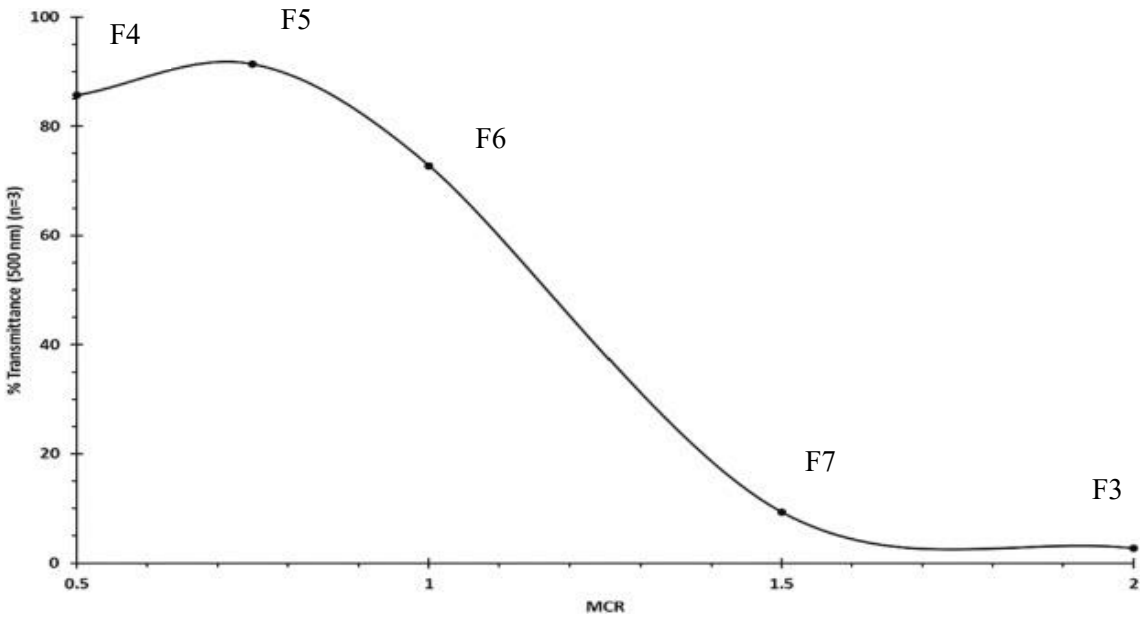

Figure 2.7: The change in % transmittance as a function of molar charge ratio at 500 nm. Data is expressed as mean ± S.D (n = 3).

2.3.6 Stoichiometry Analysis via Isothermal Titration Calorimetry

The thermodynamic properties obtained upon titration of HA with PLL and PLL with HA, respectively, in ultrapure water at pH 5.5 are highlighted in Table 2.5.

The PLL vs. HA titration mimics the dropwise titration of the polyelectrolyte of small MW to the polyelectrolyte of larger MW. The experimental parameters highlighted in Table 2.2 were optimised to achieve a sigmoidal factor of between 5 and 500. A sigmoidal factor, or c, value within this range allows for the generation of analysable data in which the binding constants between the polyelectrolytes, and the magnitude of enthalpic changes upon binding, are accounted for [407]. Initial titrations were conducted in accordance with the recommended experimental parameters outlined by TA instruments. However, these parameters generated c values out of the specified range. The respective ITC titrations were then optimised using the Experiment Design module on NanoAnalyze software to yield sigmoidal curves, as shown in Figure 2.8, with c values of 100 (PLL vs. HA titrations) and 104.3 (HA vs. PLL titrations)

(a)

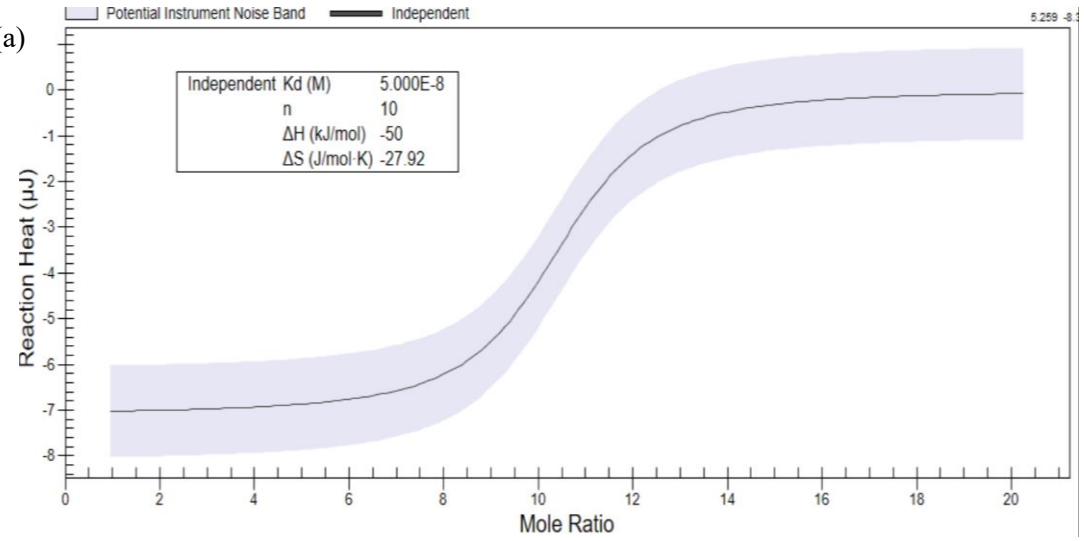

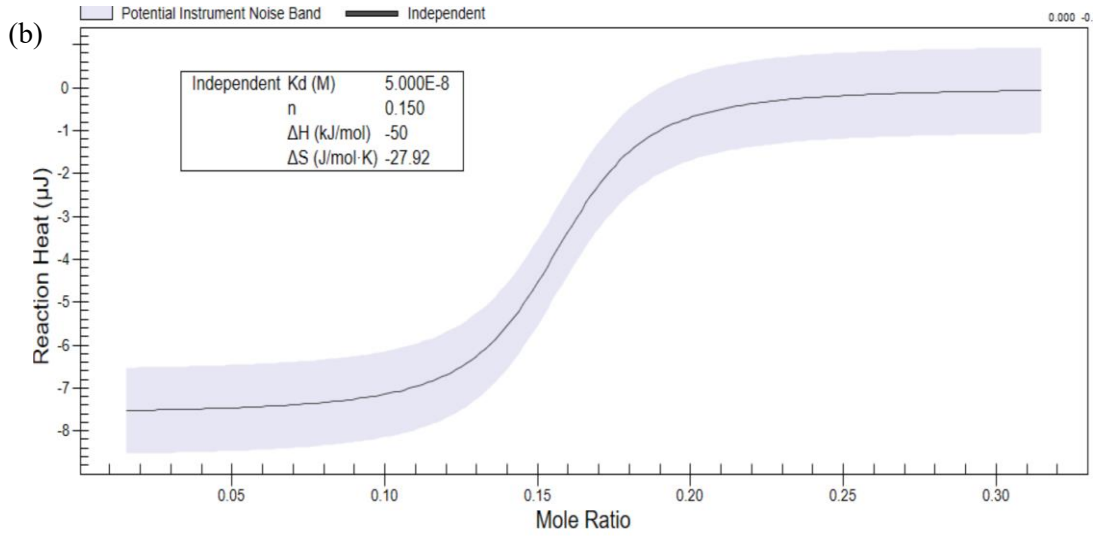

Figure 2.8: Theoretical binding isotherms for both PLL vs. HA (a) and HA vs. PLL (b) ITC titrations upon optimisation of the sigmoidal factor value. (K_D – equilibrium dissociation constant, n – reaction stoichiometry, ΔH – change in enthalpy, ΔS – change in entropy).

Table 2.5: Thermodynamic properties obtained upon fitting the ITC titration data from the PLL vs. HA titration to the independent site-binding model. Data is expressed as mean ± S.D (n = 3). The titration PLL with HA was conducted as a screening study (n = 1) to highlight changes in binding stoichiometry when the low MW polyelectrolyte is in excess.

Titration (titrant vs. titrand)	**ΔH (kJ/mol)**	**ΔS ($J/K^{-1}/mol^{-1}$)**	**Polyelectrolyte Molar Ratio at Reaction Stoichiometry**	**ΔH_{Comp} at Reaction Stoichiometry (kJ/mol)**
PLL vs. HA	-100.00 ± 38.98	-163.10 ± 0.00	7.49 ± 0.39	-88.76 ± 2.02
HA vs. PLL	-44.60	22.70	0.1	-32.66

Reaction stoichiometry was achieved at a PLL:HA molar ratio of 7.49 ± 0.39, which equates to a molar charge ratio of approximately 0.89 to 1.03. At this molar charge ratio, maximal electrostatic interaction should occur between HA and PLL. This supports the observations made upon analysis of the influence of charge ratio on PEC size. At molar charge ratios of approximately 1, maximal interaction is achieved. However, if electrostatic interactions between HA and PLL are at a maximum, the number of residual charges available for

electrostatic stabilisation will also decrease, thus resulting in the irreversible formation of complex aggregates. The properties obtained upon titration of PLL with HA are also in agreement with the size data shown in Figure 2.5 (b). A HA:PLL molar ratio of 0.1 equates to a HA:PLL molar charge ratio of approximately 0.77. This suggested that, when the polyelectrolyte in excess is smaller in MW than the polyelectrolyte in default, maximal complexation is achieved at a non-stoichiometric charge ratio, i.e., the residual cationic charges required for stabilisation are being utilised prior to achieving charge ratio stoichiometry. ITC has been utilised in previous studies to investigate the binding of respective polyelectrolytes in various reaction media. Dubashynskaya *et al.* [330] reported similar heats of reaction upon sequential titration of HA (750 kDa) with a smaller MW cationic chitosan derivative, diethylaminoethyl chitosan (37 kDa). The binding of HA to diethylaminoethyl chitosan was found to be entropically driven. It would have been expected that the release of counter ions, (Na^+- HA and Cl^- - PLL, respectively) upon disruption of the EDL of the polyelectrolytes and subsequent complexation, would result in a significant increase in entropy. However, the loss of conformational entropy, resulting from entanglement and fixation of the polyelectrolytes in the PEC meshwork seems to far exceed that of the increase in entropy originating from counter ion displacement. Interestingly, the titration of PLL with HA exhibited a small yet positive entropic change. This may be attributed to increased binding between HA and PLL, with maximal complexation being achieved prior to reaching a stoichiometric charge ratio. As such there may have been an increased number of counter ions available for release from the additional free HA chains titrated into the sample cell.

To investigate the effect of ionic strength on HA and PLL binding stoichiometry, additional ITC titrations were conducted under equivalent conditions, utilising 0.01 M PBS (pH 5.5) as the reaction media. The resulting thermodynamic properties are highlighted in Table 2.6.

Table 2.6: Thermodynamic properties obtained upon fitting the ITC titration data from the PLL vs. HA titrations, conducted in 0.01 M PBS (pH 5.5) to the independent site-binding model.

Titration (titrant vs. titrand)	ΔH (kJ/mol)	ΔS ($J/K^{-1}/mol^{-1}$)	Polyelectrolyte Molar Ratio at Reaction Stoichiometry	ΔH_{Comp} at Reaction Stoichiometry (kJ/mol)
PLL vs. HA	35.01 ± 11.44	263.1 ± 31.9	6.85 ± 2.96	20.64 ± 22.94

Both a positive shift in enthalpy and entropy were observed upon titration of HA with PLL in 0.01 M PBS. In ultrapure water, the counter ion clouds within the slipping plane, a highly charged atmosphere in which the counter ion concentration surrounding the polyelectrolytes decreases with distance until equilibrium with the bulk liquid phase is reached, are dilute. Therefore, upon release of counter ions from the polyelectrolyte structures into the slipping plane, entropy is increased. Also, the small increase in enthalpy originating from the breaking of the polyelectrolyte-counter ion electrostatic bonds does not overshadow the large decrease in enthalpy originating from the formation of the interpolyelectrolyte electrostatic interactions. In an ionic medium, counter ions would still be released into an ion-saturated medium, thus contributing to system entropy. However, the large increase in enthalpy required to release counter ions into an ion-saturated, compact slipping plane far exceeds that of the decrease in enthalpy from electrostatic interactions. This trend was also observed by Ma *et al.* [408] in which positive yet negligible heat changes were observed following titrations of 11 kDa chitosan with 21 kDa HA in 25 mM 2-(N-Morpholino) ethanesulfonic acid buffer at an ionic strength of 150 mM. Upon reduction of buffer ionic strength to 18 mM, the enthalpy decreased to -91 kcal/mol, thus highlighting the screening effect of the counter ions within the electrical double layers of the PECs at the higher ionic strength. This screening effect was also observed upon comparison of the stoichiometry in ultrapure water and 0.01 M PBS. In 0.01 M PBS, stoichiometry was achieved at a PLL:HA molar ratio of 6.85 ± 2.96 equating to a charge ratio of 0.67 to 1.92. This suggested that the increased number of co- and counter-ions within the medium may be decreasing the number of charged functional groups available for complex

formation via secondary interactions, therefore effectively screening the electrostatic interactions between HA and PLL

2.3.7 Effects of Lyophilisation on Complex Size

A significant decrease in size ($p \approx 0.001 \ll 0.05$) was observed following lyophilisation of the F3 formulation with 1% (w/v) trehalose (1633.3 ± 50.5 nm – before lyophilisation and 322.7 ± 1.82 nm – after lyophilisation). Although a decrease in size was also observed in F4 after lyophilisation (4714.7 ± 1832.4 nm vs. 790.7 ± 39.7 nm), this decrease was not statistically significant ($p = 0.066 > 0.05$). Furthermore, as its size remained over 500 nm, and in combination with previous results, this PEC was excluded from further characterisation. Trehalose was selected based on the results of a screening cryoprotectant addition study in which 1% (w/v) sucrose, glycerol and trehalose were added to three individual F3 formulations. In comparison to the other cryoprotective agents, the PECs lyophilised with 1% (w/v) trehalose attained more suitable size parameters after lyophilisation, after dilution by a factor of ten and after two weeks stored at 4 °C. Trehalose is also relatively inert, exhibits low hygroscopicity and readily undergoes conformational adaptations to aid hydrogen bond formation with nanoparticles.

The impact of PEC physicochemical size parameters following lyophilisation was identified as a critical formulation parameter. Lyophilisation of the PEC formulations would be required to ensure sufficient stability over the timeframe required for physicochemical characterisation, and preservation of the final PEC product during transport and long-term storage. Lyophilisation is typically associated with nanoparticle aggregation during the drying step and particulate damage due to external mechanical stress imparted by ice crystallisation [409]. The significant decrease in particle size observed following lyophilisation contradicted this assumption. The addition of trehalose may have preserved hydrogen bond-mediated particle structure and stability by replacing water molecules on the surface of the particles during sublimation [410]. Increased hydrogen bonding may have led to further compaction of the residual HA chains within the PEC corona, thus leading to a reduction in particle size. HA itself can also behave as a cryoprotectant due to its remarkable water retention capabilities and ability to form intra- and intermolecular hydrogen bonds [411]. As demonstrated by Rampino *et al.*

[412], the preservation of this "pseudo-hydrated" state during lyophilisation prevented PEC aggregation during lyophilisation, thus improving their dispersibility upon reconstitution in an aqueous medium. In agreement with our study, Umerska *et al.* [347] and Yan *et al.* [413] have both reported on the improved dispersibility of HA and chitosan polyelectrolyte complexes and bovine serum albumin-loaded chitosan and tripolyphosphate nanoparticles, respectively, following lyophilisation with varying concentrations of trehalose cryoprotectant. Van Le *et al.* [414] also observed the preservation of particle size following lyophilisation of a 2.7 x 10^5 Da HA with a 7 x 10^5 Da diethylaminoethyl dextran hydrochloride PEC with 0.2% (w/v) trehalose.

2.4 CONCLUSIONS

In this chapter, hyaluronic acid (HA) and poly (L-lysine) (PLL) polyelectrolyte complexes were successfully formulated via polyelectrolyte complexation, namely via electrostatic interactions, under ambient formulation conditions. Optimisation of the critical formulation parameters, and selection of the reference PEC for further characterisation and NAD+ loading, was conducted accordingly.

Based on the results obtained following DLS and FT-IR analysis, a complexation time of 24 hours was selected to allow for maximal secondary complexation of primary complexes that could be further streamlined during purification work-up. The optimal complexation pH range of 5 to 6 was selected based on the percentage of ionisation of both HA and PLL. Within this range, over 90% of the required functional groups (COO^- - HA and NH_3^+ - PLL) were present in their desired ionised state thus allowing for maximal ionic complexation during formation. The formation of gel aggregates following mixing of the individual polyelectrolyte solutions was found to be independent of HA molecular weight yet dependent on the mode of addition, leading to the selection of a dropwise mode of addition for subsequent formulations. Following extensive centrifugation trials, centrifugation of the complexes for 50 minutes at 4000 g in ultracentrifuge filters was selected for PEC purification. This method may also allow for the efficient isolation of free NAD+ molecules from complex-bound NAD+ without exposing PECs to harsh centrifugal force thus reducing the likelihood of PEC degradation.

The molar charge ratio had a significant effect on complex formation, with cationic PECs tending towards macroscopic aggregation via interparticle forces of attraction, primarily attributed to hindered electrostatic repulsion between residual amino groups within the PEC corona. However, anionic PECs, prepared with HA in excess, yielded highly turbid, colloidal suspensions with suitable size and zeta potential values for drug delivery application. These results were confirmed via DLS and UV-Vis spectroscopic analysis, and further supported by the reaction stoichiometry values obtained upon titration of HA with PLL using ITC methodologies. The screening effect of counter ions during PEC formation was also confirmed upon analysis of the inverse shifts in enthalpic and entropic effects upon titration of HA with PLL.

Lyophilisation of PECs with molar charge ratios of both 0.5 (F4) and 2 (F3) with 1% (w/v) trehalose cryoprotectant greatly improved the monodispersity of the formulations and reduced the diameter of the particle size distribution (F4 - 790.7 ± 39.7 and F3 - 322.7 ± 1.82) post-lyophilisation. However, F3 was chosen as a suitable candidate for subsequent characterisation due to its increased colloidal stability and reproducible physicochemical size parameters. Chapter 2 details the preparation of NAD+-associated complexes, in which F3 will be loaded with NAD+ during preparation and subsequently characterised using both qualitative and quantitative methodologies to investigate the effect of NAD+ association.

CHAPTER 3:

PREPARATION OF NAD+-ASSOCIATED PEC FORMULATIONS

3. PREPARATION OF NAD+-ASSOCIATED PEC FORMULATIONS

3.1 INTRODUCTION

As outlined in Chapter 1, a direct link exists between the age-related decline in intracellular NAD+ concentration and the initial pathogeneses of several ocular diseases [135]. Replenishment of the NAD+ intracellular pools via the dietary and parenteral supplementation of both NAD+ and NAD+ precursors has shown promising therapeutic efficacy in several neurodegenerative diseases, including age-related macular degeneration and glaucoma [141], [415]–[420]. However, regarding the ocular delivery of NAD+ supplements, oral administration typically results in poor bioavailability due to the unpredictable nature of enteric drug absorption and delocalised absorption in other parts of the body [421], [422]. Parenteral intraocular administration could provide more targeted delivery of NAD+, particularly within the posterior segment, at almost 100% bioavailability. However, the invasive and costly nature of such injections, particularly for the administration of a supplementary molecule, could prove unappealing to patients. NAD+ is also readily reduced to NADH during cellular respiration and is continually degraded and regenerated via enzymatic action, thus limiting its inherent stability *in vivo*.

The entrapment of NAD+ within a nanoparticulate system may provide a non-invasive alternative to the aforementioned administration methods whilst improving both its intraocular bioavailability and intrinsic stability. To the best of our knowledge, NAD+ has not been entrapped or encapsulated within a nanoparticulate system intended for ocular administration to date. Therefore, the studies conducted here present a proof of concept for formulating stable NAD+-associated HA and PLL polyelectrolyte complexes (PECs), with reproducible physicochemical properties, via polyelectrolyte complexation in an aqueous medium. From the results obtained in Chapter 2, the lyophilised F3 formulation (2% (w/v), HA:PLL charge ratio: 2) was identified as an ideal candidate for further characterisation and NAD+ loading as it exhibited suitable physicochemical size parameters for drug delivery application (size: ≈ 300 nm, zeta potential: > − 30 mV, PDI: < 0.25) and maximal colloidal stability (maximal turbidity). Due to the supplementary nature of NAD+, and the intended use of the PEC formulation as a prophylactic treatment for ocular cell dysfunction before disease progression,

it was intended that this formulation be designed as a topical administration. Topical administration of ocular drug delivery systems (ODDS) is favourable in comparison to intravitreal or surgical treatment options, in terms of both patient compliance and ease of administration [25], [423]–[425]. Therefore, dynamic conditions mimicking that of the ocular surface environment (37 °C, pH 7.4, tear flowrate = ~ 3 µL/min) were used to assess the behaviour of the NAD+-associated PECs during physicochemical characterisation.

Regarding this study, it was hypothesised that NAD+, being hydrophilic, would preferentially associate with the hydrophilic corona of the PECs. Also, as depicted in Figure 3.1, NAD+ possesses both a formal cationic charge, due to the nitrogen atom within the pyridine ring, and two anionic phosphate groups within the pyrophosphate bridging group between the adenosine and nicotinamide moieties.

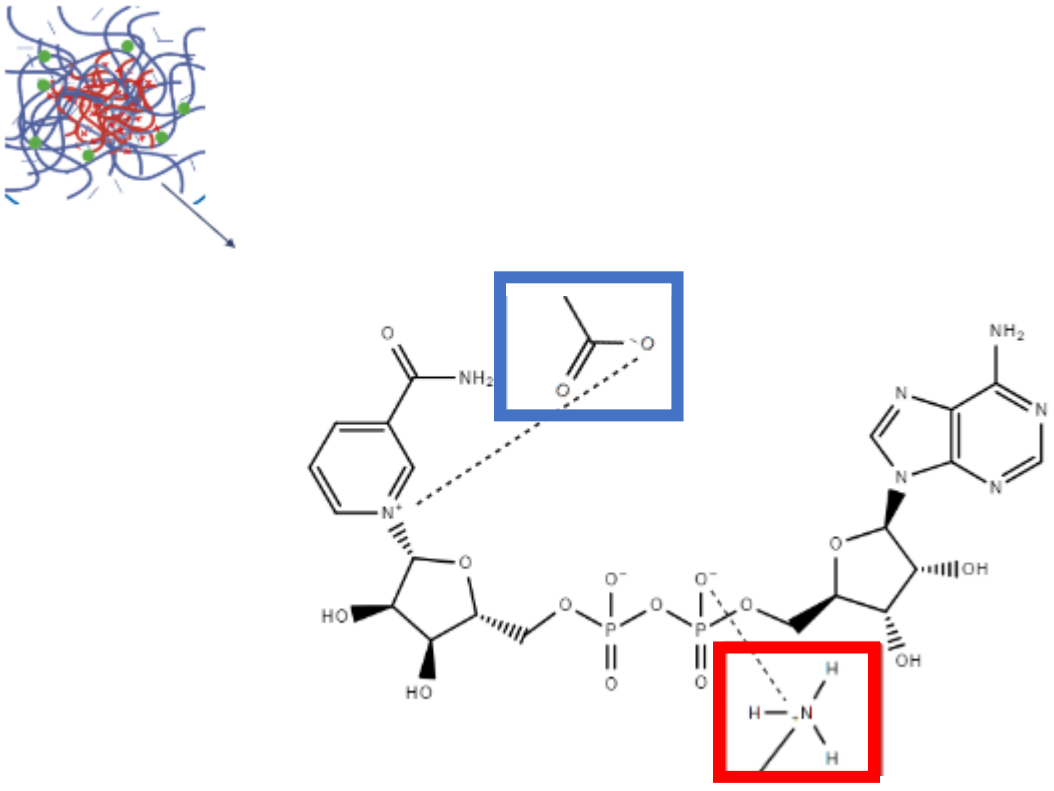

Figure 3.1: A schematic of the potential interactions of NAD+ with the charged functional groups of both HA (blue) and PLL (red).

As such, NAD+ can also partake in electrostatic interactions with the charged polyelectrolyte groups. Hydrogen bonding is also possible due to the abundance of hydroxyl groups within the molecular structure of NAD+.

The pivotal aim of the current study was to investigate the effect of NAD+ addition on the physicochemical parameters of the reference PEC identified from the optimisation studies outlined in Chapter 2. The behaviour of the NAD+-associated PECs, in terms of NAD+ release and stability, under physiological conditions, was also of key focus. NAD+ binding to both HA and PLL was investigated using ITC methodology, with DLS analysis utilised to investigate the effect of NAD+ loading and polyelectrolyte concentration on PEC physicochemical size parameters. The presence of NAD+ within the PEC formulations was analysed using FT-IR and SEM-EDX. NAD+ association efficiency (AE) and loading capacity (LC) within the PECs were quantified using RP-HPLC methodology. NAD+-associated PEC stability, both under storage conditions (4 °C and 25 °C) for one month and under physiological conditions (37 °C, pH 7.4) was assessed using UV/Vis spectroscopy, DLS and RP-HPLC. Cumulative *in vitro* release of NAD+ under conditions mimicking those of the physiological anterior segment was quantified and fit to five mathematical models to determine the mechanism and kinetics of *in vitro* NAD+ release.

3.2 EXPERIMENTAL METHODOLOGY

3.2.1 Materials

The materials outlined in Section 2.2.1 were used in the preparation and physicochemical characterisation of NAD+-associated HA and PLL PECs with the addition of the following:

β-nicotinamide adenine dinucleotide (MW: 663.43 g/mol, purity ≥ 95%) (NAD+), was purchased from Carbosynth Ltd. (Berkshire, England). An additional quantity of NAD+ (MW: 663.43 g/mol, purity ≥ 95%) was later purchased from VWR International (Dublin, Ireland). Vivaspin® Turbo 15 centrifugal filters (10 kDa MWCO) were purchased from Analab (Antrim, Northern Ireland). High-performance liquid chromatography (HPLC) grade methanol (purity ≥ 99.9%) and Spectra/Por Biotech dialysis tubing (molecular weight cut off (MWCO): 1000 kDa, 31 mm width) were purchased from Fischer Scientific Ireland (Dublin, Ireland).

3.2.2 Preparation of NAD+-Associated HA and PLL Polyelectrolyte Complexes

NAD+-associated PECs were prepared in a similar fashion to that of the blank PECs as outlined in Section 2.2.3. 2% (w/v) solutions of NAD+ were premixed with the PLL solutions before dropwise addition to the HA solutions. NAD+ loading concentrations of 50 and 100% (w/w), relative to the combined mass of both HA and PLL in each formulation, were selected for investigation. NAD+-associated PECs were prepared with total concentrations of 2% (w/v) and a molar charge ratio of 2. A list of the formulations mentioned throughout this chapter is given in Table 3.1.

Table 3.1: The formulation parameters of the formulations (F8-F10) referenced throughout the chapter.

Sample Name	F8	F9	F10
Formulation Concentration (% (w/v))	2	2	5
HA:PLL Charge Ratio	2	2	2
HA Average Molecular Weight (kDa)	90	90	90
Concentration of NAD+ (% (w/w))	100	50	50
HA:PLL:NAD+ Charge Ratio	0.83	1.2	1.2

Following complexation, the NAD+-associated PECs were centrifuged at 4000 g for 50 min at 4 °C in Vivaspin® Turbo 15 centrifugal filter tubes to both isolate the sub-micron-sized PECs and remove free NAD+ from the formulation. Subsequent lyophilisation of both the PEC and free NAD+ fractions was conducted in accordance with Section 2.2.4.3.

3.2.3 Polyelectrolyte Complex Physicochemical Characterisation

3.2.3.1 Isothermal Titration Calorimetry (ITC)

ITC analysis was conducted in accordance with the procedure outlined in Section 2.2.5.4. Briefly, 50 µL of NAD+ was loaded into the titrant syringe and 300 µL of either HA or PLL solution was injected into the sample cell following thorough rinsing with ultrapure water at pH 5.5. The ITC titrations were conducted following the experimental parameters highlighted in Table 3.2.

Table 3.2: Optimised experimental parameters utilised for ITC titrations of NAD+ (titrant syringe) vs. HA (sample cell) and NAD+ (titrant syringe) vs. PLL (sample cell).

Titration (titrant vs. titrand).	Sample Cell Volume (µL)	Conc. Sample Cell (µM)	Total Syringe Volume (µL)	Conc. Syringe Volume (µM)	Injection Volume (µL)	Stirring Speed (rpm)	Injection Interval (s)
NAD+ vs. HA	300	10.69	50	11624.4	2	200	180
NAD+ vs. PLL	300	11.62	50	11624.4	2	200	300

The concentrations of both the polyelectrolytes and NAD+ were chosen to yield NAD+ % (w/w) between 5 and 100%, relative to the mass of polyelectrolytes in the sample cell, after each injection.

3.2.3.2 DLS Analysis of Polyelectrolyte Complexes

DLS analysis of the NAD+-associated PECs was conducted as outlined in Section 2.2.5.2.

3.2.3.3 Fourier-Transform Infrared Spectroscopy (FT-IR)

FT-IR analysis of the NAD+-associated PECs was conducted as outlined in Section 2.2.5.12.2.5.2. However, a physical mixture of HA:PLL and NAD+ in a 1:1:1 mass ratio, was also analysed via FT-IR.

3.2.3.4 Scanning Electron Microscopy with Energy Dispersive X-Ray Spectroscopy (SEM-EDX)

SEM-EDX analysis was conducted using a TM4000 Plus II benchtop scanning electron microscope and AZtecOneXplore® software (Hitachi High-Tech Corporation, United Kingdom). PEC samples were mounted onto SEM stubs using conductive tape and sputter-coated with a thin layer of gold for approximately 2 hours. SEM images of the PEC lyophilisates were taken at various magnifications at an accelerating voltage of 15 kV using a Mix vacuum mode (Backscattering Electron Mode + Secondary Electron mode). For

qualitative analysis of NAD+, EDX analysis was used to generate elemental line profiles on the SEM images of the PECs obtained. Lines were drawn *in situ* on the SEM image, followed by irradiation of the PEC sample with the incident high-energy electron beam. The elemental composition of the area of analysis is depicted following the generation of elemental peaks from the emission of X-rays with energies that are equivalent to the difference between the higher and lower electron level binding energies of each element. A blank PEC was also analysed to validate that any elements specific to that of NAD+ were arising from the presence of NAD+ and not an external source.

3.2.3.5 NAD+ Chromatographic Conditions

Quantitative analysis of NAD+ was conducted using reverse-phase HPLC (RP-HPLC) methodology with chromatographic conditions selected from the HPLC method developed and validated by Forrow *et al.* [38]. The mobile phase consisted of a 95:5 (% (v/v)) mixture of 20 mM potassium phosphate buffer (pH 8):HPLC grade methanol. A flow rate of 1.0 mL/min, an injection volume of 10 µL and an autosampler temperature of 35 °C were used and each injection was conducted in triplicate. At a wavelength of 260 nm, retention times of approximately 2 minutes (for 150 x 4.6 mm columns) and 4.4 min (for 250 x 4.6 mm columns) were observed for NAD+.

Validation of the HPLC analytical method was conducted on both an Agilent 1200 HPLC system, equipped with the following modules: G1312B SL binary pump, G1329B autosampler, G1316B column compartment and a G1365B multiple UV wavelength detector (Agilent Technologies, California, United States), and a Waters e2695 separations module (Waters, Massachusetts, United States). Xterra RP 18, 5 µm HPLC column (250 x 4.6 mm and 150 x 4.6 mm) (Waters Technologies Ireland Ltd., Wexford, Ireland) were utilised throughout this study. Intra-assay precision was conducted upon injection of 12 NAD+ working standards, ranging in concentrations from 2 to 200 µg/mL, prepared in duplicate from one NAD+ stock standard solution. The coefficient of variation (% CV) for each peak area was calculated using Equation 3.1.

$$\%\ \mathrm{CV} = \frac{\text{Standard deviation of each NAD + working standard}}{\text{Mean peak area of each NAD + working standard}} \qquad \text{Equation 3.1}$$

Linearity across the desired concentration range, and the limits of detection and quantification (LOD and LOQ, respectively), were calculated from the resulting calibration curve using regression analysis on Microsoft Excel®. The peak area of a 100 µg/mL bracketing NAD+ standard was used to quantify NAD+ in subsequent runs.

3.2.3.6 Quantification of NAD+ Association Efficiency

The association efficiency (AE) of NAD+ was quantified via indirect and direct methods by measuring both the quantity of free NAD+ in the bottom fraction of the Vivaspin® Turbo 15 centrifugal filters and the quantity of PEC-associated NAD+ in the top fraction. A given mass of PEC and free NAD+ lyophilisates were weighed out and dispersed in various extraction solvents to yield solutions with concentrations of 1% (w/v). The resulting solutions were vortexed for 30 s at 500 rpm and centrifuged at 10,000 rpm for 10 minutes to aid PEC destabilisation. 100 uL aliquots of the supernatants were pipetted into amber HPLC vials, diluted to a final volume of 1 mL with mobile phase and analysed via RP-HPLC.

3.2.3.7 NAD+ Stability in Sample Media

10 mg/mL solutions of NAD+ were prepared in both ultrapure water and 0.01 M PBS, at pH 5.5 and pH 7.4, in triplicate. The resulting solutions were maintained at 37 °C and pH 7.4 for 48 hours in total. At predetermined time points, 100 µL aliquots from each solution were withdrawn and the concentration of NAD+ in the aliquots was quantified via RP-HPLC analysis. The stability of NAD+ was calculated based on the percentage recovery of NAD+ at each time point in comparison to the initial concentration of NAD+ at t_0 using Equation 3.2.

$$\left(\frac{\text{Concentration of NAD + at time 't'}}{\text{Initial Concentration of NAD +}}\right) \text{x } 100 \qquad \text{Equation 3.2}$$

3.2.3.8 In Vitro NAD+ Release under Microfluidic Conditions

Preparation of microfluidic device moulds: Sylgard 184 Silicone base and curing agents (10:1 ratio) were mixed for 4 minutes. The resulting mixture was then poured onto a glass plate within a circular mould. Needles (1.27 mm outer diameter) were placed at opposing ends of the mould to create inlet and outlet channels. As shown in

Figure ***3.2***, the hemisphere on the glass plate, with a 9.00 ± 0.10 mm radius of curvature, created a well within the mould for PEC placement. The device was then cured for 6 hours at 60 °C. The interior of the well was lined with dialysis membrane tubing prior to the addition of 400 µL of NAD+-associated PEC suspension, equivalent to 15 mg of NAD+. Two moulds were then clamped together to yield an enclosed mould containing two inlets and two outlet flow lines, thus mimicking the anatomical shape of the anterior segment of the eye.

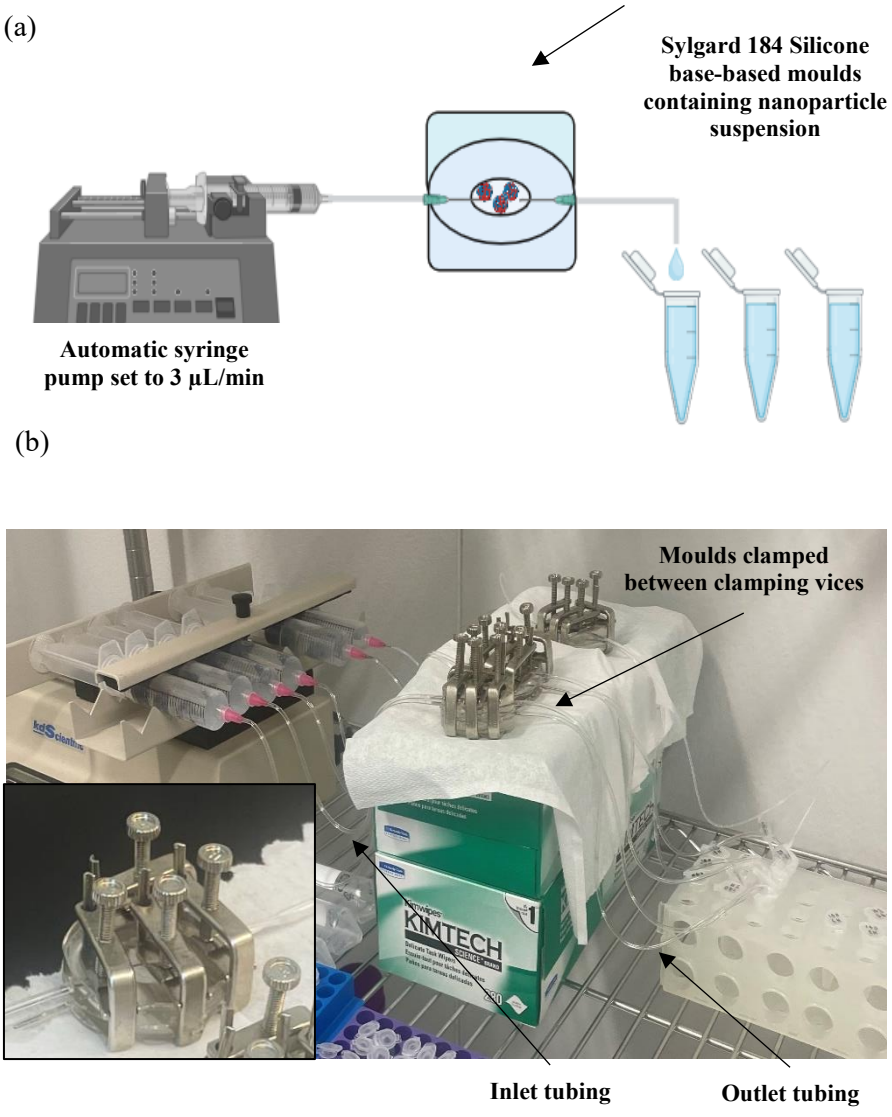

Figure 3.2: A schematic (a) and photograph (b) of the microfluidic release set-up. A close-up of the microfluidic device mould is shown in part (b).

In vitro microfluidic release: One end of a length of PVC tubing was connected to each needle of the inlet and outlet channel, with the other end being attached to a syringe filled with degassed 0.01 M PBS (pH 7.4). A syringe pump (Model 220, KD Scientific Inc, Massachusetts, United States) was set to deliver 1.5 µL/min through each length of tubing, thus allowing for a total flow rate of 3 µL/min through the PEC-laden well. *In vitro* release was conducted at 37 °C. Outlet flow samples were collected at predetermined time points for RP-HPLC analysis of NAD+ concentration. Cumulative NAD+ release was calculated using Equation 3.3.

$$\left(\frac{M_t}{M_{inf}}\right) \text{ x } 100 \qquad \text{Equation 3.3}$$

M_t = Total mass of NAD+ at time (t) (Total = Mass of NAD+ in receptor medium at time (t) + cumulative mass of NAD+ removed during sample withdrawal).
M_{inf} = Mass of NAD+ released at infinite t. (Mass released at the last time point).

3.2.3.9 Kinetic Modelling of In Vitro NAD+ Release

Both the kinetics and mechanism of *in vitro* NAD+ release were evaluated by modelling the *in vitro* microfluidic release data to the following mathematical models [426]–[430].

Zero-order release kinetics was assessed by plotting a graph of the percentage cumulative release as a function of time in hours as per Equation 3.4.

$$C_t = C_o + K_{ot} \qquad \text{Equation 3.4}$$

Where C_t is the amount of NAD+ released during time t, C_0 is the initial concentration of NAD+ ($C_0 = 0$) and k_0 is the zero-order rate constant.

As shown in Equation 3.5, first-order release kinetics was assessed by plotting the log of the cumulative NAD+ release as a function of time in hours.

Where log(C) is the log of the amount of NAD+ released at time t, C_0 is the initial amount of NAD+ dissolved, and k_t is the first-order rate constant.

$$Log(C) = \log(C_o) - \frac{K_t}{2.303} \qquad \text{Equation 3.5}$$

NAD+ release following the Higuchi model, describing therapeutic release via diffusion from an insoluble matrix, shown in Equation 3.6, was assessed by plotting the cumulative NAD+ release as a function of the square root of time, in hours.

$$Q_t = K_H t^{1/2} \quad \text{Equation 3.6}$$

Where Q_t is the amount of drug released in time t and K_H is the release rate constant for the Higuchi model.

The first 60% of NAD+ release was assessed as per the Korsmeyer-Peppas kinetic model by plotting a graph of the log of cumulative NAD+ release as a function of the log of time in hours [431]–[433]. The adaptation of the Korsmeyer-Peppas model equation to fit the slope-intercept form of a line (y = mx + c) is shown in Equation 3.7

$$\frac{Mt}{M\infty} = Kt^n \rightarrow \log\left(\frac{Mt}{M\infty}\right) = \log(k) + n\log(t) \quad \text{Equation 3.7}$$

Where Mt/M is the fraction of NAD+ released at time t, k is the release rate constant and n is the release exponent value.

The Hixson-Crowell mathematical model was used to assess whether a change in diameter and surface area governs NAD+ release. A plot of the cube root of drug remaining vs. time in hours was plotted as per Equation 3.8

$$\sqrt[3]{Q_o} - \sqrt[3]{Q_t} = K_{hc}t \quad \text{Equation 3.8}$$

Where Q_o is the initial amount of drug, Q_t is the amount of drug remaining, K_{hc} is the release rate constant and t is time in hours.

3.2.3.10 Changes in PEC Stability in Response to Environmental Stimuli

% Transmittance: 4 mL aliquots of crude NAD+-associated PECs were mixed thoroughly with 2 mL aliquots of either 0.01 M PBS (pH 7.4) or ultrapure water (pH 5.5). 3 mL of the resulting solutions were placed into a quartz cuvette. The percentage transmittance of the solutions was recorded in transmittance mode at 500 nm using a UV/Vis spectrophotometer (Cary® 50, Agilent Technologies, Ireland). Blank solutions (buffer solutions containing no PEC) were

scanned concurrently during analysis to ensure that the percentage transmittance values recorded were generated via the absorption of light by the PECs alone and not the ions within the media.

Change in physicochemical size parameters: NAD+-associated PECs were dispersed in 10 mL of sample medium (ultrapure water – pH 5.5 and pH 7.4 and 0.01 M PBS – pH 5.5 and pH 7.4), in triplicate. 1 mL of the resulting solutions was then diluted to 10 mL in 20 mL clear, glass vials with the same media and shaken at 200 rpm at 37 °C. At t_0, a 1 mL aliquot was withdrawn from each glass vial and analysed via DLS analysis. To maintain sink conditions, equal volumes of fresh sample media were re-added to the glass vials upon sample withdrawal.

Changes in NAD+ association: 10 cm sections of dialysis tubing membrane were pre-soaked overnight in 500 mL of ultrapure water. A mass of NAD+-associated PECs suspensions equivalent to 15 mg of NAD+ was pipetted into the prepared dialysis membranes and sealed using dialysis tubing closures. Following equilibration of the sample media to 37 °C, the loaded dialysis membranes were suspended in each sample media under continuous stirring at 200 rpm in a sealed, temperature-controlled incubator (S160D, Stuart Equipment, UK). At predetermined time points, 500 µL aliquots were withdrawn from the receptor medium, diluted to 1 mL with mobile phase, and analysed via RP-HPLC.

3.2.3.11 Storage Stability of PECs

1 mg/mL solutions of NAD+-associated PECs were prepared in ultrapure water (pH 5.5), in triplicate. 4 x 1 mL aliquots of each solution were pipetted into 1.5 mL Eppendorf® tubes, two of which were stored at 4 °C and the remaining 2 at 25 °C. Of the 2 aliquots, 1 was analysed via DLS analysis as outlined in Section 2.2.5.2. The remaining aliquot, intended for analysis of changes in NAD+ concentration, was centrifuged at 15,000 rpm for 10 minutes. The resulting supernatant was withdrawn and filtered through sterile, 0.45 µM syringe filters. 100 µL of the resulting filtrate was diluted to a final volume of 1 mL with mobile phase diluent and analysed via RP-HPLC. Samples were analysed at 0, 1, 7, 14, 21 and 28 days.

3.2.4 Statistical Analysis

Two sample t-tests (two-tailed) and one-way analysis of variance (ANOVA) analysis, coupled with Tukey's/Games-Howell post-hoc comparison tests were used throughout the studies outlined. Normality tests and tests for equal variances in the experimental data were also conducted. Ryan-Joiner normality tests and 2 Variances tests were also conducted to assess whether the experimental data was normally distributed and whether the standard deviations of two sample populations were equal to the hypothesised ratio, respectively. A p-value of less than 0.05 was considered statistically significant, while a p-value > 0.05 was considered statistically insignificant at the 95% confidence interval.

3.3 RESULTS & DISCUSSION

3.3.1 NAD+-Polyelectrolyte Binding via ITC Analysis

The binding of NAD+ to both HA and PLL is exothermic, as indicated by the generation of downward peaks (-µJ/s) within the respective thermograms shown in Figure 3.3. This was as expected as, upon binding of NAD+ to the respective polyelectrolytes, the newly formed complex system should release heat to the surroundings, thus resulting in a reduction in system enthalpy.

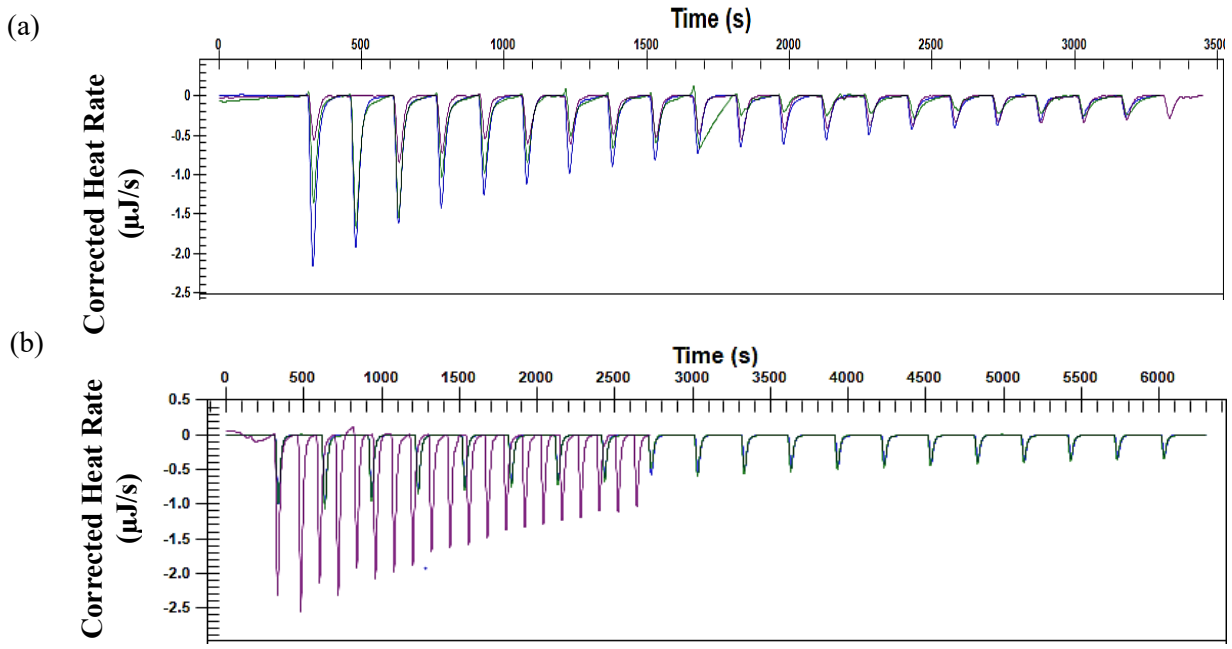

Figure 3.3: Representative ITC binding isotherms obtained upon titration of PLL with NAD+ (a) and HA with NAD+ (b).

Equilibrium dissociation constants (K_D) within the upper limit of the micromolar range (10^{-4} to 10^{-6} M) were recorded for both the titrations of NAD+ vs. PLL (6.2×10^{-4} M) and NAD+ vs. HA (9.9×10^{-4} M). Such binding constants were statistically equivalent ($p = 0.217 > 0.05$), thus indicating that NAD+ exhibited equivalent affinity for HA and PLL binding. Santos *et al.* [434] obtained a similar K_D value for the binding of tacrine ($0.93 \pm 0.08 \times 10^{-3}$ M) to HA. However, compared to that of aminacrine ($70 \pm 1 \times 10^{-3}$ M), NAD+ exhibits a much higher binding affinity. This may be attributed to the increased number of NAD+ functional groups that can readily partake in hydrogen bonding with the HA glycosaminoglycan backbone.

The reduction in differential power between the reference and sample cells after sequential injection of NAD+ also suggested that as the molar ratio of NAD+ to each polyelectrolyte increased, the polyelectrolyte became saturated, resulting in a decrease in both NAD+ binding and heat change after subsequent injections [435], [436]. Reaction stoichiometries of high variability were found upon fitting the isotherms to the independent site binding model after each titration (10.0 ± 6.7 – NAD+ vs. PLL and 10 ± 4.5 – NAD+ vs. HA). This suggested that stoichiometric binding of NAD+ to PLL occurs between NAD+ % (w/w) ratios of 2.8 and 14%

(w/w) whereas between 4.3 and 11.2% (w/w) of NAD+ is sufficient to achieve stoichiometric binding with HA.

3.3.2 Qualitative Analysis of NAD+ Association

3.3.2.1 Fourier-Transform Infrared Spectroscopy Analysis

Firstly, upon analysis of a physical mixture of HA, PLL and NAD+ powder, in a 1:1:1 mass ratio, no significant interactions were evident between NAD+ and the respective polyelectrolyte materials. NAD+ exhibited four characteristic infrared (IR) absorption bands, as highlighted in Figure 3.4. The IR absorption peaks at 1072 cm^{-1} and 1239 cm^{-1} were attributed to the symmetric and asymmetric stretching of the pyrophosphate bridge linking the adenosine and nicotinamide moieties ($O=P-O^-$) [437], [438]. Stretching of the 3-carboxamide carbonyl group of the nicotinamide moiety generated a strong IR absorption peak at 1697 cm^{-1} [439]. Finally, the IR absorption band at 1417 cm^{-1} was characteristic of stretching vibrations within both the nicotinamide and adenine moieties of NAD+ [437]. The in-plane bending of the oxygen to hydrogen in the hydroxyl groups of ribose may also have contributed to the generation of this absorption band.

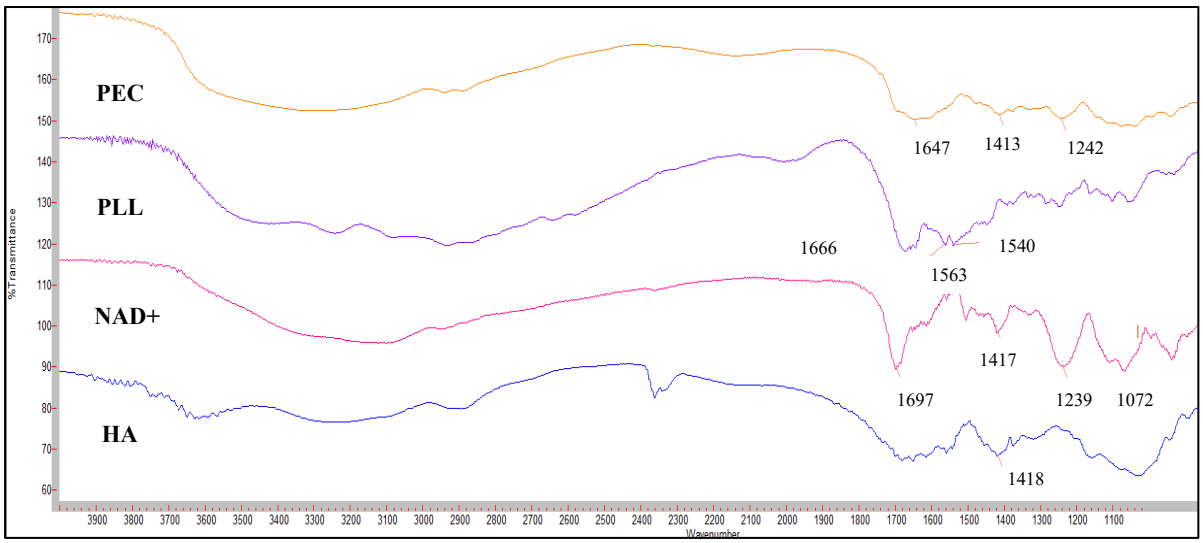

Figure 3.4: FT-IR spectra generated upon analysis of the individual starting materials and the HA:PLL PECs. (Resolution – 2 cm^{-1}).

A slight downward shift in the NAD+ absorption band, representing the C_4-N_9-C_8-H stretching vibrations in the nicotinamide and adenine moieties, from 1417 to 1413 cm^{-1} was observed in the PEC FT-IR spectrum in Figure 3.4. This may be attributed to an overlap with the absorption band representing the symmetric stretching of the HA carboxylate (COO^-) group that occurs at 1411 cm^{-1} [380], [437]. With this PEC, prepared with 50% (w/w) NAD+ and a molar charge ratio of 2, residual COO^- would likely still be present in the PEC formulation. The absorption bands corresponding to the amide I carboxyl (C=O) stretching vibrations (1666 cm^{-1}) and the amide II (C-N and N-H) in-plane bending vibrations (1563 cm^{-1}) of PLL are not present in the spectrum of the NAD+-associated PEC [381]. This may be due to the significant overlap of absorption bands generated by HA, PLL and NAD+ within this absorption region, including the asymmetric stretching of the HA carboxylate anion (1625 cm^{-1}), the stretching of the amide I (C=O) and bending of the amide II (N-H) absorption bands of HA and the stretching of the carbon to nitrogen bond with the carboxamide groups of NAD+ [378], [379], [439], [440]. Also, the complexation of PLL to HA would have enhanced the double bond character of the PLL amide group due to its proximity to the cationic amine group. As such, the in-plane bending of the N-H bonds within the PLL amide group would have shifted upfield to a higher frequency from its initial wavelength at 1563 cm^{-1}.

3.3.2.2 Scanning Electron Microscopy with Energy Dispersive Spectroscopy

The presence of sub-micron-sized PECs is evident from the SEM micrograph shown in Figure 3.5 (a). Both larger PEC particles, within the micron range, and dense, non-porous, three-dimensional sheets were also observed in the sample. This may be attributed to the association of macroscopic PECs, thus forming aggregated, irregular-shaped clusters. Ferreira *et al.* [441] made a similar observation upon analysis of chitosan and carboxymethylcellulose PECs, in which macroscopic PECs, with approximate particle size distributions between 0 and 1000 nm, appeared as dense, highly aggregated networks. The correlogram shown in Figure 3.5 (b), obtained upon analysis of the PECs in the present study, corroborated this assumption.

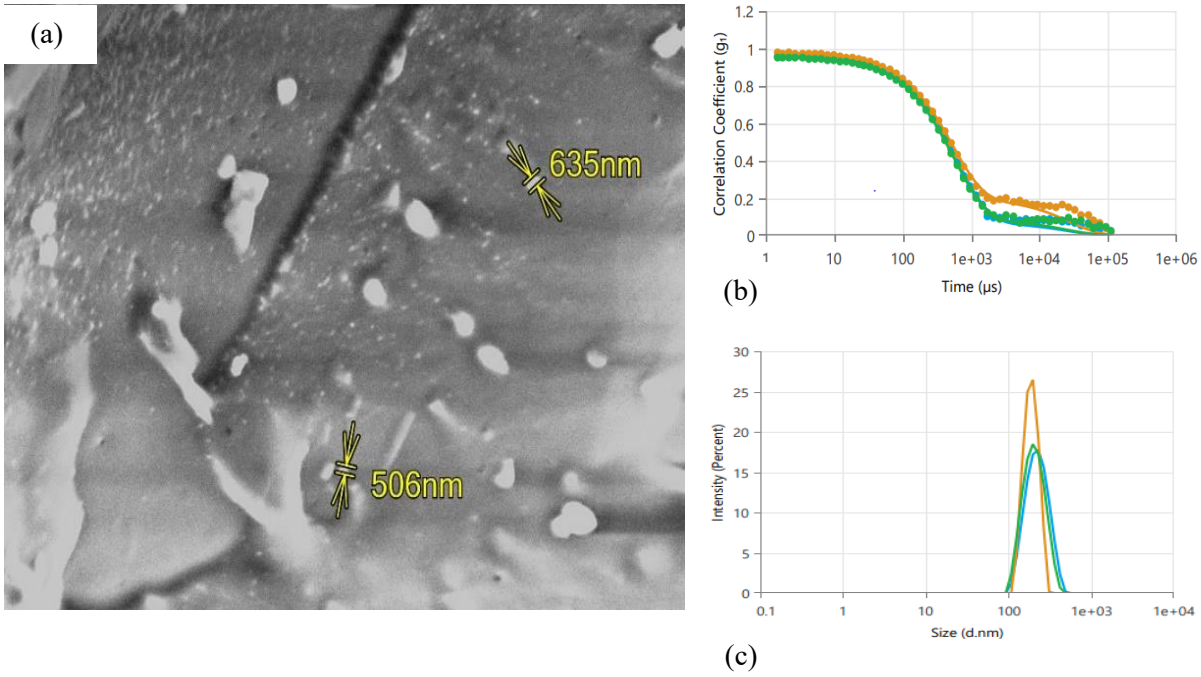

Figure 3.5: Representative SEM micrographs of the PEC (a). Images were taken under the following conditions: Mixed image (backscattered and secondary electrons), 10 kV accelerating voltage, 6.5 mm x 2.00 k, scale – 20 µM). The correlogram (b) and the particle size distribution plot (c) of the sample are also shown for information purposes.

Detection of scattering intensity from a small number of large particles that were outside the specified range of detection (> 10,000 nm) in the scattering volume results in number fluctuations. This ultimately results in poor baseline definition in the resulting correlogram, as shown in Figure 3.5 (b).

The elemental line profiles shown in Figure 3.6, generated by drawing lines in situ on the SEM images captured, confirm the complexation of NAD+ to the complexes analysed, primarily due to the presence of the phosphorous peak within the profiles. The energy of the resulting x-ray emission detected following irradiation of the PEC sample with the incident high-energy electron beam is equivalent to the difference between the higher and lower energy levels of phosphorus, an element specific to the molecular structure of NAD+ [442].

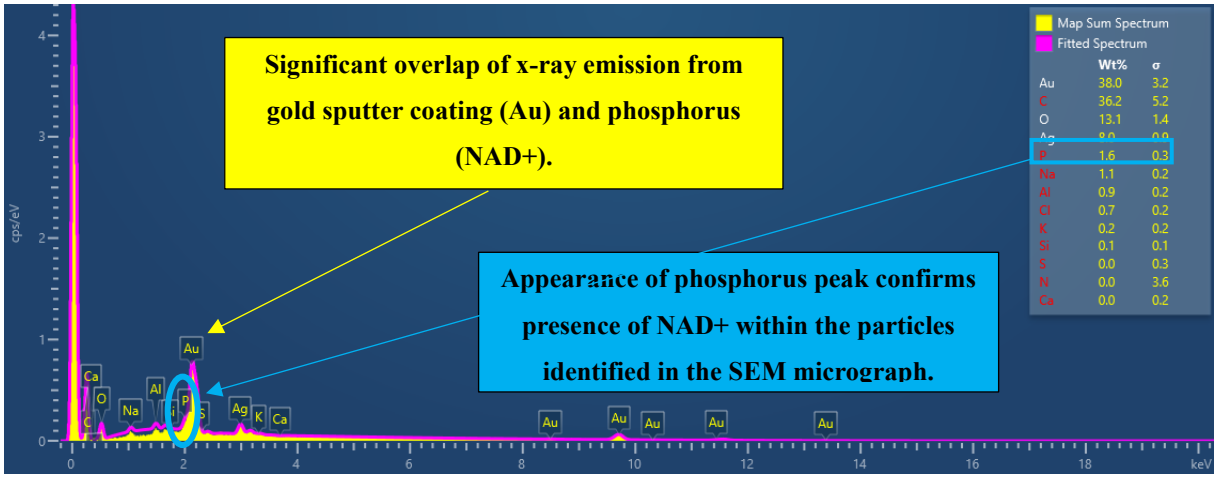

Figure 3.6: EDX elemental spectrum profiles, generated using the SEM micrographs of F9 shown in Figure 3.5.

However, phosphorous appears to be present in relatively low abundance (1.6 ± 0.3 wt. % - two PEC particles were identified in the micrograph. This may be attributed to the sputter coating of the SEM stubs before analysis. Sputter coating is advantageous for SEM analysis as it enhances the emission of secondary electrons from the surface of the sample, thus amplifying the signal-to-noise ratio and improving overall image quality [443]. Sputter coating with a highly conductive material, such as gold, can conceal the contrast between elements of varying atomic numbers. As such, the prominent peak within the EDX spectrum representing the x-ray emission from gold was overlapping that of phosphorus [444]. Although the phosphorous peak is present and given the typical error associated with the identification of minor elements using EDX (approximately ± 2 to 5%), SEM-EDX alone should not be used to determine sample composition and should be used to support observations made using alternative qualitative methodologies.

3.3.3 Quantification of NAD+ Association Efficiency

3.3.3.1 Validation of NAD+ HPLC Method

The key validation data, calculated upon analysis of NAD+ analytical standard solutions in the concentration range of 0 to 200 µg/mL, are summarised in Table 3.3.

Table 3.3: The correlation coefficient (R^2), limit of detection (LOD) and limit of quantification (LOQ) values generated upon analysis of twelve NAD+ analytical standard solutions using the Agilent 1200 HPLC system. Intra-assay precision is also represented by the coefficient of variation (CV) values obtained for each analytical standard. Data is expressed as mean ± S.D (conducted in duplicate).

			INTRA-ASSAY PRECISION	LINEARITY		
Standard Concentration (µg/ml)	**Mean Area (mAu*s)**	**Standard Deviation**	**CV (%)**	**Correlation Coefficient (R^2)**	**LOD (µg/ml)**	**LOQ (µg/ml)**
2	9.75	0.212	2.18			
4	18.90	0.141	0.75			
6	32.70	1.273	3.89			
8	44.45	0.071	0.16			
10	54.85	0.071	0.13			
20	104.95	0.071	0.07	0.9999	3.16	9.58
40	214.25	0.495	0.23			
60	322.65	0.354	0.11			
80	434.00	2.121	0.49			
100	555.15	0.636	0.11			
200	1090.90	1.980	0.18			

The NAD+ standard solutions exhibit linearity within the specified ranges, as indicated by R^2 value of > 0.95. The LOD value of 3.16 µg/mL represented the lowest analyte concentration that can be reliably distinguished from the analytical noise whereas 9.58 µg/mL was identified as the lowest concentration of NAD+ that can be quantitatively detected with a stated accuracy and precision [445]. To facilitate the accurate quantitation of NAD+ in sample solutions, at least five replicate injections of a bracketing standard with a concentration of 100 µg/mL (bracketing standard A) were included in each analytical run [446]. System suitability was verified by standard compliance via the preparation and injection of a duplicate standard of equivalent concentration (bracketing standard B). Compliance was achieved if the response ratio of the duplicate standards did not differ by more than 2%. Regarding system suitability, fresh bracketing standards were prepared if the replicate standard injections exhibited a percentage relative standard deviation value (%RSD) of ≥ 2.0% during the analytical run [447].

The HPLC analytical method was also validated on the Waters e2695 separations module used to analyse the *in vitro* release samples. Linearity was confirmed within the aforementioned concentration range (R^2 = 1) with LOD and LOQ values of 2.09 µg/mL and 6.33 µg/mL, respectively.

3.3.3.2 NAD+ Association Efficiency

Drug encapsulation efficiency is a critical quality attribute of nanomaterial formulations. Encapsulation efficiency (EE) studies are used to estimate the pharmacodynamic profile of the formation via the estimation of the amount of drug directly encapsulated within, or associated with, the nanomaterial [448]. As NAD+ is both hydrophilic and positively charged at a pH of 5.5, it was hypothesised that NAD+ would complex directly to residual carboxylate anions of HA and preferentially reside within the hydrophilic corona as opposed to being entrapped within the charge-neutralised, hydrophobic complex core. As such, the NAD+ EE was more appropriately referred to as NAD+ association efficiency (AE).

As the quantification of AE is dependent on solvation and degradation of the nanomaterial, direct NAD+ AE, using F8 as a model PEC, was first investigated in various solvent systems to determine the optimal solvent system for accurate NAD+ AE determination. The results of this study are shown in Table 3.4.

Table 3.4: The extraction of NAD+ from the F8 formulation using various extraction solvent systems.

Solvent System	% Association Efficiency (n = 5)
Mobile phase diluent	22.2 ± 3.8
pH 5.5 ultrapure water	21.5 ± 3.9
Phosphate buffer saline (PBS)	18.7 ± 2.8
Mobile Phase:Methanol (50:50)	29.2 ± 11.2
PBS:Methanol (50:50)	25.2 ± 4.7
PBS:Methanol:Hydrochloric acid	19.2 ± 2.1

The difference in NAD+ AE values in each of the solvent systems analysed was found to be statistically insignificant ($p = 0.134 > 0.05$) using a one-way ANOVA combined with a Games-Howell non-parametric post-hoc test. As such, mobile phase was used as the extraction solvent for NAD+ AE determination going forward. Not only is it used as a diluent in the study from

which the HPLC chromatographic method was adapted, but it was hypothesised that the increasing ionic strength imparted by the 20 mM potassium phosphate buffer may contribute to the destabilisation of the complexes, facilitating NAD+ release into the extraction solvent [449], [450].

Aside from economic advantages, high AE values are desirable as it decreases the quantity of the nanomaterial formulation required to deliver a therapeutic concentration of the drug in question. This is particularly advantageous as it reduces unwanted adverse effects that the administration of a large quantity of nanomaterial may evoke [451]. For example, nanoparticles exhibit a higher surface area in comparison to bulk reagents which can lead to increased biological activity due to the higher likelihood of surface-mediated interactions [452], [453]. For example, Zhu *et al.* [454] demonstrated a poly(ethylene glycol)-poly(ε-caprolactone) nanoparticle concentration-dependent decrease in kidney and liver function in an *in vivo* murine model. A reduction in cell viability to approximately 70% was observed by Azadi *et al.* [455] upon incubation of human corneal epithelial cells with 100 μg/ml of surface-modified poly(lactic-co-glycolic) acid nanoparticles. AE values are highly dependent on both the individual physicochemical parameters of both the nanomaterial and the drug and the extent to which they interact via intra and intermolecular bonding [456]. Indirect AE values, calculated following quantification of the NAD+ within the uncomplexed fraction after centrifugation, were statistically similar to the direct AE values. Direct AE values were calculated upon quantification of the NAD+ within the PECs isolated in the filter during centrifugation.

A reduction in theoretical NAD+ loading concentration from 100% to 50% (w/w) (F8 vs. F9), led to a significant increase in NAD+ AE, as shown in Table 3.5 ($p = 0.001 < 0.05$).

Table 3.5: The quantification of NAD+ AE and loading capacities (LC) in the F8 to F10 PECs. Data is expressed as mean % ± S.D (n = 3).

Parameter	F8	F9	F10
Concentration of NAD+ (% (w/w))	100	50	50
HA:PLL:NAD+ Charge Ratio	0.83	1.2	1.2
Direct AE (%)	22.3 ± 3.8	77.2 ± 9.5	65.4 ± 4.4
Indirect AE (%)	30.6 ± 9.0	90.3 ± 1.3	84.1 ± 1.5
LC (%)	56.9 ± 6.9	42.3 ± 5.3	36.3 ± 4.5

A lower NAD+ loading concentration may have established a smaller concentration gradient between areas of high and low NAD+ concentration within the formulation medium, thus decreasing the rate of free NAD+ diffusion into the uncomplexed fraction during centrifugation and improving the AE value. However, assuming the surface area available for NAD+ association in both F8 and F9 are equal, a larger number of free NAD+ molecules would be present in the medium of the F8 formulation (polyelectrolyte:NAD+ mass ratio of 1:1) following NAD+ association via physical adsorption in comparison to F9 (polyelectrolyte:NAD+ mass ratio of 2:1). Such free NAD+ molecules would be ultimately removed via centrifugation, thus resulting in the calculation of a low % AE value, as depicted in Figure 3.7.

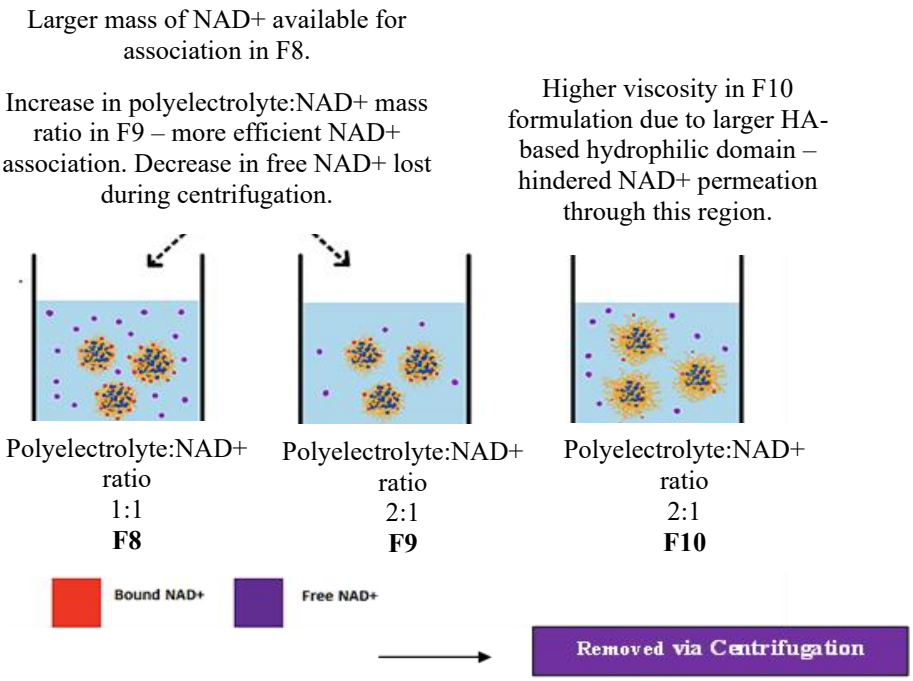

Figure 3.7: A schematic representing the proposed trends in AE values calculated for the F8, F9 and F10 formulations.

Interestingly, an increase in polyelectrolyte concentration did not increase NAD+ AE. Hypothetically, the F10 formulation should exhibit higher NAD+ loading than F9 due to the larger number of carboxyl and hydroxyl functional groups that are available for NAD+ binding via intermolecular interactions [457]. This may be attributed to the increase in chain entanglement and intermolecular bonding with an increase in polyelectrolyte concentration from 2% to 5% (w/v). This increase in intermolecular bonding leads to an increase in HA intrinsic viscosity and strengthens the rigidity of the entangled network created by overlapping HA chains on the PEC surface [458]. Kim *et al.* [459] also commented on the ability of HA to form a dense diffusion barrier on the surface of the PECs when present in excess of chitosan. However, contrary to what was observed in this study, an increase in propolis entrapment was attributed to this physicochemical characteristic. This may be attributed to both the size and hydrophobicity of propolis in comparison to NAD+. Propolis would preferentially reside within the charge-neutralised PEC core during complexation and would therefore be enveloped by the residual HA chains within the corona during complexation. Conversely, NAD+,

preferentially binding to the surface of the 5% (w/v) PECs, would exhibit hindered diffusion through the rigid HA meshwork during PEC formation in comparison to the more weakly associated network at 2% (w/v), rendering it more susceptible to premature release during preparation. Ortiz *et al.* [460] reported a decrease in diclofenac sodium, exhibiting higher aqueous solubility than propolis, loading capacity with an increase in carboxymethylagarose:chitosan wt. % ratio from 1:1 to 2:1. Nikolova *et al.* [461] attributed the decrease in diclofenac sodium encapsulation efficiency from 89 ± 1 to 29 ± 7% with an increase in 0.05 wt.% chitosan:0.05 wt% alginate volume ratio from 1:1 to 2:1 to the limited intra-PEC diffusion of diclofenac sodium due to preferential surface absorption with the cationic PEC surface.

3.3.4 Effect of Polyelectrolyte and NAD+ Loading Concentration on Size Parameters

The size distribution plots obtained for the F8 to F10 formulations prepared in this study are shown in Figure 3.8.

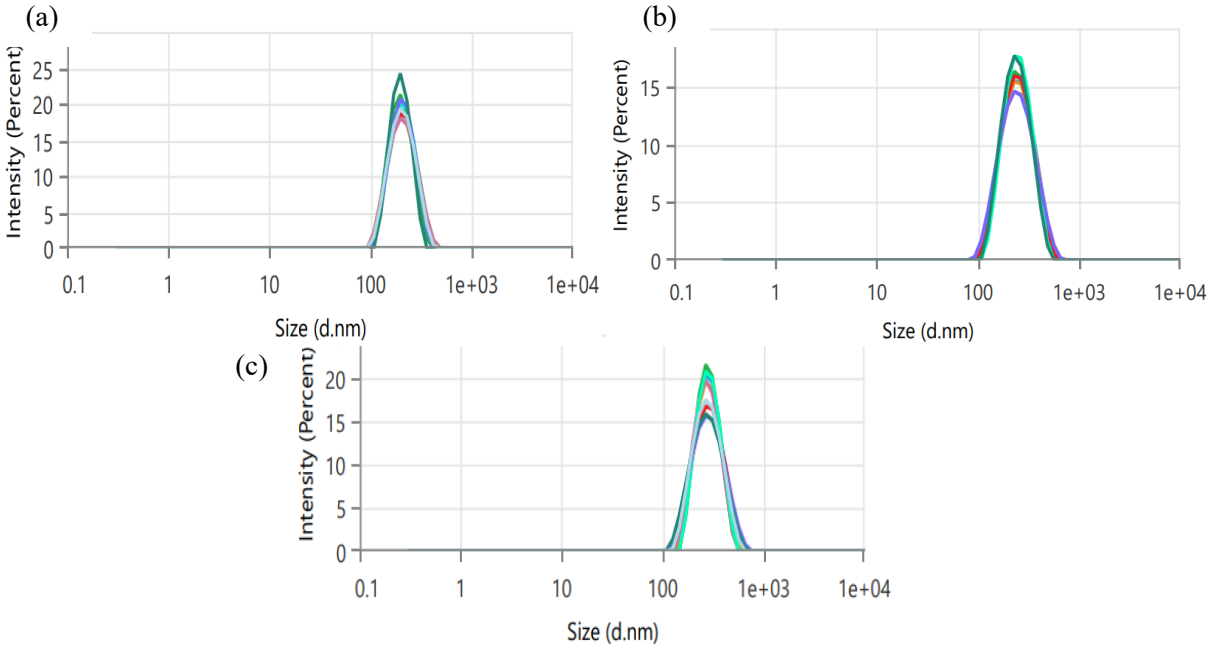

Figure 3.8: Size distribution plots of the F8 (a), F9 (b) and F10 (c) formulations, by intensity (after lyophilisation with 1% (w/w) trehalose). (n = 9 – 3 samples of each formulation with 3 runs each).

Upon comparing the values obtained for F9 and F10, an increase in polyelectrolyte concentration from 2% (F9) to 5% (w/v) (F10) resulted in a slight increase in PEC size from 235.1 ± 19.0 nm to 267.7 ± 1.8 nm. The F10 formulation exhibited ZP and PDI values of -31.3 ± 9.4 mV and 0.129 ± 0.045, respectively. However, the hydrodynamic diameter ($p = 0.099 > 0.05$) and ZP values ($p = 0.348 > 0.05$) of F9 and F10 were found to be statistically equivalent. This was not as expected as an increase in polyelectrolyte concentration should correspond to an increase in PEC size, primarily due to secondary PEC aggregation. An increase in polyelectrolyte concentration results in a corresponding decrease in Debye length (λD), primarily due to an increase in surface electrostatic charge screening by a larger number of released sodium (Na^+) and chloride (Cl^-) counter ions [462], [287], [395], [401]. This dual reduction in λD and electrostatic stabilisation promotes secondary aggregation of primary PECs, resulting in an increase in size. Also, due to the weakening of the electrostatic cross-linking bonds between PLL and HA as a result of enhanced electrostatic screening, the PECs formed may adopt a more loosely bound structure. Intracomplex water ingression will increase as a result, causing the PECs to swell and continually grow in size [355]. Gao *et al.* [463] observed a poly(diallyldimethylammonium) chloride (PDADMAC) concentration-dependent increase in size for PDADMAC and polyacrylic acid (PAA)-based PECs. At PDADMAC concentrations above the critical polyelectrolyte concentration (c*), the concentration at which the PECs transitioned from a soluble to a colloidal state, occurred at lower PAA:PDADMAC charge ratios, primarily due to enhanced chain entanglement and overlap. Aggregation, as evidenced by the formation of macroscopic aggregates and a clear supernatant with chitosan and carboxymethylcellulose PECs containing high CMC mass ratios, was also observed by Ferreira *et al.* [464]. The concentrations investigated as part of the present study may be below the c* value of this system. Therefore, only relatively small fluctuations in size parameters are observed below this point.

F9 (235.1 ± 19.0 nm) exhibited a larger hydrodynamic diameter than that of F8 (194.8 1 ± 2.4 nm). Similar ZP values of -35.0 ± 1.9 mV and -38.0 ± 1.1 mV were also obtained for F8 and F9, respectively. However, no significant difference was found between the hydrodynamic diameter ($p = 0.068 > 0.05$) and ZP values ($p = 0.078 > 0.05$). The small decrease in size observed may be attributed to the increase in NAD+ LC with an increase in theoretical NAD+

loading concentration from 50% (w/w) to 100% (w/w) in F8, as highlighted in Table 3.5. Possessing both charged functional groups and a number of electronegative atoms, NAD+ can readily partake in both electrostatic bonding and hydrogen bonding with the respective polyelectrolytes. Upon neutralisation of the residual charges, the associated NAD+ and HA/PLL moieties may migrate towards the more charge-neutralised, hydrophobic domain within the PEC core, resulting in a more compact PEC structure. The higher the NAD+ LC, the greater the likelihood of such bond formation. This trend is further supported upon comparing the size of the NAD+-laden PECs to that of the reference PECs (F3) described in Section 2.3.7. Matha *et al.* [319] also observed a decrease in anionic HA and poly(arginine) complex size from 206 nm to 161 nm after the addition of cationic diaminocyclohexane-platinum, attributed to enhanced electrostatic interaction between the individual components. Conversely, Sladek *et al.* [465] reported an increase in HA and chitosan PEC size from 232 ± 36 nm to 295 ± 58 nm with an increase in insulin loading from 100 to 500 μg/mL. This may be attributed to the association of a therapeutic (insulin = 5.8 kDa) that is approximately 10 times larger than that of NAD+ (0.663 kDa).

3.3.5 Stability of PECs under Various Conditions

3.3.5.1 NAD+ Stability in Sample Media

The stability of NAD+, calculated as the recovery of NAD+ as a percentage of the initial concentration of the NAD+ solutions, was first assessed in each sample media under the conditions to be used in both the stability and *in vitro* release studies. As shown in Table 3.6, no significant difference was found between the % recovery of NAD+ at t_0 and after 24 hours in each sample medium, thus indicating that NAD+ remained stable in each sample medium over this period of time. Stability was also maintained over one week, as evidenced by the statistically equivalent % NAD+ recoveries obtained between 24 and 48 hours, and 48 hours and 168 hours, respectively. Aside from the sample in ultrapure water at pH 5.5, % NAD+ recoveries significantly decreased between the one-week and two-week time points, suggesting NAD+ degradation ($p \sim 0.000 << 0.05$). This was further elucidated by the increase in the area of a secondary peak within the NAD+ chromatogram, eluting at a retention time of approximately 3.2 minutes, from 0 to 168 hours in all sample medium analysed. The time-

dependent increase in peak area of this secondary peak is shown in the example chromatogram in Figure 3.9.

Table 3.6: Percentage NAD+ recoveries in each sample medium over a weeklong period. Data is expressed as mean % recovery ± S.D (n = 3).

Sample Media	% at 0 Hours	% at 8 Hours	% at 24 Hours	% at 48 Hours	% at 168 Hours	% at 336 Hours
0.01 M PBS (pH 7.4)	93.4 ± 2.3	90.9 ± 1.4	89.5 ± 5.3	90.2 ±11.7	85.0 ± 3.8	53.3 ± 3.6
0.01 M PBS (pH 5.5)	89.4 ± 0.1	85.8 ± 1.7	89.6 ± 7.3	82.9 ± 2.7	90.2 ± 1.7	65.4 ± 3.9
Ultrapure Water (pH 7.4)	88.8 ± 5.6	95.9 ± 3.6	83.9 ± 7.0	86.6 ± 8.2	93.7 ± 3.9	65.6 ± 2.5
Ultrapure Water (pH 5.5)	84.4 ± 2.4	82.3 ± 2.9	80.6 ± 1.3	79.4 ± 6.2	77.7 ± 13.9	61.1 ± 1.6

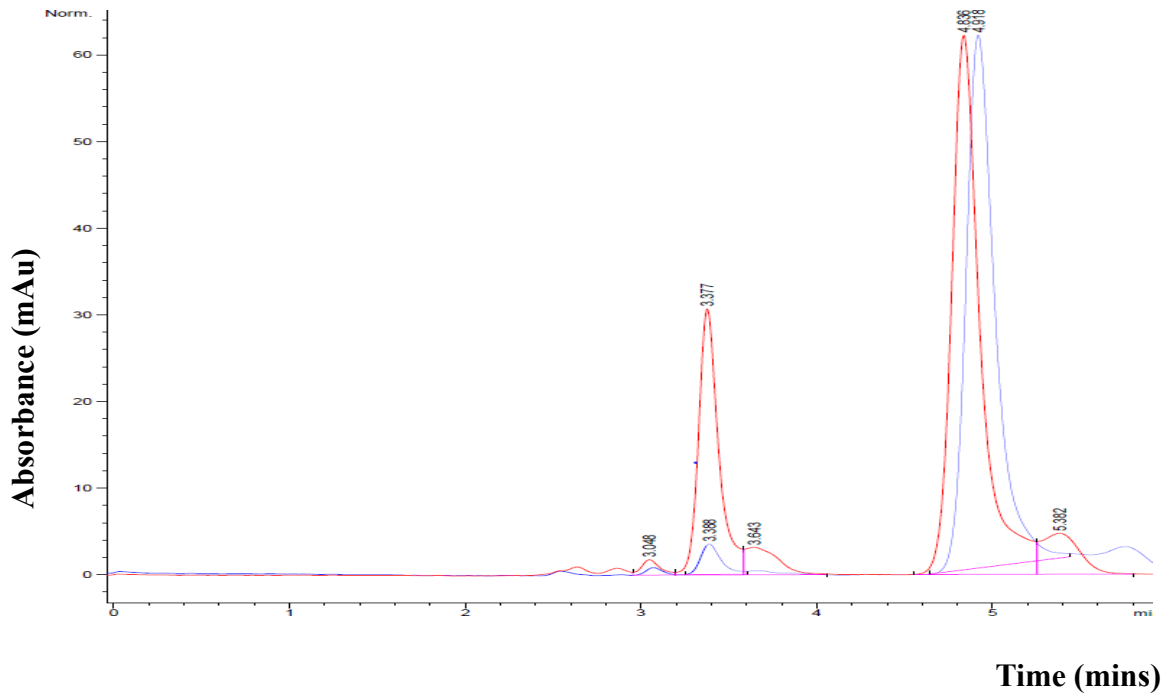

Figure 3.9: Representative HPLC chromatograms generated upon analysis of NAD+ at t_0 (blue) and after 168 hours post-incubation in 0.01 M PBS (pH 7.4) (red).

Although stability data was not provided, Yoshino *et al.* [466] reported that 100 µM NAD+ solutions, prepared in water, were stable for at least two weeks when stored at 4 °C. Anderson *et al.* [467] demonstrated that the rate of NAD+ degradation via hydroxyl ion-mediated hydrolysis of the nicotinamide-ribose linkage was higher in various phosphate buffers than in nitrogen-based buffers at neutral pH. However, when investigating the stability of NADH in phosphate buffer at pH 6.8, Rover *et al.* [468] discovered that the decomposition of NADH in phosphate buffer via phosphate ion-mediated oxidation, indicated by a decrease in the UV absorption peak at 340 nm, led to an increase in NAD+ generation. Overall, NAD+ exhibited suitable stability in the sample media to be analysed over the desired timeframe for analysis of once- or twice-daily topical ocular delivery systems [469].

3.3.5.2 PEC Matrix Stability in Response to Environmental Stimuli

Based on the pH and ionic strength-dependent behaviour of the respective polyelectrolytes outlined in Sections 2.3.1 and 2.3.6, the stability of the formulated PECs in conditions simulating that of the physiological tear film was identified as a critical quality attribute. Sensitivity to such conditions could prove detrimental to the use of NAD+-laden PECs as ocular drug delivery systems, as rapid PEC destabilisation in tear film could result in premature NAD+ loss to systemic circulation via the nasolacrimal duct and conjunctival vasculature [145], [147], [193], [470]. Average human tear fluid exhibits an electrolyte concentration (based on Na^+, K^+, Cl^- and HCO_3^-) of ~ 300 mmol/L (0.3 M) with an approximate ionic strength of 0.18 M [471]–[473].

Stability of the reference NAD+-associated PEC (F9), in physiological medium was first assessed via changes in percentage transmittance. As shown in

Table ***3.7***, the percentage transmittance increased (decrease in turbidity) upon dilution in 0.01 M PBS, providing a preliminary indication that the presence of ions has an impact on PEC formation.

Table 3.7: The mean percentage transmittance (%T) values of the F9 stability solutions in 0.01 M PBS buffer, compared to that of the control F9 solution diluted with ultrapure water at pH 5.5. Data is expressed as % mean transmittance at 500 nm ± S.D (n = 3).

PEC	Diluent	Ionic Strength (M)	%T
F9	Water (Control)	0.229	0.67 ± 0.13
	PBS (0.01 M)	0.211	36.92 ± 2.40

A time-dependent increase in NAD+-associated PEC size was observed in 0.01 M PBS at pH 7.4. As shown in Figure 3.10, an increase in size from 248 ± 84.6 nm to 429.3 ± 51.1 nm to 1340.3 ± 204.8 nm was evident between 0 and 8, and 8 to 24 hours, post-incubation. The PECs stored in 0.01 M PBS (pH 7.4) were also significantly larger than those stored in ultrapure water at equivalent pH at each time point apart from t_0.

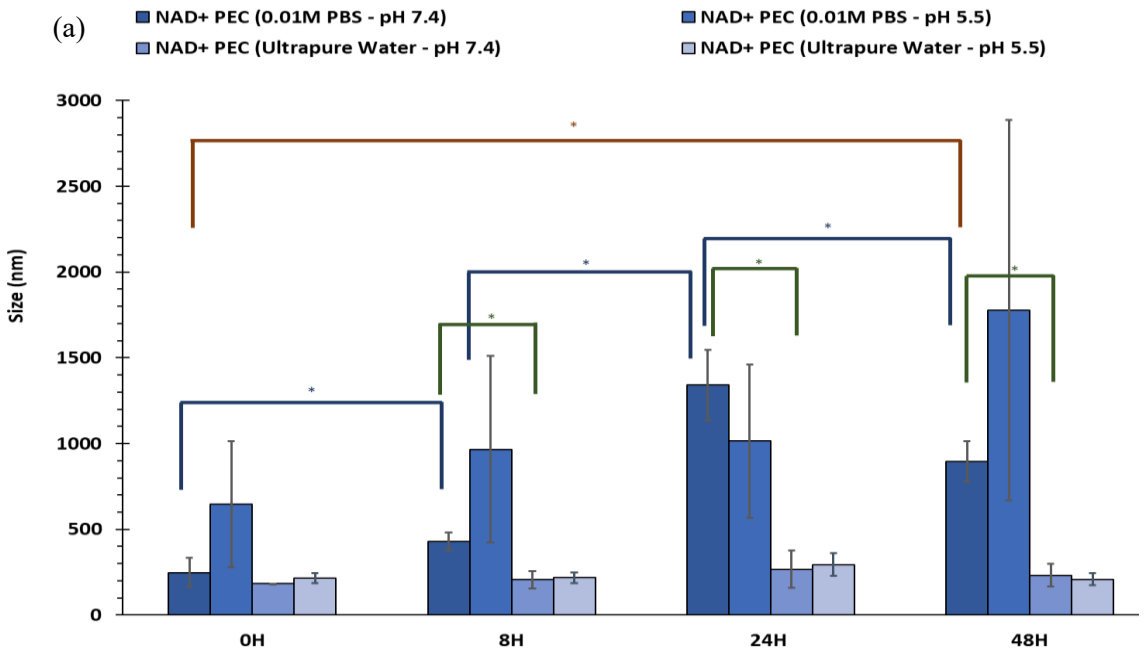

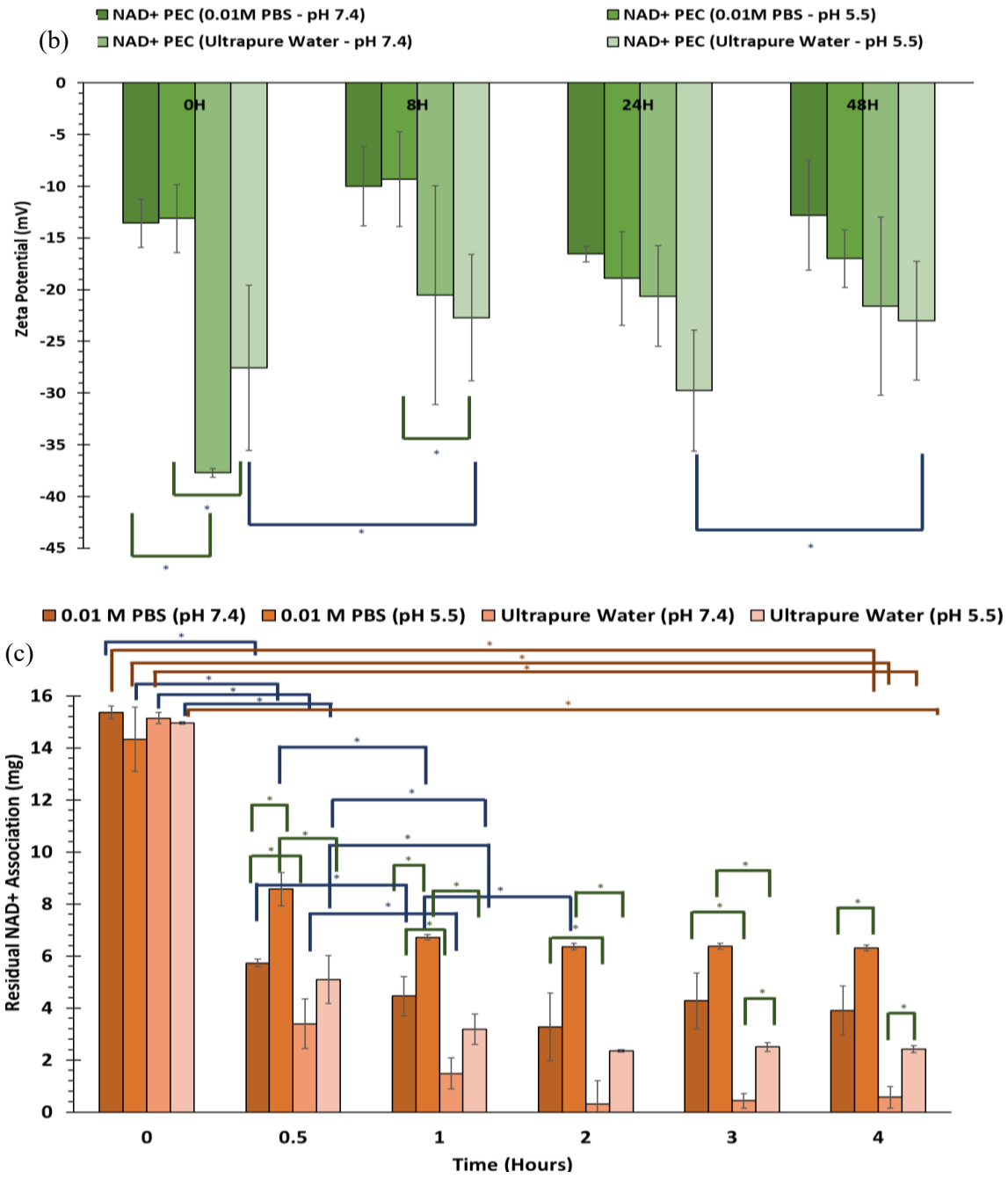

Figure 3.10: The change in size (a), ZP (b) and % NAD+ association (c) values for the NAD+ -associated PECs as a function of time in each of the sample media analysed. Data is expressed as mean ± S.D (n = 3). (* - statistically significant at a 5% confidence interval. Colour of the statistical significance bar: blue – between time points, green – between conditions and orange – from first to last time point).

This further supports the hypothesis that, due to the enhanced charge screening between neighbouring PECs, PECs may tend towards aggregation via a loss in electrostatic repulsion in a physiological medium. This phenomenon has been well documented in literature, with almost a direct correlation between PEC size and salt concentration and irreversible, macroscopic aggregation being observed above a certain salt concentration [291], [474]. Above a critical ionic strength value, the infiltration of large amounts of ions into the PEC structures results in the compression of polyelectrolyte-polyelectrolyte ion pairing, leading to a reduction in PEC nucleation, re-dissolution of the individual polyelectrolytes, and the formation of an optically clear system [293], [401], [475]. Kayitmazer *et al.* [476] demonstrated that the critical ionic strength of hyaluronic acid and chitosan-based PEC systems was 0.35 M (NaCl), equating to a Debye length of approximately 0.5 nm. The critical ionic strength was also found to be dependent on the pH of the formulation, primarily due to its effect on the ionisation and subsequent charge density of the individual polyelectrolytes. At a constant charge ratio of 7, the size of PLL, bioreducible-PLL and polyethylamine polyplexes, laden with DNA, increased with an increase in NaCl concentration from 0 to 160 mM [477]. At low ionic NaCl concentration (> 30 mM), polyplexes synthesised in the presence of 20 mM (4-(2-hydroxyethyl)-1-piperazineethanesulfonic acid) HEPES buffer were more resistant to ion-mediated aggregation, presumably attributed to the ability of a small concentration of ions to facilitate primary complex reconfiguration during complexation. This was also observed by Wu *et al.* [317] in which the addition of zinc (II) chloride or zinc (II) sulphate to HA and chitosan-based PECs preserved their stability, with respect to size, over 35 days in 0.01 M PBS maintained at 20 °C, attributed to the ability of zinc (II) to form bridging coordinate bonds with electron-rich donor groups on neighbouring HA chains.

In 0.01 M PBS, a reduction in pH to 5.5 resulted in an instantaneous increase in PEC size. This may be attributed to the dual effects of both ion-aggregation, combined with the swelling of the individual PECs due to the preservation of the electrostatic interactions between the individual HA and PLL chains when placed in an ionic medium at a pH equal to the pH at which maximal complexation occurs. No significant change in particle size was observed in ultrapure water over 48 hours, regardless of pH, ($p = 0.336 > 0.05$ – pH 7.4 (0–48 hours) and

$p = 0.678 > 0.05$ – pH 5.5 (0–48 hours)), thus highlighting the enhanced stability of the NAD+-associated PECs in the absence of ions.

As per Derjaguin, Landau, Verwey and Overbeek (DLVO) theory, to attain colloidal metastability, the energy of the PECs must not exceed that of the electrostatic energy barrier that exists between the primary and secondary minimum [478]. This is achieved via the establishment of a balance between the electrostatically repulsive surface forces, or ZP, and Van der Waals attractive forces [479]. Regardless of pH, there was an instantaneous reduction in ZP in the PECs stored in 0.01 M PBS in comparison to those stored in ultrapure water at t_0. Overall, the PECs in 0.01 M PBS exhibited lower ZP values at each time point. ZP was preserved from 0 to 48 hours in ultrapure water ($p = 0.087 > 0.05$ – pH 7.4 and $p = 0.467 > 0.05$ – pH 5.5). This ion-mediated reduction in ZP effectively decreases the extent of interparticle repulsion, thus lowering the energy of the electrostatic barrier [480]. This would lead to a metastable PEC dispersion with an increased number of particles having sufficient energy to exceed this electrostatic barrier and subsequently and irreversibly aggregate due to the predominance of Van der Waals attractive forces at short interparticle distances [478].

In both 0.01 M PBS and ultrapure water, a higher quantity of NAD+ remained associated with the PECs stored at pH 5.5, as shown in Figure 3.10 (c). The mass of NAD+ remaining within the PECs maintained at pH 7.4 in 0.01 M PBS (3.90 ± 0.95 mg) was significantly lower than that complexed to those maintained at pH 5.5 after 4 hours under equivalent ionic conditions (6.31 ± 0.11 mg). Similarly, the mass of NAD+ retained in the PEC sample at pH 7.4 in ultrapure water dropped below 1 mg (0.57 ± 0.41 mg) whilst 2.42 ± 0.14 mg was retained at pH 5.5 after 4 hours. At pH 7.4, ionisation of the cationic amino groups (NH_3^+) of PLL decreases to 23.2%. With the predominance of $-NH_2$ groups, such groups may now preferentially react via hydrophobic interactions, thus resulting in further collapse of the charge-neutralised, hydrophobic core and loosening of the dense HA to PLL meshwork, Such processes may limit the remaining surface area available for NAD+ association. At pH 5.5, preservation of the electrostatic interactions between HA and PLL allows for sequential diffusion and binding of NAD+ with the intact network via intermolecular interaction.

In general, a significant reduction in NAD+ association was observed in each sample medium over 4 hours. This may be attributed to the volume of sample media used. A large volume (100 mL) scale was used to ensure a rapid comparison of the environmental conditions under investigation [481]. However, the release of NAD+ into a sample volume that was significantly smaller than that of the receptor volume may have created a steep, osmotic gradient between the donor and the receptor compartment, thus driving NAD+ dissociation from the PECs.

3.3.5.3 PEC Stability under Storage Conditions

A significant increase in PEC size was observed upon storage at 25 °C in ultrapure water at pH 5.5 over 28 days ($p = 0.019 < 0.05$), as depicted in Figure 3.11 (a).

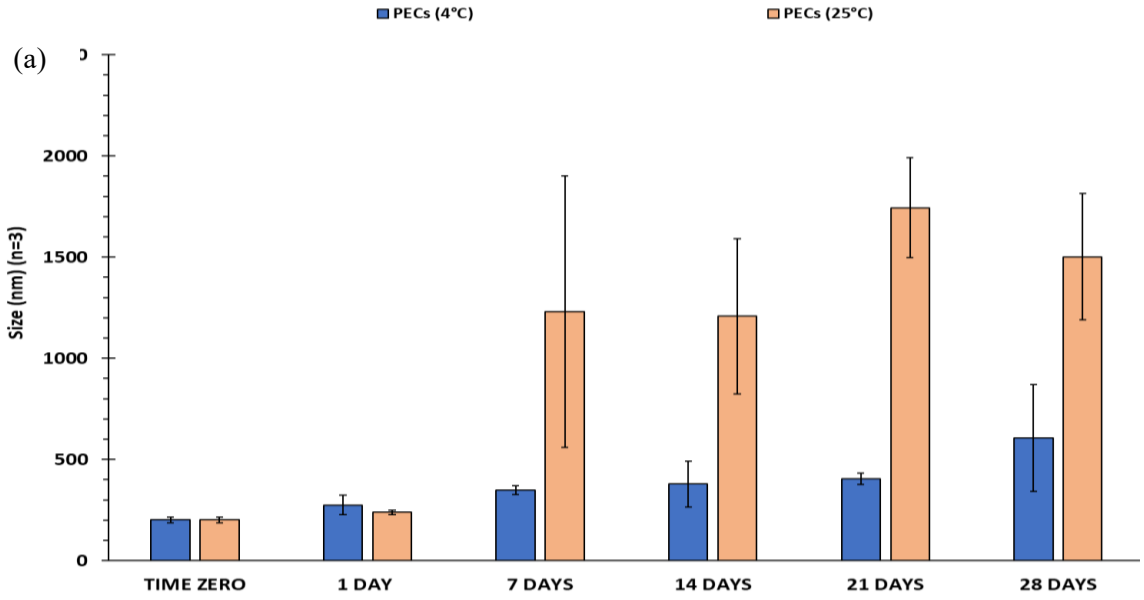

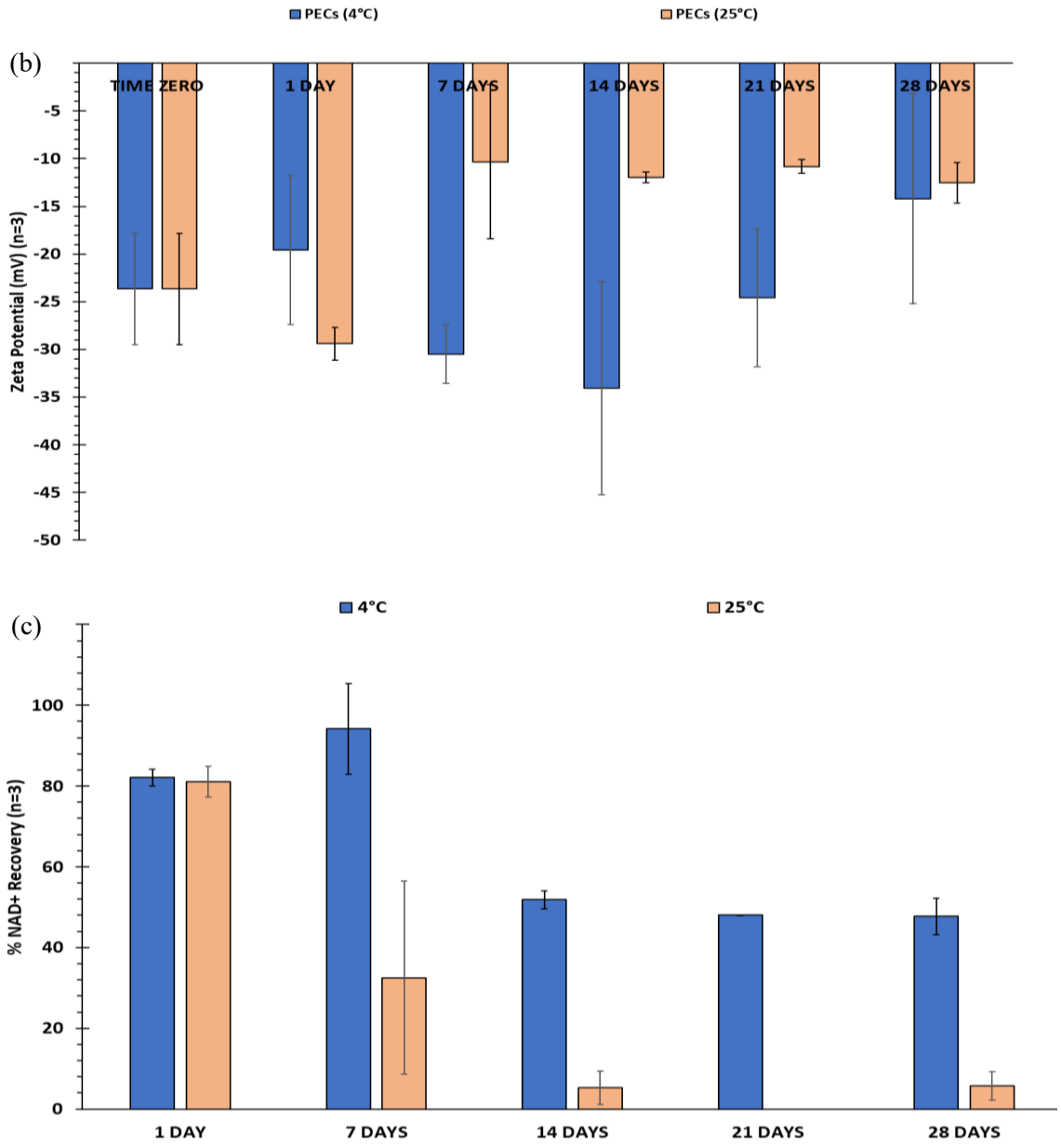

Figure 3.11: Changes in size (a), zeta potential (b) and NAD+ concentration (c) upon storage of NAD+-associated PECs formulations at 4 and 25 °C over one month (Data is expressed as mean ± S.D (n = 3).

This increase in PEC correlates to the significant loss in % NAD+ recovery from the PECs over one month ($p \sim 0.000 << 0.05$), particularly at 25 °C. Only 5.7 ± 3.5% of the loaded NAD+ concentration was recovered at 25 °C whereas 47.7 ± 4.5% was recovered at 4 °C. This

suggested that over time, PECs began to aggregate. In the absence of a colloidally stable PEC matrix barrier, NAD+ may have begun to degrade due to exposure to formulation conditions during storage. The decrease in NAD+ peak:secondary peak ratio from 19.3 ± 5.9 (initial – t_0) to 2.7 ± 1.8 (25 °C) and 11.6 ± 0.8 (4 °C), supported this hypothesis.

Ali *et al.* [482] demonstrated that the critical solution temperature of a PEC system composed of potassium-poly(styrenesulfonate) and poly(diallyl dimethylammonium) bromide was approximately 28 °C, as indicated by a significant decrease in transmittance within the temperature region. It was noted that further heating to 32 °C led to the formation of micron-sized droplets and subsequent macroscopic phase separation. Although not investigated by our group, maintaining PECs at critical temperatures for an extended period of time may invoke the same phase separation response.

A number of studies have demonstrated the prolonged stability of polymeric nanoparticles intended for ocular application when stored at 4 °C [483]–[485]. An increase in size from 200.8 ± 13.9 nm to 606.3 ± 264.9 nm was also observed over the same timeframe for PECs stored at 4 °C. However, this was found to be statistically insignificant ($p = 0.118 > 0.05$). Carton *et al.* [331] also observed an increase in HA and poly(arginine)-based PEC size over 28 days, particularly in PECs prepared with a large excess of HA in comparison to poly(arginine). This may have been attributed to the inherent water retention capabilities of HA as water immobilisation on HA chains results in the expansion of its hydrophilic domain, which may cause an increase in PEC size. However, despite a significant increase in PDI from 0.200 ± 0.046 to 0.360 ± 0.036 ($p = 0.009 < 0.05$) in our study, preservation of a negative zeta potential below – 20 mV (-24.58 ± 7.23 mV) up to 21 days suggests that significant aggregation of the discreet PECs was largely attenuated.

Overall, PEC stability, in terms of size, zeta potential and PDI, was attained for up to 21 days at 4 °C. However, the loss of over 50% of the loaded NAD+ concentration during storage of rehydrated, lyophilised PECs in aqueous medium at low temperatures severely limits their shelf-life under these conditions. Also, the PECs do not exhibit suitable stability for storage under ambient conditions. In terms of their translation into a product for end-patient use,

storage of the PECs in lyophilised form, followed by rehydration of the lyophilisate immediately before daily use, may be a suitable alternative.

3.3.6 Dynamic *In Vitro* NAD+ Release

3.3.6.1 In Vitro NAD+ Release Profile

In vitro release studies are crucial steps in the development process of a nanomaterial as it allows for simulation and estimation of the *in vivo* behaviour of the nanomaterial and is a critical indicator of its safety and efficacy [387], [486], [487]. Such studies also allow for the assessment of a nanomaterial to modify the release of the therapeutic via desorption, diffusion, and polymer erosion mechanisms [488]. NAD+ is inherently hydrophilic, exhibiting an experimental solubility of 1.10 ± 0.12 g/mL in 0.01 M PBS. As such, NAD+ is likely to complex with the residual HA chains on the surface of the PECs as opposed to being encapsulated within the hydrophobic, charge-neutralised core and may experience rapid *in vitro* release. Rapid release kinetics will result in the release of the therapeutic from the formulation within a short time after administration, thus potentially leading to the premature loss of the therapeutic away from the target site [487], [489]. The analysis of therapeutic release using a microfluidic physiological flow device allows for closer alignment of *in vitro* release results with *in vivo* conditions in comparison to infinite sink methodologies [481], [490]–[492]. The mean flowrate of tears on the corneal surface is ≈ 3 µL/min the dynamic inflow and outflow of aqueous humour via the trabecular and uveoscleral pathways is maintained at 2 and 3 µL/min [163], [493]. By analysing NAD+ release at a flow rate of ≈ 3 µL/min, the *in vivo* release behaviour of the PECs within the anterior segment can be more accurately predicted.

The F9 formulation was chosen for analysis of *in vitro* release under microfluidic conditions based on preliminary studies conducted under infinite sink conditions. F9, containing a lower NAD+ loading concentration (50% (w/w)), demonstrated a more sustained release of a smaller percentage of NAD+ over 8 hours (74.9 ± 6.5%) in comparison to that of both the F8 and F10 formulations (80.3 ± 3.6% and 66.6 ± 13.2%, respectively). Also, the release from F9 was statistically lower than that from an NAD+ control solution ($p = 0.0187 < 0.05$) under equivalent conditions, thus indicating that the PECs were providing some form of a steric barrier to NAD+ diffusion.

As shown in Figure 3.12, sustained release of 10.9 ± 0.2 mg of NAD+ was achieved for up to 14 hours under simulated ocular volumetric flowrates, delivering over 73.0 ± 2.1% of the total NAD+ payload/

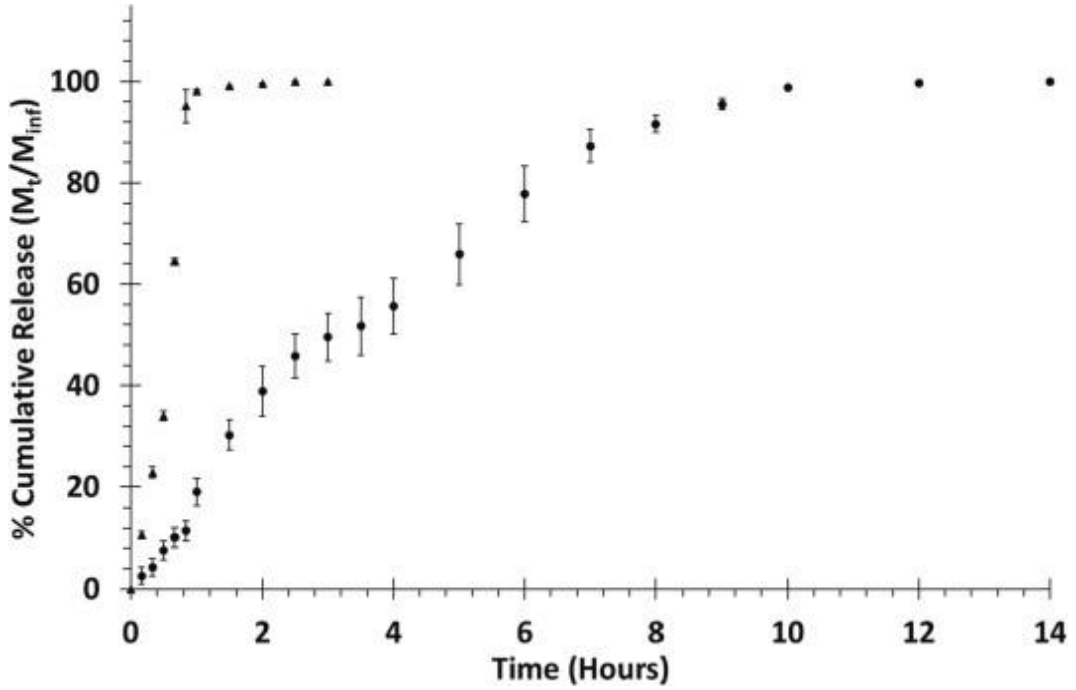

Figure 3.12: Cumulative *in vitro* NAD+ release profiles from the F9 formulation (circle) and an NAD+ bolus control (triangle) in 0.01 M PBS (pH 7.4) under microfluidic conditions. (Data is expressed as mean % Mt/Minf ± S.D (n = 3).

Regarding the release of NAD+ from an NAD+ solution under equivalent conditions, 11.6 ± 1.6 mg of NAD+ was released within an hour, whereas a statistically lower quantity of NAD+ (2.4 ± 0.3 mg) was released from the PECs over the same timeframe. Complete NAD+ release was obtained from the NAD+ control solution after just 3 hours. The release duration obtained from analysis of the PECs suggests gradual NAD+ diffusion through the nanochannels created in the PEC matrix, and that surface desorption is not the primary governing factor of NAD+ release.

Interestingly, a burst release of a large quantity of NAD+ was prevented under microfluidic conditions, with only 31.6 ± 3.4% of the total payload being released within the first 2 hours.

Burst release is attributed to the initial release of therapeutic molecules that are weakly associated with the surface of the nanomaterial formulation upon administration to the dispersion medium [488]. However, burst release phenomena can also be attributed to the formation of heterogeneous polymer matrices at the surface of the nanomaterial, drug loading via equilibrium partitioning, particularly at high loading concentrations and particle instability within the ocular environment [494], [495]. Although burst release is desirable for certain applications (wound treatments designed for immediate pain relief), the uncontrolled release of large concentrations of therapeutics, particularly for highly potent drugs, can result in local toxicity and unfavourable adverse effects [6], [7]. A burst release of hydrophilic therapeutics from polysaccharidic PEC systems is often observed, presumably due to a higher degree of surface adsorption in comparison to encapsulation. Dubashynskaya *et al.* [330] reported the ion-dependent rapid release of between 85-90% of the theoretical loading concentration of a hydrophilic, cationic antibiotic, colistin, from a HA-based PEC within one hour. Rapid release of between 80 to 100% of the theoretical concentration of dianionic adenosine 5′-triphosphate disodium salt (ATP) loaded into HA and phosphonium polyelectrolyte complexes was observed by Harrison *et al.* [496]. Similar to NAD+, ATP is also inherently soluble in water and was therefore rapidly released into the PBS release media in comparison to the other, more hydrophobic anionic salts analysed (fluorescein sodium salt - 40 – 100% release in 60 days, diclofenac sodium salt - 80 – 90% released in 60 days), thus demonstrating the importance of hydrophobic interactions in sustaining therapeutic release from the PEC matrix. Amato *et al.* [348] observed that over 60% of the loaded berberine concentration was released from HA and ε-poly(L-lysine) nanogels prepared via polyelectrolyte complexation within the first hour post-addition to a dialysis membrane submerged in 12 mL of a 0.9% (w/v) saline solution. The *in vitro* release of lidocaine hydrochloride from HA, chitosan, and pectin PECs was dependent on the concentration of HA used. PECs containing a higher % w/w of HA exhibited a more sustained lidocaine hydrochloride release, presumably due to the formation of a highly viscous HA meshwork on the PEC surface. Due to its supplementary nature, the multifactorial application of NAD+-associated PECs within both the anterior and posterior segments is possible. Therefore, if sustained release over a longer duration is required, the delaying effect of an increased concentration of HA in excess of both PLL and NAD+ may be a suitable starting

point for investigation. However, the effect of such an increase on the physicochemical attributes of the PECs must be considered, particularly regarding their electrochemical stability.

3.3.6.2 Mathematical Modelling of NAD+ Release Kinetics from PECs

The release of NAD+ from F9 in 0.01 M PBS (pH 7.4) was initially fitted to five different kinetic models to illustrate the mechanism of release from the PECs prepared. The model of best fit to the cumulative NAD+ release profile was selected based on the value of correlation coefficient (R^2) value obtained from each of the graphs plotted. The highest degree of correlation indicates the model of best fit to the experimental data. The kinetic data obtained upon fitting NAD+ release to each of the mathematical models used are summarised in Table 3.8.

Table 3.8: Kinetic analysis of NAD+ release from the F9 formulation using various mathematic models.

Kinetic Parameter	**Kinetic Models**				
	Zero Order	First-Order	Higuchi	Hixson-Crowell	Korsmeyer-Peppas
R^2	0.8847	0.9269	0.9626	0.1853	0.9424
k	5.901 %/min	0.171 min^{-1}	24.488 $\%/min^{1/2}$	-0.6891 $\%^{1/3}$/min	0.5591
n	-	-	-	-	0.8441

On the basis of best-fit, *in vitro* NAD+ release under microfluidic conditions was best fitted to the Higuchi mathematical model ($R^2 = 0.9626$), providing a good indication that diffusion was the primary phenomenon driving the release of NAD+ from the PEC. The release exponent value, or 'n', obtained following fitting to the Korsmeyer-Peppas model (0.8441, $R^2 = 0.9424$), also lies between 0.45 and 1, indicating that NAD+ release was governed by anomalous or non-Fickian diffusion, in which the rates of intrapolyelectrolyte NAD+ diffusion and polyelectrolyte relaxation are comparable [497], [498]. This may be attributed to the polyelectrolyte:NAD+ mass ratio of 2:1 within F9, resulting in increased PEC-NAD+ association and deeper NAD+ permeation through the corona of the PECs. Therefore, the release of NAD+ may have been a combination of the release of surface-bound NAD+,

governed by polyelectrolyte relaxation due to the absence of a diffusion barrier, and the release of the more deeply associated NAD+ molecules that must diffuse through nano-channels created in the polyelectrolyte matrix during the ingression of release media. Such behaviour is typical for polymer-based nanomaterial formulations that exhibit high swelling ability or when the release of the therapeutic may be due to a combination of release mechanisms [499], [500]. Ćirić *et al.* [501] demonstrated that the release of escin from xanthan gum and chitosan PECs was best fit either to the Higuchi or Korsmeyer-Peppas mathematical models, depending on the escin:polymer mass ratio. Colistin release from hyaluronic acid-based PECs was also best fit to the Higuchi model, thus confirming that the rapid *in vitro* release of over 85% of the total loaded concentration of colistin from the lyophilised PECs in the first hour was controlled by colistin diffusion [502]. The *in vitro* release of aceclofenac from chitosan and pectin PEC microparticles was best fit to the Korsmeyer-Peppas model but also demonstrated a high degree of correlation to the Higuchi model [502]. In agreement with our study, release was governed by anomalous diffusion, as indicated by the release exponent value. Magalhaes Jr. and co-workers [503] also fit the *in vitro* release of chloroquine from PECs composed of chitosan and an anionic rhamnogalacturonoglycan polysaccharide to the Korsmeyer-Peppas model.

3.5 CONCLUSIONS

NAD+-associated PECs were successfully formulated using the polyelectrolyte complexation method that was optimised in Chapter 2.

The reduction in total enthalpic changes following sequential injection of NAD+ into both HA and PLL solutions confirmed the saturation of the respective polyelectrolytes with NAD+ as the NAD+ % (w/w) ratio increased. Although not statistically significant, the dependence of particle size on both NAD+ loading concentration and total polyelectrolyte concentration was also observed. Qualitative analysis of the F9 formulation via FT-IR and SEM-EDX analysis confirmed the association of NAD+ to the HA and PLL PEC meshwork. The downward shift in the IR absorption bands specific to the vibrational frequencies of the functional groups of NAD+ can be attributed to hydrogen bond formation between the electronegative atoms of NAD+, HA and PLL and significant overlap between NAD+, HA and PLL absorption bands

in particular regions. The elemental spectrum profile confirms the presence of phosphorus at a weight percentage of 1.6 ± 0.3 wt.% within the submicron particles identified from the SEM micrographs. The low abundance of phosphorus is attributed to the sputter coating of the SEM stubs, resulting in a significant overlap of the gold and phosphorus peaks within the elemental profile.

The association efficiency (AE) of NAD+ was successfully quantified using the HPLC method adapted from that used by Forrow *et al.* [449]. The LOD and LOQ of NAD+ using the HPLC method were determined to be 3.16 and 9.58 µg/mL (Agilent 1200 HPLC system) and 2.09 and 6.33 µg/mL (Waters e2695 separations module), respectively. Potassium phosphate buffer (pH 8):100% methanol (95:5) mobile phase was chosen as the optimal extraction solvent. An inverse correlation between NAD+ loading concentration and % AE was also observed, potentially due to the increased polyelectrolyte:NAD+ ratio, allowing for increased NAD+ to polyelectrolyte interactions with a reduction in free NAD+ concentration within the formulation medium. The F9 formulation, with a polyelectrolyte concentration of 2% (w/v) and a molar charge ratio of 2, was selected for further characterisation based on its physicochemical size parameters (235.1 ± 19.0 nm and -38.0 ± 1.1 mV) and NAD+ association efficiency. (77.2 ± 9.5%).

Sustained release of 10.9 ± 0.2 mg of NAD+ from F9 over 14 hours was demonstrated under physiological ocular flow rates. Diffusion was the primary phenomenon driving NAD+ release from the PECs, based on the high correlation of NAD+ release kinetics with both the Higuchi and Korsmeyer-Peppas mathematical release models. The significant changes in size, zeta potential and NAD+ association as a function of both pH and ionic condition highlighted the dependence of the physicochemical behaviour of the PEC matrix on changes in environmental conditions, thus providing evidence of two formulation parameters that must be tightly controlled during PEC formulation. Stability, in terms of size and zeta potential, was achieved upon storage of the PECs in ultrapure water (pH 5.5) at 4 °C for 21 days. However, the significant reduction in NAD+ association by more than 50% over this timeframe may warrant storage of the PECs in lyophilisate form.

The results obtained suggest that the NAD+-associated PECs are suitable for use as a delivery system for the once- or twice-daily topical administration of NAD+. An evaluation of the *in vitro* safety and efficacy of this formulation on human corneal epithelial cell cultures and porcine anterior segment tissues will be of primary focus in later chapters. Such studies are required to obtain a well-rounded evaluation of the PECs as an ocular drug delivery system.

CHAPTER 4:

PREPARATION OF CHITOSAN-NAD+ COMPLEXES

4. PREPARATION OF CHITOSAN-NAD+ COMPLEXES

4.1 INTRODUCTION

Complexation of HA and PLL via electrostatic interaction yielded sub-micron-sized nanoparticles that could effectively associate with NAD+ and sustain its release under physiological ocular conditions. However, the anionic surface charge of the PECs, attributed to residual HA carboxylate anions at the chosen molar charge ratio, may impede their retention upon administration. This is primarily attributed to mutual electrostatic repulsion between the PECs and the anionic sulfate and sialic acid residues of mucin glycoproteins, the glycocalyx bordering apical corneal and conjunctival epithelial cells and the phospholipid head groups within the cell membrane bilayer [504], [505]. Nanoparticles with an overall cationic charge may be more suitable to prolong ocular retention times and enhance intracellular permeation due to favourable electrostatic interactions. PECs formulated with an excess of cationic PLL (molar charge ratio < 1) were unstable and exhibited macroscopic phase separation into gelatinous aggregates during the screening studies outlined in Chapter 2. As such, the use of alternative, cationic polyelectrolytes for NAD+-laden nanoparticle formation was investigated.

Aside from its mucoadhesive capabilities, chitosan can enhance the paracellular permeation of nanoformulations via reversible modification of the transmembrane protein complexes within the tight junctions. Such attributes may reduce the loss of NAD+ via nasolacrimal drainage upon administration and improve its precorneal bioavailability. Chitosan is also hydrophilic and biocompatible as it can undergo enzymatic degradation via cleavage of the β-1,4-glycosidic bonds by chitosanases to form non-toxic oligosaccharides [506]. As discussed in Section 1.4.3.2, conversion of the N-acetyl-D-glucosamine moieties via alkaline deacetylation renders chitosan cationic at pH values below the pKa (6.5) of the newly formed D-glucosamine groups. Although protonation of such groups will begin to decline at physiological pH, a lower cationic charge density is advantageous to prevent potential cytotoxic effects arising from excessive binding of chitosan to the anionic phospholipid bilayer of the cell membrane. Therefore, the degree of deacetylation must be carefully selected to ensure that a sufficient number of amine groups remain in their protonated state during administration to the ocular surface to attain

nanoparticle structure and maximise mucoadhesion, whilst minimising cytotoxic binding effects.

The self-assembly of chitosan is often aided by the introduction of an ionic crosslinker, such as tripolyphosphate (TPP) [507]–[509]. However, research has also been conducted into the complexation of chitosan with alternative compounds with phosphate to amino crosslinking capabilities, such as deoxyribonucleic acid (DNA), calcium phosphate, and β-glycerophosphate [510]–[512]. Ionotropic gelation of chitosan with TPP results in the formation of nano-sized particles comprised of a dense, electrostatically crosslinked network [513]. Similar to TPP, NAD+ also possesses two anionic phosphate groups that are negatively charged (99.5 to 100.0% deprotonated (PO_4^-)) between pH 4.5 and 6. Therefore, it was hypothesised that chitosan and NAD+ could also form ionically crosslinked nano-sized complexes without the addition of either an ionic crosslinker or a secondary polyelectrolyte. Also, due to the absence of a binding moiety competing for electrostatic interaction, it was postulated that NAD+ association with chitosan may be greater than that achieved with the HA and PLL PEC. Increased association may also have a delaying effect on the *in vitro* release of NAD+ from the chitosan network.

The work outlined in Chapter 4 was predominantly focused on the assessment of chitosan and NAD+ binding, utilising the same methodology used in the characterisation of the NAD+-associated HA and PLL PECs outlined in Chapter 3. Where appropriate, the physicochemical characteristics of the chitosan-NAD+ (CH-NAD+) complexes were compared to those of the PECs to assess their suitability for further *in vitro* safety and efficacy trials.

4.2 EXPERIMENTAL METHODOLOGY

4.2.1 Materials

The materials outlined in Sections 2.2.1 and 3.2.1 were used in the preparation and physicochemical characterisation of the chitosan and NAD+ complexes (CH-NAD+) with the addition of the following:

Water soluble chitosan (10-100 kDa, degree of deacetylation = > 90%) was purchased from Carbosynth Ltd. (Berkshire, England).

4.2.2 CH-NAD+ Complex Preparation

500 µL of NAD+ solutions, ranging in concentration from 20-180% (w/w), relative to the mass of chitosan, was pipetted into 5 mL of a 2% (w/v) solution of chitosan under constant stirring at 200 rpm. The pH of the respective solutions was adjusted to a pH of 4.5 prior to addition. After 24 hours, the resulting complexes were purified and lyophilised as outlined in Section 2.2.4.1. The charge ratios (chitosan:NAD+) of the complex formulations prepared are outlined in Table 4.1.

Table 4.1 Formulation parameters of the CH:NAD+ formulations prepared.

Mass of CH (g)	Average MW of CH (kDa)	Moles of CH	No. of CH Chains	Units of Charge per Moles of CH	Mass of NAD+ (g)	MW of NAD+	Moles of NAD+	Charge Ratio CH:NAD+
0.1	55	1.82×10^{-6}	332	0.00054	0.02	663.43	$3.02 \times 10^{--5}$	18.00
					0.04		6.03×10^{-5}	9.02
					0.06		9.05×10^{-5}	6.02
					0.08		0.00010	4.5
					0.1		0.00015	3.61
					0.12		0.00018	3.01
					0.14		0.00020	2.58
					0.16		0.00024	2.26
					0.18		0.00030	2.01

4.2.3 Characterisation of the CH-NAD+ Complexes.

The characterisation of the resulting CH-NAD+ complexes was conducted per the procedures outlined in Section 3.2.3, with the exception of the following:

4.2.3.1 ITC Analysis of CH-NAD+

As per the methodology outlined in Section 3.2.3.1, 50 µL of NAD+ was loaded into the titrant syringe and 300 µL of a 16.36 µM chitosan solution was injected into the sample cell following thorough rinsing with ultrapure water at pH 5.5. 2 µL of a 20348.8 µM solution of NAD+ was injected into the sample cell at intervals of 180 seconds under constant stirring at 200 rpm at 25 °C. The concentrations of both chitosan and NAD+ were chosen to yield a NAD+ % (w/w) between 10 and 200%, relative to the mass of chitosan in the sample cell, after each injection.

4.2.3.2 CH-NAD+ Complex Stability as a Function of pH

pH-mediated analysis of the CH-NAD+ complexes was conducted in accordance with Section 3.2.3.10. However, the sample media (ultrapure water and 0.01 M PBS) was adjusted to pH 4.5 to maximise the ionisation of the amine groups of chitosan.

4.2.3.3 Storage Stability of CH-NAD+ Formulations

The stability of both the 120% (w/w) and 140% (w/w) CH-NAD+ formulations over 28 days was assessed in accordance with Section 3.2.3.11. However, the sample medium was adjusted to pH 7.4 to preserve the sub-micron size of the complexes.

4.2.4 Statistical Analysis

Two sample t-tests (two-tailed) and one-way analysis of variance (ANOVA) analysis, coupled with Tukey's/Games-Howell post-hoc comparison tests were used throughout the studies outlined. Normality tests and tests for equal variances in the experimental data were also conducted. Ryan-Joiner normality tests and 2 Variances tests were also conducted to assess whether the experimental data was normally distributed and whether the standard deviations of two sample populations were equal to the hypothesised ratio, respectively. A p-value of less than 0.05 was considered statistically significant, while a p-value > 0.05 was considered statistically insignificant.

4.3 RESULTS AND DISCUSSION

4.3.1 Screening of Chitosan-NAD+ Complexes

At a pH of 4.5, NAD+ possesses two negatively charged phosphate groups within the pyrophosphate bridge. We hypothesised that the addition of NAD+ to chitosan, possessing cationic amine groups at this pH, may result in the formation of discreet, complex nanoparticles via ionotropic gelation. The formation of particles within the sub-micron range with the gradual increase in NAD+ concentration is shown in Table 4.2.

Table 4.2: The size, zeta potential (ZP) and polydispersity index (PDI) values recorded for crude CH-NAD+ complexes ranging from 20 to 180% (w/w) of NAD+.

Chitosan:NAD+ (% (w/w))	**20**	**40**	**60**	**80**	**100**
Size (nm)	51335 ± 71228	735 ± 104	637 ± 397	812 ± 12	680 ± 327
Zeta Potential (mV)	22.3 ± 31.0	32.0 ± 5.1	43.4 ± 3.5	43.2 ± 11.2	47.5 ± 4.2
Polydispersity Index (PDI)	0.8 ± 0.3	0.8 ± 0.02	0.8 ± 0.2	0.6 ± 0.1	0.7 ± 0.1
Intercept (DLS Correlation Curve)	0.3 ± 0.4	0.6 ± 0.04	0.7 ± 0.3	0.5 ± 0.03	0.5 ± 0.3
Chitosan:NAD+ (% (w/w))	**120**	**140**	**160**	**180**	
Size (nm)	494 ± 11	350 ± 81	497 ± 194	577 ± 107	
ZP (mV)	39.6 ± 9.1	36.3 ± 14.2	38.7 ± 15.8	45.7 ± 5.3	
PDI	0.8 ± 0.1	0.8 ± 0.1	0.9 ± 0.1	0.8 ± 0.2	
Intercept (DLS Correlation Curve)	0.4 ± 0.04	0.7 ± 0.8	0.5 ± 0.2	0.6 ±0.5	

At lower concentrations of NAD+, particularly at 20% (w/w) of NAD+, the hydrodynamic diameter of the complexes formed was large and irreproducible, suggesting that there may be insufficient NAD+ present to ionically crosslink the individual chitosan chains via electrostatic interaction. Conversely, at NAD+ concentrations of 120 and 140% (w/w), the larger quantity of NAD+ present within the system may be sufficient for the compaction of the chitosan chains via NAD+-mediated crosslinking into nanoparticles composed of a dense, highly crosslinked, polymeric network. Although not statistically significant, a further increase in NAD+ concentration led to an increase in particle size with a higher degree of variability. A similar trend was observed by Algharib *et al.* [514], in which an increase in nanoparticle formation was attributed to an increase in tripolyphosphate (TPP) crosslinker concentration. However, a concurrent increase in particle size was also observed, with precipitation occurring upon the addition of 83% (0.25 mg/mL), 167% (0.5 mg/mL) and 333% (w/w) (1 mg/mL) of TPP. This suggests that a combination of increased crosslinking and neutralisation of an increased number

of chitosan amine groups promotes intercomplex aggregation beyond a certain crosslinker concentration. Cai *et al.* [515] also demonstrated the formation of macroscopic chitosan and TPP precipitates upon doubling the concentration of DNA from 2.5 x 10^{-3} to 5.0 ×10^{-3} wt%. As DNA possesses a highly negatively charged phosphate backbone, it was hypothesised that this macroscopic aggregation was due to the reduction in available residual chitosan amine groups available for intercomplex electrostatic repulsion. However, the direct effect of a stepwise increase in DNA concentration on both size and zeta potential was not analysed. The effect of an increase in the concentration of various polyphosphates on nanoparticle size was also investigated by Goncalves *et al.* [516]. Fluctuations in particle size were not only dependent on the concentration of the individual polyphosphate crosslinkers but also on their respective charge densities, the speed of complex nucleation upon addition, and the order of chitosan and polyphosphate mixing.

Based on their small and reproducible particle size in the initial screening trial, CH-NAD+ complexes containing 120% and 140% (w/w) were selected to investigate the impact of lyophilisation, with and without 1% (w/v) trehalose cryoprotectant, on complex size. As shown in Figure 4.1, conversely to what was observed in the HA-PLL system described in Section 2.3.7, the addition of 1% (w/v) trehalose did not have a significant effect on complex size, suggesting that complex size was preserved during lyophilisation [517]. Also, a statistically significant increase in particle size was observed upon analysis of the 120% (w/w) and 140% (w/w) complexes 24 hours post-addition of NAD+ ($p = 0.008$ and 0.013, respectively). This supports the trends observed in the HA and PLL PEC systems, in which intracomplex correction and reconfiguration of bonds formed during primary complexation results in an increase in particle size over time.

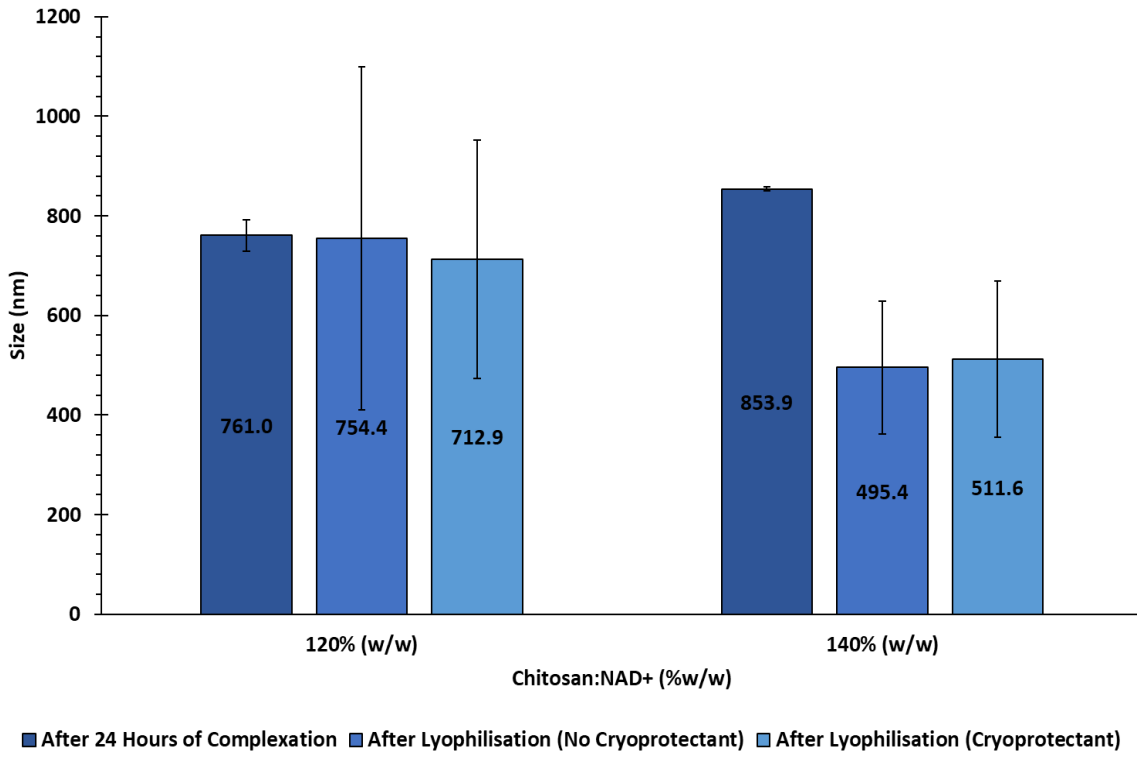

Figure 4.1: The size values recorded for chitosan and NAD+ complexes with 120 and 140% (w/w) of NAD+ after 24 hours, after lyophilisation and after lyophilisation with 1% (w/v) trehalose cryoprotectant. Data is expressed as the mean size ± S.D (n = 2)).

The quantification of NAD+ associated with chitosan following complex purification is outlined in Table 4.3.

Table 4.3: Percentage association efficiencies (AE) (indirect and direct) recorded for CH-NAD+ complexes with 120 to 140% (w/w) NAD+. Data is expressed as mean ± S.D (n = 6).

CH-NAD+ % (w/w)	120% (w/w)	140% (w/w)
Direct AE (%)	68.2 ± 12.3	65.4 ± 15.0
Indirect AE (%)	87.5 ± 8.5	92.2 ± 7.0
LC (%)	67.1 ± 5.6	69.4 ± 5.0

Contrary to the HA and PLL PEC systems, NAD+ plays more of a critical role in the cross-linking of the polymeric network due to the absence of the second polyelectrolyte. As such,

both the intra and intermolecular crosslinking may be more uncontrolled and randomly orientated, resulting in some NAD+ molecules becoming more deeply complexed within the network and not being quantified during analysis. Although the AE values obtained have higher associated error, the values are in agreement with those previously obtained for chitosan-based complex nanoparticles formed via polyelectrolyte complexation and ionotropic gelation [518]–[520]. One study conducted by Elkady *et al.* [521] in which risedronate sodium hemi-pentahydrate (RS) was complexed directly to a 150 kDa chitosan with a similar degree of deacetylation to that used in the present study, reported entrapment efficiencies of between 80 and 99%, depending on set critical quality attributes. This may be attributed to the steric hindrance imparted by the cyclic moieties surrounding the pyrophosphate bridge of NAD+. Although similar in molecular weight to NAD+, the phosphate groups of RS (700.26 g/mol) are not in close proximity to the pyridine ring, rendering them more accessible for electrostatic interaction with the cationic amine groups. The AE values obtained by Bin-Jumah *et al.* [522] support this hypothesis, with the complexation of a 120 kDa chitosan (degree of deacetylation = 85%) to clarithromycin (747.85 g/mol), a highly branched antibiotic with two cyclic functional groups, achieving an AE of a maximum of 70.33%. As such, and in conjunction with the high LC values obtained, the CH-NAD+ complexes were deemed suitable for further binding analysis and *in vitro* release studies.

4.3.2 Association via Changes in Infrared Absorption Peaks

The binding of NAD+ to chitosan was evident upon analysis of both the shifts and disappearances of the IR absorption bands relating to the characteristic functional groups of the respective components, as shown in Figure 4.2.

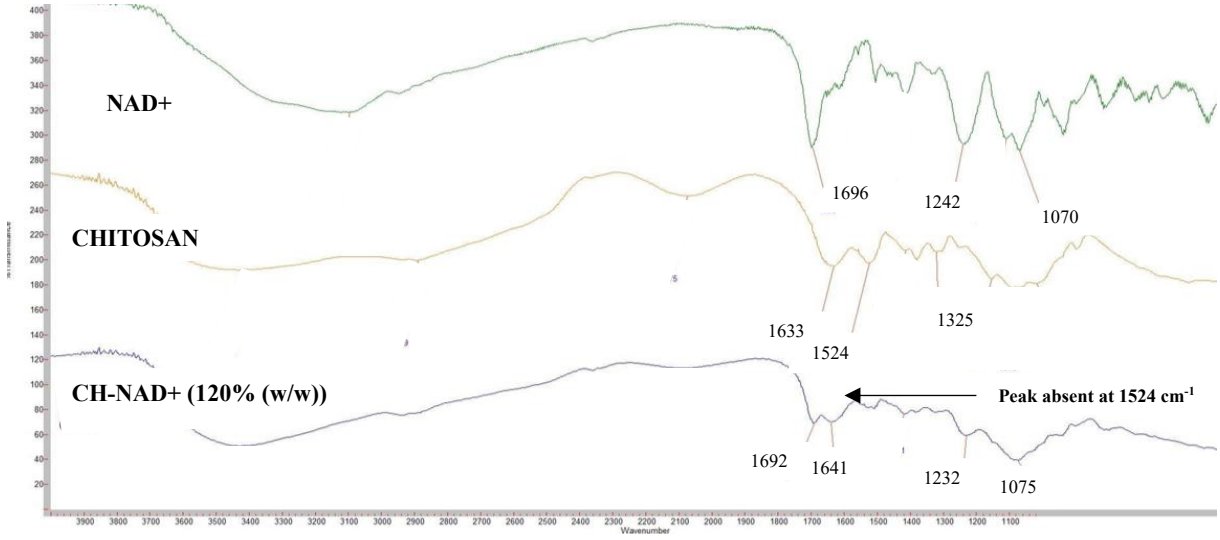

Figure 4.2: The FT-IR spectra of chitosan and NAD+. For comparative purposes, the FT-IR spectra of the chitosan-NAD+ complex with 120% (w/w) NAD+ are shown. (64 scans at a resolution of 2 cm^{-1}).

The stretching of the 3-carboxamide carbonyl bond within the nicotinamide group of NAD+ is present in the spectrum of the complex at 1692 cm^{-1}. However, the stretching of the same group within the amide I functional group of the residual N-acetyl groups of chitosan shifted from 1633 cm^{-1} to 1641 cm^{-1}. A concurrent decrease in the intensity of the peaks identified, and the disappearance of the amide III C-N stretching vibration at 1325 cm^{-1}, was also observed, thus supporting the interaction between complementary functional groups of NAD+ and chitosan. Furthermore, the peak representing the bending N-H vibration of the protonated amine group of chitosan at 1524 cm^{-1} was absent from the complex spectrum. This, combined with the reduction in intensity of the sharp peak representing the asymmetric stretching of the pyrophosphate bridge of NAD+ at 1242 cm^{-1}, and the presence of the symmetric phosphate stretching vibration at 1075 cm^{-1}, confirms the electrostatic interaction between NAD+ and chitosan. Similar trends have been observed for the electrostatic crosslinking of phosphate TPP functional groups to the amino groups of chitosan, as depicted in Figure 4.3 [523]–[525].

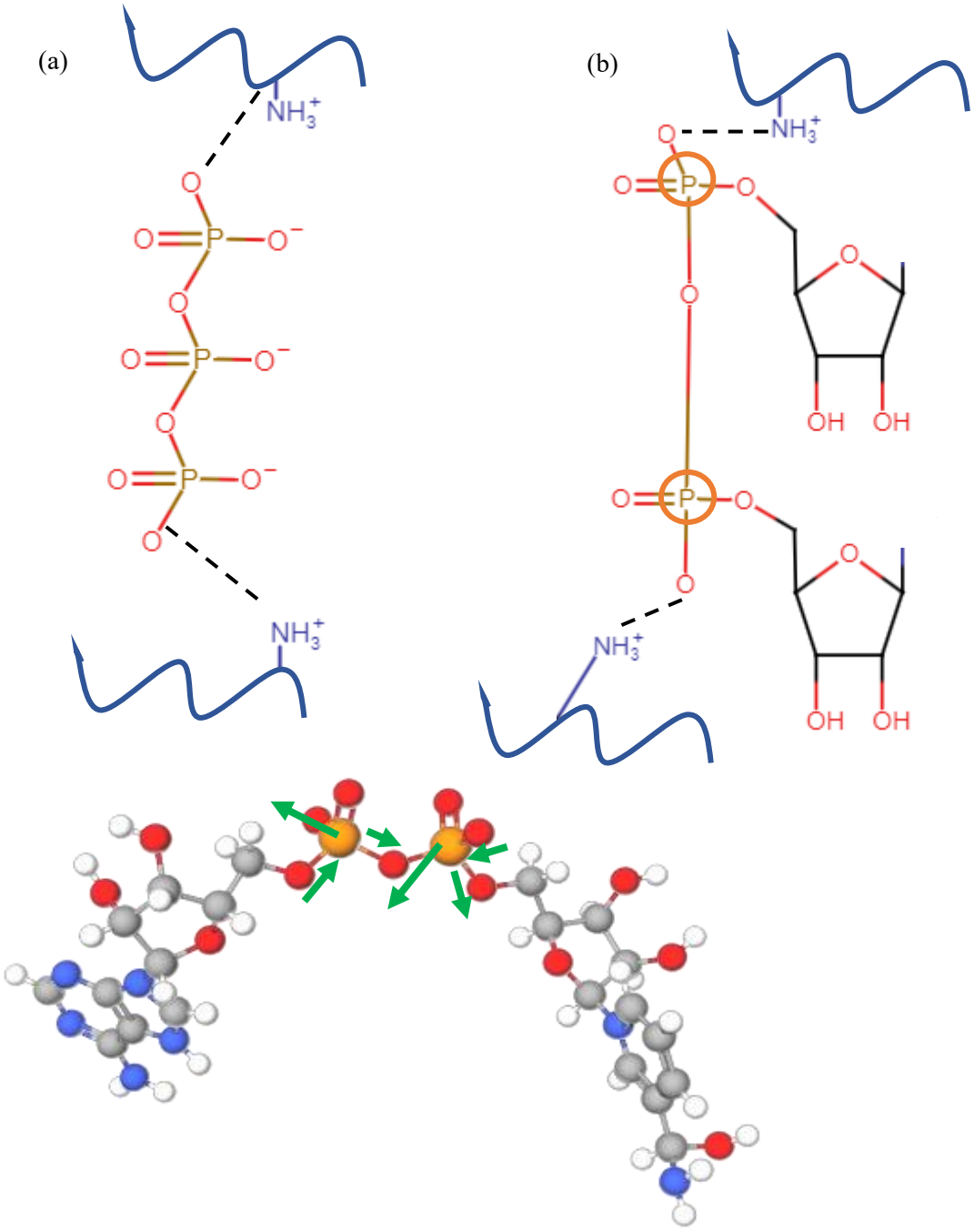

Figure 4.3: Schematic of the binding of TPP to chitosan (a) and NAD+ to chitosan (b) via phosphate-to-amine group electrostatic binding. The asymmetric stretching of the pyrophosphate bridge is represented in the 3D molecular structure of NAD+.

4.3.3 NAD+ Binding via Isothermal Titration Calorimetry

Similar to the binding of NAD+ to both HA and PLL (Section 3.3.1), negative peaks (-µJ/s) were generated upon titration of chitosan with NAD+, thus suggesting that the interaction between chitosan and NAD+ was exothermic, leading to an overall reduction in system enthalpy. The resulting thermogram is depicted in Figure 4.4.

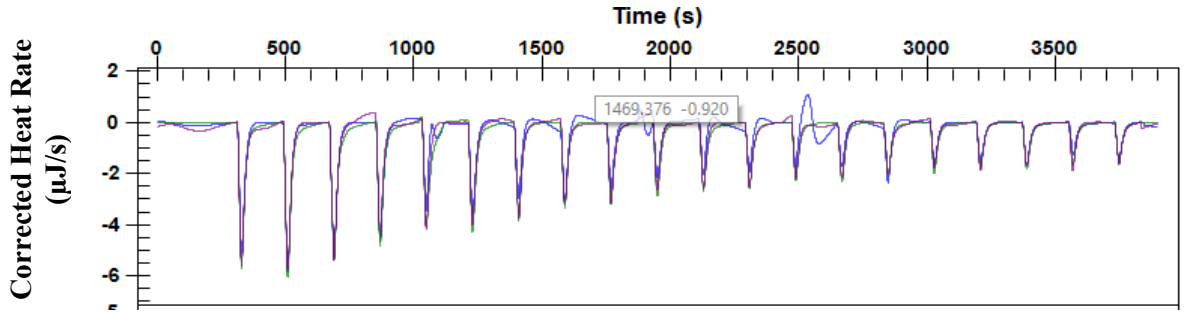

Figure 4.4: The sequential titration of chitosan with NAD+ in ultrapure water at 25 °C (pH 4.5).

However, upon fitting the ITC data to the independent binding model, the overall enthalpy was positive (28.24 ± 7.14 kJ/mol), indicating that the binding of NAD+ to chitosan was endothermic. This may be attributed to the large excess of NAD+ in comparison to chitosan, particularly at (w/w) ratios exceeding 100% (w/w). As NAD+ possess two anionic phosphate groups at a pH of 4.5, free NAD+ molecules that did not associate with chitosan during the titration would exist in solution as free ions. As such, the decrease in enthalpy arising from the ionic complexation of NAD+ to chitosan would be overshadowed by the large increase in enthalpy required to release counterions from the chitosan into an ion-saturated bulk medium. Dehydration, resulting from disruption of a large number of solvation bonds, and disentanglement of individual chitosan chains upon binding to NAD+ would also contribute to an increase in system enthalpy. The overall increase in entropy supports this hypothesis as the increase in entropy originating from the release of counterions predominates over the loss of conformational entropy from electrostatic interaction formation.

A similar equilibrium dissociation constant (K_D) to those obtained for both PLL (6.2 x 10^{-4} M) and HA (9.9 x 10^{-4} M) was obtained for the binding of NAD+ to chitosan (8.8 x 10^{-4} M).

Although statistically equivalent ($p = 0.310 > 0.05$), NAD+ may exhibit a greater binding affinity for PLL as PLL in smaller in size and can therefore access the anionic phosphate groups more readily in comparison to chitosan.

A reaction stoichiometry of 10, equating to a chitosan:NAD+ mole ratio of 100, was achieved following the fitting of the thermogram to the independent binding site model. This suggests that, at an NAD+:Chitosan mole ratio of 100, equating to an NAD+ loading of 110% (w/w), saturation of the cationic amine groups of chitosan is achieved. This further corroborated the trends observed upon investigation of the impact of NAD+ addition on complex size. At low NAD+ concentrations (e.g. 20% (w/w) - mole ratio of 17:1) the binding of a small number of NAD+ molecules to an abundance of available amine groups evokes a significant heat change in the system. However, a large fraction of the available chitosan remains uncomplexed and exists as individual, expansive chains due to intramolecular repulsion with a maximum level of solvation. At NAD+:chitosan mole ratios above stoichiometry (> 100:1), the heat change in the system drastically decreases due to the collapse of the respective charged species into nanostructured complex particles. Almost all of the available chitosan amine groups have now been saturated with NAD+ and can therefore no longer bind with additional quantities of NAD+. A similar trend was observed by de Carvalho *et al.* [526], in which the DLS titration of chitosan with TPP led to a reduction in complex size from approximately 2000 nm (TPP:chitosan molar ratio = 0) to 600 nm at a TPP:chitosan molar ratio of 0.2. A concurrent reduction in injection enthalpy was observed within this molar ratio range, with negligible heat changes being recorded at the induction of nanoaggregate formation (molar ratio of 0.2). As evidenced by the intensity-average particle size distributions obtained by Delas *et al.* [527], for various siRNA-chitosan complexes, particles with sizes < 10^2 nm formed at siRNA:chitosan molar ratios > 1. Further addition of siRNA to chitosan altered the resulting particle size but had a minimal effect on system enthalpy. Also, in accordance with our hypothesis, almost 100% siRNA complexation was achieved at siRNA:chitosan ratios above stoichiometry, thus indicating that saturation of chitosan had occurred.

4.3.4 pH-Mediated Stability of Chitosan-NAD+ Complexes

A significant reduction in both size ($p = 0.035 < 0.05$ (120% (w/w))) and ZP ($p = 0.024 < 0.05$ (120% (w/w)) and $p = 0.001 < 0.05$ (140% (w/w))) was observed upon redispersal of the CH-NAD+ complexes in ultrapure water adjusted to pH 7.4, as depicted in Figure 4.5.

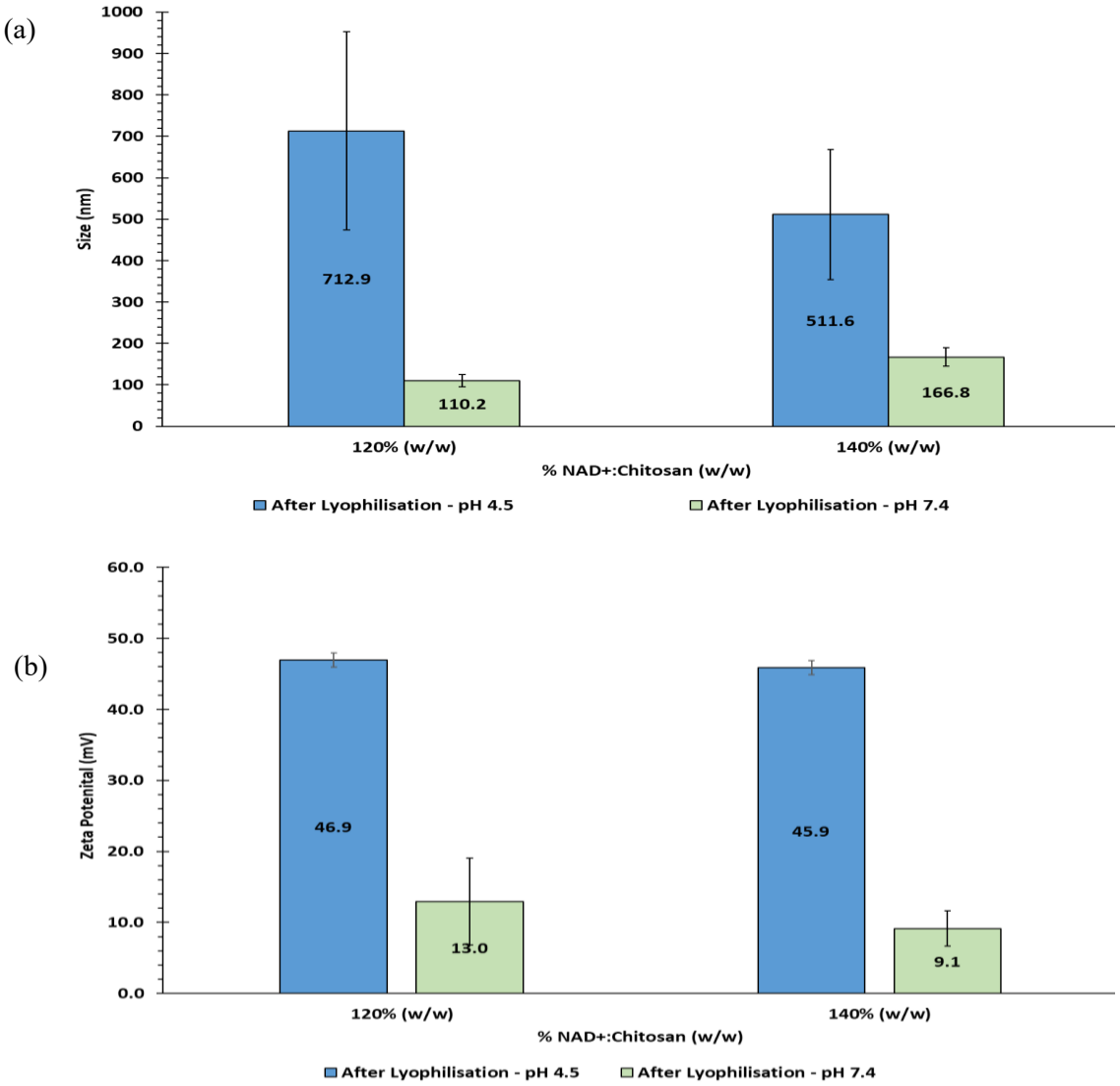

Figure 4.5: The change in size and ZP following dispersal of the lyophilised CH-NAD+ complexes in ultrapure water at pH 7.4, as compared to those dispersed in ultrapure water at pH 4.5. Data is expressed as mean size/ZP ± S.D (n = 3).

A decrease in size was also observed for the 140% (w/w) CH-NAD+ complex. However, this was not statistically significant ($p = 0.199 > 0.05$). This was potentially attributed to the compaction of the CH-NAD+ complexes due to deprotonation of the cationic charges on the D-glucosamine residues of chitosan when placed in solution with a pH above its pKa. Upon formation, the 120% and 140% (w/w) CH-NAD+ complexes should attain chitosan:NAD+ molar charge ratios of approximately 3 and 2.6, respectively. The loss of mutual electrostatic repulsion between the residual amine groups, as corroborated by the reduction in ZP values with an increase in pH, would favour the formation of intrapolymer attractive forces, thus creating a more tightly packed polymeric network.

The effect of pH on NAD+ association was also investigated using the 120% (w/w) CH-NAD+ complex as a reference. Although statistically equivalent, potentially attributed to the variation in NAD+ association arising from its irregular dispersion throughout the complex, a larger mass of NAD+ remained associated with the complex upon storage in ultrapure water at pH 7.4. As shown in Figure 4.6, just under 5 mg of NAD+ (9.8 ± 2.3 mg remaining) dissociated from the complexes during storage at pH 7.4, whereas 8.0 ± 3.3 mg of NAD+ remained associated with the complex network after 4 hours at pH 4.5.

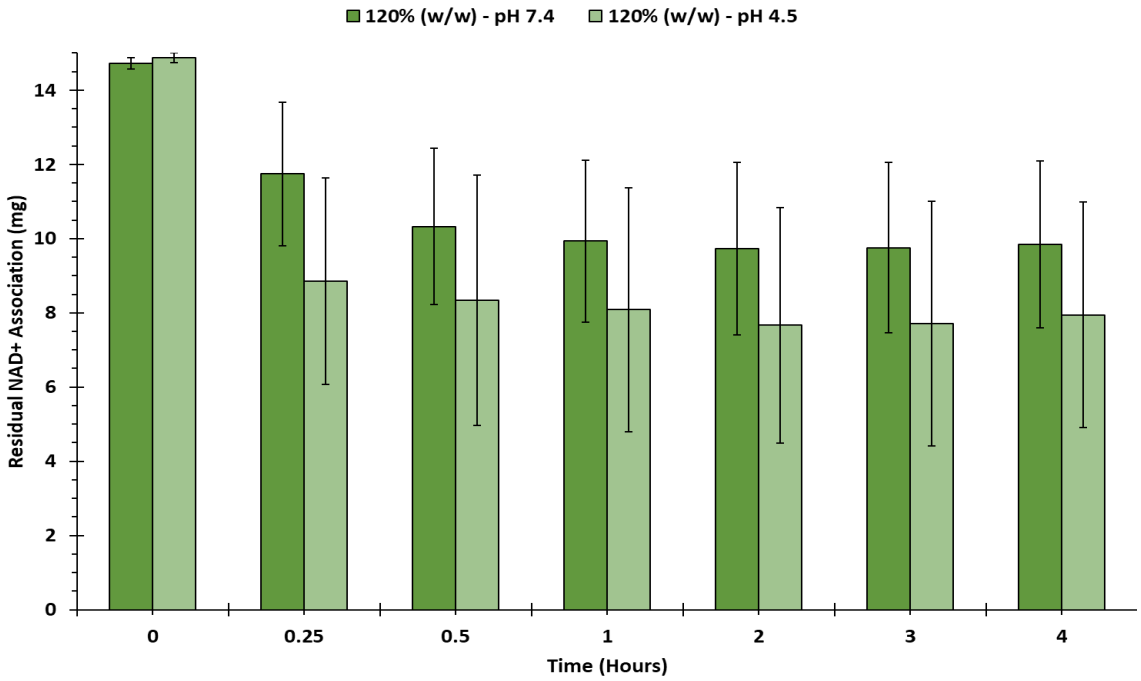

Figure 4.6: Change in NAD+ association upon storage of CH-NAD+ complexes in ultrapure water at pH 4.5 and pH 7.4 for 4 hours. Data is expressed as mean residual NAD+ association ± S.D (n = 3).

In comparison to that of the HA and PLL PECs stored under equivalent conditions (0.6 ± 0.4 mg remaining in ultrapure water at pH 7.4), a significantly larger mass of NAD+ was retained within the chitosan-based complex ($p = 0.002 < 0.05$). This supports that, upon neutralisation of the chitosan amine groups at pH 7.4, compaction of the complex aids further entrapment of NAD+ in the polymer matrix. At pH 4.5, protonation and repulsion of the cationic amine groups may allow for increased water ingression through the complex, subsequent swelling of the network and enhanced NAD+ dissociation. An increase in histatin release from chitosan and TPP ionotropic complexes with a decrease in pH from 6.3 to 3 was demonstrated by Zhu *et al.* [528]. Interestingly, an inverse correlation between particle size and pH was also observed with sizes ranging from 300 nm at pH 4 to below 200 nm at pH 6.3. This further supports the trends observed in this study and demonstrates the tendency of chitosan to swell and release associated cargo under maximal ionisation. Pilipenko *et al.* [332] also observed a pH-dependent increase in oligonucleotide release from approximately 20% to over 60% over 4 hours with a decrease in release media pH from 7.4 to 4.5. The increase in oligonucleotide release was attributed to

the enhanced swelling of the predominantly protonated chitosan chains at pH 4.5. As discussed in Section 1.4.3.2, the increase in oligonucleotide dissociation at various pH values due to the competitive association of heparin to chitosan was also evident. Competitive binding between NAD+ and PLL with HA limits the surface available for NAD+ association. As such, upon neutralisation of PLL and compaction of the HA and PLL charge-neutralised core at pH 7.4, NAD+, being more of an additive than a primary reagent of complexation in this case, is more exposed to the sample media and therefore will be displaced more readily.

In conclusion, based on the physicochemical behaviour of the CH-NAD+ complexes at physiological pH, particularly in comparison to those of the PECs, they were deemed suitable for further analysis via *in vitro* release methodologies.

4.3.5 Dynamic *In Vitro* NAD+ Release

4.3.5.1 In Vitro NAD+ Release

The release of 8.0 ± 3.1 mg (53.5 ± 20.6% cumulative release) and 10.7 ± 4.4 mg (71.6 ± 29.5% cumulative release) of NAD+ from the 120% and 140% (w/w) CH-NAD+ complexes was sustained over 36 hours under *in vitro* dynamic physiological conditions, as shown in Figure 4.7. Although no significant difference ($p = 0.207 > 0.05$) in mass of NAD+ released was found between the respective formulations at 12 hours, NAD+ release from the CH-NAD+ complexes began to plateau at 32 hours. Conversely, NAD+ release from the PECs reached a plateau after just 14 hours under physiological ocular conditions. This supports the hypothesis that, in the absence of a second polyelectrolyte, the lack of competitive binding may increase the surface area available for NAD+ sequential association, thus allowing for its delayed diffusion through the chitosan matrix.

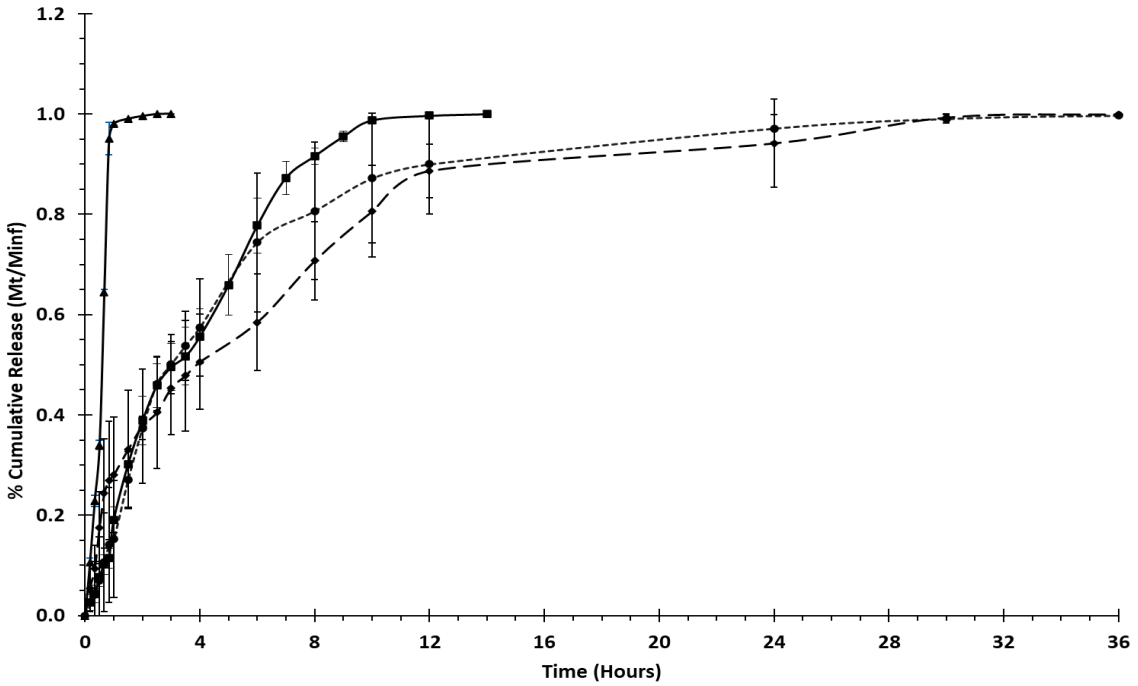

Figure 4.7: Cumulative *in vitro* NAD+ release profiles from the 120% (w/w) (large, dashed diamonds) and 140% (w/w) (small, dashed circles) CH-NAD+ complexes in 0.01 M PBS (pH 7.4) under microfluidic conditions over 36 hours. The PECs (circles) and NAD+ bolus control (triangles) are shown for comparative purposes. (Data is expressed as mean % Mt/Minf ± S.D (n = 3).

Under infinite sink conditions, Motiei *et al.* [529] reported a cumulative nicotinic acid release of approximately 60% from chitosan and TPP structured nanocomplexes at pH 7.4 over 36 hours. However, *in vitro* release was sustained for up to 72 hours in this case. The further delay in release in comparison to our study may be attributed to both the size of nicotinic acid itself and the presence of the TPP ionic crosslinker. Due to its lower MW (0.123 kDa), nicotinic acid, a precursor of NAD+ itself, may permeate through the highly crosslinked chitosan-TPP network during formation more effectively than NAD+ (0.66 kDa), resulting in hindered diffusion upon release. Between 60 to 90% of the loaded bovine serum albumin (BSA) cargo was released from chitosan and alginate polyelectrolyte complexes after 4 hours in 20 mM PBS (pH 7.4) under each condition investigated [530]. BSA is a high molecular weight (MW) compound (66 kDa). Therefore, in agreement with observations made, particularly with the HA and PLL PECs, the steric hindrance created by the complexation of alginate to chitosan of 40-

50 kDa, resulted in the preferential association of BSA with the surface of the complexes, thus aiding rapid release upon dispersion in release media.

4.3.5.2 Mathematical Modelling of NAD+ Release Kinetics from PECs

In vitro NAD+ release from both the 120% and 140% (w/w) CH-NAD+ complexes was best fit to the Korsmeyer-Peppas model. As shown in Figure 4.8, linear correlations with R^2 values above 0.9 were achieved upon plotting the first 60% of NAD+ cumulative release in each case.

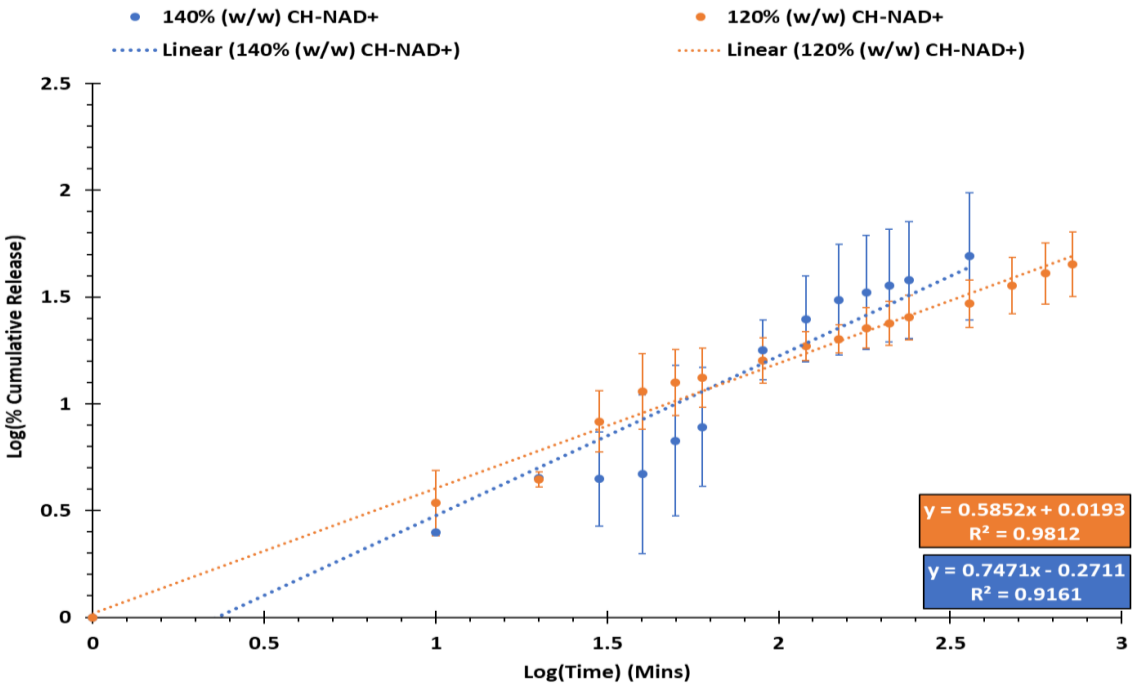

Figure 4.8: A plot of the log of cumulative NAD+ release vs. the log of time, in minutes, showing a high correlation to the Korsmeyer-Peppas mathematical model. Data is expressed as mean log(% cumulative release) ± S.D (n = 3).

Similar to that of the HA and PLL PECs, the release exponent values obtained were also within the range of 0.45 to 1, indicating that the mechanism of NAD+ release from the chitosan and NAD+ network was a combination of NAD+ diffusion and intracomplex relaxation. The high correlation to the Higuchi model in each formulation (120% (w/w) – R^2 = 0.9085 and 140% (w/w) – R^2 = 0.8120) also suggests that NAD+ diffusion may be the predominating factor that governs its mechanism of release. This further corroborates the trends outlined in Section 4.3.4. pH-mediated compaction of the polymeric network results in the further entrapment of NAD+.

In the absence of swelling resulting from electrostatic repulsion and polymer rearrangement, NAD+ would primarily diffuse through the network during release. *In vitro* NAD+ release may also be concentration dependent, as evidenced by the higher correlation to the first-order release mathematical model in comparison to the zero-order release model for each formulation. Therefore, NAD+ may not be released at a constant rate over the release timeframe and is instead dependent on fluctuations in the concentration gradient created between the complexes themselves and the surrounding environment.

4.3.6 Chitosan-NAD+ Complex Stability under Storage Conditions

No significant difference in size was observed upon storage of the 120% (w/w) ($p = 0.05$) and 140% (w/w) ($p = 0.081 > 0.05$) CH-NAD+ formulations over 28 days. Interestingly, as depicted in Figure 4.9 (b), the ZP of the 120% (w/w) CH-NAD+ formulation significantly increased from 28.0 ± 1.3 to 39.7 ± 1.9 mV over the storage period. This may be attributed to the reformation and reorganisation of the complex during release due to NAD+ disassociation from the network, exposing now free cationic chitosan amine groups that would preferentially migrate to the hydrophilic surface. Upon analysis of the changes in the ZP of chitosan and dextran sulphate-based complexes as a function of time, Carvahlo *et al.* [531] also observed a further reduction in ZP from its initial value over 4 weeks. However, as these complexes were not loaded with a therapeutic compound, and the storage medium was not stated, it was difficult to interpret what was the root cause of the reduction in ZP. Nevertheless, at 4°C, the CH-NAD+ formulations exhibited ZP values above 25 mV, indicating that electrostatic stabilisation of the complexes was preserved.

(a)

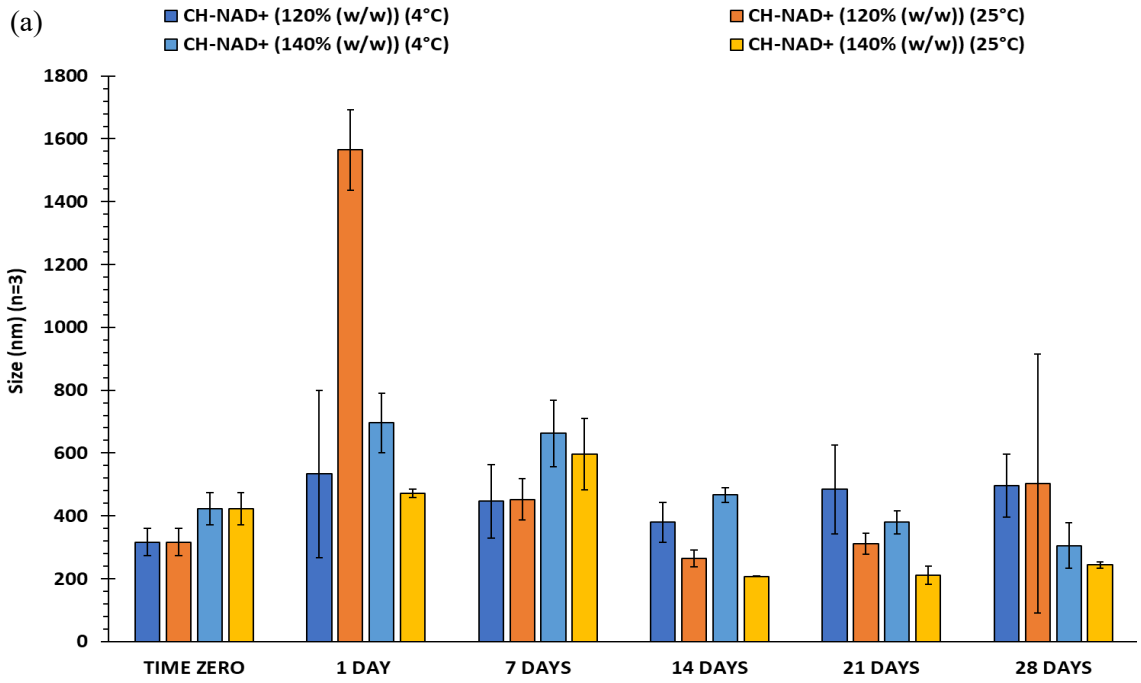
CH-NAD+ (120% (w/w)) (4°C)
CH-NAD+ (120% (w/w)) (25°C)
CH-NAD+ (140% (w/w)) (4°C)
CH-NAD+ (140% (w/w)) (25°C)
Size (nm) (n=3)
1800
1600
1400
1200
1000
800
600
400
200
0
TIME ZERO
1 DAY
7 DAYS
14 DAYS
21 DAYS
28 DAYS

(b)

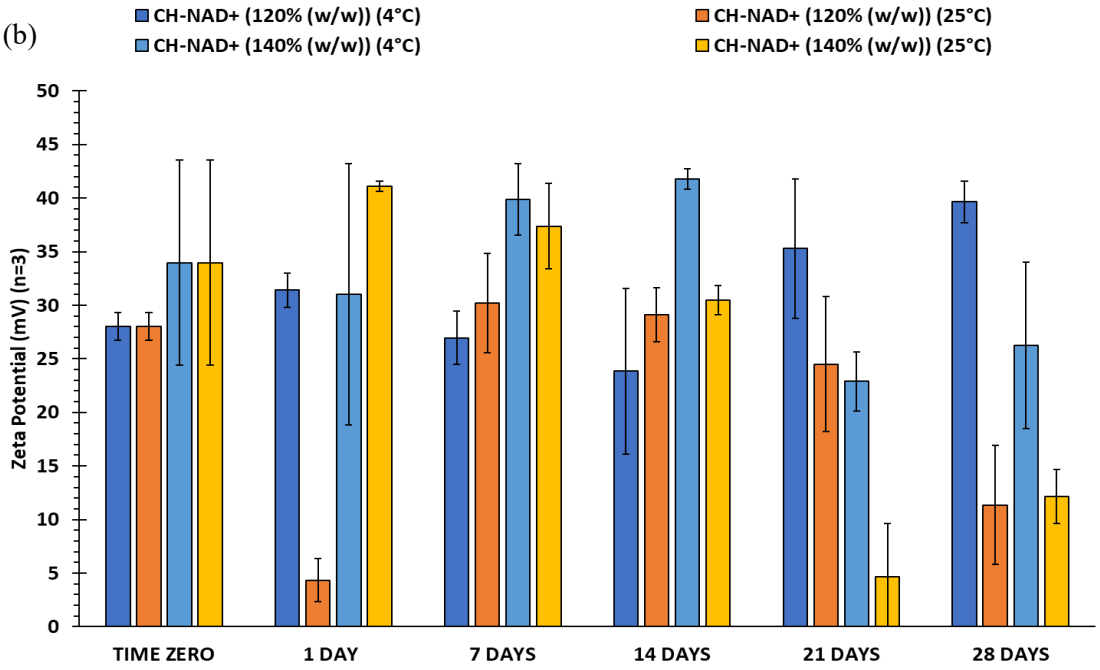
CH-NAD+ (120% (w/w)) (4°C)
CH-NAD+ (120% (w/w)) (25°C)
CH-NAD+ (140% (w/w)) (4°C)
CH-NAD+ (140% (w/w)) (25°C)
Zeta Potential (mV) (n=3)
50
45
40
35
30
25
20
15
10
5
0
TIME ZERO
1 DAY
7 DAYS
14 DAYS
21 DAYS
28 DAYS

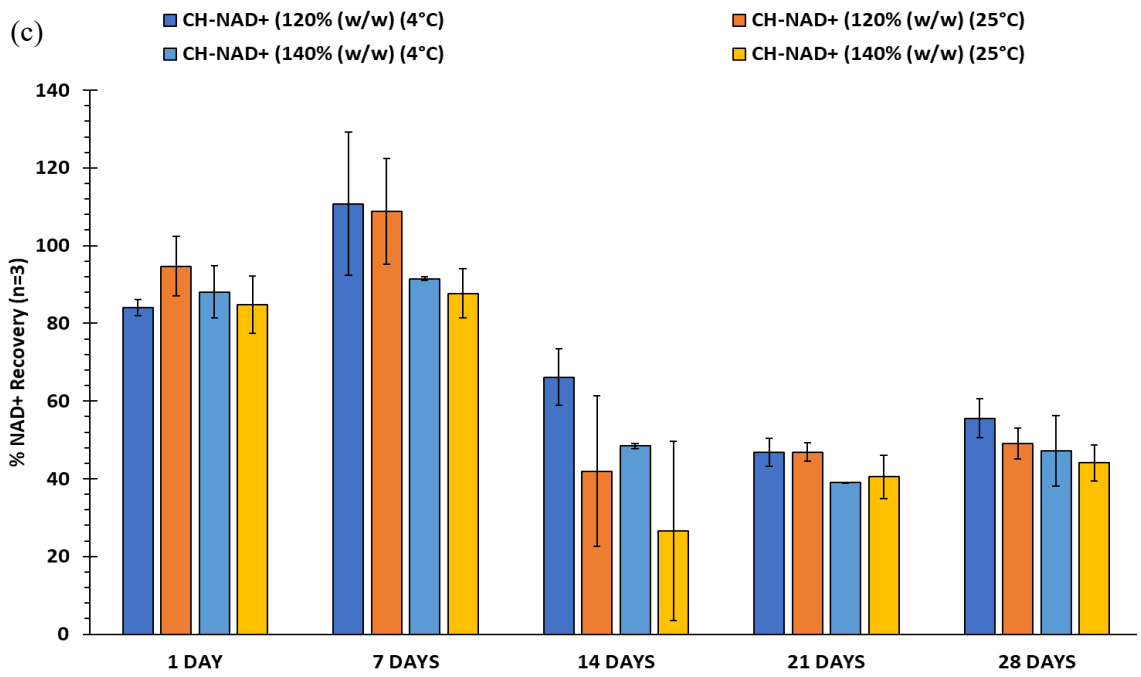

Figure 4.9: Changes size (a), zeta potential (b) and NAD+ concentration (c) upon storage of CH-NAD+ complexes at 4 (dark blue – 120% (w/w), light blue (140% (w/w)) and 25 °C (dark orange – 120% (w/w), light orange (140% (w/w)) over one month (Data is expressed as mean ± S.D (n = 3).

An almost reversible phenomenon was observed at 25 °C, particularly with the 120% (w/w) formulation. After one day post-storage, a large increase in size from 316.6 ± 42.9 to 1564.5 ± 128.0 nm, and a concurrent decrease in ZP from 28.0 ± 1.3 to 4.3 ± 2.0 was observed. However, both the size and ZP returned to similar values to those recorded initially after 7 days. This was also observed in the 140% (w/w) formulation to a lesser extent, with a small increase in size and a small decrease in ZP occurring on day seven, with opposite trends being observed on day 14. This may be indicative of reversible aggregation of the complexes at ambient temperatures, where initial placement into an aqueous medium at pH 7.4 causes intercomplex aggregation due to the limited residual cationic amine groups available for mutual repulsion. However, as seen at 4 °C, the gradual loss of NAD+ from the structured network may result in complex compaction and an increase in ZP over time. Furthermore, the significant reduction in ZP values (120% (w/w) – $p = 0.007 < 0.05$ and 140% (w/w) – $p = 0.019 < 0.05$) from t_0 to 28 days suggests that storage under ambient conditions would not be suitable to prolong the shelf-life of the

formulations. Utilising chitosan with a similar MW and degree of deacetylation to that used in this study, Yu *et al.* [532] reported a decrease in ZP over 26 hours to near-neutrality (0 mV). Fabiano *et al.* [533] reported a reduction in ZP from +24.2 ± 1.0 to 7.6 + 0.5 mV after 6 months of storage at 25 °C. The extension in shelf-life may be attributed to the difference in MW between the chitosan used (590 kDa) in comparison to the chitosan used in this study (10 - 100 kDa). A direct correlation exists between MW and charge density, with larger MW chains possessing an increased number of charged functional groups that can partake in electrostatic repulsion.

As shown in Figure 4.9 (c), NAD+ association was unaffected by the storage temperature. In each formulation, NAD+ retention within the CH-NAD+ complexes dropped below 70% after 14 days, with significant decreases in final NAD+ retention rates of 55.5 ± 5.1% (120% (w/w) (4 °C) – $p = 0.008 < 0.05$), 49.0 ± 4.0% (120% (w/w) (25 °C) – $p = 0.004 < 0.05$), 47.2 ± 9.1 (140% (w/w) (4 °C) – $p = 0.002 < 0.05$), and 44.1 ± 4.7 (140% (w/w) (25 °C) – $p = 0.001 < 0.05$), being recorded after 28 days post-storage. Similar NAD+ recovery rates of 47.7 ± 4.5% were obtained following storage of the HA and PLL PECs for 28 days at 4 °C, thus indicating they exhibited equivalent efficacy in protecting NAD+ from storage-induced degradation. Interestingly, an equivalent % NAD+ recovery was obtained from the 120% (w/w) CH-NAD+ formulation (66.1 ± 7.3%) upon comparison to NAD+ controls stored under equivalent conditions after 14 days (Table 3.6). However, the 140% formulation exhibited a lower % recovery of 48.5 ± 0.6%. Saturation of the chitosan chains with NAD+ may limit deeper entrapment of NAD+ in the 140% formulation, rendering it more susceptible to degradation due to increased surface association. As noted in Section 3.3.5.3, the large reduction in the concentration of NAD+ reserved following storage may drastically limit the shelf-life of the chitosan-based formulations and storage in lyophilised form may be more suitable.

4.4 CONCLUSIONS

CH-NAD+ complexes, prepared with 120% and 140% (w/w) of NAD+, were successfully formulated upon sequential addition of NAD+ to chitosan and subsequent analysis of the resulting physicochemical size parameters. pH was identified as a governing factor of both complex size and NAD+ association, with deionisation-mediated collapse of the chitosan

network at pH 7.4 aiding the formation of small nano-sized complexes (< 200 nm) and enhanced retention of NAD+, particularly in comparison to the HA and PLL PECs at this pH (9.8 ± 2.3 mg retained – CH-NAD+ (120% (w/v)) vs. 0.6 ± 0.4 mg retained – HA and PLL PECs). Not only did ITC analysis confirm the binding of NAD+ to chitosan but it also confirmed the large differences in size observed upon the addition of both a low (w/w) concentration of NAD+ (large, heterogenous size distributions) and a high concentration of NAD+ (smaller, more monodisperse size distribution) to chitosan via the reduction in heat changes observed during the titration. Chitosan and NAD+ binding was also confirmed through IR analysis of the shifts and intensity changes of IR absorption peaks that are specific to the binding and stretching vibrations of the respective compounds' functional groups.

In vitro release of the CH-NAD+ complexes, exhibiting association efficiencies of 68.2 ± 12.3% (120% (w/v)) and 65.4 ± 15.0% (w/v)), was also conducted under microfluidic conditions. Although the mass of NAD+ released from the PECs and CH-NAD+ formulations was statistically equivalent at 12 hours, the extension of NAD+ release to 36 hours is indicative of the enhanced ability of chitosan to impede *in vitro* NAD+ release via the aforementioned compaction of the polymeric network at physiological pH. The release of 8.0 ± 3.1 mg (120% (w/w)) and 10.7 ± 4.4 mg (140% (w/w)) of NAD+ was best-fitted to the Korsmeyer-Peppas model. However, NAD+ release was also well aligned with the Higuchi model, which suggested that even though the release exponent value suggested anomalous diffusion, NAD+ diffusion through the matrix may be the predominant mechanism of NAD+ release. Similar to that of the PECs, the size of the CH-NAD+ complexes was preserved over 28 days at 4 °C. Time-dependent increases in ZP observed in both formulations at this temperature may be indicative of structural changes within the complex arising from NAD+ release. The significant decrease in NAD+ retention over this timeframe may limit the shelf-life of the CH-NAD+ complexes in solution form.

Ultimately, the CH-NAD+ complexes exhibit suitable physicochemical attributes for ocular application and warrant further investigation using *in vitro* safety and efficacy trials on human corneal epithelial cell cultures and porcine anterior segment tissues.

CHAPTER 5:

IN VITRO SAFETY AND EFFICACY AND *EX VIVO* PERFORMANCE STUDIES ON COMPLEX FORMULATIONS

5. *IN VITRO* SAFETY AND EFFICACY AND *EX VIVO* PERFORMANCE STUDIES OF COMPLEX SYSTEMS

5.1 INTRODUCTION

In vitro and *ex vivo* safety and efficacy trials are crucial steps in the development phase of a nanoformulation as they provide an initial evaluation of the biocompatibility, pharmacokinetic and pharmacodynamic profiles of the nanoformulation under conditions closely aligned to that of the target site *in vivo* [534]. Nanoformulations exhibiting a degree of mucoadhesion may allow for enhanced contact with the pre-corneal surface following administration, thus achieving longer retention times [535]. This may also increase the likelihood of improved therapeutic bioavailability via a reduction in precorneal clearance. For example, Terreni *et al.* [536] demonstrated that the encapsulation of cyclosporine A within a d-α-Tocopherol polyethylene glycol succinate and octylphenoxy poly(ethyleneoxy)ethanol nanomicelle, functionalised with HA, led to a significant reduction in precorneal elimination rate *in vivo* (0.055 ± 0.009 min^{-1}) in comparison to a commercially available cyclosporine A nanoemulsion, Ikervis® (0.205 ± 0.033 min^{-1}). The addition of HA to the nanomicelle also increased cyclosporine A bioavailability (2142 ± 233.6 $\mu g/mL^{-1}/min$) in rabbit tear fluid in comparison to that of the unmodified nanomicelle (1813 ± 354.1 $\mu g/mL^{-1}/min$). Rhodamine B-labelled glycol chitosan and dexamethasone-conjugated nanoparticles exhibited prolonged pre-corneal retention for up to 45 minutes post-administration in a Japanese white rabbit model, attributed to the ionic bond-mediated interaction of glycol chitosan with the glycocalyx mucin corneal layer [537]. Conversely, the rhodamine B test solution was eliminated from the corneal epithelium after 15 minutes post-administration. In the work detailed in this chapter, mucoadhesion analysis of the respective nanoformulations was conducted under static conditions using mucin Type II, mimicking the MUC2 gel-forming mucin secreted on the corneal and conjunctival epithelia *in vivo* [538], [539]. Mucoadhesion under a dynamic flow rate was also conducted via QCM-D analysis in this study to further investigate the interactions of mucin with the charged functional groups of the respective polyelectrolyte materials, particularly HA and chitosan.

An immortalised human corneal epithelial cell (IMHCE) culture model was utilised in all of the *in vitro* cell studies to accurately predict the behaviours of both NAD+ and the NAD+ nanoformulations at the primary physiological barrier within the proposed site of administration. *In vitro* cytotoxicity analysis, typically conducted via a colorimetric assay of the enzymatic or metabolic activity of live cells, allows for an evaluation of changes in cell growth, replication and morphology following incubation with the chosen therapeutic [540]. The 3-(4,5-dimethylthiazol-2-yl)-2,5-diphenyltetrazolium bromide (MTT) assay has been utilised previously to assess the cytotoxic potential of self-assembled, polyelectrolyte-based nanomaterials on HCE cells [541], [542]. However, due to the cytotoxic potential of MTT itself, and its classification as hazardous to the environment, an acid phosphatase assay was used to evaluate the biocompatibility of NAD+ and NAD+-laden formulations [543]. The cleavage of *para*-nitrophenylphosphate (PNPP) substrate into p-nitrophenol via acid phosphatase enzymatic activity was utilised as a live cell biomarker. P-nitrophenol is colourless at acidic pH values. However, upon quenching the reaction using 0.1 M NaOH, the alkaline conditions result in the conversion of p-nitrophenol into p-nitrophenolate, a bright yellow compound that strongly absorbs at 405 nm. This method is highly sensitive and reproducible as it does not rely on the reduction of tetrazolium salts or their subsequent solubilisation in organic solvents.

Oxidative damage resulting from exposure to ROS is a hallmark of the initial pathological mechanisms that contribute to the progression of age-related ocular diseases [544]. As outlined in Section 1.2.1, intraocular accumulation of excess quantities of H_2O_2 can contribute to a significant imbalance in redox homeostasis and upregulation of intracellular hydroxyl radical, primarily due to its rapid permeation through cell membranes. This, in turn, contributes to oxidative stress-mediated damage and loss of cellular function. There is evidence to support that NAD+/NAD+ precursors can attenuate ROS-mediated cellular damage, mainly via upregulation of enzymatic activity responsible for maintaining basal antioxidant capacities [135], [545]. Under simulated hyperosmosis stress conditions, supplementation of primary murine corneal epithelial and RAW264.7 macrophage cell lines with 500 μM of nicotinamide mononucleotide (NMN) upregulated NAD+ concentration and alleviated ROS production and regulated lactate dehydrogenase release [546]. In a double-masked, randomised clinical trial, oral supplementation of 3.0 g of nicotinamide per day led to improvements in inner retinal

function (evidenced by significant increases in photopic negative response) in 23% of the 57 glaucoma patients treated [141]. Three days post-separation of the neurosensory retina from the RPE in a murine model, intraperitoneal injections of NMN at 500 mg/kg/day attenuated protein carbonyl content production (biomarker of oxidative stress), restoring them to a level that was comparable to that of the attached retina group (0.55 ± 0.10 nmol/mg – NMN and 0.55 ± 0.15 nmol/mg - control) [547]. Therefore, it was hypothesised that NAD+ supplementation prior to induction of ROS-mediated stress could indirectly protect the IMHCE by enhancing the cell's endogenous antioxidant defence. Although a delaying effect may be observed due to the hindered diffusion of NAD+ from the respective polymeric networks, it was not expected that the PECs and CH-NAD+ would significantly impede the ability of NAD+ to attain adequate cell viability.

Research conducted on nanoformulations for drug delivery applications suggests that nanoparticles exhibit enhanced cellular permeation at the target site due to their inherent sub-micron size. However, the morphology, charge and surface properties are also contributing factors to effective cellular internalisation [548]. Chiesa *et al.* [549] demonstrated that the kinetics of intracellular uptake of HA and chitosan-based PECs of approximately 200 nm in size in human mesenchymal stem cells was also highly dependent on the expression of CD44 receptors. In a similar study, HA-decorated gelatin-epigallocatechin gallate nanoparticles of between 273 ± 3 (cationic nanoparticle – 62.5 μg/mL of HA) and 354 ± 29 nm (anionic nanoparticle – 167 μg/mL of HA) in size exhibited enhanced permeation within an ARPE-19 cell line in comparison to that of the control dye (TAMRA) due to CD44-mediated endocytosis [550]. However, the surface charge of the nanoparticles was also a contributing factor to intracellular uptake, with the cationic nanoparticles exhibiting an increase in ARPE-19 uptake rate of over 29% 1-hour post-incubation. In a quantitative study, Kimna *et al.* [329] observed a significant increase in timolol maleate permeation through a porcine cornea upon comparison of a chitosan and alginate complex of 251 ± 96 nm in size and a timolol maleate control solution. Over 89% of the encapsulated timolol maleate was quantified within the receptor compartment following corneal permeation, attributed to the blocking of the cationic moieties of timolol maleate from the anionic porcine mucin later via complex association. Only 67% of the timolol maleate concentration in the control solution reached the receptor compartment,

whilst over 30% of the loaded concentration was retained within the tissue sample. Therefore, to obtain a complete assessment of the therapeutic efficacy of a nanoformulation, the intracellular trafficking and biodistribution of a formulation must be evaluated. As the NAD+-associated PECs and CH-NAD+ formulations exhibit similar sizes and polymer functionality to the aforementioned formulations, cell uptake studies can be used to evaluate whether further investigations of the mechanism of cell uptake are warranted. Cellular internalisation of fluorescent-tagged nanoformulations is typically monitored via flow cytometry or fluorescence microscopy [551]–[555].

In conjunction with the IMHCE culture, *ex vivo* porcine corneal and scleral tissue models were also used to investigate the pharmacokinetic of the respective formulations upon application to the pre-corneal surface. The complexity and enhanced interaction between numerous cell types and extracellular environments within the respective tissues, and their similarities in morphology to those of humans, provided a more comprehensive estimation of NAD+/NAD+-laden nanoformulation permeation and retention [556].

Ultimately, the research work detailed in this chapter provided a critical evaluation of the *in vitro* and *ex vivo* physiological behaviour of the NAD+-laden nanoformulations prepared in Chapters 3 and 4. Although both formed via the association of NAD+ to the respective polyelectrolytes during complexation, the PECs and CH-NAD+ formulations exhibit different physicochemical attributes, particularly with surface charge. As such, this provided an opportunity to compare the capabilities of the respective nanoformulations to deliver NAD+ to the corneal surface and intracorneal environment in a safe and effective manner.

5.2 EXPERIMENTAL METHODOLOGY

5.2.1 Materials

IMHCE (P10871-IM), corneal epithelial cell basal medium (4-(2-hydroxyethyl)-1-piperazineethanesulfonic acid) (HEPES) and bicarbonate buffered), corneal epithelial cell growth supplements, fetal bovine serum and penicillin/streptomycin solution were purchased from Innoprot (Bizkaia, Spain). Trypsin-EDTA (0.05%), phenol red, PNPP, and 2-(4-amidinophenyl)-1H-indole-6-carboxamide (DAPI) were purchased from Thermo Fisher

Scientific (Dublin, Ireland). Fluorescein isothiocyanate (FITC) was purchased from Sigma Aldrich Ireland Ltd. (Wicklow, Ireland). Porcine mucin (Type II – Stomach) was purchased from Merck (Darmstadt, Germany).

5.2.2 Mucoadhesion Analysis of PECs and Chitosan-NAD+ Complex Formulations

5.2.2.1 Quartz Crystal Microbalance with Dissipation (QCM-D)

The mucoadhesive capabilities of the PEC and CH-NAD+ formulations were initially analysed via a QCM-D methodology using a QSense analyser (Biolin Scientific AB, Sweden). Briefly, piezoelectric AT-cut quartz crystal sensors (fundamental frequency of 5 MHz) (QSX 301, Biolin Scientific, Sweden) were immersed in a 5:1:1 (v/v/v) solution of ultrapure water, 25% (v/v) ammonium hydroxide and 30% (v/v) hydrogen peroxide, heated to 80 $^{\circ}$C, for 10 minutes. The sensors were rinsed twice with deionised water and 99% (v/v) ethanol, dried under nitrogen and placed into the sensor chambers. A syringe pump (Model 220, KD Scientific Inc, Massachusetts, United States) was set to deliver the samples through the sensor chamber at a flow rate of 0.11 mL/min in the order outlined in Table 5.1.

Each reagent or formulation was analysed in duplicate at the 3rd, 5th, 7th, 9th, 11^{th,} and 13th overtone.

Table 5.1 Order of addition of each sample/media analysed via QCM-D.

Media/Sample	Concentration (% (w/v)	Time (min)
Air	N/A	20
Ultrapure Water	N/A	20
0.01 M PBS (pH 7.4)	N/A	20
Porcine Mucin (Type II Stomach)	0.0025	40
0.01 M PBS (pH 7.4)	N/A	15
Reagent/Formulation	0.01	40
0.01 M PBS (pH 7.4)	N/A	10

5.2.2.2 Zeta Potential Analysis

2 mg/mL solutions of each reagent, formulation and porcine mucin were prepared in ultrapure water, adjusted to pH 7.4. 500 µL of each sample solution was mixed with an equal volume of the porcine mucin solution and incubated at 37 °C in a temperature-controlled incubator

(S160D, Stuart Equipment, UK) for 2 hours. The sample controls (incubated without porcine mucin) were mixed with 500 µL of ultrapure water prior to incubation. The mucin control was also pre-mixed with ultrapure water prior to incubation. Following incubation, 1 mL aliquots of the solutions were placed into a U-shaped folded capillary zeta cell and analysed as per Section 2.2.5.2.

5.2.3 *In Vitro* Cell Studies

5.2.3.1 Human Corneal Epithelial Cell Culture

Upon thawing, an aliquot of the IMHCE cell culture, equivalent to a seeding density of 10,000 cells/cm^2, was dispensed into a Nunc^{TM} T-75 flasks containing 10 mL of ocular epithelial cell medium, supplemented with 5% (v/v) fetal bovine serum (FBS), 1% (v/v) of epithelial cell growth supplement (EpiCGS) solution and 1% (v/v) penicillin/streptomycin solution. IMHCE cell cultures were maintained at 37 °C in a humidified atmosphere with 5% carbon dioxide (CO_2) in a CO_2 incubator (Haier Biomedical, UK). To prevent dimethyl sulfoxide (DMSO)-mediated cytotoxicity, the media was changed approximately 16 hours after thawing and every 3 days thereafter. IMHCE cells were passaged upon reaching approximately 90-95% confluency, with at least two passages being conducted prior to seeding in well plates for experimental use. Cells of a passage number between 6 and 14 were used in the studies detailed in this chapter. This passage range was deemed suitable for use, as it was well within the passage range investigated by Araki-Sasaki *et al.* [557], who established an IMHCE model that continued to grow through to 100 passages (up to 400 generations). The cell line utilised was also immortalised with SV40 Large T antigen, thus allowing for long-term reproducibility, phenotypic and genotypic uniformity, and protection against stimuli-induced senescence during culture.

5.2.3.2 In Vitro Cytotoxicity via Acid Phosphatase Assay

IMHCE cells were seeded at a density of 5×10^3 cells per well into a 96-well cell culture plate. Technical replicates were conducted, with each concentration being analysed in triplicate (three wells per concentration). Once a confluency of approximately 80% was achieved (following 24 to 48 hours of incubation), the medium was withdrawn and replaced with 100 µL of fresh medium supplemented with PEC or CH-NAD+ formulations containing 40-800 µM of NAD+.

After 24 hours, the formulations were removed and the IMHCE cultures were washed thrice with ice-cold 0.01 M PBS. 100 µL of 10 mM PNPP in pH 5.5 sodium acetate buffer was added to each well, followed by incubation for 2 hours. 50 µL of a 0.1 M NaOH stop solution was added to each well prior to analysis of the absorbance of each well at 405 nm using a BioTek Epoch® microplate reader (Agilent Technologies, Dublin, Ireland). A cytotoxic evaluation of both blank formulations (HA and PLL-based PECs and chitosan alone) and NAD+ alone at equivalent concentrations was also conducted for comparative purposes. Percentage cytotoxicity was calculated in accordance with Equation 5.1. Control cells, incubated with 100 µL of fresh medium alone, were also analysed.

$$\left(\frac{\text{Absorbance of Sample Well}}{\text{Absorbance of Control}}\right) \text{x } 100 \qquad \text{Equation 5.1}$$

5.2.3.3 In Vitro Efficacy in an Oxidative Stress Model via Acid Phosphatase Assay

IMHCE cells were seeded at a density of 1 x 10^4 cells per well and incubated until optimal confluency was achieved. The trials conducted to investigate the efficacy of both NAD+ and the PEC/CH- NAD+ formulations in attenuating hydrogen peroxide (H_2O_2)-induced cellular dysfunction, using a similar methodology to that outlined in Section 5.2.3.2, are summarised in Table 5.2.

Table 5.2: Details of the *in vitro* efficacy studies conducted on IMHCE cells via an acid phosphatase assay (APA).

Trial One	***Cytotoxic Effect of H_2O_2 -*** To investigate changes in % IMHCE cell viability upon incubation with H_2O_2 in both a time and concentration dependant manner.					
Concentration (H_2O_2) (µM)	200	400	600	800	1000	1200
Exposure Time Concentration (H_2O_2) (h)	2, 6, and 24 (for each concentration)					
Trial Two	***Restorative Effect of NAD+ Supplementation on H_2O_2-Stressed Cells*** – To determine the minimum effective concentration of NAD+ against the maximum					

	concentration of H_2O_2 that induced a cytotoxic effect on IMHCE cells.
Concentration (NAD+) (µM)	20 50 100 200
Concentration (H_2O_2) (µM)	400, 800, and 1200 (for each concentration)
Exposure Time (H_2O_2) (h)	As before for each concentration of H_2O_2 analysed.
NAD+ Supplementation Time (h)	2
Trial Three:	***Effect of Supplementation Time on the Restorative Effect of NAD+ –*** To investigate if the length of time that IMHCE cells are incubated with NAD+ prior to the addition of H_2O_2 has an impact on its restorative capability.
Concentration (NAD+) (µM)	20 200
NAD+ Supplementation Time (h)	2, 6, 10, 17, and 24 (for each concentration)
Concentration (H_2O_2) (µM)	200
Exposure Time (H_2O_2) (h)	2
Trial Four:	*Restorative Effects of NAD+-Associated Formulations on H_2O_2-Stressed Cells* – To compare the efficacy of the NAD+-associated formulations to NAD+ alone in restoring cell viability after H_2O_2 exposure.
Concentration (NAD+ in Formulation) (µM)	20 (CH-NAD+) 200 (PEC)
NAD+ Supplementation Time (h)	10, 24, 32, and 48 (for each concentration)
Concentration (H_2O_2) (µM)	200
Exposure Time (H_2O_2) (h)	2

5.2.3.4 Quantification of NAD+ Cellular Uptake

IMHCE cells were seeded at a 1 x 10^5 density in a 24-well cell culture plate and incubated overnight. The media was then replaced with 1 mL of fresh medium, supplemented with increasing concentrations of NAD+ within the range of 20 to 200 µM and the cells were incubated for a further 24 hours. 1 mL of media containing PEC/CH-NAD+ formulations, with

equivalent concentrations of NAD+ to those of the controls, were added to individual wells. The media was subsequently removed, and the cells were washed twice with ice-cold 0.01 M PBS. All media and well washings were retained for indirect NAD+ quantification. 500 µL of trypsin-EDTA (0.05%) was added to each well prior to incubation for a further 5 minutes to allow for detachment. Following addition of 500 µL of 0.1 M NaOH, the cells were transferred to 1.5 mL Eppendorf® tubes, incubated at ambient temperature for an hour and subsequently centrifuged at 2,800 rpm for 5 minutes. 100 uL of the lysate was withdrawn, diluted to 1 mL with mobile phase and analysed via RP-HPLC.

5.2.3.5 Preparation of Fluorescent PECs and Chitosan-NAD+ Complex Formulations

FITC-PEC and FITC-CH-NAD+ formulations were prepared using a method adapted from Ilka *et al.* [336]. Briefly, 2 mg of FITC was dissolved in ultrapure water at pH 5.5 and added dropwise to PEC/CH-NAD+ formulations during complexation. The resulting formulations were shaken at 200 rpm at 25 °C overnight, and protected from light. Centrifugation was conducted as outlined in Section 2.2.4 to remove free FITC before lyophilisation.

5.2.3.6 Qualitative Analysis of Cellular Uptake via Fluorescent Microscopy

After seeding for 24 hours (1 x 10^5 density) in a 24-well cell culture plate, IMHCE cells were incubated with FITC-CH-NAD+ and FITC-PECs formulations, equivalent to 20 and 200 µM of NAD+, respectively. After 24 hours post-incubation, the cells were washed as before with ice-cold 0.01 M PBS, before fixation with 300 µL of 4% paraformaldehyde for 30 minutes. The cells were then rinsed with ice-cold 0.01 M PBS and treated with 100 µL of 0.0001% (w/v) DAPI for 15 minutes, followed by a final washing step. Each well was viewed using an Olympus fluorescence microscope (Olympus Life Sciences, Japan) in DAPI and FITC modes, at a set magnification of 40x, to determine the extent of internalised fluorescence.

5.2.4 *Ex Vivo* Studies using Porcine Corneal and Scleral Tissues

5.2.4.1 Tissue Dissection and Maintenance

The porcine eyes used in this study were collected from a local abattoir (Dawn Meats Grannagh, Waterford, Ireland) within an hour of slaughter and stored in 0.9% (w/v) saline solution maintained at 4 °C. Upon delivery to the laboratory, the eyes were washed thoroughly

with 0.01 M PBS (pH 7.4) and the lids and surrounding muscle tissues were carefully removed. As shown in Figure 5.1, incisions were made perpendicular to the ciliary arteries along the limbus. The anterior and posterior sections were separated by cutting around the limbus using surgical scissors, leaving 3 to 5 mm of sclera attached to the corneal tissue. Lenses were subsequently removed and the irises were carefully peeled from the endothelial side of the isolated cornea using a forceps. Intact corneal tissues were then gently cleaned with, and immersed in, fresh aliquots of sterile 0.01 M PBS (pH 7.4). A portion of scleral tissue was surgically removed from the posterior explant and the choroid was carefully scraped from the tissues using a scalpel. The RPE was then removed from the scleral tissues using filter paper before immersion of the tissues into an additional aliquot of sterile 0.01 M PBS (pH 7.4). All *ex vivo* studies were conducted within 8 hours of slaughter to ensure tissue integrity.

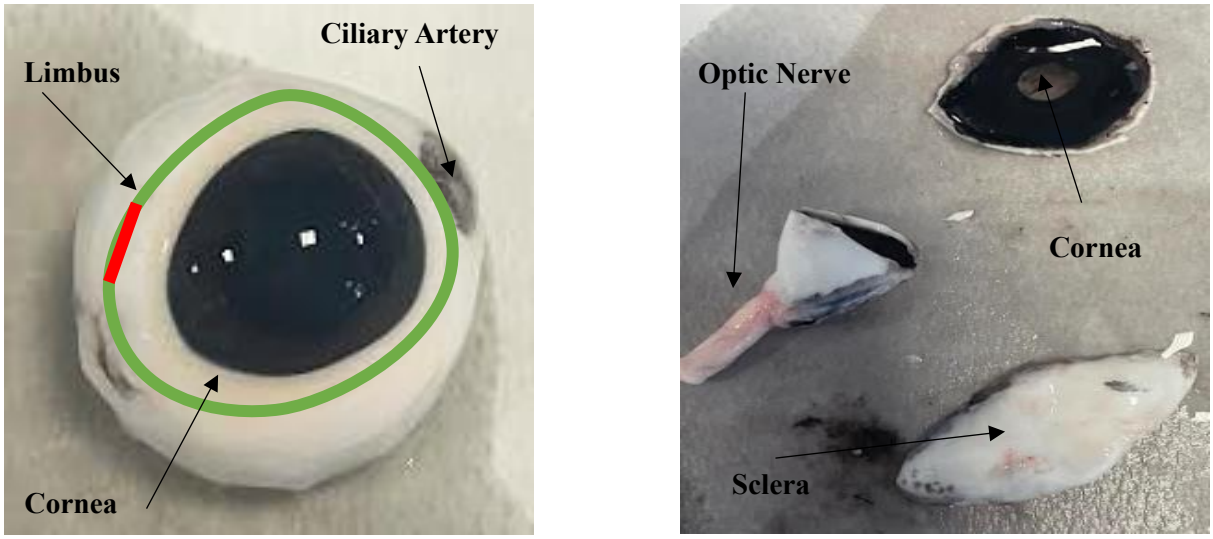

Figure 5.1: Diagram showing (a) the incision point (red) on the porcine cornea and (b) the resulting tissue segments following surgical removal.

5.2.4.2 Quantification of NAD+ Permeation

Isolated corneal and scleral tissues were clamped into Franz diffusion cells (average permeation area: 1.3 cm^2), with the corneal epithelium and exterior of the sclera facing outward. The receptor chamber was filled with 3 mL of 0.01 M PBS (pH 7.4), followed by equilibration for 30 minutes at 37 °C under gentle shaking at 200 rpm. 200 µL of PECs and CH-NAD+

formulations in 0.01 M PBS (pH 7.4), prepared with formulation masses equivalent to 15 mg of NAD+, was then pipetted into respective donor chambers. Both a positive (200 µL of an NAD+ solution) and a negative (200 µL of 0.01 M PBS (pH 7.4)) control were analysed in this study. At set timepoints between 5 minutes and 8 hours, 200 µL of the receptor medium was withdrawn and stored at 4 °C. 8 hours post-incubation, 50 µL of the donor solution was removed and diluted as before.

To analyse the mass of NAD+ retained within the tissues, a sample of each tissue was removed using a hole punch and weighed. 1 mL of mobile phase was then added before vortexing the tissue samples at high speed for 5 minutes. Extraction was left to proceed for 24 hours at ambient temperature. 200 µL of the resulting solution was removed, filtered using 0.45 µM syringe filters and diluted as before. The receptor, donor and retention samples were ultimately analysed via RP-HPLC.

5.2.4.3 Visualisation of Complex Permeation via Fluorescence Microscopy

Isolated corneal and scleral tissues were clamped into prepared Franz diffusion cells as before. After equilibration for 30 minutes at 37 °C, 200 µL of FITC-PECs and FITC-CH-NAD+ formulations in 0.01 M PBS (pH 7.4), containing a mass equivalent to 15 mg of NAD+, was pipetted into the donor chambers. 200 µL aliquots of both a FITC control solution, equivalent in FITC concentration to the formulations, and 0.01 M PBS (pH 7.4) alone, were placed into individual diffusion cells. 6 hours post-incubation, the porcine tissues were removed, washed thrice with ice-cold 0.01 M PBS, and immersed in 3 mL of DAPI (0.0001% (w/v)) solution for 5 minutes. After a final washing step with ice-cold 0.01 M PBS, the tissues were viewed using an Olympus fluorescence microscope at 20x magnification as outlined in Section 5.2.3.6.

5.2.5 Statistical Analysis

Statistical analysis was conducted as previously outlined in Sections 2.2.6, 3.2.4, and 4.2.4.

5.3 RESULTS AND DISCUSSION

5.3.1 Mucoadhesive Capabilities of Complex Formulations

QCM-D analysis was used to investigate the mucoadhesive capabilities of both the individual polyelectrolyte reagents and complex formulations via surface adsorption onto mucin-modified sensors. A QCM measures the mass of a quartz sensor, per unit area, by detecting the change in frequency. Upon application of an alternating voltage, a standing wave is generated within the quartz sensor due to the close alignment of its resonance frequency with that of the applied voltage [558]. An indirect correlation is established between the thickness, and therefore the mass, of the quartz sensors and their resonance oscillation frequency following sample deposition, as per the Sauerbrey equation shown in Equation 5.2 [559].

$$\Delta \mathrm{m} = -\frac{C\ x\ \Delta f}{n} \qquad \text{Equation 5.2}$$

Sample deposition increases sensor thickness, thus increasing the wavelength of the standing wave and a detectable decrease in oscillation frequency [560]. Changes in dissipation (ΔD) can also provide information regarding the viscoelastic properties of the absorbed layer. When the alternating voltage is switched off during an oscillation cycle, energy is dissipated from the sensor due to the exponential dampening of the oscillation [561]. Materials with higher viscoelasticity do not couple well with the oscillation and cause rapid deformation of the oscillation with high dissipation. Conversely, rigid materials couple well with the sensor, which leads to a longer oscillation decay time.

Changes in frequency (Δf) and dissipation (ΔD), indicating surface adsorption/desorption and changes in system viscosity, for each reagent/formulation, are presented in

Table ***5.3*** and Supplementary Figure 1 (Appendix 1.1). Both Δf and ΔD were measured across a range of overtones to analyse changes in both oscillation frequency and energy due to sample deposition and penetration at varying depths across the adsorbed mucin layer [562].

Table 5.3: Changes in Δf and ΔD recorded upon deposition of the individual reagent/ formulations onto the respective quartz sensors at the 5th overtone.

Δf/ ΔD	**NAD+-PEC**	**BLANK PECs**	**HA**	**PLL**
F5	0.73 ± 0.49	1.27 ± 4.75	8.85 ± 10.83	-1.36 ± 2.94
D5	-1.24 ± 0.06	-0.53 ± 1.65	-4.88 ± 1.84	-0.92 ± 0.83
Δf/ ΔD	**CHITOSAN**	**CH-NAD+ (120 % (w/v))**	**CH-NAD+ (140 % (w/v))**	
F5	-27.43 ± 18.65	-21.94 ± 23.40	-4.99 ± 14.32	
D5	2.77 ± 0.58	9.17 ± 13.67	3.03 ± 3.67	

A reduction in Δf and spreading of overtones was observed upon deposition of the chitosan-based formulations onto the mucin-coated sensors, particularly in the CH-NAD+ (120% (w/w)) formulation. Adhesion of the chitosan-based formulations to the mucin on the sensors, primarily via electrostatic interaction between free cationic amine groups and the anionic moieties of mucin, would increase the mass of the respective sensors, thus leading to a concurrent reduction in oscillation frequency. However, the increase in Δf following rinsing of the quartz sensors with 0.01 M PBS (pH 7.4) (Appendix 1.1 – (e), (f), (g)), indicating a negative shift in sensor mass, suggested that the adsorption of the respective reagents/formulations was reversible. Slight, positive shifts in ΔD within the chitosan-based samples were observed, indicating that the viscosity of the system had increased as a result of chitosan adsorption.

Negligible changes in Δf were observed upon the addition of HA and the PEC formulations to the quartz sensor, thus indicating that minimal adsorption to the mucin layer occurred. A slight negative shift in Δf was observed for PLL alone (-1.36 ± 2.94 – F5). However, although not statistically significant ($p = 0.190 > 0.05$), this shift in frequency was smaller in comparison to that of chitosan (-27.43 ± 18.65 – F5), potentially attributed to the enhanced electrostatic interaction of chitosan with mucin due to its higher charge density. However, slight reductions in ΔD were recorded for HA (-4.88 ± 1.84 – F5), blank PECs (-0.53 ± 1.7 – F5) and NAD+-associated PECs (-1.24 ± 0.06 – F5), thus suggesting that a conformational change had occurred due to association of HA with the mucin layer, increasing its rigidity. At a similar overtone, Sladek *et al*. [465] also reported a small, yet negative change in ΔD and no notable changes in

Δf following the deposition of anionic, HA and chitosan-based PECs onto a layer of porcine mucin (Type III). Cationic, chitosan-based PECs evoked a sharp increase in ΔD and a corresponding decrease in Δf. Oh *et al.* [563] also observed a decrease in ΔD following HA adsorption onto native porcine gastric mucin, attributed to conformational changes within the mucin layer followed by mutual electrostatic repulsion between the carboxyl and sulfate groups of mucin and the residual carboxylate anions of HA and the PECs with HA present in excess. The slight reduction in Δf observed following the final rinse with 0.01 M PBS after HA (Supplementary Figure 1 (a)) and NAD+-associated PEC (Supplementary Figure 1 (d)) may be due to water adsorption by residual HA chains present on the PEC surface. The expected interactions of the respective polyelectrolytes and formulations with mucin via electrostatic bond formation, mutual repulsion, and intermolecular bonding, are supported by the changes in both Δf and ΔD. To conduct a more complete evaluation of the mucoadhesive capabilities of the formulations, the ZP of the formulations upon incubation with porcine mucin was also analysed.

The changes in ZP values obtained upon incubation of the reagents/formulations with porcine mucin, as depicted in Figure 5.2, support the trends observed during QCM-D analysis. Significant, positive shifts in ZP was observed upon incubation of HA (-36.9 ± 11.1 mV to -23.5 ± 2.2 mV) and NAD+-associated PECs (-33.5 ± 1.3 mV to -17.4 ± 1.3 mV) with mucin. These values were also statistically lower in comparison to that of mucin alone. Despite its anionic nature, HA may exhibit some degree of mucoadhesion due to a combination of attractive electrostatic interactions between residual HA carboxylate anions and the cationic amino groups of the zwitterionic backbones of corneal-bound mucin, hydrophobic interactions and van der Waals forces. As observed by both Graca *et al.* [564] and Landucci *et al*. [565], a positive shift in ZP that retains a value that is more negative than mucin alone is indicative of mutual interaction between mucin and HA. In a similar study conducted by Mangiacotte *et al.* [566] with anionic poly(2-hydroxyethyl) methacrylate and 3-(acrylamido)phenylboronic acid nanoparticles, samples that were more negative than the mucin control were deemed to exhibit mucoadhesive capability due to enhanced interaction.

Regarding the cationic formulations and respective reagents, reductions in ZP values were observed in the presence of mucin, potentially attributed to the neutralisation of the anionic mucin moieties with the cationic polyelectrolyte functional groups. However, the ZP values of the formulations were statistically equivalent to those of the respective controls (reagents/formulations dispersed in ultrapure water pH 7.4 alone).

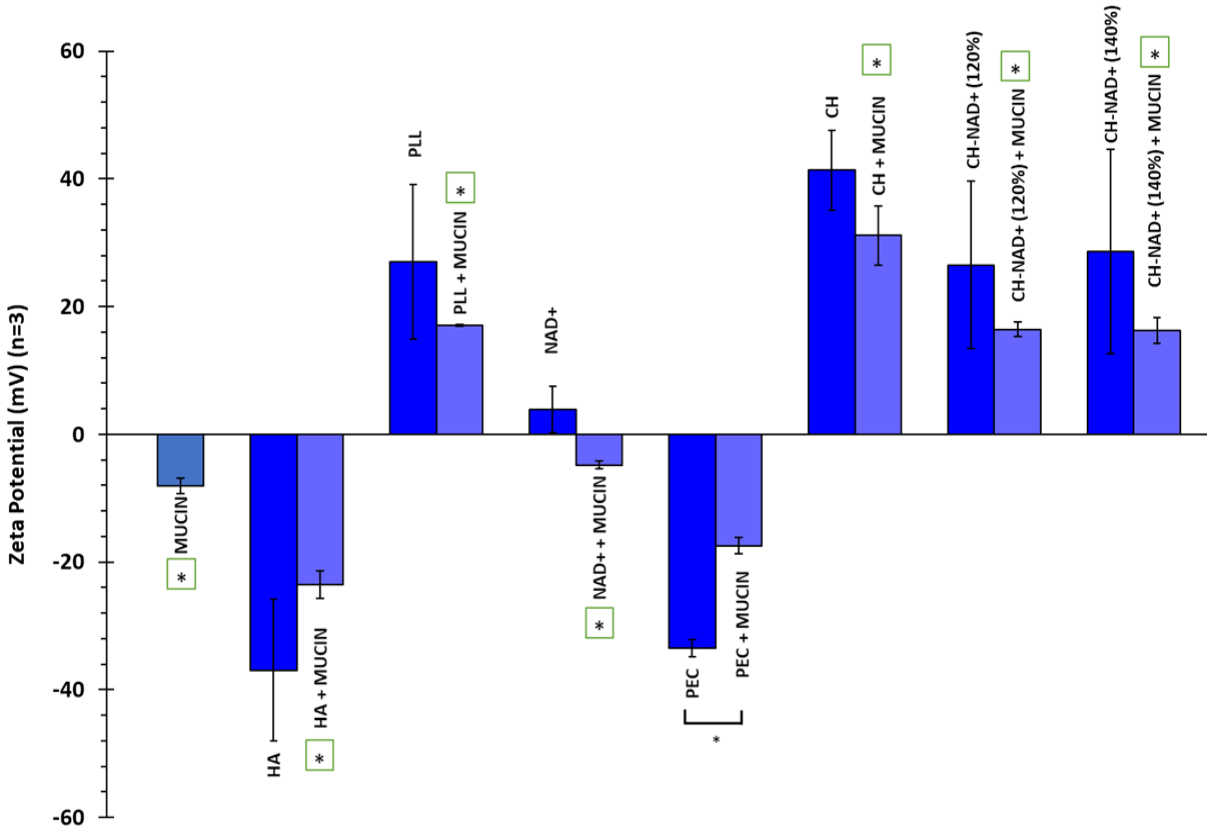

Figure 5.2: Changes in ZP observed upon incubation of the individual reagents, PECs, and chitosan-NAD+ formulations with porcine mucin (Type II) for 2 hours at 37°C. (**Dark blue** – without mucin, **light blue** – with mucin). Data is expressed as mean zeta potential ± S.D. (n = 3). (Green * - statistically different from mucin alone).

Ultimately, both the PEC and chitosan-based formulations exhibited some degree of mucoadhesive capabilities, with the chitosan-based formulations exhibiting greater affinity for mucin binding due to favourable electrostatic interaction. As such, both formulations may

exhibit extended pre-corneal retention times upon administration, thus increasing the likelihood of enhanced NAD+ permeation and increased bioavailability.

5.3.2 Cytotoxic Assessment of NAD+ on Corneal Epithelial Cells

A cytotoxic evaluation of both NAD+ alone and the NAD+-laden complex formulations was conducted to determine the maximal concentration of NAD+ that can be administered without eliciting a cytotoxic response. In line with EN ISO 10933-5:2009, a formulation exhibiting a cell viability of above 80% is considered non- cytotoxic. Percentage cell viabilities ranging from 60% to 80% indicate a weak cytotoxic response whereas a reduction in cell viability by 40% or more is considered highly cytotoxic [567], [568]. The concentration-dependant decline in cell viability following incubation of IMHCE cells with NAD+/NAD+-laden complexes is depicted in Figure 5.3.

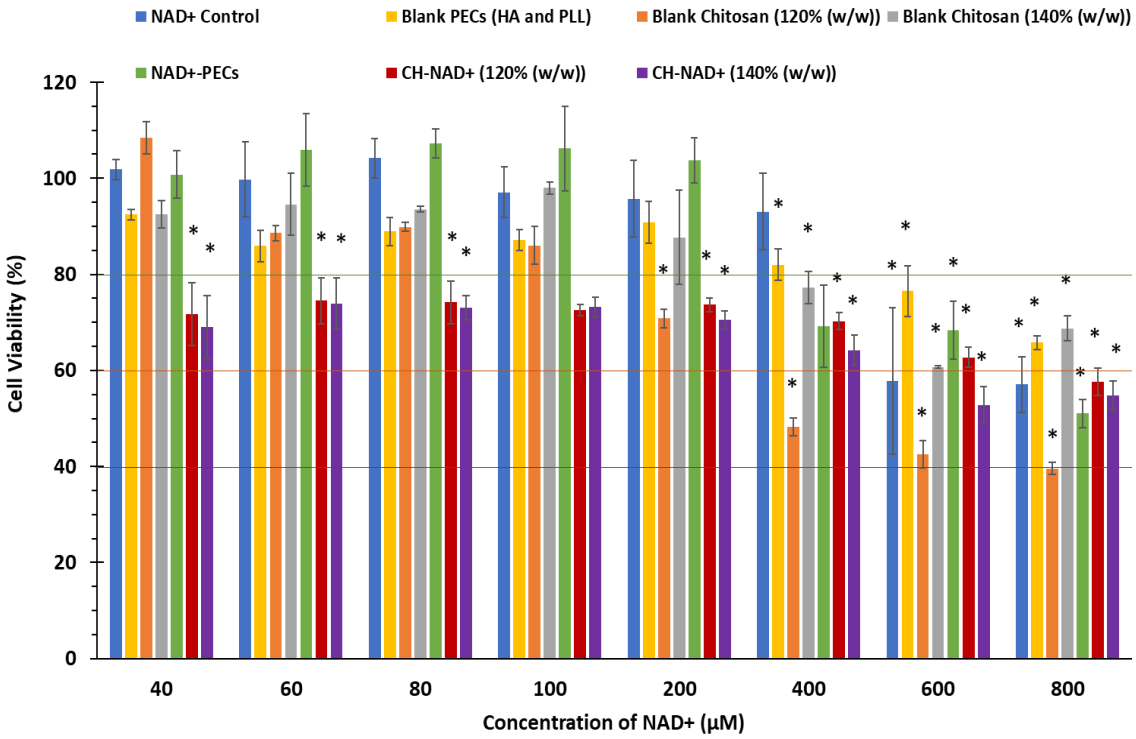

Figure 5.3: Cell viabilities of IMHCE cells with each NAD+ concentration/NAD+ complex for 24 hours at 37°C under 5% CO_2. (Dark blue – NAD+ control, yellow – blank PECs, orange – blank CH-NAD+ (120% (w/w)), grey – blank CH-NAD+ (140% (w/w)), green – NAD+-associated PECs, red – CH-NAD+ (120% (w/w)), purple – CH-NAD+ (140% (w/w)). Data is

expressed as mean % cell viability ± S.D (n = 3). (* = statistically significant difference between cell viability of the sample and that of the control (100 ± 3.7%) at a 5% confidence interval). (The cell viability categories are shown on the graph).

A significant decrease in viability in comparison to the control was observed for both the CH-NAD+ (120% (w/w)) (71.7 ± 6.6% - $p = 0.003 < 0.05$) and CH-NAD+ (140% (w/w)) (69.0 ± 6.5% - $p = 0.004 < 0.05$) at the lowest concentration of NAD+ analysed. No significant difference was found between the viability of the blank chitosan-based complexes and that of the control, thus indicating that the cytotoxic response observed was not due to chitosan alone. It was expected that chitosan may elicit a cytotoxic response, particularly at high concentrations, due to the binding of the cationic amine groups to the cell membranes. However, due to the electrostatic binding of NAD+ to the available amine groups during complexation, this would not explain the decrease in cell viability. The cytotoxic potential of crosslinked chitosan-based nanoformulations has been critically evaluated by Zoe *et al.* [569]. Although numerous *in vitro* and *in vivo* disease models, including cancer cell lines, hypercholesterolemic plasma, and zebrafish embryonic models, were summarised in this review, the vast majority of the studies highlighted observed a dose-dependent increase in cytotoxicity upon incubation with chitosan-based formulations. Zebrafish embryos exhibited an increase in mortality rate of over 80% after incubation with 40 mg/L chitosan and TPP nanoparticles (200 nm) upon comparison with those incubated with 5 mg/mL of the same formulation [570]. Incubation with 340 nm nanoparticles evoked a smaller cytotoxic response (approximately 15% mortality rate), thus highlighting that particle size is also a governing factor of the cytotoxic response. Increased cellular apoptosis, as evidenced by an increase in acridine orange dye uptake (higher degree of green fluorescence) was also observed after 96 hours of incubation of the zebrafish larvae with 20 mg/mL chitosan and TPP nanoparticles. Although not statistically significant, a decrease in corneal stromal fibroblast cell viability from above 95% to 82% was observed by Radwan *et al.* [571] for chitosan-decorated bovine serum albumin nanoparticles, with the same sample exhibiting enhanced *in vitro* cell uptake (14,000 relative fluorescent units) in comparison to the uncoated formulation (8,000 relative fluorescent units). Furthermore, a study conducted by Jesus *et al.* [572] demonstrated that the self-assembly of chitosan via TPP-mediated ionotropic gelation resulted in decreased cell viability in

comparison to an equivalent concentration of chitosan in a RAW 264.7 cell line. A more prominent decrease in cell viability was also observed when the degree of chitosan deacetylation decreased from 93 to 80%, primarily attributed to the concurrent reduction in particle size. The decline in cell viability observed in our study may be attributed to enhanced intracellular nanoparticle permeation in comparison to the individual chitosan chains. Nevertheless, a weak cytotoxic response was observed for both of the CH-NAD+ formulations containing 40 μM of NAD+ and therefore, CH-NAD+ formulations containing a lower concentration of NAD+ (20 μM) were analysed in further *in vitro* safety and efficacy studies.

The viability of IMHCE cells incubated with NAD+-associated PECs containing up to 200 μM of NAD+ was statistically equivalent to that of the control and therefore did not elicit a cytotoxic response. Despite attaining suitable cell viability upon incubation with 400 μM of NAD+ alone, high variability of viability in cells incubated with PECs containing 400 μM of NAD+ was observed. This was not observed in cell samples incubated with lower concentrations of NAD+-associated PECs. This, combined with the significant decline in viability in cells incubated with PECs alone (100.0 ± 3.7% - control vs. 82.0 ± 3.2% - PECs alone, $p = 0.003 \ll 0.05$), suggests that the PEC components themselves elicit a cytotoxic response at higher concentrations from 400 μM onwards (600 μM – 76.5 ± 5.2%, 800 μM - 65.8 ± 1.4%). This was further corroborated by a significant decline in viability with NAD+-associated PECs containing 600 (68.4 ± 6.0%) and 800 μM of NAD+ (51.0 ± 2.9%). The cationic charge of PLL may be causing a cytotoxic effect due to enhanced electrostatic interaction with the anionic phospholipid bilayers of cell membranes, with the likelihood of electrostatic bond formation increasing with an increase in concentration. Both Mohamed *et al.* [573] and Fan *et al.* [574] observed a PLL concentration-mediated decline in normal human keratinocytes and human corneal epithelial cells, respectively, upon incubation with PLL-modified polymeric nanoparticles. Kennedy *et al.* [575] also demonstrated the amoebicidal effect of PLL against trophozoites associated with *acanthamoeba* keratitis in a concentration-dependent manner. An increase in PLL-hydrogel concentration from 0.2 to 2.2 mM led to an almost 40% increase in trophozoite death. Incubation with NAD+ alone at concentrations of 600 and 800 μM also led to a reduction in cell viability to 57.8 ± 15.3% and 57.1 ± 5.8%, respectively, presumably attributed to the accumulation of potentially toxic metabolites from

increased NAD+ consumption [134]. Also, as discussed in Section 1.2.2.2, an increase in NAD+ concentration could also lead to increased competitive inhibition of NAD+-consuming enzymes due to hyperexpression, thus hindering enzymatic activity that is responsible for maintaining cellular homeostasis. Both Zhu *et al.* [140] and Zhou *et al.* [576] also observed a decrease in ARPE-19 and lens epithelial cells with an increase in NAD+ and nicotinamide riboside (NR) concentration from 0 to 1 mM, and 0 to 10 mM, respectively.

5.3.3 Analysis of Protective Effects of NAD+ in Response to Oxidative Stress

Firstly, the cytotoxic potential of H_2O_2 on IMHCE cells was confirmed via exposure of IMHCE cells to increasing concentrations of H_2O_2 over time. As shown in Figure 5.4 (a), cell viability declined in both a time- and concentration-dependent manner, with cell viability dropping to below 50% after just 2 hours upon exposure to NAD+ concentrations of 400 µM of H_2O_2 and above.

IMHCE cells were subsequently incubated for 2 hours with increasing concentrations of NAD+ before the addition of between 400 to 1200 µM of H_2O_2 for 24 hours to determine if NAD+ could effectively preserve cell viability. No significant difference was found between the viabilities of the 800 and 1200 µM H_2O_2-treated cells and those treated with an equivalent concentration of H_2O_2 and each concentration of NAD+ at any of the timepoints analysed. However, treatment with 20 to 200 µM of NAD+ after exposure to 400 µM of H_2O_2 resulted in a statistically higher cell viability (20 µM – 16.2 ± 0.5% ($p = 0.000$), 200 µM - 20.6 ± 1.8% ($p = 0.005$)) in comparison to that of the positive control (14.0 ± 0.4%) (Figure 5.4 (b)). Nguyen *et al.* [577] observed a similar trend upon incubation of ARPE-19 cells with a TPP and niacin-based polyelectrolyte complex, in which pre-supplementation for 2 hours with increasing niacin concentration protected against the deleterious effects caused by 300 µM of H_2O_2.

However, despite this seemingly positive increase in IMHCE viability with NAD+ addition in our study, over 75% of the cells were non-viable upon exposure to 400 µM of H_2O_2, indicating a severely cytotoxic response. Basal intracellular H_2O_2 concentration typically ranges from 1 to 100 nM, with the induction of biomolecule damage and oxidative distress occurring at concentrations above 100 nM [578], [579]. However, as detailed by Ransy *et al.* [580], H_2O_2 concentrations between 100 and 500 µM are typically required to observe oxidative damage in

an H_2O_2-stressed cell model, primarily due to the loss of H_2O_2 via conversion to molecular oxygen, which is subsequently utilised in the synthesis of both ATP and superoxide radicals. With this in mind, and with the assumption that these NAD+-associated formulations be used as a supplementary treatment before the accumulation of supraphysiological oxidant concentrations, an H_2O_2 concentration of 200 µM was selected for investigation of treatment supplementation time.

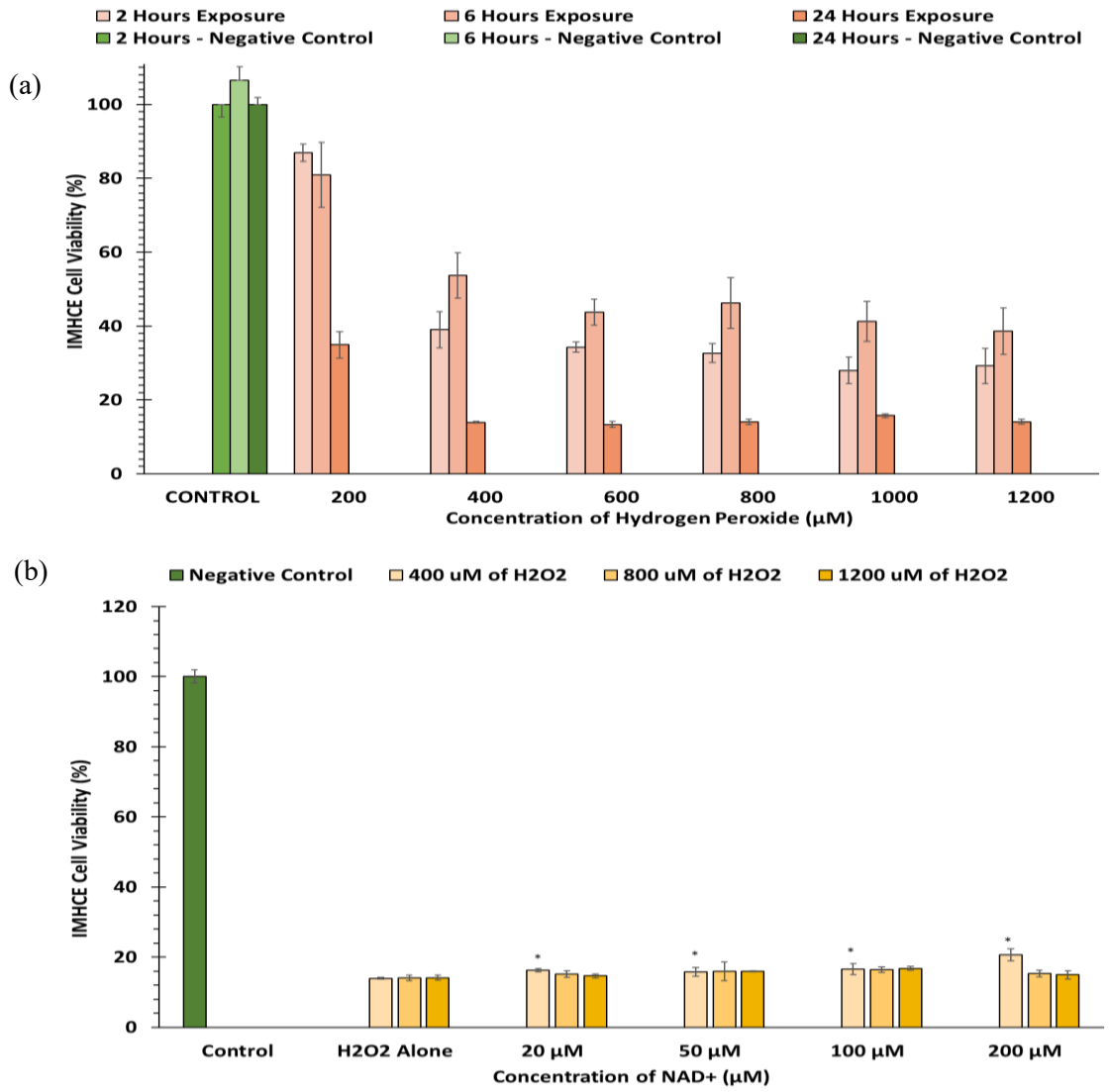

Figure 5.4: Percentage cell viabilities upon incubation of IMHCE cells with varying concentrations of H_2O_2 (200 to 1200 µM) (a) and H_2O_2 concentrations of 400, 800, and 1200

µM + NAD+ concentrations of 20 µM to 200 µM for 24 hours (b). * - significant difference between a sample and an H_2O_2-treated sample.

Pre-supplementation of IMHCE cells with 20 and 200 µM of NAD+ for 17 and 24 hours, prior to 24-hour exposure to 200 µM of H_2O_2, significantly attenuated oxidative stress-mediated damage (17 hours - 20 µM – p = 0.022 and 200 µM – p = 0.074 and 24 hours - 20 µM – p = 0.020 and 200 µM – p = 0.012), as highlighted in Figure 5.5.

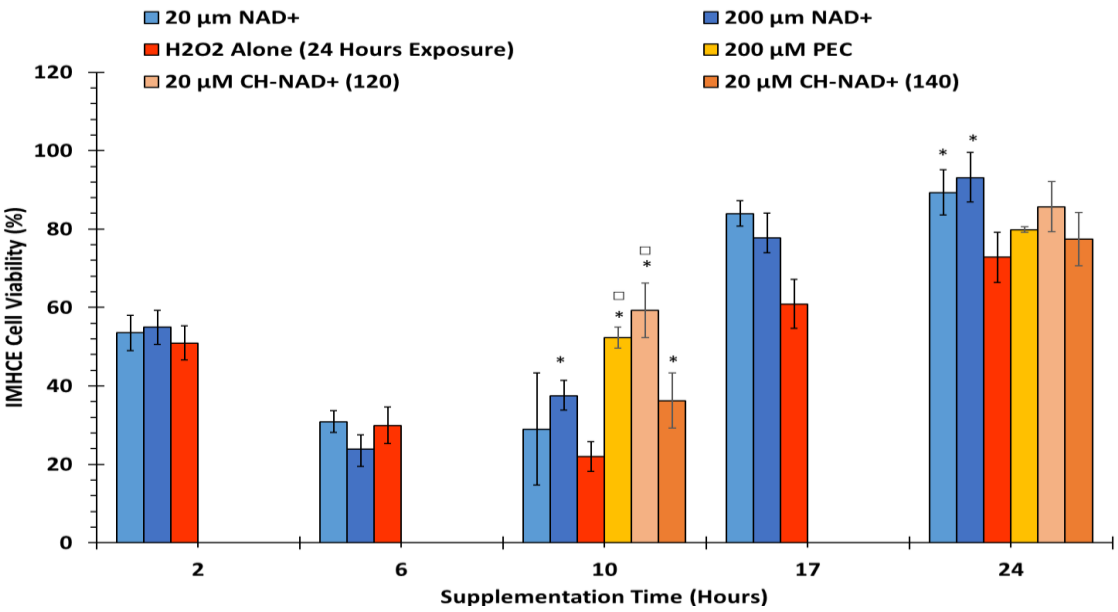

Figure 5.5: Percentage cell viabilities upon incubation of IMHCE cells with 20 µM and 200 µM NAD+/NAD+-associated formulations over set supplementation times before exposure to 200 µM of H_2O_2 for 24 hours. * - significant difference between a sample and H_2O_2-treated sample, □ - significant difference between NAD+ alone and NAD+-associated formulation, * (with bridge) - significant difference between supplementation timepoint. (Data is expressed as mean % cell viability ± S.D (n = 3).

Furthermore, the cell viabilities were statistically equivalent to that of the negative control cells (100.0 ± 6.1%), suggesting that NAD+ could restore cellular function to basal conditions even after exposure to H_2O_2. Cell morphology was also largely retained within NAD+-incubated cell samples in comparison to that of the negative control, as per the microscopic observations

presented in Figure 5.6. Conversely, floating dead cells were observed in the positive control sample, as evidenced by the detachment of cells during observation.

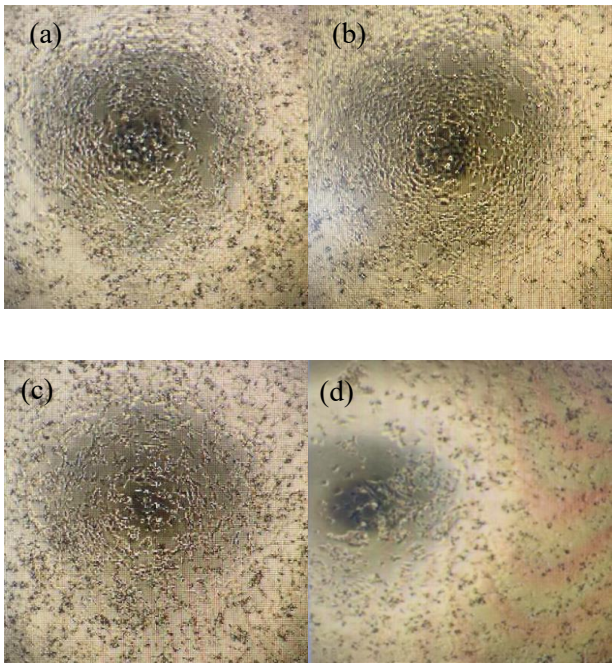

Figure 5.6: Morphology of IMHCE cells incubated with culture media (a), 20 µM NAD+ (b), 200 µM NAD+ (c), and 200 µM H_2O_2 (d). (Magnification – 20x).

The PECs loaded with 200 µM of NAD+ exhibited statistically equivalent efficacy (79.8 ± 0.7%) to that of NAD+ alone (93.1 ± 6.5%). Similarly, the viabilities of cells incubated with the CH-NAD+ (120% and 140% (w/w)) formulations containing 20 µM of NAD+ (85.7 ± 6.3% ($p = 0.507$) and 77.4 ± 6.8% ($p = 0.081$), respectively) were statistically equivalent to those obtained from 20 µM of NAD+ alone (89.3 ± 5.8%). Furthermore, the viabilities of IMHCE cells incubated with blank formulations of equivalent concentration were statistically lower than that of the NAD+-associated formulations. (blank PEC – 60.8 ± 3.2% ($p = 0.004$), blank CH-NAD+ (120% (w/w)) – 53.5 ± 7.8% ($p = 0.005$), and blank CH-NAD+ (140% (w/w)) – 35.3 ± 4.8% ($p = 0.001$)). This suggests that the formulations themselves did not invoke a therapeutic response and that association of NAD+ with polyelectrolyte-based formulations does not impact its ability to protect corneal cells against H_2O_2-mediated damage. Also, the

sustained release of NAD+ from the formulations may protect its stability *in vivo* and prevent premature NAD+ clearance from the ocular surface.

The cell viabilities calculated at the 10-hour supplementation timepoint suggested that the NAD+-associated formulations may have evoked a more significant therapeutic response in comparison to NAD+ alone. 59.3 ± 7.0% of the available IMHCE cells were metabolically active after 10 hours of pre-supplementation with the CH-NAD+ (120% (w/w)), whereas 29.0 ± 14.3% of the available cell population remained metabolically active when pre-supplemented with 20 μM of NAD+ alone. Similarly, incubation with PECs containing 200 μM of NAD+ (52.4 ± 2.7%) led to a significant increase in cell viability in comparison to an equivalent concentration of NAD+ alone (37.5 ± 3.8%) ($p = 0.005$). In comparison to that of the positive control, all of the formulations produced a higher percentage cell viability at 10 hours (PEC - $p = 0.001$, CH-NAD+ (120% (w/w)) – $p = 0.002$, and CH-NAD+ (140% (w/w)) – $p = 0.02$). This suggests that the delivery of NAD+ via nanoparticle supplementation may require a shorter supplementation time to illicit a therapeutic response in comparison to NAD+ alone, potentially attributed to enhanced intracellular permeation via polyelectrolyte bioactivity and protection due to NAD+ association to a polymeric network.

Lastly, to determine whether association with the polyelectrolyte formulations could prolong the efficacy of NAD+ in comparison to NAD+ alone, IMHCE cells were supplemented with the NAD+-associated PECs for 48 hours before oxidative stress induction. Although no outliers were detected upon conducting statistical outlier tests (PECs – $p = 0.121$, CH-NAD+ (120% (w/v)) – $p = 0.652$, and CH-NAD+ (140% (w/v)) – $p = 0.196$), high variabilities in cell viability were detected in each sample well at the 32-hour timepoint. As high variability is indicative of cell culture non-uniformity, which may introduce bias upon treatment of the cells with the respective NAD+-laden nanoformulations, results taken at the 32-hour timepoint were not considered.

However, a significant increase in cell viability was observed with an increase in supplementation time from 24 (79.8 ± 0.7%) to 48 (93.2 ± 0.6%) hours in the PEC-treated IMHCE sample ($p = 0.003$). Also, conversely to what was observed at the 24-hour supplementation timepoint, no significant difference was found between the viability of the

PEC-treated IMHCE cells and that of the negative control at 48 hours ($p = 0.416$). Equivalent efficacy was observed with the CH-NAD+-based formulations, both between 24 and 48 hours, and with the negative controls at each timepoint. Particularly with the PEC, this may be attributed to the sustained release of NAD+ from the formulation under *in vivo* conditions, thus prolonging the therapeutic activity of NAD+ over a longer period of time prior to the onset of oxidative stress. Ultimately, this study provides an initial indication of the antioxidant capabilities of NAD+, both alone and in association with a polyelectrolyte-based nanoformulation and highlights its strong potential to improve ocular health as a supplementary treatment.

5.3.4 Complex Formulation Permeation via Fluorescence Microscopy

Corneal distribution of both the FITC-CH-NAD+ and FITC-PECs was assessed using both the IMHCE cell line and an *ex vivo* porcine cornea model. Without histological preparation, fluorescence within the isolated scleral tissues could not be accurately identified due to the thickness of the tissue itself. The inverted microscopy images taken for each formulation at 20x magnification are presented in Figure 5.7.

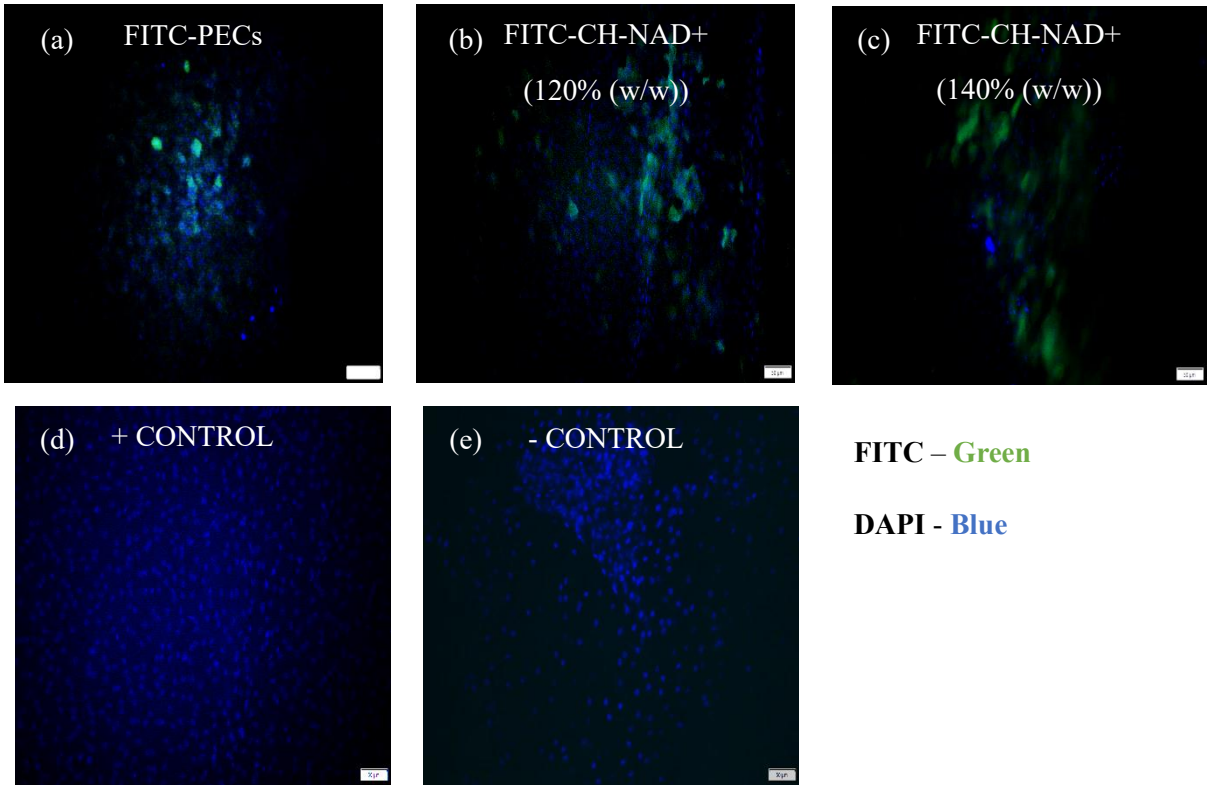

Figure 5.7: Fluorescent microscopy images of FITC-PECs (0.1% (w/v) FITC) (a), FITC-CH-NAD+ (120% (w/w)) (b), FITC-CH-NAD+ (140% (w/w)) (c), a 0.1% (w/v) FITC solution (d), and negative control (incubation with 0.01 M PBS (pH 7.4)) (e), taken after incubation of porcine corneal tissues at 37 °C for 6 hours. (20 x magnification with scale – 50 µm) (Representative images of n = 3).

The positive (Figure 5.7 (d)) and negative (Figure 5.7 (e)) control fluorescent images were equivalent. Therefore, any FITC fluorescence observed in the formulations was attributed to that associated with the formulations and not free FITC. Free FITC did not permeate through the corneal tissues and was effectively removed during the rinsing step with ice-cold 0.01 M PBS. Both the FITC-CH-NAD+ formulations and FITC-PECs were visible within the porcine apical epithelium layer 6 hours post-incubation at 37 °C, with the former exhibiting a higher fluorescent intensity. Its enhanced retention in comparison to the PECs may be attributed to the superior mucoadhesive capabilities of chitosan due to electrostatic bond-mediated association with corneal mucosa and apical epithelial tight junction disruption.

Although formulation retention was visible on the porcine cornea (FITC fluorescence following *ex vivo* permeation), internalisation of the FITC-based formulations at a cellular level was difficult to observe due to the presence of a multilayered network of cells and extracellular matrices within the tissue. In the absence of histological preparation, the extent of FITC-based formulation internalisation within a monolayer of cells was investigated using a monolayer of IMHCE cells. As depicted in Figure 5.8, FITC fluorescence was also visible within IMHCE cells after 24 hours of incubation, thus suggesting that the formulations were successfully internalised. This further supports the trends observed upon analysis of the protective effects of the formulations against H_2O_2-mediated dysfunction in IMHCE cells, in which high cell viability was attained following pre-supplementation of cells with formulations for 24 hours before stress induction. NAD+-mediated cell preservation at this timepoint may be due to maximal uptake of the formulations.

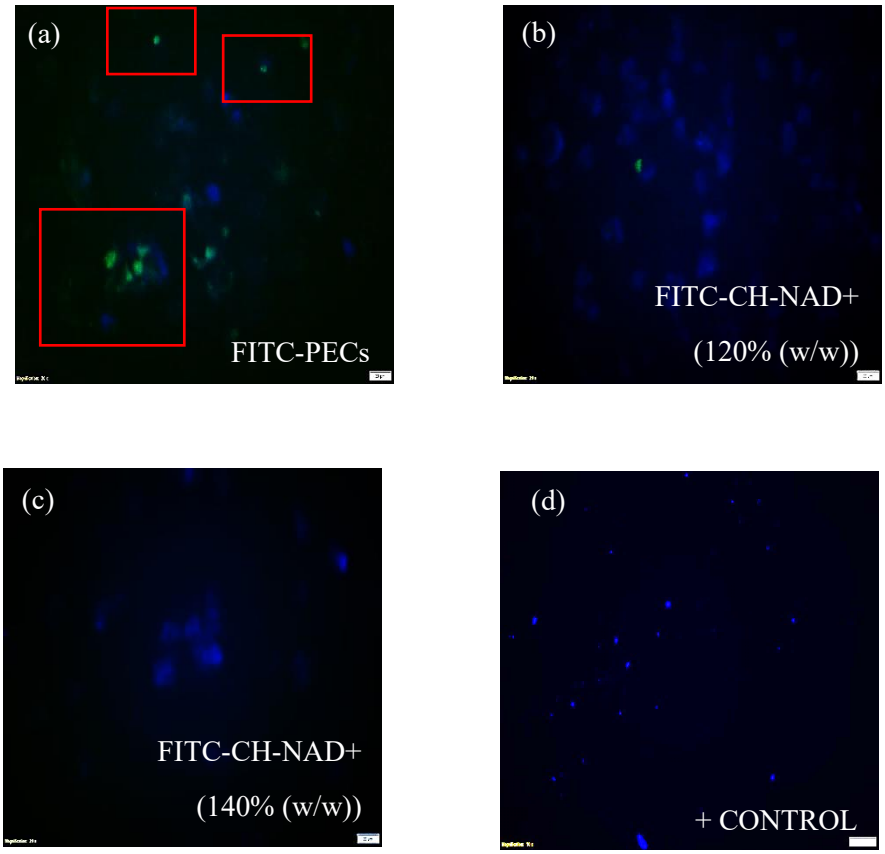

Figure 5.8: Fluorescent microscopy images of FITC-PECs (a), FITC-CH-NAD+ (120% (w/w)) (b), FITC-CH-NAD+ (140% (w/w)) (c), and FITC solution of equivalent concentration

to that of the formulations (d) taken after incubation of IMHCE cells at 37 °C for 24 hours. (40 x magnification with scale – 20 µm – SAMPLES, 20 x magnification with scale – 50 µm - CONTROL) (Representative images of n = 3).

Conversely to what was observed in the *ex vivo* tissue model, the intensity of FITC fluorescence is higher in cell samples incubated with FITC-PEC in comparison to those incubated with the FITC-CH-NAD+ formulations. This may be attributed to the size of the FITC-PECs in comparison to that of the FITC-CH-NAD+ formulation, which may experience hindered intracellular internalisation via size-mediated hindrance. Aside from the components of the cell culture media themselves, exhibiting an approximate size of 17.2 nm, PECs in cell culture media exhibited a mean hydrodynamic diameter of 22.2 ± 1.8 nm, with 51.1% of the size distribution exhibiting a size of 90.5 nm. Conversely, although a larger percentage of the size distribution was within the 80 to 200 nm range (CH-NAD+ (120% (w/w) – 83.2% at 155.4 nm and CH-NAD+ (140% (w/w) – 78.3% at 149.6 nm)), hydrodynamic diameters of 2341.0 ± 372.4 nm and 2171.0 ± 261.8 nm were observed for the respective formulations.

This study provided preliminary evidence to support the idea that both formulations were effectively retained on the corneal surface and exhibited uptake into an *in vitro* human epithelial cell line, thus further highlighting their suitability for NAD+ delivery to the ocular surface. Such results provide justification for further studies to investigate the pharmacodynamics of epithelial retention and cell uptake via analysis of receptor-mediated endocytosis and immunofluorescent staining of tight junction complex disruption. There is also scope to revisit the cell uptake of the NAD+-associated PECs to determine the progression of IMHCE cell internalisation as a function of time.

5.3.5 Quantification of NAD+ Cellular Uptake

Preliminary quantification of NAD+ internalisation, both alone and in association with the respective formulations, was conducted to determine if the formulations could deliver an equivalent, or larger concentration, of NAD+ to the intracellular environment. PEC formulations containing between 100 to 200 µM of NAD+, and CH-NAD+ formulations equivalent to 20 µM of NAD+, were analysed to directly match concentrations that exhibited efficacy in attenuating H_2O_2 cell damage whilst maintaining a sufficient percentage cell

viability. Control cells incubated with media alone were treated and lysed in a similar fashion to those treated with formulations. As depicted in Figure 5.9, a peak representing the elution of NAD+ at approximately 4 minutes was not detected in the chromatograms of the control cell lysates. Therefore, it was conclusive that the NAD+ quantified in the formulation-treated cell lysates was due to the NAD+ in the formulations alone during treatment and not from the presence of endogenously produced NAD+.

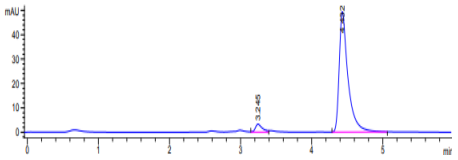

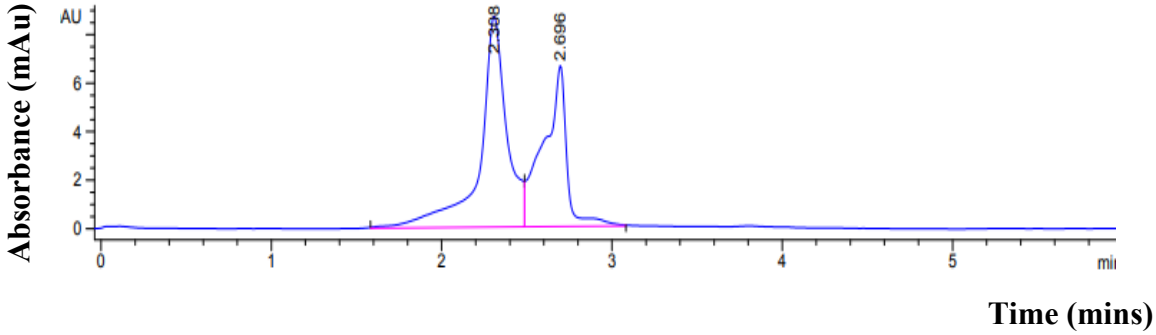

Figure 5.9: Representative HPLC chromatogram of cell lysate isolated from control IMHCE cells incubated with corneal epithelial culture medium alone for 24 hours. The peak representing typical NAD+ elution, as shown in the insert, is not present.

As shown in Table 5.4, upon lysis of the IMHCE cells, the intracellular concentration of NAD+ was higher in cells incubated with the NAD+-associated PECs at each theoretical loading concentration in comparison to those incubated with NAD+ of equivalent concentration, particularly in the 200 µM sample (NAD+ associated PECs - 27.99 ± 2.82 µM, NAD+ alone - 11.38 ± 5.81 µM). The PECs were capable of delivering an effective therapeutic dose (> 20 µM), as determined by the *in vitro* efficacy study detailed in Section 5.3.3, to the intracellular environment over 24 hours, further supporting that this timeframe is suitable for effective corneal cell supplementation.

Table 5.4: Quantification of both NAD+ internalisation in IMHCE cells and retention in cell culture media following 24-hour incubation. Data is expressed as mean ± S.D (n = 3). (LOD – 4.76 µM).

Sample	Conc. Of NAD+ Remaining in Culture Media (µM)	% of Administered NAD+	Conc. Of NAD+ Internalised (µM)	% of Administered NAD+
NAD+ (20 µM)	8.48 ± 1.83	42.41 ± 9.15	BELOW LOD	N/A
NAD+ (100 µM)	22.08 ± 1.68	22.08 ± 1.68	34.10 ± 1.68	34.10 ± 1.68
NAD+ (150 µM)	22.07 ± 3.02	14.71 ± 2.01	20.46 ± 11.73	13.65 ±7.82
NAD+ (200 µM)	18.24 ± 1.49	9.12 ± 0.74	11.38 ± 5.81	6.35 ± 2.90
NAD+ -PECs (100 µM)	17.54 ± 0.30	17.54 ± 0.30	28.77 ± 1.82	28.77 ± 1.82
NAD+ -PECs (150 µM)	18.87 ± 1.04	12.58 ± 0.69	30.79 ± 0.10	20.53 ± 0.07
NAD+ -PECs (200 µM)	19.07 ± 1.21	9.54 ± 0.61	27.99 ± 2.82	13.24 ± 1.41
CH-NAD+ (120% (w/w)) (20 µM)	21.17 ± 2.38	105.85 ± 11.90	BELOW LOD	N/A
CH-NAD+ (140% (w/w)) (20 µM)	9.45 ± 0.59	47.24 ± 2.94	BELOW LOD	N/A

Conversely, the concentration of NAD+ within the cells incubated with 20 µM of CH-NAD+ formulations was below the LOD and could not be accurately quantified. Also, although the only difference between the two CH-NAD+ formulations is the NAD+ loading during formulation, the formulations exhibited highly varied behaviour during cell uptake. None of the loaded concentrations of NAD+ were internalised in the CH-NAD+ (120% (w/w))-treated sample, with 105.9 ± 11.9% of the 20 µM of NAD+ remaining within the culture media. This supports observations made during the analysis of CH-NAD+ cell uptake via fluorescence microscopy, in which CH-NAD+ uptake was hindered in comparison to that of the PECs. Conversely, only 47.2 ± 2.9% of the 20 µM of NAD+ remained in the media in the CH-NAD+ (140% (w/w))-treated sample.

Despite the successful uptake of therapeutically relevant NAD+ concentrations, particularly in the PEC samples, a large percentage (> 50%) of the loaded NAD+ concentration was unaccounted for in each sample analysed. No NAD+ was detected within the washings withdrawn after rinsing the IMHCE cells with 0.01 M PBS. The presence of secondary peaks,

as shown in the representative HPLC chromatogram in Figure 5.10, suggests that intracellular NAD+ enzymatic degradation into its respective by-products, nicotinamide and ADP-ribose, could be occurring, thus resulting in an overall reduction in NAD+ concentration. Similarly, the generation of peaks at 340 nm may be the result of NAD+ reduction into NADH [581]. This enzymatic degradation of NAD+ could be investigated further by using HPLC coupled with mass spectroscopy to determine the structural composition of the eluted analytes in comparison to the mass spectra of reference standards of known NAD+ by-products. However, this was outside of the initial scope of the research project and due to time constraints, will be the focus of future investigations. Similarly, analysis of the cell lysates using a diode array detector could provide an indication of spectral homogeneity across the eluted peaks, which can be compared with that of the reference standards.

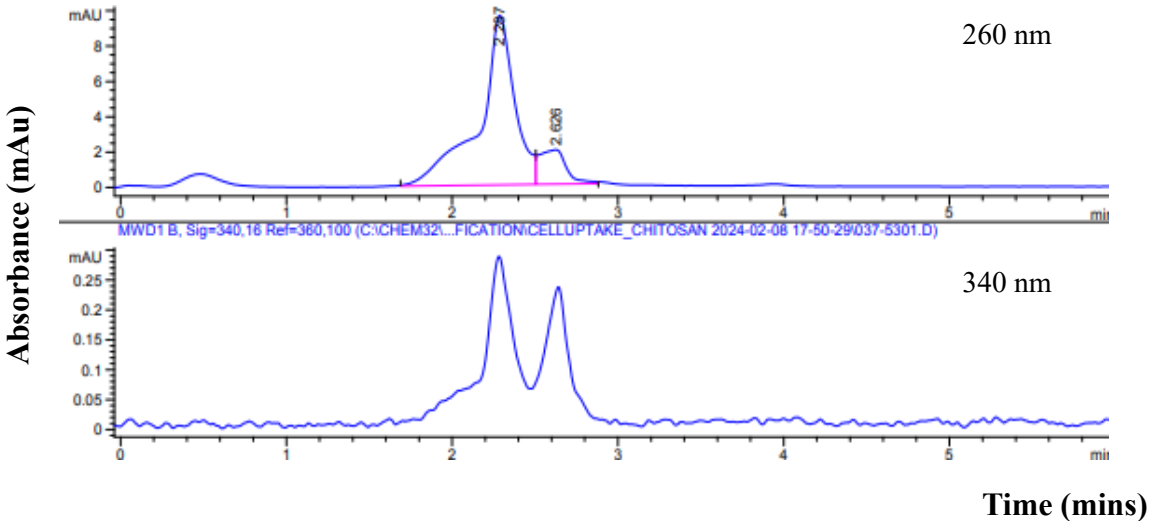

Figure 5.10: Representative HPLC chromatogram of cell lysate isolated from IMHCE cells incubated with CH-NAD+ (140% (w/w)) for 24 hours. The NAD+ peak at 260 nm is not present (4 minutes).

5.3.6 Corneal vs. Scleral Permeation of Complex Formulations

An estimation of NAD+ absorption and intraocular bioavailability was obtained using an *ex vivo* porcine tissue model [582]. As highlighted in Figure 5.11, NAD+ permeation through isolated corneal tissue, both alone and in association with the PEC formulations could be successfully quantified after 6 hours (NAD+ - 146.1 ± 103.8 µg/cm^2, PEC – 66.7 ± 17.8

µg/cm^2). However, NAD+ could not be quantified within the receptor chambers of porcine corneas treated with the CH-NAD+ (120 and 140% (w/w)) formulations. This further supports the hypothesis that transcorneal absorption of the chitosan-based formulations is hindered by comparison with the PECs, as evidenced by the decrease in intracellular fluorescence (Section 5.3.4) and intracellular NAD+ concentrations below the LOD (Section 5.3.5).

Due to its greater affinity towards the permeation of hydrophilic compounds, the permeation of NAD+ through porcine scleral tissue was also obtained. Recent studies have also conducted *ex vivo* permeability analysis for nanoparticles exhibiting high degrees of hydrophilicity and formulations intended for targeted posterior segment delivery [583], [584]. Furthermore, regarding the PECs, it was hypothesised that NAD+ permeation through the sclera may be greater than that of the cornea due to similar physicochemical attributes of residual HA on the PEC surface and the anionic scleral network of hydrophilic collagen fibrils.

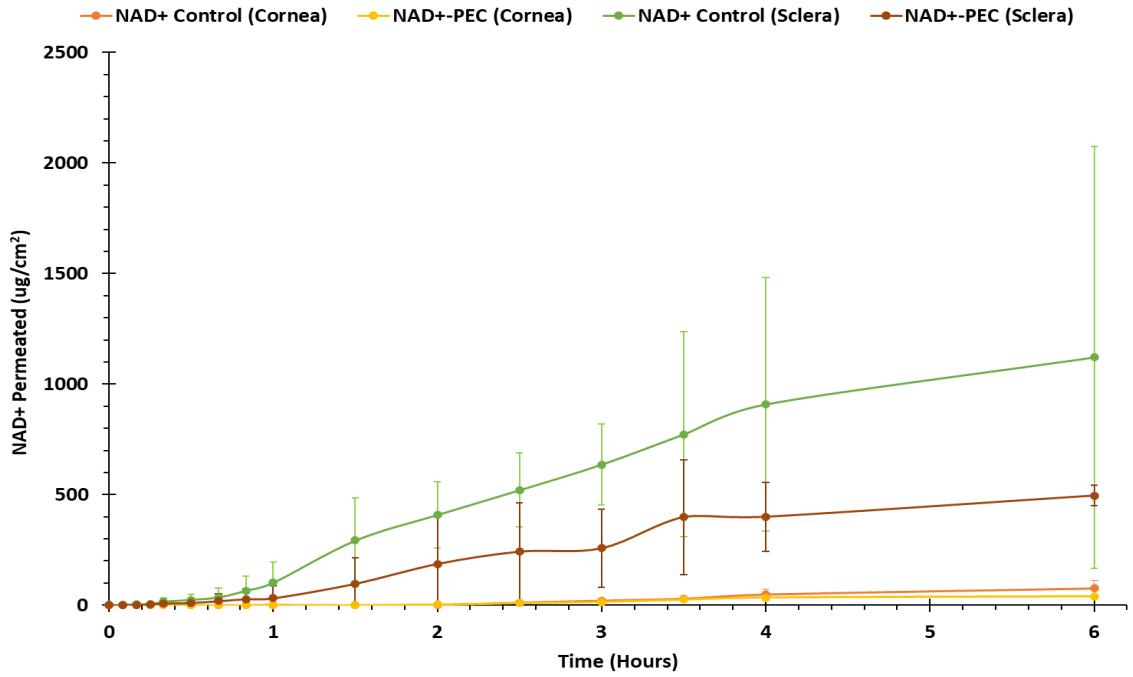

Figure 5.11: Cumulative mass of NAD+ permeated from NAD+ alone and NAD+-associated PECs per cm^2 of excised porcine corneal and scleral tissue isolates. Data is expressed as mean ± S.D (n = 3).

In both tissue samples, the mass of NAD+ permeated per cm^2 of tissue was higher for NAD+ alone in comparison to that of the NAD+-associated PECs. This could be attributed to the more sustained release of NAD+ from the PECs in comparison to NAD+ alone, thus decreasing its rate of permeation through the isolated tissues. Although each tissue was visually examined prior to and after analysis to ensure tissue integrity, there may have been a small tear in one of the scleral tissues utilised for the NAD+ control, thus resulting in the calculation of a large degree of error.

The lower flux value obtained from the corneal and scleral tissues from the NAD+-associated PECs (13.2 ± 8.0 µg/cm^2/h (cornea) and 108.6 ± 10.7 µg/cm^2/h (sclera)) in comparison to the NAD+ control (37.3 ± 33.5 µg/cm^2/h (cornea) and 122.2 ± 122.8 µg/cm^2/h (sclera)), may also be attributed to the retention of the PECs on the apical corneal surface, as highlighted in the fluorescent microscopy study. Fathalla *et al.* [585] observed a similar trend upon analysis of the permeation of ketorolac tromethamine-laden chitosan and alginate complex microparticles using *ex vivo* bovine corneal tissues. Due to its lipophilicity, ketorolac tromethamine exhibited increased corneal permeation in comparison to the results obtained for NAD+, equating to a flux of 119.6 ± 1.0 µg/cm^2/h. However, upon association to the complexes, corneal flux decreased to 91.4 ± 2.1 µg/cm^2/h (chitosan – 0.1% (w/v), alginate – 0.05% (w/v)) and 79.1 ± 1.2 µg/cm^2/h (chitosan – 0.15% (w/v), alginate – 0.1% (w/v), attributed to enhanced precorneal retention and mucoadhesion to the corneal surface via formulation-mediated bonding that increased with an increase in polyelectrolyte concentration. The hindered diffusion of NAD+ through the residual HA chains on the surface of the PECs upon application to the porcine cornea may have also limited the number of NAD+ molecules available for permeation. This trend was also observed by Tighsazzadeh *et al.* [586], in which the crosslinking of timolol maleate with HA resulted in a reduction in permeation flux through a porcine cornea from 1045.1 ± 0.2 µg/cm^2/h to 549.0 ± 0.3 µg/cm^2/h. Whilst analysing the *ex vivo* scleral and corneal permeability of meloxicam, Mohamed *et al*. [587] also observed a decrease in permeation flux through both tissues resulting from the electrostatic association of meloxicam with chitosan in comparison to meloxicam alone. Due to its lipophilicity, meloxicam demonstrated a higher degree of flux through the corneal tissue in comparison to the scleral tissue.

Cumulative NAD+ permeation from the PEC formulation through scleral tissue (495.7 ± 47.0 $\mu g/cm^2$) was also significantly higher ($p = 0.000$) in comparison to that through corneal tissue (66.7 ± 17.8 $\mu g/cm^2$). This suggests that the opposing physicochemical attributes of the NAD+-associated PECs and the multilayers of the cornea are the rate-limiting factors of NAD+ corneal permeation [588]. The large decrease in permeation flux for the PECs (cornea - 13.2 ± 8.0 $\mu g/cm^2/h$ vs. sclera - 108.6 ± 10.7 $\mu g/cm^2/h$ ($p = 0.000$)) and apparent permeability coefficient (cornea - 2.5 x 10^{-7} ± 1.5 x 10^{-7} cm/sec vs. sclera – 2.0 x 10^{-6} ± 2.0 x 10^{-7} cm/sec ($p = 0.000$)), confirm the restrictive nature of the cornea in comparison to the sclera. The CH-NAD+ formulations also exhibited a degree of transscleral permeation, with the CH-NAD+ (120% (w/w)) and CH-NAD+ (140% (w/w)) generating a flux of 67.2 ± 46.1 and 48.2 ± 22.1 $\mu g/cm^2/h$, respectively.

A large percentage of the theoretical mass of NAD+ within the donor chamber of the Franz diffusion cell remained unaccounted for. The mass of NAD+ remaining within the donor chamber, and that retained within the tissue isolate, are shown in conjunction with the mass of NAD+ permeated in Table 5.5. Similar to what was observed during the *in vitro* cell uptake studies, this could be attributed to the metabolism of NAD+ during transcorneal and transscleral permeation.

Table 5.5: Mass balance analysis of NAD+ quantified at each step during *ex vivo* corneal and scleral permeation and retention analysis. Data is expressed as mean ± S.D (n = 3).

Cornea	**NAD+ CONTROL – 15.03 mg**	**NAD+ PEC – 15.18 mg**	**Corneal Tissue Control**
Mass Permeated (mg)	0.18 ± 0.13	0.08 ± 0.02	N/A
Mass Retained in Tissue (mg)	0.30 ± 0.27	0.02 ± 0.02	N/A
Mass Remaining in Donor Chamber (mg)	6.29 ± 0.74	3.17 ± 0.67	N/A
NAD+ Recovery (%)	45.09 ± 4.29	21.55 ± 4.47	N/A
Cornea		**CH-NAD+ 120% (w/w) – 14.9 mg**	**CH-NAD+ 140% (w/w) – 14.9 mg**

Mass Permeated (mg)		BELOW LOD	BELOW LOD
Mass Retained in Tissue (mg)		0.18 ± 0.1	0.26 ± 0.25
Mass Remaining in Donor Chamber (mg)		1.06 ± 1.03	2.14 ± 1.1
NAD+ Recovery (%)		11.75 ± 9.50	18.93 ± 10.04
Sclera	**NAD+ CONTROL – 15.2 mg**	**NAD+-PEC – 15.07 mg**	**Scleral Tissue Control**
Mass Permeated (mg)	1.42 ± 1.21	0.66 ± 0.06	N/A
Mass Retained in Tissue (mg)	0.20 ± 0.34	0.10 ± 0.15	N.A
Mass Remaining in Donor Chamber (mg)	3.82 ± 0.94	2.00 ± 1.73	N/A
NAD+ Recovery (%)	32.67 ± 13.51	21.11 ± 13.76	N/A
Sclera		**CH-NAD+ 120% (w/w) – 15.1 mg**	**CH-NAD+ 140% (w/w) – 15.4 mg**
Mass Permeated (mg)		0.51 ± 0.33	0.35 ± 0.14
Mass Retained in Tissue (mg)		0.22 ± 0.10	0.31 ± 0.12
Mass Remaining in Donor Chamber (mg)		2.31 ± 0.94	2.97 ± 1.56
NAD+ Recovery (%)		21.49 ± 3.08	27.72 ± 11.77

Reference chromatograms taken from the respective donor and receptor chambers of NAD+ and NAD+-associated PECs after corneal and scleral permeation analysis also highlight a greater number of secondary peaks for the permeated NAD+ sample (

Figure ***5.12***). Conversely, the NAD+ peak is largely preserved within the donor chamber chromatograms. The CH-based formulations exhibited a similar degradation profile for samples taken from the receptor chamber in both the corneal and scleral tissue. However, the NAD+ peak is predominantly absent, thus confirming the limited capability of the CH-NAD+ formulations to deliver NAD+ across a cellular membrane. Although not initially outlined in the research objectives of this project, there is scope to repeat the *ex vivo* analysis upon obtaining reference standards of the NAD+ metabolic by-products to obtain a clear profile of NAD+ degradation under *in vivo* conditions. Also, conducting *ex vivo* permeation analysis

under static conditions in Franz diffusion cells does not provide a true evaluation of therapeutic permeation under dynamic *in vivo* conditions [589]. However, it can be used to estimate how the physiochemical properties of both therapeutics and therapeutic-laden nanoformulations can influence their interaction with ocular tissues that would be in close proximity to the target administration site. Conducting *ex vivo* permeation using an Ussing chamber or under physiological flow rates would also allow for the measurement of corneal and scleral integrity via measurement of the transepithelial electrical resistance, and an assessment of NAD+ permeation under conditions that more closely align the *in vitro-in vivo* correlation.

(a)

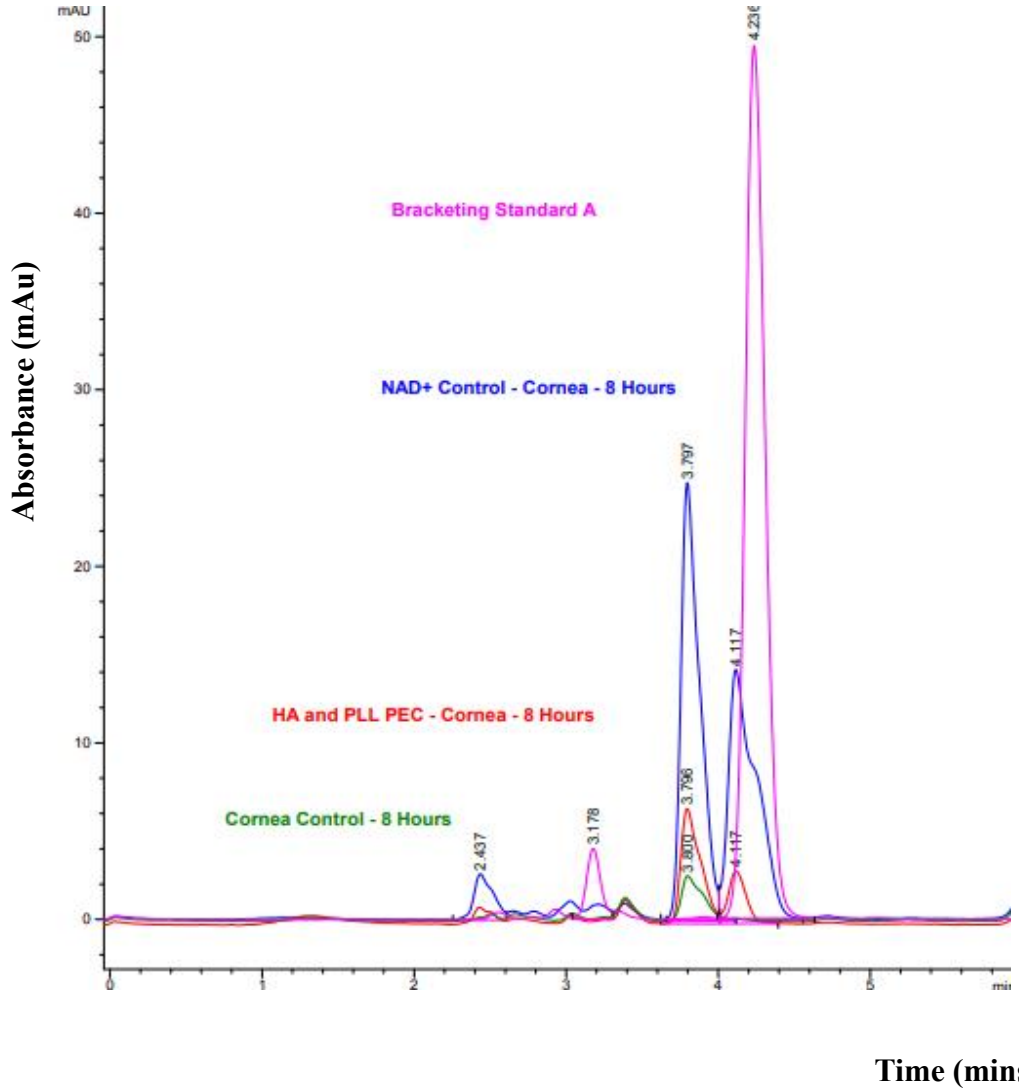

(b)

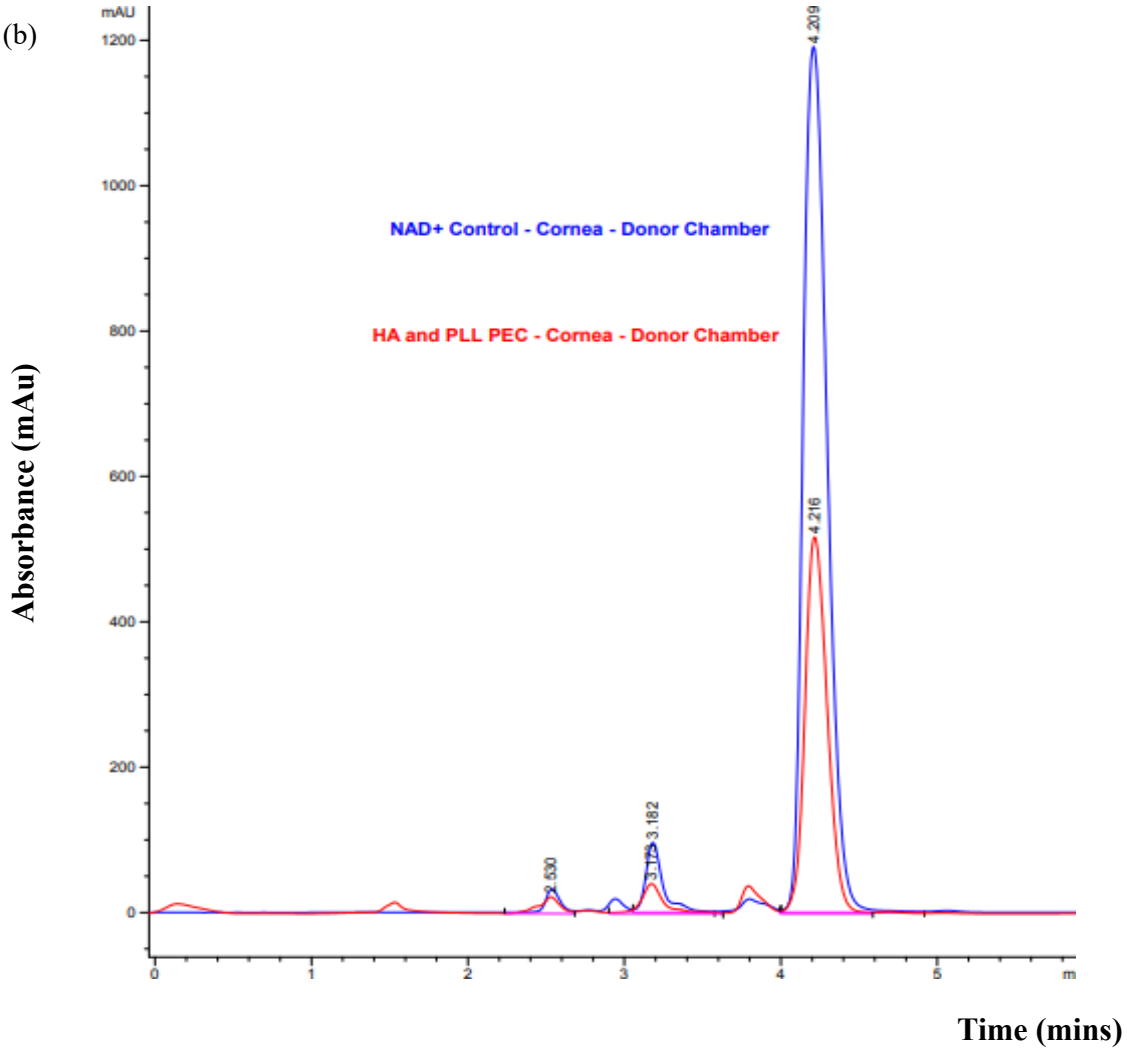

Figure 5.12: Representative HPLC chromatogram taken from the receptor chambers of the porcine cornea (a) following incubation with NAD+/NAD+-associated PECs. The donor chambers from the corneal sample (b) show preservation of the NAD+ peak at 4 minutes.

5.4 CONCLUSIONS

In vitro and *ex vivo* assessments of the respective NAD+-laden nanoformulations confirmed their suitability for the safe and effective delivery of NAD+ to the ocular surface and surrounding tissues. Both formulations (PEC and CH-NAD+ complexes), exhibited some degree of mucoadhesion when analysed concurrently with porcine mucin (Type II, stomach) via QCM-D and ZP analysis, with the mucoadhesion of the CH-NAD+ formulation being enhanced via electrostatic-mediated bonding with the anionic mucin carboxyl and sulfate

groups. Cytocompatibility, equating to cell viability values above 80%, was confirmed upon incubation of IMHCE cells with concentrations of between 20 and 200 μM of NAD+. Cells incubated with PECs containing 200 μM of NAD+ were statistically equivalent to that of NAD+ alone of equal concentration, whereas CH-NAD+ complex laden with 20 μM of NAD+ were used to prevent significant decreases in cell viability during the *in vitro* efficacy trials. NAD+ was effective in preventing a significant loss in cell viability resulting from oxidative stress-mediated dysfunction, with a direct correlation obtained between cell viability and NAD+ supplementation time. Association to the respective formulations did not hinder the ability of NAD+ to protect the IMHCE cells from H_2O_2 during supplementation, as evidenced by the non-significant difference in cell viability between the NAD+ and the NAD+-laden formulation-treated cells at 24 hours. However, association with the respective polyelectrolytes, decreased the supplementation time required to illicit a therapeutic response. NAD+ association with the HA and PLL PECs also appeared to prolong its therapeutic window over 48 hours.

The barrier properties of the cornea appeared to be the governing factor of transcorneal permeation, with both the PECs and CH-NAD+ formulations exhibiting very little to no permeation. Conversely, the hydrophilic nature of the sclera, in combination with its greater porosity in comparison to that of the corneal epithelium, allowed for enhanced permeation. Fluorescent microscopy images taken of the DAPI-stained corneal tissues highlighted the surface association of the respective formulations, with the CH-NAD+ formulations exhibiting a more intense fluorescence signal. However, upon observing the uptake of fluorescent-tagged formulations using a monolayer of IMHCE cells, those incubated with the NAD+-associated PECs showed a higher degree of fluorescence. This was further corroborated upon quantification of the mass of NAD+ internalised in IMHCE cells, with NAD+ delivery via PEC administration achieving a higher internalised mass of NAD+ (27.99 ± 2.82 μM) in comparison to NAD+ alone (11.38 ± 5.81 μM). NAD+ internalisation could not be accurately quantified within the IMHCE cell samples incubated with the respective CH-NAD+ formulations. The fluorescence intensity of the IMHCE cells incubated with the CH-NAD+ formulations was also low, potentially attributed to the electrostatic-mediated interaction of the formulations with the anionic phospholipid bilayers, resulting in subsequent removal during the removal of media

and washing steps. Further analysis of the enzymatic by-products of NAD+ is required to obtain a complete degradation profile of NAD+ *in vivo.*

The results outlined in Chapter 5 highlight the suitability of the NAD+-laden formulations, particularly the HA and PLL-based PECs, to deliver NAD+ to the ocular surface and anterior tissues in a safe and effective manner. Such studies provide scope to explore the antioxidant and respiration restorative capabilities of NAD+ further, utilising the studies outlined in Section 7.2, which would provide a thorough evaluation of its effectiveness for further pre-clinical investigations.

CHAPTER 6:

PRELIMINARY TRIALS – NAD+-LADEN NANOFORMULATIONS FOR POSTERIOR SEGMENT DELIVERY

6. PRELIMINARY TRIALS – NAD+-LADEN NANOFORMULATIONS FOR POSTERIOR SEGMENT DELIVERY

To date, this project has focused on the supplementation of the corneal surface with NAD+, primarily due to the physicochemical behaviour of the formulations when placed under physiological conditions. However, there is scope to develop NAD+-laden formulations for delivery to, and subsequent supplementation of, posterior segment tissues that are susceptible to age-related decline and dysfunction.

Due to its high oxygen consumption and enhanced mitochondrial activity, the retina is particularly predisposed to oxidative stress, which, as discussed in Section 1.1.3.1, is at the forefront of the degenerative processes of age-related diseases such as AMD. However, based on their physicochemical attributes, the complex formulations prepared may not be suitable for retinal supplementation. Due to its hydrophilic nature, NAD+ may have preferentially associated with the surface of the complex-based formulations, thus aiding its release under physiological ocular conditions over a relatively short period of time (< 48 hours). Also, surface association enhances NAD+ exposure to physiological conditions in comparison to its entrapment within a nanoparticle. This is unfavourable, particularly for posterior supplementation, primarily due to the significant potential for premature NAD+ loss during PEC/CH-NAD+ permeation through the increased number of anatomical barriers to the posterior segment.

Preliminary screening studies were conducted to investigate the development of poly (lactic-co-glycolic acid) (PLGA) and lipid-based formulations, using formulation methods such as water-in-oil-in-water emulsion, thin film hydration, and diethyl ether injection for both NAD+ and NAD+-associated PEC encapsulation. Aside from tunable release properties and improved stability *in vivo*, lipids are also inherently biocompatible and exhibit low toxicity as they possess similar characteristics to those within the phospholipid bilayers of cellular membranes. PLGA is a widely used, biodegradable, synthetic polymer that has been approved for ocular use by the Food and Drugs Administration [590]. *In vivo* enzymatic hydrolysis of PLGA into its constituent monomers - lactic acid and glycolic acid monomers, in combination with its lactic acid:glycolic acid ratio-dependent degradation and solubility, renders it a highly suitable

candidate for formulations intended for sustained therapeutic release [591], [592]. Both PLGA and lipid-based formulations have exhibited efficacy in sustaining therapeutic release within posterior tissues whilst preserving cytocompatibility and enhancing therapeutic bioavailability in comparison to free therapeutic solutions [593]–[597]. For example, Kakkar *et al.* [597] demonstrated the prolonged release of fluconazole from pegylated-Compritol® 888 ATO and Phospholipon 90 G solid-lipid nanoparticles over 25 hours in comparison to a free fluconazole solution (< 1 hour – > 90% release). The lipid nanoparticles also exhibited equivalent efficacy to free fluconazole in decreasing the colony count in a *Candida* keratitis murine model, whilst also demonstrating enhanced permeation through the Bruch's membrane, the inner plexiform layer, and the choroidal vessel endothelial cells 2 hours post instillation. Entrapment of adalimumab and aflibercept within a PLGA-PEG-PLGA triblock polymeric hydrogel reduced corneal alkali injury-mediated retinal ganglion cell loss by 45% three months post-injury, as compared to the 45% loss observed in human IgG isotype treated control group [598]. Similarly, encapsulation of bevacizumab in a PLGA-based nanoparticle was capable of inhibiting oxygen-induced retinal angiogenesis and preventing neovessel formation to a higher degree than the free bevacizumab treatment in a neonatal murine model [599].

Ultimately, the aim of this chapter was to investigate the feasibility of preparing formulations intended for sustained delivery of NAD+ to the posterior segment. Such formulations could have the potential to improve the NAD+ bioavailability within retinal tissues and provide a supplementary treatment option to attenuate cell health decline before age-related dysfunction.

6.1 EXPERIMENTAL METHODOLOGY

6.1.1 Materials

PLGA (Resomer® - RG503H – 24 -38 kDa) was purchased from Sigma Aldrich Ireland Ltd. (Wicklow, Ireland). Poly(vinyl) alcohol (PVA) (fully hydrolysed) (Mowiol 10-98 (61 kDa)) and PVA (partially hydrolysed ≈ 88%) (25 kDa) were purchased from Fisher Scientific (Loughborough, UK). Pluronic® F-127 was purchased from Sigma Aldrich (Missouri, U.S.).

Gas chromatography (GC) grade dichloromethane (DCM) (purity ≥ 99.0%) was purchased from Honeywell Specialty Chemicals Seelze GmbH (Germany).

The materials outlined in Sections 2.2.1 and 3.2.1 were used in the formulation and characterisation of lipid-PEC hybrid nanoparticles (LPHNP) and NAD+-laden liposomes (NAD+-Lipo), with the addition of the following:

Lecithin (purity:90%, soybean) and cholesterol (purity: 95%) were purchased from Fischer Scientific Ireland (Dublin, Ireland). Laboratory grade Triton™ X-100 and oleic acid (purity ≥ 99% (GC)) were purchased from Sigma Aldrich Ireland Ltd. (Wicklow, Ireland). Chloroform (purity ≥ 99.0% with ~ 50 ppm amylene stabiliser) was purchased from RCI Labscan Ltd. (Poland). GC grade diethyl ether (purity ≥ 99.5%), GC grade dichloromethane (purity ≥ 99-99.4%), and HPLC grade acetone (purity ≥ 99.8%) were purchased from Honeywell Specialty Chemicals Seelze GmbH (Germany). HPLC grade acetonitrile (purity ≥ 99.8%) was purchased from Fischer Scientific Ireland (Dublin, Ireland)

6.1.2 NAD+ Stability in Lipid Extraction Solvents

1% (w/v) Triton™ X-100 solutions were prepared by adding 107 mg of Triton™ X-100 (equivalent to 100 µL – density = 1.07 g/mL) to 10 mL volumetric flasks and diluting to volume with deionised water:methanol mixtures with volume ratios ranging from 50:50 to 95:5 (deionised water:methanol). 10 mg of NAD+ was dissolved in 5 mL of the resulting extraction solvents. NAD+ stability was assessed by monitoring peak splitting in the primary NAD+ peak (retention time: 4-5 minutes) and an increase in peak area of the known impurity peak at a retention time of 3 minutes.

6.1.3 Preparation of NAD+-Laden PLGA Nanoparticles.

NAD+-laden PLGA (NAD+-PLGA) nanoparticles were prepared using a double emulsion-solvent evaporation method. Briefly, 60 to 100 mg of PLGA was dissolved in 2 mL of DCM whereas 15 to 30 mg of NAD+ was dissolved in 50 or 250 µL of ultrapure water. The aqueous phase was added to the organic phase dropwise under sonication at 60% amplitude, yielding primary emulsions with NAD+:PLGA mass ratios of 1:3.3 to 1:4 and inner aqueous:organic ratios (AQ1:O) of 1:8 to 1:40. Under magnetic stirring at 250 rpm, the primary emulsion was

added dropwise to 10 or 20 mL ultrapure water containing 0.5 to 2% (w/v) PVA (partially or fully hydrolysed) emulsifier. The double emulsion was then sonicated for 2 minutes at 60% amplitude and left overnight, loosely covered and under magnetic stirring at 250 rpm, to allow for evaporation of DCM. Centrifugation of the resulting formulation was conducted as per Figure 6.1. Each fraction (pellet or supernatant) isolated during the work-up steps was lyophilised and retained for subsequent NAD+ quantification and encapsulation efficiency (%EE) analysis.

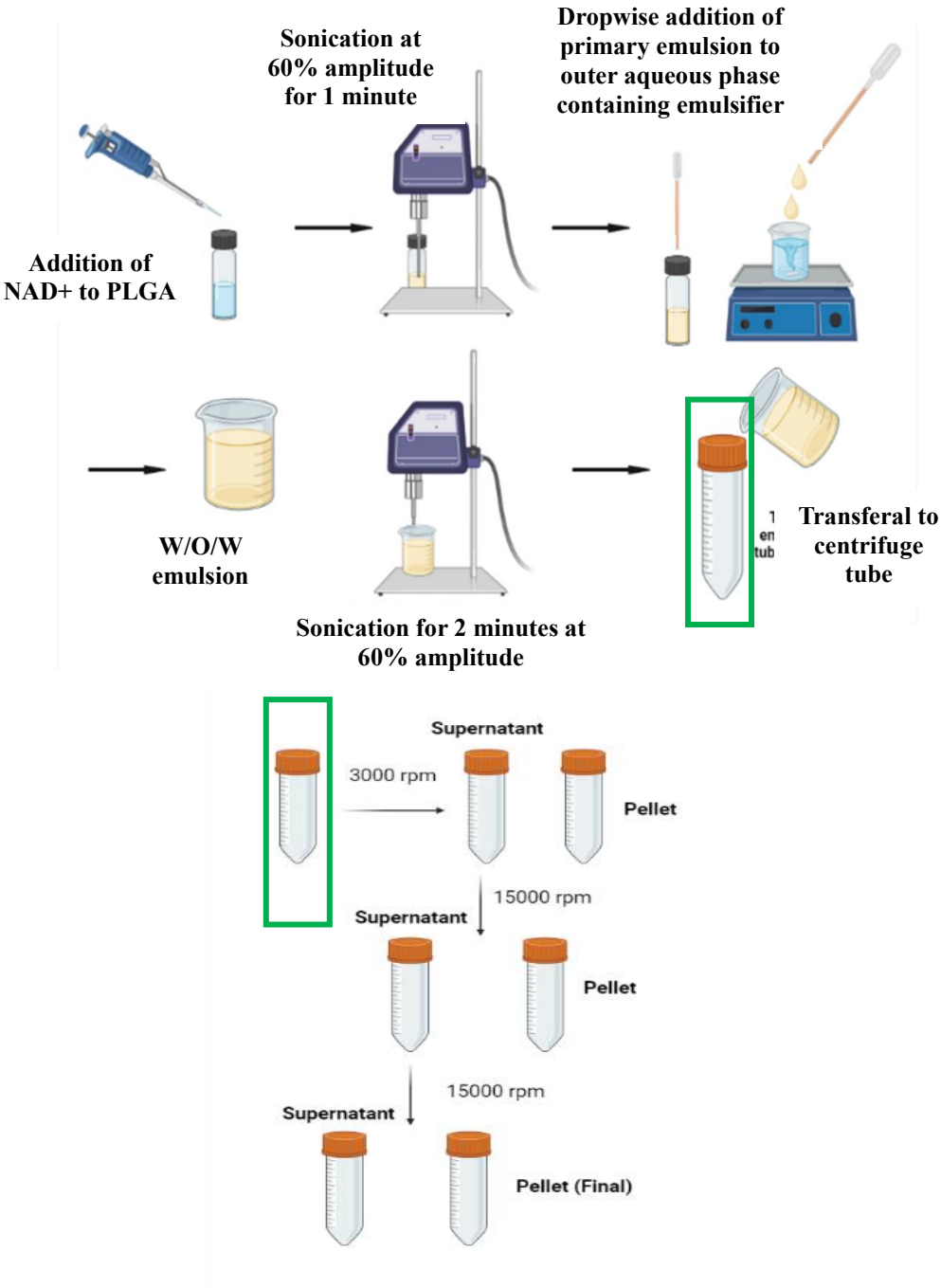

Figure 6.1: Schematic of the preparation and purification of NAD+-laden PLGA nanoparticles via ultracentrifugation. (Figure generated using templates available on Biorender.com).

6.1.4 PEC Coating via Diethyl Ether Injection

20 mg of NAD+-associated PECs were dispersed in 10 mL of ultrapure water, heated to 55 °C. 5 mL of a 0.8% (w/v) diethyl ether solution of lipid material (100% cholesterol, 4:1 (w/w)

soybean lecithin:cholesterol, or 1.5:1 (w/w) soybean lecithin:cholesterol) was gradually injected into the aqueous phase under magnetic stirring at 200 rpm. After 30 minutes, the diethyl ether was removed from the formulation via rotary evaporation under reduced pressure. The lipid-PEC hybrid nanoparticles (LPHNP) formed were then centrifuged at 3000 rpm for 10 minutes at 25 °C. Upon separation of the residual lipid material via centrifugation, the supernatant was decanted into Amicon® ultracentrifuge tubes and centrifuged a second time under the same conditions.

6.1.5 PEC Coating via Mixing-Solvent Evaporation

20 mg of NAD+-associated PECs were dispersed in 5 mL of 0.8% (w/v) diethyl ether solution of soybean lecithin or cholesterol. The resulting mixture was stirred overnight, uncovered and at ambient temperature, to allow for solvent evaporation. The resulting dried material was redispersed in 10 mL of ultrapure water and centrifuged in accordance with Section 6.1.4.

6.1.6 Preparation of Liposomal Formulations via Thin Film Hydration

Soybean lecithin and cholesterol, in a 4:1 (w/w) mass ratio, were dissolved in 15 mL of chloroform. The chloroform was left to evaporate over two to three hours via rotary evaporation (Rotavapor R 110, Buchi AG, Switzerland, and water bath Bibby RE200B, Akribis Scientific Ltd., UK) under reduced pressure at 25 °C. Hydration of the resulting thin lipid layer was carried out using 5 mL or 20 mL of a NAD+-laden PEC suspension via agitation at 55 °C. The mass of PEC dispersed within the hydration volume was selected to yield a final lipid:PEC mass ratio of 1.5:1 (w/w). Resulting PEC liposomes (PEC-Lipo) were sonicated for 5 minutes at 60% amplitude, followed by centrifugation as outlined in Section 6.1.4. The PEC-Lipo formulations were then redispersed in 5 mL of ultrapure water (pH 5) and stored under ambient conditions for further characterisation. NAD+-Lipo were also prepared in a similar fashion using thin-film hydration (TFH) methodology, using a lipid:NAD+ mass ratio of 5:1 (w/w).

6.1.7 Physicochemical Characterisation of the PLGA- and Lipid-Based NAD+ Formulations

The characterisation of the PLGA and lipid formulations, in terms of size, NAD+ %EE and *in vitro* NAD+ microfluidic release were conducted as outlined in Sections 2.2.5.2, 3.2.3.6, and 3.2.3.8, respectively, with the following additions:

NAD+ %EE (PLGA Formulations) - A given mass of the lyophilised fractions isolated during NAD+-PLGA purification were dissolved in DCM to yield 1% (w/v) solutions. A given volume of ultrapure water, equating to a DCM:water volume ratio of 1:10 was added and the mixture was vortexed using a vortex mixer (Fisherbrand™), Fisher Scientific, Ireland for 2 minutes at high speed. The mixture was left undisturbed for 24 hours to allow for the separation of the aqueous and organic layers. 500 µL of the aqueous layer was withdrawn, filtered through 0.45 µM syringe filters, diluted to volume (1 mL) with mobile phase and analysed via RP-HPLC.

NAD+ %EE (Lipid Formulations)– After the first centrifugation cycle, the resulting pellet was redispersed in 5 mL of ultrapure water, 100 µL of which was dispersed in 900 µL of 1% Triton™ X-100 in 95:5 20 mM potassium phosphate buffer (pH 8):methanol. Similarly, after the second centrifugation cycle, 100 µL of both the top (encapsulated NAD+) and bottom (unencapsulated NAD+) fractions was withdrawn and added to a fresh aliquot of the same extraction solvent. All aliquots were filtered through sterile, 0.45 µM syringe filters before RP-HPLC analysis.

6.2 RESULTS AND DISCUSSION

6.2.1 Discrepancy between Indirect and Direct NAD+ Encapsulation Efficiency in PLGA Nanoparticles

As highlighted in Table 6.1, despite optimising a number of formulation parameters in an effort to improve NAD+-PLGA nanoparticle %EE, significant discrepancies were observed between indirect and direct NAD+ %EE values.

Table 6.1: Mass balance and %EE values obtained upon analysis of the lyophilisates (pellets and supernatants) isolated during centrifugation of the NAD+-PLGA nanoparticles.

Sample	Mass of NAD+ in 1st 15,000 rpm Supernatant (mg)	Mass of NAD+ Recovered (%)	% Indirect EE	% Direct EE
Initial Trial *NAD+:PLGA Mass Ratio* – 1:4 (15 mg:60 mg) *PLGA Concentration (% (w/v))* – 3 *AQ1:O Volume Ratio* – 1:8 *O:AQ2 Volume Ratio*- 1:8.9 *Emulsifier - PVA* (Fully Hydrolysed) *Emulsifier Concentration* (% (w/v)) - 0.5	N/A	98.1 ± 0.2	1.9 ± 0.9	N/A
Increased PLGA Concentration (3 → 5% (w/v) *NAD+:PLGA Mass Ratio* – 1:6.6 (15 mg:100mg) *AQ1:O Volume Ratio* – 1:8 *O:AQ2 Volume Ratio*- 1:8.9 *Emulsifier - PVA* (Fully Hydrolysed) *Emulsifier Concentration* (% (w/v)) - 0.5	N.A	87.4	12.4	N/A

Increased W1:O Ratio (1:8 → 1:40) *PLGA Concentration (% (w/v))* – 5 *NAD+:PLGA Mass Ratio* – 1:3.3 (30 mg:100 mg) *O:AQ2 Volume Ratio*- 1:9.8 *Emulsifier - PVA* (Fully Hydrolysed) *Emulsifier Concentration* (% (w/v)) - 0.5	16.78	59.2	41.0	0.3
Different Emulsifier (PVA -≈ 88%) *PLGA Concentration (% (w/v))* – 5 *NAD+:PLGA Mass Ratio* – 1:3.3 *AQ1:O Volume Ratio* – 1:40 *O:AQ2 Volume Ratio*- 1:9.8 *Emulsifier Concentration* (% (w/v)) - 0.5	18.37	63.7	32.4	0.01
Different Emulsifier (Pluronic® F-127) *PLGA Concentration (% (w/v))* – 5 *NAD+:PLGA Mass Ratio* – 1:3.3 *AQ1:O Volume Ratio* – 1:40 *O:AQ2 Volume Ratio*- 1:9.8 *Emulsifier Concentration* (% (w/v)) - 0.5	10.26	39.9	60	0.08
Increase in PVA ≈ 88% Concentration to 2% (w/v) *PLGA Concentration (% (w/v))* – 5 *NAD+:PLGA Mass Ratio* – 1:3.3 *AQ1:O Volume Ratio* – 1:40 *O:AQ2 Volume Ratio*- 1:9.8 *Emulsifier - PVA* Partially Hydrolysed (≈ 88%)	21.14	73.1	27.6	0.09

Increase in NAD+:PLGA mass ratio (1:10 – 10 mg:100mg) *PLGA Concentration (% (w/v))* – 5 *AQ1:O Volume Ratio* – 1:40 *O:AQ2 Volume Ratio*- 1:9.8 *Emulsifier - PVA* Partially Hydrolysed (≈ 88%) *Emulsifier Concentration* (% (w/v)) - 2	6.97	74.6	25.7	0.03
Removal of the Second Sonication Step *PLGA Concentration (% (w/v))* – 5 *AQ1:O Volume Ratio* – 1:40 *O:AQ2 Volume Ratio*- 1:9.8 *Emulsifier - PVA* Partially Hydrolysed (≈ 88%) *Emulsifier Concentration* (% (w/v)) – 0.5	8.10	67.4	72.2	0.03
Decrease in Centrifugation Speed (15,000 rpm→ 10,000 rpm) *PLGA Concentration (% (w/v))* – 5 *AQ1:O Volume Ratio* – 1:40 *O:AQ2 Volume Ratio*- 1:9.8 *Emulsifier - PVA* Partially Hydrolysed (≈ 88%) *Emulsifier Concentration* (% (w/v)) – 0.5	9.20	31.9	68	≈ 0

Initial trials were conducted to determine if intermolecular interaction with the respective nanoparticle reagents (PLGA, PVA (≈ 88%), Pluronic® F-127) was leading to NAD+ entrapment within the organic layer during liquid-liquid extraction, thus resulting in a decrease in NAD+ %EE. However, upon spiking solutions of the reagents with a known mass of NAD+

and conducting NAD+ extraction and quantification as before, % NAD+ recoveries of approximately 100% were recorded (PLGA: 98.1 ± 1.1%, PVA (≈ 88%): 98.8 ± 1.7% and Pluronic® F-127: 98.6 ± 1.8%). PLGA nanoparticle stability was identified as a potential root cause for poor NAD %EE. The loss of a large percentage of nanoparticle yield during the 3,000 rpm and first 15,000 rpm centrifugation cycle, in addition to the loss of a large quantity of loaded NAD+ during the first 15,000 rpm cycle suggested that the PLGA nanoparticles were unstable, resulting in premature NAD+ loss during work-up. Optimisation of critical formulation and process parameters, such as emulsifier concentration, sonication time, PLGA concentration etc. is vital to the formation of stable PLGA nanoparticles via double emulsion-solvent evaporation [600], [601]. Failure to optimise such attributes can lead to particle instability and aggregation, which is further enhanced via compaction of particle aggregates during centrifugation at high centrifugal speeds [602].

Despite an increase in available surface area for NAD+ entrapment during emulsification, and reinforcement provided by an increased number of PLGA chains during the formation of the hardened PLGA shell during DCM evaporation [238], [603], an increase in NAD+:PLGA mass ratio from 1:33 to 1:6.6 to 1:10 did not improve direct % NAD+ %EE.

Also, lowering the volume of AQ1 from 250 to 50 μL, resulting in an increase in the AQ1:O ratio from 1:8.8 to 1:40 did not improve %EE. Hypothetically, an increase in AQ1:O ratio should have increased NAD+ entrapment, primarily due to the reduction in both primary emulsion viscosity and the resulting frequency of collisions between inner aqueous phase droplets during emulsification. A reduction in collision frequency decreases the likelihood of inner phase coalescence and hinders the formation of pores during PLGA solidification, thus increasing the stability of the primary emulsion [604]–[606]. Whilst investigating the effect of AQ1 volume on the encapsulation of antihypertensive small peptides in PLGA nanoparticles, Yu *et al.* [607] observed a decrease in peptide encapsulation from > 80% to < 60% with an increase in AQ1 volume from 33 to 200 μL. This was attributed to the insufficient encapsulation of the inner phase droplets with the organic phase during primary emulsification. Abdelkadar *et al.* [608] also reported a significant decrease in insulin entrapment efficiency from > 80% to below 40% with an increase in AQ1 volume from 0.5 to 1.0 mL at constant

organic phase volume (4mL) and PLGA concentration of 7.5% (w/v), due to leeching arising from the decreased thickness of the organic phase surrounding the aqueous phase droplets.

Neither the use of PVA (≈ 88%) (increased number of vinyl acetate groups) nor Pluronic® F-127 (poly(propylene) oxide group), resulted in an improvement in NAD+ %EE. Further, an increase in emulsifier concentration from 0.5 to 2% (w/v), did not improve NAD+ %EE. Anchoring of the hydrophobic groups to the surface of PLGA should have increased the density and thickness of the emulsifier layer at the oil-to-water interface upon addition to the aqueous continuous phase [609]. The concurrent increase in viscosity and decrease in interfacial tension at the interface should have improved PLGA stability, thus reducing particle size. The particle sizes highlighted in Table 6.2 support this hypothesis, yet direct NAD+ %EE remained below 0.1%. Ismail *et al.* [605] also observed the inverse relationship between PVA concentration and liraglutide encapsulation, with an increase in PVA concentration from 0.5 to 2% (w/w) resulting in a decrease in encapsulation from above 29% to below 24% during a seven-factor, two-level Plackett Burman analysis. This was attributed to the accelerated cavitation and breakdown of the inner aqueous phase with an increase in PVA concentration.

Table 6.2: Particle sizes of NAD+-PLGA nanoparticles prepared with various emulsifier stabilising agents. Data is expressed as mean size ± S.D (n=3).

Emulsifier	Concentration (% (w/v))	Size (nm)
PVA - fully hydrolysed	0.5	3689.3 ± 1214.8
PVA – partially hydrolysed	0.5	294.1 ± 39.6
(≈ 88%)	2	223.6 ± 6.7
Pluronic® F-127	0.5	348.9 ± 87.9

The removal of mechanical stresses (sonication, centrifugation speed, etc.) from the formulation process led to an increase in indirect NAD+ %EE and decreased the mass of NAD+ lost during the first centrifugation step at 15,000 rpm.

Ultimately, due to the continual discrepancy between the indirect and direct NAD+ %EE within the PLGA nanoparticles, the scope of the research work was shifted to focus primarily on the formulation and characterisation of lipid-based, NAD+-laden nanoformulations.

6.2.2 Selection of Lipid Extraction Solvent for NAD+

Due to its ability to permeate cellular membranes and lyse cells for organelle extraction, Triton™ X-100, a non-ionic surfactant, is typically used to disrupt the lipid bilayers in lipid-based nanoformulations during drug encapsulation analysis [610]. Increasing volumes of methanol were also analysed as methanol is a commonly used organic solvent in lipid extraction studies [611]. However, as the volume ratio of methanol increased, the area of the primary NAD+ chromatographic peak (retention time = ~ 4-5 minutes) began to decrease, with a concurrent increase in the area of the known impurity peak (retention time = ~ 3 minutes) also observed under these conditions. As shown in

Figure **6.2**, peak splitting was also observed in the extraction solvents with a 60:40 and 50:50 water:methanol volume ratio in comparison to that with a 95:5 volume ratio. To ensure that peak splitting was not resulting from the material precipitation on the head of the column, a 10 µL aliquot of the NAD+ solution with a 50:50 deionised water:methanol volume ratio was pipetted into a volume of mobile phase that was equivalent to one column volume (4.15 mL). No precipitation was observed. A HPLC equipped with a PDA detector could also be used in future studies to evaluate whether the peak splitting observed is due to the co-elution of lipid components with NAD+ at an increased methanol concentration.

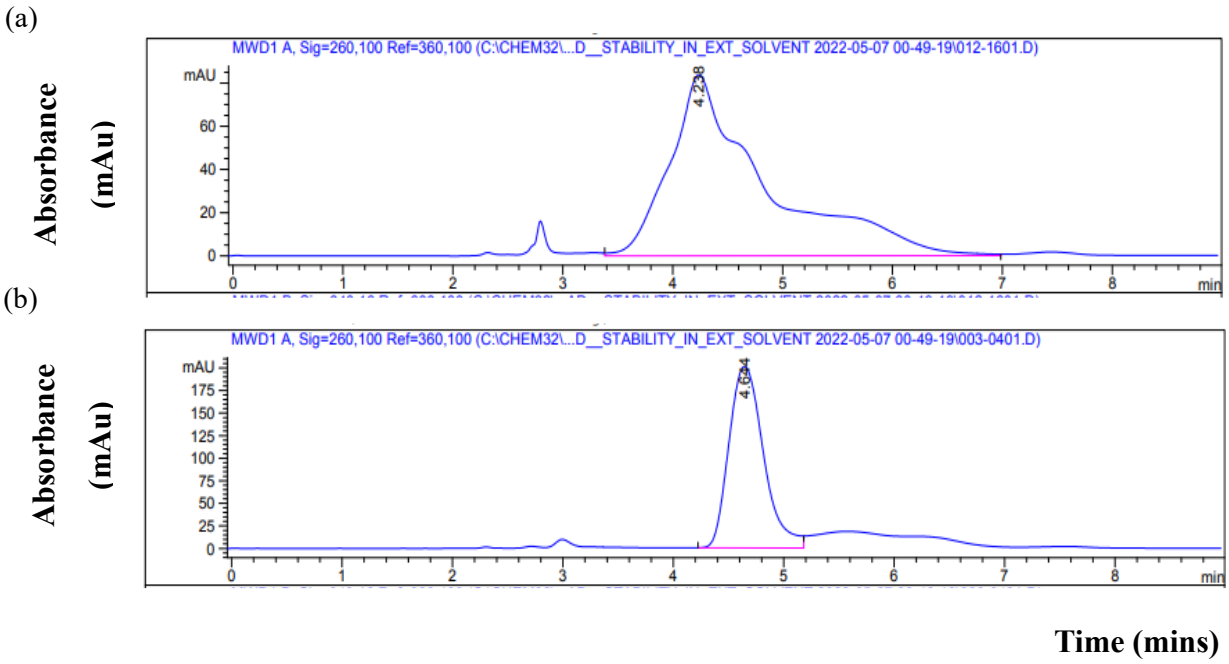

Figure 6.2: The HPLC chromatogram generated for NAD+ in 1% (w/v) Triton™ X-100 in (a) 95:5 (deionised water:methanol) and (b) 50:50 (deionised water:methanol) extraction solvent.

These trends suggest that NAD+ may be degrading in extraction solvents with larger volumes of organic solvent, with NAD+ exhibiting fluctuating elution times due to the combined polarity of the injection solvent and the mobile phase. Therefore, 1% (w/v) Triton™ X-100 in extraction solvents containing the smallest volume of methanol (95:5 – deionised water:methanol) were chosen for use in the NAD+ %EE studies.

6.2.3 PEC Coating with Lipid Material

Preliminary trials were carried out to screen potential preparation methods for effective PEC encapsulation. Diethyl ether was selected for the coating trials from preliminary results due to its ability to both dissolve the chosen lipid materials and disperse the PECs whilst preventing PEC solubilisation. Mixing-solvent evaporation was investigated due to the absence of a PEC hydration step, thus preserving NAD+ association due to affinity-mediated intracomplex diffusion during formulation work-up. However, as shown in Table 6.3, despite high NAD+ %EE values, almost 100% of the loaded mass of NAD+ dissociated from the LPHNP formulations within one hour after placement in physiological medium, conducted as per Section 3.2.3.10. The mass of NAD+ retained from the PECs alone was statistically larger than

that within the respective LPHNP formulations ($p = 0.024 < 0.05$ – 1.5:1 lecithin:cholesterol and $p = 0.022 <$ - 4:1 lecithin:cholesterol), suggesting that, even in the absence of a hydration step, NAD+ dissociation may be accelerated due to incompatibility with the lipid material.

Table 6.3: Physicochemical attributes of LPHNP formulations prepared via diethyl ether injection. Data is expressed as mean ± S.D (n=3).

	PECs + 100% Cholesterol	**PECs + 4:1 (Lecithin:Cholesterol)**	**PECs + 1.5:1 (Lecithin:Cholesterol)**
Mass of NAD+ added to formulation (mg)	7.13 (in 20.7 mg of PEC)	6.99 (in 20.3 mg of PEC)	6.88 (in 20.0 mg of PEC)
%EE	75.1 ± 1.4	91.6 ± 1.2	70.0 ± 1.2
NAD+ Disassociation (%) (at 1 Hour)	91.4 ± 8.4	87.8 ± 6.0	N/A*
Size (nm)	518.3 ± 24.0	431.9 ± 57.3	1949.7 ± 100.7*

* Sedimentation observed during DLS analysis → sample not used for subsequent % NAD+ disassociation analysis.

As shown in Figure 6.3 (a), significant coagulation of the cholesterol-coated PECs, prepared via mixing-solvent evaporation, was observed during preparation and was therefore excluded from further characterisation.

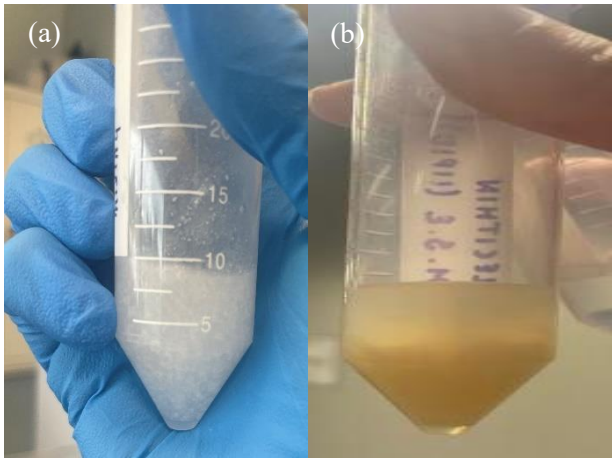

Figure 6.3: The cholesterol (a) and lecithin (b)-coated PEC formulations prepared via mixing-solvent evaporation.

Replacement of cholesterol with soybean lecithin improved the dispersibility of the LPHNP formulation. However, significant NAD+ release (98.3% (n = 1)) was observed from the LPHNP after 1 hour in 0.01 M PBS (pH 7.4). A large quantity of lecithin material, depicted in Figure 6.3 (b), was also isolated during the first centrifugation cycle at 3,000 rpm, suggesting that the majority of the added soybean lecithin was not associated with the PEC surface. Therefore, no further trials were conducted using these preparation methods and focus was shifted to investigate the formation of liposome-based formulations for PEC and NAD+ encapsulation.

6.2.4 NAD+-Laden Liposomes– Suitable Attributes but Irreproducible Release

It was proposed that the encapsulation of the NAD+-laden PECs within a liposomal bilayer may attain the beneficial physiological attributes of the PEC whilst preventing premature NAD+ release upon administration and prolonging formulation stability for effective delivery to the posterior segment *in vivo.* The TFH method used during these trials was adapted from methods previously used to coat chitosan-based PECs with mixtures of phosphatidylcholine derivatives and cationic lipids [612], [613]. Additionally, unlike methods such as nanoprecipitation and emulsification-solvent evaporation, the PECs would not be exposed to organic solvents during formulation, thus avoiding potential cytotoxicity risks [614]. The lipid:PEC mass ratio was maintained at 1.5:1 (w/w) as this mass ratio yielded PEC liposomes (PEC-Lipo) with small particle sizes and stable zeta potential (ZP) values in the aforementioned studies. As shown in Table 6.4, an increase in NAD+ %EE was observed with an increase in hydration volume from 5 mL to 20 mL during TFH.

Table 6.4: Summary of the physicochemical attributes of the PEC-Lipo and NAD+-Lipo formulations investigated. Data is expressed as mean ± S.D (n = 3).

Formulation	Hydration Volume (mL)	Size (nm)	Zeta Potential (mV)	PDI	Direct %EE	Indirect %EE
Control PECs	n/a	235.1 ± 19.0	-38.0 ± 1.1	0.21 ± 0.14	77.2. ± 9.5	90.3 ± 1.3
PEC-Lipo	5	364.3 ± 19.8	-48.8 ± 0.6	0.38 ±0.03	20.1 ± 6.0	44.7 ± 20.1
	20	163.2 ± 1.9	-66.1 ± 1.2	0.26 ± 0.0	77.8 ± 2.7	86.7 ± 1.4
NAD+-Lipo	5	132.8 ± 3.6	-45.1 ± 3.0	0.27 ± 0.03	15.8 ± 0.3	21.7 ± 0.8
	20	167.5 ± 1.9	-44.9 ± 7.3	0.30 ± 0.05	71.2 ± 0.7	77.6 ± 2.2

Regarding the PEC-Lipo formulation, a concurrent, significant decrease in particle size, yielding particles with sizes less than that of the control PECs, was observed with an increase in hydration volume ($p = 0.003 << 0.05$). This may have been attributed to the preferential association of the PECs with an increased volume of aqueous hydration volume during formulation, thus minimising PEC encapsulation within the liposomes formed. The significant decrease in zeta potential (ZP) with an increase in PEC-Lipo hydration volume corroborates this hypothesis ($p = 0.000 << 0.05$), suggesting that the anionic surface of the PECs was being measured in tandem with the anionic phosphate headgroups of the phosphatidylcholine chains. Upon comparison to the control PECs, the ZP of the PEC-Lipo (5 mL) were significantly more negative ($p = 0.000 << 0.05$). Also, statistically similar ZP values were obtained for the NAD+-Lipo formulations ($p = 0.104 > 0.05$), in which no HA carboxylate anions are present, thus suggesting the PECs were sufficiently encapsulated using a lower hydration volume and the ZP obtained was attributed to phosphatidylcholine alone. The higher %EE value for the PEC-Lipo (20 mL) formulation may have resulted from the intrapolyelectrolyte swelling and release of NAD+ from the PECs in a larger aqueous volume during hydration. This may have led to the encapsulation of now free, more readily accessible NAD+ molecules within the thin, lipid layer, rather than NAD+-associated PECs as a whole.

Regarding the PEC-Lipo 5 mL formulation, a large quantity of the mass of loaded NAD+ (21.8 ± 7.9 mg) was removed during the second centrifugation cycle. Also, similar to that observed

during the diethyl ether injection trials, over 87.1 ± 6.6% (n = 3) of the loaded mass of NAD+ leaked from the PEC-Lipo formulations within one hour under physiological conditions. Despite the trends observed during size analysis, suggesting that sufficient encapsulation of the PECs was achieved with a decrease in hydration volume, the majority of the loaded NAD+ preferentially resided in the 5 mL hydration volume during preparation and was subsequently removed during centrifugation. This may be attributed to the organisation of soybean lecithin into phospholipid bilayers during hydration, which would have hindered PEC encapsulation due to electrostatic repulsion between the phosphate headgroups and the HA carboxylate anions.

To improve the encapsulation of the hydrophilic PECs within a lipid layer, the lipid:PEC mass ratio was doubled to 3:1 (w/v) as it was postulated that a larger quantity of lipid material may be required for effective encapsulation. Oleic acid (OA) was also used in place of soybean lecithin to investigate the efficacy of a smaller, fatty acid moiety in terms of NAD+-laden PEC encapsulation. Bearing a molecular weight of 282.47 g/mol, OA may be able to penetrate the HA-based corona in comparison to soybean lecithin, which may experience increased steric hindrance during formation due to its larger molecular weight of 785.08 g/mol. Also, with a pKa value of 5.02, the negatively charged carboxylic acid group may preferentially reside at the solvent interface in the hydration medium (pH 5 ultrapure water), with the neutral fatty acid chain aligning with the PEC surface. However, although the addition of OA improved NAD+ %EE (47.9 ± 6.6%) in comparison to soybean lecithin at 1.5:1 (20.1 ± 6.0%) and 3:1 (21.8 ± 1.3%) (w/w) lipid:PEC mass ratios, large quantities of unentrapped NAD+ were quantified upon completion of the second centrifugation cycle (17.7 ± 3.5 mg). In addition, the use of double the quantity of soybean lecithin resulted in the removal of over 71.0% of the encapsulated NAD+ concentration after 1 hour, with the PEC-Lipo formulated using OA losing 74.9% within the same time period (n =1). Such trends suggested that the PECs were poorly encapsulated by the liposomal formulations, thus aiding rapid release of NAD+ due to repulsion with a highly lipophilic environment. As such, no further investigations were conducted using the PEC-Lipo.

As a high %EE value was obtained, the NAD+-Lipo (20 mL) formulations were selected for further *in vitro* release studies under microfluidic conditions. Initial studies confirmed that only 8.4 ± 0.8% (n = 3) of the total loaded mass of NAD+ was released from the NAD+-Lipo formulations over 24 hours. Conversely, an NAD+ control of equivalent concentration exhibited a release of over 86.5 ± 9.6% of the loaded NAD+ over the same time frame. Forced dissolution trials were conducted using the NAD+-Lipo formulation as a reference to ensure the true loaded concentration of NAD+ was represented in the release study. Neither the addition of 1% (w/v) Triton™ X-100 to the 0.01 M PBS (pH 7.4) release medium (14.2% (n = 1)), nor the use of an elevated temperature (55 °C) (0.09% (n = 1)) significantly enhanced NAD+ release. However, upon conducting an *in vitro* release study over 10 days, 55.9 ± 3.2% (n = 2) was released after 24 hours post-addition to the microfluidic device. The sudden increase in NAD+ mass released, and the small variations between indirect and direct %EE, suggested that the variability was not arising from the quantity of NAD+ within the particles, but instead from the stability of the particles and their physiochemical behaviour when placed in physiological medium.

The optimal physicochemical size attributes and %EE values of the NAD+-Lipo contribute to the proof-of-concept of using such formulations for NAD+ ocular delivery. Further optimisation is required to enhance particle stability. As a starting point, the mass ratio of cholesterol, with respect to soybean lecithin, will be increased. The addition of cholesterol to the liposomal bilayer enhances its rigidity and minimises its permeability via hydrogen bond-mediated packing of the bilayer structure, namely between the hydroxyl groups of cholesterol and the phospholipid fatty acid chains [615], [616]. Soni *et al.* [617] observed an increase in brimonidine tartrate %EE from below 40% to above 45% with a concurrent increase in cholesterol content from 30 to 50 mM during a Box–Behnken experimental design analysis. A significant decrease in cumulative *in vitro* release was also observed, primarily attributed to the restriction of drug permeabilisation through a more rigid, hydrophobic membrane bilayer. There is also scope to investigate alternative lipid materials for liposome formation. The double bonds present within the fatty acid chains of soybean lecithin, an unsaturated phosphatidylcholine derivative, may introduce kinks within the bilayer structure, resulting in disordered packing and enhanced fluidity [618], [619]. Conversely, the use of a saturated

phospholipid, such as dipalmitoylphosphatidylcholine or stearic acid, would form a more structured bilayer, this rendering it more impermeable to therapeutic diffusion. However, as investigated by Chaw *et al*. [620], a balance is needed between high %EE values and suitable *in vitro* efficacy, as the use of a fully saturated lipid building block significantly upregulated intraocular clearance of liposomal formulations post-administration to the subconjunctival region due to protein-mediated interaction and enhanced removal to circulation. The incorporation of a cationic phospholipid may be advantageous for prolonged intraocular retention within both the anterior and posterior segments. For example, Jounaki *et al.* [621] added stearylamine, a saturated, cationic lipid, to a stearic acid-based liposome to aid vancomycin encapsulation via electrostatic interaction with its negatively charged carboxyl groups. A similar technique could be used to enhance NAD+ entrapment within the aqueous core of the liposome via interaction with the anionic pyrophosphate bridge moiety. Finally, to attain the biological functionality of the PECs without their direct entrapment, HA may be deposited onto the surface of the optimised NAD+ liposomal formulation, a technique that has been used previously to improve permeabilisation *in vivo* whilst preserving physiological stability [619], [622].

6.3 CONCLUSIONS

The research work highlighted in this chapter provides the first stepping stone for the optimisation of both PLGA and lipid-based formulations for the posterior segment delivery of NAD+. The initial optimisation studies conducted during the formulation an development of the NAD+-PLGA nanoparticles yielded large discrepancies between the direct and indirect %EE values. Although beyond the initial scope of this phase of work, the studies highlighted a number of critical quality attributes that could be optimised further using statistical Design of Experiment methodologies. There is also potential to investigate the effect of lactic acid:glycolic acid ratio and the addition of a hydrophobic emulsifier with a low hydrophilic-lipophilic balance value to stabilise the primary emulsion [623]–[625].

Preparation of NAD+-laden liposomes via TFH was selected due to poor retention of NAD+ in physiological medium from the lipid-based formulations prepared via diethyl ether injection and mixing-solvent evaporation. A monodisperse nanoparticle formulation with an average size

of 167.5 ± 1.9 nm was prepared upon hydrating the NAD+-Lipo with 20 ml of ultrapure water. Although encapsulating over 77% of the loaded concentration of NAD+, NAD+ release from this formulation over 24 hours was not reproducible (8.4 ± 0.8% (n = 3) – initial study, 55.9 ± 3.2% (n = 2) – long-term release study), potentially attributed to formulation instability in physiological medium. As only one lipid mixture (soybean lecithin and cholesterol) at one mass ratio (4:1 (w/w)) was investigated, there is scope to optimise the composition of the liposomal bilayer to improve physiological stability, particularly for the encapsulation and sustained release of NAD+ to the posterior segment.

CHAPTER 7:

FUTURE WORK AND CONCLUDING REMARKS

7. FUTURE WORK AND CONCLUDING REMARKS

7.1 FUTURE PERSPECTIVES

Chapters 2 to 5 detailed the preparation and physicochemical characterisation of NAD+-associated HA and PLL PECs and CH-NAD+ complex formulations as potential candidates for the once or twice-daily supplementation of the corneal surface. The *in vitro* cell studies conducted provide a baseline estimation of the *in vitro* safety and efficacy of the complex formulations. Building on the work conducted, one of the primary focuses of future research is the further characterisation of the complex-based formulations using *in vitro* cellular models to assess the pharmacological activity of NAD+, both in free form and upon association with the respective formulations. Cellular models that closely mimic the early-onset pathogenesis of corneal surface disorders will be selected for investigation to provide a well-rounded examination of the *in vitro* efficacy of the respective formulations. Completion of such studies, in combination with pre-clinical investigations using *in vivo* pharmacokinetic and pharmacodynamic methodologies, will aid the translation of these formulations into clinical application.

In terms of energy efficiency and cost-effectiveness, complex-based formulations are highly suitable for commercial scalability due to their ability to form in aqueous solution under ambient conditions. However, despite their favourable physiochemical attributes, polyelectrolytes, exhibiting the dual character of a macromolecule and electrolyte, exhibit high variability and their functionality is particularly susceptible to changes in environmental conditions. Therefore, critical assessments of their feasibility for commercial scale-up and mass production must be conducted to ensure the stability of the formulations over the production process, including sterilisation and subsequent storage. An assessment of their stability upon exposure to additives and stabilisers during commercial formulation development should also be of pivotal focus.

Future work should also focus on the feasibility of delivering the complex-based formulations via a pre-existing method of ocular administration. Due to the intended supplementary mode of action of these formulations, modes of administration involving frequent subjection to invasive procedures, such as intravitreal injections or implantations, would not be favourable

in terms of patient compliance. The delivery of the developed formulations utilising a topical delivery system, such as a hydrogel contact lens or eye-drop formulation, would be more suitable for the intended application whilst maximising user safety and ease of use, provided the addition of the complex-based formulations does not hinder the critical quality attributes of the chosen delivery system.

7.2 PROPOSED EXPERIMENTAL WORK

7.2.1 Addressing the Limitations of the Study

The baseline safety and efficacy of the PEC and CH-NAD+ formulations were established on a secondary corneal epithelial cell line. Although the use of a secondary cell culture is more cost effective and minimises culture-to-culture variability between replicate experiments, manipulation of their proliferation for indefinite subculture can alter their physiological properties. This, in turn, affects their alignment to basal physiology of corneal cells *in vivo.* To provide a more accurate model of the biological and genetic properties of the corneal epithelium, both the cytotoxic potential and antioxidant behaviour of the formulations will also be evaluated using a primary human corneal epithelial cell (PHCECs) culture. Also, only corneal epithelial cells were utilised in this study as the formulations were initially evaluated as supplementary drug delivery systems or administration to the ocular surface. However, there is scope to investigate the safety and pharmacokinetic profiles of the formulations on a retinal cell line, such as ARPE-19, to evaluate their potential to deliver NAD+ to the posterior segment.

As described in Section 5.3.6, Franz diffusion cells were used during the *ex vivo* permeation and retention study. Neither the impact of release media flow rate nor blinking mechanism on NAD+ permeation through the corneal tissue was considered. To ensure a high degree of correlation with *in vivo* condition, there is scope to repeat the *ex vivo* studies using an Ussing chamber under a dynamic physiological flow rate with transepithelial electrical resistance measurements to ensure tissue integrity throughout the study. Blinking and the spreading of tear fluid across the corneal explants could also be simulated via the use of a mechanical arm, thus allowing for the quantification of NAD+ loss to tear film clearance during re-establishment of equilibrium tear volume.

As outlined in Chapter 5, *in vitro* cellular and *ex vivo* porcine models were used to establish the baseline safety an efficacy of the formulations. In order to fully assess the pharmacokinetic and pharmacodynamic properties of the formulations, with a high degree of correlation to the complex anatomy and physiology of the ocular environment *in vivo*, experimental animal models must be used. To reduce the number of animal subjects required for trials. The tolerability and irritation potential of the formulations could be assessed using the hen's egg-chorioallantonic membrane test (HET-CAM) and the corresponding score classification. A pharmacokinetic and pharmacodynamic assessment of the formulations could be conducted using a healthy rabbit or murine model, with NAD+ bioavailability and mean residence time being quantified in tear fluid and aqueous humour. Mild-dry eye in the rabbit or murine model could be induced using benzalkonium chloride and used to assess *in vivo* NAD+ pharmacodynamics. Tear fluid production (Schirmers test), tear film break-up time and corneal and conjunctival injury (ocular surface staining score ‑ observation under cobalt blue light from a slip lamp) could be used to assess the efficacy of both NAD+ and the NAD+-laden formulations in attenuating the deleterious effects of dry eye.

7.2.2 Soft X-Ray Microscopy for Complex Internalisation

7.2.2.1 Visualisation of Mitochondrial Dysfunction

Soft x-ray microscopy (SXM) can be utilised to obtain a 3D tomogram of the intracellular environment via imaging intact, hydrated cells using soft x-ray radiation in the range of 2.3 to 4.4 nm (the water window), achieving a spatial resolution of between 25 to 60 nm [626]. Water and oxygen molecules weakly absorb soft x-rays within the water window. Conversely, carbon and nitrogen molecules strongly absorb soft x-rays within this region, thus allowing for natural contrast between the organelles and the surrounding cytoplasm. More specifically, SXM can be utilised to quantify mitochondrial molecular densities, using theoretical linear absorption coefficient (LAC) values, and assess mitochondrial cristae morphology in both basal and diseased cellular states [627], [628]. Therefore, there is scope to utilise this technique to compare the subcellular arrangement of control corneal epithelial cells and those under oxidative stress. PHCECs will be purchased from ATCC and cultured in accordance with the subculture protocol. Following subculture and growth in media for 24 the media will be replaced with

either 100 µL of fresh media (negative control) or 100 µL of media containing 200 µM of H_2O_2, before incubation for a further 24 hours. Cell preparation for loading into the capillary sample holders and subsequent cryofixation will be conducted in accordance with the protocol detailed by Parkinson *et al.* [629]. The cryo-preserved cells will then be analysed via SXM and compared to investigate changes in cell morphology resulting from oxidative stress. Additionally, the mitochondria from both cell types can be extracted and imaged using a similar methodology outlined by Polo *et al.* [630]. Calculation of the LAC values and mitochondrial matrix shapes using the mitochondrial complexity index will provide an indication of mitochondrial decline or dysfunction resulting from oxidative stress.

7.2.2.2 Restoration of Mitochondrial Homeostasis Following Complex Uptake

Additionally, the impact of complex internalisation on the morphology of the intracellular environment can also be visualised using SXM. *In vitro* cell uptake will be conducted as per Section 5.2.3.4, without the work-up and quantification steps. Following incubation, the formulation-laden PHCECs will be prepared and imaged via SXM as before. Not only will this provide a clear visualisation of formulation intracellular uptake, but there is potential to visualise the restoration of mitochondrial function following supplementation of the cells with the respective formulations and induction of oxidative stress. PHCECs will be supplemented with either NAD+ alone, NAD+-associated PECs or CH-NAD+ complex for 24 hours prior to exposure to 200 µM of H_2O_2. Comparison of the SXM images of treated PHCECs to those obtained from the H_2O_2-stressed cells should yield changes in cell organelle morphology.

7.2.3 Restoration of Basal Respiration via Seahorse Mito Stress Assay

Induction of oxidative stress within mitochondria can significantly damage the mitochondrial respiratory chain, thus significantly upregulating mitochondrial dysfunction [631]. However, NAD+ plays a pivotal role in mitochondrial respiration, namely by acting as a central hydride donor to ATP synthesis through mitochondrial oxidative phosphorylation [632]. As such, it is hypothesised that the incubation of H_2O_2-stressed PHCECs with NAD+/NAD+-laden complex formulations may enhance mitochondrial respiratory function in comparison to PHCECs incubated with H_2O_2 alone. PHCECs will be incubated at a seeding density of 20 x 10^3 cells/well in a Seahorse XF cell culture plate for 24 hours. The cells will be incubated for a

further 24 hours with 100 µL of media supplemented with; fresh media (negative control), fresh media (positive control), NAD+, NAD+-associated PECs, and CH-NAD+ formulations. The final 24-hour incubation period will involve the removal of the treatments and the addition of 100 µL of media containing 200 µM of H_2O_2.

Before analysis, the media will be removed and replaced with Seahorse XF assay media (1 mM HEPES buffer containing 25 mM glucose, 2 Mm GlutaMax and 1 mM sodium pyruvate) before incubating the plate in a humidified incubator at 37 °C (no CO_2). Oxygen consumption rate (OCR), an indicator of mitochondrial respiratory function, will be assessed using a Seahorse XF Analyzer and a Seahorse XF Cell Mito Stress Kit. Baseline mitochondrial respiration, an indicator of the basal metabolic demands of the PHCECs, will be assessed prior to the addition of the mitochondrial stress test reagents. Measurements of ATP-linked respiration, maximal oxygen consumption rate, and residual OCR originating from non-mitochondrial sources, will also be analysed via sequential injection of 1 µM of oligomycin, 2 µM of phenylhydrazone (FCCP), and 0.5 µM of rotenone/antimycin A to each well, respectively [633]–[635]. The results obtained will be combined with those from the *in vitro* cell internalisation studies to critically evaluate the efficacy of the NAD+-associated formulations upon internalisation.

7.2.4 Etheno-NAD+ Assay for Sirtuin Function Analysis

A quantitative assessment of NAD+ hydrolase activity would be highly beneficial to both gain a thorough understanding of NAD+ consumption in PHCECs and to investigate whether association to a formulation impacts its enzymatic activity [636]. Upon washing and trypsinising the cells from the cell culture plates, the cells will be homogenised in NETN lysis buffer and centrifuged. Quantification of the total hydrolase content (CD38, PARP, SIRTS) in cell supernatants will be conducted using a bicinchoninic acid (BCA) assay and normalised across the cell samples. 10 µL of the sample lysates will be added to a 96-well cell culture plate, followed by the immediate addition of either nicotinamide $1,N_6$-ethenoadenine dinucleotide (etheno-NAD+), a fluorescent ADP-ribose byproduct of NAD+ hydrolysis, or 10 µL of PEC/CH-NAD+ solutions containing an equivalent etheno-NAD+ concentration. Fluorescence will be read using a fluorescence microplate reader. The total NAD+ hydrolase activity of each well will be calculated by plotting the active fluorescent units as a function of

time and obtaining the slope of the resulting curve. There is also scope to analyse the behaviour of select NAD+ hydrolases via the addition of 10 µL of inhibitor solutions (apigenin – CD38, 3-aminobenzamide – PARPs, etc.) before the addition of etheno-NAD+. This can also be applied to the analysis of PHCECs in a diseased state to quantify the effect of cellular dysfunction on NAD+ hydrolase activity.

7.2.5 CD44 Receptor-Mediated Uptake of HA and PLL PECs

As outlined in Section 1.4.1, corneal intracellular uptake of HA and PLL PECs may be governed by the binding of HA to CD44 receptors expressed on the corneal epithelium [637]. To investigate whether PEC uptake is mediated by receptor binding, PEC uptake will be conducted under conditions of CD44 inhibition. Firstly, the expression of CD44 receptors in the PHCEC line will be confirmed via Western blotting and immunofluorescence assays [638]. Based on the methods outlined by Conteras-Ruiz *et al*. [639], upon reaching the desired confluency, PHCECs will be incubated with anti-CD44 Hermes-1 antibody for 30 minutes prior to incubation with FITC-PEC and FITC-CH-NAD+ formulations for 24 hours. Changes in fluorescence upon comparison with that obtained during the cell uptake study outlined in Section 5.2.3.6 can be visualised via fluorescence microscopy. However, there is scope to quantify the hypothesised decline in fluorescence via analysis of the fluorescence intensity of the lysates from formulation-laden cells using a fluorescence microplate reader.

7.2.6 Investigation of Chitosan-Mediated Tight Junction Opening

Tight junction disruption and subsequent opening via CH-NAD+ formulation permeation will be investigated via means of immunofluorescence staining and fluorescence microscopy. PHCECs will be incubated with both CH-NAD+ formulations and chitosan alone (positive control – equivalent in concentration to the formulations) for 1, 6, 10 and 24 hours. Upon incubation with a primary antibody for zona occludens (ZO-1), an integral scaffold protein for tight junction integrity, for 1 hour and subsequent fixation, PHCECs will be stained with a FITC-labelled secondary antibody for 2 hours, protected from light. Control cells will be incubated in the absence of the primary antibody. Following counterstaining with 0.0001% (w/w) DAPI to highlight cell nuclei, the PHCECs will be imaged. A decrease in fluorescence and boundary pattern integrity upon incubation with chitosan/CH-NAD+ is indicative of tight

junction destabilisation. For example, as shown in Figure 7.1, Shi *et al.* [640] observed a decrease in ZO-1 fluorescence and discontinuity of the cell borders after incubation of human corneal epithelial cells with a chitosan conjugate eye drop formulation (CCH).

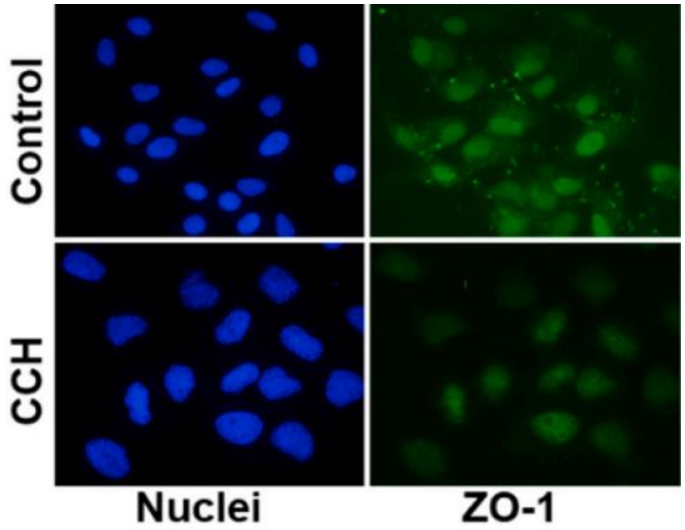

Figure 7.1: A reduction in ZO-1 fluorescence observed in human corneal epithelial cells after pre-incubation with CCH for 2 hours [640].

FINAL REMARKS

This research work details, for the first time, the development of a number of biopolymer-based nanoformulations exhibiting optimal physicochemical attributes for the direct delivery of NAD+ to the corneal surface and supplementary treatment of age-related ocular dysfunction. Further investigations are required to optimise the chosen NAD+-laden formulations intended for posterior segment supplementation. Particularly regarding the NAD+-associated PECs, the *in vitro* safety and efficacy profiles obtained within conditions mimicking that of the corneal environment render them a suitable candidate for further *in vitro* and *in vivo* pre-clinical trials.

With NAD+ and NAD+ precursor oral and intravenous supplementation gaining increasing popularity in the field of anti-ageing research, the direct, targeted delivery of NAD+ provides a novel avenue of investigation for the preventative treatment of numerous age-related ocular diseases. This research work has provided a proof-of-concept for the development of a number

of promising nanoformulation platforms for ocular NAD+ delivery, with strong potential to improve ocular health and reduce susceptibility to the deleterious effects of ageing.

RESEARCH DISSEMINATION

Based on the literature review conducted in Chapter 1, a gap in scientific knowledge regarding the development of HA-based PECs specifically for ophthalmic applications was identified. Limited research has also been published regarding the considerations that must be made for the optimisation of the intrinsic and extrinsic properties of HA-based PECs during formulation. To fill the identified gap in the literature, a review article, entitled "Hyaluronic Acid: Its Versatile Use in Ocular Drug Delivery with a Specific Focus on Hyaluronic Acid-Based Polyelectrolyte Complexes" was successfully published in the Special Issue of the Pharmaceutics journal "Innovative Technologies to Treat Diseases of the Back of the Eye" (DOI: https://doi.org/10.3390/pharmaceutics14071479).

Chapters 2,3, and 5 detail the successful development and characterisation of NAD+-associated PECs, in terms of method optimisation (Chapter 2), size parameters (Chapters 2 and 3), NAD+ loading and release (Chapter 3), *in vitro* biocompatibility (Chapter 5) and *ex vivo* permeation and retention (Chapter 5). Based on this experimental work, a research article, entitled "NAD+-associated-hyaluronic acid and poly(L-lysine) polyelectrolyte complexes: An evaluation of their potential for ocular drug delivery", was successfully published in the International Journal of Pharmaceutics and Biopharmaceutics (DOI: https://doi.org/10.1016/j.ejpb.2023.10.004). This work was also selected for poster presentation at the Association for Research in Vision and Ophthalmology Annual Meeting (ARVO) in New Orleans, Lousiana in April 2023, with the abstract later published in the corresponding book of meeting abstracts, Investigative Ophthalmology & Visual Science: An ARVO Journal (Link: https://iovs.arvojournals.org/article.aspx?articleid=2787647).

A research paper, entitled "Preliminary, Comparative Evaluation of the Safety and Efficacy of Polyelectrolyte Complex-Based Nanoformulations for NAD+ Ocular Surface Delivery using *In vitro* and *Ex vivo* Models – Working Title", is currently under preparation and is due for

submission in 2024. This paper will highlight the development and characterisation of the CH-NAD+ formulations (Chapter 4) and provide a comparative analysis of the *in vitro* mucoadhesion, efficacy, uptake, and *ex vivo* permeation and retention of the NAD+-associated PECs and CH-NAD+ formulations, based on the work detailed in Chapter 5.

REFERENCES

[1] Gupta, M. P.; Herzlich, A. A.; Sauer, T.; Chan, C. C. Retinal Anatomy and Pathology. In *Retinal Pharmacotherapeutics*; Nguyen, Q. D., Rodrigues, E. B., Farah, M. E., Mieler, W. F., Do, D. V., Eds.; Karger, 2016; Vol. 55, pp 7–17. https://doi.org/10.1159/000431128.

[2] Galetta, S. L. Occipital Lobe. *Encyclopedia of the Neurological Sciences (Second Edition)* **2014**, *2*, 626–632. https://doi.org/10.1016/B978-0-12-809324-5.03810-4.

[3] SMART - Servier Medical ART. Servier. Available online: https://smart.servier.com/ (Accessed on: 23 April 2020).

[4] Cholkar, Kishore.; Dasari, S. R.; Pal, D.; Mitra, A. K. Eye: Anatomy, Physiology and Barriers to Drug Delivery. *Ocular Transporters and Receptors: Their Role in Drug Delivery* **2013**, No. February, 1–36. https://doi.org/10.1533/9781908818317.1.

[5] Ng, P. C.; Oliver, J. J. Anatomy of the Eye. In *Handbook of Emergency Ophthalmology*; Long, B., Koyfman, A., Eds.; Springer US, 2018; pp 1–12. https://doi.org/10.1007/978-3-319-78945-3_1.

[6] Vision Eye Institute. The Vitreous Humour Fact Sheet - Vision Eye Institute. Eye Matters. Available online: https://visioneyeinstitute.com.au/eyematters/the-vitreous-humour/ (Accessed on: 09 October 2019).

[7] Moiseev, R. V.; Morrison, P. W. J.; Steele, F.; Khutoryanskiy, V. V. Penetration Enhancers in Ocular Drug Delivery. *Pharmaceutics* **2019**, *11* (7). https://doi.org/10.3390/pharmaceutics11070321.

[8] Tsai, C.-H.; Wang, P.-Y.; Lin, I.-C.; Huang, H.; Liu, G.-S.; Tseng, C.-L. Ocular Drug Delivery: Role of Degradable Polymeric Nanocarriers for Ophthalmic Application. *Int J Mol Sci* **2018**, *19* (9). https://doi.org/10.3390/ijms19092830.

[9] Huerta Ángeles, G.; Nešporová, K. Hyaluronan and Its Derivatives for Ophthalmology: Recent Advances and Future Perspectives. *Carbohydr. Polym.* **2021**, *259*, 1–15. https://doi.org/10.1016/j.carbpol.2021.117697.

[10] Crowell, S. R.; Wang, K.; Famili, A.; Shatz, W.; Loyet, K. M.; Chang, V.; Liu, Y.; Prabhu, S.; Kamath, A. V; Kelley, R. F. Influence of Charge, Hydrophobicity, and Size on Vitreous Pharmacokinetics of Large Molecules. **2019**. https://doi.org/10.1167/tvst.8.6.1.

[11] Blindness and Visual Impairment. Available online: https://www.who.int/en/news-room/fact-sheets/detail/blindness-and-visual-impairment (Accessed on: 14 October 2019).

[12] Vision Loss Expert Group IAPB. Magnitude and Projections - The International Agency for the Prevention of Blindness. Vision Atlas \ Magnitude and Projections. Available online: https://www.iapb.org/learn/vision-atlas/magnitude-and-projections/ (Accessed on: 11 January 2021).

[13] Ackland, P.; Resnikoff, S.; Bourne, R. World Blindness and Visual Impairment: Despite Many Successes, the Problem Is Growing. *Community Eye Health Journal* **2017**, *30* (100), 71–73.

[14] The Department of Economic and Social Affairs Population Division of the United Nations. Globally, Population Aged 60 or over Is the Fastest Growing. In *World Population Prospects: The 2015 Revision, Key Findings and Advance Tables*; New York, 2015; p 7.

[15] Projected Change in Vision Loss 2020 to 2050. Available online: https://www.iapb.org/learn/vision-atlas/magnitude-and-projections/projected-change/ (Accessed on: 06 January 2021).

[16] Fighting Blindness. Vision impairment and blindness | Fighting Blindness. Fighting Blindness Website. Available online: https://www.fightingblindness.ie/how-we-can-help/advocacy/information-and-resource-hub/vision-impairment-and-blindness/ (Accessed on: 15 April 2020).

[17] Adelson, J.; Bourne, R. R. A.; Birant, P. S.; Flaxman, S.; Taylor, H.; Jonas, J. B. Under Review - Causes of Blindness and Vision Impairment in 2020 and Trends over 30 Years : Evaluating the Prevalence of Avoidable Blindness in Relation to " VISION 2020 : The Right to Sight ". The Lancet Global Health. Available online: https://www.iapb.org/learn/vision-atlas/causes-of-vision-loss/ (Accessed on: 30 November 2020).

[18] Schaeffer Eye Center. Hyperopia vs. Myopia: Understanding Two Common Refractive Errors : Schaeffer Eye Center. Schaeffer Eye Center Website. Available online:

https://schaeffereyecenter.com/about-your-eyes/hyperopia-vs-myopia/ (Accessed on: 24 October 2019).

[19] Liu, Y.-C.; Wilkins, M.; Kim, T.; Malyugin, B.; Mehta, J. S. Cataracts. *The Lancet* **2017**, *390* (10094), 600–612. https://doi.org/10.1016/S0140-6736(17)30544-5.

[20] World Health Organisation. WHO | Priority eye diseases. WHO Website. Available online: https://www.who.int/blindness/causes/priority/en/ (Accessed on: 29 October 2019).

[21] Age-Related Macular Degeneration: Facts & Figures | BrightFocus Foundation. Available online: https://www.brightfocus.org/macular/article/age-related-macular-facts-figures (Accessed on: 09 November 2023).

[22] Vyawahare, H.; Shinde, P. Age-Related Macular Degeneration: Epidemiology, Pathophysiology, Diagnosis, and Treatment. *Cureus* **2022**, *14* (9). https://doi.org/10.7759/CUREUS.29583.

[23] Jun, S.; Datta, S.; Wang, L.; Pegany, R.; Cano, M.; Handa, J. T. The Impact of Lipids, Lipid Oxidation, and Inflammation on AMD, and the Potential Role of MiRNAs on Lipid Metabolism in the RPE. *Exp Eye Res* **2019**, *181* (2019), 346–355. https://doi.org/10.1016/j.exer.2018.09.023.

[24] Hernández-Zimbrón, L. F.; Zamora-Alvarado, R.; Ochoa-De La Paz, L.; Velez-Montoya, R.; Zenteno, E.; Gulias-Cañizo, R.; Quiroz-Mercado, H.; Gonzalez-Salinas, R. Age-Related Macular Degeneration: New Paradigms for Treatment and Management of AMD. *Oxid Med Cell Longev* **2018**, *2018*, 14. https://doi.org/10.1155/2018/8374647.

[25] Kharuna, A. Ocular Pharmacology. In *Comprehensive Ophthalmology*; Kharuna, A., Kharuna, B., Eds.; Jaypee Brothers Medical Publishers: New Delhi, 2015; pp 441–464.

[26] Kauppinen, A.; Paterno, J. J.; Blasiak, J.; Salminen, A.; Kaarniranta, K. Inflammation and Its Role in Age-Related Macular Degeneration. *Cellular and Molecular Life Sciences* **2016**, *73* (9), 1765–1786. https://doi.org/10.1007/s00018-016-2147-8.

[27] Roche Group Media Relations. *Media Release | Roche Reports Very Strong Results in 2019*; Basel, Switzerland, 2020.

[28] Regeneron Pharmaceuticals. *Regeneron Reports Fourth Quarter and Full Year 2019 Financial and Operating Results | Regeneron Pharmaceuticals Inc.*; Tarrytown, New York State, 2020.

[29] Dugel, P. U.; Jaffe, G. J.; Sallstig, P.; Warburton, J.; Weichselberger, A.; Wieland, M.; Singerman, L. Brolucizumab Versus Aflibercept in Participants with Neovascular Age-Related Macular Degeneration: A Randomized Trial. *Ophthalmology* **2017**, *124* (9), 1296–1304. https://doi.org/10.1016/j.ophtha.2017.03.057.

[30] RxList.Inc. Drugs A-Z List - A on RxList. RxList Website. Available online: https://www.rxlist.com/drugs/alpha_a.htm (Accessed on: 10 January 2022).

[31] Global age-related macular degeneration market will more than double in size by 2028 - GlobalData. Available online: https://www.globaldata.com/global-age-related-macular-degeneration-market-will-more-than-double-in-size-by-2028/ (Accessed on: 11 January 2021).

[32] Kim, H. M.; Woo, S. J. Ocular Drug Delivery to the Retina: Current Innovations and Future Perspectives. *Pharmaceutics* **2021**, *13* (1), 108. https://doi.org/10.3390/pharmaceutics13010108.

[33] Genentech. Port Delivery System With Ranibizumab Shows Positive Phase III Results in Neovascular Age-Related Macular Degeneration. Media \ Press Releases \ Genentech Websites. Available online: https://www.gene.com/media/press-releases/14854/2020-05-26/port-delivery-system-with-ranibizumab-sh (Accessed on: 11 January 2021).

[34] Weksler, M.; McDougal, A.; Williams, S.; Pegoraro, T.; Randles, E.; deLong, M. A.; Kopczynski, C. C. AR-14034 SR Implant Inhibits Retinal Vascular Leakage In A VEGF Challenge Model For Up To 12 Months. *Invest Ophthalmol Vis Sci* **2023**, *64* (8), 2114–2114.

[35] Aerie Pharmaceuticals Inc. Study of AR-14034 in Participants With Neovascular Age-Related Macular Degeneration (nAMD). ClinicalTrials.gov. Available online: https://classic.clinicaltrials.gov/ct2/show/NCT05769153 (Accessed on: 09 November 2023).

[36] GlobalData. *Age-Related Macular Degeneration - Global Drug Forecast and Market Analysis to 2028*; 2020.

[37] Medicine, ClinicalTrials. gov | N. L. of. *Phase II/III Study of the Efficacy and Safety of MacuCLEAR MC-1101 in Treating DryAge-Related Macular Degeneration - Full Text View - ClinicalTrials.Gov*; 2014.

[38] Bandello, F.; Sacconi, R.; Querques, L.; Corbelli, E.; Cicinelli, M. V.; Querques, G. Recent Advances in the Management of Dry Age-Related Macular Degeneration: A Review. *F1000Res* **2017**, *6* (May), 1–10. https://doi.org/10.12688/f1000research.10664.1.

[39] Vision Loss Expert Group IAPB. Glaucoma - The International Agency for the Prevention of Blindness. Causes of Vision Loss / Glaucoma. Available online: https://www.iapb.org/learn/vision-atlas/causes-of-vision-loss/glaucoma/ (Accessed on: 09 November 2023).

[40] Zetterberg, M. Age-Related Eye Disease and Gender. *Maturitas* **2016**, *83*, 19–26. https://doi.org/10.1016/j.maturitas.2015.10.005.

[41] Yadav, K. S.; Rajpurohit, R.; Sharma, S. Glaucoma: Current Treatment and Impact of Advanced Drug Delivery Systems. *Life Sci* **2019**, *221*, 362–376. https://doi.org/10.1016/j.lfs.2019.02.029.

[42] Chen, G.; Chan, I.; Lam, D. C. C. Sensors and Actuators A : Physical Capacitive Contact Lens Sensor for Continuous Non-Invasive Intraocular Pressure Monitoring. *Sensors & Actuators A* **2013**, *203*, 112–118. https://doi.org/10.1016/j.sna.2013.08.029.

[43] National Eye Institute. Eye Disease Simulations | National Eye Institute (NEI) Media Library. National Eye Insitute Media Library. Available online: https://medialibrary.nei.nih.gov/search?keywords=&f[0]=category:8 (Accessed on: 11 January 2021).

[44] Knobbe, C. A. Optic Neuritis and Neuropathy: Symptoms, Causes, Treatments. All About Vision Website. Available online: https://www.allaboutvision.com/conditions/optic-neuritis.htm (Accessed on: 29 October 2019).

[45] National Eye Institute. Glaucoma | Eye Conditions and Diseases. National Eye Insitute Website. Available online: https://www.nei.nih.gov/learn-about-eye-health/eye-conditions-and-diseases/glaucoma (Accessed on: 11 January 2021).

[46] Glaucoma Research Foundation. Symptoms of Angle-Closure Glaucoma | Glaucoma Research Foundation. Available online: https://www.glaucoma.org/glaucoma/symptoms-of-angle-closure-glaucoma.php (Accessed on: 15 October 2019).

[47] Shirley, M. Bimatoprost Implant: First Approval. *Drugs Aging* **2020**, *37* (6), 457. https://doi.org/10.1007/S40266-020-00769-8.

[48] Singh, R. B.; Ichhpujani, P.; Thakur, S.; Jindal, S. Promising Therapeutic Drug Delivery Systems for Glaucoma: A Comprehensive Review. *Ther Adv Ophthalmol* **2020**, *12*, 251584142090574. https://doi.org/10.1177/2515841420905740.

[49] Al-Kharashi, A. S. Role of Oxidative Stress, Inflammation, Hypoxia and Angiogenesis in the Development of Diabetic Retinopathy. *Saudi Journal of Ophthalmology* **2018**, *32* (4), 318–323. https://doi.org/10.1016/j.sjopt.2018.05.002.

[50] Wang, W.; Lo, A. C. Y. Diabetic Retinopathy: Pathophysiology and Treatments. *Int J Mol Sci* **2018**, *19* (6). https://doi.org/10.3390/ijms19061816.

[51] Semeraro, F.; Morescalchi, F.; Cancarini, A.; Russo, A.; Rezzola, S.; Costagliola, C. Diabetic Retinopathy, a Vascular and Inflammatory Disease: Therapeutic Implications. *Diabetes Metab* **2019**, No. 2018. https://doi.org/10.1016/j.diabet.2019.04.002.

[52] Duh, E. J.; Sun, J. K.; Stitt, A. W. Diabetic Retinopathy: Current Understanding, Mechanisms, and Treatment Strategies. *JCI Insight* **2017**, *2* (14), 1–13. https://doi.org/10.1172/jci.insight.93751.

[53] Brănişteanu, D. C.; Bilha, A.; Moraru, A. Vitrectomy Surgery of Diabetic Retinopathy Complications. *Rom J Ophthalmol* **2016**, *60* (1), 31–36.

[54] Zhao, Y.; Singh, R. P. The Role of Anti-Vascular Endothelial Growth Factor (Anti-VEGF) in the Management of Proliferative Diabetic Retinopathy. *Drugs Context* **2018**, *7*, 1–10. https://doi.org/10.7573/dic.212532.

[55] Roche Group Media Relations. Roche - New phase III data show Roche's faricimab is the first investigational injectable eye medicine to extend time between treatments up to four months in two leading causes of vision loss, potentially reducing treatment burden for patients. Roche Media Releases. Available online: https://www.roche.com/media/releases/med-cor-2021-02-12.htm (Accessed on: 08 December 2021).

[56] Hoffman La Roche. A Study to Evaluate the Long-Term Safety and Tolerability of Faricimab in Participants With Diabetic Macular Edema - Full Text View - ClinicalTrials.gov. ClinicalTrials.gov. Available online: https://clinicaltrials.gov/ct2/show/NCT04432831 (Accessed on: 09 November 2023).

[57] Hoffman La Roche. A Multicenter, Randomized Study in Participants With Diabetic Retinopathy Without Center-involved Diabetic Macular Edema To Evaluate the Efficacy, Safety, and Pharmacokinetics of Ranibizumab Delivered Via the Port Delivery System Relative to the Comparato. ClinicalTrials.gov. Available online: https://clinicaltrials.gov/ct2/show/NCT04503551 (Accessed on: 09 November 2023).

[58] Dieckmann, G.; Fregni, F.; Hamrah, P. Neurostimulation in Dry Eye Disease—Past, Present, and Future. *Ocul Surf* **2019**, *17* (1), 20–27. https://doi.org/10.1016/j.jtos.2018.11.002.

[59] Sharma, A.; Hindman, H. B. Aging: A Predisposition to Dry Eyes. *J Ophthalmol* **2014**, *2014*, 1–8. https://doi.org/10.1155/2014/781683.

[60] Boyd, K. How Hormones Can Affect Eyes and Vision - American Academy of Ophthalmology. American Academy of Ophthalmology Website. Available online: https://www.aao.org/eye-health/tips-prevention/how-hormones-can-affect-eyes-vision (Accessed on: 22 October 2019).

[61] Matossian, C.; McDonald, M.; Donaldson, K. E.; Nichols, K. K.; Maciver, S.; Gupta, P. K. Dry Eye Disease: Consideration for Women's Health. *J Womens Health* **2019**, *28* (4), 502–514. https://doi.org/10.1089/jwh.2018.7041.

[62] De Paiva, C. S. Effects of Aging in Dry Eye. *Int Ophthalmol Clin* **2017**, *57* (2), 47–64. https://doi.org/10.1097/IIO.0000000000000170.

[63] Stevenson, W.; Chauhan, S. K.; Dana, R. Dry Eye Disease. *Archives of Ophthalmology* **2012**, *130* (1), 90. https://doi.org/10.1001/archophthalmol.2011.364.

[64] Ganesalingam, K.; Ismail, S.; Sherwin, T.; Craig, J. P. Molecular Evidence for the Role of Inflammation in Dry Eye Disease. *Optom* **2019**, *102*, 446–454. https://doi.org/10.1111/cxo.12849.

[65] Ames, P.; Galor, A. Cyclosporine Ophthalmic Emulsions for the Treatment of Dry Eye: A Review of the Clinical Evidence. *Clin Investig (Lond)* **2015**, *5* (3), 267–285. https://doi.org/10.4155/cli.14.135.

[66] Agarwal, P.; Craig, J. P.; Rupenthal, I. D. Formulation Considerations for the Management of Dry Eye Disease. *Pharmaceutics* **2021**, *13* (2), 1–19. https://doi.org/10.3390/pharmaceutics13020207.

[67] Fallacara, A.; Vertuani, S.; Panozzo, G.; Pecorelli, A.; Valacchi, G.; Manfredini, S. Molecules Novel Artificial Tears Containing Cross-Linked Hyaluronic Acid: An In Vitro Re-Epithelialization Study. **2017**. https://doi.org/10.3390/molecules22122104.

[68] Schmidl, D.; MD, P.; Schmetterer, L.; Witkowska, K.; MD, P.; Unterhuber, A.; Aranha dos Santos, V.; Kaya, S.; Nepp, J.; Baar, C.; et al. Tear Film Thickness After Treatment With Artificial Tears in Patients With Moderate Dry Eye Disease. *Cornea* **2015**, *34* (4), 421–426.

[69] Harrer, D.; Sanchez Armengol, E.; Friedl, J. D.; Jalil, A.; Jelkmann, M.; Leichner, C.; Laffleur, F. Is Hyaluronic Acid the Perfect Excipient for the Pharmaceutical Need? *Int. J. Pharm.* **2021**, *601* (February), 120589. https://doi.org/10.1016/j.ijpharm.2021.120589.

[70] Selyanin, M. A.; Boykov, P. YA.; Khabarov, V. N. Molecular and Supramolecular Structure of Hyaluronic Acid. In *Hyaluronic Acid - Preparation, Properties, Application in Biology and Medicine*; Polyak, F., Ed.; John Wiley & Sons Ltd.: West Sussex, United Kingdom, 2015; Vol. 1, pp 101–104.

[71] Novaliq GmbH. NOV03. Novaliq GmbH Website. Available online: https://www.novaliq.com/products/nov03/ (Accessed on: 08 December 2021).

[72] Johnson & Johnson Consumer Inc. VISINE® Dry Eye Relief Lubricant Eye Drops | VISINE®. Visine Website. Available online: https://www.visine.com/eye-drops/dry-eye-relief (Accessed on: 08 December 2021).

[73] Oyster Point Pharma. Tyrvaya (Varenicline solution) Nasal Spray | A New Treatment Option for Dry Eye Disease. Tyrvaya Website. Available online: https://www.tyrvaya-pro.com/ (Accessed on: 08 December 2021).

[74] Sheppard, J. D.; Kurata, F.; Epitropoulos, A. T.; Krösser, S.; Vittitow, J. L. NOV03 for Signs and Symptoms of Dry Eye Disease Associated With Meibomian Gland Dysfunction: The Randomized Phase 3 MOJAVE Study. *Am J Ophthalmol* **2023**, *252*, 265–274. https://doi.org/10.1016/j.ajo.2023.03.008.

[75] Vittitow, J.; Protzko, E.; Segal, B. A.; Korenfeld, M. S.; Krösser, S. Long-Term Safety and Efficacy of NOV03 (Perfluorohexyloctane) for the Treatment of Patients with Dry Eye Disease Associated with Meibomian Gland Dysfunction: The KALAHARI Study. *Invest Ophthalmol Vis Sci* **2023**, *64* (8), 3995–3995.

[76] Bausch + Lomb and Novaliq Announce FDA Approval of MIEBOTM (Perfluorohexyloctane Ophthalmic Solution) for the Treatment of the Signs and Symptoms of Dry Eye Disease - Novaliq. Available online: https://www.novaliq.com/press-releases/2023/05/19/bausch-lomb-and-novaliq-announce-fda-approval-of-miebotm-perfluorohexyloctane-ophthalmic-solution-for-the-treatment-of-the-signs-and-symptoms-of-dry-eye-disease/ (Accessed on: 03 January 2024).

[77] Petrov, A.; Perekhvatova, N.; Skulachev, M.; Stein, L.; Ousler, G. SkQ1 Ophthalmic Solution for Dry Eye Treatment: Results of a Phase 2 Safety and Efficacy Clinical Study in the Environment and During Challenge in the Controlled Adverse Environment Model. *Adv Ther* **2016**, *33* (1), 96–115. https://doi.org/10.1007/s12325-015-0274-5.

[78] Stephenson, M. Dry Eye: What's in the Pipeline? Review of Ophthalmology Website. Available online: https://www.reviewofophthalmology.com/article/dry-eye-whats-in-the-pipeline-2021 (Accessed on: 08 December 2021).

[79] Han, H.; Li, S.; Xu, M.; Zhong, Y.; Fan, W.; Xu, J.; Zhou, T.; Ji, J.; Ye, J.; Yao, K. Polymer- and Lipid-Based Nanocarriers for Ocular Drug Delivery: Current Status and Future Perspectives. *Adv Drug Deliv Rev* **2023**, *196*, 114770. https://doi.org/10.1016/J.ADDR.2023.114770.

[80] Karamali, F.; Behtaj, S.; Babaei-Abraki, S.; Hadady, H.; Atefi, A.; Savoj, S.; Soroushzadeh, S.; Najafian, S.; Nasr Esfahani, M. H.; Klassen, H. Potential Therapeutic Strategies for Photoreceptor Degeneration: The Path to Restore Vision. *J Transl Med* **2022**, *20* (1), 572. https://doi.org/10.1186/S12967-022-03738-4.

[81] Tian, B.; Bilsbury, E.; Doherty, S.; Teebagy, S.; Wood, E.; Su, W.; Gao, G.; Lin, H. Ocular Drug Delivery: Advancements and Innovations. *Pharmaceutics* **2022**, *14* (9). https://doi.org/10.3390/PHARMACEUTICS14091931.

[82] Hydrogels, S.; Zemła, J.; Metwally, S.; Wu, K. Y.; Akbar, D.; Giunta, M.; Kalevar, A.; Tran, S. D. Hydrogels in Ophthalmology: Novel Strategies for Overcoming Therapeutic Challenges. *Materials 2024, Vol. 17, Page 86* **2023**, *17* (1), 86. https://doi.org/10.3390/MA17010086.

[83] Hirst, J.; King, M. S.; Pryde, K. R. The Production of Reactive Oxygen Species by Complex I. *Biochem Soc Trans* **2008**, *36* (5), 976–980. https://doi.org/10.1042/BST0360976.

[84] Zorov, D. B.; Juhaszova, M.; Sollott, S. J. Mitochondrial Reactive Oxygen Species (ROS) and ROS-Induced ROS Release. *Physiol Rev* **2014**, *94* (3), 909–950. https://doi.org/10.1152/physrev.00026.2013.

[85] Agrawal, A.; Mabalirajan, U. Rejuvenating Cellular Respiration for Optimizing Respiratory Function: Targeting Mitochondria. *Am J Physiol Lung Cell Mol Physiol* **2016**, *310* (2), L103–L113. https://doi.org/10.1152/ajplung.00320.2015.

[86] Scialò, F.; Fernández-Ayala, D. J.; Sanz, A. Role of Mitochondrial Reverse Electron Transport in ROS Signaling: Potential Roles in Health and Disease. *Front Physiol* **2017**, *8* (JUN), 1–7. https://doi.org/10.3389/fphys.2017.00428.

[87] Valko, M.; Leibfritz, D.; Moncol, J.; Cronin, M. T. D.; Mazur, M.; Telser, J. Free Radicals and Antioxidants in Normal Physiological Functions and Human Disease. *International Journal of Biochemistry and Cell Biology* **2007**, *39* (1), 44–84. https://doi.org/10.1016/j.biocel.2006.07.001.

[88] Jomova, K.; Valko, M. Free Radicals, Signal Transduction, and Human Disease. *Oxidative Stress in Vertebrates and Invertebrates: Molecular Aspects of Cell Signaling* **2011**, No. November 2011, 17–32. https://doi.org/10.1002/9781118148143.ch2.

[89] Umapathy, A.; Donaldson, P.; Lim, J. Antioxidant Delivery Pathways in the Anterior Eye. *Biomed Res Int* **2013**, *2013*. https://doi.org/10.1155/2013/207250.

[90] Zhang, J.; Wang, X.; Vikash, V.; Ye, Q.; Wu, D.; Liu, Y.; Dong, W. ROS and ROS-Mediated Cellular Signaling. *Oxid Med Cell Longev* **2016**, *2016* (4350965). https://doi.org/10.1155/2016/4350965.

[91] Redza-Dutordoir, M.; Averill-Bates, D. A. Activation of Apoptosis Signalling Pathways by Reactive Oxygen Species. *Biochim Biophys Acta Mol Cell Res* **2016**, *1863* (12), 2977–2992. https://doi.org/10.1016/j.bbamcr.2016.09.012.

[92] Son, Y.; Kim, S.; Chung, H. T.; Pae, H. O. *Reactive Oxygen Species in the Activation of MAP Kinases*, 1st ed.; Elsevier Inc., 2013; Vol. 528. https://doi.org/10.1016/B978-0-12-405881-1.00002-1.

[93] Zhang, W.; Liu, H. T. MAPK Signal Pathways in the Regulation of Cell Proliferation in Mammalian Cells. *Cell Res* **2002**, *12* (1), 9–18. https://doi.org/10.1007/BF00568631.

[94] Selim, K.; Abdelrasoul, H.; Aboelmagd, M.; Tawila, A. The Role of the MAPK Signaling, Topoisomerase and Dietary Bioactives in Controlling Cancer Incidence. *Diseases* **2017**, *5* (13). https://doi.org/10.3390/diseases5020013.

[95] Kansanen, E.; Kuosmanen, S. M.; Leinonen, H.; Levonenn, A. L. The Keap1-Nrf2 Pathway: Mechanisms of Activation and Dysregulation in Cancer. *Redox Biol* **2013**, *1* (1), 45–49. https://doi.org/10.1016/j.redox.2012.10.001.

[96] Bellezza, I.; Giambanco, I.; Minelli, A.; Donato, R. Nrf2-Keap1 Signaling in Oxidative and Reductive Stress. *Biochim Biophys Acta Mol Cell Res* **2018**, *1865* (5), 721–733. https://doi.org/10.1016/j.bbamcr.2018.02.010.

[97] Batliwala, S.; Xavier, C.; Liu, Y.; Wu, H.; Pang, I.-H. Involvement of Nrf2 in Ocular Diseases. *Oxid Med Cell Longev* **2017**, *2017*, 18. https://doi.org/10.1155/2017/1703810.

[98] Ali, S. S.; Ahsan, H.; Zia, M. K.; Siddiqui, T.; Khan, F. H. Understanding Oxidants and Antioxidants: Classical Team with New Players. *J Food Biochem* **2020**, *44* (3), 1–13. https://doi.org/10.1111/jfbc.13145.

[99] Ankamah, E.; Sebag, J.; Ng, E.; Nolan, J. M. Vitreous Antioxidants , Degeneration , and Vitreo-Retinopathy : Exploring the Links. **2020**, 1–20.

[100] Boddu, S.; Gupta, H.; Patel, S. Drug Delivery to the Back of the Eye Following Topical Administration: An Update on Research and Patenting Activity. *Recent Pat. Drug Deliv. Formul.* **2014**, *8* (1), 27–36. https://doi.org/10.2174/1872211308666140130093301.

[101] Cabrera, M. P.; Chihuailaf, R. H. Antioxidants and the Integrity of Ocular Tissues. *Vet Med Int* **2011**, *2011*, 8. https://doi.org/10.4061/2011/905153.

[102] Verdin, E. NAD+ in Aging, Metabolism, and Neurodegeneration. *Science (1979)* **2015**, *350* (6265), 1208–1213. https://doi.org/10.1126/science.aac4854.

[103] Khansari, N.; Shakiba, Y.; Mahmoudi, M. Chronic Inflammation and Oxidative Stress as a Major Cause of Age- Related Diseases and Cancer. *Recent Pat Inflamm Allergy Drug Discov* **2009**, *3* (1), 73–80. https://doi.org/10.2174/187221309787158371.

[104] Kamel, K.; Farrell, M.; O'Brien, C. Mitochondrial Dysfunction in Ocular Disease: Focus on Glaucoma. *Mitochondrion* **2017**, *35* (March), 44–53. https://doi.org/10.1016/j.mito.2017.05.004.

[105] Sachdeva, M. M.; Cano, M.; Handa, J. T. Nrf2 Signaling Is Impaired in the Aging RPE given an Oxidative Insult. *Exp Eye Res* **2014**, *119*, 111–114. https://doi.org/10.1016/j.exer.2013.10.024.

[106] Bungau, S.; Abdel-Daim, M. M.; Tit, D. M.; Ghanem, E.; Sato, S.; Maruyama-Inoue, M.; Yamane, S.; Kadonosono, K. Health Benefits of Polyphenols and Carotenoids in Age-Related Eye Diseases. *Oxid Med Cell Longev* **2019**, *2019*, 22. https://doi.org/10.1155/2019/9783429.

[107] Zhou, Y.; Jiang, Z.; Lu, H.; Xu, Z.; Tong, R.; Shi, J.; Jia, G. Recent Advances of Natural Polyphenols Activators for Keap1-Nrf2 Signaling Pathway. *Chem Biodivers* **2019**, *16* (11). https://doi.org/10.1002/cbdv.201900400.

[108] Ceravolo, I.; Mannino, F.; Irrera, N.; Squadrito, F.; Altavilla, D.; Ceravolo, G.; Pallio, G.; Minutoli, L. Health Potential of Aloe Vera against Oxidative Stress Induced Corneal Damage : An " In Vitro " Study. **2021**.

[109] Duncan, R. S.; Hurtado, D. T.; Hall, C. W.; Koulen, P. Differential Mechanisms of Action and Ef Fi Cacy of Vitamin E Components in Antioxidant Cytoprotection of Human Retinal Pigment Epithelium. **2022**, *12* (January), 1–14. https://doi.org/10.3389/fphar.2021.798938.

[110] Yang, M.; Wang, Y. Recent Advances and the Mechanism of Astaxanthin in Ophthalmological Diseases. **2022**, *2022*.

[111] Pang, Y.; Qin, M.; Hu, P.; Ji, K.; Xiao, R. Resveratrol Protects Retinal Ganglion Cells against Ischemia Induced Damage by Increasing Opa1 Expression. **2020**, 1707–1720. https://doi.org/10.3892/ijmm.2020.4711.

[112] Tsai, C.; Woung, L.; Yen, J.; Tseng, P. Thermosensitive Chitosan-Based Hydrogels for Sustained Release of Ferulic Acid on Corneal Wound Healing. *Carbohydr Polym* **2016**, *135*, 308–315. https://doi.org/10.1016/j.carbpol.2015.08.098.

[113] Chen, W.; Ye, Y.; Wu, Z.; Lin, J.; Wang, Y.; Ding, Q.; Yang, X.; Yang, W.; Lin, B.; Lin, B. Temporary Upregulation of Nrf2 by Naringenin Alleviates Oxidative Damage in the Retina and ARPE-19 Cells.

[114] Abengózar-vela, A.; Schaumburg, C. S.; Stern, M. E.; Enríquez-de-salamanca, A.; González-garcía, M. J.; Schaumburg, C. S.; Stern, M. E.; Enríquez-de-salamanca, A.; Topical, M. J. G.; Abengózar-vela, A.; et al. Topical Quercetin and Resveratrol Protect the Ocular Surface in Experimental Dry Eye Disease Topical Quercetin and Resveratrol Protect the Ocular Surface in

Experimental Dry Eye Disease. *Ocul Immunol Inflamm* **2019**, *27* (6), 1023–1032. https://doi.org/10.1080/09273948.2018.1497664.

[115] Zhang, Y.; An, Y.; He, X.; Zhang, D.; He, W. Esculetin Protects Human Corneal Epithelial Cells from Oxidative Stress through Nrf-2 Signaling Pathway. *Exp Eye Res* **2021**, *202* (May 2020), 108360. https://doi.org/10.1016/j.exer.2020.108360.

[116] Ghosh, A. K.; Thapa, R.; Hariani, H. N.; Volyanyuk, M.; Ogle, S. D.; Orloff, K. A.; Ankireddy, S.; Lai, K.; Kalesnykas, G.; Hakkarainen, J. J.; et al. Poly (Lactic-Co-Glycolic Acid) Nanoparticles Encapsulating the Prenylated Flavonoid , Xanthohumol , Protect Corneal Epithelial Cells from Dry Eye Disease-Associated Oxidative Stress. **2021**.

[117] Tohari, A. M.; Almarhoun, M.; Alhasani, R. H.; Biswas, L.; Zhou, X.; Reilly, J.; Zeng, Z.; Shu, X. Protection by Vitamin D against High-Glucose-Induced Damage in Retinal Pigment Epithelial Cells. *Exp Cell Res* **2020**, *392* (1), 112023. https://doi.org/10.1016/J.YEXCR.2020.112023.

[118] Dai, Y.; Zhang, J.; Xiang, J.; Li, Y.; Wu, D.; Xu, J. Calcitriol Inhibits ROS-NLRP3-IL-1β Signaling Axis via Activation of Nrf2-Antioxidant Signaling in Hyperosmotic Stress Stimulated Human Corneal Epithelial Cells. *Redox Biol* **2019**, *21*, 101093. https://doi.org/10.1016/J.REDOX.2018.101093.

[119] Leung, H. H.; · Jean-Marie Galano2; Crauste2, · Céline; Durand2, · Thierry; Lee1, · Jetty Chung-Yung. Combination of Lutein and Zeaxanthin, and DHA Regulated Polyunsaturated Fatty Acid Oxidation in H2O2-Stressed Retinal Cells. Available online: https://sci-hub.se/https://doi.org/10.1007/s11064-020-02994-4 (Accessed on: 31 October 2023).

[120] Johansson, I.; Monsen, V. T.; Pettersen, K.; Mildenberger, J.; Misund, K.; Kaarniranta, K.; Schønberg, S.; Bjørkøy, G. The Marine N-3 PUFA DHA Evokes Cytoprotection against Oxidative Stress and Protein Misfolding by Inducing Autophagy and NFE2L2 in Human Retinal Pigment Epithelial Cells. *Autophagy* **2015**, *11* (9), 1636–1651. https://doi.org/10.1080/15548627.2015.1061170.

[121] Jiao, Y.; Ma, S.; Wang, Y.; Li, J.; Shan, L.; Chen, J. Epigallocatechin-3-Gallate Reduces Cytotoxic Effects Caused by Dental Monomers : A Hypothesis Epigallocatechin-3-Gallate Reduces Cytotoxic Effects Caused by Dental Monomers : A Hypothesis. *Med Sci Monit* **2015**, *21*, 3197–3202. https://doi.org/10.12659/MSM.895628.

[122] Miyagawa, T.; Chen, Z. Y.; Chang, C. Y.; Chen, K. H.; Wang, Y. K.; Liu, G. S.; Tseng, C. L. Topical Application of Hyaluronic Acid-RGD Peptide-Coated Gelatin/Epigallocatechin-3 Gallate (EGCG) Nanoparticles Inhibits Corneal Neovascularization via Inhibition of VEGF Production. *Pharmaceutics* **2020**, *12* (5). https://doi.org/10.3390/pharmaceutics12050404.

[123] Huang, H.-Y.; Wang, M.-C.; Chen, Z.-Y.; Chiu, W.-Y.; Chen, K.-H.; Lin, I.-C.; Yang, W.-C. V.; Wu, C.-C.; Tseng, C.-L. Gelatin-Epigallocatechin Gallate Nanoparticles with Hyaluronic Acid Decoration as Eye Drops Can Treat Rabbit Dry-Eye Syndrome Effectively via Inflammatory Relief. *Int. J. Nanomedicine* **2018**, *Volume 13*, 7251–7273. https://doi.org/10.2147/IJN.S173198.

[124] Hosseini, L.; Vafaee, M. S.; Mahmoudi, J.; Badalzadeh, R. Nicotinamide Adenine Dinucleotide Emerges as a Therapeutic Target in Aging and Ischemic Conditions. *Biogerontology* **2019**, *6*. https://doi.org/10.1007/s10522-019-09805-6.

[125] Hogan, K. A.; Chini, C. C. S.; Chini, E. N. The Multi-Faceted Ecto-Enzyme CD38: Roles in Immunomodulation, Cancer, Aging, and Metabolic Diseases. *Front Immunol* **2019**, *10* (MAY), 1–12. https://doi.org/10.3389/fimmu.2019.01187.

[126] Camacho-Pereira, J.; Tarragó, M. G.; Chini, C. C. S.; Nin, V.; Escande, C.; Warner, G. M.; Puranik, A. S.; Schoon, R. A.; Reid, J. M.; Galina, A.; et al. CD38 Dictates Age-Related NAD Decline and Mitochondrial Dysfunction through an SIRT3-Dependent Mechanism. *Cell Metab* **2016**, *23* (6), 1127–1139. https://doi.org/10.1016/j.cmet.2016.05.006.

[127] Johnson, S.; Imai, S. NAD+ Biosynthesis, Aging, and Disease. *F1000Res* **2018**, *7* (132), 132. https://doi.org/10.12688/f1000research.12120.1.

[128] Xie, N.; Zhang, L.; Gao, W.; Huang, C.; Huber, P. E.; Zhou, X.; Li, C.; Shen, G.; Zou, B. NAD+ Metabolism: Pathophysiologic Mechanisms and Therapeutic Potential. *Signal Transduct Target Ther* **2020**, *5* (227), 1–37. https://doi.org/10.1038/s41392-020-00311-7.

[129] Tribble, J. R.; Hagström, A.; Jusseaume, K.; Lardner, E.; Wong, R. C.-B.; Stålhammar, G.; Williams, P. A. NAD Salvage Pathway Machinery Expression in Normal and Glaucomatous Retina and Optic Nerve. *Acta Neuropathol Commun* **2023**, *11* (1), 18. https://doi.org/10.1186/s40478-023-01513-0.

[130] Yaku, K.; Okabe, K.; Nakagawa, T. NAD Metabolism: Implications in Aging and Longevity. *Ageing Res Rev* **2018**, *47* (June), 1–17. https://doi.org/10.1016/j.arr.2018.05.006.

[131] Billingham, L. K.; Chandel, N. S. NAD-Biosynthetic Pathways Regulate Innate Immunity. *Nat Immunol* **2019**, *20* (4), 380–382. https://doi.org/10.1038/s41590-019-0353-x.

[132] Chiang, B.; Jung, J. H.; Prausnitz, M. R. The Suprachoroidal Space as a Route of Administration to the Posterior Segment of the Eye. *Adv Drug Deliv Rev* **2018**, *126*, 58–66. https://doi.org/10.1016/j.addr.2018.03.001.

[133] Zhou, M.; Luo, J.; Zhang, H. Role of Sirtuin 1 in the Pathogenesis of Ocular Disease (Review). *Int J Mol Med* **2018**, *42* (1), 13–20. https://doi.org/10.3892/ijmm.2018.3623.

[134] Braidy, N.; Liu, Y. NAD+ Therapy in Age-Related Degenerative Disorders: A Benefit/ Risk Analysis. *Exp Gerontol* **2020**, *132* (110831). https://doi.org/10.1016/j.pharmthera.2019.107402.

[135] Cimaglia, G.; Votruba, M.; Morgan, J. E.; Andr, H.; Williams, P. A. Supplementation for Glaucoma and Age-Related Macular Degeneration. *Nutrients* **2020**, *12* (9), 2871. https://doi.org/10.3390/nu12092871.

[136] Williams, P. A.; Harder, J. M.; Foxworth, N. E.; Cochran, K. E.; Philip, V. M.; Porciatti, V.; Smithies, O.; John, S. W. M. Vitamin B3 Modulates Mitochondrial Vulnerability and Prevents Glaucoma in Aged Mice. *Science (1979)* **2017**, *760* (February), 756–760. https://doi.org/10.1120/science.aal0092.

[137] Poddar, S. K.; Sifat, A. E.; Haque, S.; Nahid, N. A.; Chowdhury, S.; Mehedi, I. Nicotinamide Mononucleotide: Exploration of Diverse Therapeutic Applications of a Potential Molecule. *Biomolecules* **2019**, *9* (1). https://doi.org/10.3390/biom9010034.

[138] Nacarelli, T.; Lau, L.; Fukumoto, T.; Zundell, J.; Fatkhytdinov, N.; Wu, S.; Aird, K. M.; Iwasaki, O.; Kossenkov, A. V.; Schultz, D.; et al. NAD+ Metabolism Governs the Proinflammatory Senescence- Associated Secretome. *Nat Cell Biol* **2019**, *21* (3), 397–407. https://doi.org/10.1016/j.physbeh.2017.03.040.

[139] Bai, S.; Sheline, C. T. NAD+ Maintenance Attenuates Light Induced Photoreceptor Degeneration. *Exp Eye Res* **2013**, *108*, 76–83. https://doi.org/10.1016/j.exer.2012.12.007.

[140] Zhu, Y.; Zhao, K. K.; Tong, Y.; Zhou, Y. L.; Wang, Y. X.; Zhao, P. Q.; Wang, Z. Y. Exogenous NAD+ Decreases Oxidative Stress and Protects H2O2-Treated RPE Cells against Necrotic

Death through the up-Regulation of Autophagy. *Sci Rep* **2016**, *6* (January), 1–12. https://doi.org/10.1038/srep26322.

[141] Hui, F.; Tang, J.; Williams, P. A.; McGuinness, M. B.; Hadoux, X.; Casson, R. J.; Coote, M.; Trounce, I. A.; Martin, K. R.; van Wijngaarden, P.; et al. Improvement in Inner Retinal Function in Glaucoma with Nicotinamide (Vitamin B3 Supplementation: A Crossover Randomized Clinical Trial. *Clin Exp Ophthalmol* **2020**, *48* (7), 903–914. https://doi.org/10.1111/ceo.13818.

[142] Ren, C.; Hu, C.; Wu, Y.; Li, T.; Zou, A.; Yu, D.; Shen, T.; Cai, W.; Yu, J. Nicotinamide Mononucleotide Ameliorates Cellular Senescence and Inflammation Caused by Sodium Iodate in RPE. *Oxid Med Cell Longev* **2022**, *2022*. https://doi.org/10.1155/2022/5961123.

[143] Gote, V.; Sikder, S.; Sicotte, J.; Pal, D. Ocular Drug Delivery: Present Innovations and Future Challenges. *Journal of Pharmacology and Experimental Therapeutics* **2019**, *370* (3), 602–624. https://doi.org/10.1124/jpet.119.256933.

[144] Nayak, K.; Misra, M. A Review on Recent Drug Delivery Systems for Posterior Segment of Eye. *Biomedicine and Pharmacotherapy* **2018**, *107* (February), 1564–1582. https://doi.org/10.1016/j.biopha.2018.08.138.

[145] Lakhani, P.; Patil, A.; Majumdar, S. Recent Advances in Topical Nano Drug-Delivery Systems for the Anterior Ocular Segment. *Ther Deliv* **2018**, *9* (2), 137–153. https://doi.org/10.4155/tde-2017-0088.

[146] Wakshull, E.; Quarmby, V.; Mahler, H. C.; Rivers, H.; Jere, D.; Ramos, M.; Szczesny, P.; Bechtold-Peters, K.; Masli, S.; Gupta, S. Advancements in Understanding Immunogenicity of Biotherapeutics in the Intraocular Space. *AAPS Journal* **2017**, *19* (6), 1656–1668. https://doi.org/10.1208/s12248-017-0128-y.

[147] Suri, R.; Beg, S.; Kohli, K. Target Strategies for Drug Delivery Bypassing Ocular Barriers. *J Drug Deliv Sci Technol* **2020**, *55* (October 2019), 101389. https://doi.org/10.1016/j.jddst.2019.101389.

[148] Varela-Fernández, R.; Díaz-Tomé, V.; Luaces-Rodríguez, A.; Conde-Penedo, A.; García-Otero, X.; Luzardo-álvarez, A.; Fernández-Ferreiro, A.; Otero-Espinar, F. J. Drug Delivery to the Posterior Segment of the Eye: Biopharmaceutic and Pharmacokinetic Considerations. *Pharmaceutics* **2020**, *12* (3), 1–39. https://doi.org/10.3390/pharmaceutics12030269.

[149] Young, S. M.; Lim, A. Y. N.; Lang, S. S.; Lee, K. O.; Sundar, G. Efficacy and Safety of Pulsed Intravenous Methylprednisolone in Early Active Thyroid Eye Disease. *Orbit* **2019**, *38* (5), 362–369. https://doi.org/10.1080/01676830.2018.1553189.

[150] Mohammadi, M.; Shahram, F.; Shams, H.; Akhlaghi, M.; Ashofteh, F.; Davatchi, F. High-Dose Intravenous Steroid Pulse Therapy in Ocular Involvement of Behcet's Disease: A Pilot Double-Blind Controlled Study. *Int J Rheum Dis* **2017**, *20* (9), 1269–1276. https://doi.org/10.1111/1756-185X.13095.

[151] Deboer, C. M. T.; Agrawal, R.; Rahimy, E. Novel Oral Medications for Retinal Disease: An Update on Clinical Development. *Curr Opin Ophthalmol* **2023**, *34* (3), 203–210. https://doi.org/10.1097/ICU.0000000000000948.

[152] Karaca, I.; Tran, E. M.; Park, S. W.; Khojasteh, H.; Tran, A. N. T.; Bromeo, A. J.; Akhavanrezayat, A.; Yavari, N.; Yasar, C.; Uludag, G.; et al. Intravenous Cyclophosphamide Therapy for Patients with Severe Ocular Inflammatory Diseases Who Failed Other Immunomodulatory Therapies. *Invest Ophthalmol Vis Sci* **2023**, *64* (8), 3574–3574.

[153] Xu, J.; Xue, Y.; Hu, G.; Lin, T.; Gou, J.; Yin, T.; He, H.; Zhang, Y.; Tang, X. A Comprehensive Review on Contact Lens for Ophthalmic Drug Delivery. *J. Control. Release* **2018**, *281*, 97–118. https://doi.org/10.1016/j.jconrel.2018.05.020.

[154] Vaajanen, A.; Vapaatalo, H. A Single Drop in the Eye – Effects on the Whole Body? *Open Ophthalmol J* **2017**, *11* (1), 305–314. https://doi.org/10.2174/1874364101711010305.

[155] Tao, Y.; Li, C.; Yao, A.; Qu, Y.; Qin, L.; Xiong, Z.; Zhang, J.; Wang, W. Intranasal Administration of Erythropoietin Rescues the Photoreceptors in Degenerative Retina: A Noninvasive Method to Deliver Drugs to the Eye. *Drug Deliv* **2019**, *26* (1), 78–88. https://doi.org/10.1080/10717544.2018.1556361.

[156] Cabrera, F. J.; Wang, D. C.; Reddy, K.; Acharya, G.; Shin, C. S. Challenges and Opportunities for Drug Delivery to the Posterior of the Eye. *Drug Discov. Today* **2019**, *24* (8), 1679–1684. https://doi.org/10.1016/j.drudis.2019.05.035.

[157] Cao, Y.; Samy, K. E.; Bernards, D. A.; Desai, T. A. Recent Advances in Intraocular Sustained-Release Drug Delivery Devices. *Drug Discov. Today* **2019**, *24* (8), 1694–1700. https://doi.org/10.1016/j.drudis.2019.05.031.

[158] Garaszczuk, I. K.; Montes Mico, R.; Iskander, D. R.; Expósito, A. C. The Tear Turnover and Tear Clearance Tests–a Review. *Expert Rev Med Devices* **2018**, *15* (3), 219–229. https://doi.org/10.1080/17434440.2018.1435271.

[159] Achouri, D.; Alhanout, K.; Piccerelle, P.; Andrieu, V. Recent Advances in Ocular Drug Delivery. *Drug Dev Ind Pharm* **2013**, *39* (11), 1599–1617. https://doi.org/10.3109/03639045.2012.736515.

[160] Mundada, A. S. Pharmacokinetics of Drug Delivered through the Ocular Route. In *Update on Polymers for Ocular Drug Delivery*; Smithers Rapra, 2011; pp 5–8.

[161] Sánchez-López, E.; Espina, M.; Doktorovova, S.; Souto, E. B.; García, M. L. Lipid Nanoparticles (SLN, NLC): Overcoming the Anatomical and Physiological Barriers of the Eye – Part I - Barriers and Determining Factors in Ocular Delivery Barriers and Determining Factors in Ocular Deliver. *European Journal of Pharmaceutics and Biopharmaceutics* **2016**, *16*.

[162] Agrahari, V.; Mandal, A.; Agrahari, V.; Trinh, H. M.; Joseph, M.; Ray, A.; Hadji, H.; Mitra, R.; Pal, D.; Mitra, A. K. A Comprehensive Insight on Ocular Pharmacokinetics. *Drug Deliv. and Transl. Res.* **2016**, *6* (6), 735–754. https://doi.org/10.1007/s13346-016-0339-2.

[163] Dartt, D.; Willcox, M. Complexity of the Tear Film: Importance in Homeostasis and Dysfunction during Disease. *Exp. Eye. Res.* **2013**, *117* (1), 1–3. https://doi.org/10.1038/jid.2014.371.

[164] Biorender.com. BioRender. Available online: https://biorender.com/ (Accessed on: 17 January 2022).

[165] Sridhar, M. S. Anatomy of the Cornea and Ocular Surface. *Indian J Ophthalmol* **2018**, *66* (2), 190–194. https://doi.org/10.4103/ijo.IJO.

[166] Tomlinson, A.; Doane, M. G.; McFadyen, A. Inputs and Outputs of the Lacrimal System: Review of Production and Evaporative Loss. *Ocular Surface* **2009**, *7* (4), 186–198. https://doi.org/10.1016/S1542-0124(12)70186-6.

[167] Sánchez-López, E.; Espina, M.; Doktorovova, S.; Souto, E. B.; García, M. L. Lipid Nanoparticles (SLN, NLC): Overcoming the Anatomical and Physiological Barriers of the Eye – Part I – Barriers and Determining Factors in Ocular Delivery. *European Journal of Pharmaceutics and Biopharmaceutics* **2017**, *110*, 70–75. https://doi.org/10.1016/j.ejpb.2016.10.009.

[168] Xu, J.; Xue, Y.; Hu, G.; Lin, T.; Gou, J.; Yin, T.; He, H.; Zhang, Y.; Tang, X. A Comprehensive Review on Contact Lens for Ophthalmic Drug Delivery. *J. Control. Release* **2018**, *281* (May), 97–118. https://doi.org/10.1016/j.jconrel.2018.05.020.

[169] Sebbag, L.; Moody, L. M.; Mochel, J. P. Albumin Levels in Tear Film Modulate the Bioavailability of Medically-Relevant Topical Drugs. *Front Pharmacol* **2020**, *10* (January), 1–9. https://doi.org/10.3389/fphar.2019.01560.

[170] Malhotra, M.; Majumdar, D. K. Permeation through Cornea. *Indian J Exp Biol* **2001**, *39* (1), 11–24.

[171] Pöyry, S.; Vattulainen, I. Role of Charged Lipids in Membrane Structures — Insight given by Simulations. *Biochim Biophys Acta Biomembr* **2016**, *1858* (10), 2322–2333. https://doi.org/10.1016/j.bbamem.2016.03.016.

[172] Liaw, J.; Rojanasakul, Y.; Robinson, J. R. The Effect of Drug Charge Type and Charge Density on Corneal Transport. *Int J Pharm* **1992**, *88* (1–3), 111–124. https://doi.org/10.1016/0378-5173(92)90308-O.

[173] Liu, C.; Tai, L.; Zhang, W.; Wei, G.; Pan, W.; Lu, W. Penetratin, a Potentially Powerful Absorption Enhancer for Noninvasive Intraocular Drug Delivery. *Mol Pharm* **2014**, *11* (4), 1218–1227. https://doi.org/10.1021/MP400681N/SUPPL_FILE/MP400681N_SI_001.PDF.

[174] Balla, A.; Auriola, S.; Grey, A. C.; Demarais, N. J.; Valtari, A.; Heikkinen, E. M.; Toropainen, E.; Urtti, A.; Vellonen, K. S.; Ruponen, M. Partitioning and Spatial Distribution of Drugs in Ocular Surface Tissues. *Pharmaceutics* **2021**, *13* (5), 1–15. https://doi.org/10.3390/pharmaceutics13050658.

[175] Toropainen, E.; Ranta, V. P.; Vellonen, K. S.; Palmgrén, J.; Talvitie, A.; Laavola, M.; Suhonen, P.; Hämäläinen, K. M.; Auriola, S.; Urtti, A. Paracellular and Passive Transcellular Permeability in Immortalized Human Corneal Epithelial Cell Culture Model. *European Journal of Pharmaceutical Sciences* **2003**, *20* (1), 99–106. https://doi.org/10.1016/S0928-0987(03)00173-8.

[176] Kidron, H.; Vellonen, K. S.; Del Amo, E. M.; Tissari, A.; Urtti, A. Prediction of the Corneal Permeability of Drug-like Compounds. *Pharm Res* **2010**, *27* (7), 1398–1407. https://doi.org/10.1007/s11095-010-0132-8.

[177] Laksitorini, M.; Prasasty, V. D.; Kiptoo, P. K.; Siahaan, T. J. Pathways and Progress in Improving Drug Delivery through the Intestinal Mucosa and Blood-Brain Barriers. *Ther Deliv* **2014**, *5* (10), 1143–1163. https://doi.org/10.4155/tde.14.67.

[178] Rijo, J.; Vaswani, H.; Dandekar, P.; Devarajan, P. V. Brain Cancer Receptors and Targeting Strategies. In *Targeted Receptor Mediated Delivery by Intracellular Drug Endocytosis - Volume 39*; Devarajan, P. V., Dandekar, P., D'Souza, A. A., Eds.; Springer Nature Switzerland AG, 2019; pp 45–79. https://doi.org/https://doi.org/10.1007/978-3-030-29168-6.

[179] Campbell, M.; Humphries, P. The Blood-Retina Barrier Tight Junctions and Barrier Modulation. *Adv Exp Med Biol* **2013**, *763*, 70–84. https://doi.org/10.1007/978-1-4614-4711-5_3.

[180] Lee, B.; Moon, K. M.; Kim, C. Y. Tight Junction in the Intestinal Epithelium: Its Association with Diseases and Regulation by Phytochemicals. *J Immunol Res* **2018**, *2018* (Figure 2). https://doi.org/10.1155/2018/2645465.

[181] Hämäläinen, K. M.; Kananen, K.; Auriola, S.; Kontturi, K.; Urtti, A. Characterization of Paracellular and Aqueous Penetration Routes in Cornea, Conjunctiva, and Sclera. *Invest Ophthalmol Vis Sci* **1997**, *38* (3), 627–634.

[182] Edwards, A.; Prausnitz, M. R. Predicted Permeability of the Cornea. *Pharm Res* **2001**, *18* (11), 1497–1508. https://doi.org/10.1023/a:1013061926851.

[183] Shirasaki, Y. Molecular Design for Enhancement of Ocular Penetration. *J Pharm Sci* **2008**, *97* (7), 2462–2496. https://doi.org/10.1002/jps.

[184] Djebli, N.; Khier, S.; Griguer, F.; Coutant, A. L.; Tavernier, A.; Fabre, G.; Leriche, C.; Fabre, D. Ocular Drug Distribution After Topical Administration: Population Pharmacokinetic Model in Rabbits. *Eur J Drug Metab Pharmacokinet* **2017**, *42* (1), 59–68. https://doi.org/10.1007/s13318-016-0319-4.

[185] Zhang, W.; Prausnitz, M. R.; Edwards, A. Model of Transient Drug Diffusion across Cornea. *Journal of Controlled Release* **2004**, *99* (2), 241–258. https://doi.org/10.1016/j.jconrel.2004.07.001.

[186] Suri, R.; Beg, S.; Kohli, K. Target Strategies for Drug Delivery Bypassing Ocular Barriers. *J Drug Deliv Sci Technol* **2020**, *55*, 101389. https://doi.org/10.1016/j.jddst.2019.101389.

[187] Sangly P. Srinivas. Dynamic Regulation of Barrier Integrity of the Corneal Endothelium. *Optometry and Vision Science* **2010**, *87* (4), 239–254. https://doi.org/10.1097/OPX.0b013e3181d39464.Dynamic.

[188] Roy, O.; Leclerc, V. B.; Bourget, J. M.; Thériault, M.; Proulx, S. Understanding the Process of Corneal Endothelial Morphological Change in Vitro. *Invest Ophthalmol Vis Sci* **2015**, *56* (2), 1228–1237. https://doi.org/10.1167/iovs.14-16166.

[189] Urtti, A. Challenges and Obstacles of Ocular Pharmacokinetics and Drug Delivery. *Adv Drug Deliv Rev* **2006**, *58* (11), 1131–1135. https://doi.org/10.1016/j.addr.2006.07.027.

[190] Lee, V. H. l. Review: New Directions in the Optimization of Ocular Drug Delivery. *J Ocul Pharmacol* **1990**, *6* (2), 157–164. https://doi.org/10.1089/jop.1990.6.157.

[191] Hosoya, K. I.; Lee, V. H. L.; Kim, K. J. Roles of the Conjunctiva in Ocular Drug Delivery: A Review of Conjunctival Transport Mechanisms and Their Regulation. *European Journal of Pharmaceutics and Biopharmaceutics* **2005**, *60* (2), 227–240. https://doi.org/10.1016/j.ejpb.2004.12.007.

[192] Hämäläinen, K. M.; Kananen, K.; Auriola, S.; Kontturi, K.; Urtti, A. Characterization of Paracellular and Aqueous Penetration Routes in Cornea, Conjunctiva, and Sclera. *Invest Ophthalmol Vis Sci* **1997**, *38* (3), 627–634.

[193] Ramsay, E.; del Amo, E. M.; Toropainen, E.; Tengvall-Unadike, U.; Ranta, V. P.; Urtti, A.; Ruponen, M. Corneal and Conjunctival Drug Permeability: Systematic Comparison and Pharmacokinetic Impact in the Eye. *European Journal of Pharmaceutical Sciences* **2018**, *119* (January), 83–89. https://doi.org/10.1016/j.ejps.2018.03.034.

[194] Huang, A. J. W.; Tseng, S. C. G.; Kenyon, K. R. Paracellular Permeability of Corneal and Conjunctival Epithelia. *Invest Ophthalmol Vis Sci* **1989**, *30* (4), 684–689.

[195] Geroski, D. H.; Edelhauser, H. F. Transscleral Drug Delivery for Posterior Segment Disease. *Adv Drug Deliv Rev* **2001**, *52* (1), 37–48. https://doi.org/10.1016/S0169-409X(01)00193-4.

[196] Gaudana, R.; Ananthula, H. K.; Parenky, A.; Mitra, A. K. Ocular Drug Delivery. *AAPS J* **2010**, *12* (3), 348–360. https://doi.org/10.1208/s12248-010-9183-3.

[197] Dunlevy, J. R.; Summers Rada, J. A. Interaction of Lumican with Aggrecan in the Aging Human Sclera. *Invest Ophthalmol Vis Sci* **2004**, *45* (11), 3849–3856. https://doi.org/10.1167/iovs.04-0496.

[198] Chopra, P.; Hao, J.; Li, S. K. Iontophoretic Transport of Charged Macromolecules across Human Sclera. *Int J Pharm* **2010**, *388* (1–2), 107–113. https://doi.org/10.1016/j.ijpharm.2009.12.046.

[199] Kim, Y. C.; Chiang, B.; Wu, X.; Prausnitz, M. R. Ocular Delivery of Macromolecules. *Journal of Controlled Release* **2014**, *190*, 172–181. https://doi.org/10.1016/j.jconrel.2014.06.043.

[200] Wen, H.; Hao, J.; Li, S. K. Characterization of Human Sclera Barrier Properties for Transscleral Delivery of Bevacizumab and Ranibizumab. *J Pharm Sci* **2013**, *102* (3), 892–903. https://doi.org/10.1002/jps.23387.

[201] Labelle, P. The Eye. In *Pathologic Basis of Veterinary Disease Expert Consult*; Zachary, J. F., Ed.; Elservier, 2017; pp 1265–1318. https://doi.org/10.1016/B978-0-323-35775-3.00021-7.

[202] Coca-Prados, M. The Blood-Aqueous Barrier in Health and Disease. *J Glaucoma* **2014**, *23* (8), S36–S38. https://doi.org/10.1097/IJG.0000000000000107.

[203] Delamere, N. A. Ciliary Body and Ciliary Epithelium. *Adv Organ Biol* **2005**, *10*, 127–148. https://doi.org/10.1016/S1569-2590(05)10005-6.Ciliary.

[204] Simó, R.; Villarroel, M.; Corraliza, L.; Hernández, C.; Garcia-Ramírez, M. The Retinal Pigment Epithelium: Something More than a Constituent of the Blood-Retinal Barrier-Implications for the Pathogenesis of Diabetic Retinopathy. *J Biomed Biotechnol* **2010**, *2010*. https://doi.org/10.1155/2010/190724.

[205] del Amo, E. M.; Rimpelä, A. K.; Heikkinen, E.; Kari, O. K.; Ramsay, E.; Lajunen, T.; Schmitt, M.; Pelkonen, L.; Bhattacharya, M.; Richardson, D.; et al. Pharmacokinetic Aspects of Retinal Drug Delivery. *Prog. Retin. Eye Res.* **2017**, *57*, 134–185. https://doi.org/10.1016/j.preteyeres.2016.12.001.

[206] Pitkänen, L.; Ranta, V. P.; Moilanen, H.; Urtti, A. Permeability of Retinal Pigment Epithelium: Effects of Permeant Molecular Weight and Lipophilicity. *Investig. Ophthalmol. Vis. Sci.* **2005**, *46* (2), 641–646. https://doi.org/10.1167/iovs.04-1051.

[207] Rimpelä, A. K.; Schmitt, M.; Latonen, S.; Hagström, M.; Antopolsky, M.; Manzanares, J. A.; Kidron, H.; Urtti, A. Drug Distribution to Retinal Pigment Epithelium: Studies on Melanin

Binding, Cellular Kinetics, and Single Photon Emission Computed Tomography/Computed Tomography Imaging. *Mol Pharm* **2016**, *13* (9), 2977–2986. https://doi.org/10.1021/acs.molpharmaceut.5b00787.

[208] Attar, M.; Brassard, J. A.; Kim, A. S.; Matsumoto, S.; Ramos, M.; Vangyi, C. *Safety Evaluation of Ocular Drugs*; 2013. https://doi.org/10.1016/B978-0-12-387815-1.00024-1.

[209] Cheruvu, N. P. S.; Amrite, A. C.; Kompella, U. B. Effect of Eye Pigmentation on Transscleral Drug Delivery. *Invest Ophthalmol Vis Sci* **2008**, *49* (1), 333–341. https://doi.org/10.1167/iovs.07-0214.

[210] Cunha-Vaz, J. The Blood–Retinal Barrier in Retinal Disease. *European Ophthalmic Review* **2009**, *03* (02), 105. https://doi.org/10.17925/eor.2009.03.02.105.

[211] Rattanakijsuntorn, K.; Penkova, A.; Sadha, S. S. Mass Diffusion Coefficient Measurement for Vitreous Humor Using FEM and MRI. *IOP Conf Ser Mater Sci Eng* **2018**, *297*, 012024. https://doi.org/10.1088/1757-899X/297/1/012024.

[212] Penkova, A.; Moats, R.; Humayun, M. S.; Fraser, S.; Sadhal, S. S. Diffusive Transport in the Vitreous Humor: Experimental and Analytical Studies. *J Heat Transfer* **2019**, *141* (5), 1–11. https://doi.org/10.1115/1.4042297.

[213] Johannsdottir, S.; Jansook, P.; Stefansson, E.; Kristinsdottir, I. M.; Fulop, Z.; Asgrimsdottir, G. M.; Thorsteindsottir, M.; Eiriksson, F. F.; Loftsson, T. Topical Drug Delivery to the Posterior Segment of the Eye: Dexamethasone Concentrations in Various Eye Tissues after Topical Administration for up to 15 Days to Rabbits. *J. Drug Deliv. Sci. Technol.* **2018**, *45*, 449–454. https://doi.org/10.1016/j.jddst.2018.04.007.

[214] Chen; Yin; Ma; Tu; Shen. Preparation and Evaluation of Topically Applied Azithromycin Based on Sodium Hyaluronate in Treatment of Conjunctivitis. *Pharmaceutics* **2019**, *11* (4), 183. https://doi.org/10.3390/pharmaceutics11040183.

[215] Jiang, Q.; Zhang, P.; Li, J. Elucidation of Colloid Performances of Thermosensitive in Situ-Forming Ophthalmic Gel Formed by Poloxamer407 for Loading Drugs. *J Pharm Sci* **2020**. https://doi.org/10.1016/j.xphs.2020.01.021.

[216] Kojima, T.; Nagata, T.; Kudo, H.; Müller-Lierheim, W. G. K.; van Setten, G.-B.; Dogru, M.; Tsubota, K. The Effects of High Molecular Weight Hyaluronic Acid Eye Drop Application in

Environmental Dry Eye Stress Model Mice. *Int. J. Mol. Sci.* **2020**, *21* (10), 3516. https://doi.org/10.3390/ijms21103516.

[217] Badiee, P.; Varshochian, R.; Rafiee-Tehrani, M.; Abedin Dorkoosh, F.; Khoshayand, M. R.; Dinarvand, R. Ocular Implant Containing Bevacizumab-Loaded Chitosan Nanoparticles Intended for Choroidal Neovascularization Treatment. *J. Biomed. Mater. Res. - Part A* **2018**, *106* (8), 2261–2271. https://doi.org/10.1002/jbm.a.36424.

[218] Jiang, P.; Chaparro, F. J.; Cuddington, C. T.; Palmer, A. F. Injectable Biodegradable Bi-Layered Capsule for Sustained Delivery of Bevacizumab in Treating Wet Age-Related Macular Degeneration. *Journal of Controlled Release* **2020**, *320* (January), 442–456. https://doi.org/10.1016/j.jconrel.2020.01.036.

[219] Kim, J.; Kudisch, M.; da Silva, N. R. K.; Asada, H.; Aya-Shibuya, E.; Bloomer, M. M.; Mudumba, S.; Bhisitkul, R. B.; Desai, T. A. Long-Term Intraocular Pressure Reduction with Intracameral Polycaprolactone Glaucoma Devices That Deliver a Novel Anti-Glaucoma Agent. *Journal of Controlled Release* **2018**, *269* (November 2017), 45–51. https://doi.org/10.1016/j.jconrel.2017.11.008.

[220] Alvarez-Rivera, F.; Concheiro, A.; Alvarez-Lorenzo, C. Epalrestat-Loaded Silicone Hydrogels as Contact Lenses to Address Diabetic-Eye Complications. *European Journal of Pharmaceutics and Biopharmaceutics* **2018**, *122* (October 2017), 126–136. https://doi.org/10.1016/j.ejpb.2017.10.016.

[221] Mun, J.; Mok, J. W.; Jeong, S.; Cho, S.; Joo, C. K.; Hahn, S. K. Drug-Eluting Contact Lens Containing Cyclosporine-Loaded Cholesterol-Hyaluronate Micelles for Dry Eye Syndrome. *RSC Adv* **2019**, *9* (29), 16578–16585. https://doi.org/10.1039/c9ra02858g.

[222] Deng, J.; Chen, S.; Chen, J.; Ding, H.; Deng, D.; Xie, Z. Self-Reporting Colorimetric Analysis of Drug Release by Molecular Imprinted Structural Color Contact Lens. *ACS Appl Mater Interfaces* **2018**, *10* (40), 34611–34617. https://doi.org/10.1021/acsami.8b11655.

[223] Wei, Y.; Hu, Y.; Shen, X.; Zhang, X.; Guan, J.; Mao, S. Design of Circular-Ring Film Embedded Contact Lens for Improved Compatibility and Sustained Ocular Drug Delivery. *European Journal of Pharmaceutics and Biopharmaceutics* **2020**, *157*, 28–37. https://doi.org/10.1016/j.ejpb.2020.09.010.

[224] Zhu, Q.; Wei, Y.; Li, C.; Mao, S. Inner Layer-Embedded Contact Lenses for Ion-Triggered Controlled Drug Delivery. *Materials Science and Engineering: C* **2018**, *93*, 36–48. https://doi.org/10.1016/j.msec.2018.07.065.

[225] Bian, F.; Shin, C. S.; Wang, C.; Pflugfelder, S. C.; Acharya, G.; de Paiva, C. S. Dexamethasone Drug Eluting Nanowafers Control Inflammation in Alkali-Burned Corneas Associated with Dry Eye. *Invest Ophthalmol Vis Sci* **2016**, *57* (7), 3222–3230. https://doi.org/10.1167/iovs.16-19074.

[226] Coursey, T. G.; Henriksson, J. T.; Marcano, D. C.; Shin, C. S.; Isenhart, L. C.; Ahmed, F.; De Paiva, C. S.; Pflugfelder, S. C.; Acharya, G. Dexamethasone Nanowafer as an Effective Therapy for Dry Eye Disease. *Journal of Controlled Release* **2015**, *213*, 168–174. https://doi.org/10.1016/j.jconrel.2015.07.007.

[227] Abdel-Rashid, R. S.; Helal, D. A.; Omar, M. M.; El Sisi, A. M. Nanogel Loaded with Surfactant Based Nanovesicles for Enhanced Ocular Delivery of Acetazolamide. *Int J Nanomedicine* **2019**, *14*, 2973–2983. https://doi.org/10.2147/IJN.S201891.

[228] Osorno, L. L.; Maldonado, D. E.; Whitener, R. J.; Brandley, A. N.; Yiantsos, A.; Medina, J. D. R.; Byrne, M. E. Amphiphilic PLGA-PEG-PLGA Triblock Copolymer Nanogels Varying in Gelation Temperature and Modulus for the Extended and Controlled Release of Hyaluronic Acid. *J. Appl. Polym. Sci.* **2019**, *48678*, 1–11. https://doi.org/10.1002/app.48678.

[229] Lee, S. H.; Kim, H. J.; Kim, D. H.; Chang, W. S.; Vales, T. P.; Kim, J. W.; Kim, K. H.; Kim, J. K. Thermo-Sensitive Nanogel-Laden Bicontinuous Microemulsion Drug-Eluting Contact Lenses. *J Biomed Mater Res B Appl Biomater* **2018**, *107* (4), 1159–1169. https://doi.org/10.1002/jbm.b.34209.

[230] Gorantla, S.; Rapalli, V. K.; Waghule, T.; Singh, P. P.; Dubey, S. K.; Saha, R. N.; Singhvi, G. Nanocarriers for Ocular Drug Delivery: Current Status and Translational Opportunity. *RSC Adv* **2020**, *10* (46), 27835–27855. https://doi.org/10.1039/d0ra04971a.

[231] Zielinska, A.; Carreiró, F.; Oliveira, A. M.; Neves, A.; Pires, B.; Venkatesh, N.; Durazzo, A.; Lucarini, M.; Eder, P.; Silva, A. M.; et al. Polymeric Nanoparticles: Production, Characterization, Toxicology and Ecotoxicology. *Molecules* **2020**, *25* (16), 3731. https://doi.org/10.1201/9780429031236-8.

[232] Meng, T.; Kulkarni, V.; Simmers, R.; Brar, V.; Xu, Q. Therapeutic Implications of Nanomedicine for Ocular Drug Delivery. *Drug Discov Today* **2019**, *24* (8), 1524–1538. https://doi.org/10.1016/j.drudis.2019.05.006.

[233] Rina Juliana, F.; Kesse, S.; Oti Boakye-Yiadom, K.; Veroniaina, H.; Wang, H.; Sun, M.; Paduano, L.; Luciani, P. Promising Approach in the Treatment of Glaucoma Using Nanotechnology and Nanomedicine-Based Systems. *Molecules* **2019**, *24* (20), 3805. https://doi.org/10.3390/molecules24203805.

[234] Jiang, S.; Franco, Y. L.; Zhou, Y.; Chen, J. Nanotechnology in Retinal Drug Delivery. *Int. J. Ophthalmol.* **2018**, *11* (6), 1038–1044. https://doi.org/10.18240/ijo.2018.06.23.

[235] Luis de Redín, I.; Boiero, C.; Recalde, S.; Agüeros, M.; Allemandi, D.; Llabot, J. M.; García-Layana, A.; Irache, J. M. In Vivo Effect of Bevacizumab-Loaded Albumin Nanoparticles in the Treatment of Corneal Neovascularization. *Exp Eye Res* **2019**, *185*, 107697. https://doi.org/10.1016/j.exer.2019.107697.

[236] Liu, Y.; Sun, D.; Fan, Q.; Ma, Q.; Dong, Z.; Tao, W.; Tao, H.; Liu, Z.; Wang, C. The Enhanced Permeability and Retention Effect Based Nanomedicine at the Site of Injury. *Nano Res* **2020**, *13* (2), 564–569. https://doi.org/10.1007/s12274-020-2655-6.

[237] López-Machado, A.; Díaz, N.; Cano, A.; Espina, M.; Badía, J.; Baldomà, L.; Calpena, A. C.; Biancardi, M.; Souto, E. B.; García, M. L.; et al. Development of Topical Eye-Drops of Lactoferrin-Loaded Biodegradable Nanoparticles for the Treatment of Anterior Segment Inflammatory Processes. *Int J Pharm* **2021**, *609* (June), 121188. https://doi.org/10.1016/j.ijpharm.2021.121188.

[238] Warsi, M. H. Development and Optimization of Vitamin E TPGS Based PLGA Nanoparticles for Improved and Safe Ocular Delivery of Ketorolac. *J Drug Deliv Sci Technol* **2021**, *61*, 102121. https://doi.org/10.1016/j.jddst.2020.102121.

[239] Koo, H.; Moon, H.; Han, H.; Na, J. H.; Huh, M. S.; Park, J. H.; Woo, S. J.; Park, K. H.; Chan Kwon, I.; Kim, K.; et al. The Movement of Self-Assembled Amphiphilic Polymeric Nanoparticles in the Vitreous and Retina after Intravitreal Injection. *Biomaterials* **2012**, *33* (12), 3485–3493. https://doi.org/10.1016/j.biomaterials.2012.01.030.

[240] Zhu, S.; Gong, L.; Li, Y.; Xu, H.; Gu, Z.; Zhao Zhu, Y. S.; Gong, L.; Gu, Z.; Zhao, Y.; Li, Y.; et al. Safety Assessment of Nanomaterials to Eyes: An Important but Neglected Issue. *Advanced Science News* **2019**, *6* (1802289), 1–16. https://doi.org/10.1002/advs.201802289.

[241] Taghe, S.; Mirzaeei, S. Preparation and Characterization of Novel, Mucoadhesive of Loxacin Nanoparticles for Ocular Drug Delivery. *Brazilian Journal of Pharmaceutical Sciences* **2019**, *55*, 1–12. https://doi.org/10.1590/s2175-97902019000117105.

[242] Ikuta, Y.; Aoyagi, S.; Tanaka, Y.; Sato, K.; Inada, S.; Koseki, Y.; Onodera, T.; Oikawa, H.; Kasai, H. Creation of Nano Eye-Drops and Effective Drug Delivery to the Interior of the Eye. *Sci Rep* **2017**, *7*, 1–10. https://doi.org/10.1038/srep44229.

[243] Ibrahim, M. M.; Abd-Elgawad, A.-E. H.; Soliman, O. A.-E.; Jablonski, M. M. Natural Bioadhesive Biodegradable Nanoparticle-Based Topical Ophthalmic Formulations for Management of Glaucoma. *Transl Vis Sci Technol* **2015**, *4* (3), 12. https://doi.org/10.1167/tvst.4.3.12.

[244] Natarajan, J. V.; Darwitan, A.; Barathi, V. A.; Ang, M.; Htoon, H. M.; Boey, F.; Tam, K. C.; Wong, T. T.; Venkatraman, S. S. Sustained Drug Release in Nanomedicine: A Long-Acting Nanocarrier-Based Formulation for Glaucoma. *ACS Nano* **2014**, *8* (1), 419–429. https://doi.org/10.1021/nn4046024.

[245] Huang, J.; Peng, T.; Li, Y.; Zhan, Z.; Zeng, Y.; Huang, Y.; Pan, X.; Wu, C. Y.; Wu, C. Ocular Cubosome Drug Delivery System for Timolol Maleate: Preparation, Characterization, Cytotoxicity, Ex Vivo, and In Vivo Evaluation. *AAPS PharmSciTech* **2017**, *18* (8), 2919–2926. https://doi.org/10.1208/s12249-017-0763-8.

[246] Karami, Z.; Hamidi, M. Cubosomes: Remarkable Drug Delivery Potential. *Drug Discov Today* **2016**, *21* (5), 789–801. https://doi.org/10.1016/j.drudis.2016.01.004.

[247] Omerović, N.; Vranić, E. Application of Nanoparticles in Ocular Drug Delivery Systems. *Health Technol (Berl)* **2020**, *10* (1), 61–78. https://doi.org/10.1007/s12553-019-00381-w.

[248] Silva, M. M.; Calado, R.; Marto, J.; Bettencourt, A.; Almeida, A. J.; Gonçalves, L. M. D. Chitosan Nanoparticles as a Mucoadhesive Drug Delivery System for Ocular Administration. *Mar Drugs* **2017**, *15* (12), 1–16. https://doi.org/10.3390/md15120370.

[249] Ma, Q.; Gao, Y.; Sun, W.; Cao, J.; Liang, Y.; Han, S.; Wang, X.; Sun, Y. Self-Assembled Chitosan / Phospholipid Nanoparticles : From Fundamentals to Preparation for Advanced Drug Delivery. *Drug Deliv* **2020**, *27* (1), 200–215. https://doi.org/10.1080/10717544.2020.1716878.

[250] Kalam, M. A. Development of Chitosan Nanoparticles Coated with Hyaluronic Acid for Topical Ocular Delivery of Dexamethasone. *Int. J. Biol. Macromol.* **2016**, *89*, 127–136. https://doi.org/10.1016/j.ijbiomac.2016.04.070.

[251] Kianersi, S.; Solouk, A.; Saber-Samandari, S.; Keshel, S. H.; Pasbakhsh, P. Alginate Nanoparticles as Ocular Drug Delivery Carriers. *J Drug Deliv Sci Technol* **2021**, *66* (September), 102889. https://doi.org/10.1016/j.jddst.2021.102889.

[252] Mahaling, B.; Katti, D. S. Physicochemical Properties of Core-Shell Type Nanoparticles Govern Their Spatiotemporal Biodistribution in the Eye. *Nanomedicine* **2016**, *12* (7), 2149–2160. https://doi.org/10.1016/j.nano.2016.05.017.

[253] Li, J.; Cheng, T.; Tian, Q.; Cheng, Y.; Zhao, L.; Zhang, X.; Qu, Y. A More Efficient Ocular Delivery System of Triamcinolone Acetonide as Eye Drop to the Posterior Segment of the Eye. *Drug Deliv* **2019**, *26* (1), 188–198. https://doi.org/10.1080/10717544.2019.1571122.

[254] Radwan, S. E. S.; El-Kamel, A.; Zaki, E. I.; Burgalassi, S.; Zucchetti, E.; El-Moslemany, R. M. Hyaluronic-Coated Albumin Nanoparticles for the Non-Invasive Delivery of Apatinib in Diabetic Retinopathy. *Int. J. Nanomedicine* **2021**, *16*, 4481–4494. https://doi.org/10.2147/IJN.S316564.

[255] Mattheolabakis, G.; Milane, L.; Singh, A.; Amiji, M. M. Hyaluronic Acid Targeting of CD44 for Cancer Therapy: From Receptor Biology to Nanomedicine. *J Drug Target* **2015**, *23* (7–8), 605–618. https://doi.org/10.3109/1061186X.2015.1052072.

[256] Kwon, M. Y.; Wang, C.; Galarraga, J. H.; Puré, E.; Han, L.; Burdick, J. A. Influence of Hyaluronic Acid Modification on CD44 Binding towards the Design of Hydrogel Biomaterials. *Biomaterials* **2019**, *222*, 119451. https://doi.org/10.1016/j.biomaterials.2019.119451.

[257] Sagbas Suner, S.; Ari, B.; Onder, F. C.; Ozpolat, B.; Ay, M.; Sahiner, N. Hyaluronic Acid and Hyaluronic Acid: Sucrose Nanogels for Hydrophobic Cancer Drug Delivery. *Int J Biol Macromol* **2019**, *126* (August), 1150–1157. https://doi.org/10.1016/j.ijbiomac.2019.01.021.

[258] Yao, J.; Zhang, L.; Zhou, J.; Liu, H.; Zhang, Q. Efficient Simultaneous Tumor Targeting Delivery of All-Trans Retinoid Acid and Paclitaxel Based on Hyaluronic Acid-Based Multifunctional Nanocarrier. *Molecular Pharmaceutics*. 2013, pp 1080–1091. https://doi.org/10.1021/mp3005808.

[259] Zhong, Y.; Zhang, J.; Cheng, R.; Deng, C.; Meng, F.; Xie, F.; Zhong, Z. Reversibly Crosslinked Hyaluronic Acid Nanoparticles for Active Targeting and Intelligent Delivery of Doxorubicin to Drug Resistant CD44 + Human Breast Tumor Xenografts. *Journal of Controlled Release* **2015**, *205*, 144–154. https://doi.org/10.1016/j.jconrel.2015.01.012.

[260] Chandola, C.; Casteleijn, M. G.; Chandola, U. M.; Gopalan, L. N.; Urtti, A.; Neerathilingam, M. CD44 Aptamer Mediated Cargo Delivery to Lysosomes of Retinal Pigment Epithelial Cells to Prevent Age-Related Macular Degeneration. *Biochem Biophys Rep* **2019**, *18* (May), 100642. https://doi.org/10.1016/j.bbrep.2019.100642.

[261] Gote, V.; Sikder, S.; Sicotte, J.; Pal, D. Ocular Drug Delivery: Present Innovations and Future Challenges. *Journal of Pharmacology and Experimental Therapeutics* **2019**, *370* (3), 602–624. https://doi.org/10.1124/jpet.119.256933.

[262] Huang, D.; Chen, Y. S.; Rupenthal, I. D. Hyaluronic Acid Coated Albumin Nanoparticles for Targeted Peptide Delivery to the Retina. *Mol. Pharm.* **2017**, *14* (2), 533–545. https://doi.org/10.1021/acs.molpharmaceut.6b01029.

[263] Amoabediny, G.; Haghiralsadat, F.; Naderinezhad, S.; Helder, M. N.; Akhoundi Kharanaghi, E.; Mohammadnejad Arough, J.; Zandieh-Doulabi, B. Overview of Preparation Methods of Polymeric and Lipid-Based (Niosome, Solid Lipid, Liposome) Nanoparticles: A Comprehensive Review. *International Journal of Polymeric Materials and Polymeric Biomaterials* **2018**, *67* (6), 383–400. https://doi.org/10.1080/00914037.2017.1332623.

[264] Wang, Y.; Li, P.; Tran, T. T. D.; Zhang, J.; Kong, L. Manufacturing Techniques and Surface Engineering of Polymer Based Nanoparticles for Targeted Drug Delivery to Cancer. *Nanomaterials* **2016**, *6* (2), 26. https://doi.org/10.3390/nano6020026.

[265] Ealias, A. M.; Saravanakumar, M. P. A Review on the Classification, Characterisation, Synthesis of Nanoparticles and Their Application. *IOP Conf Ser Mater Sci Eng* **2017**, *263* (3). https://doi.org/10.1088/1757-899X/263/3/032019.

[266] Sur, S.; Rathore, A.; Dave, V.; Reddy, K. R.; Chouhan, R. S.; Sadhu, V. Recent Developments in Functionalized Polymer Nanoparticles for Efficient Drug Delivery System. *Nano-Structures and Nano-Objects* **2019**, *20*, 100397. https://doi.org/10.1016/j.nanoso.2019.100397.

[267] Rodrigues, P. R.; Vieira, R. P. Advances in Atom-Transfer Radical Polymerization for Drug Delivery Applications. *Eur Polym J* **2019**, *115* (February), 45–58. https://doi.org/10.1016/j.eurpolymj.2019.03.023.

[268] Barreras-Urbina, C. G.; Ramírez-Wong, B.; López-Ahumada, G. A.; Burruel-Ibarra, S. E.; Martínez-Cruz, O.; Tapia-Hernández, J. A.; Rodríguez Félix, F. Nano- and Micro-Particles by Nanoprecipitation: Possible Application in the Food and Agricultural Industries. *Int J Food Prop* **2016**, *19* (9), 1912–1923. https://doi.org/10.1080/10942912.2015.1089279.

[269] Mishra, V.; Bansal, K. K.; Verma, A.; Yadav, N.; Thakur, S.; Sudhakar, K.; Rosenholm, J. M. Solid Lipid Nanoparticles: Emerging Colloidal Nano Drug Delivery Systems. *Pharmaceutics* **2018**, *10* (4), 191. https://doi.org/10.3390/pharmaceutics10040191.

[270] Ganesan, P.; Narayanasamy, D. Lipid Nanoparticles: Different Preparation Techniques, Characterization, Hurdles, and Strategies for the Production of Solid Lipid Nanoparticles and Nanostructured Lipid Carriers for Oral Drug Delivery. *Sustain Chem Pharm* **2017**, *6* (August), 37–56. https://doi.org/10.1016/j.scp.2017.07.002.

[271] Arredondo-Ochoa, T.; Silva-Martínez, G. A. Microemulsion Based Nanostructures for Drug Delivery. *Frontiers in Nanotechnology* **2022**, *3*, 753947. https://doi.org/10.3389/FNANO.2021.753947/BIBTEX.

[272] Pande, S. Liposomes for Drug Delivery: Review of Vesicular Composition, Factors Affecting Drug Release and Drug Loading in Liposomes. *Artif Cells Nanomed Biotechnol* **2023**, *51* (1), 428–440. https://doi.org/10.1080/21691401.2023.2247036.

[273] Malakouti-Nejad, M.; Bardania, H.; Aliakbari, F.; Baradaran-Rafii, A.; Elahi, E.; Monti, D.; Morshedi, D. Formulation of Nanoliposome-Encapsulated Bevacizumab (Avastin): Statistical Optimization for Enhanced Drug Encapsulation and Properties Evaluation. *Int J Pharm* **2020**, *590*, 119895. https://doi.org/10.1016/J.IJPHARM.2020.119895.

[274] Shirakawa, M.; Nakai, K.; Sato, Y.; Nakamura, S.; Harada, M.; Ishihara, K.; Yoshida, F.; Matsumura, A.; Tomida, H. Optimization of Preparation Methods for High Loading Content and

High Encapsulation Efficiency of BSH into Liposomes. *Applied Radiation and Isotopes* **2021**, *169*, 109260. https://doi.org/10.1016/J.APRADISO.2020.109260.

[275] Gonzalez Gomez, A.; Syed, S.; Marshall, K.; Hosseinidoust, Z. Liposomal Nanovesicles for Efficient Encapsulation of Staphylococcal Antibiotics. *ACS Omega* **2019**, *4* (6), 10866–10876. https://doi.org/10.1021/ACSOMEGA.9B00825/ASSET/IMAGES/MEDIUM/AO-2019-008254_M001.GIF.

[276] Pandit, S.; Roy, S.; Pillai, J.; Banerjee, S. Formulation and Intracellular Trafficking of Lipid-Drug Conjugate Nanoparticles Containing a Hydrophilic Antitubercular Drug for Improved Intracellular Delivery to Human Macrophages. *ACS Omega* **2020**, *5* (9), 4433–4448. https://doi.org/10.1021/acsomega.9b03523.

[277] Becker Peres, L.; Becker Peres, L.; de Araújo, P. H. H.; Sayer, C. Solid Lipid Nanoparticles for Encapsulation of Hydrophilic Drugs by an Organic Solvent Free Double Emulsion Technique. *Colloids Surf B Biointerfaces* **2016**, *140*, 317–323. https://doi.org/10.1016/j.colsurfb.2015.12.033.

[278] Dragan, E. S.; Dinu, M. V. Polysaccharides Constructed Hydrogels as Vehicles for Proteins and Peptides. A Review. *Carbohydr Polym* **2019**, *225* (May), 115210. https://doi.org/10.1016/j.carbpol.2019.115210.

[279] Quiñones, J. P.; Brüggemann, O.; Covas, C. P.; Ossipov, D. A. Self-Assembled Hyaluronic Acid Nanoparticles for Controlled Release of Agrochemicals and Diosgenin. *Carbohydr Polym* **2017**, *173*, 157–169. https://doi.org/10.1016/j.carbpol.2017.05.048.

[280] Rho, J. G.; Han, H. S.; Han, J. H.; Lee, H.; Nguyen, V. Q.; Lee, W. H.; Kwon, S.; Heo, S.; Yoon, J.; Shin, H. H.; et al. Self-Assembled Hyaluronic Acid Nanoparticles: Implications as a Nanomedicine for Treatment of Type 2 Diabetes. *Journal of Controlled Release* **2018**, *279* (March), 89–98. https://doi.org/10.1016/j.jconrel.2018.04.006.

[281] Gonçalves, C.; Pereira, P.; Gama, M. Self-Assembled Hydrogel Nanoparticles for Drug Delivery Applications. *Materials* **2010**, *3* (2), 1420–1460. https://doi.org/10.3390/ma3021420.

[282] Shah, S.; Eyler, A.; Tabandeh, S.; Leon, L. Electrostatically Driven Self-Assembled Nanoparticles and Coatings. In *Nanoparticles for Biomedical Applications*; Chung, E. J.,

Rinaldi, L., Leon, C., Eds.; Elsevier, 2020; pp 349–370. https://doi.org/10.1016/B978-0-12-816662-8.00020-5.

[283] Ou, Z.; Muthukumar, M. Entropy and Enthalpy of Polyelectrolyte Complexation: Langevin Dynamics Simulations. *J. Chem. Phys.* **2006**, *124* (154902). https://doi.org/10.1063/1.2178803.

[284] Srivastava, S.; Tirrell, M. V. Polyelectrolyte Complexation. In *Advances in Chemical Physics*; Rice, S. A., Dinner, A. R., Eds.; 2016; Vol. 161, pp 499–544.

[285] Philipp, B.; Dautzenberg, H.; Linow, K. J.; Kötz, J.; Dawydoff, W. Polyelectrolyte Complexes - Recent Developments and Open Problems. *Prog. Polym. Sci.* **1989**, *14* (1), 91–172. https://doi.org/10.1016/0079-6700(89)90018-X.

[286] Inamdar, N.; Mourya, V. K. Chitosan and Anionic Polymers - Complex Formation and Applications. In *Polysaccharides: Development, Properties and Applications*; 2010; pp 333–377.

[287] Gucht, J. van der; Spruijt, E.; Lemmers, M.; Cohen Stuart, M. A. Polyelectrolyte Complexes: Bulk Phases and Colloidal Systems. *J. Colloid Interface Sci.* **2011**, *361* (2), 407–422. https://doi.org/10.1016/j.jcis.2011.05.080.

[288] Leite, E. R.; Ribeiro, C. Basic Principles: Thermodynamics and Colloidal Chemistry. In *Crystallization and Growth of Colloidal Nanocrystals*; Springer Verlag: New York, 2012; pp 7–17. https://doi.org/10.1007/978-1-4614-1308-0_2.

[289] Casey-Power, S.; Ryan, R.; Behl, G.; McLoughlin, P.; Byrne, M. E.; Fitzhenry, L. Hyaluronic Acid: Its Versatile Use in Ocular Drug Delivery with a Specific Focus on Hyaluronic Acid-Based Polyelectrolyte Complexes. *Pharmaceutics* **2022**, *14* (7), 1–41. https://doi.org/10.3390/pharmaceutics14071479.

[290] Wang, Q.; Schlenoff, J. B. The Polyelectrolyte Complex/Coacervate Continuum. *Macromolecules* **2014**, *47* (9), 3108–3116. https://doi.org/10.1021/ma500500q.

[291] Van Le, H.; Dulong, V.; Picton, L.; Le Cerf, D. Polyelectrolyte Complexes of Hyaluronic Acid and Diethylaminoethyl Dextran: Formation, Stability and Hydrophobicity. *Colloids Surfaces A Physicochem. Eng. Asp.* **2021**, *629* (September), 127485. https://doi.org/10.1016/j.colsurfa.2021.127485.

[292] Thünemann, A. F.; Müller, M.; Dautzenberg, H.; Joanny, J.-F.; Löwen, H. Polyelectrolytes with Defined Molecular Architecture II. In *Adv Polym Sci*; Springer Berlin Heidelberg, 2004; Vol. 166, pp 113–171. https://doi.org/10.1007/b11350.

[293] Koetz, J.; Kosmella, S. Semi Diluted Polyanion-Polycation Systems (Turbid Polyelectolyte Complexes). In *Polyelectrolytes and Nanoparticles*; Barth, H. G., Pasch, H., Eds.; Springer-Verlag Berlin Heidelberg: New York, 2007; pp 41–43.

[294] Villamizar-Sarmiento, M. G.; Moreno-Villoslada, I.; Martínez, S.; Giacaman, A.; Miranda, V.; Vidal, A.; Orellana, S. L.; Concha, M.; Pavicic, F.; Lisoni, J. G.; et al. Ionic Nanocomplexes of Hyaluronic Acid and Polyarginine to Form Solid Materials: A Green Methodology to Obtain Sponges with Biomedical Potential. *Nanomaterials* **2019**, *9* (7). https://doi.org/10.3390/nano9070944.

[295] Hartig, S. M.; Greene, R. R.; Dikov, M. M.; Prokop, A.; Davidson, J. M. Multifunctional Nanoparticulate Polyelectrolyte Complexes. *Pharm. Res.* **2007**, *24* (12), 2353–2369. https://doi.org/10.1007/s11095-007-9459-1.

[296] Kulkarni, A. D.; Vanjari, Y. H.; Sancheti, K. H.; Patel, H. M.; Belgamwar, V. S.; Surana, S. J.; Pardeshi, C. V. Polyelectrolyte Complexes: Mechanisms, Critical Experimental Aspects, and Applications. *Artif. Cells, Nanomedicine Biotechnol.* **2016**, *44* (7), 1615–1625. https://doi.org/10.3109/21691401.2015.1129624.

[297] Sæther, H. V.; Holme, H. K.; Maurstad, G.; Smidsrød, O.; Stokke, B. T. Polyelectrolyte Complex Formation Using Alginate and Chitosan. *Carbohydr Polym* **2008**, *74* (4), 813–821. https://doi.org/10.1016/j.carbpol.2008.04.048.

[298] Mohammed, A. S. A.; Naveed, M.; Jost, N. Polysaccharides; Classification, Chemical Properties, and Future Perspective Applications in Fields of Pharmacology and Biological Medicine (A Review of Current Applications and Upcoming Potentialities). *J Polym Environ* **2021**, *29* (8), 2359. https://doi.org/10.1007/S10924-021-02052-2.

[299] Barclay, T. G.; Day, C. M.; Petrovsky, N.; Garg, S. Review of Polysaccharide Particle-Based Functional Drug Delivery. *Carbohydr Polym* **2019**, *221*, 94–112. https://doi.org/10.1016/j.carbpol.2019.05.067.

[300] Chandra, N. S.; Gorantla, S.; Priya, S.; Singhvi, G. Insight on Updates in Polysaccharides for Ocular Drug Delivery. *Carbohydr Polym* **2022**, *297*, 120014. https://doi.org/10.1016/J.CARBPOL.2022.120014.

[301] Chen, Q.; Yin, C.; Ma, J.; Tu, J.; Shen, Y. Preparation and Evaluation of Topically Applied Azithromycin Based on Sodium Hyaluronate in Treatment of Conjunctivitis. *Pharmaceutics* **2019**, *11* (4). https://doi.org/10.3390/pharmaceutics11040183.

[302] Trombino, S.; Servidio, C.; Curcio, F.; Cassano, R. Strategies for Hyaluronic Acid-Based Hydrogel Design in Drug Delivery. *Pharmaceutics* **2019**, *11* (8), 1–17. https://doi.org/10.3390/pharmaceutics11080407.

[303] Ferreira, L. M. B.; dos Santos, A. M.; Boni, F. I.; dos Santos, K. C.; Robusti, L. M. G.; de Souza, M. P. C.; Ferreira, N. N.; Carvalho, S. G.; Cardoso, V. M. O.; Chorilli, M.; et al. Design of Chitosan-Based Particle Systems: A Review of the Physicochemical Foundations for Tailored Properties. *Carbohydr Polym* **2020**, *250* (May), 1–20. https://doi.org/10.1016/j.carbpol.2020.116968.

[304] Lapčík, L.; Lapčík, L.; De Smedt, S.; Demeester, J.; Chabreček, P. Hyaluronan: Preparation, Structure, Properties, and Applications. *Chem. Rev.* **1998**, *98* (8). https://doi.org/10.1021/cr941199z.

[305] Dovedytis, M.; Liu, Z. J.; Bartlett, S. Hyaluronic Acid and Its Biomedical Applications: A Review. *Eng. Regen.* **2020**, *1* (October), 102–113. https://doi.org/10.1016/j.engreg.2020.10.001.

[306] Vasvani, S.; Kulkarni, P.; Rawtani, D. Hyaluronic Acid: A Review on Its Biology, Aspects of Drug Delivery, Route of Administrations and a Special Emphasis on Its Approved Marketed Products and Recent Clinical Studies. *Int. J. Biol. Macromol.* **2020**, *151*, 1012–1029. https://doi.org/10.1016/j.ijbiomac.2019.11.066.

[307] Fallacara, A.; Baldini, E.; Manfredini, S.; Vertuani, S. Hyaluronic Acid in the Third Millennium. *Polymers (Basel)* **2018**, *10* (7), 701. https://doi.org/10.3390/polym10070701.

[308] Müller-Lierheim, W. G. K. Why Chain Length of Hyaluronan in Eye Drops Matters. *Diagnostics* **2020**, *10* (8). https://doi.org/10.3390/diagnostics10080511.

[309] Rubenicia, A. M. L.; Cubillan, L. D. P.; Sicam, V. A. D. P.; Macabeo, A. P. G.; Villaflores, O. B.; Castillo, A. L. Intraocular Pressure Reduction Effect of 0.005% Latanoprost Eye Drops in a

Hyaluronic Acid-Chitosan Nanoparticle Drug Delivery System in Albino Rabbits. *Transl. Vis. Sci. Technol.* **2021**, *10* (4), 2–2. https://doi.org/10.1167/TVST.10.4.2.

[310] Sonaje, K.; Chuang, E. Y.; Lin, K. J.; Yen, T. C.; Su, F. Y.; Tseng, M. T.; Sung, H. W. Opening of Epithelial Tight Junctions and Enhancement of Paracellular Permeation by Chitosan: Microscopic, Ultrastructural, and Computed-Tomographic Observations. *Mol Pharm* **2012**, *9* (5), 1271–1279. https://doi.org/10.1021/mp200572t.

[311] Yeh, T.; Hsu, L.; Tseng, M. T.; Lee, P.; Sonjae, K.; Ho, Y.; Sung, H. Mechanism and Consequence of Chitosan-Mediated Reversible Epithelial Tight Junction Opening. *Biomaterials* **2011**, *32* (26), 6164–6173. https://doi.org/10.1016/j.biomaterials.2011.03.056.

[312] Sun, H.; Li, S.; Qi, W.; Xing, R.; Zou, Q.; Yan, X. Stimuli-Responsive Nanoparticles Based on Co-Assembly of Naturally- Occurring Biomacromolecules for in Vitro Photodynamic Therapy. *Colloids and Surfaces A* **2018**, *538*, 795–801.

[313] Mero, A.; Campisi, M. Hyaluronic Acid Bioconjugates for the Delivery of Bioactive Molecules. *Polymers (Basel)* **2014**, *6*, 346–369. https://doi.org/10.3390/polym6020346.

[314] Liao, Y. H.; Jones, S. A.; Forbes, B.; Martin, G. P.; Brown, M. B. Hyaluronan: Pharmaceutical Characterization and Drug Delivery. *Drug Delivery: Journal of Delivery and Targeting of Therapeutic Agents* **2005**, *12* (6), 327–342. https://doi.org/10.1080/10717540590952555.

[315] Grimaudo, M. A.; Amato, G.; Carbone, C.; Diaz-Rodriguez, P.; Musumeci, T.; Concheiro, A.; Alvarez-Lorenzo, C.; Puglisi, G. Micelle-Nanogel Platform for Ferulic Acid Ocular Delivery. *Int. J. Pharm.* **2020**, *576*, 1–9. https://doi.org/10.1016/j.ijpharm.2019.118986.

[316] Kale, N. R.; Dutta, D.; Carstens, W.; Mallik, S.; Quadir, M. Functional Applications of Polyarginine-Hyaluronic Acid-Based Electrostatic Complexes. *Bioelectricity* **2020**, *2* (2), 158–166. https://doi.org/10.1089/bioe.2020.0011.

[317] Wu, D.; Delair, T. Stabilization of Chitosan/Hyaluronan Colloidal Polyelectrolyte Complexes in Physiological Conditions. *Carbohydr. Polym.* **2015**, *119*, 149–158. https://doi.org/10.1016/j.carbpol.2014.11.042.

[318] Chaharband, F.; Daftarian, N.; Kanavi, M. R.; Varshochian, R.; Hajiramezanali, M.; Norouzi, P.; Arefian, E.; Atyabi, F.; Dinarvand, R. Trimethyl Chitosan-Hyaluronic Acid Nano-Polyplexes for Intravitreal VEGFR-2 SiRNA Delivery: Formulation and in Vivo Efficacy Evaluation.

Nanomedicine Nanotechnology, Biol. Med. **2020**, *26* (102181). https://doi.org/10.1016/j.nano.2020.102181.

[319] Matha, K.; Lollo, G.; Taurino, G.; Respaud, R.; Marigo, I.; Shariati, M.; Bussolati, O.; Vermeulen, A.; Remaut, K.; Benoit, J. P. Bioinspired Hyaluronic Acid and Polyarginine Nanoparticles for DACHPt Delivery. *European Journal of Pharmaceutics and Biopharmaceutics* **2020**, *150* (February), 1–13. https://doi.org/10.1016/j.ejpb.2020.02.008.

[320] Tang, J. D.; Caliari, S. R.; Lampe, K. J. Temperature-Dependent Complex Coacervation of Engineered Elastin-like Polypeptide and Hyaluronic Acid Polyelectrolytes. *Biomacromolecules* **2018**, *19* (10), 3925–3935. https://doi.org/10.1021/acs.biomac.8b00837.

[321] Mohammed, M. A.; Syeda, J. T. M.; Wasan, K. M.; Wasan, E. K. An Overview of Chitosan Nanoparticles and Its Application in Non-Parenteral Drug Delivery. *Pharmaceutics* **2017**, *9* (4). https://doi.org/10.3390/pharmaceutics9040053.

[322] Sieval, A. B.; Thanou, M.; Kotzé, A. F.; Verhoef, J. C.; Brussee, J.; Junginger, H. E. Preparation and NMR Characterization of Highly SubstitutedN-Trimethyl Chitosan Chloride. *Carbohydr Polym* **1998**, *36* (2–3), 157–165. https://doi.org/10.1016/S0144-8617(98)00009-5.

[323] Hu, X.; Wang, Y.; Zhang, L.; Xu, M. Construction of Self-Assembled Polyelectrolyte Complex Hydrogel Based on Oppositely Charged Polysaccharides for Sustained Delivery of Green Tea Polyphenols. *Food Chem* **2020**, *306* (June 2019), 125632. https://doi.org/10.1016/j.foodchem.2019.125632.

[324] Wu, C. L.; Chen, Q. H.; Li, X. Y.; Su, J. hui; He, S.; Liu, J.; Yuan, Y. Formation and Characterisation of Food Protein–Polysaccharide Thermal Complex Particles: Effects of PH, Temperature and Polysaccharide Type. *Int J Food Sci Technol* **2020**, *55* (3), 1368–1374. https://doi.org/10.1111/ijfs.14416.

[325] Brar, V.; Kaur, G. Preparation and Characterization of Polyelectrolyte Complexes of Hibiscus Esculentus (Okra) Gum and Chitosan. *Int J Biomater* **2018**, *2018*. https://doi.org/10.1155/2018/4856287.

[326] Gennari, A.; de la Rosa, J. M. R.; Hohn, E.; Pelliccia, M.; Lallana, E.; Donno, R.; Tirella, A.; Tirelli, N. The Different Ways to Chitosan/Hyaluronic Acid Nanoparticles: Templated vs Direct Complexation. Influence of Particle Preparation on Morphology, Cell Uptake and Silencing

Efficiency. *Beilstein journal of nanotechnology* **2019**, *10*, 2594–2608. https://doi.org/10.3762/BJNANO.10.250.

[327] de Carvalho, F. G.; Magalhães, T. C.; Teixeira, N. M.; Gondim, B. L. C.; Carlo, H. L.; dos Santos, R. L.; de Oliveira, A. R.; Denadai, Â. M. L. Synthesis and Characterization of TPP/Chitosan Nanoparticles: Colloidal Mechanism of Reaction and Antifungal Effect on C. Albicans Biofilm Formation. *Materials Science and Engineering C* **2019**, *104* (October 2018). https://doi.org/10.1016/j.msec.2019.109885.

[328] Abdullah, T.; Ibrahim, N.; Warsi, M. Chondroitin Sulfate-Chitosan Nanoparticles for Ocular Delivery of Bromfenac Sodium: Improved Permeation, Retention, and Penetration. *Int J Pharm Investig* **2016**, *6* (2), 96. https://doi.org/10.4103/2230-973X.177823.

[329] Kimna, C.; Winkeljann, B.; Hoffmeister, J.; Lieleg, O. Biopolymer-Based Nanoparticles with Tunable Mucoadhesivity Efficiently Deliver Therapeutics across the Corneal Barrier. *Materials Science and Engineering C* **2021**, *121* (September 2020), 111890. https://doi.org/10.1016/j.msec.2021.111890.

[330] Dubashynskaya, N. V.; Raik, S. V.; Dubrovskii, Y. A.; Demyanova, E. V.; Shcherbakova, E. S.; Poshina, D. N.; Shasherina, A. Y.; Anufrikov, Y. A.; Skorik, Y. A. Hyaluronan/Diethylaminoethyl Chitosan Polyelectrolyte Complexes as Carriers for Improved Colistin Delivery. *Int J Mol Sci* **2021**, *22* (16). https://doi.org/10.3390/ijms22168381.

[331] Carton, F.; Chevalier, Y.; Nicoletti, L.; Tarnowska, M.; Stella, B.; Arpicco, S.; Malatesta, M.; Jordheim, L. P.; Briançon, S.; Lollo, G. Rationally Designed Hyaluronic Acid-Based Nano-Complexes for Pentamidine Delivery. *Int. J. Pharm.* **2019**, *568*, 1–39. https://doi.org/10.1016/j.ijpharm.2019.118526.

[332] Pilipenko, I.; Korzhikov-Vlakh, V.; Sharoyko, V.; Zhang, N.; Schäfer-Korting, M.; Rühl, E.; Zoschke, C.; Tennikova, T. PH-Sensitive Chitosan–Heparin Nanoparticles for Effective Delivery of Genetic Drugs into Epithelial Cells. *Pharmaceutics* **2019**, *11* (7). https://doi.org/10.3390/PHARMACEUTICS11070317.

[333] Silva, B.; Marto, J.; Braz, B. S.; Delgado, E.; Almeida, A. J.; Gonçalves, L. New Nanoparticles for Topical Ocular Delivery of Erythropoietin. *Int J Pharm* **2020**, *576* (August 2019), 119020. https://doi.org/10.1016/j.ijpharm.2020.119020.

[334] de Vasconcelos, C. L.; Pereira, M. R.; Fonseca, J. L. C. Polyelectrolytes in Solution and the Stabilization of Colloids. *J. Dispers. Sci. Technol.* **2005**, *26* (1), 59–70. https://doi.org/10.1081/DIS-200040170.

[335] Resende, A. P.; Silva, B.; Braz, B. S.; Nunes, T.; Gonçalves, L.; Delgado, E. Ex Vivo Permeation of Erythropoietin through Porcine Conjunctiva, Cornea, and Sclera. *Drug Deliv Transl Res* **2017**, *7* (5), 625–631. https://doi.org/10.1007/s13346-017-0399-y.

[336] Ilka, R.; Mohseni, M.; Kianirad, M.; Naseripour, M.; Ashtari, K.; Mehravi, B. Nanogel-Based Natural Polymers as Smart Carriers for the Controlled Delivery of Timolol Maleate through the Cornea for Glaucoma. *Int J Biol Macromol* **2018**, *109*, 955–962. https://doi.org/10.1016/j.ijbiomac.2017.11.090.

[337] Bachu, R. D.; Chowdhury, P.; Al-saedi, Z. H. F.; Karla, P. K.; Boddu, S. H. S. Ocular Drug Delivery Barriers — Role of Nanocarriers in the Treatment of Anterior Segment Ocular Diseases. **2018**, 1–31. https://doi.org/10.3390/pharmaceutics10010028.

[338] Plucinski, A.; Lyu, Z.; Schmidt, B. V. K. J. Polysaccharide Nanoparticles: From Fabrication to Applications. *J Mater Chem B* **2021**, *9* (35), 7030–7062. https://doi.org/10.1039/d1tb00628b.

[339] Tsai, C. H.; Wang, P. Y.; Lin, I. C.; Huang, H.; Liu, G. S.; Tseng, C. L. Ocular Drug Delivery: Role of Degradable Polymeric Nanocarriers for Ophthalmic Application. *Int J Mol Sci* **2018**, *19* (9), 2830. https://doi.org/10.3390/IJMS19092830.

[340] Jo, D. H.; Lee, T. G.; Kim, J. H. Nanotechnology and Nanotoxicology in Retinopathy. *Int J Mol Sci* **2011**, *12* (11), 8288–8301. https://doi.org/10.3390/IJMS12118288.

[341] Almeida, H.; Helena, M.; Lobão, P.; Silva, A. C.; Manuel, J.; Lobo, S. Applications of Polymeric and Lipid Nanoparticles in Ophthalmic Pharmaceutical Formulations : Present and Future Considerations. *J Pharm Pharm Sci (www.cspsCanada.org)* **2014**, *17* (3), 278–293.

[342] Jo, D. H.; Kim, J. H.; Lee, T. G.; Kim, J. H. Size, Surface Charge, and Shape Determine Therapeutic Effects of Nanoparticles on Brain and Retinal Diseases. *Nanomedicine* **2015**, *11* (7), 1603–1611. https://doi.org/10.1016/j.nano.2015.04.015.

[343] Petros, R. A.; Desimone, J. M. Strategies in the Design of Nanoparticles for Therapeutic Applications. *Nat Rev Drug Discov* **2010**, *9* (8), 615–627. https://doi.org/10.1038/nrd2591.

[344] Chang, W. H.; Liu, P. Y.; Lin, M. H.; Lu, C. J.; Chou, H. Y.; Nian, C. Y.; Jiang, Y. T.; Hsu, Y. H. H. Applications of Hyaluronic Acid in Ophthalmology and Contact Lenses. *Molecules* **2021**, *26* (9), 1–15. https://doi.org/10.3390/molecules26092485.

[345] Zhang, X.; Wei, D.; Xu, Y.; Zhu, Q. Hyaluronic Acid in Ocular Drug Delivery. *Carbohydr Polym* **2021**, *264* (January), 118006. https://doi.org/10.1016/j.carbpol.2021.118006.

[346] Lynch, C. R.; Kondiah, P. P. D.; Choonara, Y. E.; du Toit, L. C.; Ally, N.; Pillay, V. Hydrogel Biomaterials for Application in Ocular Drug Delivery. *Front Bioeng Biotechnol* **2020**, *8* (March), 1–18. https://doi.org/10.3389/fbioe.2020.00228.

[347] Umerska, A.; Paluch, K. J.; Santos-Martinez, M. J.; Corrigan, O. I.; Medina, C.; Tajber, L. Freeze Drying of Polyelectrolyte Complex Nanoparticles: Effect of Nanoparticle Composition and Cryoprotectant Selection. *Int J Pharm* **2018**, *552* (1–2), 27–38. https://doi.org/10.1016/j.ijpharm.2018.09.035.

[348] Amato, G.; Grimaudo, M. A.; Alvarez-lorenzo, C.; Concheiro, A.; Carbone, C.; Bonaccorso, A.; Puglisi, G.; Musumeci, T. Hyaluronan / Poly-L-Lysine / Berberine Nanogels for Impaired Wound Healing. *Pharmaceutics* **2021**, *13* (34), 1–11. https://doi.org/10.3390/pharmaceutics13010034.

[349] Chen, X. S.; Wang, K. F.; Zheng, G. C.; Gao, Y.; Mao, Z. G. Preparation, Characterization and Antimicrobial Activity of ε-Poly-L-Lysine with Short Chain Length Produced from Glycerol by Streptomyces Albulus. *Process Biochemistry* **2018**, *68* (February), 22–29. https://doi.org/10.1016/j.procbio.2018.03.001.

[350] Heo, J. S.; Kim, H. O.; Song, S. Y.; Lew, D. H.; Choi, Y.; Kim, S. Poly-L-Lysine Prevents Senescence and Augments Growth in Culturing Mesenchymal Stem Cells Ex Vivo. *Biomed Res Int* **2016**, *2016*. https://doi.org/10.1155/2016/8196078.

[351] Sasaki, H.; Karasawa, K.; Hironaka, K.; Tahara, K.; Tozuka, Y.; Takeuchi, H. Retinal Drug Delivery Using Eyedrop Preparations of Poly-l-Lysine-Modified Liposomes. *European Journal of Pharmaceutics and Biopharmaceutics* **2013**, *83* (3), 364–369. https://doi.org/10.1016/j.ejpb.2012.10.014.

[352] Hyldgaard, M.; Mygind, T.; Vad, B. S.; Stenvang, M.; Otzen, D. E.; Meyer, R. L. The Antimicrobial Mechanism of Action of Epsilon-Poly-L-Lysine. *Appl Environ Microbiol* **2014**, *80* (24), 7758–7770. https://doi.org/10.1128/AEM.02204-14.

[353] Jordan, A. R.; Racine, R. R.; P Hennig, M. J.; Lokeshwar, V. B. The Role of CD44 in Disease Pathophysiology and Targeted Treatment. *Front. Immunol* **2015**, *6* (182). https://doi.org/10.3389/fimmu.2015.00182.

[354] Meka, V. S.; Sing, M. K. G.; Pichika, M. R.; Nali, S. R.; Kolapalli, V. R. M.; Kesharwani, P. A Comprehensive Review on Polyelectrolyte Complexes. *Drug Discov Today* **2017**, *22* (11), 1697–1706. https://doi.org/10.1016/j.drudis.2017.06.008.

[355] Dakhara, S. L.; Anajwala, C. C. Polyelectrolyte Complex: A Pharmaceutical Review. *Systematic Reviews in Pharmacy* **2010**, *1* (2), 121–127. https://doi.org/10.4103/0975-8453.75046.

[356] Schatz, C.; Lucas, J. M.; Viton, C.; Domard, A.; Pichot, C.; Delair, T. Formation and Properties of Positively Charged Colloids Based on Polyelectrolyte Complexes of Biopolymers. *Langmuir* **2004**, *20* (18), 7766–7778. https://doi.org/10.1021/LA049460M.

[357] Lalwani, S. M.; Eneha, C. I.; Lutkenhaus, J. L. Emerging Trends in the Dynamics of Polyelectrolyte Complexes. *Physical Chemistry Chemical Physics* **2020**, *22*, 24157–24177. https://doi.org/10.1039/x0xx00000x.

[358] Le, H. Van; Le Cerf, D.; Le, H. V; Le Cerf, D. Colloidal Polyelectrolyte Complexes from Hyaluronic Acid: Preparation and Biomedical Applications. *Small* **2022**, *18* (51), 2204283. https://doi.org/10.1002/SMLL.202204283.

[359] Coelho, F.; Botelho, C.; Paris, J. L.; Marques, E. F.; Silva, B. F. B. Influence of the Media Ionic Strength on the Formation and in Vitro Biological Performance of Polycation-DNA Complexes. *J Mol Liq* **2021**, *344*, 117930. https://doi.org/10.1016/J.MOLLIQ.2021.117930.

[360] Gao, J.; Zhan, Q. wei; Tang, Z.; Huang, Y. The Critical Transition from Soluble Complexes to Colloidal Aggregates of Polyelectrolyte Complexes at Non-Stoichiometric Charge Ratios. *Macromol Rapid Commun* **2022**, *43* (7), 2100880. https://doi.org/10.1002/MARC.202100880.

[361] Trefalt, G.; Ruiz-Cabello, F. J. M.; Borkovec, M. Interaction Forces, Heteroaggregation, and Deposition Involving Charged Colloidal Particles. *Journal of Physical Chemistry B* **2014**, *118*

(23), 6346–6355. https://doi.org/10.1021/JP503564P/ASSET/IMAGES/LARGE/JP-2014-03564P_0006.JPEG.

[362] Priftis, D.; Tirrell, M. Phase Behaviour and Complex Coacervation of Aqueous Polypeptide Solutions. *Soft Matter* **2012**, *8* (36), 9396–9405. https://doi.org/10.1039/C2SM25604E.

[363] Sanchez-Ballester, N. M.; Sciortino, F.; Mir, S. H.; Rydzek, G. Weak Polyelectrolytes as Nanoarchitectonic Design Tools for Functional Materials: A Review of Recent Achievements. *Molecules 2022, Vol. 27, Page 3263* **2022**, *27* (10), 3263. https://doi.org/10.3390/MOLECULES27103263.

[364] Shah, S.; Leon, L. Structural Dynamics, Phase Behavior, and Applications of Polyelectrolyte Complex Micelles. *Curr Opin Colloid Interface Sci* **2021**, *53*, 101424. https://doi.org/10.1016/J.COCIS.2021.101424.

[365] Li, L.; Srivastava, S.; Andreev, M.; Marciel, A. B.; de Pablo, J. J.; Tirrell, M. V. Phase Behavior and Salt Partitioning in Polyelectrolyte Complex Coacervates. *Macromolecules* **2018**, *51* (8), 2988–2995. https://doi.org/10.1021/acs.macromol.8b00238.

[366] Kaur, J.; Kaur, G. Optimization of PH Conditions and Characterization of Polyelectrolyte Complexes between Gellan Gum and Cationic Guar Gum. *Polymer Advanced Technologies* **2018**, *29*, 3035–3048.

[367] Sproncken, C. C. M.; Gumí-Audenis, B.; Foroutanparsa, S.; Magana, J. R.; Voets, I. K. Controlling the Formation of Polyelectrolyte Complex Nanoparticles Using Programmable PH Reactions. *Macromolecules* **2023**, *56* (1), 226–233. https://doi.org/10.1021/ACS.MACROMOL.2C01431/ASSET/IMAGES/LARGE/MA2C01431_0008.JPEG.

[368] Musin, E. V.; Dubrovskii, A. V.; Kim, A. L.; Tikhonenko, S. A. A Study of the Buffer Capacity of Polyelectrolyte Microcapsules Depending on Their Concentration and the Number of Layers of the Polyelectrolyte Shell. *Int J Mol Sci* **2022**, *23* (17). https://doi.org/10.3390/IJMS23179917.

[369] Bravo-Anaya, L. M.; Garbay, B.; Nando-Rodríguez, J. L. E.; Carvajal Ramos, F.; Ibarboure, E.; Bathany, K.; Xia, Y.; Rosselgong, J.; Joucla, G.; Garanger, E.; et al. Nucleic Acids Complexation with Cationic Elastin-like Polypeptides: Stoichiometry and Stability of Nano-Assemblies. *J Colloid Interface Sci* **2019**, *557*, 777–792. https://doi.org/10.1016/j.jcis.2019.09.054.

[370] Schatz, C.; Domard, A.; Viton, C.; Pichot, C. Versatile and Efficient Formation of Colloids of Biopolymer-Based Polyelectrolyte Complexes. *Biomacromolecules* **2004**, *5* (5), 1882–1892. https://doi.org/10.1021/bm049786+.

[371] Chen, Y.; Mohanraj, V. J.; Wang, F.; Benson, H. A. E. Designing Chitosan-Dextran Sulfate Nanoparticles Using Charge Ratios. *AAPS PharmSciTech* **2007**, *8* (4). https://doi.org/10.1208/pt0804098.

[372] de la Fuente, M.; Seijo, B.; Alonso, M. J. Novel Hyaluronan-Based Nanocarriers for Transmucosal Delivery of Macromolecules. *Macromol Biosci* **2008**, *8* (5), 441–450. https://doi.org/10.1002/mabi.200700190.

[373] Akolade, J. O.; Oloyede, H. O. B.; Onyenekwe, P. C. Encapsulation in Chitosan-Based Polyelectrolyte Complexes Enhances Antidiabetic Activity of Curcumin. *J Funct Foods* **2017**, *35*, 584–594. https://doi.org/10.1016/j.jff.2017.06.023.

[374] Tsuchida, E. Formation of Polyelectrolyte Complexes and Their Structures. *Journal of Macromolecular Science, Part A: Pure and Applied Chemistry* **1994**, *31* (1), 1–15.

[375] Veis, A.; Aranyi, C. Phase Separation in Polyelectrolyte Systems. I. Complex Coacervates of Gelatin. *Journal of Physical Chemistry A* **1960**, *64* (9), 1203–1210.

[376] Kulkarni, A. D.; Vanjari, Y. H.; Sancheti, K. H.; Patel, H. M.; Belgamwar, V. S.; Surana, S. J.; Pardeshi, C. V; Kulkarni, A. D.; Vanjari, Y. H.; Sancheti, K. H.; et al. Polyelectrolyte Complexes : Mechanisms , Critical Experimental Aspects , and Applications. *Artif Cells Nanomed Biotechnol* **2016**, *44* (7), 1615–1625. https://doi.org/10.3109/21691401.2015.1129624.

[377] Ankerfors, C. *Polyelectrolyte Complexes: Preparation, Characterization, and Use for Control of Wet and Dry Adhesion between Surfaces*; 2012.

[378] Dumitriu, R. P.; Profire, L.; Nita, L. E.; Dragostin, O. M.; Ghetu, N.; Pieptu, D.; Vasile, C. Sulfadiazine-Chitosan Conjugates and Their Polyelectrolyte Complexes with Hyaluronate Destined to the Management of Burn Wounds. *Materials* **2015**, *8* (1), 317–338. https://doi.org/10.3390/ma8010317.

[379] Barroso, N.; Guaresti, O.; Pérez-Álvarez, L.; Ruiz-Rubio, L.; Gabilondo, N.; Vilas-Vilela, J. L. Self-Healable Hyaluronic Acid/Chitosan Polyelectrolyte Complex Hydrogels and Multilayers. *Eur Polym J* **2019**, *120* (September), 109268. https://doi.org/10.1016/j.eurpolymj.2019.109268.

[380] de Oliveira, S. A.; da Silva, B. C.; Riegel-Vidotti, I. C.; Urbano, A.; de Sousa Faria-Tischer, P. C.; Tischer, C. A. Production and Characterization of Bacterial Cellulose Membranes with Hyaluronic Acid from Chicken Comb. *Int J Biol Macromol* **2017**, *97* (January), 642–653. https://doi.org/10.1016/j.ijbiomac.2017.01.077.

[381] Yang, G.; Zhang, B.; Wang, J.; Xie, S.; Li, X. Preparation of Polylysine-Modified Superparamagnetic Iron Oxide Nanoparticles. *J Magn Magn Mater* **2015**, *374*, 205–208. https://doi.org/10.1016/j.jmmm.2014.08.040.

[382] Liu, T.; Liu, Y.; Chen, Y.; Liu, S.; Maitz, M. F.; Wang, X.; Zhang, K.; Wang, J.; Wang, Y.; Chen, J.; et al. Immobilization of Heparin/Poly-L-Lysine Nanoparticles on Dopamine-Coated Surface to Create a Heparin Density Gradient for Selective Direction of Platelet and Vascular Cells Behavior. *Acta Biomater* **2014**, *10* (5), 1940–1954. https://doi.org/10.1016/j.actbio.2013.12.013.

[383] Smith, Brian, C. The Infrared Spectra of Primary, Secondary, and Tertiery Amines. In *Infrared Spectral Interpretation : A Systematic Approach*; CRC Press LLC, 2018; pp 136–138.

[384] Fornaro, T.; Burini, D.; Biczysko, M.; Barone, V. Hydrogen-Bonding Effects on Infrared Spectra from Anharmonic Computations: Uracil-Water Complexes and Uracil Dimers. *Journal of Physical Chemistry A* **2015**, *119* (18), 4224–4236. https://doi.org/10.1021/acs.jpca.5b01561.

[385] Ruiz-Rubio, L.; Lizundia, E.; Vilas, J. L.; León, L. M.; Rodríguez, M. Influence of N-Alkyl and α-Substitutions on the Thermal Behaviour of H-Bonded Interpolymer Complexes Based on Polymers with Acrylamide or Lactame Groups and Poly(4-Vinylphenol). *Thermochim Acta* **2015**, *614*, 191–198. https://doi.org/10.1016/j.tca.2015.06.030.

[386] Yi, J. Z.; Goh, S. H. Interactions in Miscible Blends and Complexes of Poly(N-Acryloylmorpholine) with Poly (p-Vinylphenol). *Polymer (Guildf)* **2002**, *43* (16), 4515–4522. https://doi.org/10.1016/S0032-3861(02)00291-4.

[387] Souza, S. D. '; Keck, C. M. A Review of In Vitro Drug Release Test Methods for Nano-Sized Dosage Forms. **2014**. https://doi.org/10.1155/2014/304757.

[388] Quiñones, J. P.; Brüggemann, O.; Covas, C. P.; Ossipov, D. A. Self-Assembled Hyaluronic Acid Nanoparticles for Controlled Release of Agrochemicals and Diosgenin. *Carbohydr Polym* **2017**, *173*, 157–169. https://doi.org/10.1016/j.carbpol.2017.05.048.

[389] Fakhari, A. Biomedical Application of Hyaluronic Acid Nanoparticles, 2012.

[390] Choi, K. Y.; Min, K. H.; Na, J. H.; Choi, K.; Kim, K.; Park, J. H.; Kwon, I. C.; Jeong, S. Y. Self-Assembled Hyaluronic Acid Nanoparticles as a Potential Drug Carrier for Cancer Therapy: Synthesis, Characterization, and in Vivo Biodistribution. *J Mater Chem* **2009**, *19* (24), 4102–4107. https://doi.org/10.1039/b900456d.

[391] Sigma Aldrich Inc. *Poly-L-Lysine Hydrochloride Product Informataion Leaflet*.

[392] Oyarzun-Ampuero, F. A., Goycoolea, F. M., Torres, D., Alonso, M., J. A New Drug Nanocarrier Consisting of Polyarginine and Hyaluronic Acid. *European Journal of Pharmaceutics and Biopharmaceutics* **2011**, 54–57.

[393] Oyarzun-Ampuero, F. A.; Goycoolea, F. M.; Torres, D.; Alonso, M. J. A New Drug Nanocarrier Consisting of Polyarginine and Hyaluronic Acid. *European Journal of Pharmaceutics and Biopharmaceutics* **2011**, *79* (1), 54–57. https://doi.org/10.1016/j.ejpb.2011.04.008.

[394] Pan, W.; Yin, D.-X.; Jing, H.-R.; Chang, H.-J.; Wen, H.; Liang, D.-H. Core-Corona Structure Formed by Hyaluronic Acid and Poly(L-Lysine) via Kinetic Path. *Chinese Journal of Polymer Science* **2019**, *37*, 36–42.

[395] Golchoobi, A.; Khosravi, A.; Modarress, H.; Ahmadzadeh, A. Effect of Charge, Size and Temperature on Stability of Charged Colloidal Nano Particles. *Chinese Journal of Chemical Physics* **2012**, *25* (5), 617–624. https://doi.org/10.1088/1674-0068/25/05/617-624.

[396] Drogoz, A.; David, L.; Rochas, C.; Domard, A.; Delair, T. Polyelectrolyte Complexes from Polysaccharides: Formation and Stoichiometry Monitoring. *Langmuir* **2007**, *23* (22), 10950–10958. https://doi.org/10.1021/la7008545.

[397] Danaei, M.; Dehghankhold, M.; Ataei, S.; Davarani, F. H.; Javanmard, R.; Dokhani, A.; Khorasani, S.; Mozafari, M. R. Impact of Particle Size and Polydispersity Index on the Clinical Applications of Lipidic Nanocarrier Systems. *Pharmaceutics* **2018**, *10* (57), 1–17. https://doi.org/10.3390/pharmaceutics10020057.

[398] Otoni, C. G.; Queirós, M. V. A.; Sabadini, J. B.; Rojas, O. J.; Loh, W. Charge Matters: Electrostatic Complexation As a Green Approach to Assemble Advanced Functional Materials. *ACS Omega* **2020**, *5* (3), 1296–1304. https://doi.org/10.1021/acsomega.9b03690.

[399] Zheng, M.; Pan, M.; Zhang, W.; Lin, H.; Wu, S.; Lu, C.; Tang, S.; Liu, D.; Cai, J. Poly(α-L-Lysine)-Based Nanomaterials for Versatile Biomedical Applications: Current Advances and Perspectives. *Bioact Mater* **2021**, *6* (7), 1878–1909. https://doi.org/10.1016/j.bioactmat.2020.12.001.

[400] Marras, A. E.; Ting, M.; Stevens, K. C.; Tirrell, M. V. Advances in the Structural Design of Polyelectrolyte Complex Micelles. *Journal of Physical Chemistry B* **2021**, *125* (26), 7076–7089. https://doi.org/10.1021/acs.jpcb.1c01258.

[401] Zhang, Y.; Yildirim, E.; Antila, H. S.; Valenzuela, L. D.; Sammalkorpi, M.; Lutkenhaus, J. L. The Influence of Ionic Strength and Mixing Ratio on the Colloidal Stability of PDAC/PSS Polyelectrolyte Complexes. *Soft Matter* **2015**, *11* (37), 7392–7401. https://doi.org/10.1039/C5SM01184A.

[402] Honary, S.; Zahir, F. Effect of Zeta Potential on the Properties of Nano-Drug Delivery Systems - A Review (Part 2). *Tropical Journal of Pharmaceutical Research* **2013**, *12* (2), 265–273. https://doi.org/10.4314/tjpr.v12i2.20.

[403] Sapsford, K. E.; Tyner, K. M.; Dair, B. J.; Deschamps, J. R.; Medintz, I. L. Analyzing Nanomaterial Bioconjugates: A Review of Current and Emerging Purification and Characterization Techniques. *Anal Chem* **2011**, *83* (12), 4453–4488. https://doi.org/10.1021/ac200853a.

[404] Strand, A.; Vähäsalo, L.; Ketola, A.; Salminen, K.; Retulainen, E.; Sundberg, A. In-Situ Analysis of Polyelectrolyte Complexes by Flow Cytometry. *Cellulose* **2018**, *25* (7), 3781–3795. https://doi.org/10.1007/s10570-018-1832-1.

[405] Ferreira, D. C. M.; Ferreira, S. O.; de Alvarenga, E. S.; Soares, N. de F. F.; Coimbra, J. S. dos R.; de Oliveira, E. B. Polyelectrolyte Complexes (PECs) Obtained from Chitosan and Carboxymethylcellulose: A Physicochemical and Microstructural Study. *Carbohydrate Polymer Technologies and Applications* **2022**, *3*, 100197. https://doi.org/10.1016/J.CARPTA.2022.100197.

[406] Holkar, A.; Toledo, J.; Srivastava, S. Structure of Nanoparticle-Polyelectrolyte Complexes: Effects of Polyelectrolyte Characteristics and Charge Ratio. *AIChE Journal* **2021**, *67* (12), e17443. https://doi.org/10.1002/AIC.17443.

[407] Wiseman, T.; Williston, S.; Brandts, J. F.; Lin, L. N. Rapid Measurement of Binding Constants and Heats of Binding Using a New Titration Calorimeter. *Anal Biochem* **1989**, *179* (1), 131–137. https://doi.org/10.1016/0003-2697(89)90213-3.

[408] Ma, P. L.; Lavertu, M.; Winnik, F. M.; Buschmann, M. D. Stability and Binding Affinity of DNA/Chitosan Complexes by Polyanion Competition. *Carbohydr Polym* **2017**, *176*, 167–176. https://doi.org/10.1016/J.CARBPOL.2017.08.002.

[409] Date, P. V.; Samad, A.; Devarajan, P. V. Freeze Thaw: A Simple Approach for Prediction of Optimal Cryoprotectant for Freeze Drying. *AAPS PharmSciTech* **2010**, *11* (1), 304–313. https://doi.org/10.1208/s12249-010-9382-3.

[410] Siddhanta, S.; Barman, I.; Narayana, C. Revealing the Trehalose Mediated Inhibition of Protein Aggregation through Lysozyme–Silver Nanoparticle Interaction. *Soft Matter* **2015**, *11* (37), 7241–7249. https://doi.org/10.1039/C5SM01896J.

[411] Le, H. Van; Le Cerf, D. Colloidal Polyelectrolyte Complexes from Hyaluronic Acid: Preparation and Biomedical Applications. *Small* **2022**, *18*, 1–26. https://doi.org/10.1002/smll.202204283.

[412] Rampino, A.; Borgogna, M.; Blasi, P.; Bellich, B.; Cesàro, A. Chitosan Nanoparticles: Preparation, Size Evolution and Stability. *Int J Pharm* **2013**, *455* (1–2), 219–228. https://doi.org/10.1016/j.ijpharm.2013.07.034.

[413] Yan, Q.; Weng, J.; Wu, X.; Wang, W.; Yang, Q.; Guo, F.; Wu, D.; Song, Y.; Chen, F.; Yang, G. Characteristics, Cryoprotection Evaluation and in Vitro Release of BSA-Loaded Chitosan Nanoparticles. *Mar Drugs* **2020**, *18* (6). https://doi.org/10.3390/md18060315.

[414] Le, H. Van; Dulong, V.; Picton, L.; Le Cerf, D. Lyophilization for Formulation Optimization of Drug-Loaded Thermoresponsive Polyelectrolyte Complex Nanogels from Functionalized Hyaluronic Acid. *Pharmaceutics* **2023**, *15* (3), 929. https://doi.org/10.3390/PHARMACEUTICS15030929/S1.

[415] Williams, P. A.; Harder, J. M.; Cardozo, B. H.; Foxworth, N. E.; John, S. W. M. Nicotinamide Treatment Robustly Protects from Inherited Mouse Glaucoma. **2018**, *1356956*.

[416] Gadol, E.; Mestayer, R. F.; Grant, R.; Grigoryev, Y.; Gibson, S. B.; Happel, M. A Case of Parkinson ' s Disease Symptom Reduction with Intravenous NAD + A Case of Parkinson ' s Disease Symptom Reduction with Intravenous. *On Journ Online Publishers* **2019**, *3* (April), 1–4.

[417] Saini, J. S.; Corneo, B.; Miller, J. D.; Kiehl, T. R.; Wang, Q.; Boles, N. C.; Blenkinsop, T. A.; Stern, J. H.; Temple, S. Nicotinamide Ameliorates Disease Phenotypes in a Human IPSC Model of Age-Related Macular Degeneration. *Cell Stem Cell* **2017**, *20* (5), 635-647.e7. https://doi.org/10.1016/j.stem.2016.12.015.

[418] Hou, Y.; Lautrupa, S.; Cordonnier, S.; Wang, Y.; Croteau, D. L.; Zavala, E.; Zhang, Y.; Moritoh, K.; O'Connell, J. F.; Baptiste, B. A.; et al. NAD + Supplementation Normalizes Key Alzheimer's Features and DNA Damage Responses in a New AD Mouse Model with Introduced DNA Repair Deficiency. *Proc Natl Acad Sci U S A* **2018**. https://doi.org/10.1073/pnas.1718819115.

[419] de Picciotto, N. E.; Gano, L. B.; Johnson, L. C.; Martens, C. R.; Sindler, A. L.; Mills, K. F.; Imai, S. ichiro; Seals, D. R. Nicotinamide Mononucleotide Supplementation Reverses Vascular Dysfunction and Oxidative Stress with Aging in Mice. *Aging Cell* **2016**, *15* (3), 522–530. https://doi.org/10.1111/acel.12461.

[420] Mills, K. F.; Yoshida, S.; Stein, L. R.; Grozio, A.; Kubota, S.; Sasaki, Y.; Redpath, P.; Migaud, M. E.; Apte, R. S.; Uchida, K.; et al. Long-Term Administration of Nicotinamide Mononucleotide Mitigates Age-Associated Physiological Decline in Mice. *Cell Metab* **2017**, *24* (6), 795–806. https://doi.org/10.1016/j.physbeh.2017.03.040.

[421] Alqahtani, M. S.; Kazi, M.; Alsenaidy, M. A.; Ahmad, M. Z. Advances in Oral Drug Delivery. *Front Pharmacol* **2021**, *12* (February). https://doi.org/10.3389/fphar.2021.618411.

[422] Homayun, B.; Lin, X.; Choi, H. J. Challenges and Recent Progress in Oral Drug Delivery Systems for Biopharmaceuticals. *Pharmaceutics* **2019**, *11* (3). https://doi.org/10.3390/pharmaceutics11030129.

[423] Campos, P. M.; Petrilli, R.; Lopez, R. F. V. The Prominence of the Dosage Form Design to Treat Ocular Diseases. *Int J Pharm* **2020**, *586* (March), 119577. https://doi.org/10.1016/j.ijpharm.2020.119577.

[424] Ross, A. E.; Bengani, L. C.; Tulsan, R.; Maidana, D. E.; Salvador-Culla, B.; Kobashi, H.; Kolovou, P. E.; Zhai, H.; Taghizadeh, K.; Kuang, L.; et al. Topical Sustained Drug Delivery to the Retina with a Drug-Eluting Contact Lens. *Biomaterials* **2019**, *217* (March), 119285. https://doi.org/10.1016/j.biomaterials.2019.119285.

[425] Jumelle, C.; Gholizadeh, S.; Annabi, N.; Dana, R. Advances and Limitations of Drug Delivery Systems Formulated as Eye Drops. *Journal of Controlled Release* **2020**, *321* (January), 1–22. https://doi.org/10.1016/j.jconrel.2020.01.057.

[426] Bohrey, S.; Chourasiya, V.; Pandey, A. Polymeric Nanoparticles Containing Diazepam: Preparation, Optimization, Characterization, in-Vitro Drug Release and Release Kinetic Study. *Nano Converg* **2016**, *3* (1), 3–9. https://doi.org/10.1186/s40580-016-0061-2.

[427] Son, G. H.; Lee, B. J.; Cho, C. W. Mechanisms of Drug Release from Advanced Drug Formulations Such as Polymeric-Based Drug-Delivery Systems and Lipid Nanoparticles. *J Pharm Investig* **2017**, *47* (4), 287–296. https://doi.org/10.1007/s40005-017-0320-1.

[428] Ahmed, L.; Atif, R.; Eldeen, T. S.; Yahya, I.; Omara, A.; Eltayeb, M. Study the Using of Nanoparticles as Drug Delivery System Based on Mathematical Models for Controlled Release. *International Journal of Latest Technology in Engineering, Management & Applied Science* **2019**, *8* (5), 52–56.

[429] Bhasarkar, J.; Bal, D. Kinetic Investigation of a Controlled Drug Delivery System Based on Alginate Scaffold with Embedded Voids. *J Appl Biomater Funct Mater* **2019**, *17* (2). https://doi.org/10.1177/2280800018817462.

[430] Sreedharan, S. M.; Singh, R. Ciprofloxacin Functionalized Biogenic Gold Nanoflowers as Nanoantibiotics against Pathogenic Bacterial Strains. *Int J Nanomedicine* **2019**, *14*, 9905–9916. https://doi.org/10.2147/IJN.S224488.

[431] Dash, S.; Murthy, P. N.; Nath, L.; Chowdhury, P. Kinetic Modeling on Drug Release from Controlled Drug Delivery Systems. *Acta Poloniae Pharmaceutica - Drug Research* **2010**, *67* (3), 217–223.

[432] Mircioiu, C.; Voicu, V.; Anuta, V.; Tudose, A.; Celia, C.; Paolino, D.; Fresta, M.; Sandulovici, R.; Mircioiu, I. Mathematical Modeling of Release Kinetics from Supramolecular Drug Delivery Systems. *Pharmaceutics* **2019**, *11* (3). https://doi.org/10.3390/pharmaceutics11030140.

[433] Wójcik-Pastuszka, D.; Krzak, J.; Macikowski, B.; Berkowski, R.; Osí Nski, B.; Musiał, W. Materials Evaluation of the Release Kinetics of a Pharmacologically Active Substance from Model Intra-Articular Implants Replacing the Cruciate Ligaments of the Knee. https://doi.org/10.3390/ma12081202.

[434] Santos, H. A.; Manzanares, J. A.; Murtomäki, L.; Kontturi, K. Thermodynamic Analysis of Binding between Drugs and Glycosaminoglycans by Isothermal Titration Calorimetry and Fluorescence Spectroscopy. *Eur J Pharm Sci* **2007**, *32* (2), 105–114. https://doi.org/10.1016/J.EJPS.2007.06.003.

[435] Lima Cavalcanti, I. D.; Xavier Junior, F. H.; Santos Magalhães, N. S.; Lira Nogueira, M. C. de B. Isothermal Titration Calorimetry (ITC) as a Promising Tool in Pharmaceutical Nanotechnology. *Int J Pharm* **2023**, *641*, 123063. https://doi.org/10.1016/J.IJPHARM.2023.123063.

[436] Saponaro, A. Isothermal Titration Calorimetry: A Biophysical Method to Characterize the Interaction between Label-Free Biomolecules in Solution. *Bio Protoc* **2018**, *8* (15). https://doi.org/10.21769/BIOPROTOC.2957.

[437] Li, L.; Xie, Y.; Wang, Y.; Yang, X.; Fu, R.; Fang, R. Colloids and Surfaces B : Biointerfaces Study on Nicotinamide Adenine Dinucleotide Adsorbed at Nano-Boehmite / Water and Nano-Corundum / Water Interfaces. **2013**, *102*, 398–404. https://doi.org/10.1016/j.colsurfb.2012.07.029.

[438] Brewer, S. H.; Anthireya, S. J.; Lappi, S. E.; Drapcho, D. L.; Franzen, S. Detection of DNA Hybridization on Gold Surfaces by Polarization Modulation Infrared Reflection Absorption Spectroscopy. *Langmuir* **2002**, *18* (11), 4460–4464. https://doi.org/10.1021/la025613z.

[439] Iwaki, M.; Cotton, N. P. J.; Quirk, P. G.; Rich, P. R.; Jackson, J. B. Molecular Recognition between Protein and Nicotinamide Dinucleotide in Intact, Proton-Translocating Transhydrogenase Studied by ATR-FTIR Spectroscopy. *J Am Chem Soc* **2006**, *128* (8), 2621–2629. https://doi.org/10.1021/ja0556272.

[440] Damian, A.; Omanovic, S. Interactive Adsorption Behavior of NAD+ at a Gold Electrode Surface. *Langmuir* **2007**, *23* (6), 3162–3171. https://doi.org/10.1021/la062385q.

[441] Ferreira, D. C. M.; Ferreira, S. O.; de Alvarenga, E. S.; Soares, N. de F. F.; Coimbra, J. S. dos R.; de Oliveira, E. B. Polyelectrolyte Complexes (PECs) Obtained from Chitosan and Carboxymethylcellulose: A Physicochemical and Microstructural Study. *Carbohydrate Polymer Technologies and Applications* **2022**, *3*, 100197. https://doi.org/10.1016/J.CARPTA.2022.100197.

[442] Abraham, J.; Jose, B.; Jose, A.; Thomas, S. Characterization of Green Nanoparticles from Plants. In *Phytonanotechnology*; Thajuddin, N., Mathew, S., Eds.; Elsevier Inc., 2020; pp 21–39. https://doi.org/10.1016/b978-0-12-822348-2.00002-4.

[443] Electron Microscopy Sciences. Sputter Coater Principles Technical Data Sheet. Electron Microscopy Sciences - Data Sheets. Available online: https://www.emsdiasum.com/microscopy/technical/datasheet/sputter_coating.aspx (Accessed on: 12 November 2021).

[444] Groarke, R.; Vijayaraghavan, R. K.; Powell, D.; Rennie, A.; Brabazon, D. Powder Characterization—Methods, Standards, and State of the Art. *Fundamentals of Laser Powder Bed Fusion of Metals* **2021**, 491–527. https://doi.org/10.1016/B978-0-12-824090-8.00006-8.

[445] Armbruster, D. A.; Pry, T. Limit of Blank, Limit of Detection and Limit of Quantitation. *Clin Biochem Rev* **2008**, *29 Suppl 1* (August), S49-52.

[446] Ettre, L. S. Nonmenclature for Chromatography. *Pure and Applied Chemistry* **1993**, *65* (4), 819–872.

[447] The United States Pharmacopeial Convention. *Physical Tests / <625> Chromatography*; 2012.

[448] Yamamoto, E.; Miyazaki, S.; Aoyama, C.; Kato, M. A Simple and Rapid Measurement Method of Encapsulation Efficiency of Doxorubicin Loaded Liposomes by Direct Injection of the Liposomal Suspension to Liquid Chromatography. *Int J Pharm* **2018**, *536* (1), 21–28. https://doi.org/10.1016/j.ijpharm.2017.11.035.

[449] Forrow, N. J.; Shabir, G. A. Development and Validation of a HPLC Method for NAD: Application to Stability Studies in Buffered Solutions and Dry Test Strips. *J Liq Chromatogr Relat Technol* **2009**, *32* (19), 2805–2821. https://doi.org/10.1080/10826070903288680.

[450] Maiti, S.; Jana, S.; Laha, B. *Cationic Polyelectrolyte–Biopolymer Complex Hydrogel Particles for Drug Delivery*; Elsevier Inc., 2018. https://doi.org/10.1016/b978-0-12-813627-0.00006-5.

[451] Amini, Y.; Amel Jamehdar, S.; Sadri, K.; Zare, S.; Musavi, D.; Tafaghodi, M. Different Methods to Determine the Encapsulation Efficiency of Protein in PLGA Nanoparticles. *Biomed Mater Eng* **2017**, *28* (6), 613–620. https://doi.org/10.3233/BME-171705.

[452] Ali, M. What Function of Nanoparticles Is the Primary Factor for Their Hyper-Toxicity? *Adv Colloid Interface Sci* **2023**, *314*, 102881. https://doi.org/10.1016/j.cis.2023.102881.

[453] Yildirimer, L.; Thanh, N. T. K.; Loizidou, M.; Seifalian, A. M. Toxicology and Clinical Potential of Nanoparticles. *Nano Today* **2011**, *6* (6), 585–607. https://doi.org/10.1016/J.NANTOD.2011.10.001.

[454] Zhu, G.; Wang, K.; Qin, H.; Zhao, X.; Chen, W.; Xu, L.; Cao, W.; Guo, H. Internal Cross-Linked Polymeric Nanoparticles with Dual Sensitivity for Combination Therapy of Muscle-Invasive Bladder Cancer. *J Nanobiotechnology* **2020**, *18* (1), 1–13. https://doi.org/10.1186/S12951-020-00686-3/FIGURES/7.

[455] Azadi, M.; David, A. E. Enhancing Ocular Drug Delivery: The Effect of Physicochemical Properties of Nanoparticles on the Mechanism of Their Uptake by Human Cornea Epithelial Cells. *ACS Biomater Sci Eng* **2023**. https://doi.org/10.1021/ACSBIOMATERIALS.3C01144/ASSET/IMAGES/MEDIUM/AB3C01144_0011.GIF.

[456] Vrignaud, S.; Benoit, J. P.; Saulnier, P. Strategies for the Nanoencapsulation of Hydrophilic Molecules in Polymer-Based Nanoparticles. *Biomaterials* **2011**, *32* (33), 8593–8604. https://doi.org/10.1016/j.biomaterials.2011.07.057.

[457] Li, Q.; Li, X.; Zhao, C. Strategies to Obtain Encapsulation and Controlled Release of Small Hydrophilic Molecules. *Front Bioeng Biotechnol* **2020**, *8* (May), 1–6. https://doi.org/10.3389/fbioe.2020.00437.

[458] Snetkov, P.; Zakharova, K.; Morozkina, S.; Olekhnovich, R. Hyaluronic Acid : The Influence of Molecular Weight and Degradable Properties of Biopolymer. *Polymers (Basel)* **2020**, *12*, 1800.

[459] Kim, D. H.; Jeong, E. W.; Baek, Y.; Lee, H. G. Development of Propolis Extract-Loaded Nanoparticles with Chitosan and Hyaluronic Acid for Improving Solubility and Stability. *LWT* **2023**, *181*, 114738. https://doi.org/10.1016/J.LWT.2023.114738.

[460] Ortiz, J. A.; Sepúlveda, F. A.; Panadero-Medianero, C.; Murgas, P.; Ahumada, M.; Palza, H.; Matsuhiro, B.; Zapata, P. A. Cytocompatible Drug Delivery Hydrogels Based on Carboxymethylagarose/Chitosan PH-Responsive Polyelectrolyte Complexes. *Int J Biol Macromol* **2022**, *199*, 96–107. https://doi.org/10.1016/J.IJBIOMAC.2021.12.093.

[461] Nikolova, D.; Simeonov, M.; Tzachev, C.; Apostolov, A.; Christov, L.; Vassileva, E. Polyelectrolyte Complexes of Chitosan and Sodium Alginate as a Drug Delivery System for Diclofenac Sodium. *Polym Int* **2022**, *71* (6), 668–678. https://doi.org/10.1002/PI.6273.

[462] Starchenko, V.; Müller, M.; Lebovka, N. Sizing of PDADMAC/PSS Complex Aggregates by Polyelectrolyte and Salt Concentration and PSS Molecular Weight. *Journal of Physical Chemistry B* **2012**, *116* (51), 14961–14967. https://doi.org/10.1021/jp3095243.

[463] Gao, J.; Zhan, Q. wei; Tang, Z.; Huang, Y. The Critical Transition from Soluble Complexes to Colloidal Aggregates of Polyelectrolyte Complexes at Non-Stoichiometric Charge Ratios. *Macromol Rapid Commun* **2022**, *43* (7), 2100880. https://doi.org/10.1002/MARC.202100880.

[464] Ferreira, D. C. M.; Ferreira, S. O.; de Alvarenga, E. S.; Soares, N. de F. F.; Coimbra, J. S. dos R.; de Oliveira, E. B. Polyelectrolyte Complexes (PECs) Obtained from Chitosan and Carboxymethylcellulose: A Physicochemical and Microstructural Study. *Carbohydrate Polymer Technologies and Applications* **2022**, *3*, 100197. https://doi.org/10.1016/J.CARPTA.2022.100197.

[465] Sladek, S.; McCartney, F.; Eskander, M.; Dunne, D. J.; Santos-Martinez, M. J.; Benetti, F.; Tajber, L.; Brayden, D. J. An Enteric-Coated Polyelectrolyte Nanocomplex Delivers Insulin in Rat Intestinal Instillations When Combined with a Permeation Enhancer. *Pharmaceutics* **2020**, *12* (3). https://doi.org/10.3390/pharmaceutics12030259.

[466] Yoshino, J.; Imai, S.-I. Accurate Measurement of Nicotinamide Adenine Dinucleotide (NAD +) with High-Performance Liquid Chromatography. https://doi.org/10.1007/978-1-62703-637-5_14.

[467] Anderson, B. M.; Anderson, C. D. The Effect of Buffers on Nicotinamide Adenine Dinucleotide Hydrolysis. *J Biol Chem* **1963**, *238* (4), 1475–1478. https://doi.org/10.1016/s0021-9258(18)81208-x.

[468] Rover, L.; Fernandes, J. C. B.; Neto, G. D. O.; Kubota, L. T.; Katekawa, E.; Serrano, S. H. P. Study of NADH Stability Using Ultraviolet-Visible Spectrophotometric Analysis and Factorial Design. *Anal Biochem* **1998**, *260* (1), 50–55. https://doi.org/10.1006/abio.1998.2656.

[469] D'Souza, S. A Review of In Vitro Drug Release Test Methods for Nano-Sized Dosage Forms . *Advances in Pharmaceutics* **2014**, *2014*, 1–12. https://doi.org/10.1155/2014/304757.

[470] Ranta, V. P.; Mannermaa, E.; Lummepuro, K.; Subrizi, A.; Laukkanen, A.; Antopolsky, M.; Murtomäki, L.; Hornof, M.; Urtti, A. Barrier Analysis of Periocular Drug Delivery to the Posterior Segment. *Journal of Controlled Release* **2010**, *148* (1), 42–48. https://doi.org/10.1016/j.jconrel.2010.08.028.

[471] van Haeringen, N. J. Clinical Biochemistry of Tears. *Surv Ophthalmol* **1981**, *26* (2), 84–96. https://doi.org/10.1016/0039-6257(81)90145-4.

[472] Stahl, U.; Willcox, M.; Stapleton, F. Osmolality and Tear Film Dynamics. *Clin Exp Optom* **2012**, *95* (1), 3–11. https://doi.org/10.1111/j.1444-0938.2011.00634.x.

[473] Mitsubayashi, K.; Ogasawara, K.; Yokoyama, K.; Takeuchi, T.; Tsuru, T.; Karube, I. Measurement of Tear Electrolyte Concentration and Turnover Rate Using a Flexible Conductimetric Sensor. *Technology and Health Care* **1995**, *3* (2), 117–121. https://doi.org/10.3233/thc-1995-3206.

[474] Kapelner, R. A.; Fisher, R. S.; Elbaum-Garfinkle, S.; Obermeyer, A. C. Protein Charge Parameters That Influence Stability and Cellular Internalization of Polyelectrolyte Complex Micelles. *Chem Sci* **2022**, *13* (48), 14346–14356. https://doi.org/10.1039/D2SC00192F.

[475] Dautzenberg, H.; Karibyants, N. Polyelectrolyte Complex Formation in Highly Aggregating Systems. Effect of Salt: Response to Subsequent Addition of NaCl. *Macromol Chem Phys* **1999**, *200* (1), 118–125. https://doi.org/10.1002/(SICI)1521-3935(19990101)200:1<118::AID-MACP118>3.0.CO;2-K.

[476] Kayitmazer, A. B.; Koksal, A. F.; Kilic Iyilik, E. Complex Coacervation of Hyaluronic Acid and Chitosan: Effects of PH, Ionic Strength, Charge Density, Chain Length and the Charge Ratio. *Soft Matter* **2015**, *11* (44), 8605–8612. https://doi.org/10.1039/c5sm01829c.

[477] Coelho, F.; Botelho, C.; Paris, J. L.; Marques, E. F.; Silva, B. F. B. Influence of the Media Ionic Strength on the Formation and in Vitro Biological Performance of Polycation-DNA Complexes. *J Mol Liq* **2021**, *344*, 117930. https://doi.org/10.1016/J.MOLLIQ.2021.117930.

[478] Horinek, D. DLVO Theory. In *Encyclopedia of Applied Electrochemistry*; Kreysa, G., Ota, K., Savinell, Robert. F., Eds.; Springer, New York: New York, 2014; pp 343–346. https://doi.org/10.1007/978-1-4419-6996-5.

[479] Ohshima, H. The Derjaguin – Landau – Verway – Overbeek (DLVO) Theory of Colloidal Stability. In *Electrical Phenomena at Interfaces and Bionterfaces - Fundamentals and Applications in Nano-, Bio-, and Environmental Sciences*; Ohshima, H., Ed.; John Wiley & Sons Ltd: New Jersey, 2012; pp 27–34.

[480] Dukhin, A. S.; Goetz, P. J. Fundamentals of Interface and Colloid Science. In *Characterization of Liquids, Dispersions, Emulsions, and Porous Materials Using Ultrasound*; Elservier, 2017; pp 19–83. https://doi.org/10.1016/b978-0-444-63908-0.00002-8.

[481] Tieppo, A.; Boggs, A. C.; Pourjavad, P.; Byrne, M. E. Analysis of Release Kinetics of Ocular Therapeutics from Drug Releasing Contact Lenses: Best Methods and Practices to Advance the Field. *Contact Lens and Anterior Eye* **2014**, *37* (4), 305–313. https://doi.org/10.1016/j.clae.2014.04.005.

[482] Ali, S.; Bleuel, M.; Prabhu, V. M. Lower Critical Solution Temperature in Polyelectrolyte Complex Coacervates. *ACS Macro Lett* **2019**, *8* (3), 289–293. https://doi.org/10.1021/ACSMACROLETT.8B00952.

[483] Romeo, A.; Musumeci, T.; Carbone, C.; Bonaccorso, A.; Corvo, S.; Lupo, G.; Anfuso, C. D.; Puglisi, G.; Pignatello, R. Ferulic Acid-Loaded Polymeric Nanoparticles for Potential Ocular Delivery. *Pharmaceutics 2021, Vol. 13, Page 687* **2021**, *13* (5), 687. https://doi.org/10.3390/PHARMACEUTICS13050687.

[484] Salama, A. H.; AbouSamra, M. M.; Awad, G. E. A.; Mansy, S. S. Promising Bioadhesive Ofloxacin-Loaded Polymeric Nanoparticles for the Treatment of Ocular Inflammation: Formulation and in Vivo Evaluation. *Drug Deliv Transl Res* **2021**, *11* (5), 1943–1957. https://doi.org/10.1007/S13346-020-00856-8/FIGURES/11.

[485] Jacinto, T. A.; Oliveira, B.; Miguel, S. P.; Ribeiro, M. P.; Coutinho, P. Ciprofloxacin-Loaded Zein/Hyaluronic Acid Nanoparticles for Ocular Mucosa Delivery. *Pharmaceutics* **2022**, *14* (8), 1557. https://doi.org/10.3390/PHARMACEUTICS14081557/S1.

[486] Weng, J.; Tong, H. H. Y.; Chow, S. F. In Vitro Release Study of the Polymeric Drug Nanoparticles: Development and Validation of a Novel Method. *Pharmaceutics* **2020**, *12* (8), 1–18. https://doi.org/10.3390/pharmaceutics12080732.

[487] Modi, S.; Anderson, B. D. *Determination of Drug Release Kinetics from Nanoparticles: Overcoming Pitfalls of the Dynamic Dialysis Method*; 2013; Vol. 10. https://doi.org/10.1021/mp400154a.

[488] Lu, X. Y.; Wu, D. C.; Li, Z. J.; Chen, G. Q. Drug Release. In *Progress in Molecular Biology and Translational Science*; Villaverde, A., Ed.; Elsevier Inc., 2011; Vol. 104, p 307. https://doi.org/10.1016/B978-0-12-416020-0.00007-3.

[489] Carradori, D.; Gaudin, A.; Brambilla, D.; Andrieux, K. Application of Nanomedicine to the CNS Diseases. *Int Rev Neurobiol* **2016**, *130*, 73–113. https://doi.org/10.1016/BS.IRN.2016.06.002.

[490] Pimenta, A. F. R.; Valente, A.; Pereira, J. M. C.; Pereira, J. C. F.; Filipe, H. P.; Mata, J. L. G.; Colaço, R.; Saramago, B.; Serro, A. P. Simulation of the Hydrodynamic Conditions of the Eye to Better Reproduce the Drug Release from Hydrogel Contact Lenses: Experiments and Modeling. *Drug Deliv Transl Res* **2016**, *6* (6), 755–762. https://doi.org/10.1007/s13346-016-0303-1.

[491] Meany, E. L.; Andaya, R.; Tang, S.; Kasse, C. M.; Fuji, R. N.; Grosskopf, A. K.; D'aquino, A. L.; Bartoe, J. T.; Ybarra, R.; Shelton, A.; et al. Injectable Polymer-Nanoparticle Hydrogel for the Sustained Intravitreal Delivery of Bimatoprost. **2022**. https://doi.org/10.1002/adtp.202200207.

[492] Hou, H.; Wang, C.; Nan, K.; Freeman, W. R.; Sailor, M. J.; Cheng, L. Controlled Release of Dexamethasone From an Intravitreal Delivery System Using Porous Silicon Dioxide. *Invest Ophthalmol Vis Sci* **2016**, *57* (2), 557–566. https://doi.org/10.1167/IOVS.15-18559.

[493] Kotecha, A.; Lim, K. S.; Hirn, C.; Garway-Heath, D. Tonometry and Intraocular Pressure Fluctuation. *Glaucoma: Second Edition* **2015**, *1*, 98–108. https://doi.org/10.1016/B978-0-7020-5193-7.00010-8.

[494] Bhattacharjee, S. Understanding the Burst Release Phenomenon: Toward Designing Effective Nanoparticulate Drug-Delivery Systems. *Ther Deliv* **2020**, *12* (1), 21–36. https://doi.org/10.4155/TDE-2020-0099.

[495] Kamaly, N.; Yameen, B.; Wu, J.; Farokhzad, O. C. Degradable Controlled-Release Polymers and Polymeric Nanoparticles: Mechanisms of Controlling Drug Release. *Chem Rev* **2016**, *116* (4), 2602–2663. https://doi.org/10.1021/acs.chemrev.5b00346.

[496] Harrison, T. D.; Yunyaeva, O.; Borecki, A.; Hopkins, C. C.; de Bruyn, J. R.; Ragogna, P. J.; Gillies, E. R. Phosphonium Polyelectrolyte Complexes for the Encapsulation and Slow Release of Ionic Cargo. *Biomacromolecules* **2020**, *21* (1), 152–162. https://doi.org/10.1021/acs.biomac.9b01115.

[497] Fu, Y.; Kao, W. J. Drug Release Kinetics and Transport Mechanisms of Non- Degradable and Degradable Polymeric Delivery Systems. *Expert Opin Drug Deliv* **2011**, *7* (4), 429–444. https://doi.org/10.1517/17425241003602259.Drug.

[498] Brusch, M. L. Mathematical Models of Drug Release. In *Strategies to Modify the Drug Release from Pharmaceutical Systems*; Marcos Luciano Bruschi, Ed.; Elsevier, 2015; pp 63–86. https://doi.org/10.1016/B978-0-08-100092-2.00005-9.

[499] Putro, J. N.; Lunardi, V. B.; Soetaredjo, F. E.; Yuliana, M.; Santoso, S. P.; Wenten, I. G.; Ismadji, S. A Review of Gum Hydrocolloid Polyelectrolyte Complexes (Pec) for Biomedical Applications: Their Properties and Drug Delivery Studies. *Processes* **2021**, *9* (10). https://doi.org/10.3390/pr9101796.

[500] Ahmed, L.; Atif, R.; Eldeen, T. S.; Yahya, I.; Omara, A.; Eltayeb, M. Study the Using of Nanoparticles as Drug Delivery System Based on Mathematical Models for Controlled Release. *International Journal of Latest Technology in Engineering, Management & Applied Science* **2019**, *8* (5), 52–56.

[501] Ćirić, A.; Budinčić, J. M.; Medarević, Đ.; Dobričić, V.; Rmandić, M.; Barudžija, T.; Malenović, A.; Petrović, L.; Djekic, L. Evaluation of Chitosan/Xanthan Gum Polyelectrolyte Complexes Potential for PH-Dependent Oral Delivery of Escin. *Int J Biol Macromol* **2022**, *221*, 48–60. https://doi.org/10.1016/J.IJBIOMAC.2022.08.190.

[502] Jana, S.; Banerjee, A.; Gandhi, A. Preparation and Characterization of Chitosan Based Polyelectrolyte Complex as a Carrier of Aceclofenac. *Journal of PharmaSciTech* **2014**, *3* (2), 1–4.

[503] Magalhães, G. A.; Moura Neto, E.; Sombra, V. G.; Richter, A. R.; Abreu, C. M. W. S.; Feitosa, J. P. A.; Paula, H. C. B.; Goycoolea, F. M.; de Paula, R. C. M. Chitosan/Sterculia Striata Polysaccharides Nanocomplex as a Potential Chloroquine Drug Release Device. *Int J Biol Macromol* **2016**, *88*, 244–253. https://doi.org/10.1016/j.ijbiomac.2016.03.070.

[504] Shamloo, K.; Mistry, P.; Barbarino, A.; Ross, C.; Jhanji, V.; Sharma, A. Differential Effect of Proinflammatory Cytokines on Corneal and Conjunctival Epithelial Cell Mucins and Glycocalyx. *Transl Vis Sci Technol* **2021**, *10* (7). https://doi.org/10.1167/TVST.10.7.17.

[505] Burhan, A. M.; Klahan, B.; Cummins, W.; Andrés-Guerrero, V.; Byrne, M. E.; O'reilly, N. J.; Chauhan, A.; Fitzhenry, L.; Hughes, H. Posterior Segment Ophthalmic Drug Delivery: Role of Muco-Adhesion with a Special Focus on Chitosan. *Pharmaceutics 2021, Vol. 13, Page 1685* **2021**, *13* (10), 1685. https://doi.org/10.3390/PHARMACEUTICS13101685.

[506] Aranaz, I.; Alcántara, A. R.; Civera, M. C.; Arias, C.; Elorza, B.; Caballero, A. H.; Acosta, N.; Velasco, H.; Mecerreyes, D.; Antonio, R.; et al. Chitosan: An Overview of Its Properties and Applications. *Polymers 2021, Vol. 13, Page 3256* **2021**, *13* (19), 3256. https://doi.org/10.3390/POLYM13193256.

[507] Hassan, H. A. F. M.; Ali, A. I.; ElDesawy, E. M.; ElShafeey, A. H. Pharmacokinetic and Pharmacodynamic Evaluation of Gemifloxacin Chitosan Nanoparticles As an Antibacterial Ocular Dosage Form. *J Pharm Sci* **2022**, *111* (5), 1497–1508. https://doi.org/10.1016/J.XPHS.2021.12.016.

[508] Benamer Oudih, S.; Tahtat, D.; Nacer Khodja, A.; Mahlous, M.; Hammache, Y.; Guittoum, A. E.; Kebbouche Gana, S. Chitosan Nanoparticles with Controlled Size and Zeta Potential. *Polym Eng Sci* **2023**, *63* (3), 1011–1021. https://doi.org/10.1002/PEN.26261.

[509] Kalam, M. A.; Iqbal, M.; Alshememry, A.; Alkholief, M.; Alshamsan, A. Development and Evaluation of Chitosan Nanoparticles for Ocular Delivery of Tedizolid Phosphate. *Molecules* **2022**, *27* (7). https://doi.org/10.3390/MOLECULES27072326.

[510] Bravo-Anaya, L. M.; Fernández-Solís, K. G.; Rosselgong, J.; Nano-Rodríguez, J. L. E.; Carvajal, F.; Rinaudo, M. Chitosan-DNA Polyelectrolyte Complex: Influence of Chitosan Characteristics and Mechanism of Complex Formation. *Int J Biol Macromol* **2019**, *126*, 1037–1049. https://doi.org/10.1016/J.IJBIOMAC.2019.01.008.

[511] Popova, E. V.; Tikhomirova, V. E.; Beznos, O. V.; Chesnokova, N. B.; Grigoriev, Y. V.; Klyachko, N. L.; Kost, O. A. Chitosan-Covered Calcium Phosphate Particles as a Drug Vehicle for Delivery to the Eye. *Nanomedicine* **2022**, *40*, 102493. https://doi.org/10.1016/J.NANO.2021.102493.

[512] Asfour, M. H.; Abd El-Alim, S. H.; Awad, G. E. A.; Kassem, A. A. Chitosan/β-Glycerophosphate in Situ Forming Thermo-Sensitive Hydrogel for Improved Ocular Delivery of Moxifloxacin Hydrochloride. *European Journal of Pharmaceutical Sciences* **2021**, *167*, 106041. https://doi.org/10.1016/J.EJPS.2021.106041.

[513] Henao, E.; Delgado, E.; Contreras, H.; Quintana, G. Polyelectrolyte Complexation versus Ionotropic Gelation for Chitosan-Based Hydrogels with Carboxymethylcellulose, Carboxymethyl Starch, and Alginic Acid. *International Journal of Chemical Engineering* **2018**, *2018*. https://doi.org/10.1155/2018/3137167.

[514] Algharib, S. A.; Dawood, A.; Zhou, K.; Chen, D.; Li, C.; Meng, K.; Zhang, A.; Luo, W.; Ahmed, S.; Huang, L.; et al. Preparation of Chitosan Nanoparticles by Ionotropic Gelation Technique: Effects of Formulation Parameters and in Vitro Characterization. *J Mol Struct* **2022**, *1252*, 132129. https://doi.org/10.1016/j.molstruc.2021.132129.

[515] Cai, Y.; Lapitsky, Y. Biomolecular Uptake Effects on Chitosan/Tripolyphosphate Micro- and Nanoparticle Stability. *Colloids Surf B Biointerfaces* **2020**, *193*, 111081. https://doi.org/10.1016/J.COLSURFB.2020.111081.

[516] Marques Gonçalves, M.; Florencio Maluf, D.; Pontarolo, R.; Ketzer Saul, C.; Almouazen, E.; Chevalier, Y. Negatively Charged Chitosan Nanoparticles Prepared by Ionotropic Gelation for Encapsulation of Positively Charged Proteins. *Int J Pharm* **2023**, *642*, 123164. https://doi.org/10.1016/J.IJPHARM.2023.123164.

[517] Mohammady, M.; mohammadi, Y.; Yousefi, G. Freeze-Drying of Pharmaceutical and Nutraceutical Nanoparticles: The Effects of Formulation and Technique Parameters on

Nanoparticles Characteristics. *J Pharm Sci* **2020**, *109* (11), 3235–3247. https://doi.org/10.1016/J.XPHS.2020.07.015.

[518] Malviya, R.; Raj, S.; Fuloria, S.; Subramaniyan, V.; Sathasivam, K.; Kumari, U.; Meenakshi, D. U.; Porwal, O.; Kumar, D. H.; Singh, A.; et al. Evaluation of Antitumor Efficacy of Chitosan-Tamarind Gum Polysaccharide Polyelectrolyte Complex Stabilized Nanoparticles of Simvastatin. *Int J Nanomedicine* **2021**, *16*, 2533–2553. https://doi.org/10.2147/IJN.S300991.

[519] Mohan, P.; Rangari, V. D.; Kesavan, K. Cationic Chitosan/Pectin Polyelectrolyte Nanocapsules of Moxifloxacin as Novel Topical Management System for Bacterial Keratitis. *Curr Eye Res* **2022**, *47* (11), 1498–1507. https://doi.org/10.1080/02713683.2022.2124274.

[520] Dubey, V.; Mohan, P.; Dangi, J. S.; Kesavan, K. Brinzolamide Loaded Chitosan-Pectin Mucoadhesive Nanocapsules for Management of Glaucoma: Formulation, Characterization and Pharmacodynamic Study. *Int J Biol Macromol* **2020**, *152*, 1224–1232. https://doi.org/10.1016/J.IJBIOMAC.2019.10.219.

[521] Elkady, O. A.; Tadros, M. I.; El-laithy, H. M. QbD Approach for Novel Crosslinker-Free Ionotropic Gelation of Risedronate Sodium–Chitosan Nebulizable Microspheres: Optimization and Characterization. *AAPS PharmSciTech* **2020**, *21* (1), 1–18. https://doi.org/10.1208/S12249-019-1561-2/FIGURES/9.

[522] Bin-Jumah, M.; Gilani, S. J.; Jahangir, M. A.; Zafar, A.; Alshehri, S.; Yasir, M.; Kala, C.; Taleuzzaman, M.; Imam, S. S. Clarithromycin-Loaded Ocular Chitosan Nanoparticle: Formulation, Optimization, Characterization, Ocular Irritation, and Antimicrobial Activity. *Int J Nanomedicine* **2020**, *15*, 7861–7875. https://doi.org/10.2147/IJN.S269004.

[523] Benamer Oudih, S.; Tahtat, D.; Nacer Khodja, A.; Mahlous, M.; Hammache, Y.; Guittoum, A. E.; Kebbouche Gana, S. Chitosan Nanoparticles with Controlled Size and Zeta Potential. *Polym Eng Sci* **2023**, *63* (3), 1011–1021. https://doi.org/10.1002/PEN.26261.

[524] Khoerunnisa, F.; Nurhayati, M.; Dara, F.; Rizki, R.; Nasir, M.; Aziz, H. A.; Hendrawan, H.; Poh, N. E.; Kaewsaneha, C.; Opaprakasit, P. Physicochemical Properties of TPP-Crosslinked Chitosan Nanoparticles as Potential Antibacterial Agents. *Fibers and Polymers* **2021**, *22* (11), 2954–2964. https://doi.org/10.1007/S12221-021-0397-Z/METRICS.

[525] Martins, A. F.; de Oliveira, D. M.; Pereira, A. G. B.; Rubira, A. F.; Muniz, E. C. Chitosan/TPP Microparticles Obtained by Microemulsion Method Applied in Controlled Release of Heparin. *Int J Biol Macromol* **2012**, *51* (5), 1127–1133. https://doi.org/10.1016/J.IJBIOMAC.2012.08.032.

[526] de Carvalho, F. G.; Magalhães, T. C.; Teixeira, N. M.; Gondim, B. L. C.; Carlo, H. L.; dos Santos, R. L.; de Oliveira, A. R.; Denadai, Â. M. L. Synthesis and Characterization of TPP/Chitosan Nanoparticles: Colloidal Mechanism of Reaction and Antifungal Effect on C. Albicans Biofilm Formation. *Materials Science and Engineering: C* **2019**, *104*, 109885. https://doi.org/10.1016/J.MSEC.2019.109885.

[527] Delas, T.; Mock-Joubert, M.; Faivre, J.; Hofmaier, M.; Sandre, O.; Dole, F.; Chapel, J. P.; Crépet, A.; Trombotto, S.; Delair, T.; et al. Effects of Chain Length of Chitosan Oligosaccharides on Solution Properties and Complexation with SiRNA. *Polymers 2019, Vol. 11, Page 1236* **2019**, *11* (8), 1236. https://doi.org/10.3390/POLYM11081236.

[528] Zhu, Y.; Marin, L. M.; Xiao, Y.; Gillies, E. R.; Siqueira, W. L. Ph-Sensitive Chitosan Nanoparticles for Salivary Protein Delivery. *Nanomaterials* **2021**, *11* (4). https://doi.org/10.3390/NANO11041028/S1.

[529] Motiei, M.; Sedlařík, V.; Lucia, L. A.; Fei, H.; Münster, L. Stabilization of Chitosan-Based Polyelectrolyte Nanoparticle Cargo Delivery Biomaterials by a Multiple Ionic Cross-Linking Strategy. *Carbohydr Polym* **2020**, *231*, 115709. https://doi.org/10.1016/J.CARBPOL.2019.115709.

[530] Li, J.; Jin, H.; Abdur Razzak, M.; Ji Kim, E.; Sik Choi, S. Crosslinker-Free Bovine Serum Albumin-Loaded Chitosan/Alginate Nanocomplex for PH-Responsive Bursting Release of Oral-Administered Protein. *Biotechnology and Bioprocess Engineering* **2021**, *26*, 40–50. https://doi.org/10.1007/s12257-021-0243-6.

[531] Carvalho, S. G.; dos Santos, A. M.; Silvestre, A. L. P.; Meneguin, A. B.; Ferreira, L. M. B.; Chorilli, M.; Gremião, M. P. D. New Insights into Physicochemical Aspects Involved in the Formation of Polyelectrolyte Complexes Based on Chitosan and Dextran Sulfate. *Carbohydr Polym* **2021**, *271*, 118436. https://doi.org/10.1016/J.CARBPOL.2021.118436.

[532] Yu, H.; Nguyen, M. H.; Hadinoto, K. Effects of Chitosan Molecular Weight on the Physical and Dissolution Characteristics of Amorphous Curcumin–Chitosan Nanoparticle Complex. *Drug Dev Ind Pharm* **2018**, *44* (1), 82–88. https://doi.org/10.1080/03639045.2017.1373802.

[533] Fabiano, A.; De Leo, M.; Cerri, L.; Piras, A. M.; Braca, A.; Zambito, Y. Saffron Extract Self-Assembled Nanoparticles to Prolong the Precorneal Residence of Crocin. *J Drug Deliv Sci Technol* **2022**, *74*, 103580. https://doi.org/10.1016/J.JDDST.2022.103580.

[534] Józsa, L.; Nemes, D.; Pető, Á.; Kósa, D.; Révész, R.; Bácskay, I.; Haimhoffer, Á.; Vasvári, G. Recent Options and Techniques to Assess Improved Bioavailability: In Vitro and Ex Vivo Methods. *Pharmaceutics* **2023**, *15* (4). https://doi.org/10.3390/PHARMACEUTICS15041146.

[535] Dave, R. S.; Goostrey, T. C.; Ziolkowska, M.; Czerny-Holownia, S.; Hoare, T.; Sheardown, H. Ocular Drug Delivery to the Anterior Segment Using Nanocarriers: A Mucoadhesive/Mucopenetrative Perspective. *Journal of Controlled Release* **2021**, *336*, 71–88. https://doi.org/10.1016/J.JCONREL.2021.06.011.

[536] Terreni, E.; Chetoni, P.; Tampucci, S.; Burgalassi, S.; Al-Kinani, A. A.; Alany, R. G.; Monti, D. Assembling Surfactants-Mucoadhesive Polymer Nanomicelles (ASMP-Nano) for Ocular Delivery of Cyclosporine-A. *Pharmaceutics 2020, Vol. 12, Page 253* **2020**, *12* (3), 253. https://doi.org/10.3390/PHARMACEUTICS12030253.

[537] Yu, A.; Shi, H.; Liu, H.; Bao, Z.; Dai, M.; Lin, D.; Lin, D.; Xu, X.; Li, X.; Wang, Y. Mucoadhesive Dexamethasone-Glycol Chitosan Nanoparticles for Ophthalmic Drug Delivery. *Int J Pharm* **2020**, *575*, 118943. https://doi.org/10.1016/J.IJPHARM.2019.118943.

[538] Fini, M. E.; Jeong, S.; Gong, H.; Martinez-Carrasco, R.; Laver, N. M. V.; Hijikata, M.; Keicho, N.; Argüeso, P. Membrane-Associated Mucins of the Ocular Surface: New Genes, New Protein Functions and New Biological Roles in Human and Mouse. *Prog Retin Eye Res* **2020**, *75*, 100777. https://doi.org/10.1016/j.preteyeres.2019.100777.

[539] Hori, Y. Secreted Mucins on the Ocular Surface. *Invest Ophthalmol Vis Sci* **2018**, *59* (14), DES151–DES156. https://doi.org/10.1167/IOVS.17-23623.

[540] LI, W.; ZHOU, J.; XU, Y. Study of the in Vitro Cytotoxicity Testing of Medical Devices. *Biomed Rep* **2015**, *3* (5), 617. https://doi.org/10.3892/BR.2015.481.

[541] Fathalla, Z.; Fatease, A. Al; Abdelkader, H. Formulation and In-Vitro/Ex-Vivo Characterization of Pregelled Hybrid Alginate–Chitosan Microparticles for Ocular Delivery of Ketorolac Tromethamine. *Polymers 2023, Vol. 15, Page 2773* **2023**, *15* (13), 2773. https://doi.org/10.3390/POLYM15132773.

[542] Ch, S.; Paul, M.; Padaga, S. G.; Ghosh, B.; Biswas, S. Cationized Gelatin-Sodium Alginate Polyelectrolyte Nanoparticles Encapsulating Moxifloxacin as an Eye Drop to Treat Bacterial Keratitis. *Int J Biol Macromol* **2024**, *264*, 130457. https://doi.org/10.1016/J.IJBIOMAC.2024.130457.

[543] Ghasemi, M.; Turnbull, T.; Sebastian, S.; Kempson, I. The Mtt Assay: Utility, Limitations, Pitfalls, and Interpretation in Bulk and Single-Cell Analysis. *Int J Mol Sci* **2021**, *22* (23), 12827. https://doi.org/10.3390/IJMS222312827/S1.

[544] Zhang, J.; Hong, Y.; Cao, W.; Yin, S.; Shi, H.; Ying, W. SIRT2, ERK and Nrf2 Mediate NAD+ Treatment-Induced Increase in the Antioxidant Capacity of PC12 Cells under Basal Conditions. *Front Mol Neurosci* **2019**, *12*, 443450. https://doi.org/10.3389/FNMOL.2019.00108/BIBTEX.

[545] Yoshida, M.; Apte, R. S. NAD+ Boosting Brings Tears to Aging Eyes. *Nature Aging 2022 2:2* **2022**, *2* (2), 97–99. https://doi.org/10.1038/s43587-022-00172-5.

[546] Meng, Y. F.; Pu, Q.; Dai, S. Y.; Ma, Q.; Li, X.; Zhu, W. Nicotinamide Mononucleotide Alleviates Hyperosmolarity-Induced Il-17a Secretion and Macrophage Activation in Corneal Epithelial Cells/ Macrophage Co-Culture System. *J Inflamm Res* **2021**, *14*, 479–493. https://doi.org/10.2147/JIR.S292764.

[547] Chen, X.; Amorim, J. A.; Moustafa, G. A.; Lee, J. J.; Yu, Z.; Ishihara, K.; Iesato, Y.; Barbisan, P.; Ueta, T.; Togka, K. A.; et al. Neuroprotective Effects and Mechanisms of Action of Nicotinamide Mononucleotide (NMN) in a Photoreceptor Degenerative Model of Retinal Detachment. *Aging (Albany NY)* **2020**, *12* (24), 24504. https://doi.org/10.18632/AGING.202453.

[548] Augustine, R.; Hasan, A.; Primavera, R.; Wilson, R. J.; Thakor, A. S.; Kevadiya, B. D. Cellular Uptake and Retention of Nanoparticles: Insights on Particle Properties and Interaction with Cellular Components. *Mater Today Commun* **2020**, *25*, 101692. https://doi.org/10.1016/J.MTCOMM.2020.101692.

[549] Chiesa, E.; Greco, A.; Riva, F.; Dorati, R.; Conti, B.; Modena, T.; Genta, I. CD44-Targeted Carriers: The Role of Molecular Weight of Hyaluronic Acid in the Uptake of Hyaluronic Acid-Based Nanoparticles. *Pharmaceuticals 2022, Vol. 15, Page 103* **2022**, *15* (1), 103. https://doi.org/10.3390/PH15010103.

[550] Tsai, C. H.; Hoang, L. N.; Lin, C. C.; Pan, L. C.; Wu, C. L.; Lin, I. C.; Wang, P. Y.; Tseng, C. L. Evaluation of Topical and Subconjunctival Injection of Hyaluronic Acid-Coated Nanoparticles for Drug Delivery to Posterior Eye. *Pharmaceutics 2022, Vol. 14, Page 1253* **2022**, *14* (6), 1253. https://doi.org/10.3390/PHARMACEUTICS14061253.

[551] Bongiovì, F.; Fiorica, C.; Palumbo, F. S.; Pitarresi, G.; Giammona, G. Hyaluronic Acid Based Nanohydrogels Fabricated by Microfluidics for the Potential Targeted Release of Imatinib: Characterization and Preliminary Evaluation of the Antiangiogenic Effect. *Int J Pharm* **2020**, *573*, 118851. https://doi.org/10.1016/J.IJPHARM.2019.118851.

[552] Christensen, G.; Urimi, D.; Lorenzo-Soler, L.; Schipper, N.; Paquet-Durand, F. Ocular Permeability, Intraocular Biodistribution of Lipid Nanocapsule Formulation Intended for Retinal Drug Delivery. *European Journal of Pharmaceutics and Biopharmaceutics* **2023**, *187*, 175–183. https://doi.org/10.1016/J.EJPB.2023.04.012.

[553] Delrish, E.; Ghassemi, F.; Jabbarvand, M.; Lashay, A.; Atyabi, F.; Soleimani, M.; Dinarvand, R. Biodistribution of Cy5-Labeled Thiolated and Methylated Chitosan-Carboxymethyl Dextran Nanoparticles in an Animal Model of Retinoblastoma. *J Ophthalmic Vis Res* **2022**, *17* (1), 58. https://doi.org/10.18502/JOVR.V17I1.10171.

[554] Liu, R.; Fei, S.; Zhang, X.; Hua, Z.; Tan, M. Layer-by-Layer Oral-Deliverable Nanoparticles Targeted Microfold Cells to Promote Lutein Absorption in Alleviating Dry Eye Disease. *Chemical Engineering Journal* **2024**, *479*, 147590. https://doi.org/10.1016/J.CEJ.2023.147590.

[555] Kicková, E.; Salmaso, S.; Mastrotto, F.; Caliceti, P.; Urtti, A. Pullulan Based Bioconjugates for Ocular Dexamethasone Delivery. *Pharmaceutics* **2021**, *13* (6), 791. https://doi.org/10.3390/PHARMACEUTICS13060791/S1.

[556] Dang, Y.; Waxman, S.; Wang, C.; Loewen, R. T.; Sun, M.; Loewen, N. A. A Porcine Ex Vivo Model of Pigmentary Glaucoma. *Scientific Reports 2018 8:1* **2018**, *8* (1), 1–14. https://doi.org/10.1038/s41598-018-23861-x.

[557] Araki-Sasaki, K.; Ohashi, Y.; Sasabe, T.; Hayashi, K.; Watanabe, H.; Tano, Y.; Handa\, H. An SV40-Immortalized Human Corneal Epithelial Cell Line and Its Characterization. *Invest Ophthalmol Vis Sci* **1995**, *36* (3), 614–621.

[558] Reviakine, I.; Johannsmann, D.; Richter, R. P. Hearing What You Cannot See and Visualizing What You Hear: Interpreting Quartz Crystal Microbalance Data from Solvated Interfaces. *Anal Chem* **2011**, *83* (23), 8838–8848. https://doi.org/10.1021/AC201778H/ASSET/IMAGES/LARGE/AC-2011-01778H_0006.JPEG.

[559] Dave, R. S.; Goostrey, T. C.; Ziolkowska, M.; Czerny-Holownia, S.; Hoare, T.; Sheardown, H. Ocular Drug Delivery to the Anterior Segment Using Nanocarriers: A Mucoadhesive/Mucopenetrative Perspective. *Journal of Controlled Release* **2021**, *336*, 71–88. https://doi.org/10.1016/J.JCONREL.2021.06.011.

[560] Mosley, R. J.; Talarico, M. V; Byrne, M. E. Recent Applications of QCM-D for the Design, Synthesis, and Characterization of Bioactive Materials. *J Bioact Compat Polym* **2021**, *36* (4), 261–275. https://doi.org/10.1177/08839115211014216.

[561] Grießinger, J.; Dünnhaupt, S.; Cattoz, B.; Griffiths, P.; Oh, S.; Gómez, S. B. i; Wilcox, M.; Pearson, J.; Gumbleton, M.; Abdulkarim, M.; et al. Methods to Determine the Interactions of Micro- and Nanoparticles with Mucus. *European Journal of Pharmaceutics and Biopharmaceutics* **2015**, *96*, 464–476. https://doi.org/10.1016/j.ejpb.2015.01.005.

[562] Watchorn, J.; Clasky, A. J.; Prakash, G.; Johnston, I. A. E.; Chen, P. Z.; Gu, F. X. Untangling Mucosal Drug Delivery: Engineering, Designing, and Testing Nanoparticles to Overcome the Mucus Barrier. *ACS Biomater Sci Eng* **2022**, *8* (4), 1396–1426. https://doi.org/10.1021/ACSBIOMATERIALS.2C00047/ASSET/IMAGES/MEDIUM/AB2C00047_0010.GIF.

[563] Oh, S.; Wilcox, M.; Pearson, J. P.; Borrós, S. Optimal Design for Studying Mucoadhesive Polymers Interaction with Gastric Mucin Using a Quartz Crystal Microbalance with Dissipation (QCM-D): Comparison of Two Different Mucin Origins. *European Journal of Pharmaceutics and Biopharmaceutics* **2015**, *96*, 477–483. https://doi.org/10.1016/j.ejpb.2015.08.002.

[564] Graça, A.; Gonçalves, L. M.; Raposo, S.; Ribeiro, H. M.; Marto, J. Useful in Vitro Techniques to Evaluate the Mucoadhesive Properties of Hyaluronic Acid-Based Ocular Delivery Systems. *Pharmaceutics* **2018**, *10* (3). https://doi.org/10.3390/pharmaceutics10030110.

[565] Landucci, E.; Mazzantini, C.; Calvani, M.; Pellegrini-Giampietro, D. E.; Bergonzi, M. C. Evaluation of Conventional and Hyaluronic Acid-Coated Thymoquinone Liposomes in an In Vitro Model of Dry Eye. *Pharmaceutics* **2023**, *15* (2). https://doi.org/10.3390/PHARMACEUTICS15020578.

[566] Mangiacotte, N.; Prosperi-Porta, G.; Liu, L.; Dodd, M.; Sheardown, H. Mucoadhesive Nanoparticles for Drug Delivery to the Anterior Eye. *Nanomaterials* **2020**, *10* (7), 1–16. https://doi.org/10.3390/nano10071400.

[567] López-García, J.; Lehocký, M.; Humpolíček, P.; Sáha, P. HaCaT Keratinocytes Response on Antimicrobial Atelocollagen Substrates: Extent of Cytotoxicity, Cell Viability and Proliferation. *J Funct Biomater* **2014**, *5* (2), 43. https://doi.org/10.3390/JFB5020043.

[568] ISO 10993-5:2009 - Biological evaluation of medical devices — Part 5: Tests for in vitro cytotoxicity. Available online: https://www.iso.org/standard/36406.html (Accessed on: 04 April 2024).

[569] Zoe, L. H.; David, S. R.; Rajabalaya, R. Chitosan Nanoparticle Toxicity: A Comprehensive Literature Review of in Vivo and in Vitro Assessments for Medical Applications. *Toxicol Rep* **2023**, *11*, 83–106. https://doi.org/10.1016/J.TOXREP.2023.06.012.

[570] Hu, Y. L.; Qi, W.; Han, F.; Shao, J. Z.; Gao, J. Q. Toxicity Evaluation of Biodegradable Chitosan Nanoparticles Using a Zebrafish Embryo Model. *Int J Nanomedicine* **2011**, *6*, 3351. https://doi.org/10.2147/IJN.S25853.

[571] Radwan, S. E. S.; El-Moslemany, R. M.; Mehanna, R. A.; Thabet, E. H.; Abdelfattah, E. Z. A.; El-Kamel, A. Chitosan-Coated Bovine Serum Albumin Nanoparticles for Topical Tetrandrine Delivery in Glaucoma: In Vitro and in Vivo Assessment. *Drug Deliv* **2022**, *29* (1), 1150–1163. https://doi.org/10.1080/10717544.2022.2058648.

[572] Jesus, S.; Marques, A. P.; Duarte, A.; Soares, E.; Costa, J. P.; Colaço, M.; Schmutz, M.; Som, C.; Borchard, G.; Wick, P.; et al. Chitosan Nanoparticles: Shedding Light on Immunotoxicity

and Hemocompatibility. *Front Bioeng Biotechnol* **2020**, *8*, 509196. https://doi.org/10.3389/FBIOE.2020.00100/BIBTEX.

[573] Mohamed, A.; Korzhikov-Vlakh, V.; Zhang, N.; Said, A.; Pilipenko, I.; Schäfer-Korting, M.; Zoschke, C.; Tennikova, T. Effect of Poly(L-Lysine) and Heparin Coatings on the Surface of Polyester-Based Particles on Prednisolone Release and Biocompatibility. *Pharmaceutics* **2021**, *13* (6). https://doi.org/10.3390/PHARMACEUTICS13060801/S1.

[574] Fan, W.; Han, H.; Lu, Z.; Huang, Y.; Zhang, Y.; Chen, Y.; Zhang, X.; Ji, J.; Yao, K. ε-Poly-L-Lysine-Modified Polydopamine Nanoparticles for Targeted Photothermal Therapy of Drug-Resistant Bacterial Keratitis. *Bioeng Transl Med* **2023**, *8* (1), e10380. https://doi.org/10.1002/BTM2.10380.

[575] Kennedy, S. M.; Deshpande, P.; Gallagher, A. G.; Horsburgh, M. J.; Allison, H. E.; Kaye, S. B.; Wellings, D. A.; Williams, R. L. Amoebicidal Activity of Poly-Epsilon-Lysine Functionalized Hydrogels. *Invest Ophthalmol Vis Sci* **2022**, *63* (1), 11–11. https://doi.org/10.1167/IOVS.63.1.11.

[576] Zhou, B.; Zhao, G.; Zhu, Y.; Chen, X.; Zhang, N.; Yang, J.; Lin, H. Protective Effects of Nicotinamide Riboside on H2O2-Induced Oxidative Damage in Lens Epithelial Cells. *Curr Eye Res* **2021**, *46* (7), 961–970. https://doi.org/10.1080/02713683.2020.1855662.

[577] Nguyen, H. P.; Shin, S.; Shin, K. J.; Tran, P. H.; Park, H.; De Tran, Q.; No, M. H.; Sun, J. S.; Kim, K. W.; Kwak, H. B.; et al. Protective Effect of TPP-Niacin on Microgravity-Induced Oxidative Stress and Mitochondrial Dysfunction of Retinal Epithelial Cells. *Biochimica et Biophysica Acta (BBA) - Molecular Cell Research* **2023**, *1870* (1), 119384. https://doi.org/10.1016/J.BBAMCR.2022.119384.

[578] Sies, H. Hydrogen Peroxide as a Central Redox Signaling Molecule in Physiological Oxidative Stress: Oxidative Eustress. *Redox Biol* **2017**, *11*, 613–619. https://doi.org/10.1016/J.REDOX.2016.12.035.

[579] Di Marzo, N.; Chisci, E.; Giovannoni, R. The Role of Hydrogen Peroxide in Redox-Dependent Signaling: Homeostatic and Pathological Responses in Mammalian Cells. *Cells 2018, Vol. 7, Page 156* **2018**, *7* (10), 156. https://doi.org/10.3390/CELLS7100156.

[580] Ransy, C.; Vaz, C.; Lombès, A.; Bouillaud, F. Use of H2O2 to Cause Oxidative Stress, the Catalase Issue. *Int J Mol Sci* **2020**, *21* (23), 1–14. https://doi.org/10.3390/IJMS21239149.

[581] Saba, T.; Burnett, J. W. H.; Li, J.; Kechagiopoulos, P. N.; Wang, X. A Facile Analytical Method for Reliable Selectivity Examination in Cofactor NADH Regeneration. *Chemical Communications* **2020**, *56* (8), 1231–1234. https://doi.org/10.1039/C9CC07805C.

[582] Pescina, S.; Govoni, P.; Potenza, A.; Padula, C.; Santi, P.; Nicoli, S. Development of a Convenient Ex Vivo Model for the Study of the Transcorneal Permeation of Drugs: Histological and Permeability Evaluation. *J Pharm Sci* **2015**, *104* (1), 63–71. https://doi.org/10.1002/JPS.24231.

[583] Pandit, J.; Sultana, Y.; Aqil, M. Chitosan Coated Nanoparticles for Efficient Delivery of Bevacizumab in the Posterior Ocular Tissues via Subconjunctival Administration. *Carbohydr Polym* **2021**, *267*, 118217. https://doi.org/10.1016/J.CARBPOL.2021.118217.

[584] Lorenzo-Veiga, B.; Diaz-Rodriguez, P.; Alvarez-Lorenzo, C.; Loftsson, T.; Sigurdsson, H. H. In Vitro and Ex Vivo Evaluation of Nepafenac-Based Cyclodextrin Microparticles for Treatment of Eye Inflammation. *Nanomaterials 2020, Vol. 10, Page 709* **2020**, *10* (4), 709. https://doi.org/10.3390/NANO10040709.

[585] Fathalla, Z.; Fatease, A. Al; Abdelkader, H. Formulation and In-Vitro/Ex-Vivo Characterization of Pregelled Hybrid Alginate–Chitosan Microparticles for Ocular Delivery of Ketorolac Tromethamine. *Polymers 2023, Vol. 15, Page 2773* **2023**, *15* (13), 2773. https://doi.org/10.3390/POLYM15132773.

[586] Tighsazzadeh, M.; Boateng, J. Matrix Hyaluronic Acid and Bilayer Poly-Hydroxyethyl Methacrylate-Hyaluronic Acid Films as Potential Ocular Drug Delivery Platforms. *Int J Biol Macromol* **2024**, *260*, 129496. https://doi.org/10.1016/J.IJBIOMAC.2024.129496.

[587] Mohamed, H. B.; Attia Shafie, M. A.; Mekkawy, A. I. Chitosan Nanoparticles for Meloxicam Ocular Delivery: Development, In Vitro Characterization, and In Vivo Evaluation in a Rabbit Eye Model. *Pharmaceutics* **2022**, *14* (5), 893. https://doi.org/10.3390/pharmaceutics14050893.

[588] Santana, C. P.; Matter, B. A.; Patil, M. A.; Silva-Cunha, A.; Kompella, U. B. Corneal Permeability and Uptake of Twenty-Five Drugs: Species Comparison and Quantitative

Structure–Permeability Relationships. *Pharmaceutics* **2023**, *15* (6). https://doi.org/10.3390/PHARMACEUTICS15061646/S1.

[589] Singh, M.; Bharadwaj, S.; Lee, K. E.; Kang, S. G. Therapeutic Nanoemulsions in Ophthalmic Drug Administration: Concept in Formulations and Characterization Techniques for Ocular Drug Delivery. *Journal of Controlled Release* **2020**, *328*, 895–916. https://doi.org/10.1016/J.JCONREL.2020.10.025.

[590] Allyn, M. M.; Luo, R. H.; Hellwarth, E. B.; Swindle-Reilly, K. E. Considerations for Polymers Used in Ocular Drug Delivery. *Front Med (Lausanne)* **2022**, *8*, 787644. https://doi.org/10.3389/FMED.2021.787644/BIBTEX.

[591] Swetledge, S.; Carter, R.; Stout, R.; Astete, C. E.; Jung, J. P.; Sabliov, C. M. Stability and Ocular Biodistribution of Topically Administered PLGA Nanoparticles. *Scientific Reports 2021 11:1* **2021**, *11* (1), 1–11. https://doi.org/10.1038/s41598-021-90792-5.

[592] Marquina, S.; Ozgul, M.; Robertson-Brown, K.; Kenney, M. C. A Review on PLGA Particles as a Sustained Drug-Delivery System and Its Effect on the Retina. *Exp Eye Res* **2023**, *235*, 109626. https://doi.org/10.1016/J.EXER.2023.109626.

[593] Zhang, E.; Zhukova, V.; Semyonkin, A.; Osipova, N.; Malinovskaya, Y.; Maksimenko, O.; Chernikov, V.; Sokolov, M.; Grigartzik, L.; Sabel, B. A.; et al. Release Kinetics of Fluorescent Dyes from PLGA Nanoparticles in Retinal Blood Vessels: In Vivo Monitoring and Ex Vivo Localization. *European Journal of Pharmaceutics and Biopharmaceutics* **2020**, *150*, 131–142. https://doi.org/10.1016/J.EJPB.2020.03.006.

[594] Joseph, R. R.; Tan, D. W. N.; Ramon, M. R. M.; Natarajan, J. V.; Agrawal, R.; Wong, T. T.; Venkatraman, S. S. Characterization of Liposomal Carriers for the Trans-Scleral Transport of Ranibizumab. *Scientific Reports 2017 7:1* **2017**, *7* (1), 1–10. https://doi.org/10.1038/s41598-017-16791-7.

[595] Lai, S.; Wei, Y.; Wu, Q.; Zhou, K.; Liu, T.; Zhang, Y.; Jiang, N.; Xiao, W.; Chen, J.; Liu, Q.; et al. Liposomes for Effective Drug Delivery to the Ocular Posterior Chamber. *J Nanobiotechnology* **2019**, *17* (1), 1–12. https://doi.org/10.1186/S12951-019-0498-7/FIGURES/5.

[596] Platania, C. B. M.; Fisichella, V.; Fidilio, A.; Geraci, F.; Lazzara, F.; Leggio, G. M.; Salomone, S.; Drago, F.; Pignatello, R.; Caraci, F.; et al. Topical Ocular Delivery of TGF-B1 to the Back of the Eye: Implications in Age-Related Neurodegenerative Diseases. *International Journal of Molecular Sciences 2017, Vol. 18, Page 2076* **2017**, *18* (10), 2076. https://doi.org/10.3390/IJMS18102076.

[597] Kakkar, S.; Singh, M.; Mohan Karuppayil, S.; Raut, J. S.; Giansanti, F.; Papucci, L.; Schiavone, N.; Nag, T. C.; Gao, N.; Yu, F. S. X.; et al. Lipo-PEG Nano-Ocular Formulation Successfully Encapsulates Hydrophilic Fluconazole and Traverses Corneal and Non-Corneal Path to Reach Posterior Eye Segment. *J Drug Target* **2021**, *29* (6), 631–650. https://doi.org/10.1080/1061186X.2020.1871483.

[598] Zhou, C.; Lei, F.; Sharma, J.; Hui, P. C.; Wolkow, N.; Dohlman, C. H.; Vavvas, D. G.; Chodosh, J.; Paschalis, E. I. Sustained Inhibition of VEGF and TNF-α Achieves Multi-Ocular Protection and Prevents Formation of Blood Vessels after Severe Ocular Trauma. *Pharmaceutics 2023, Vol. 15, Page 2059* **2023**, *15* (8), 2059. https://doi.org/10.3390/PHARMACEUTICS15082059.

[599] Zhang, X. P.; Sun, J. G.; Yao, J.; Shan, K.; Liu, B. H.; Yao, M. Di; Ge, H. M.; Jiang, Q.; Zhao, C.; Yan, B. Effect of Nanoencapsulation Using Poly (Lactide-Co-Glycolide) (PLGA) on Anti-Angiogenic Activity of Bevacizumab for Ocular Angiogenesis Therapy. *Biomedicine & Pharmacotherapy* **2018**, *107*, 1056–1063. https://doi.org/10.1016/J.BIOPHA.2018.08.092.

[600] Lagreca, E.; Onesto, V.; Di Natale, C.; La Manna, S.; Netti, P. A.; Vecchione, R. Recent Advances in the Formulation of PLGA Microparticles for Controlled Drug Delivery. *Progress in Biomaterials 2020 9:4* **2020**, *9* (4), 153–174. https://doi.org/10.1007/S40204-020-00139-Y.

[601] Panigrahi, D.; Sahu, P. K.; Swain, S.; Verma, R. K. Quality by Design Prospects of Pharmaceuticals Application of Double Emulsion Method for PLGA Loaded Nanoparticles. *SN Applied Sciences 2021 3:6* **2021**, *3* (6), 1–21. https://doi.org/10.1007/S42452-021-04609-1.

[602] Hernández-Giottonini, K. Y.; Rodríguez-Córdova, R. J.; Gutiérrez-Valenzuela, C. A.; Peñuñuri-Miranda, O.; Zavala-Rivera, P.; Guerrero-Germán, P.; Lucero-Acuña, A. PLGA Nanoparticle Preparations by Emulsification and Nanoprecipitation Techniques: Effects of Formulation Parameters. *RSC Adv* **2020**, *10* (8), 4218. https://doi.org/10.1039/C9RA10857B.

[603] López-Machado, A.; Díaz, N.; Cano, A.; Espina, M.; Badía, J.; Baldomà, L.; Calpena, A. C.; Biancardi, M.; Souto, E. B.; García, M. L.; et al. Development of Topical Eye-Drops of

Lactoferrin-Loaded Biodegradable Nanoparticles for the Treatment of Anterior Segment Inflammatory Processes. *Int J Pharm* **2021**, *609*, 121188. https://doi.org/10.1016/J.IJPHARM.2021.121188.

[604] Yushu, H.; Venkatraman, S. The Effect of Process Variables on the Morphology and Release Characteristics of Protein-Loaded PLGA Particles. *J Appl Polym Sci* **2006**, *101* (5), 3053–3061. https://doi.org/10.1002/app.23933.

[605] Ismail, R.; Sovány, T.; Gácsi, A.; Ambrus, R.; Katona, G.; Imre, N.; Csóka, I. Synthesis and Statistical Optimization of Poly (Lactic-Co-Glycolic Acid) Nanoparticles Encapsulating GLP1 Analog Designed for Oral Delivery. *Pharm Res* **2019**, *36* (7). https://doi.org/10.1007/s11095-019-2620-9.

[606] Leister, N.; Karbstein, H. P. Evaluating the Stability of Double Emulsions—A Review of the Measurement Techniques for the Systematic Investigation of Instability Mechanisms. *Colloids and Interfaces 2020, Vol. 4, Page 8* **2020**, *4* (1), 8. https://doi.org/10.3390/COLLOIDS4010008.

[607] Yu, T.; Zhao, S.; Li, Z.; Wang, Y.; Xu, B.; Fang, D.; Wang, F.; Zhang, Z.; He, L.; Song, X.; et al. Enhanced and Extended Anti-Hypertensive Effect of VP5 Nanoparticles. *Int J Mol Sci* **2016**, *17* (12). https://doi.org/10.3390/IJMS17121977.

[608] Abdelkader, D. H.; El-Gizawy, S. A.; Faheem, A. M.; McCarron, P. A.; Osman, M. A. Effect of Process Variables on Formulation, in-Vitro Characterisation and Subcutaneous Delivery of Insulin PLGA Nanoparticles: An Optimisation Study. *J Drug Deliv Sci Technol* **2018**, *43*, 160–171. https://doi.org/10.1016/J.JDDST.2017.10.004.

[609] Sahoo, S. K.; Panyam, J.; Prabha, S.; Labhasetwar, V. Residual Polyvinyl Alcohol Associated with Poly (d,l-Lactide-Co-Glycolide) Nanoparticles Affects Their Physical Properties and Cellular Uptake. *Journal of Controlled Release* **2002**, *82* (1), 105–114. https://doi.org/10.1016/S0168-3659(02)00127-X.

[610] Gonzalez Gomez, A.; Syed, S.; Marshall, K.; Hosseinidoust, Z. Liposomal Nanovesicles for Efficient Encapsulation of Staphylococcal Antibiotics. *ACS Omega* **2019**, *4* (6), 10866–10876. https://doi.org/10.1021/ACSOMEGA.9B00825/SUPPL_FILE/AO9B00825_SI_001.PDF.

[611] Axelsson, M.; Gentili, F. A Single-Step Method for Rapid Extraction of Total Lipids from Green Microalgae. *PLoS One* **2014**, *9* (2). https://doi.org/10.1371/JOURNAL.PONE.0089643.

[612] Gan, L.; Wang, J.; Zhao, Y.; Chen, D.; Zhu, C.; Liu, J.; Gan, Y. Hyaluronan-Modified Core-Shell Liponanoparticles Targeting CD44-Positive Retinal Pigment Epithelium Cells via Intravitreal Injection. *Biomaterials* **2013**, *34* (24), 5978–5987. https://doi.org/10.1016/j.biomaterials.2013.04.035.

[613] Liu, D.; Lian, Y.; Fang, Q.; Liu, L.; Zhang, J.; Li, J. Hyaluronic-Acid-Modified Lipid-Polymer Hybrid Nanoparticles as an Efficient Ocular Delivery Platform for Moxifloxacin Hydrochloride. *Int. J. Biol. Macromol.* **2018**, *116*, 1026–1036. https://doi.org/10.1016/j.ijbiomac.2018.05.113.

[614] Martínez Rivas, C. J.; Tarhini, M.; Badri, W.; Miladi, K.; Greige-Gerges, H.; Nazari, Q. A.; Galindo Rodríguez, S. A.; Román, R. Á.; Fessi, H.; Elaissari, A. Nanoprecipitation Process: From Encapsulation to Drug Delivery. *Int J Pharm* **2017**, *532* (1), 66–81. https://doi.org/10.1016/j.ijpharm.2017.08.064.

[615] Juszkiewicz, K.; Sikorski, A. F.; Czogalla, A. Building Blocks to Design Liposomal Delivery Systems. *Int J Mol Sci* **2020**, *21* (24), 1–22. https://doi.org/10.3390/IJMS21249559.

[616] Nsairat, H.; Ibrahim, A. A.; Jaber, A. M.; Abdelghany, S.; Atwan, R.; Shalan, N.; Abdelnabi, H.; Odeh, F.; El-Tanani, M.; Alshaer, W. Liposome Bilayer Stability: Emphasis on Cholesterol and Its Alternatives. *J Liposome Res* **2023**, 1–25. https://doi.org/10.1080/08982104.2023.2226216.

[617] Soni, P. K.; Saini, T. R. Formulation Design and Optimization of Cationic-Charged Liposomes of Brimonidine Tartrate for Effective Ocular Drug Delivery by Design of Experiment (DoE) Approach. *Drug Dev Ind Pharm* **2021**, *47* (11), 1847–1866. https://doi.org/10.1080/03639045.2022.2070198.

[618] Ballweg, S.; Sezgin, E.; Doktorova, M.; Covino, R.; Reinhard, J.; Wunnicke, D.; Hänelt, I.; Levental, I.; Hummer, G.; Ernst, R. Regulation of Lipid Saturation without Sensing Membrane Fluidity. *Nat Commun* **2020**, *11* (1), 756. https://doi.org/10.1038/s41467-020-14528-1.

[619] López-Cano, J. J.; González-Cela-Casamayor, M. A.; Andrés-Guerrero, V.; Herrero-Vanrell, R.; Molina-Martínez, I. T. Liposomes as Vehicles for Topical Ophthalmic Drug Delivery and Ocular Surface Protection. *Expert Opin Drug Deliv* **2021**, *18* (7), 819–847. https://doi.org/10.1080/17425247.2021.1872542.

[620] Chaw, S. Y.; Novera, W.; Chacko, A.-M.; Wong, T. T. L.; Venkatraman, S. In Vivo Fate of Liposomes after Subconjunctival Ocular Delivery. *Journal of Controlled Release* **2021**, *329*, 162–174. https://doi.org/10.1016/j.jconrel.2020.11.053.

[621] Jounaki, K.; Makhmalzadeh, B. S.; Feghhi, M.; Heidarian, A. Topical Ocular Delivery of Vancomycin Loaded Cationic Lipid Nanocarriers as a Promising and Non-Invasive Alternative Approach to Intravitreal Injection for Enhanced Bacterial Endophthalmitis Management. *European Journal of Pharmaceutical Sciences* **2021**, *167*, 105991. https://doi.org/10.1016/j.ejps.2021.105991.

[622] Landucci, E.; Bonomolo, F.; De Stefani, C.; Mazzantini, C.; Pellegrini-Giampietro, D. E.; Bilia, A. R.; Bergonzi, M. C. Preparation of Liposomal Formulations for Ocular Delivery of Thymoquinone: In Vitro Evaluation in HCEC-2 e HConEC Cells. *Pharmaceutics* **2021**, *13* (12), 2093. https://doi.org/10.3390/pharmaceutics13122093.

[623] Panigrahi, D.; Sahu, P. K.; Swain, S.; Verma, R. K. Quality by Design Prospects of Pharmaceuticals Application of Double Emulsion Method for PLGA Loaded Nanoparticles. *SN Applied Sciences 2021 3:6* **2021**, *3* (6), 1–21. https://doi.org/10.1007/S42452-021-04609-1.

[624] Kumar, A.; Kaur, R.; Kumar, V.; Kumar, S.; Gehlot, R.; Aggarwal, P. New Insights into Water-in-Oil-in-Water (W/O/W) Double Emulsions: Properties, Fabrication, Instability Mechanism, and Food Applications. *Trends Food Sci Technol* **2022**, *128*, 22–37. https://doi.org/10.1016/J.TIFS.2022.07.016.

[625] Wang, J.; Helder, L.; Shao, J.; Jansen, J. A.; Yang, M.; Yang, F. Encapsulation and Release of Doxycycline from Electrospray-Generated PLGA Microspheres: Effect of Polymer End Groups. *Int J Pharm* **2019**, *564* (January), 1–9. https://doi.org/10.1016/j.ijpharm.2019.04.023.

[626] Golyshev, S. A.; Kazakov, E. P.; Kireev, I. I.; Reunov, D. G.; Malyshev, I. V. Soft X-Ray Microscopy in Cell Biology: Current Status, Contributions and Prospects. *Acta Naturae* **2023**, *15* (4), 32. https://doi.org/10.32607/ACTANATURAE.26551.

[627] Ekman, A. A.; Chen, J. H.; Guo, J.; McDermott, G.; Le Gros, M. A.; Larabell, C. A. Mesoscale Imaging with Cryo-Light and X-Rays: Larger than Molecular Machines, Smaller than a Cell. *Biol Cell* **2017**, *109* (1), 24–38. https://doi.org/10.1111/BOC.201600044.

[628] Loconte, V.; White, K. L. The Use of Soft X-Ray Tomography to Explore Mitochondrial Structure and Function. *Mol Metab* **2022**, *57*, 101421. https://doi.org/10.1016/J.MOLMET.2021.101421.

[629] Parkinson, D. Y.; Epperly, L. R.; McDermott, G.; Le Gros, M. A.; Boudreau, R. M.; Larabell, C. A. Nanoimaging Cells Using Soft X-Ray Tomography. *Methods in Molecular Biology* **2013**, *950*, 457–481. https://doi.org/10.1007/978-1-62703-137-0_25.

[630] Polo, C. C.; Fonseca-Alaniz, M. H.; Chen, J.-H.; Ekman, A.; McDermott, G.; Meneau, F.; Krieger, J. E.; Miyakawa, A. A. Three-Dimensional Imaging of Mitochondrial Cristae Complexity Using Cryo-Soft X-Ray Tomography. *Sci Rep* **2020**, *10* (1), 21045. https://doi.org/10.1038/s41598-020-78150-3.

[631] Bhatti, J. S.; Bhatti, G. K.; Reddy, P. H. Mitochondrial Dysfunction and Oxidative Stress in Metabolic Disorders — A Step towards Mitochondria Based Therapeutic Strategies. *Biochimica et Biophysica Acta (BBA) - Molecular Basis of Disease* **2017**, *1863* (5), 1066–1077. https://doi.org/10.1016/J.BBADIS.2016.11.010.

[632] Xie, N.; Zhang, L.; Gao, W.; Huang, C.; Huber, P. E.; Zhou, X.; Li, C.; Shen, G.; Zou, B. NAD+ Metabolism: Pathophysiologic Mechanisms and Therapeutic Potential. *Signal Transduction and Targeted Therapy 2020 5:1* **2020**, *5* (1), 1–37. https://doi.org/10.1038/s41392-020-00311-7.

[633] Tabatabaie, F.; Franich, R.; Feltis, B.; Geso, M. Oxidative Damage to Mitochondria Enhanced by Ionising Radiation and Gold Nanoparticles in Cancer Cells. *Int J Mol Sci* **2022**, *23* (13). https://doi.org/10.3390/IJMS23136887.

[634] Tsujioka, T.; Sasaki, D.; Takeda, A.; Harashima, H.; Yamada, Y. Resveratrol-Encapsulated Mitochondria-Targeting Liposome Enhances Mitochondrial Respiratory Capacity in Myocardial Cells. *Int J Mol Sci* **2022**, *23* (1). https://doi.org/10.3390/IJMS23010112.

[635] Fitch, T. C.; Frank, S. I.; Li, Y. K.; Saint-Geniez, M.; Kim, L. A.; Shu, D. Y. Real-Time Analysis of Bioenergetics in Primary Human Retinal Pigment Epithelial Cells Using High-Resolution Respirometry. *J Vis Exp* **2023**, *2023* (192). https://doi.org/10.3791/64572.

[636] Schultz, M. B.; Lu, Y.; Braidy, N.; Sinclair, D. A. Assays for NAD + -Dependent Reactions and NAD + Metabolites. *Methods in Molecular Biology* **2018**, *1813*, 77–90. https://doi.org/10.1007/978-1-4939-8588-3_6.

[637] Kim, D. J.; Jung, M. Y.; Pak, H. J.; Park, J. H.; Kim, M.; Chuck, R. S.; Park, C. Y. Development of a Novel Hyaluronic Acid Membrane for the Treatment of Ocular Surface Diseases. *Sci Rep* **2021**, *11* (1), 1–16. https://doi.org/10.1038/s41598-021-81983-1.

[638] García-Posadas, L.; Contreras-Ruiz, L.; López-García, A.; Villarón Álvarez, S.; Maldonado, M. J.; Diebold, Y. Hyaluronan Receptors in the Human Ocular Surface: A Descriptive and Comparative Study of RHAMM and CD44 in Tissues, Cell Lines and Freshly Collected Samples. *Histochem. Cell Biol.* **2012**, *137* (2), 165–176. https://doi.org/10.1007/s00418-011-0878-z.

[639] Contreras-Ruiz, L.; De La Fuente, M.; Párraga, J. E.; López-García, A.; Fernández, I.; Seijo, B.; Sánchez, A.; Calonge, M.; Diebold, Y. Intracellular Trafficking of Hyaluronic Acid-Chitosan Oligomer-Based Nanoparticles in Cultured Human Ocular Surface Cells. *Mol Vis* **2011**, *17*, 279–290.

[640] Shi, L.; Li, Z.; Liang, Z.; Zhang, J.; Liu, R.; Chu, D.; Han, L.; Zhu, L.; Shen, J.; Li, J. A Dual-Functional Chitosan Derivative Platform for Fungal Keratitis. *Carbohydr Polym* **2022**, *275*, 118762. https://doi.org/10.1016/j.carbpol.2021.118762.

APPENDIX I

SUPPLEMENTARY DATA

APPENDIX 1.1 QCM-D DATA

(a)

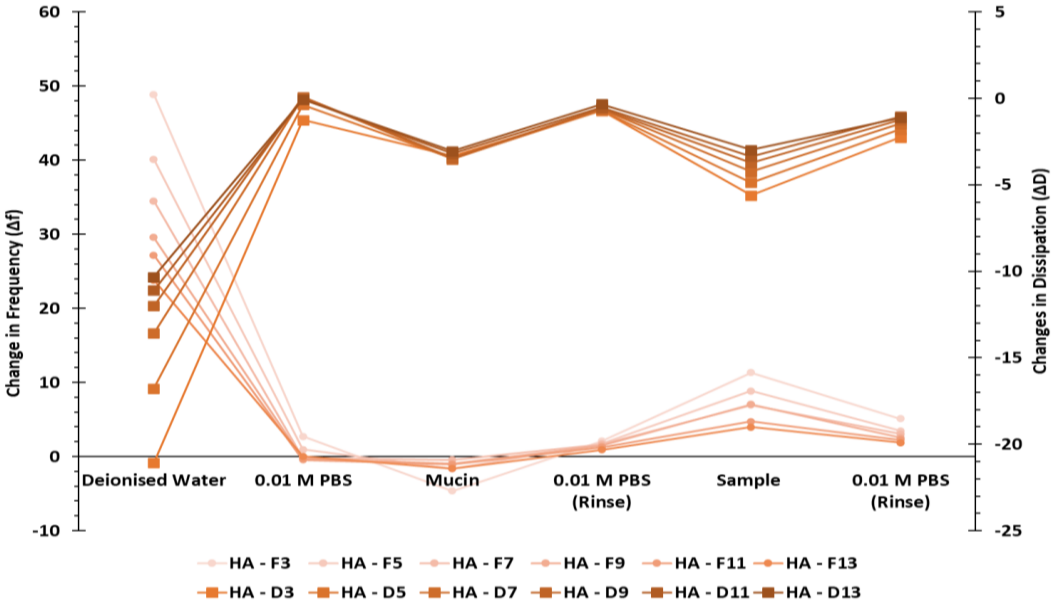

(b)

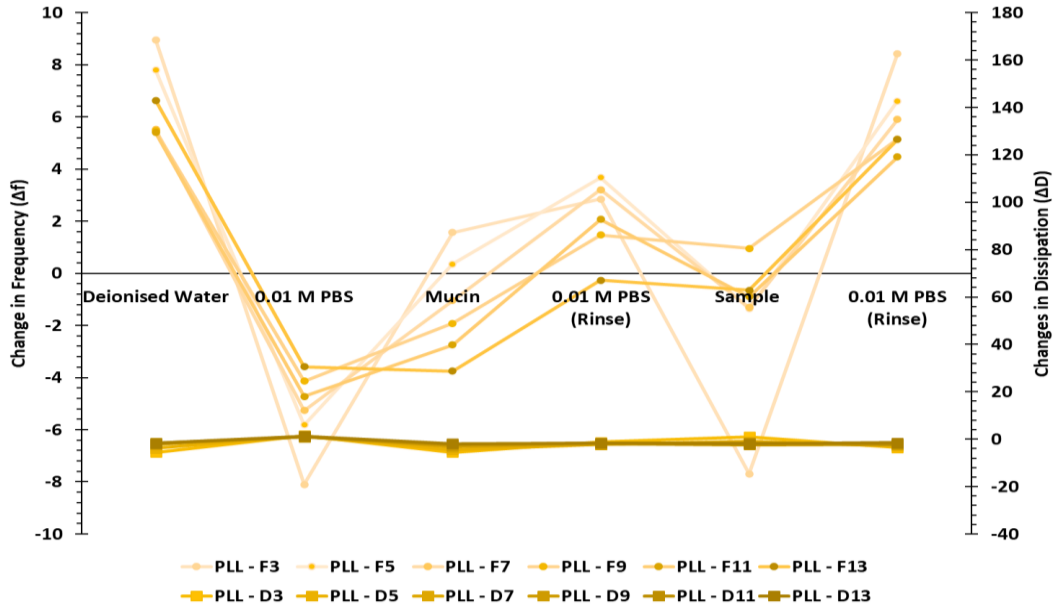

(c)

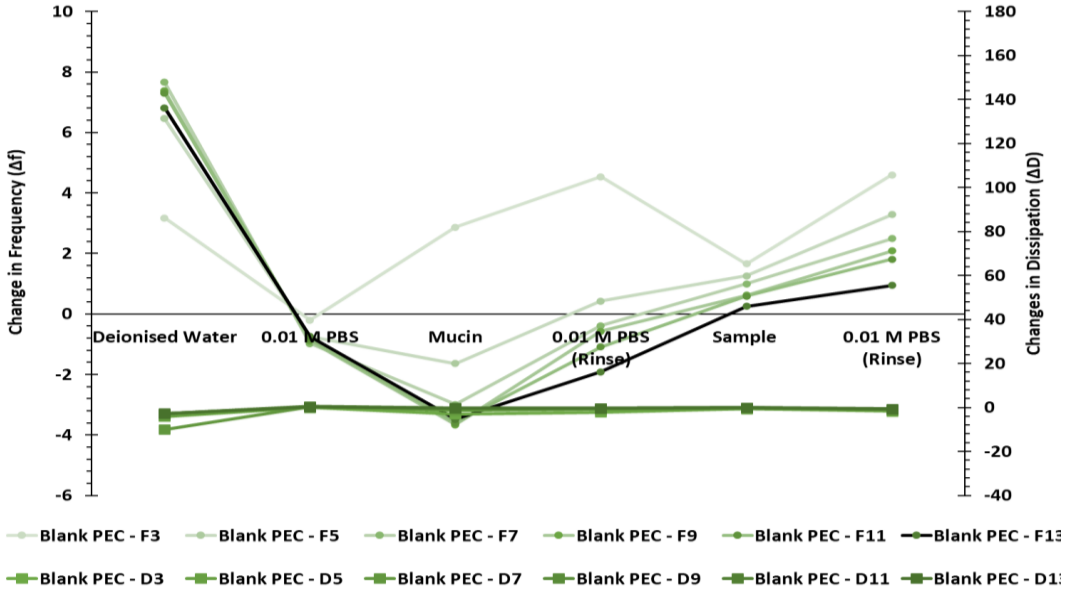
Change in Frequency (Δf)
Changes in Dissipation (ΔD)
Deionised Water
0.01 M PBS
Mucin
0.01 M PBS (Rinse)
Sample
0.01 M PBS (Rinse)
Blank PEC - F3
Blank PEC - F5
Blank PEC - F7
Blank PEC - F9
Blank PEC - F11
Blank PEC - F13
Blank PEC - D3
Blank PEC - D5
Blank PEC - D7
Blank PEC - D9
Blank PEC - D11
Blank PEC - D13

(d)

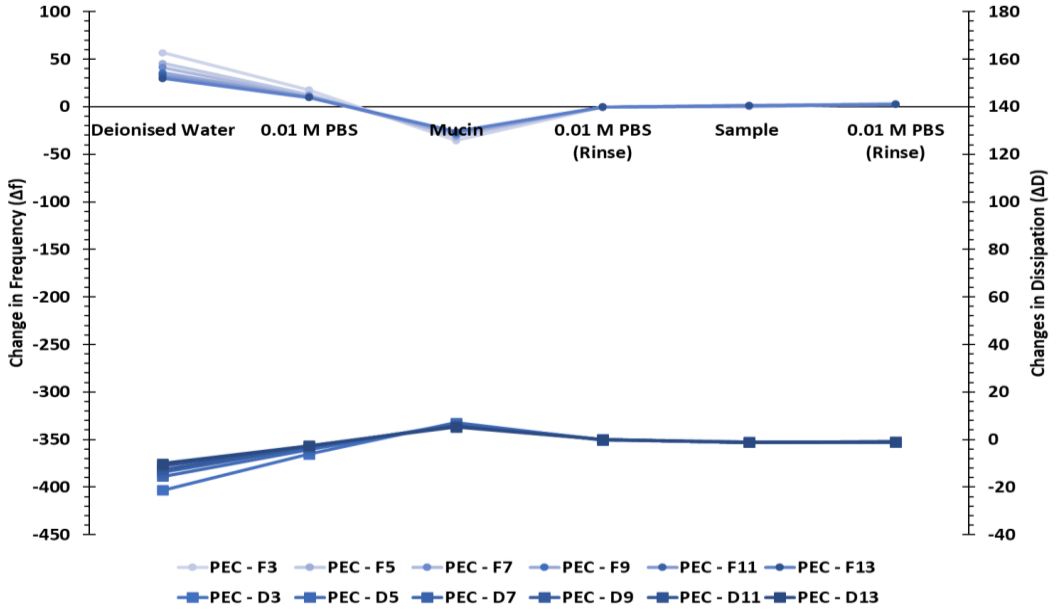
Change in Frequency (Δf)
Changes in Dissipation (ΔD)
Deionised Water
0.01 M PBS
Mucin
0.01 M PBS (Rinse)
Sample
0.01 M PBS (Rinse)
PEC - F3
PEC - F5
PEC - F7
PEC - F9
PEC - F11
PEC - F13
PEC - D3
PEC - D5
PEC - D7
PEC - D9
PEC - D11
PEC - D13

(e)

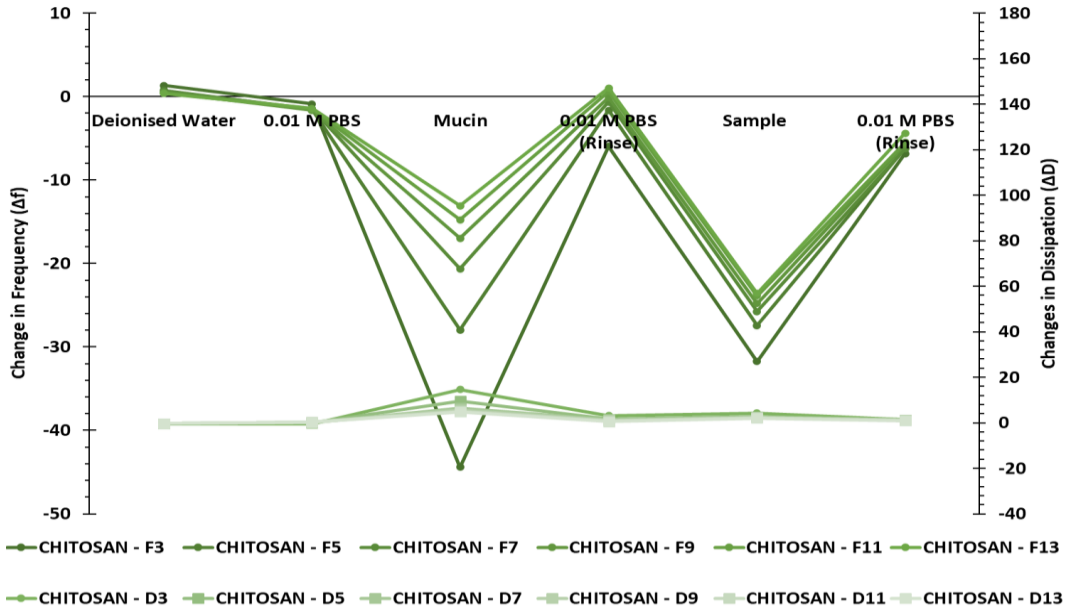
Deionised Water
0.01 M PBS
Mucin
0.01 M PBS (Rinse)
Sample
0.01 M PBS (Rinse)
Change in Frequency (Δf)
Changes in Dissipation (ΔD)
CHITOSAN - F3
CHITOSAN - F5
CHITOSAN - F7
CHITOSAN - F9
CHITOSAN - F11
CHITOSAN - F13
CHITOSAN - D3
CHITOSAN - D5
CHITOSAN - D7
CHITOSAN - D9
CHITOSAN - D11
CHITOSAN - D13

(f)

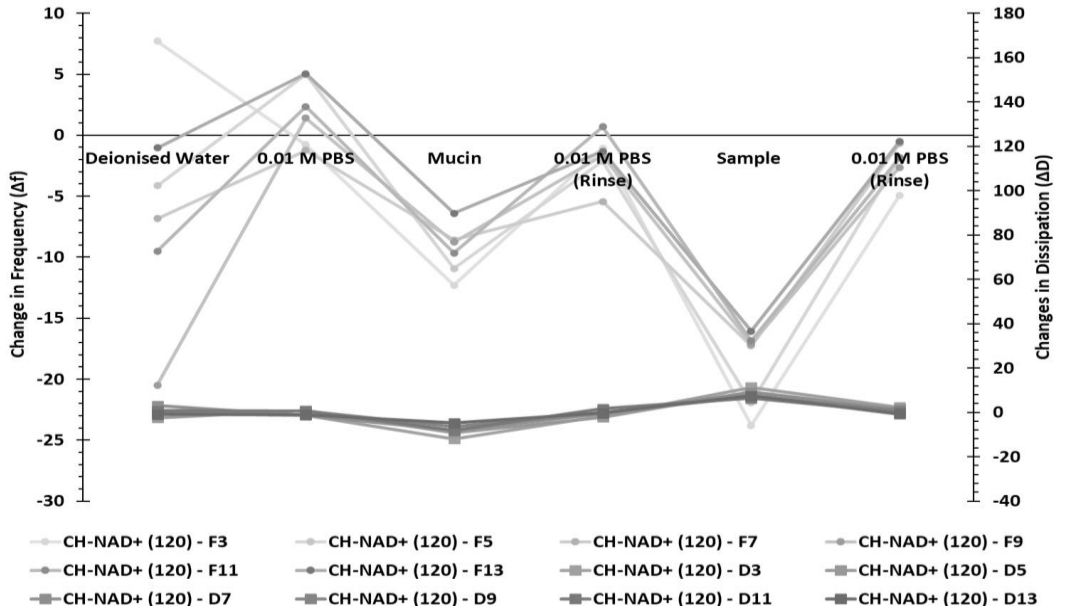
Deionised Water
0.01 M PBS
Mucin
0.01 M PBS (Rinse)
Sample
0.01 M PBS (Rinse)
Change in Frequency (Δf)
Changes in Dissipation (ΔD)
CH-NAD+ (120) - F3
CH-NAD+ (120) - F5
CH-NAD+ (120) - F7
CH-NAD+ (120) - F9
CH-NAD+ (120) - F11
CH-NAD+ (120) - F13
CH-NAD+ (120) - D3
CH-NAD+ (120) - D5
CH-NAD+ (120) - D7
CH-NAD+ (120) - D9
CH-NAD+ (120) - D11
CH-NAD+ (120) - D13

(g)

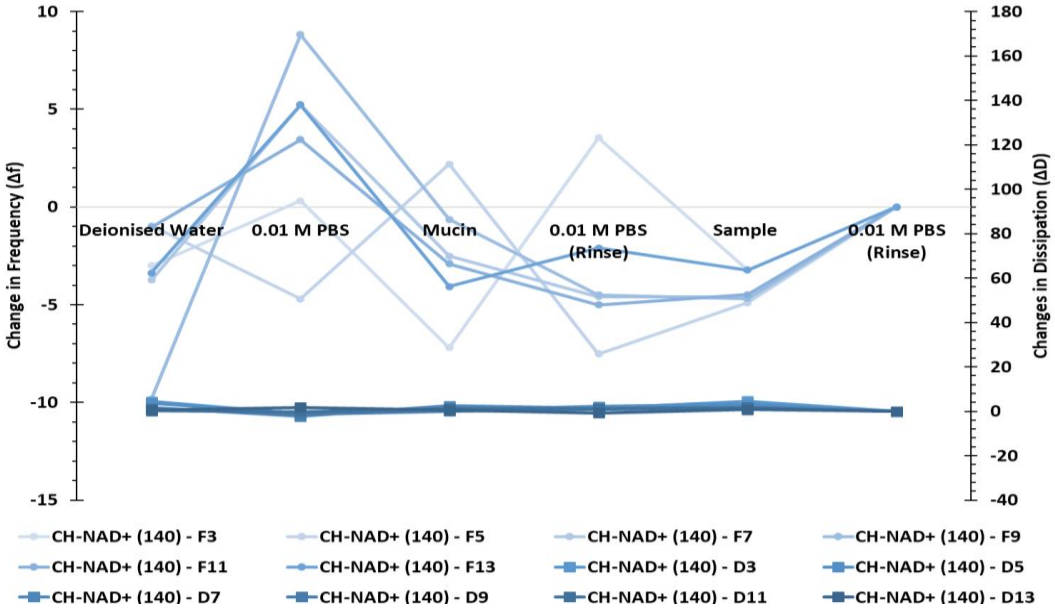

Supplementary Figure 1: QCM-D raw data plots of the changes in Δf and ΔD after each equilibration, sample deposition and rinsing cycle for (a) HA, (b) PLL, (c) blank PECs, (d) NAD+-associated PECs, (e) chitosan, (f) CH-NAD+ (120% (w/w)), and (g) CH-NAD+ (140% (w/w)).

APPENDIX 1.2 *EX VIVO* PERMEATION – HPLC CHROMATOGRAMS

(a)

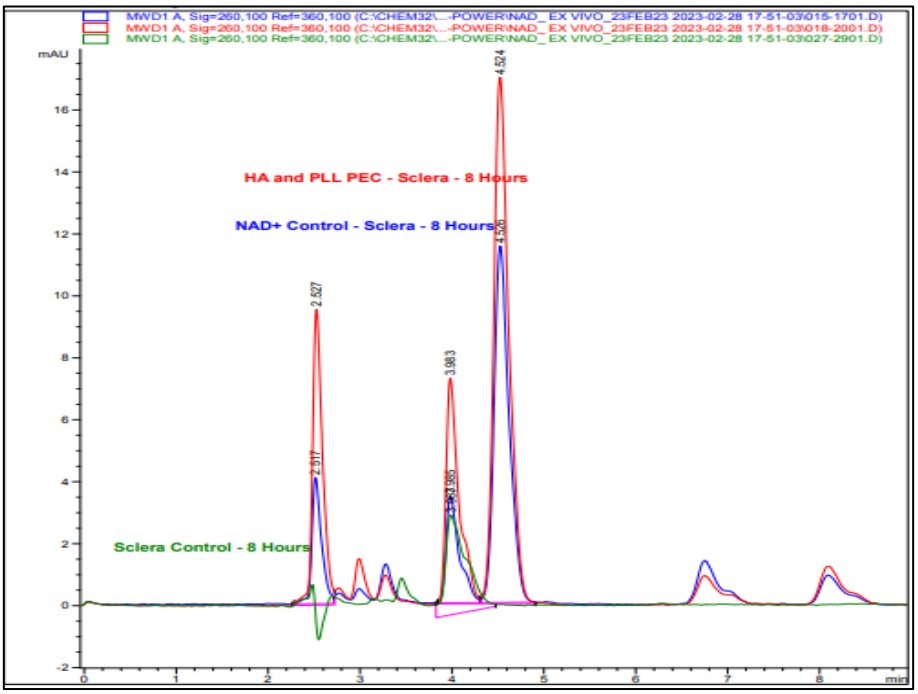

(b)

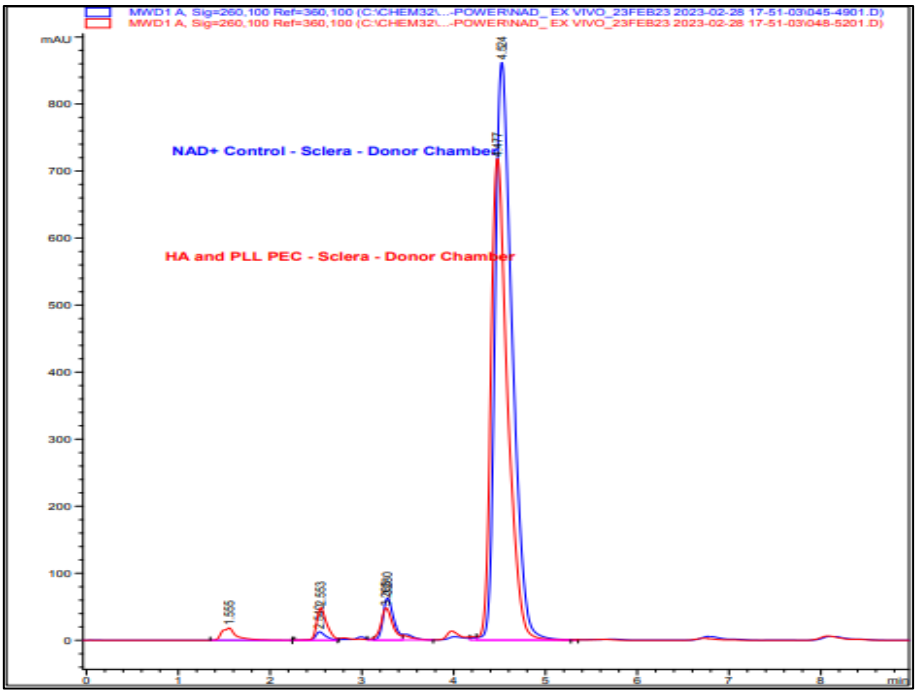

(c)

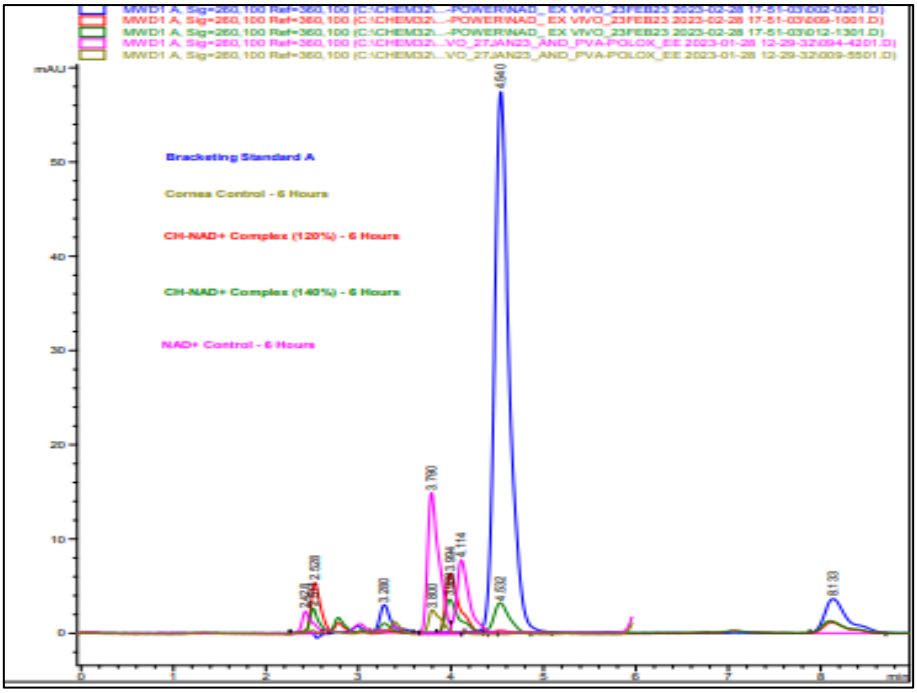

(d)

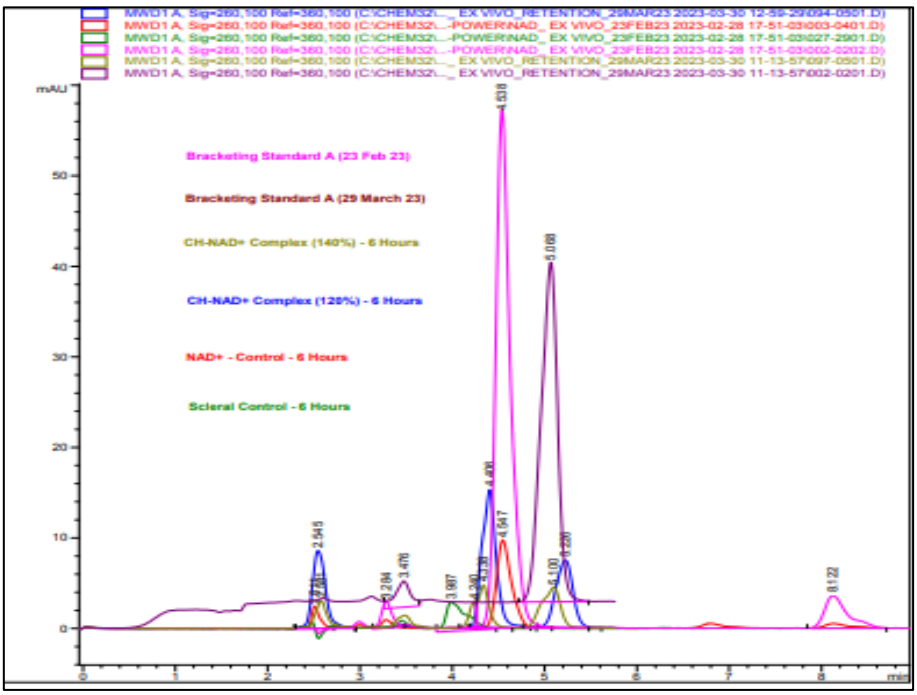

Supplementary Figure 2: Representative HPLC chromatogram taken from the receptor chambers (a) and donor chambers (b) of the porcine scleral tissues following incubation with NAD+/NAD+-associated PECs. The receptor chambers of the corneal (c) and scleral (d) tissues following incubation with the CH-NAD+ formulations are also included.

APPENDIX 2

RESEARCH DISSEMINATION

APPENDIX 2.1: REVIEW ARTICLE

pharmaceutics

MDPI

Review

Hyaluronic Acid: Its Versatile Use in Ocular Drug Delivery with a Specific Focus on Hyaluronic Acid-Based Polyelectrolyte Complexes

Saoirse Casey-Power [1,*], Richie Ryan [1], Gautam Behl [1], Peter McLoughlin [1], Mark E. Byrne [2,3] and Laurence Fitzhenry [1]

[1] Ocular Therapeutics Research Group, Pharmaceutical and Molecular Biotechnology Research Centre, Waterford Campus, South East Technological University, X91 K0EK Waterford, Ireland; richie.j.ryan@setu.ie (R.R.); gautam.behl@setu.ie (G.B.); peter.mcloughlin@setu.ie (P.M.); laurence.fitzhenry@setu.ie (L.F.)
[2] Biomimetic & Biohybrid Materials, Biomedical Devices & Drug Delivery Laboratories, Department of Biomedical Engineering, Henry M. Rowan College of Engineering, Rowan University, 201 Mullica Hill Road, Glassboro, NJ 08028, USA; byrnem@rowan.edu
[3] Department of Chemical Engineering, Henry M. Rowan College of Engineering, Rowan University, 201 Mullica Hill Road, Glassboro, NJ 08028, USA
* Correspondence: saoirse.casey-power@postgrad.wit.ie

Abstract: Extensive research is currently being conducted into novel ocular drug delivery systems (ODDS) that are capable of surpassing the limitations associated with conventional intraocular anterior and posterior segment treatments. Nanoformulations, including those synthesised from the natural, hydrophilic glycosaminoglycan, hyaluronic acid (HA), have gained significant traction due to their enhanced intraocular permeation, longer retention times, high physiological stability, inherent biocompatibility, and biodegradability. However, conventional nanoformulation preparation methods often require large volumes of organic solvent, chemical cross-linkers, and surfactants, which can pose significant toxicity risks. We present a comprehensive, critical review of the use of HA in the field of ophthalmology and ocular drug delivery, with a discussion of the physicochemical and biological properties of HA that render it a suitable excipient for drug delivery to both the anterior and posterior segments of the eye. The pivotal focus of this review is a discussion of the formation of HA-based nanoparticles via polyelectrolyte complexation, a mild method of preparation driven primarily by electrostatic interaction between opposing polyelectrolytes. To the best of our knowledge, despite the growing number of publications centred around the development of HA-based polyelectrolyte complexes (HA-PECs) for ocular drug delivery, no review articles have been published in this area. This review aims to bridge the identified gap in the literature by (1) reviewing recent advances in the area of HA-PECs for anterior and posterior ODD, (2) describing the mechanism and thermodynamics of polyelectrolyte complexation, and (3) critically evaluating the intrinsic and extrinsic formulation parameters that must be considered when designing HA-PECs for ocular application.

Keywords: hyaluronic acid; nanoformulations; ocular drug delivery; physicochemical properties; polyelectrolyte complexes; electrostatic interaction; artificial tears; comfort agent; mucoadhesion; viscosity enhancer

check for updates

Citation: Casey-Power, S.; Ryan, R.; Behl, G.; McLoughlin, P.; Byrne, M.E.; Fitzhenry, L. Hyaluronic Acid: Its Versatile Use in Ocular Drug Delivery with a Specific Focus on Hyaluronic Acid-Based Polyelectrolyte Complexes. *Pharmaceutics* **2022**, *14*, 1479. https://doi.org/10.3390/pharmaceutics14071479

Academic Editor: Francisco Javier Otero-Espinar

Received: 30 May 2022
Accepted: 12 July 2022
Published: 15 July 2022

Publisher's Note: MDPI stays neutral with regard to jurisdictional claims in published maps and institutional affiliations.

Copyright: © 2022 by the authors. Licensee MDPI, Basel, Switzerland. This article is an open access article distributed under the terms and conditions of the Creative Commons Attribution (CC BY) license (https://creativecommons.org/licenses/by/4.0/).

1. Introduction

Recent advances made in the development of novel therapeutic delivery systems for the treatment of ocular diseases affecting both the anterior and posterior segments can be seen in the review of Gote et al. [1]. Such delivery systems include, but are not limited to, thermosensitive in situ gelling systems for enhanced corneal adhesion [2,3], nanoformulations for enhanced therapeutic solubility, targetability and intraocular migration and

retention [4–7], modified contact lenses for dual vision correction and therapeutic delivery [8–12], and bioerodible implants for the sustained, intravitreal delivery of anti-vascular endothelial growth factors [13,14]. Our understanding of the pathogenesis and origination of such diseases has also significantly improved, thus allowing for the development of targeted, stimuli-responsive delivery systems that exploit various routes of administration.

However, despite such successes, the global prevalence of moderate-to-severe visual impairment (MSVI) is continually increasing due to the combined effects of population growth and the increasing longevity of an ageing global population [15]. By 2050, the population of people over the age of 60 is set to reach approximately 2.1 billion [16,17]. As ageing is a primary risk factor for several moderate-to-severe visual abnormalities and ocular diseases, a concurrent exponential increase in MSVI cases is also expected. By 2050, it is estimated that over 474 million people will be suffering from some form of MSVI, a percentage increase of over 60% from 2020 [17]. In 2020, a total of 5.4% of the 206 million reported cases of MSVI within the global population of people over the age of 50 were attributed to ocular diseases such as age-related macular degeneration (AMD) (3%), glaucoma (2%), and diabetic retinopathy (1.4%) [18].

The global market for both therapeutics and drug delivery systems intended for the treatment of such diseases is set to expand exponentially in the coming years. It is predicted that the global market for therapeutics indicated in the treatment of AMD will reach USD 18.7 billion in 2028, an increase of USD 10.1 billion from the 2018 market value [19]. Due to increased demand for prostaglandin analogue-based formulations for the treatment of glaucoma in the ageing population, the global market for glaucoma treatment is predicted to reach USD 11 billion by 2027 [20]. Within the same timeframe, the global market for diabetic retinopathy is expected to reach USD 13 billion, predominantly due to the increasing prevalence of diabetes and the subsequent increase in hyperglycaemia-related retinal haemorrhaging in developed countries [21,22].

Posterior segment ocular diseases are primarily treated via intravitreal injections (IVI) or surgical intervention [23,24]. Such treatment options offer higher therapeutic retinal bioavailability in comparison to those administrated via topical or systemic administration [25]. A high concentration of the therapeutic is administered in the direct vicinity of the retina, thus bypassing the static and dynamic anatomical barriers within the anterior segment [26]. However, multiple administration of such injections over long periods can result in persistent, cumulative fluctuations in intraocular pressure (IOP), which can result in irreversible degeneration of the optic nerve [27]. Depending on the implantation site, surgical procedures involving delivery system implants pose the risk of moderate-to-severe adverse effects such as retinal haemorrhaging, acute inflammation, and ciliary body puncture [28].

Topical formulations such as eye drop formulations, ophthalmic gels, Ocuserts, and therapeutic-soaked contact lenses are non-invasive and can be self-administered in a non-clinical setting [29,30]. Treatments based on the topical administration of ocular therapeutics dominated the global ophthalmic market in 2020, equating to a total revenue share of over 62% [31]. However, selective inhibition of deeper intraocular therapeutic permeation through the static anatomical barriers, combined with precorneal clearance mechanisms such as the upregulation of tear film clearance via nasolacrimal drainage and reflex blinking, significantly reduces corneal retention time and therapeutic bioavailability at the target site [32]. Typically, only 3 to 5% of topically applied drugs penetrate the cornea and are available for further migration into the posterior intraocular tissues, whilst therapeutic bioavailability within the retinal tissues is highly dependent on the physiochemical attributes (molecular radius, lipophilicity) of the drug itself [33–37]. As such, to elicit a therapeutic response, repeated, more frequent administration may be required, thus resulting in the sporadic administration of the therapeutic in a manner that deviates from the recommended administration regime [38].

Polymeric ODDS such as nanoformulations, hydrogels, and biological stimuli-responsive systems have been developed to counteract the pitfalls of conventional ophthalmic for-

mulations. Both synthetic and biological polymers have been used in the development of ODDs, with synthetic polymers exhibiting increased mechanical strength and stability in vivo, whereas the latter has the added advantages of biomimetic cell receptor targeting and enhanced biocompatibility resulting from fast in vivo enzymatic degradation. A thorough understanding of polysaccharidic and protein biopolymers such as chitosan, alginate, albumin, dextran, and gelatin can be seen in the reviews of Irimia et al. and Allyn et al. [39,40]. For the purpose of this review, hyaluronic acid (HA), a naturally occurring, high-molecular-weight (MW) glycosaminoglycan biopolymer, will be discussed in detail. HA has become a popular excipient in ocular drug delivery formulations as it possesses favourable characteristics such as pseudoplasticity, biocompatibility, water retention capacity, and biodegradability. Its tuneable viscosity and mucoadhesive properties are favourable for prolonging the precorneal residence time of various topical formulations. Its inherent hydrophilicity, attributed to the sequestration of water molecules within its network structure upon dispersion in aqueous media, allows for greater nanoformulation and therapeutic stability in vivo [41,42]. Targeted delivery in vivo is also achievable due to CD44 receptor-mediated endocytosis. Such prolonged and targeted therapeutic delivery at the target site is highly beneficial for reducing the frequency of administration and improving patient compliance, particularly for diseases affecting the posterior segment that are treated via invasive surgical procedures. However, HA undergoes rapid enzymatic degradation in vivo and may require physical or chemical modification to achieve therapeutically relevant stability in vivo [40].

2. Hyaluronic Acid: "Nature's Sponge"

HA is a linear, non-sulphated glycosaminoglycan composed of repeating units of D-glucuronic acid and N-acetyl-D-glucosamine units [43–45]. Alternating β-1-3 glycosidic bonds link the individual monosaccharides, and β-1-4-glycosidic bonds link the disaccharide monomer units to one another [46]. HA has been branded 'nature's sponge' due to its remarkable ability to absorb and retain water. When hydrated, HA has the capability of increasing its initial solid volume thousand-fold [47]. For this reason, it has become a primary component in several skincare and cosmetology products as a hydrating agent [48,49]. HA is a primary component of the extracellular matrices (ECM) surrounding connective tissues and exhibits inherent biocompatibility, biodegradability, and mucoadhesive capabilities [45,50–52]. It is found in abundance in synovial fluid, the umbilical cord and vitreous humour, at average concentrations of 2550 $\mu g/cm^3$, 4100 $\mu g/cm^3$, and 250 $\mu g/cm^3$, respectively [46]. Such properties render it an ideal excipient for medical and pharmaceutical applications, such as artificial joint lubrication, hydrogel scaffolding for tissue engineering, and drug delivery systems.

2.1. Molecular Structure

As depicted in Figure 1, when both D-glucuronic acid and *N*-acetyl-D-glucosamine are in the β conformation, the functional moieties in the equatorial positions are sterically stabilised, whereas the hydrogen atoms on each monosaccharide unit occupy the more energetically and sterically unfavourable axial positions, forming the energetically stable conformation of HA [53–55]. Each disaccharide unit is inverted respective to the preceding disaccharide unit in the polysaccharide chain, allowing HA to adapt a coiled, yet semi-rigid, ribbon conformation in solution [56–58].

In aqueous solution, rigidity is further enhanced by the formation of intermolecular and intramolecular hydrogen bonds and solvent interactions [43,58]. The secondary, two-fold helical structure is stabilised by hydrogen bond formation between both the carboxylate and acetylamine moieties on neighbouring monosaccharide units and the equatorial hydroxyl groups and the oxygen atoms of the glycosidic bonds [59].

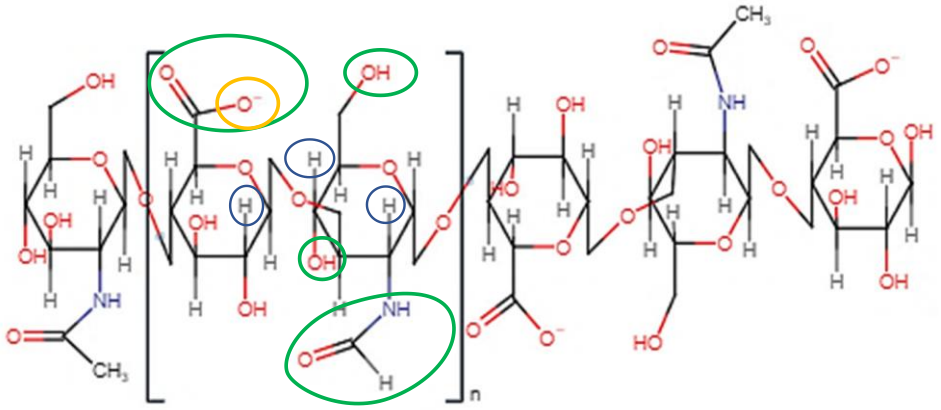

Figure 1. A schematic of the two-fold helical structure of HA. Colour coding is used to indicate the axial hydrogen atoms (blue), the equatorial side chains (green), and the anionic carboxylate group (orange) within the repeating disaccharide unit.

Mutual repulsion of the charged carboxylate anions and solvent–disaccharide interactions expand the rigid polysaccharide coils [58]. This expansion, coupled with the inherent rigidity of the chains, results in the formation of an expansive, hydrophilic domain and the entrapment of water molecules between the individual chains [60]. The MW of the individual HA chains is a critical factor in the reorganisation of such chains into a network structure. HA with a MW greater than 1600 kDa has exhibited enhanced polymer network formation in comparison to HA with a MW of less than 350 kDa, which has been attributed to increased chain entanglement and intermolecular hydrogen bond formation [61]. The hydrophobic regions of individual HA chains self-associate via supramolecular interactions such as hydrophobic interactions and intermolecular hydrogen bonds. Each of these supramolecular interactions contributes to the formation of the tertiary β sheet structure of HA [53]. This structure appears as an entangled, highly viscous network of individual HA chains aligned with one another in an anti-parallel configuration. Water molecules, electrolytes and nutrient molecules can freely diffuse throughout the domain. However, the diffusion of molecules with large hydrodynamic volumes, such as proteins and biopolymers, is hindered by the chain network. Tuneable diffusive properties can be beneficial for achieving sustained drug release from HA-based ODDs, particularly if the system is designed for the dual loading of therapeutic molecules with varying sizes.

2.2. Ionisation and Rheological Properties

HA is considered a weak polyelectrolyte. The degree of ionisation, or charge density, of the anionic carboxylate group is dependent on the pH of the reaction medium [62,63]. HA carboxylate anions possess a pKa of approximately 3 to 4 [64]. As such, at physiological pH, HA is negatively charged and can readily complex with cationic salts or cationic polyelectrolytes. The physicochemical state of HA, in relation to its ionisation, stability, and rheological behaviour, within specific pH ranges, is depicted in Table 1.

Table 1. The physicochemical state of HA from pH 1 to 14 [65–68].

pH	Ionisation	Stability	Viscosity
1–3	The **carboxylate anion** primarily exists in its protonated state (COOH). Protonation of the **-NH- group** of the acetylamine groups may also occur at a pH < 1.6. 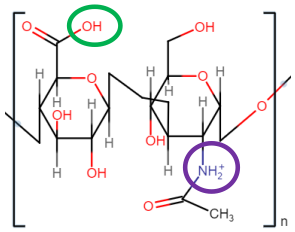	At a pH of <2, cleavage of the β-1-3 and β-1-4 glycosidic bonds via acid hydrolysis occurs. This results in the reformation of the individual monosaccharide units coupled with a decrease in molecular mass. 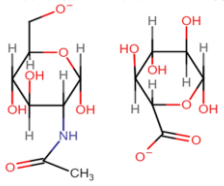	A significant decrease in HA viscosity occurs within this pH range. pH-induced degradation of the individual HA chains reduces both the rigidity and the extent of interchain entanglement. Suppression of electrostatic repulsion between the COO^- anions contributes to the formation of a more densely compact gel state. Below 1.6, a gel-sol transition occurs due to acetylamino group protonation.
4–11	The **carboxylate anion** exists in its deprotonated state (COO^-). Electrostatic repulsion between COO- anions allows for hydrophilic domain expansion. Protonation of the **-NH- groups** is at a minimum. 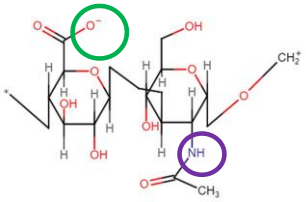	The stability of the tertiary β sheet structure is enhanced by the formation of an intermolecular hydrogen bond between the hydroxyl and ether groups 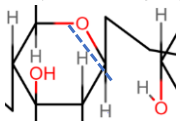 and carboxylate anions and acetylamine groups. 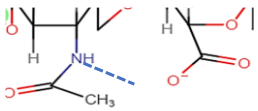 Water molecules can also indirectly facilitate the formation of these hydrogen bonds by behaving as bridging molecules.	HA exhibits both viscoelastic and pseudoplastic flow behaviour. Increasing shear rate disrupts hydrogen bonding and hydrophobic interactions, resulting in increased chain flexibility and network degradation. This allows the individual chains to align in the direction of the applied flow, leading to a temporary decrease in viscosity. However, HA is also non-thixotropic. Reformation of the network occurs over time upon removal of the shear stress.

Table 1. *Cont.*

pH	Ionisation	Stability	Viscosity
12–14	At pH > 12, the **COO- anions** remain in their deprotonated state. The **hydroxyl (OH) atoms** also exist as alkoxyl anions due to the removal of the hydrogen atoms via excess hydroxide ions. 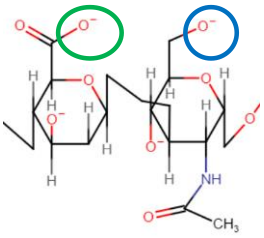	Base-catalysed hydrolysis of the β-1-3 and β-1-4 glycosidic bonds occurs. Due to the deprotonation of the hydroxyl groups, the hydrogen bonds responsible for the stabilisation of the tertiary network begin to degrade. 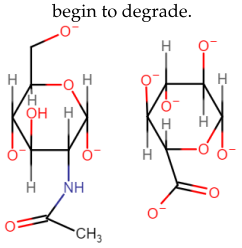	Deformation of the intermolecular hydrogen bonds reduces the rigidity of the backbones of the HA chains. This results in the degradation of the entangled network, coupled with an increase in chain flexibility and mobility.

Aside from pH, the rheological properties of HA are also heavily dependent on intrinsic parameters such as MW and concentration. A direct correlation exists between both the MW and concentration of HA in solution and its intrinsic viscosity. However, the MW of HA is the primary deciding factor in the viscosity of the resulting solution. Endogenous HA, with a typical MW of approximately 1×10^6 Da, exists as a highly cross-linked, entangled network, even at concentrations as low as 1 μg/cm^3 [53]. Cowman et al. [69] demonstrated the inverse correlation between the MW and the concentration of HA on intrinsic viscosity. Upon evaluation of the intrinsic viscosity of HA solutions, 8600 μg/cm^3 of 1×10^5 Da HA was required to reach critical coil-overlap concentration. However, to reach critical coil-overlap within the sample prepared using 6×10^6 Da HA, only 320 μg/cm^3 was required. The specific volume occupied by HA increases with an increase in MW. Further expansion of the hydrophilic domain via electrostatic repulsion of an increased number of COO^- anions also contributes to an increase in both specific volume and intrinsic viscosity. Intermolecular hydrogen bond formation and hydrophobic self-association also increase with increasing MW, thus strengthening the rigidity of the entangled network and enhancing interchain entanglement.

At concentrations of between 1 and 4% (w/v), HA solutions form pseudo-gel structures with considerable intrinsic viscosity [46]. As the mass concentration in a given solution volume increases, intermolecular bonding and chain entanglement also increase. The individual HA chains cannot adapt configurations independently of one another and become fixed within the network. At a fixed HA MW, Bothner et al. [70] demonstrated an increase in HA zero shear viscosity with an increase in HA concentration from 10 to 20 mg/mL. At lower polymer concentrations, HA chains are weakly associated with one another and can behave independently of one another.

Fluctuations in extrinsic parameters, such as ionic strength and temperature, not only induce conformational changes but can also impact the charge density and rheological properties of HA in solution. The addition of cationic electrolytes, such as Na^+, Li+, etc. can lead to a substantial decline in its intrinsic viscosity [46]. Cationic electrolytes suppress the electrostatic repulsion between the carboxylate anions on adjacent D-glucuronic acid units via the formation of extrinsic electrostatic pairs. Coupled with the weakening of the intermolecular hydrogen bonds, this results in the contraction of the dimensions of the established network domain, an increase in hydrophobic region self-association, and increased chain flowability [71]. Cations with a valence greater than two can behave as bridging molecules between two adjacent HA chains [43]. The formation of these

intermolecular crosslinks results in the formation of a gel structure that attains the ability to retain large volumes of water.

The stability of the HA β-conformation is attributed to the steric hindrance imparted by the bulkier functional groups on the equatorial face of the disaccharide unit, which prevents free rotation about the β-1-4-glycosidic bonds. An increase in temperature allows for increased rotation, thus aiding chain mobility. The specific volume occupied decreases, resulting in a corresponding decrease in viscosity [71,72]. This increase in kinetic energy disrupts intramolecular and intermolecular hydrogen bond formation, thus hindering the stabilisation of the entangled network and promoting contraction via mutual aggregation.

The viscosity of HA-based ODDs can be fine-tuned depending on the preferred mode of administration. Viscous formulations are often preferred for topical administration to prolong the corneal residence times of the therapeutic. Conversely, formulations of low viscosity are preferable for posterior segment delivery due to the smaller injection force required for administration, thus preventing excess damage to the fragile posterior tissues [73].

2.3. Biological Properties of HA

2.3.1. HA—A Fundamental Component of Vitreous Humour

The vitreous humour is composed of 98% water and 2% structural proteins [74]. A total of 75% of this structural protein network is composed of collagen type II [75]. The remaining 25% is composed of collagen type IX, HA, and other structural proteins such as fibrillin and opticin [76,77]. HA chains infiltrate the fibrillar structures composed of collagen type II and IX. A combination of water immobilisation and mutual electrostatic repulsion between HA chains results in the expansion of the collagen scaffold via an established swelling pressure. This ultimately increases the viscosity of the vitreous humour. The gelatinous nature of the vitreous humour imparts sufficient IOP on the retina to attain the overall spherical shape of the eye. HA is not uniformly distributed throughout the vitreous humour [78]. Higher concentrations of HA tend to accumulate within the posterior segment (1200 $\mu g/cm^3$) whilst lower concentrations of approximately 250 $\mu g/cm^3$ are present within the anterior segment [79].

2.3.2. HA and Mucoadhesion

HA exhibits substantial mucoadhesive capabilities, readily forming hydrogen bonds with the MUC5AC glycoprotein oligomers within the mucoaqueous tear layer and the protective glycocalyx coating on the apical corneal epithelial cells [80]. Such binding forces significantly enhance the precorneal residence time of HA-based formulations.

2.3.3. HA-CD44 Binding: An Essential Cellular Signalling Mechanism

HA can indirectly mediate several cell signal transduction pathways by binding to cell surface receptors such as Cluster determinant 44 (CD44), Toll-like receptors (TLR), and lymphatic vessel endothelial HA receptors (LYVE-1) [55]. CD44, a ubiquitously produced, transmembrane glycoprotein, is considered to be the primary HA receptor and its binding to HA directly influences a large number of physiological cellular processes. HA binds to specific amino acid residues on the extracellular HA-binding domain (HABD) of CD44. The C6 primary alcohol on the *N*-acetyl-D-glucosamine units binds to the tyrosine-109 residue of the HABD [81]. HA carboxylate anions also indirectly bind to the alanine 102 and 103 residues via the formation of water-bridged hydrogen bonds. Such interactions evoke conformational changes in the cytoplasmic domain of CD44, triggering several signalling cascades that are responsible for cellular proliferation, HA endocytosis, lymphocyte activation, inflammation, cytokine release, and cellular migration [45,82,83].

CD44-HA binding is of particular importance in corneal wound healing. The binding of HA to CD44 receptors within the corneal epithelium and endothelium layer stimulates cytoplasmic CD44 domain phosphorylation, which ultimately enhances fibroblast migration to the affected site [83,84]. HA can also facilitate corneal re-epithelisation and

wound healing resulting from ocular damage via receptor-mediated activation of the pro-inflammatory response and angiogenesis. CD44 receptors are also expressed within the iris, conjunctival cells, and Muller glia within the retina under physiological conditions [60].

Increased proinflammatory cytokine expression and release are characteristic of the pathogeneses of several ocular diseases, such as AMD, glaucoma, and uveitis. Alternate splicing of CD44 messenger RNA (mRNA) in response to pro-inflammatory cytokine expression results in an increase in CD44 receptor expression [85]. Increased CD44 expression has been linked to the induction of choroidal neovascularisation in the retinal cells of a murine model post-laser-photocoagulation [86,87]. In primary open-angle glaucoma, a progressive decrease in HA concentration within the ECM of the trabecular network results in a corresponding increase in CD44 accumulation, a degradant of CD44 that is cytotoxic to retinal ganglion cells [88]. The overexpression of CD44 on the surface of ocular cells under pathological conditions presents a unique opportunity for the receptor-targeted delivery of HA-based ocular therapeutic systems.

2.3.4. The Relationship between HA MW and Biological Activity

The biological activity of HA is highly dependent on MW. HA is endogenously produced within the inner plasma membrane via the enzymatic action of three isoenzymes, HA synthases 1, 2 and 3 [56,89]. The MW of the chains produced is controlled by the differential expression of the synthases in response to varying intracellular conditions. Native HA (NHA) has a MW of over 1×10^6 Da and exhibits both anti-angiogenic and immunosuppressive properties [54,90,91]. NHA regulates the hydration, viscoelasticity, and structural integrity of the ECM via proteoglycan-mediated binding [53]. The exertion of swelling pressure due to the binding of NHA to water creates channels between adjacent tissues, creating an optimal environment for cellular migration. Low-MW HA (LMWHA) typically exhibits MWs of between 20 kDa and 500 kDa [45]. Polydispersity arises from NHA fragmentation via NHA synthases and degrading enzyme dysregulation under pathological conditions and via free-radical-mediated degradation [80]. LMWHA stimulates angiogenesis and cell mobility in response to cellular damage, enhancing wound healing and scar formation with the simultaneous activation of several pro-inflammatory mediators and growth factors [92,93].

The MW of HA also has an impact on the extent of CD44 receptor binding. NHA binds to CD44 via the formation of multivalent, cooperative interactions and has the capability of clustering CD44 receptors on the cellular surface, allowing CD44 to bind with secondary ligands [90,94]. Although the use of a high-MW HA will enhance the binding affinity of the therapeutic system to the target cells, it can also simultaneously induce adverse reactions that are stimulated by the transduction of the activated signal. This can prove detrimental to cells that are already under pathological stress. Through monovalent binding interactions, LMWHA and HA oligosaccharides (6–18 HA residues) bind to CD44 receptors with lower affinity in comparison to NHA [95].

2.4. Enzymatic Degradation of HA

An average-sized human has approximately 15 g of HA, 5 g of which is continuously turned over each day via enzymatic hydrolysis [95]. HA exhibits an approximate half-life of 10 weeks within the vitreous humour [55]. Hydrolysis of HA occurs via the enzymatic action of hyaluronidases (HYAL). HYAL-1 and HYAL-2 comprise the predominant hyaluronidases in somatic cells, cleaving the β-1-4-glycosidic bonds between the repeating units of D-glucuronic acid and *N*-acetyl-D-glucosamine via hydrolysis [44,83]. Rapid enzymatic degradation is unfavourable, particularly for HA-based ODDs that are designed for sustained therapeutic release within the posterior segment. As such, HA is often cross-linked via chemical modification to prolong its residence time and stability within the intraocular environment. The resulting fragments are internalised into lysosomes within the cytosol where HYAL-1 hydrolyses the fragments further, primarily forming tetrasaccharide residues [96]. Two exoglycosidases, β-glucuronidase and β-N-acetyl-D-

hexosaminidase, cleave the tetrasaccharide residues further to yield monosaccharide units. Upon binding to CD44 receptors on the cell membrane surface, NHA and high-MW HA (HMWHA) are cleaved by HYAL-2, thus forming fragments of up to 20 kDa in size [92].

2.5. Potential Cytotoxicity of HA under Inflammatory Conditions

The relationship between HA MW and its inflammatory activity has been well documented in the literature, particularly in osteoarthritis models. The sequestration of multiple CD44 receptors via NHA and HMWHA-mediated divalent bonding suppresses both the expression of the pro-inflammatory cytokines and the formation of proteoglycans [97].

Conversely, LMWHA preferentially binds to TLR 2 and 4, transmembrane receptors that are primarily responsible for immune response initiation via pathogen-associated molecular pattern recognition [98]. The complexation of LMWHA and TLR triggers the nuclear translocation of the NF-κB protein, thus triggering the expression of several pro-inflammatory cytokines such as tumour necrosis factor-α (TNF-α), interleukin (IL)-1β, IL-6, and IL-8 [94]. As such, LMWHA fragments serve as potential biomarkers of cellular damage.

Under oxidative stress conditions, an inverse correlation exists between the concentration of HA and the chain length of the respective HA chains at the site of tissue injury [83]. The fragmentation of NHA via reactive oxygen (ROS) and nitrogen (RNS) species production, and imbalances in HA synthase and hyaluronidase activity, can result in excessive HA degradation via glycosidic bond cleavage, thus forming biologically active, pro-inflammatory HA fragments [99]. A vicious cycle between the mass production of ROS/RNS during tissue injury and pro-inflammatory cytokine activation via LMWHA-receptor binding is established, which may further amplify the inflammatory state and disease progression. It is also postulated that the reduction in thickness and viscosity of the HA protective barrier surrounding cells via ROS mediation contributes to both increased cell receptor accessibility and enhancement of the innate immune and inflammatory response [53].

Cytotoxicity can also arise due to the covalent modification of HA resulting from overexpression of tumour necrosis factor-stimulated gene-6 (TSG-6), an inflammation-associated secreted protein induced by TNF- α and IL-1, during inflammation [100]. TSG-6 catalyses the covalent bonding of the heavy chain (HC) domains of the chondroitin sulphate chains of IαI to HA, which results in the sequestration and aggregation of HA chains within a gelatinous hyaluronic acid–heavy chain (HA–HC) complex [71,101,102]. It is possible that HA–HC complexes can form within ocular tissues, due to the detection of both TSG-6 within human corneal epithelia and IαI within porcine trabecular meshwork cells, respectively [103,104]. The complexed aggregates are immobile and more viscous in comparison to NHA and, as such, exhibit enhanced resistance to biodegradation [105]. However, although such characteristics are favourable for the attenuation of joint degradation in arthritis, the intraocular sequestration of HA–HC aggregates may result in increased intraocular pressure and enhanced inflammation via the enzymatic and chemical fragmentation of localised HA within the complexes.

3. Hyaluronic Acid Biomaterials for Ocular Drug Delivery

Due to its tuneable physicochemical properties and inherent biocompatibility, the use of HA as an ophthalmic excipient has gained significant traction in recent years [51]. Many reviews have discussed the development of HA biomaterials, such as injectable hydrogels, nanofibrous membranes and films, and vitreous substitutes [59,60]. Similarly, recent studies have also demonstrated the efficacy in enhancing wound healing, protecting corneal epithelium cells, and attaining sufficient intraocular ocular lubrication and pressure during vitro-retinal and cataract surgery [3,42,79,106–108]. Therapeutic-laden nanomaterials and injectable hydrogels composed of HA have previously been injected into the posterior segment of the eye to both improve therapeutic accumulation at the target site and prolong its intra-retinal residence time [109–112]. Critical analysis of recent developments in HA-

based ocular delivery systems is a primary focus of this review and will be discussed in greater detail in the following sections.

3.1. Artificial Tears for Dry Eye Disease

Artificial tear (AT) solutions are one of the primary treatment options to alleviate the discomfort and burning sensation caused by dry eye disease [113]. Dry eye is a multifactorial disease characterised by poor quality, unstable tear film secretion, primarily resulting from both the dysfunction of meibomian glands and loss of lubricating efficacy due to the progressive decrease in MUC5AC concentration within the mucoaqueous layer. Its pseudoplastic, rheological behaviour mimics that of the physiological tear film, thus allowing for increased flowability and distribution across the corneal surface during blinking upon application. The efficacy of AT solutions can be quantified by evaluating the stability of the tear film as a function of its break-up time.

You et al. [114] demonstrated the concentration-dependant therapeutic effect of HA-based AT solutions on tear film break-up time (TFBT) and conjunctival goblet cell stability in a dry eye-induced murine model. In comparison to the control groups, the 0.1%, 0.18%, and 0.3% (w/v) HA solutions significantly prolonged the TFBT, with the 0.3% (w/v) solution exhibiting superior efficacy by increasing TFBT by approximately 1.25 seconds. The 0.3% (w/v) solution also exhibited a protective effect against the deleterious effects of increased pro-inflammatory cytokine expression on conjunctival goblet cells.

Fallacara et al. [115] demonstrated the in vitro efficacy of a cross-linked HA and urea AT solution to stimulate corneal re-epithelisation upon induction of epithelial damage resulting from tear film dysregulation. After 72 h, the cells treated with the 0.02% and 0.4% (w/v) AT solutions exhibited similar viability of epithelial wound closure to that of the negative control. However, the corneal residence time of the AT formulations was not investigated as part of this study. Therefore, the results were inconclusive as to whether the crosslinking of carboxylate anions of HA with urea impacts its ability to bind to the mucin moieties on the corneal epithelium via hydrogen-bond-mediated adhesion. Graca et al. [116] evaluated the mucoadhesion of 0.15% and 0.30% (w/v) HA containing AT solutions using in vitro rheological studies. The 0.3% (w/v) HA formulation exhibited superior viscosity (382.2 mPa·s) when combined with hydrated porcine mucin in comparison to that of the 0.15% (w/v) formulation (53.2 mPa·s); this was attributed to the combined anionic charges of HA's physiological pH and the negatively charged carbohydrate-bound ester sulphate residues and carboxyl groups on mucin oligosaccharides.

As a general note, none of the aforementioned studies included an investigation into the effect of MW on the viscosity of the HA formulations. As MW has a predominating effect on the intrinsic viscosity of HA in solution, this would be considered a critical parameter to investigate. Kojima et al. [117] demonstrated the increased efficacy of high-MW HA (HMWHA) in minimising the deleterious effects of dry eye in an environmental dry eye-stress murine model.

3.2. Eye Drop Formulations—Viscosity, Mucoadhesion, and Solubility Enhancement

Previous reviews have reported on the use of HA in therapeutic-laden eye drop formulations to both increase ocular residence time and enhance the therapeutic bioavailability and aqueous solubility of lipophilic therapeutics [52,118]. An increase in precorneal residence time ultimately reduces the rate at which the therapeutic is eliminated via nasolacrimal and conjunctival sac drainage. However, the viscosity of the formulation may be controlled to allow for sufficient mucoadhesion without adversely affecting vision clarity. Formulations should not exhibit an equivalent viscosity of greater than 30 mPa·s as the increased viscosity of the formulation may result in ocular discomfort and blurred vision [119].

Chen et al. [120] demonstrated the enhanced bioavailability and aqueous solubility of nimesulide, a non-steroidal anti-inflammatory drug, via conjugation to HMWHA (360 kDa) and LMWHA (36 kDa). Exhibiting equivalent tear osmolarity to that of normal human

tears (296.7 ± 0.5 mOsm/L–LMWHA, 303.3 ± 4.2 mOsm/L–HMWHA), the nimesulide–HA conjugates significantly decreased interleukin 6 expression post-lipopolysaccharide-stimulated inflammation. Tredici et al. [121] also reported on the multi-factorial use of cross-linked HA as both a stabilising excipient and a therapeutic molecule to enhance in vivo corneal surface regeneration in a group of professional swimmers exposed to chlorinated water. Whilst therapeutic efficacy was proven, indicated by a reduction in tear osmolarity of 1.82 mOsm/L from baseline measurements, an investigation into the efficacy of the combination treatment in reducing the frequency of instillation was not conducted. Theoretically, HA should prolong the precorneal residence time of Coenzyme Q10 due to its mucoadhesive capabilities, enhancing its bioavailability whilst concurrently reducing the need for frequent administration. As shown in Figure 2, White et al. [122] demonstrated that HA exhibited superior water retention properties in comparison to the alternative polysaccharidic and acrylic comfort agents. HA also exhibited high values of zero-shear viscosity and flow viscosity with increasing MW, indicating its ability to reduce the rate of tear film drainage, attain tear film stability and volume, and maximise comfortability.

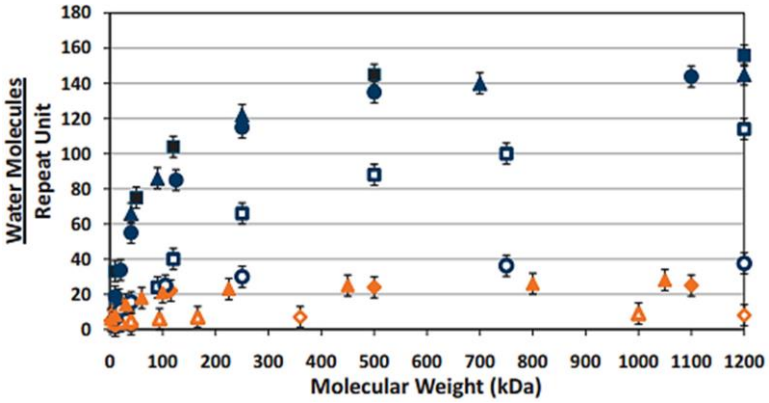

Figure 2. Water retention per polymer repeat unit of various polyelectrolyte polysaccharides and acrylics. The water retention of HA, (■) exhibiting superior water retention in comparison to the other polyelectrolyte materials, increases as a function of MW. (●—dextran sodium sulfate, ▫—hydroxypropyl methylcellulose, ○—dextran, ▲—carboxymethylcellulose, ♦—poly(acrylic acid), ▲—poly(methacrylic acid), ◇—polyvinyl alcohol, △—polyvinyl pyrrilidone). (Reproduced with permission from Ref. [122]. 2014, White, C.J., Thomas, C.R. and Byrne, M.E. "Bringing comfort to the masses: A novel evaluation of comfort agent solution properties"; published by Contact Lens and Anterior Eye.

Jansook et al. [123] demonstrated the enhanced mucoadhesion of celecoxib and cyclodextrin ophthalmic solutions prepared with HA (MW 1000–1400 kDa). An increase in HA concentration from 0.1% to 0.5% (w/v) resulted in a significant increase in the concentration of celecoxib retained on the mucin-coated membrane. Salzillo et al. [124] also reported an increase in viscosity and mucoadhesion of the HA-based samples on simulated corneal–conjunctival epithelial mucin with an increase in HA concentration, with a more marked increase in such parameters with an increase in HA MW from 250 to 1120 kDa. Chen et al. [125] demonstrated the enhanced mucoadhesion of sodium hyaluronate (SH)–azithromycin eye drops in comparison to an azithromycin formulation containing hydroxypropyl methylcellulose (HPMC). The mean residence time of the SH formulation on rabbit eyes was approximately 1.56 times greater than that of the HPMC formulation, which they attributed to the combined viscoelasticity and bioadhesive nature of SH.

3.3. In Situ-Forming Hydrogel Systems

In situ-forming hydrogels, comprised of three-dimensional polymer networks cross-linked by physical or chemical bonds, exhibit remarkable swelling ability in aqueous media whilst attaining structural integrity [126]. Hydrogels exhibit remarkable swelling ability in aqueous media whilst retaining structural integrity [50]. Additionally, unlike the direct administration of therapeutics via IVI, hydrogel-based drug delivery systems can be designed to control and sustain the localised intraocular release of therapeutics, thus reducing the need for frequent administration. The use of bioerodible hydrogel systems also eliminates the need for subsequent surgical removal procedures, a quality that has become increasingly popular in the field of ophthalmology in recent years, particularly in the treatment of posterior segment pathologies [127]. Although HA exhibits physiochemical characteristics that are highly beneficial for hydrogel formation, it cannot form a physical gel by itself. [128]. Furthermore, its high elimination rate hinders its structural integrity in vivo [50,51]. Therefore, chemically modified or cross-linked HA derivatives are often used to formulate hydrogel systems intended for sustained therapeutic release.

3.3.1. Injectable Formulations

Awwad et al. [129] prepared pNPAAM-based hydrogels, cross-linked with acrylated HA for the sustained release of infliximab and bevacizumab (BEVA) following IVI. Upon comparing in vitro enzymatic degradation, approximately 68% of the theoretical mass of the hydrogel containing 2.0 mg/mL of acrylated HA had degraded in 50 units per mL (U/mL) hyaluronidase over 4 days, whilst a weight loss of 41.5% was observed in the hydrogel prepared with 4.0 mg/mL of acrylated HA under the same conditions. This was attributed to the reduced enzyme ingression into the more densely cross-linked hydrogel. However, as a control pNIPAAM hydrogel was not analysed, it is difficult to evaluate the enhanced biodegradation capabilities of the hydrogels functionalised with HA.

Egbu et al. [130] reported the enzymatic and chemical crosslinking of in situ injectable hydrogels prepared with HA. Although the authors demonstrated a more sustained infliximab release over nine days from a pNIPAAM-HA hydrogel ($24.9 \pm 0.4\%$) in comparison to a 5% tyrosine-modified HA hydrogel ($45.49 \pm 0.3\%$), the reason why HA was added to the hydrogels prepared was unclear. HA may enhance the degradation and excretion of non-biodegradable pNIPAAM, thus improving the overall biocompatibility of the formulation. However, no in vitro degradation nor clearance studies were conducted to evaluate this hypothesis. Bora et al. [106] formulated a HA-based poly(D, L-lactide-co-glycide) (PLGA) microparticle-laden composite hydrogel system intended for the subconjunctival delivery of 5-fluorouracil. Optimal syringeability was obtained for the microparticle formulation that was dispersed in a 0.5% (w/v) solution of HA in comparison to those dispersed in solutions of lower concentration, attributed to the increased viscosity of the more concentrated HA solution. The in vitro release study highlighted the superior efficacy of the 4% methacrylated HA hydrogel in comparison to the 0.5% (w/v) solution in sustaining 5-fluorouracil release over 15 days, presumably due to the hindered diffusion of 5-fluorouracil through the hydrogel meshwork. Although capable of sustained release, the 4% methacrylated HA composite hydrogel was not characterised in terms of optical transparency, syringeability or rheological properties.

Yu et al. [131] conducted an in vivo release and biocompatibility study in which vinyl sulfone-functionalised HA hydrogels were administered to a rabbit eye via IVI. The hydrogels exhibited excellent cytocompatibility and exhibited similar retinal morphology and function to that of the control group over three months, whilst also attaining a BEVA concentration of approximately double the therapeutic concentration of BEVA after six months post-administration. The direct injection of BEVA into the pars plana attained a concentration of 2×10^{-5} ng/mL, a concentration that is 2.5×10^{6} times less than the therapeutically relevant dose.

3.3.2. Vitreous Substitutes

Upon removal of the phase-separated vitreous during a vitrectomy, an artificial vitreous substitute is administered to both stabilise and tamponade the retina. A successful vitreous substitute must attain a density of 1.0071 g/cm^3 and a refractive index of 1.3347, and exhibit porosity, biocompatibility, and stability equivalent to that of natural vitreous humour [132]. Silicone oil is a cornerstone vitreous substitute. However, due to the risk of emulsification post-administration, long-term intraocular cytotoxicity, and the need for a second removal surgery associated with silicone oil, alternative vitreous substitute components have been investigated in recent years [133]. HA-based hydrogels are of particular interest as they exhibit similar physicochemical properties to that of the natural vitreous humour.

A carboxymethyl chitosan-based in situ hydrogel, cross-linked with oxidised HA, for vitreous substitute application, was formulated by Wang et al. [134]. The hydrogels exhibited a comparable equilibrium water content, refractive index, and density to that of the physiological vitreous humour. As the HA concentration increased from 1% (*w*/*v*) to 4% (*w*/*v*), the aforementioned physicochemical properties also increased. The hydrogel preserved the original position of the retina 90 days after vitrectomy surgery whilst attaining a normal murine IOP of approximately 6 mmHg, with no adverse effects such as retinal detachment or opacification of the vitreous or haemorrhaging reported.

Thakur et al. [135] investigated the use of HA- and agar-based hydrogels for use as artificial vitreous humour in in vitro intravitreal drug delivery assays. The lower-viscosity HA–agar hydrogel, containing 0.7 mg/mL of HA, exhibited comparable sodium fluorescein neutral nanoparticle migration to that of excised bovine vitreous humour.

A glycidyl methacrylated HA hydrogel, cross-linked via the application of UV light at 365 nm in the presence of N-vinylpyrrolidone, was successfully formulated by Schulz et al. [136]. Although a slight decrease in viscoelasticity was observed upon passing the HA hydrogel through a 23G cannula, resulting from disruption of the hydrogel network under mechanical stress, the hydrogel attained similar viscoelastic behaviour to that of physiological vitreous humour.

3.4. HA-Based Topical Gels

HA-based hydrogels have also been developed as an alternative formulation to topical drug-laden ointments. Exhibiting the dual advantages of both an aqueous solution and an ointment, in situ hydrogels can prolong precorneal residence time due to their viscous nature whilst attaining optical transparency similar to that of natural vitreous humour [79].

Kim et al. [137] developed a 1,4-butanediol diglycidyl ether cross-linked HA membrane that exhibited a twofold increase in diameter after 5 days post-hydration. Transforming from a dry, rigid membrane to a soft, pliable hydrogel upon application, the hydrogel exhibited accelerated corneal re-epithelialisation and wound healing 72 h post-corneal-alkali-burn induction in a murine model. Interestingly, although the membrane was prepared using HA with an average MW of 700 kDa, the membrane released fragments ranging from 15 to 885 kDa. It was hypothesised that the wound healing induced by the membrane was attributed to the dual effect of both low- and high-MW HA fragments. Although it is known that both low- and high-MW HA exhibit regenerative properties, the preparation of a membrane with low-MW HA would have been beneficial to truly compare the in vivo efficacy against corneal injury.

Bao et al. [138] utilised oxidised HA with an average MW of 800 kDa and a glycol-chitosan and dexamethasone (DEX) conjugate to fabricate dual DEX and levofloxacin-laden hydrogel films for corneal application. One hundred percent of the theoretical levofloxacin concentration was released from the hydrogels of varying crosslinking density after 10 min. Conversely, following a burst release equating to 18% of the theoretical DEX concentration, a release of 720 µg of DEX was sustained over 24 h. Assuming a bioavailability of 10%, a single drop of DEX 0.1% (*w*/*v*) eye drop solution delivers 5 µg of DEX per application (30 µg a day with 6 applications). Therefore, via swelling and sustained diffusion mechanisms,

the HA hydrogel was capable of delivering a therapeutic concentration of DEX that was 24 times higher than that of DEX 0.1% (*w*/*v*) eye drops in a single application.

Tomes et al. [139] synthesised an HA-based hydrogel to improve the aqueous solubility and corneal retention time of econazole, an antifungal therapeutic commonly prescribed for fungal keratitis. Solubilised with α-cyclodextrin, econazole release from the HA hydrogel was more sustained in comparison to the positive control econazole solution. Although the hydrogels exhibited a lower clearance rate and a mean residence time of 71 min on the ocular surface, viscosity and mucoadhesion studies would have been useful to demonstrate the superior retention capabilities in comparison to the econazole–cyclodextrin solution.

3.5. Contact Lenses: Comfort and Wettability via HA Modification

HA is an excellent comfort and wetting agent due to its water retention capabilities, a characteristic that is essential for the development of contact lenses designed for enhanced patient comfort. The addition of HA as a releasable wetting agent, as a conditioning agent in a soft contact lens care solution, or as an additive immobilised directly into the lenses via chemical crosslinking has demonstrated efficacy in increasing lens surface wettability, improving biocompatibility with the ocular surface, and preventing protein fouling [140].

Poly-2-hydroxyethyl methacrylate (pHEMA) lenses exhibit high water swellability and oxygen permeability due to co-polymerisation with hydrophilic monomers [141,142]. However, the addition of such monomers also increases surface protein deposition due to the electrostatic interaction-mediated bond formation between the electrochemically charged monomers and the cationic and anionic amino acid residues of lysozyme and albumin [143]. Van Beek et al. [144] demonstrated that immobilisation of HA within a pHEMA hydrogel via ethyl-3-[3-dimethylaminopropyl]carbodiimide hydrochloride crosslinking resulted in a significant decrease in both lysozyme and albumin surface absorption in comparison to the control. However, the optical transparency of the lenses decreased as the MW of the HA cross-linked into the pHEMA hydrogel increased due to the formation of large HA domains within the polymer matrix.

Silicone hydrogel (SIHy) contact lenses containing lipophilic silicone-based polymers such as poly(dimethyl siloxane) and tris (trimethylsiloxy) methacryloxy propyl silane (TRIS) are highly susceptible to lipid deposition and protein denaturation at the tear film–lens surface interface [145–147]. This, coupled with the inherent hydrophobicity and mechanical strength of SIHy lenses, contributes to decreased surface wettability, ocular irritation, and overall patient discomfort. Yamasaki et al. [148] compared the wettability of commercial SIHy lenses prepared with a low-MW, hydrophobically modified HA derivative (~10 kDa) to SIHy lenses prepared with 1000 kDa HA. Soaking the four commercial lenses in a multipurpose solution (MPS) containing the modified HA derivative (cleadew MPS) resulted in decreased contact angles in comparison to the lenses soaked in Biotrue® (unmodified HA) and EOBO-41® (polyoxyethylene-polyoxybutylene) after 13 cycles. The lower the contact angle, the higher the degree of wetting when the lenses come into contact with an aqueous solution [149]. Lower contact angles and lysozyme and human serum albumin deposition were also achieved by Korogiannaki et al. [140] by covalently attaching HA to the surface of a pHEMA lens co-polymerised with a TRIS monomer using thiol-ene "click" chemistry.

Utilising biomimetic molecular imprinting to create binding sites mimicking that of the CD44 receptor in daily disposable nelfilcon A lenses, Ali et al. [150] exhibited the dependence of HA release on both the percentage-by-mass of functional monomer and 2-(diethylamino) ethyl methacrylate (DEAEM) concentration. Additionally, utilising HA as a therapeutic, Maulvi et al. [151] designed UV photopolymerised pHEMA lenses containing an HA-laden ring implant. Although sustained release of HA in vivo was achieved over 15 days, pHEMA lenses are typically designed for daily, single-use application. As there was no significant difference between the degree of corneal staining in the positive control and HA-laden implant lenses group after one day post-application, the therapeutic efficacy of these lenses in promoting corneal wound healing may be limited. Additionally, a study

to evaluate the effect of HA ring implantation on the critical optical properties of the pHEMA lenses was not conducted.

3.6. HA-Based Nanoformulations

The development of ophthalmic nanoformulations has been at the forefront of ophthalmology research in recent years as a means of overcoming the limitations associated with conventional ocular drug delivery systems [79,152,153]. The modification of such nanomaterials with HA presents unique advantages such as improved migration through the static anatomical ocular barriers, enhanced trans-membrane cellular permeation and enhanced bioadhesive capabilities through ligand-mediated CD44 receptor binding, and mucoadhesion [42,51,118]. Table 2 summarises the recent advances in the use of HA as an excipient in ophthalmic nanomaterial formulations and the impact of the addition of HA on the physicochemical attributes of the nanomaterials. As highlighted in Table 2, a variety of formulation methods are used in the synthesis of HA-based nanoformulations. However, preparation methods involving the use of desolvating agents, cross-linking moieties, large volumes of organic solvent, or high-energy formulation conditions to formulate nanoparticles with optimal physicochemical attributes that are suitable for mass scale-up are becoming increasingly unfavourable [154,155]. This is due to the potential cytotoxicity risks imparted by organic residues and the cost of the extensive purification steps to eliminate such residual material. The examples below highlight that HA-based nanoformulations prepared via self-assembly exhibit greater efficacy than alternative formulation methods in alleviating adverse conditions in both in vitro and in vivo ocular disease models, with the added advantage of mild formulation conditions.

Table 2. A synopsis of HA-based nanoformulations in ocular drug delivery.

Formulation	Preparation Method	Excipients	Function	HA MW (kDa)	Desired Effect	Therapeutic	Key Findings	Further Investigation	Ref.
Nanoparticles	Ionotropic Gelation	Chitosan (CS) and tripolyphoshapte (TPP)	Coating agent	200	Improved cellular targeting via receptor-mediated internalisation.	Dexamethasone sodium phosphate (DEX-SP)	Increase in size from 305 ± 14 nm to 386 ± 13 nm and reversal of ZP values from high positive to high negative with HA coating. Coating with HA decreased initial DEX -SP in vitro burst release by approximately 15%. Similar release profiles were obtained between the 1 and 12 h time points.	In vitro/ex vivo mucoadhesion In vitro cytotoxicity analysis In vitro CD44- binding and cellular uptake analysis (study conducted by Matha et al. [156] to investigate HA-CD44 mediated cellular uptake).	[157]
Nanofibres	Electrospinning	Polyvinylpyrrolidone	Excipient	600–1100	Enhanced ocular bioavailability after conjunctival application.	Ferulic acid (FA) and ε-poly(L-lysine) (ε-PLL)	Crosslinking the HA nanofibres with ε-PLL formed electrostatically cross-linked nanofibre-laden inserts (blank inserts only). Blank and FA-loaded inserts preserved chorioallantoic membrane integrity (embryonated hen's egg).	Ex vivo conjunctival permeation and retention studies.	[158]
Nanoparticles	Desolvation	Human serum albumin	Surface ligand	120	Targeted retinal delivery via active CD44 targeting.	Connexin 43 mimetic peptide (Cx43-MP)	The HA-coated nanoparticles exhibited enhanced ex vivo retinal penetration into the outer nuclear layer and retinal pigment epithelium in comparison to the uncoated control group 4 h post-incubation due to high CD44 ligand interaction. 1.2- and 1.5-fold increase in fluorescence intensity in neural retina and retinal pigment epithelium/choroid with HA-coated particles in comparison to the uncoated group. HA-modification exhibited superior ARPE-19 in vitro internalisation in comparison to control.	In vivo permeation studies. In vivo Cx43-MP quantification to determine whether nanoparticle encapsulation prolongs the half-life of Cx43-MP in the vitreal injection site after injection.	[159]

Table 2. *Cont.*

Formulation	Preparation Method	Excipients	Function	HA MW (kDa)	Desired Effect	Therapeutic	Key Findings	Further Investigation	Ref.
Lipid–polymer hybrid nanoparticles (LPHNP)	Ionotropic gelation and thin-film hydration	CS, TPP, Lipoid E 80, cholesterol and DPPE	Surface Ligand	10	Enhanced corneal retention and permeability.	Moxifloxacin hydrochloride (MCF.HCL)	The apparent permeability coefficient of the HA-coated LPHNPs through excised rabbit cornea was 3.29- and 1.69-fold higher than those of the MXF commercial product and the uncoated LPHNP formulation. The area under the curve of the HA-coated LPHNPs between 0 and 6 h was 6.74 and 2.56 times higher than that of the commercial MXF product and the control chitosan nanoparticle formulation, respectively. Fluorescent-labelled HA-coated LPHNPs exhibited stronger fluorescence within the corneal and conjunctival tissues of a rabbit model after ex vivo fluorescent imaging analysis.	Although the enhanced precorneal retention of the HA-coated LPHNP formulation was attributed to the mucoadhesive capabilities of HA, no mucoadhesion studies were conducted. In vitro stability studies to evaluate the stability of the HA-coated LPHNPs in comparison to the uncoated LPHNP and control nanoparticle formulations.	[160]
Nanogels	Physical crosslinking	ε-PLL	Excipient	200/700/1200	General wound healing capabilities.	Berberine	Due to macrogelation and polydispersity index values above 0.3, nanogels formulated with 700 and 1200 kDa HA or HA concentrations above 2 mg/mL were excluded from further characterisation studies. In vitro berberine release was sustained for 24 h after an initial burst release of approximately 50% of the total loaded berberine within 45 min. Blank nanogels exhibited greater efficacy in promoting in vitro wound healing over 48 h in comparison to the berberine-loaded nanogels, which they attributed to the decreased availability of HA as a result of electrostatic interaction with berberine.	A rheological assessment of optimised nanogels. These nanogels were prepared for general wound healing purposes. If designed for corneal wound healing, nanogels exhibiting high viscosity may be beneficial for increasing the retention time and pharmacological profile of the formulation.	[161]

Table 2. *Cont.*

Formulation	Preparation Method	Excipients	Function	HA MW (kDa)	Desired Effect	Therapeutic	Key Findings	Further Investigation	Ref.
Nanoparticles	Self-assembly	Gelatin	Surface ligand	Not Listed	Mucoadhesion to the corneal–conjunctival interface.	Epigallocatechin gallate (EGCG)	HA-coated gelatin–EGCG nanoparticles (GEH) exhibited greater accumulation in human corneal epithelial cells in comparison to control gelatin–EGCG nanoparticles. 100 min after in vivo administration in a murine model, the GEH formulation demonstrated longer retention on the ocular surface in comparison to both the control nanoparticles and an EGCG solution. After twice-daily administrations for three weeks, the GEH formulation restored normal corneal architecture following benzalkonium chloride-induced dry eye syndrome (DES) in a rabbit model.	A study to evaluate the effect of HA MW on the mucoadhesive capabilities and ocular surface retention times of the GEH formulation.	[162]
Nanomicelles	Self-assembly	D-α-Tocopherolpolyethylene glycol succinate (VitE-TPGS) and octylphenoxy poly(ethyleneoxy)ethanol	Excipient	1650	Mucoadhesion to the corneal surface and prevention of corneal damage caused by surfactant excipients.	Cyclosporine A (CyA)	The addition of HA to the micellar formulation significantly decreased the rate of cyclosporine A elimination from the corneal surface in a rabbit model, as evidenced by an elimination rate constant that was almost 4 times smaller than that of the commercial product (Ikervis®) and a five-fold increase in CyA half-life.	Additional in vivo efficacy studies to determine the effective dose of CyA required to treat DES. The dual efficacy of the nanomicellar formulation in delivering CyA for DES treatment and minimising corneal surface abnormalities via HA-mediated re-epithelisation and wound healing.	[7]

Table 2. *Cont.*

Formulation	Preparation Method	Excipients	Function	HA MW (kDa)	Desired Effect	Therapeutic	Key Findings	Further Investigation	Ref.
Nanoparticles	Ionotropic gelation	CS and TPP	Surface ligand	Not Listed	Mucoadhesion to the corneal and conjunctival surface.	Latanoprost	Treatment with HA-CS-latanoprost link nanoparticles led to a significant reduction in daily IOP measurements (27.3 ± 2.2% reduction) in comparison to a 0.005% latanoprost eye drop and Xalatan® (0.005%) over a three-day treatment period in a rabbit model.	In vivo cytotoxicity and ocular tolerability analysis. In vivo latanoprost release and quantification in rabbit tear fluid and/or the mucus layer.	[163]
Nanomicelles	Co-solvent evaporation	HA-ethylenediamine-hexadecyl group derivatives	Excipient	7.3	Mucoadhesion and enhanced retention time on the corneal surface.	Imatinib	HA micellar decoration with polyethylene glycol (PEG) and L-carnitine (CRN) improved transcorneal permeation in an in vitro human corneal epithelial cell model and an ex vivo bovine cornea model. Corneal permeation coefficients increased by 10.5 (free HA), 20.5 (HA-PEG), and 16.5 (HA-CRN) times in comparison to an imatinib suspension (0.5 mg/mL).	In vivo imatinib pharmacokinetic analysis.	[164]
Nanoparticles	Turkevich method	Gold	Coating agent	5	Improved intraocular mobility and targetability.	N/A	Chemical conjugation of thiolated HA to the surface of the gold nanoparticles allowed for enhanced diffusion through retinal explants (from the ganglion cell layer to the photoreceptor layer) in comparison to the uncoated nanoparticles.	Long-term in vitro analysis of antiangiogenic and antioxidant effects of gold nanoparticles. Physicochemical analysis of therapeutic-laden, HA-coated gold nanoparticles.	[165]

Table 2. *Cont.*

Formulation	Preparation Method	Excipients	Function	HA MW (kDa)	Desired Effect	Therapeutic	Key Findings	Further Investigation	Ref.
Nanoparticle	Desolvation	Bovine serum albumin	Coating agent	1400	Enhanced binding to CD44 receptors expressed on RPE-19 cells and minimisation of diabetic vascular adverse effects.	Apatinib	In comparison to uncoated nanoparticles (3.55 ± 0.81 fluorescence intensity), the HA-coated nanoparticles exhibited greater retinal accumulation (12.28 ± 1.39 fluorescence intensity) 5 h post-topical administration in a murine diabetic retinopathy model. The viscosity of the experimental mucin increased from 10.5 ± 0.2 cP to 28.42 ± 1.25 cP upon mixing with the HA-coated albumin nanoparticles. The ZP values of the coated nanoparticles also decreased from -37.3 ± 1.8 mV to -11.9 ± 0.8 mV upon incubation with mucin.	Evaluation of increased apatinib-laden HA-coated nanoparticle cellular uptake resulting from CD44-mediated endocytosis.	[166]
Nanogels	Mixing of amphiphilic polymers at various mass ratios	PLGA-PEG-PLGA triblock copolymer	Therapeutic	800	Extended and controlled release of HA via non-covalent modification.	Fluorescein isothiocyanate-HA	5–30 kDa and 30–70 kDa PLL chains sustained the release of HA from the nanogels up to 30 days via counterion-mediated overlap of the anionic HA chains and cationic PLL. This prevented excessive swelling of the electrostatic complexes and allowed for a more gradual in vitro release of HA.	In vivo HA release and pharmacodynamic study to ensure that sustained HA release and optical transparency can be obtained in physiological conditions.	[167]

3.6.1. Enhanced Pharmacokinetics of HA-Based Nanoformulations

The addition of an HA coating can effectively enhance the intraocular migration of nanomaterials, particularly in the vitreous humour due to charge-mediated repulsion between the anionic carboxylate anions of HA and the negatively charged vitreal glycosaminoglycan moieties at physiological pH. HA-coated, mRNA-loaded lipoplexes of less than 100 nm exhibited enhanced mobility through bovine vitreous humour in an ex vivo model in comparison to the positively charged, uncoated lipoplexes [168]. The coating of the lipoplexes with HA with MWs of 22 and 2700 kDa did not trigger mRNA release in biological media, thus preserving the initial mRNA complexation efficiency of approximately 100%.

Conversely, the adsorption of 120 kDa HA onto the surface of positively charged, human serum-albumin nanoparticles resulted in a decrease in fluorescently labelled connexin43 mimetic peptide (Cx43-MP) encapsulation efficiency from 98.4 ± 0.1% to 85.4 ± 3.7%, with a concurrent reduction in zeta potential from 11.4 ± 0.2 mV to −18.2 ± 0.7 mV. The chemical conjugation of HA to nanoparticles, in which CX43-MP was loaded via an incorporation method, also resulted in a reduction in Cx43-MP encapsulation efficiency from 79.0 ± 1.9% to 71.1 ± 0.8%. However, the chemically modified nanoparticles also exhibited a highly negative surface charge (−44.0 ± 0.4 mV), which ultimately enhanced penetration through both the outer nuclear and RPE layer of an ex vivo bovine retinal model after 4 h of incubation. Conversely, the intraretinal diffusion of the uncoated nanoparticles was limited to the ganglion cell layer after 2 h [159]. In comparison to uncoated gold nanoparticles, HA-coated gold nanoparticles exhibited enhanced diffusion from the vitreal injection site within 4 h post-administration in an ex vivo porcine model [165]. The coated nanoparticles also maintained their inherent red-brown colour within the vitreous humour for up to 24 h, whereas the uncoated nanoparticles began to aggregate, indicated by a red-brown to purple colour change over the same period [158]. Ex vivo corneal permeability in a murine model increased significantly upon integrating HA within and around liposomal vesicles [169]. Hydrating a thin layer of soybean phosphatidylcholine with 0.7% (*w*/*v*) HA resulted in the spontaneous formation of gel-integrated liposomes. As the concentration of HA was fixed at 0.7% (*w*/*v*), it was unclear how the addition of HA affected fluconazole (FLZ) encapsulation efficiency. However, FLZ encapsulation efficiency increased from 25.8 ± 4.9% to 56.8 ± 2.5%, with an increase in FLZ loading from 0.3 to 1.2% (*w*/*v*). Corneal permeation was enhanced following HA modification, with the HA-modified liposomes allowing for the permeation of over 350 μg/cm^3 of FLZ, an amount that was 1.9 and 2.6 times higher than that of the unmodified liposomes (~200 μg/cm^3) and FLZ suspension (~140 μg/cm^3), respectively. Stabilisation of the liposome core via HA gel integration also contributed to the sustained release of FLZ in vivo. The creation of a highly viscous, mucoadhesive diffusion network within the liposomes allowed for the sustained delivery of FLZ at a concentration above its minimum inhibitory concentration of 8 μg/mL for over 24 h post-instillation in an in vivo murine model. Conversely, the FLZ suspension reached a Cmax of 60 μg/mL 2 h post-instillation, followed by a rapid reduction in FLZ permeation after 6 h. Methyl ether poly(ethylene) glycol and 3-amino-1-propanol block copolymer micelles coated with HA exhibited a 1.5-fold increase in genistein corneal penetration in comparison to a genistein eye drop formulation in an ex vivo murine model after 10 h post-administration; this was attributed to the increase in precorneal retention time via hydrogen-bond-mediated mucoadhesion between HA and mucin chains [170].

3.6.2. Cytotoxicity and Safety of HA-Based Nanoformulations

Although HA itself plays a significant role in corneal wound healing via enhanced corneal epithelium proliferation, the cytotoxic and safety evaluation of HA-based nanoformulations for ocular drug delivery remains an imperative step in the development process [107,115,171]. Kalam et al. [157] developed HA-coated CS nanoparticles that exhibited refractive indices (1.33 ± 0.08) and viscosity values (31.25 ± 2.05) that were suitable for topical ocular drug delivery without evoking adverse reactions such as blurred vision,

nanoparticulate sensitivity, and discomfort. Huang et al. [162] developed an eye drop formulation laden with gelatin nanoparticles containing 20 µg/mL of EGCG and 62.5 µg/mL of HA. The nanoparticles exhibited an osmolality value (291 ± 11.1 mOsm/kg) that was within the acceptable range for normal human tear osmolality. An HA concentration-dependent increase in human corneal epithelial (HCE) and IOBA-NHC cellular viability was observed by de la Fuente et al. [172] after cytotoxic evaluation of chitosan-HA nanoparticles. The addition of 0.01% (*w*/*w*) HA to a CyA-laden nanomicellar formulation consisting of VitE-TPGS and octylphenoxy poly(ethyleneoxy)ethanol increased rabbit corneal epithelial cell viability from 56–58% to 77% (1.0% (*w*/*v*) CyA) and 93% (0.0001% (*w*/*v*) CyA) [7].

3.7. Clinical Applications of HA-Based Ocular Drug Delivery Systems

Due to its remarkable hydrating properties, HA is now the predominant active pharmaceutical ingredient in several commercially available AT formulations (Vismed®, Blink® Tears, and Hyalein®) and contact lens multi-purpose solution (BioTrue® and Hidro Health) [52,173]. The treatment of moderate-to-severe dry eye disease (DED) has been the primary focus of clinical trials involving HA-based topical eye drop formulations in recent years. A meta-analysis conducted by Yang et al. [157], in which 19 studies with a total of 2078 cases were evaluated, highlighted the superior efficacy of HA-based artificial tear (AT) formulations in comparison to alternative AT and saline solutions in improving DED symptoms. Similarly, Hynnekleiv et al. [174] previously summarised the results of 53 clinical trials involving the use of AT solutions containing 0.1–0.4% HA in the treatment of DED over 3 months. The safety and efficacy of HA-based formulations, demonstrated in some completed clinical trials with published results, will be discussed here.

When compared to autologous serum eye drops derived from the patients' blood samples, Beck et al. [175] observed that Comfort Shield®, an eye drop formulation containing 0.15% HMWHA, exhibited comparable efficacy in treating patients with severe, late-stage dry eye disease in an initial, randomised clinical trial. However, it was noted that, although comparable efficacy was achieved between the two formulations, severe corneal surface irregularities limited the reliability of the corneal fluorescein staining score. Additionally, the authors reported that due to the small size of the cohort (8 in total, 4—control group, 4—Comfort Shield®), further clinical trials with a larger cohort would be required to ensure the validity of the results obtained.

In an investigator-masked, randomised clinical assessment, a combination eye drop formulation containing glycerine and erythritol, carboxymethyl cellulose (0.5%), and HA (0.1%) exhibited comparable efficacy to a 0.18% HA formulation, indicated by a statistically similar reduction in Global Ocular Staining Score from baseline after 3 months [176]. Although both formulations were well tolerated, indicated by minimal changes in best-corrected visual acuity and a low incidence of treatment-related adverse effects, there was a significant decrease in the number of reported cases of subjective DED symptoms (burning sensation, itching, etc.) in the combination treatment in comparison to the 0.18% HA formulation. A statistically significant increase in tear film break-up time (TFBT) was reported for patients treated with 0.9% saline solution and 0.1–0.3% sodium hyaluronate-based eye drop formulations (Ocudry®) 30 min after instillation in a double-masked, randomised trial [177]. Subjective vision significantly improved post-instillation, with the 0.2% and 0.3% Ocudry® solutions exhibiting a marked improvement from 1 min to 20 min post-instillation. In terms of comfort, Ocudry® 0.3% scored significantly less at 1 min and 5 min post-instillation, attributed to the higher viscosity of the formulation with increasing sodium hyaluronate concentration. However, there was a significant improvement in the subjective comfort score after 20 min from baseline in the Ocudry® 0.3% cohort.

Pinto-Fraga et al. [178] demonstrated the superior efficacy of Visaid®, a 0.2% sodium hyaluronate solution, in comparison to a 0.9% saline solution in reducing the Ocular Surface Disease Index (OSDI) score after daily instillation of 3–8 drops in a phase II, double-blind clinical trial. Patients treated with 0.2% Visaid® exhibited a percentage reduction in OSDI index value of −19.5 ± 27.3% from baseline after 1 month, with over 31.2%

of patients reporting an OSDI comfort value of greater than 5 points. No significant changes in intraocular pressure (IOP), TFBT, or visual acuity from baseline were reported, thus confirming the tolerability of the formulations. Interestingly, when 0.3% Visaid® was compared to 0.9% saline in a later phase III double-blind clinical trial, a statistically significant increase in TFBT from baseline was recorded (+13.98 ± 26.19%, $p > 0.05$) for patients treated with 0.3% Visaid® [179]. A significant difference in the percentage change in TFBT from baseline was also reported between those treated with 0.3% Visaid® and 0.9% saline control after 1 month. The MW of the sodium hyaluronate within the Visaid® solutions was not reported. Assuming the MW of the solutions is similar, it would have been interesting to investigate whether a similar therapeutic response could be achieved with a lower dose of the 0.3% Visaid® solution due to the concentration-dependent increase in viscosity. A recent clinical evaluation was conducted by Alcon Research to evaluate the safety and efficacy of the dual implantation of a CyPass® Micro-Stent and a commercially available viscoadaptive ophthalmic viscosurgical device (Healon5®) in lowering IOP in a cohort with open-angle glaucoma [180]. A total of 83.3% and 73.5% of the patients treated with the CyPass® Micro-Stent and 30 µL of 60 µL of Healon 5, respectively, experienced a reduction in IOP of over 20% from baseline 12 months post-implantation.

4. HA Polyelectrolyte Complexes

Self-assembled nanoformulations, particularly those synthesised from biopolyelelectrolytes, such as HA, are gaining considerable scientific interest in the biomedical field. Formed via electrostatic interaction under mild, aqueous formulation conditions, polyelectrolyte complexes (PECs) present a biocompatible, biodegradable drug delivery system with functionalities that can be tailored for a wide variety of pharmaceutical applications during formulation. As reviewed by Cazorla-Luna et al. [181] and Papagiannopoulos [182], PECs have been adapted for use in multiple dosage forms, including films, hydrogels, porous scaffolds for tissue engineering, and nanovesicles for the delivery of genetic material, protein, and small therapeutic molecules. Taking advantage of the pH-dependant stability of PECs, combined with the cell-binding and penetrating capabilities of biopolyelectrolytes, targeted, responsive therapeutic release can be obtained in vivo.

Despite the proven, multi-purpose efficacy of HA in a variety of ocular drug delivery systems (ODDs), and the favourable characteristics of PECs for drug delivery application, limited research has been conducted into the use of HA-based PECs for ocular application. Following a description of colloidally stable PEC formation with respect to intrinsic formulation parameters and complexation thermodynamics, recent publications in the area of HA-based PECs in ODDs will be reviewed.

4.1. Polyelectrolyte Complex Assembly Mechanism

Polyelectrolyte complexation is an example of supramolecular self-assembly of polyelectrolyte macromolecules of opposing charge into structurally ordered nano-aggregates in an aqueous solution [183]. In such environments, polyelectrolytes adapt either cationic or anionic surface charges due to the ionisation of the acidic (carboxyl or sulphate) or basic (amine) functional groups within the polyelectrolyte chains. The electrostatically driven self-assembly of polymeric material into submicron-sized particles is advantageous in comparison to more conventional nanoparticle preparation methods. Formed under mild formulation conditions and in the absence of harsh organic solvents, chemical crosslinkers, and surfactants, polyelectrolyte complexes (PECs) exhibit high biocompatibility and are free from residual toxic by-products [184]. Extensive purification post-formation is not required, rendering polyelectrolyte complexation a more cost-effective and environmentally friendly method of nanoparticle preparation.

The supramolecular packing of oppositely charged polyacid and polybase moieties via electrostatic charge compensation and the increase in entropy resulting from counter-ion displacement are the driving forces for the self-assembly of polyelectrolyte chains into a complex coacervate phase [185–187]. Polyelectrolyte complexation occurs in three primary

steps [188,189]. Firstly, the kinetically driven mutual entanglement and self-assembly of polyelectrolyte chains via Coulomb interactions result in the formation of primary complexes. Thermodynamic stability is attained via intracomplex reconfiguration. Conformational changes or distortions that occurred during primary complexation are corrected via the establishment of secondary supramolecular or non-covalent interactions. Intercomplex aggregation of the structurally organised secondary complexes composes the final step in the complexation process. Two structural models have also been proposed for PEC assembly and conformation [190–192]. The ladder-like structural model describes PEC assembly as the ordered packing of opposing polyelectrolyte chains resulting from electrostatic charge compensation via a zip mechanism, followed by conformational adaptation to maximise charge neutralisation. The resulting PECs consist of both ionised, hydrophilic, single-stranded blocks and neutralised, hydrophobic, double-stranded blocks.

Conversely, the "scrambled egg" theory of PEC assembly follows a more chaotic approach. Opposing polyelectrolyte chains randomly entangle and aggregate, resulting in partial charge compensation and the formation of ionised sites within a highly entangled polymeric matrix. Theoretically, the true model of PEC assembly is a combination of both the ladder and "scrambled egg" structural models. The predominating assembly mechanism is contingent on many intrinsic characteristics, such as the MWs, concentrations, and charge densities of the respective polyelectrolytes and the molar charge ratio (MCR), shown below in Equation (1) [193].

$$\text{Molar Charge Ratio (MCR)} = \frac{\text{Molar units of anionic } (-) \text{ charge}}{\text{Molar units of cationic } (+) \text{ charge}} \quad (1)$$

The MCR represents the ratio of moles of anionic to cationic polyionic charges in a PEC system and plays a vital role in both the formation and stabilisation of PEC structures. As shown in Figure 3, the structure of PECs can be sub-divided into three primary categories: water-soluble PECs, colloidally stable PECs, and macroscopically precipitated PEC aggregates. However, for the purpose of this review, colloidally stable PECs will be of particular focus as they are the most suitable structural model for nanoparticle-facilitated drug delivery. The complexation of polyelectrolytes exhibiting non-stoichiometric charge ratios under very high dilution results in the formation of colloidally stable, insoluble PECs. Such complexes do not exhibit thermodynamic stability but are kinetically stabilised via mutual electrostatic repulsion of the residual surface charges, the sign of which is dependent on the polyelectrolyte in excess [194]. Such electrostatic stabilisation is imperative to prevent aggregation in vivo, thus ultimately reducing size-exclusion during intraocular transport and subsequent delocalised, uncontrolled therapeutic release [195].

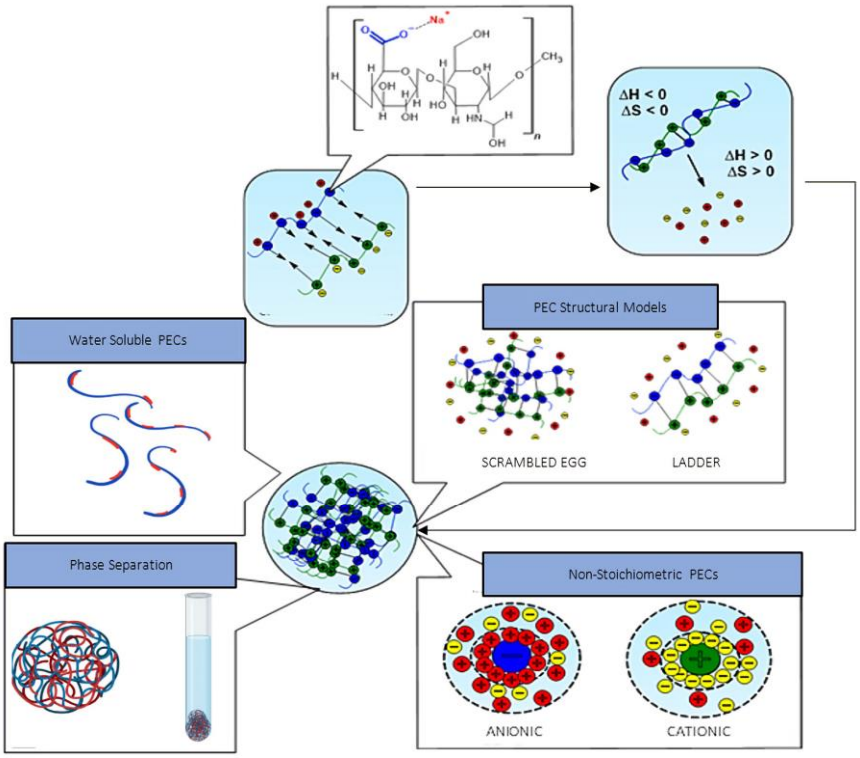

Figure 3. An overview of the complexation between HA and a cationic polyelectrolyte with the resulting physiochemical attribute-dependent structural models (blue—carboxylate anion, red—cationic counterion, green—cationic polyelectrolyte, yellow—anionic counterion; ΔH—change in enthalpy, ΔS—change in entropy) (Created using Biorender.com [196]).

4.2. Thermodynamics of Polyelectrolyte Complexation

The increase in entropy upon disruption of the electrical double layer (EDL) of the individual polyelectrolyte chains and subsequent release of both counterions and solvent molecules into the bulk medium drives complexation [185,197]. The increase in entropy from counterion displacement far exceeds the loss of conformational entropy from the mutual entanglement of the polyelectrolyte chains via supramolecular bond formation. Such favourable entropic contributions, coupled with the decrease in enthalpy resulting from interpolyelectrolyte electrostatic bond formation, ultimately result in a reduction in total Gibb's free energy of the system and the spontaneous formation of PECs [198].

PECs are not thermodynamically stable. In the absence of kinetic stabilisation via residual surface charges, dispersed PECs will tend towards aggregation to decrease the area at the PEC–bulk medium interface, resulting in macroscopic, thermodynamically stable phase separation [198]. Hydrophobic interactions form between the polyelectrolyte hydrophobic moieties to lower the interfacial energy at the hydrophobe–water molecule interface. The increase in entropy resulting from the displacement and disruption of the hydrogen bonds between the water molecules surrounding the hydrophobic moieties drives hydrophobic interaction further. The surface-to-surface separation distance decreases as a result, thus increasing the formation of attractive Van der Waal's forces. As per the Derjaguin, Landau, Verwey, and Overbeek (DLVO) theory, describing the theoretical

analysis of colloidal stability based on the attractive and repulsive forces acting on charged colloidal particles in solution, the system now exists in a deep potential-energy well due to the predominance of attractive forces at short interparticle distances [188,199]. This results in the irreversible formation of a macroscopic, thermodynamically stable PEC aggregate. To attain colloidal metastability, the energy of the PECs must not exceed that of the electrostatic energy barrier $(\Delta_{int}(G))$max, achievable via kinetic stabilisation of the PECs via surface charge.

4.3. Applications of HA Polyelectrolyte Complexes in Ocular Drug Delivery

At physiological pH, HA possesses a negative charge due to deprotonation of the carboxylate anion (pKa 3–4) and can readily complex with cationic species [200,201]. Such polycations include CS, chitosan derivatives such as trimethyl chitosan, poly(L-lysine), silk fibroin, dextran derivates, and poly(arginine) [194,202–208]. Silva et al. [209] synthesised chitosan and HA nanoparticles via electrostatic complexation for use in a topical eye drop solution of erythropoietin. Optimal ZP values and nanoparticle sizes were obtained when the concentration of chitosan and HA of varying MWs were in equal ratios. Significant aggregation was observed when chitosan was present in excess (chitosan:HA ratio—1:0.5), which they attributed to the mixing order of the polyelectrolytes during formulation. The addition of chitosan in excess of HA at this charge ratio may have resulted in the neutralisation of the anionic carboxylate moieties of the initial coacervates before all of the chitosan was introduced to the formulation. Enhanced ex vivo erythropoietin permeation through porcine conjunctiva (0.71 ± 0.04%), sclera (0.52 ± 0.08%), and cornea (0.17 ± 0.04%) were achieved via HA–chitosan complex encapsulation when compared to the percentage ex vivo permeation values obtained for erythropoietin alone (0.52%, 0.35%, and 0.07%). However, an in vitro burst release of erythropoietin, equating to approximately 70% of the erythropoietin loaded, was observed within 30 min. This may prove problematic for treatments designed for topical ocular administration as a faster rate of release shortly after administration may result in increased therapeutic elimination from the pre-corneal area due to nasolacrimal clearance.

The release of 50% of the loading concentration of pentamidine isethionate (PTM), a hydrophilic antiprotozoal and antifungal agent, from HA and poly(arginine)-based PECs was also observed by Carton et al. after 8 h [210]. This was primarily attributed to the hydrophilicity of PTM, resulting in both faster permeation through the HA-poly(arginine) matrix upon release and a higher degree of PEC swelling. Similar in vitro release profiles for the PTM-PEC and free PTM were also recorded, demonstrating that the PECs may not have provided a sufficient diffusion barrier to PTM release when dispersed in the receptor medium. Through ion-mediated diffusion and exchange with the protonated amino groups of timolol maleate™ in 0.9% NaCl solution, Battistini et al. [211] reported an approximate 10% increase in the cumulative release of TM) from sodium hyaluronate (NaHA)-TM ionic complexes over 8 h in comparison to that obtained when water was used as the receptor medium. The NaHA-TM complexes also exhibited superior efficacy in reducing IOP in comparison to a 0.5% TM commercial eye drop (Zopirol®) in a rabbit model over 10 h, attributed to the enhanced mucoadhesive capabilities of the NaHA-based formulation. Increased TM bioavailability in rabbit aqueous humour over 4 h, evidenced by a significantly higher area under the curve (607.7 ± 53.4 μg·h/mL) was also observed for the NaHA-TM formulation in comparison to Zopirol® (400.5 ± 12.2 μg·h/mL).

Chaharband et al. [208] designed trimethyl chitosan and HA nanopolyplexes for the intravitreal delivery of vascular endothelial growth factor 2 (VEGF-2)-small interfering RNA (siRNA). Complete retinal penetration of the nanopolyplexes was visible after one-hour post-IVI in a rabbit model, which they attributed to the ability of HA to permeate the blood-retinal barrier and vitreous humour. Retinal distribution was still detected 120 h post-IVI. Laser-induced choroidal neovascularisation was reduced in the nanopolyplex-treated group (46,501 ± 21,739 μm^2) in comparison to the control group (113,728 ± 32,289 μm^2) in a murine model.

4.4. HA-PECs: Design Considerations and Critical Quality Attributes

Many reviews have discussed the dependence of PEC stability and formation on numerous critical intrinsic and extrinsic factors [63,184,212]. To design an HA-PEC formulation that is both stable under physiological ocular conditions and capable of releasing a drug in a sustained and controlled manner, such attributes must be optimised during formulation method development.

4.4.1. pH

The pH value of the formulation medium has a significant impact on the degree of ionisation of the respective polyelectrolytes within the PECs, thus ultimately affecting the extent of electrostatic bond formation and the separation of PECs into a polymer-rich phase [194,210,213]. A pH value of 7.2 has been reported for the outer nuclear retinal layer, whilst tear fluid exhibits an average pH value of 7.4 [214,215]. Based on its pKa, the carboxylic acid groups of HA should be completely ionised at the aforementioned pH values in the anterior and posterior segments. However, to ensure maximal complexation, the pKa value of the cationic polyelectrolyte should also be taken into consideration. Potentiometric titrations are often conducted to determine the pH value at which both polyelectrolytes exhibit maximal ionisation [216,217]. The extent of ionisation of the PEC formulation at physiological pH should also be determined to ensure that the electrostatic interactions formed are not diminished upon application.

4.4.2. PEC Surface Charge

PECs in which HA is present in excess ($n^-/n^+ > 1$) will preferentially adopt an anionic surface charge. It has been suggested that HA chains will form a peripheral corona, surrounding the charge-neutralised, hydrophobic core, with the electrostatically charged, hydrophilic carboxylate anions residing at the interface of the PEC and the aqueous media [218]. PECs bearing an anionic surface charge are desirable for particular ocular applications. For example, high therapeutic bioavailability within the inner retinal tissues post-intravitreal-administration can be attained via encapsulation within an anionic PEC, primarily due to increased vitreal permeation resulting from the electrostatic repulsion between HA and the negatively charged vitreal glycosaminoglycan moieties [168]. Anionic HA-PECs would also pose a lower risk of cytotoxicity in comparison to cationic PECs. This is also attributed to increased electrostatic repulsion between the residual carboxylate anions and both the phosphate head groups and anionic glycoproteins within the phospholipid bilayer of the cell membrane [219].

4.4.3. Ionic Strength and Stability

When dispersed in a medium of high ionic strength, the ingression of ions into the PEC matrices can effectively screen the electrostatic repulsive forces between kinetically stabilised, charged, colloidal PECs. In comparison to Figure 4a, the reduction in the thickness of the EDL, i.e., the Debye length (λD) (shown in Figure 4b), due to high surface electrostatic charge screening, results in counterion cloud compaction. The increase in energy (+H) required to displace ions from this compact counterion cloud is far greater than the reduction in energy (−H) from the formation of polyelectrolyte ion pairs. As such, PEC formation under these conditions is endothermic. Such processes lead to a reduction in interparticle repulsion, allowing for increased overlap between the EDLs of PECs in close proximity to one another. As per the DLVO theory, at short interparticle distances, Van der Waals forces of attraction tend to predominate. This, coupled with the elimination of the electrostatic energy barrier in high-ionic-strength conditions, can result in irreversible, thermodynamically favourable aggregation [220–223]. Above a critical ionic strength value, PEC nucleation is drastically hindered due to extensive electrostatic charge screening, resulting in the re-dissolution of the individual polyelectrolytes [220,221,224]. The average electrolyte concentration of human tear fluid, based on the concentration of sodium, potassium, chloride, and bicarbonate ions, is approximately 0.3 M (300 mmol/L) [225–227].

Therefore, it is imperative that the stability of PECs in a medium with an ionic strength mimicking that of physiological tear fluid be evaluated during the formulation design stage. Premature PEC degradation in vivo could result in delocalised drug absorption away from the desired target site, thus ultimately reducing the bioavailability of the formulation. As a means of preserving the stability of chitosan and HA-based PECs, Wu et al. [207] investigated the addition of zinc (II) salts to the PECs during formation. This may be a suitable option to enhance stability under physiological conditions as zinc (II) can readily form bridging coordinate bonds with electron-rich donor groups on neighbouring HA chains.

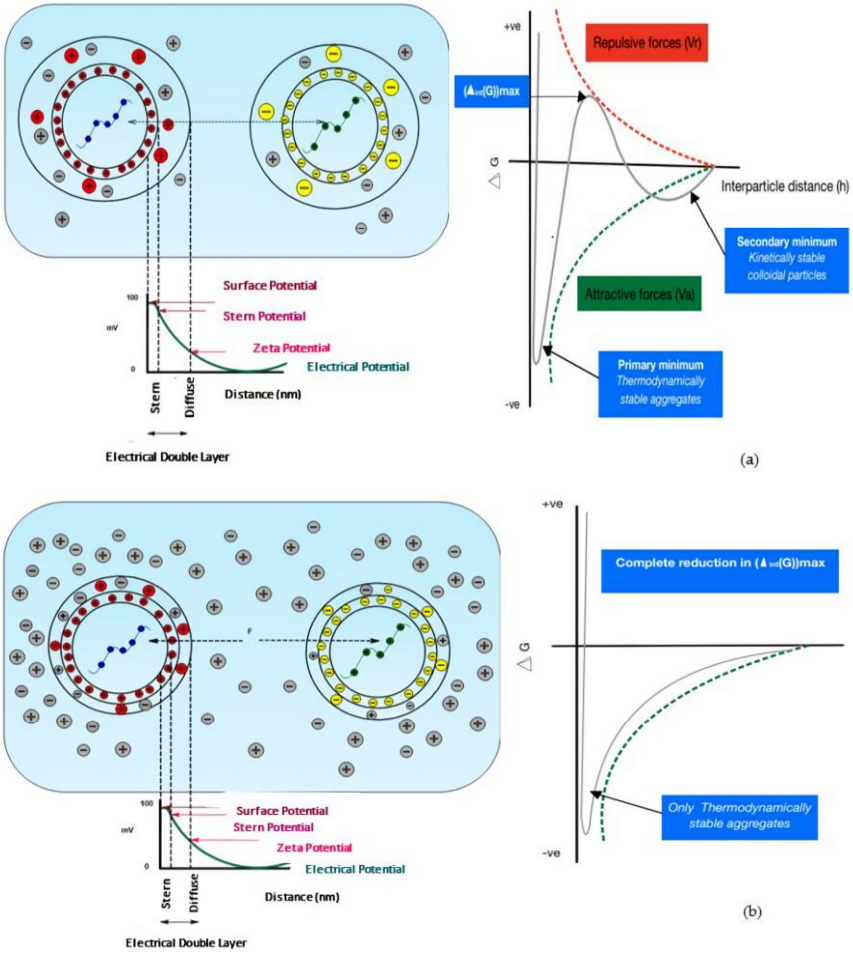

Figure 4. The complexation of two polyelectrolytes of opposing charges under low–(**a**) and high–(**b**) ionic–strength conditions. The effect of both low and high ionic strength on colloidal stability is also represented by the energy vs. interparticulate distance graph drawn per DLVO theory (Red (+)—cations within the electrical double layer (EDL) of HA that are strongly attracted to the anionic carboxylate groups. Yellow (−)—anions within the EDL of the cationic polyelectrolyte that are strongly attracted to the cationic groups. Grey (+/−)—counterions within and outside the EDL of the polyelectrolytes that are more weakly attracted to the surface charges).

4.4.4. The Control of Therapeutic Release from PECs

As highlighted in Section 4.3, therapeutic-laden PECs tend to exhibit fast in vitro release kinetics when placed in an aqueous receptor medium. Hydrophilic drugs will preferentially associate with the hydrophilic corona of the PECs. Cationic drugs can also complex to HA-PECs with non-stoichiometric MCRs ($n^-/n^+ > 1$) directly, due to the presence of residual carboxylate anions. However, the absence of a highly complexed polymeric diffusion barrier at the PEC surface, and the establishment of an osmotic gradient between the aqueous donor phase and the receptor phase, could result in accelerated therapeutic release. Fast intraocular release is unfavourable, particularly for sustained-release ocular drug delivery systems designed to minimise frequent, invasive administration. Additionally, similar to the issues arising from PEC instability in high-ionic-strength conditions, premature release, coupled with the limited migration of therapeutics through the anatomical ocular barriers, will significantly reduce the bioavailability of the therapeutic at the target site, particularly if that target site lies within the posterior segment. Drug molecules with a higher degree of lipophilicity tend to associate with the charge-neutralised hydrophobic core via supermolecular interactions, and would assumingly exhibit slower rates of release due to incompatibility with the external aqueous phase. However, the initial entrapment of lipophilic molecules may prove problematic due to limited solubility in the aqueous formulation media. To control the release of hydrophilic drugs, and to ensure the maximal complexation of lipophilic drugs within the PEC core, the chemical conjugation of drugs to the polymeric backbone of HA via a cleavable linkage may be required. Although it overcomes the pitfalls of physical therapeutic absorption, chemical conjugation may introduce toxicity via residual solvent and coupling agents, thus ultimately affecting the biocompatibility of the PEC formulation [51,118,200,228].

4.4.5. The Influence of HA Concentration and MW

As discussed in Section 2.3, both the concentration and MW of HA have a considerable impact on the viscosity of the final formulation, an attribute that must be carefully optimised to ensure maximal ocular retention whilst minimising potential adverse effects such as ocular irritation and blurred vision. Regarding the administration of drug-laden HA-PECs via IVI, the intrinsic viscosity of the formulation should not exceed that of the vitreous humour (0.1–0.85 Pas) [229]. However, an inverse correlation exists between viscosity and injection volume. Therefore, the formulation should exhibit sufficient viscosity to ensure a minimal volume of the formulation is required for injection, thus preventing potential increases in IOP resulting from the injection of a large volume into the small, fixed vitreal volume of 4 mL [73,230].

With HA-PECs, the effect of HA concentration and MW on PEC stability must also be evaluated. With increasing concentration and MW, an increased number of counterions are released into the EDL surrounding the newly formed PECs. The dual reduction in Debye length and electrostatic stabilisation with increasing counterion concentration promotes the secondary aggregation of primary PECs, leading to the formation of PECs with unfavourable size characteristics. Additionally, similar to what was observed by Schatz et al. [231] when developing chitosan and dextran sulphate PECs, the MW and flexibility of the polyelectrolyte in excess play a fundamental role in PEC colloidal stability. For the formation of anionic PECs (HA in excess), if the MW of the HA used is less than that of the cationic polyelectrolyte, flocculation may occur due to complete polyelectrolyte–polyelectrolyte ion-pairing via the conformational adaptation of HA. However, due to the rigidity of the 1-4-glycosidic bonds, HA may resist adaptation in favour of ion-pairing, allowing the cationic polyelectrolyte of higher MW to behave as a host molecule whilst attaining residual anionic charges for electrostatic stabilisation.

5. Conclusions

In summary, this review highlights the suitability of HA, based on its favourable physicochemical and biological properties, for use as an excipient in ocular drug delivery

systems. The mucoadhesive and viscoelastic properties of HA, combined with its increased cellular uptake via CD44-mediated endocytosis, allow for localised, targeted delivery of therapeutics within the anterior and posterior segments in a sustained manner. Due to its inherent hydrophilicity and biocompatibility, HA has shown great success in providing maximal comfort whilst preserving cellular homeostasis and avoiding potentially harmful adverse effects upon application. However, despite the extensive use of HA-based formulations in ophthalmology and ocular drug delivery, limited research has been conducted into the use of HA-PECs for ocular applications, particularly for posterior segment delivery. There is scope to formulate a system that combines the favourable physicochemical and biological attributes of HA with highly biocompatible PECs that offer similar advantages to those of conventional nanoparticle formulations, whilst avoiding the use of harsh formulation conditions. However, to achieve maximal efficacy with posterior segment delivery, the PEC formulation must remain stable within the intraocular environment whilst permeating through the various anatomical diffusion barriers. Due to the fragility of the interpolyelectrolyte electrostatic interactions, particularly in high-ionic-strength conditions and fluctuating pH, further modification of HA-PECs via chemical conjugation, salt-based stabilisers, or lipoidal coatings may be required for maximal stability and controlled release at the target site. However, with careful optimisation of the critical quality attributes and formulation parameters, HA-based PECs yielding optimal physicochemical parameters have been successfully formulated in the selected examples, which opens the possibility for the development of HA-based PECs for a diverse range of ophthalmic applications.

Author Contributions: Conceptualisation, S.C.-P., R.R., P.M., M.E.B. and L.F.; methodology, S.C.-P., R.R., P.M., G.B., M.E.B. and L.F.; writing—original draft preparation, S.C.-P.; writing—review and editing, S.C.-P., R.R., P.M., M.E.B. and L.F.; supervision, R.R., P.M., G.B., M.E.B. and L.F.; project administration, L.F.; funding acquisition, R.R., P.M., G.B., M.E.B. and L.F. All authors have read and agreed to the published version of the manuscript.

Funding: This work was funded under the SETU PhD Scholarship Programme.

Institutional Review Board Statement: Not applicable.

Informed Consent Statement: Not applicable.

Data Availability Statement: Not applicable.

Conflicts of Interest: The authors declare no conflict of interest.

Abbreviations

AMD	Age-related macular degeneration
AT	Artificial tears
BEVA	Bevacizumab
CD44	Cluster determinant 44
CH	Chitosan
CRN	L-carnitine
Cx43	MP Connexin 43 mimetic peptide
CyA	Cyclosporine A
DEAEM	2-(diethylamino) ethyl methacrylate
DED	Dry eye disease
DEX	Dexamethasone
DEX-SP	Dexamethasone sodium phosphate
DLVO	Derjaguin, Landau, Verwey, and Overbeek
ECM	Extracellular matrices
EDL	Electrical double layer
EGCG	Epigallocatechin gallate
EPR	Enhanced permeation and retention
FA	Ferulic acid

FLZ	Fluconazole
GEH	Gelatin–EGCG nanoparticles
HA	Hyaluronic acid
HABD	HA-binding domain
HA–HC	Hyaluronic acid–heavy chain
HA-PEC	HA-based polyelectrolyte complexes
HC	Heavy chain
HCE	Human corneal epithelial
HMWHA	High-MW HA
HPMC	Hydroxypropyl methylcellulose
HYAL	Hyaluronidases
IL	Interleukin
IOBA-NHC	Spontaneously immortalised normal human conjunctival cell line
IOP	Intraocular pressure
IVI	Intravitreal injection
LMWHA	Low-MW HA
LPHNP	Lipid–polymer hybrid nanoparticles
LYVE-1	Lymphatic vessel endothelial HA receptors
MCF.HCL	Moxifloxacin hydrochloride
MCR	Molar charge ratio
MPS	Multipurpose solution
mRNA	Messenger RNA
MSVI	Moderate-to-severe visual impairment
MW	Molecular weight
NaHA	Sodium hyaluronate
NHA	Native HA
ODDS	Ocular drug delivery systems
OSDI	Ocular Surface Disease Index
PECs	Polyelectrolyte complexes
pHEMA	poly-2-hydroxyethyl methacrylate
PLGA	Poly(D, L-lactide-co-glycide)
PLL	Poly(L-lysine)
pNIPAAM	Poly(N-isopropylacrylamide)
PTM	Pentamidine isethionate
RNS	Reactive nitrogen species
ROS	Reactive oxygen species
SH	Sodium hyaluronate
SIHy	Silicone hydrogel
siRNA	Small interfering RNA
TFBT	Tear film break-up time
TLR	Toll-like receptors
TM	Timolol maleate
TNF-α	Tumour necrosis factor-α
TPP	Tripolyphosphate
TRIS	Tris (trimethylsiloxy) methacryloxy propyl silane
TSG-6	Tumour necrosis factor-stimulated gene-6
VEGF-2	Vascular endothelial growth factor 2
$VEGF_{165}$	Vascular endothelial growth factor 165
VEGF	Vascular endothelial growth factor
VitE-TPGS	D-α-Tocopherolpolyethylene glycol succinate
ZP	Zeta potential

References

1. Gote, V.; Sikder, S.; Sicotte, J.; Pal, D. Ocular Drug Delivery: Present Innovations and Future Challenges. *J. Pharmacol. Exp. Ther.* **2019**, *370*, 602–624. [CrossRef] [PubMed]
2. Jiang, Q.; Zhang, P.; Li, J. Elucidation of Colloid Performances of Thermosensitive in situ—Forming Ophthalmic Gel Formed by Poloxamer 407 for Loading Drugs. *J. Pharm. Sci.* **2020**, *109*, 1703–1713. [CrossRef]
3. Zhu, M.; Wang, J.; Li, N. A Novel Thermo-Sensitive Hydrogel-Based on Poly(N-Isopropylacrylamide)/Hyaluronic Acid of Ketoconazole for Ophthalmic Delivery. *Artif. Cells Nanomed. Biotechnol.* **2018**, *46*, 1282–1287. [CrossRef]
4. Cheng, Y.-H.; Ko, Y.-C.; Chang, Y.-F.; Huang, S.-H.; Liu, C.J.-L. Thermosensitive Chitosan-Gelatin-Based Hydrogel Containing Curcumin-Loaded Nanoparticles and Latanoprost as a Dual-Drug Delivery System for Glaucoma Treatment. *Exp. Eye Res.* **2019**, *179*, 179–187. [CrossRef] [PubMed]
5. Suwannoi, P.; Chomnawang, M.; Tunsirikongkon, A.; Phongphisutthinan, A.; Müller-Goymann, C.C.; Sarisuta, N. TAT-Surface Modified Acyclovir-Loaded Albumin Nanoparticles as a Novel Ocular Drug Delivery System. *J. Drug Deliv. Sci. Technol.* **2019**, *52*, 624–631. [CrossRef]
6. Luis de Redín, I.; Boiero, C.; Martínez-Ohárriz, M.C.; Agüeros, M.; Ramos, R.; Peñuelas, I.; Allemandi, D.; Llabot, J.M.; Irache, J.M. Human Serum Albumin Nanoparticles for Ocular Delivery of Bevacizumab. *Int. J. Pharm.* **2018**, *541*, 214–223. [CrossRef] [PubMed]
7. Terreni, E.; Chetoni, P.; Tampucci, S.; Burgalassi, S.; Al-Kinani, A.A.; Alany, R.G.; Monti, D. Assembling Surfactants-Mucoadhesive Polymer Nanomicelles (ASMP-Nano) for Ocular Delivery of Cyclosporine-A. *Pharmaceutics* **2020**, *12*, 253. [CrossRef]
8. Bengani, L.C.; Kobashi, H.; Ross, A.E.; Zhai, H.; Salvador-Culla, B.; Tulsan, R.; Kolovou, P.E.; Mittal, S.K.; Chauhan, S.K.; Kohane, D.S.; et al. Steroid-Eluting Contact Lenses for Corneal and Intraocular Inflammation. *Acta Biomater.* **2020**, *116*, 149–161. [CrossRef]
9. Zhu, Y.; Sheng, Y. Sustained Delivery of Epalrestat to the Retina Using PEGylated Solid Lipid Nanoparticles Laden Contact Lens. *Int. J. Pharm.* **2020**, *587*, 119688. [CrossRef]
10. Ross, A.E.; Bengani, L.C.; Tulsan, R.; Maidana, D.E.; Salvador-Culla, B.; Kobashi, H.; Kolovou, P.E.; Zhai, H.; Taghizadeh, K.; Kuang, L.; et al. Topical Sustained Drug Delivery to the Retina with a Drug-Eluting Contact Lens. *Biomaterials* **2019**, *217*, 119285. [CrossRef]
11. Mun, J.; Mok, J.W.; Jeong, S.; Cho, S.; Joo, C.K.; Hahn, S.K. Drug-Eluting Contact Lens Containing Cyclosporine-Loaded Cholesterol-Hyaluronate Micelles for Dry Eye Syndrome. *RSC Adv.* **2019**, *9*, 16578–16585. [CrossRef] [PubMed]
12. Lee, S.H.; Kim, H.J.; Kim, D.H.; Chang, W.S.; Vales, T.P.; Kim, J.W.; Kim, K.H.; Kim, J.K. Thermo-Sensitive Nanogel-Laden Bicontinuous Microemulsion Drug-Eluting Contact Lenses. *J. Biomed. Mater. Res. B Appl. Biomater.* **2018**, *107*, 1159–1169. [CrossRef] [PubMed]
13. Badiee, P.; Varshochian, R.; Rafiee-Tehrani, M.; Abedin Dorkoosh, F.; Khoshayand, M.R.; Dinarvand, R. Ocular Implant Containing Bevacizumab-Loaded Chitosan Nanoparticles Intended for Choroidal Neovascularization Treatment. *J. Biomed. Mater. Res. A* **2018**, *106*, 2261–2271. [CrossRef]
14. Jiang, P.; Chaparro, F.J.; Cuddington, C.T.; Palmer, A.F. Injectable Biodegradable Bi-Layered Capsule for Sustained Delivery of Bevacizumab in Treating Wet Age-Related Macular Degeneration. *J. Control. Release* **2020**, *320*, 442–456. [CrossRef] [PubMed]
15. Blindness and Visual Impairment. Available online: https://www.who.int/en/news-room/fact-sheets/detail/blindness-and-visual-impairment (accessed on 14 October 2019).
16. The World Population Prospects: 2015 Revision. Available online: https://www.un.org/en/development/desa/publications/world-population-prospects-2015-revision.html (accessed on 14 October 2019).
17. Projected Change in Vision Loss 2020 to 2050. Available online: https://www.iapb.org/learn/vision-atlas/magnitude-and-projections/projected-change/ (accessed on 6 January 2021).
18. Adelson, J.D.; Bourne, R.R.A.; Briant, P.S.; Flaxman, S.R.; Taylor, H.R.B.; Jonas, J.B.; Abdoli, A.A.; Abrha, W.A.; Abualhasan, A.; Abu-Gharbieh, E.G.; et al. Causes of Blindness and Vision Impairment in 2020 and Trends over 30 Years, and Prevalence of Avoidable Blindness in Relation to VISION 2020: The Right to Sight: An Analysis for the Global Burden of Disease Study. *Lancet Glob. Health* **2020**, *1*, E144–E160. [CrossRef]
19. Global Age-Related Macular Degeneration Market Will More Than Double in Size by 2028—GlobalData. Available online: https://www.globaldata.com/global-age-related-macular-degeneration-market-will-more-than-double-in-size-by-2028/ (accessed on 11 January 2021).
20. Glaucoma Therapeutics Market to Reach USD 11.05 Billion at 6.1% CAGR by 2027; Rising Research on Prostaglandin Analogs, Says Fortune Business InsightsTM. Available online: https://www.globenewswire.com/news-release/2020/09/09/2090664/0/en/Glaucoma-Therapeutics-Market-to-Reach-USD-11-05-Billion-at-6-1-CAGR-by-2027-Rising-Research-on-Prostaglandin-Analogs-says-Fortune-Business-Insights.html (accessed on 2 May 2022).
21. Diabetic Retinopathy Market to Reach USD 13.04 Billion by 2026. Available online: https://www.globenewswire.com/news-release/2019/06/06/1865544/0/en/Diabetic-Retinopathy-Market-to-Reach-USD-13-04-billion-By-2026-Reports-And-Data.html (accessed on 2 May 2022).
22. Nentwich, M.M.; Ulbig, M.W. Diabetic Retinopathy—Ocular Complications of Diabetes Mellitus. *World J. Diabetes* **2015**, *6*, 489. [CrossRef]

23. García-Quintanilla, L.; Luaces-Rodríguez, A.; Gil-Martínez, M.; Mondelo-García, C.; Maroñas, O.; Mangas-Sanjuan, V.; González-Barcia, M.; Zarra-Ferro, I.; Aguiar, P.; Otero-Espinar, F.J.; et al. Pharmacokinetics of Intravitreal Anti-VEGF Drugs in Age-Related Macular Degeneration. *Pharmaceutics* **2019**, *11*, 365. [CrossRef]
24. Varela-Fernández, R.; Díaz-Tomé, V.; Luaces-Rodríguez, A.; Conde-Penedo, A.; García-Otero, X.; Luzardo-álvarez, A.; Fernández-Ferreiro, A.; Otero-Espinar, F.J. Drug Delivery to the Posterior Segment of the Eye: Biopharmaceutic and Pharmacokinetic Considerations. *Pharmaceutics* **2020**, *12*, 269. [CrossRef] [PubMed]
25. del Amo, E.M.; Rimpelä, A.K.; Heikkinen, E.; Kari, O.K.; Ramsay, E.; Lajunen, T.; Schmitt, M.; Pelkonen, L.; Bhattacharya, M.; Richardson, D.; et al. Pharmacokinetic Aspects of Retinal Drug Delivery. *Prog. Retin. Eye Res.* **2017**, *57*, 134–185. [CrossRef]
26. Edelhauser, H.F.; Rowe-Rendleman, C.L.; Robinson, M.R.; Dawson, D.G.; Chader, G.J.; Grossniklaus, H.E.; Rittenhouse, K.D.; Wilson, C.G.; Weber, D.A.; Kuppermann, B.D.; et al. Ophthalmic Drug Delivery Systems for the Treatment of Retinal Diseases: Basic Research to Clinical Applications. *Investig. Ophthalmol. Vis. Sci.* **2010**, *51*, 5403–5420. [CrossRef]
27. Meduri, E.; Gillmann, K.; Mansouri, K. Intraocular Pressure Variations After Intravitreal Injections Measured with an Implanted Suprachoroidal Telemetry Sensor. *J. Glaucoma* **2021**, *30*, E360–E363. [CrossRef] [PubMed]
28. Falavarjani, K.G.; Nguyen, Q.D. Adverse Events and Complications Associated with Intravitreal Injection of Anti-VEGF Agents: A Review of Literature. *Eye* **2013**, *27*, 787–794. [CrossRef] [PubMed]
29. Cabrera, F.J.; Wang, D.C.; Reddy, K.; Acharya, G.; Shin, C.S. Challenges and Opportunities for Drug Delivery to the Posterior of the Eye. *Drug Discov. Today* **2019**, *24*, 1679–1684. [CrossRef] [PubMed]
30. Cao, Y.; Samy, K.E.; Bernards, D.A.; Desai, T.A. Recent Advances in Intraocular Sustained-Release Drug Delivery Devices. *Drug Discov. Today* **2019**, *24*, 1694–1700. [CrossRef]
31. Ophthalmic Drugs Market Size, Share & Trends Analysis Report by Disease (Dry Eye, Eye Allergy, Glaucoma, Eye Infection), by Drug Class, by Dosage form, by Route of Administration, by Product Type, by Region, and Segment Forecasts, 2021–2028. Available online: https://www.grandviewresearch.com/industry-analysis/ophthalmic-therapeutics-drug-market (accessed on 2 May 2022).
32. Patel, A. Ocular Drug Delivery Systems: An Overview. *World J. Pharmacol.* **2013**, *2*, 47. [CrossRef]
33. Boddu, S.; Gupta, H.; Patel, S. Drug Delivery to the Back of the Eye Following Topical Administration: An Update on Research and Patenting Activity. *Recent Pat. Drug Deliv. Formul.* **2014**, *8*, 27–36. [CrossRef]
34. Johannsdottir, S.; Jansook, P.; Stefansson, E.; Kristinsdottir, I.M.; Fulop, Z.; Asgrimsdottir, G.M.; Thorsteindsottir, M.; Eiriksson, F.F.; Loftsson, T. Topical Drug Delivery to the Posterior Segment of the Eye: Dexamethasone Concentrations in Various Eye Tissues after Topical Administration for up to 15 Days to Rabbits. *J. Drug Deliv. Sci. Technol.* **2018**, *45*, 449–454. [CrossRef]
35. Gaudana, R.; Ananthula, H.K.; Parenky, A.; Mitra, A.K. Ocular Drug Delivery. *AAPS J.* **2010**, *12*, 348–360. [CrossRef]
36. Rodrigues, G.A.; Lutz, D.; Shen, J.; Yuan, X.; Shen, H.; Cunningham, J.; Rivers, H.M. Topical Drug Delivery to the Posterior Segment of the Eye: Addressing the Challenge of Preclinical to Clinical Translation. *Pharm. Res.* **2018**, *35*, 245. [CrossRef]
37. Pitkänen, L.; Ranta, V.P.; Moilanen, H.; Urtti, A. Permeability of Retinal Pigment Epithelium: Effects of Permeant Molecular Weight and Lipophilicity. *Investig. Ophthalmol. Vis. Sci.* **2005**, *46*, 641–646. [CrossRef]
38. Jumelle, C.; Gholizadeh, S.; Annabi, N.; Dana, R. Advances and Limitations of Drug Delivery Systems Formulated as Eye Drops. *J. Control. Release* **2020**, *321*, 1–22. [CrossRef] [PubMed]
39. Irimia, T.; Ghica, M.V.; Popa, L.; Anuța, V.; Arsene, A.L.; Dinu-Pîrvu, C.E. Strategies for Improving Ocular Drug Bioavailability and Cornealwound Healing with Chitosan-Based Delivery Systems. *Polymers* **2018**, *10*, 1221. [CrossRef] [PubMed]
40. Allyn, M.M.; Luo, R.H.; Hellwarth, E.B.; Swindle-Reilly, K.E. Considerations for Polymers Used in Ocular Drug Delivery. *Front. Med.* **2022**, *8*, 787644. [CrossRef] [PubMed]
41. Park, Y.; Huh, K.M.; Kang, S.W. Applications of Biomaterials in 3D Cell Culture and Contributions of 3D Cell Culture to Drug Development and Basic Biomedical Research. *Int. J. Mol. Sci.* **2021**, *22*, 2491. [CrossRef] [PubMed]
42. Chang, W.H.; Liu, P.Y.; Lin, M.H.; Lu, C.J.; Chou, H.Y.; Nian, C.Y.; Jiang, Y.T.; Hsu, Y.H.H. Applications of Hyaluronic Acid in Ophthalmology and Contact Lenses. *Molecules* **2021**, *26*, 2485. [CrossRef]
43. Snetkov, P.; Zakharova, K.; Morozkina, S.; Olekhnovich, R.; Uspenskaya, M. Hyaluronic Acid: The Influence of Molecular Weight on Structural, Physical, Physico-Chemical, and Degradable Properties of Biopolymer. *Polymers* **2020**, *12*, 1800. [CrossRef]
44. Papakonstantinou, E.; Roth, M.; Karakiulakis, G. Hyaluronic Acid: A Key Molecule in Skin Aging. *Dermato-Endocrinol.* **2012**, *4*, 253–258. [CrossRef]
45. Vasvani, S.; Kulkarni, P.; Rawtani, D. Hyaluronic Acid: A Review on Its Biology, Aspects of Drug Delivery, Route of Administrations and a Special Emphasis on Its Approved Marketed Products and Recent Clinical Studies. *Int. J. Biol. Macromol.* **2020**, *151*, 1012–1029. [CrossRef]
46. Selyanin, M.A.; Boykov, P.Y.; Khabarov, V.N. Molecular and Supramolecular Structure of Hyaluronic Acid. In *Hyaluronic Acid—Preparation, Properties, Application in Biology and Medicine*; Polyak, F., Ed.; John Wiley & Sons Ltd.: West Sussex, UK, 2015; Volume 1, pp. 101–104.
47. Lapčík, L.; Lapčík, L.; de Smedt, S.; Demeester, J.; Chabreček, P. Hyaluronan: Preparation, Structure, Properties, and Applications. *Chem. Rev.* **1998**, *98*, 2663–2684. [CrossRef]
48. Juncan, A.M.; Moisă, D.G.; Santini, A.; Morgovan, C.; Rus, L.L.; Vonica-Țincu, A.L.; Loghin, F. Advantages of Hyaluronic Acid and Its Combination with Other Bioactive Ingredients in Cosmeceuticals. *Molecules* **2021**, *26*, 4429. [CrossRef]

49. Bukhari, S.N.A.; Roswandi, N.L.; Waqas, M.; Habib, H.; Hussain, F.; Khan, S.; Sohail, M.; Ramli, N.A.; Thu, H.E.; Hussain, Z. Hyaluronic Acid, a Promising Skin Rejuvenating Biomedicine: A Review of Recent Updates and Pre-Clinical and Clinical Investigations on Cosmetic and Nutricosmetic Effects. *Int. J. Biol. Macromol.* **2018**, *120*, 1682–1695. [CrossRef] [PubMed]
50. Lynch, C.R.; Kondiah, P.P.D.; Choonara, Y.E.; du Toit, L.C.; Ally, N.; Pillay, V. Hydrogel Biomaterials for Application in Ocular Drug Delivery. *Front. Bioeng. Biotechnol.* **2020**, *8*, 228. [CrossRef]
51. Zhang, X.; Wei, D.; Xu, Y.; Zhu, Q. Hyaluronic Acid in Ocular Drug Delivery. *Carbohydr. Polym.* **2021**, *264*, 118006. [CrossRef] [PubMed]
52. Harrer, D.; Sanchez Armengol, E.; Friedl, J.D.; Jalil, A.; Jelkmann, M.; Leichner, C.; Laffleur, F. Is Hyaluronic Acid the Perfect Excipient for the Pharmaceutical Need? *Int. J. Pharm.* **2021**, *601*, 120589. [CrossRef] [PubMed]
53. Fallacara, A.; Baldini, E.; Manfredini, S.; Vertuani, S. Hyaluronic Acid in the Third Millennium. *Polymers* **2018**, *10*, 701. [CrossRef] [PubMed]
54. Knopf-Marques, H.; Pravda, M.; Wolfova, L.; Velebny, V.; Schaaf, P.; Vrana, N.E.; Lavalle, P. Hyaluronic Acid and Its Derivatives in Coating and Delivery Systems: Applications in Tissue Engineering, Regenerative Medicine and Immunomodulation. *Adv. Healthc. Mater.* **2016**, *5*, 2841–2855. [CrossRef]
55. Gallo, N.; Nasser, H.; Salvatore, L.; Natali, M.L.; Campa, L.; Mahmoud, M.; Capobianco, L.; Sannino, A.; Madaghiele, M. Hyaluronic Acid for Advanced Therapies: Promises and Challenges. *Eur. Polym. J.* **2019**, *117*, 134–147. [CrossRef]
56. Necas, J.; Bartosikova, L.; Brauner, P.; Kolar, J. Hyaluronic Acid (Hyaluronan): A Review. *Vet. Med.* **2008**, *53*, 397–411. [CrossRef]
57. Toole, B.P. Hyaluronan: From Extracellular Glue to Pericellular Cue. *Nat. Rev. Cancer* **2004**, *4*, 528–539. [CrossRef]
58. Fakhari, A.; Berkland, C. Applications and Emerging Trends of Hyaluronic Acid in Tissue Engineering, as a Dermal Filler and in Osteoarthritis Treatment. *Acta Biomater.* **2013**, *9*, 7081–7092. [CrossRef]
59. Dovedytis, M.; Liu, Z.J.; Bartlett, S. Hyaluronic Acid and Its Biomedical Applications: A Review. *Eng. Regen.* **2020**, *1*, 102–113. [CrossRef]
60. Guter, M.; Breunig, M. Hyaluronan as a Promising Excipient for Ocular Drug Delivery. *Eur. J. Pharm. Biopharm.* **2017**, *113*, 34–49. [CrossRef] [PubMed]
61. Yanaki, T.; Yamaguchi, T. Temporary Network Formation of Hyaluronate under a Physiological Condition. 1. Molecular-weight Dependence. *Biopolymers* **1990**, *30*, 415–425. [CrossRef] [PubMed]
62. Kabanov, V.A. Polyelectrolyte Complexes in Solution and in Bulk. *Russ. Chem. Rev.* **2005**, *74*, 3–20. [CrossRef]
63. Insua, I.; Wilkinson, A.; Fernandez-Trillo, F. Polyion Complex (PIC) Particles: Preparation and Biomedical Applications. *Eur. Polym. J.* **2016**, *81*, 198–215. [CrossRef]
64. Khunmanee, S.; Jeong, Y.; Park, H. Crosslinking Method of Hyaluronic-Based Hydrogel for Biomedical Applications. *J. Tissue Eng.* **2017**, *8*, 2041731417726464. [CrossRef]
65. Gatej, I.; Popa, M.; Rinaudo, M. Role of the PH on Hyaluronan Behavior in Aqueous Solution. *Biomacromolecules* **2005**, *6*, 61–67. [CrossRef]
66. Ghosh, S.; Kobal, I.; Zanette, D.; Reed, W.F. Conformational Contraction and Hydrolysis of Hyaluronate in Sodium Hydroxide Solutions. *Macromolecules* **1993**, *26*, 4685–4693. [CrossRef]
67. Morris, E.R.; Rees, D.A.; Welsh, E.J. Conformation and Dynamic Interactions in Hyaluronate Solutions. *J. Mol. Biol.* **1980**, *138*, 383–400. [CrossRef]
68. Maleki, A.; Kjøniksen, A.L.; Nyström, B. Effect of PH on the Behavior of Hyaluronic Acid in Dilute and Semidilute Aqueous Solutions. *Macromol. Symp.* **2008**, *274*, 131–140. [CrossRef]
69. Cowman, M.K.; Matsuoka, S. The Intrinsic Viscosity of Hyaluronan. In *Hyaluronan*; Elsevier: Amsterdam, The Netherlands, 2002; pp. 75–78. [CrossRef]
70. Bothner, H.; Wik, O. Rheology of Hyaluronate. *Acta Oto-Laryngol.* **1987**, *104*, 25–30. [CrossRef] [PubMed]
71. Cowman, M.K.; Schmidt, T.A.; Raghavan, P.; Stecco, A. Viscoelastic Properties of Hyaluronan in Physiological Conditions. *F1000Research* **2015**, *4*, 622. [CrossRef] [PubMed]
72. Cleland, R.L. Effect of Temperature on the Limiting Viscosity Number of Hyaluronic Acid and Chondroitin 4-sulfate. *Biopolymers* **1979**, *18*, 1821–1828. [CrossRef]
73. Shetty, G.N.; Whelton, R. Ophthalmic Injection of Viscous Formulations—Why Unique Needs Require a Novel Delivery System. *ONdrugdelivery* **2022**, *130*, 54–58.
74. Ng, P.C.; Oliver, J.J. Anatomy of the Eye. In *Handbook of Emergency Ophthalmology*; Long, B., Koyfman, A., Eds.; Springer: Cham, Switzerland, 2018; pp. 1–12. [CrossRef]
75. Nickerson, C.S. The Vitreous Humor: Mechanics and Structure. Ph.D. Thesis, California Institute of Technology, Pasadena, CA, USA, 2005.
76. Moiseev, R.V.; Morrison, P.W.J.; Steele, F.; Khutoryanskiy, V.V. Penetration Enhancers in Ocular Drug Delivery. *Pharmaceutics* **2019**, *11*, 321. [CrossRef]
77. Crowell, S.R.; Wang, K.; Famili, A.; Shatz, W.; Loyet, K.M.; Chang, V.; Liu, Y.; Prabhu, S.; Kamath, A.V.; Kelley, R.F. Influence of Charge, Hydrophobicity, and Size on Vitreous Pharmacokinetics of Large Molecules. *Transl. Vis. Sci. Technol.* **2019**, *8*, 1. [CrossRef]
78. Bishop, P. The Biochemical Structure of Mammalian Vitreous. *Eye* **1996**, *10*, 664–670. [CrossRef]
79. Ángeles, G.H.; Nešporová, K. Hyaluronan and Its Derivatives for Ophthalmology: Recent Advances and Future Perspectives. *Carbohydr. Polym.* **2021**, *259*, 117697. [CrossRef]

80. Müller-Lierheim, W.G.K. Why Chain Length of Hyaluronan in Eye Drops Matters. *Diagnostics* **2020**, *10*, 511. [CrossRef]
81. Kwon, M.Y.; Wang, C.; Galarraga, J.H.; Puré, E.; Han, L.; Burdick, J.A. Influence of Hyaluronic Acid Modification on CD44 Binding towards the Design of Hydrogel Biomaterials. *Biomaterials* **2019**, *222*, 119451. [CrossRef]
82. Girish, K.S.; Kemparaju, K. The Magic Glue Hyaluronan and Its Eraser Hyaluronidase: A Biological Overview. *Life Sci.* **2007**, *80*, 1921–1943. [CrossRef] [PubMed]
83. Passi, A.; Vigetti, D. Hyaluronan as Tunable Drug Delivery System. *Adv. Drug Deliv. Rev.* **2019**, *146*, 83–96. [CrossRef] [PubMed]
84. García-Posadas, L.; Contreras-Ruiz, L.; López-García, A.; Álvarez, S.V.; Maldonado, M.J.; Diebold, Y. Hyaluronan Receptors in the Human Ocular Surface: A Descriptive and Comparative Study of RHAMM and CD44 in Tissues, Cell Lines and Freshly Collected Samples. *Histochem. Cell Biol.* **2012**, *137*, 165–176. [CrossRef] [PubMed]
85. Chen, C.; Zhao, S.; Karnad, A.; Freeman, J.W. The Biology and Role of CD44 in Cancer Progression: Therapeutic Implications. *J. Hematol. Oncol.* **2018**, *11*, 64. [CrossRef]
86. Mochimaru, H.; Takahashi, E.; Tsukamoto, N.; Miyazaki, J.; Yaguchi, T.; Koto, T.; Kurihara, T.; Noda, K.; Ozawa, Y.; Ishimoto, T.; et al. Involvement of Hyaluronan and Its Receptor CD44 with Choroidal Neovascularization. *Investig. Ophthalmol. Vis. Sci.* **2009**, *50*, 4410–4415. [CrossRef]
87. Shen, W.Y.; Yu, M.J.T.; Barry, C.J.; Constable, I.J.; Rakoczy, P.E. Expression of Cell Adhesion Molecules and Vascular Endothelial Growth Factor in Experimental Choroidal Neovascularisation in the Rat. *Br. J. Ophthalmol.* **1998**, *82*, 1063–1071. [CrossRef]
88. Knepper, P.A.; Miller, A.M.; Choi, J.; Wertz, R.D.; Nolan, M.J.; Goossens, W.; Whitmer, S.; Yue, B.Y.J.T.; Ritch, R.; Liebmann, J.M.; et al. Hypophosphorylation of Aqueous Humor SCD44 and Primary Open-Angle Glaucoma. *Investig. Ophthalmol. Vis. Sci.* **2005**, *46*, 2829–2837. [CrossRef]
89. de Oliveira, J.D.; Carvalho, L.S.; Gomes, A.M.V.; Queiroz, L.R.; Magalhães, B.S.; Parachin, N.S. Genetic Basis for Hyper Production of Hyaluronic Acid in Natural and Engineered Microorganisms. *Microb. Cell Factories* **2016**, *15*, 119. [CrossRef]
90. Yang, C.; Cao, M.; Liu, H.; He, Y.; Xu, J.; Du, Y.; Liu, Y.; Wang, W.; Cui, L.; Hu, J.; et al. The High and Low Molecular Weight Forms of Hyaluronan Have Distinct Effects on CD44 Clustering. *J. Biol. Chem.* **2012**, *287*, 43094–43107. [CrossRef]
91. Wight, T.N. Provisional Matrix: A Role for Versican and Hyaluronan. *J. Int. Soc. Matrix Biol.* **2017**, *60–61*, 38–56. [CrossRef]
92. Stern, R.; Jedrzejas, M.J. The Hyaluronidases: Their Genomics, Structures, and Mechanisms of Action. *Chem. Rev.* **2006**, *106*, 818–839. [CrossRef] [PubMed]
93. Cyphert, J.M.; Trempus, C.S.; Garantziotis, S. Size Matters: Molecular Weight Specificity of Hyaluronan Effects in Cell Biology. *Int. J. Cell Biol.* **2015**, *2015*, 563818. [CrossRef] [PubMed]
94. Vigetti, D.; Karousou, E.; Viola, M.; Deleonibus, S.; de Luca, G.; Passi, A. Hyaluronan: Biosynthesis and Signaling. *Biochim. Et Biophys. Acta Gen. Subj.* **2014**, *1840*, 2452–2459. [CrossRef] [PubMed]
95. Mestorino, N.; Bełdowski, P.; Martinez-Larrañaga, M.-R.; Gupta, R.C.; Lall, R.; Srivastava, A.; Sinha, A. Hyaluronic Acid: Molecular Mechanisms and Therapeutic Trajectory. *Front. Vet. Sci.* **2019**, *6*, 192. [CrossRef]
96. Erickson, M.; Stern, R. Chain Gangs: New Aspects of Hyaluronan Metabolism. *Biochem. Res. Int.* **2012**, *2012*, 893947. [CrossRef]
97. Marinho, A.; Nunes, C.; Reis, S. Hyaluronic Acid: A Key Ingredient in the Therapy of Inflammation. *Biomolecules* **2021**, *11*, 1518. [CrossRef]
98. Fan, C.; Wang, H. Connection between Hyaluronic Acid and Toll-Like Receptor in Signal Transduction. In *Proceedings of the International Conference in Medical Science and Biological Engineering*; Deng, J., Qingjun, L., Eds.; World Scientific: Kowloon, Hong Kong, 2015; pp. 387–393. [CrossRef]
99. Kotla, N.G.; Bonam, S.R.; Rasala, S.; Wankar, J.; Bohara, R.A.; Bayry, J.; Rochev, Y.; Pandit, A. Recent Advances and Prospects of Hyaluronan as a Multifunctional Therapeutic System. *J. Control. Release* **2021**, *336*, 598–620. [CrossRef]
100. Jiang, D.; Liang, J.; Noble, P.W. Hyaluronan as an Immune Regulator in Human Diseases. *Physiol. Rev.* **2011**, *91*, 221–264. [CrossRef]
101. Petrey, A.C.; de la Motte, C.A. Hyaluronan, a Crucial Regulator of Inflammation. *Front. Immunol.* **2014**, *5*, 101. [CrossRef]
102. Lee-Sayer, S.S.M.; Dong, Y.; Arif, A.A.; Olsson, M.; Brown, K.L.; Johnson, P. The Where, When, How and Why of Hyaluronan Binding by Immune Cells. *Front. Immunol.* **2015**, *6*, 150. [CrossRef]
103. Lardner, E.; van Setten, G.B. Detection of TSG-6-like Protein in Human Corneal Epithelium. Simultaneous Presence with CD44 and Hyaluronic Acid. *J. Fr. D'ophtalmologie* **2020**, *43*, 879–883. [CrossRef] [PubMed]
104. Sun, Y.Y.; Keller, K.E. Hyaluronan Cable Formation by Ocular Trabecular Meshwork Cells. *Exp. Eye Res.* **2015**, *139*, 97–107. [CrossRef] [PubMed]
105. Day, A.J.; de La Motte, C.A. Hyaluronan Cross-Linking: A Protective Mechanism in Inflammation? *Trends Immunol.* **2005**, *26*, 637–643. [CrossRef]
106. Bora, M.; Mundargi, R.C.; Chee, Y.; Wong, T.T.L.; Venkatraman, S.S. 5-Flurouracil Microencapsulation and Impregnation in Hyaluronic Acid Hydrogel as Composite Drug Delivery System for Ocular Fibrosis. *Cogent Med.* **2016**, *3*, 1182108. [CrossRef]
107. Carlson, E.; Kao, W.W.Y.; Ogundele, A. Impact of Hyaluronic Acid-Containing Artificial Tear Products on Reepithelialization in an In Vivo Corneal Wound Model. *J. Ocul. Pharmacol. Ther.* **2018**, *34*, 360. [CrossRef] [PubMed]
108. Xu, W.; Wang, Z.; Liu, Y.; Wang, L.; Jiang, Z.; Li, T.; Zhang, W.; Liang, Y. Carboxymethyl Chitosan/Gelatin/Hyaluronic Acid Blended-Membranes as Epithelia Transplanting Scaffold for Corneal Wound Healing. *Carbohydr. Polym.* **2018**, *192*, 240–250. [CrossRef]

109. Saraswathy, K.; Agarwal, G.; Srivastava, A. Hyaluronic Acid Microneedles-Laden Collagen Cryogel Plugs for Ocular Drug Delivery. *J. Appl. Polym. Sci.* **2020**, *137*, 49285. [CrossRef]
110. Ilochonwu, B.C.; Urtti, A.; Hennink, W.E.; Vermonden, T. Intravitreal Hydrogels for Sustained Release of Therapeutic Proteins. *J. Control. Release* **2020**, *326*, 419–441. [CrossRef]
111. Chittasupho, C.; Posritong, P.; Ariyawong, P. Stability, Cytotoxicity, and Retinal Pigment Epithelial Cell Binding of Hyaluronic Acid-Coated PLGA Nanoparticles Encapsulating Lutein. *AAPS PharmSciTech* **2019**, *20*, 4. [CrossRef]
112. Silva, B.; Gonçalves, L.M.; Braz, B.S.; Delgado, E. Chitosan and Hyaluronic Acid Nanoparticles as Vehicles of Epoetin Beta for Subconjunctival Ocular Delivery. *Mar. Drugs* **2022**, *20*, 151. [CrossRef]
113. Agarwal, P.; Craig, J.P.; Rupenthal, I.D. Formulation Considerations for the Management of Dry Eye Disease. *Pharmaceutics* **2021**, *13*, 207. [CrossRef] [PubMed]
114. You, I.C.; Li, Y.; Jin, R.; Ahn, M.; Choi, W.; Yoon, K.C. Comparison of 0.1%, 0.18%, and 0.3% Hyaluronic Acid Eye Drops in the Treatment of Experimental Dry Eye. *J. Ocul. Pharmacol. Ther.* **2018**, *34*, 557–564. [CrossRef] [PubMed]
115. Fallacara, A.; Vertuani, S.; Panozzo, G.; Pecorelli, A.; Valacchi, G.; Manfredini, S. Novel Artificial Tears Containing Cross-Linked Hyaluronic Acid: An in Vitro Re-Epithelialization Study. *Molecules* **2017**, *22*, 2104. [CrossRef]
116. Graça, A.; Gonçalves, L.M.; Raposo, S.; Ribeiro, H.M.; Marto, J. Useful in Vitro Techniques to Evaluate the Mucoadhesive Properties of Hyaluronic Acid-Based Ocular Delivery Systems. *Pharmaceutics* **2018**, *10*, 110. [CrossRef] [PubMed]
117. Kojima, T.; Nagata, T.; Kudo, H.; Müller-Lierheim, W.G.K.; van Setten, G.-B.; Dogru, M.; Tsubota, K. The Effects of High Molecular Weight Hyaluronic Acid Eye Drop Application in Environmental Dry Eye Stress Model Mice. *Int. J. Mol. Sci.* **2020**, *21*, 3516. [CrossRef]
118. Manju, S.; Sreenivasan, K. Conjugation of Curcumin onto Hyaluronic Acid Enhances Its Aqueous Solubility and Stability. *J. Colloid Interface Sci.* **2011**, *359*, 318–325. [CrossRef] [PubMed]
119. Oechsner, M.; Keipert, S. Polyacrylic Acid/Polyvinylpyrrolidone Bipolymeric Systems. I. Rheological and Mucoadhesive Properties of Formulations Potentially Useful for the Treatment of Dry-Eye-Syndrome. *Eur. J. Pharm. Biopharm.* **1999**, *47*, 113–118. [CrossRef]
120. Chen, T.; Tseng, C.; Lin, C.-A.; Lin, H.; Venkatesan, P.; Lai, P. Effects of Eye Drops Containing Hyaluronic Acid-Nimesulide Conjugates in a Benzalkonium Chloride-Induced Experimental Dry Eye Rabbit Model. *Pharmaceutics* **2021**, *13*, 1366. [CrossRef]
121. Tredici, C.; Fasciani, R.; Villano, A.; Gambini, G.; Caporossi, A. Efficacy of Eye Drops Containing Crosslinked Hyaluronic Acid and CoQ10 in Restoring Ocular Health Exposed to Chlorinated Water. *Eur. J. Ophthalmol.* **2020**, *30*, 430–438. [CrossRef]
122. White, C.J.; Thomas, C.R.; Byrne, M.E. Bringing Comfort to the Masses: A Novel Evaluation of Comfort Agent Solution Properties. *Contact Lens Anterior Eye* **2014**, *37*, 81–91. [CrossRef]
123. Jansook, P.; Kulsirachote, P.; Asasutjarit, R.; Loftsson, T. Development of Celecoxib Eye Drop Solution and Microsuspension: A Comparative Investigation of Binary and Ternary Cyclodextrin Complexes. *Carbohydr. Polym.* **2019**, *225*, 115209. [CrossRef] [PubMed]
124. Salzillo, R.; Schiraldi, C.; Corsuto, L.; D'Agostino, A.; Filosa, R.; de Rosa, M.; la Gatta, A. Optimization of Hyaluronan-Based Eye Drop Formulations. *Carbohydr. Polym.* **2016**, *153*, 275–283. [CrossRef] [PubMed]
125. Chen, Q.; Yin, C.; Ma, J.; Tu, J.; Shen, Y. Preparation and Evaluation of Topically Applied Azithromycin Based on Sodium Hyaluronate in Treatment of Conjunctivitis. *Pharmaceutics* **2019**, *11*, 183. [CrossRef] [PubMed]
126. Sun, X.; Agate, S.; Salem, K.S.; Lucia, L.; Pal, L. Hydrogel-Based Sensor Networks: Compositions, Properties, and Applications—A Review. *ACS Appl. Bio Mater.* **2021**, *4*, 140–162. [CrossRef] [PubMed]
127. Li, J.; Mooney, D.J.; Paulson, J.A. Designing Hydrogels for Controlled Drug Delivery. *Nat. Rev. Mater.* **2016**, *1*, 16071. [CrossRef]
128. Trombino, S.; Servidio, C.; Curcio, F.; Cassano, R. Strategies for Hyaluronic Acid-Based Hydrogel Design in Drug Delivery. *Pharmaceutics* **2019**, *11*, 407. [CrossRef]
129. Awwad, S.; Abubakre, A.; Angkawinitwong, U.; Khaw, P.T.; Brocchini, S. In Situ Antibody-Loaded Hydrogel for Intravitreal Delivery. *Eur. J. Pharm. Sci.* **2019**, *137*, 104993. [CrossRef] [PubMed]
130. Egbu, R.; Brocchini, S.; Khaw, P.T.; Awwad, S. Antibody Loaded Collapsible Hyaluronic Acid Hydrogels for Intraocular Delivery. *Eur. J. Pharm. Biopharm.* **2018**, *124*, 95–103. [CrossRef]
131. Yu, Y.; Lau, L.C.M.; Lo, A.C.; Chau, Y. Injectable Chemically Crosslinked Hydrogel for the Controlled Release of Bevacizumab in Vitreous: A 6-Month In Vivo Study. *Transl. Vis. Sci. Technol.* **2015**, *4*, 5. [CrossRef]
132. Donati, S.; Caprani, S.M.; Airaghi, G.; Vinciguerra, R.; Bartalena, L.; Testa, F.; Mariotti, C.; Porta, G.; Simonelli, F.; Azzolini, C. Vitreous Substitutes: The Present and the Future. *BioMed Res. Int.* **2014**, *2014*, 351804. [CrossRef]
133. Alovisi, C.; Panico, C.; De Sanctis, U.; Eandi, C.M. Vitreous Substitutes: Old and New Materials in Vitreoretinal Surgery. *J. Ophthalmol.* **2017**, *2017*, 3172138. [CrossRef] [PubMed]
134. Wang, S.; Chi, J.; Jiang, Z.; Hu, H.; Yang, C.; Liu, W.; Han, B. A Self-Healing and Injectable Hydrogel Based on Water-Soluble Chitosan and Hyaluronic Acid for Vitreous Substitute. *Carbohydr. Polym.* **2021**, *256*, 117519. [CrossRef] [PubMed]
135. Thakur, S.S.; Shenoy, S.K.; Suk, J.S.; Hanes, J.S.; Rupenthal, I.D. Validation of Hyaluronic Acid-Agar-Based Hydrogels as Vitreous Humor Mimetics for in Vitro Drug and Particle Migration Evaluations. *Eur. J. Pharm. Biopharm.* **2020**, *148*, 118–125. [CrossRef] [PubMed]
136. Schulz, A.; Rickmann, A.; Wahl, S.; Germann, A.; Stanzel, B.V.; Januschowski, K.; Szurman, P. Alginate-and Hyaluronic Acid–Based Hydrogels as Victreous Substitutes: An in Vitro Evaluation. *Transl. Vis. Sci. Technol.* **2020**, *9*, 34. [CrossRef] [PubMed]

137. Kim, D.J.; Jung, M.Y.; Pak, H.J.; Park, J.H.; Kim, M.; Chuck, R.S.; Park, C.Y. Development of a Novel Hyaluronic Acid Membrane for the Treatment of Ocular Surface Diseases. *Sci. Rep.* **2021**, *11*, 2351. [CrossRef]
138. Bao, Z.; Yu, A.; Shi, H.; Hu, Y.; Jin, B.; Lin, D.; Dai, M.; Lei, L.; Li, X.; Wang, Y. Glycol Chitosan/Oxidized Hyaluronic Acid Hydrogel Film for Topical Ocular Delivery of Dexamethasone and Levofloxacin. *Int. J. Biol. Macromol.* **2021**, *167*, 659–666. [CrossRef]
139. Díaz-Tomé, V.; Luaces-Rodríguez, A.; Silva-Rodríguez, J.; Blanco-Dorado, S.; García-Quintanilla, L.; Llovo-Taboada, J.; Blanco-Méndez, J.; García-Otero, X.; Varela-Fernández, R.; Herranz, M.; et al. Ophthalmic Econazole Hydrogels for the Treatment of Fungal Keratitis. *J. Pharm. Sci.* **2018**, *107*, 1342–1351. [CrossRef]
140. Korogiannaki, M.; Zhang, J.; Sheardown, H. Surface Modification of Model Hydrogel Contact Lenses with Hyaluronic Acid via Thiol-Ene "Click" Chemistry for Enhancing Surface Characteristics. *J. Biomater. Appl.* **2017**, *32*, 446–462. [CrossRef]
141. Luensmann, D.; Jones, L. Protein Deposition on Contact Lenses: The Past, the Present, and the Future. *Contact Lens Anterior Eye* **2012**, *35*, 53–64. [CrossRef]
142. Xu, J.; Xue, Y.; Hu, G.; Lin, T.; Gou, J.; Yin, T.; He, H.; Zhang, Y.; Tang, X. A Comprehensive Review on Contact Lens for Ophthalmic Drug Delivery. *J. Control. Release* **2018**, *281*, 97–118. [CrossRef]
143. Musgrave, C.S.A.; Fang, F. Contact Lens Materials: A Materials Science Perspective. *Materials* **2019**, *12*, 261. [CrossRef] [PubMed]
144. Van Beek, M.; Jones, L.; Sheardown, H. Hyaluronic Acid Containing Hydrogels for the Reduction of Protein Adsorption. *Biomaterials* **2008**, *29*, 780–789. [CrossRef] [PubMed]
145. Williams, L.; Stapleton, F.; Carnt, N. Microbiology, Lens Care and Maintenance. In *Contact Lenses*; Phillips, A.J., Speedwell, L., Hough, T., Eds.; Elsevier: Amsterdam, The Netherlands, 2019; Volume 16, pp. 65–96. [CrossRef]
146. Weeks, A.; Boone, A.; Luensmann, D.; Jones, L.; Sheardown, H. The Effects of Hyaluronic Acid Incorporated as a Wetting Agent on Lysozyme Denaturation in Model Contact Lens Materials. *J. Biomater. Appl.* **2013**, *28*, 323–333. [CrossRef]
147. Boone, A.; Heynen, M.; Joyce, E.; Varikooty, J.; Jones, L. Ex Vivo Protein Deposition on Bi-Weekly Silicone Hydrogel Contact Lenses. *Optom. Vis. Sci.* **2009**, *86*, 1241–1249. [CrossRef] [PubMed]
148. Yamasaki, K.; Drolle, E.; Nakagawa, H.; Hisamura, R.; Ngo, W.; Jones, L. Impact of a Low Molecular Weight Hyaluronic Acid Derivative on Contact Lens Wettability. *Contact Lens Anterior Eye* **2021**, *44*, 101334. [CrossRef] [PubMed]
149. Yuan, Y.; Lee, T.R. Contact Angle and Wetting Properties. In *Surface Science Techniques*; Bracco, G., Holst, B., Eds.; Springer: Berlin/Heidelberg, Germany, 2013; Volume 51, pp. 3–34. [CrossRef]
150. Ali, M.; Byrne, M.E. Controlled Release of High Molecular Weight Hyaluronic Acid from Molecularly Imprinted Hydrogel Contact Lenses. *Pharm. Res.* **2009**, *26*, 714–726. [CrossRef] [PubMed]
151. Maulvi, F.A.; Shaikh, A.A.; Lakdawala, D.H.; Desai, A.R.; Pandya, M.M.; Singhania, S.S.; Vaidya, R.J.; Ranch, K.M.; Vyas, B.A.; Shah, D.O. Design and Optimization of a Novel Implantation Technology in Contact Lenses for the Treatment of Dry Eye Syndrome: In Vitro and in Vivo Evaluation. *Acta Biomater.* **2017**, *53*, 211–221. [CrossRef]
152. Jiang, S.; Franco, Y.L.; Zhou, Y.; Chen, J. Nanotechnology in Retinal Drug Delivery. *Int. J. Ophthalmol.* **2018**, *11*, 1038–1044. [CrossRef]
153. Gorantla, S.; Rapalli, V.K.; Waghule, T.; Singh, P.P.; Dubey, S.K.; Saha, R.N.; Singhvi, G. Nanocarriers for Ocular Drug Delivery: Current Status and Translational Opportunity. *RSC Adv.* **2020**, *10*, 27835–27855. [CrossRef]
154. Pinto Reis, C.; Neufeld, R.J.; Ribeiro, A.J.; Veiga, F.; Nanoencapsulation, I. Methods for Preparation of Drug-Loaded Polymeric Nanoparticles. *Nanomed. Nanotechnol. Biol. Med.* **2006**, *2*, 8–21. [CrossRef]
155. Vauthier, C.; Bouchemal, K. Methods for the Preparation and Manufacture of Polymeric Nanoparticles. *Pharm. Res.* **2009**, *26*, 1025–1058. [CrossRef] [PubMed]
156. Matha, K.; Lollo, G.; Taurino, G.; Respaud, R.; Marigo, I.; Shariati, M.; Bussolati, O.; Vermeulen, A.; Remaut, K.; Benoit, J.P. Bioinspired Hyaluronic Acid and Polyarginine Nanoparticles for DACHPt Delivery. *Eur. J. Pharm. Biopharm.* **2020**, *150*, 1–13. [CrossRef] [PubMed]
157. Kalam, M.A. Development of Chitosan Nanoparticles Coated with Hyaluronic Acid for Topical Ocular Delivery of Dexamethasone. *Int. J. Biol. Macromol.* **2016**, *89*, 127–136. [CrossRef]
158. Grimaudo, M.A.; Concheiro, A.; Alvarez-Lorenzo, C. Crosslinked Hyaluronan Electrospun Nanofibers for Ferulic Acid Ocular Delivery. *Pharmaceutics* **2020**, *12*, 274. [CrossRef] [PubMed]
159. Huang, D.; Chen, Y.S.; Rupenthal, I.D. Hyaluronic Acid Coated Albumin Nanoparticles for Targeted Peptide Delivery to the Retina. *Mol. Pharm.* **2017**, *14*, 533–545. [CrossRef]
160. Liu, D.; Lian, Y.; Fang, Q.; Liu, L.; Zhang, J.; Li, J. Hyaluronic-Acid-Modified Lipid-Polymer Hybrid Nanoparticles as an Efficient Ocular Delivery Platform for Moxifloxacin Hydrochloride. *Int. J. Biol. Macromol.* **2018**, *116*, 1026–1036. [CrossRef] [PubMed]
161. Amato, G.; Grimaudo, M.A.; Alvarez-Lorenzo, C.; Concheiro, A.; Carbone, C.; Bonaccorso, A.; Puglisi, G.; Musumeci, T. Hyaluronan/Poly-L-Lysine/Berberine Nanogels for Impaired Wound Healing. *Pharmaceutics* **2020**, *13*, 34. [CrossRef]
162. Huang, H.-Y.; Wang, M.-C.; Chen, Z.-Y.; Chiu, W.-Y.; Chen, K.-H.; Lin, I.-C.; Yang, W.-C.V.; Wu, C.-C.; Tseng, C.-L. Gelatin-Epigallocatechin Gallate Nanoparticles with Hyaluronic Acid Decoration as Eye Drops Can Treat Rabbit Dry-Eye Syndrome Effectively via Inflammatory Relief. *Int. J. Nanomed.* **2018**, *13*, 7251–7273. [CrossRef]
163. Rubenicia, A.M.L.; Cubillan, L.D.P.; Sicam, V.A.D.P.; Macabeo, A.P.G.; Villaflores, O.B.; Castillo, A.L. Intraocular Pressure Reduction Effect of 0.005% Latanoprost Eye Drops in a Hyaluronic Acid-Chitosan Nanoparticle Drug Delivery System in Albino Rabbits. *Transl. Vis. Sci. Technol.* **2021**, *10*, 2. [CrossRef]

164. Bongiovì, F.; Fiorica, C.; Palumbo, F.S.; di Prima, G.; Giammona, G.; Pitarresi, G. Imatinib-Loaded Micelles of Hyaluronic Acid Derivatives for Potential Treatment of Neovascular Ocular Diseases. *Mol. Pharm.* **2018**, *15*, 5031–5045. [CrossRef]
165. Apaolaza, P.S.; Busch, M.; Asin-Prieto, E.; Peynshaert, K.; Rathod, R.; Remaut, K.; Dünker, N.; Göpferich, A. Hyaluronic Acid Coating of Gold Nanoparticles for Intraocular Drug Delivery: Evaluation of the Surface Properties and Effect on Their Distribution. *Exp. Eye Res.* **2020**, *198*, 14–4835. [CrossRef] [PubMed]
166. Radwan, S.E.S.; El-Kamel, A.; Zaki, E.I.; Burgalassi, S.; Zucchetti, E.; El-Moslemany, R.M. Hyaluronic-Coated Albumin Nanoparticles for the Non-Invasive Delivery of Apatinib in Diabetic Retinopathy. *Int. J. Nanomed.* **2021**, *16*, 4481–4494. [CrossRef] [PubMed]
167. Osorno, L.L.; Maldonado, D.E.; Whitener, R.J.; Brandley, A.N.; Yiantsos, A.; Medina, J.D.R.; Byrne, M.E. Amphiphilic PLGA-PEG-PLGA Triblock Copolymer Nanogels Varying in Gelation Temperature and Modulus for the Extended and Controlled Release of Hyaluronic Acid. *J. Appl. Polym. Sci.* **2019**, *48678*, 48678. [CrossRef]
168. Devoldere, J.; Wels, M.; Peynshaert, K.; Dewitte, H.; de Smedt, S.C.; Remaut, K. The Obstacle Course to the Inner Retina: Hyaluronic Acid-Coated Lipoplexes Cross the Vitreous but Fail to Overcome the Inner Limiting Membrane. *Eur. J. Pharm. Biopharm.* **2019**, *141*, 161–171. [CrossRef]
169. Moustafa, M.A.; Elnaggar, Y.S.R.; El-Refaie, W.M.; Abdallah, O.Y. Hyalugel-Integrated Liposomes as a Novel Ocular Nanosized Delivery System of Fluconazole with Promising Prolonged Effect. *Int. J. Pharm.* **2017**, *534*, 14–24. [CrossRef] [PubMed]
170. Li, C.; Chen, R.; Xu, M.; Qiao, J.; Yan, L.; Guo, X.D. Hyaluronic Acid Modified MPEG-b-PAE Block Copolymer Aqueous Micelles for Efficient Ophthalmic Drug Delivery of Hydrophobic Genistein. *Drug Deliv.* **2018**, *25*, 1258–1265. [CrossRef]
171. Gomes, J.A.P.; Amankwah, R.; Powell-Richards, A. Sodium Hyaluronate (Hyaluronic Acid) Promotes Migration of Human Corneal Epithelial Cells in Vitro. *Br. J. Ophthalmol.* **2004**, *88*, 821–825. [CrossRef]
172. De La Fuente, M.; Seijo, B.; Alonso, M.J. Novel Hyaluronic Acid-Chitosan Nanoparticles for Ocular Gene Therapy. *Investig. Ophthalmol. Vis. Sci.* **2008**, *49*, 2016–2024. [CrossRef]
173. Karpecki, P.M. HA: No Laughing Matter. Available online: https://www.reviewofoptometry.com/article/ha-no-laughing-matter (accessed on 25 June 2022).
174. Hynnekleiv, L.; Magno, M.; Vernhardsdottir, R.R.; Moschowits, E.; Tønseth, K.A.; Dartt, D.A.; Vehof, J.; Utheim, T.P. Hyaluronic Acid in the Treatment of Dry Eye Disease. *Acta Ophthalmol.* **2022**. [CrossRef]
175. Beck, R.; Stachs, O.; Koschmieder, A.; Mueller-Lierheim, W.G.K.; Peschel, S.; van Setten, G.B. Hyaluronic Acid as an Alternative to Autologous Human Serum Eye Drops: Initial Clinical Results with High-Molecular-Weight Hyaluronic Acid Eye Drops. *Case Rep. Ophthalmol.* **2019**, *10*, 244–255. [CrossRef]
176. Labetoulle, M.; Chiambaretta, F.; Shirlaw, A.; Leaback, R.; Baudouin, C. Osmoprotectants, Carboxymethylcellulose and Hyaluronic Acid Multi-Ingredient Eye Drop: A Randomised Controlled Trial in Moderate to Severe Dry Eye. *Eye* **2017**, *31*, 1409–1416. [CrossRef] [PubMed]
177. Carracedo, G.; Pastrana, C.; Serramito, M.; Rodriguez-Pomar, C. Evaluation of Tear Meniscus by Optical Coherence Tomography after Different Sodium Hyaluronate Eyedrops Instillation. *Acta Ophthalmol.* **2019**, *97*, 162–169. [CrossRef] [PubMed]
178. Pinto-Fraga, J.; López-De La Rosa, A.; Arauzo, F.B.; Rodríguez, R.U.; González-García, M.J. Efficacy and Safety of 0.2% Hyaluronic Acid in the Management of Dry Eye Disease. *Eye Contact Lens* **2017**, *43*, 57–63. [CrossRef] [PubMed]
179. López-De La Rosa, A.; Pinto-Fraga, J.; Blázquez Arauzo, F.; Rodríguez, R.U.; González-García, M.J. Safety and Efficacy of an Artificial Tear Containing 0.3% Hyaluronic Acid in the Management of Moderate-to-Severe Dry Eye Disease. *Eye Contact Lens* **2017**, *43*, 383–388. [CrossRef]
180. Clinical Evaluation of Visco-Assisted CyPass®Micro-Stent Implantation in Patients with Open Angle Glaucoma. Available online: https://clinicaltrials.gov/ct2/show/NCT02448875 (accessed on 22 June 2022).
181. Cazorla-Luna, R.; Martín-Illana, A.; Notario-Pérez, F.; Ruiz-Caro, R.; Veiga, M.D. Naturally Occurring Polyelectrolytes and Their Use for the Development of Complex-Based Mucoadhesive Drug Delivery Systems: An Overview. *Polymers* **2021**, *13*, 2241. [CrossRef]
182. Papagiannopoulos, A. Current Research on Polyelectrolyte Nanostructures: From Molecular Interactions to Biomedical Applications. *Macromol* **2021**, *1*, 155–172. [CrossRef]
183. Yadav, S.; Sharma, A.K.; Kumar, P. Nanoscale Self-Assembly for Therapeutic Delivery. *Front. Bioeng. Biotechnol.* **2020**, *8*, 127. [CrossRef]
184. Kulkarni, A.D.; Vanjari, Y.H.; Sancheti, K.H.; Patel, H.M.; Belgamwar, V.S.; Surana, S.J.; Pardeshi, C.V. Polyelectrolyte Complexes: Mechanisms, Critical Experimental Aspects, and Applications. *Artif. Cells Nanomed. Biotechnol.* **2016**, *44*, 1615–1625. [CrossRef]
185. van der Gucht, J.; Spruijt, E.; Lemmers, M.; Stuart, M.A.C. Polyelectrolyte Complexes: Bulk Phases and Colloidal Systems. *J. Colloid Interface Sci.* **2011**, *361*, 407–422. [CrossRef]
186. Shah, S.; Eyler, A.; Tabandeh, S.; Leon, L. Electrostatically Driven Self-Assembled Nanoparticles and Coatings. In *Nanoparticles for Biomedical Applications*; Chung, E.J., Rinaldi, L., Leon, C., Eds.; Elsevier: Amsterdam, The Netherlands, 2020; pp. 349–370. [CrossRef]
187. Ou, Z.; Muthukumar, M. Entropy and Enthalpy of Polyelectrolyte Complexation: Langevin Dynamics Simulations. *J. Chem. Phys.* **2006**, *124*, 154902. [CrossRef]
188. Lebovka, N.I. Aggregation of Charged Colloidal Particles. In *Polyelectrolyte Complexes in the Dispersed and Solid State I: Principles and Theory*; Muller, M., Ed.; Springer: Berlin/Heidelberg, Germany, 2013; pp. 57–97.

189. Tsuchida, E. Formation of Polyelectrolyte Complexes and Their Structures. *J. Macromol. Sci. Part A* **1994**, *31*, 1–15. [CrossRef]
190. Philipp, B.; Dautzenberg, H.; Linow, K.J.; Kötz, J.; Dawydoff, W. Polyelectrolyte Complexes—Recent Developments and Open Problems. *Prog. Polym. Sci.* **1989**, *14*, 91–172. [CrossRef]
191. Ankerfors, C. Polyelectrolyte Complexes: Preparation, Characterization, and Use for Control of Wet and Dry Adhesion between Surfaces. Ph.D. Thesis, KTH Royal Institute of Technology, Stockholm, Sweden, 2012.
192. Hartig, S.M.; Greene, R.R.; Dikov, M.M.; Prokop, A.; Davidson, J.M. Multifunctional Nanoparticulate Polyelectrolyte Complexes. *Pharm. Res.* **2007**, *24*, 2353–2369. [CrossRef]
193. Quiñones, J.P.; Peniche, H.; Peniche, C. Chitosan Based Self-Assembled Nanoparticles in Drug Delivery. *Polymers* **2018**, *10*, 235. [CrossRef]
194. van Le, H.; Dulong, V.; Picton, L.; le Cerf, D. Polyelectrolyte Complexes of Hyaluronic Acid and Diethylaminoethyl Dextran: Formation, Stability and Hydrophobicity. *Colloids Surf. A Physicochem. Eng. Asp.* **2021**, *629*, 127485. [CrossRef]
195. Hotze, E.M.; Phenrat, T.; Lowry, G.V. Nanoparticle Aggregation: Challenges to Understanding Transport and Reactivity in the Environment. *J. Environ. Qual.* **2010**, *39*, 1909–1924. [CrossRef]
196. Biorender. BioRender. Available online: https://biorender.com/ (accessed on 17 January 2022).
197. Ferreira, L.M.B.; dos Santos, A.M.; Boni, F.I.; dos Santos, K.C.; Robusti, L.M.G.; de Souza, M.P.C.; Ferreira, N.N.; Carvalho, S.G.; Cardoso, V.M.O.; Chorilli, M.; et al. Design of Chitosan-Based Particle Systems: A Review of the Physicochemical Foundations for Tailored Properties. *Carbohydr. Polym.* **2020**, *250*, 116968. [CrossRef]
198. Leite, E.R.; Ribeiro, C. Basic Principles: Thermodynamics and Colloidal Chemistry. In *Crystallization and Growth of Colloidal Nanocrystals*; Springer: New York, NY, USA, 2012; pp. 7–17. [CrossRef]
199. Ohshima, H. The Derjaguin—Landau—Verway—Overbeek (DLVO) Theory of Colloidal Stability. In *Electrical Phenomena at Interfaces and Bionterfaces—Fundamentals and Applications in Nano-, Bio-, and Environmental Sciences*; Ohshima, H., Ed.; John Wiley & Sons Ltd.: New Jersey, NJ, USA, 2012; pp. 27–34.
200. Mero, A.; Campisi, M. Hyaluronic Acid Bioconjugates for the Delivery of Bioactive Molecules. *Polymers* **2014**, *6*, 346–369. [CrossRef]
201. Liao, Y.H.; Jones, S.A.; Forbes, B.; Martin, G.P.; Brown, M.B. Hyaluronan: Pharmaceutical Characterization and Drug Delivery. *Drug Deliv. J. Deliv. Target. Ther. Agents* **2005**, *12*, 327–342. [CrossRef]
202. Meka, V.S.; Sing, M.K.G.; Pichika, M.R.; Nali, S.R.; Kolapalli, V.R.M.; Kesharwani, P. A Comprehensive Review on Polyelectrolyte Complexes. *Drug Discov. Today* **2017**, *22*, 1697–1706. [CrossRef]
203. Grimaudo, M.A.; Amato, G.; Carbone, C.; Diaz-Rodriguez, P.; Musumeci, T.; Concheiro, A.; Alvarez-Lorenzo, C.; Puglisi, G. Micelle-Nanogel Platform for Ferulic Acid Ocular Delivery. *Int. J. Pharm.* **2020**, *576*, 118986. [CrossRef]
204. Kale, N.R.; Dutta, D.; Carstens, W.; Mallik, S.; Quadir, M. Functional Applications of Polyarginine-Hyaluronic Acid-Based Electrostatic Complexes. *Bioelectricity* **2020**, *2*, 158–166. [CrossRef]
205. Malay, Ö.; Yal, D.Ï.; Bat, A.Ï.; Bayraktar, O. Characterisation of Silk Fibroin/Hyaluronic Acid Polyelectrolyte Complex (PEC) Films. *J. Therm. Anal. Calorim.* **2008**, *94*, 749–755. [CrossRef]
206. Deb Nath, S.; Abueva, C.; Kim, B.; Taek, B. Chitosan—Hyaluronic Acid Polyelectrolyte Complex Scaffold Crosslinked with Genipin for Immobilization and Controlled Release of BMP-2. *Carbohydr. Polym.* **2015**, *115*, 160–169. [CrossRef]
207. Wu, D.; Delair, T. Stabilization of Chitosan/Hyaluronan Colloidal Polyelectrolyte Complexes in Physiological Conditions. *Carbohydr. Polym.* **2015**, *119*, 149–158. [CrossRef]
208. Chaharband, F.; Daftarian, N.; Kanavi, M.R.; Varshochian, R.; Hajiramezanali, M.; Norouzi, P.; Arefian, E.; Atyabi, F.; Dinarvand, R. Trimethyl Chitosan-Hyaluronic Acid Nano-Polyplexes for Intravitreal VEGFR-2 SiRNA Delivery: Formulation and in Vivo Efficacy Evaluation. *Nanomed. Nanotechnol. Biol. Med.* **2020**, *26*, 102181. [CrossRef]
209. Silva, B.; Marto, J.; Braz, B.S.; Delgado, E.; Almeida, A.J.; Gonçalves, L. New Nanoparticles for Topical Ocular Delivery of Erythropoietin. *Int. J. Pharm.* **2020**, *576*, 119020. [CrossRef]
210. Carton, F.; Chevalier, Y.; Nicoletti, L.; Tarnowska, M.; Stella, B.; Arpicco, S.; Malatesta, M.; Jordheim, L.P.; Briançon, S.; Lollo, G. Rationally Designed Hyaluronic Acid-Based Nano-Complexes for Pentamidine Delivery. *Int. J. Pharm.* **2019**, *568*, 118526. [CrossRef]
211. Battistini, F.D.; Tártara, L.I.; Boiero, C.; Guzmán, M.L.; Luciani-Giaccobbe, L.C.; Palma, S.D.; Allemandi, D.A.; Manzo, R.H.; Olivera, M.E. The Role of Hyaluronan as a Drug Carrier to Enhance the Bioavailability of Extended Release Ophthalmic Formulations. Hyaluronan-Timolol Ionic Complexes as a Model Case. *Eur. J. Pharm. Sci.* **2017**, *105*, 188–194. [CrossRef]
212. Siyawamwaya, M.; Choonara, Y.E.; Bijukumar, D.; Kumar, P.; du Toit, L.C.; Pillay, V. A Review: Overview of Novel Polyelectrolyte Complexes as Prospective Drug Bioavailability Enhancers. *Int. J. Polym. Mater. Polym. Biomater.* **2015**, *64*, 955–968. [CrossRef]
213. Wu, D.; Zhu, L.; Li, Y.; Zhang, X.; Xu, S.; Yang, G.; Delair, T. Chitosan-Based Colloidal Polyelectrolyte Complexes for Drug Delivery: A Review. *Carbohydr. Polym.* **2020**, *238*, 116126. [CrossRef]
214. Dreffs, A.; Henderson, D.; Dmitriev, A.V.; Antonetti, D.A.; Linsenmeier, R.A. Retinal PH and Acid Regulation during Metabolic Acidosis. *Curr. Eye Res.* **2018**, *43*, 902. [CrossRef]
215. Rawas-Qalaji, M.; Williams, C.A. Advances in Ocular Drug Delivery. *Curr. Eye Res.* **2012**, *37*, 345–356. [CrossRef]
216. Kaur, J.; Kaur, G. Optimization of PH Conditions and Characterization of Polyelectrolyte Complexes between Gellan Gum and Cationic Guar Gum. *Polym. Adv. Technol.* **2018**, *29*, 3035–3048. [CrossRef]

217. Kayitmazer, A.B.; Koksal, A.F.; Kilic Iyilik, E. Complex Coacervation of Hyaluronic Acid and Chitosan: Effects of PH, Ionic Strength, Charge Density, Chain Length and the Charge Ratio. *Soft Matter* **2015**, *11*, 8605–8612. [CrossRef]
218. Pan, W.; Yin, D.-X.; Jing, H.-R.; Chang, H.-J.; Wen, H.; Liang, D.-H. Core-Corona Structure Formed by Hyaluronic Acid and Poly(L-Lysine) via Kinetic Path. *Chin. J. Polym. Sci.* **2019**, *37*, 36–42. [CrossRef]
219. Sukhanova, A.; Bozrova, S.; Sokolov, P.; Berestovoy, M.; Karaulov, A.; Nabiev, I. Dependence of Nanoparticle Toxicity on Their Physical and Chemical Properties. *Nanoscale Res. Lett.* **2018**, *13*, 44. [CrossRef]
220. Dautzenberg, H.; Karibyants, N. Polyelectrolyte Complex Formation in Highly Aggregating Systems. Effect of Salt: Response to Subsequent Addition of NaCl. *Macromol. Chem. Phys.* **1999**, *200*, 118–125. [CrossRef]
221. Zhang, Y.; Yildirim, E.; Antila, H.S.; Valenzuela, L.D.; Sammalkorpi, M.; Lutkenhaus, J.L. The Influence of Ionic Strength and Mixing Ratio on the Colloidal Stability of PDAC/PSS Polyelectrolyte Complexes. *Soft Matter* **2015**, *11*, 7392–7401. [CrossRef]
222. Golchoobi, A.; Khosravi, A.; Modarress, H.; Ahmadzadeh, A. Effect of Charge, Size and Temperature on Stability of Charged Colloidal Nano Particles. *Chin. J. Chem. Phys.* **2012**, *25*, 617–624. [CrossRef]
223. de Vasconcelos, C.L.; Pereira, M.R.; Fonseca, J.L.C. Polyelectrolytes in Solution and the Stabilization of Colloids. *J. Dispers. Sci. Technol.* **2005**, *26*, 59–70. [CrossRef]
224. Koetz, J.; Kosmella, S. Semi Diluted Polyanion-Polycation Systems (Turbid Polyelectrolyte Complexes). In *Polyelectrolytes and Nanoparticles*; Barth, H.G., Pasch, H., Eds.; Springer: Berlin/Heidelberg, Germany, 2007; pp. 41–43.
225. Mitsubayashi, K.; Ogasawara, K.; Yokoyama, K.; Takeuchi, T.; Tsuru, T.; Karube, I. Measurement of Tear Electrolyte Concentration and Turnover Rate Using a Flexible Conductimetric Sensor. *Technol. Health Care* **1995**, *3*, 117–121. [CrossRef] [PubMed]
226. van Haeringen, N.J. Clinical Biochemistry of Tears. *Surv. Ophthalmol.* **1981**, *26*, 84–96. [CrossRef]
227. Stahl, U.; Willcox, M.; Stapleton, F. Osmolality and Tear Film Dynamics. *Clin. Exp. Optom.* **2012**, *95*, 3–11. [CrossRef]
228. Li, Q.; Li, X.; Zhao, C. Strategies to Obtain Encapsulation and Controlled Release of Small Hydrophilic Molecules. *Front. Bioeng. Biotechnol.* **2020**, *8*, 437. [CrossRef]
229. Henein, C.; Awwad, S.; Ibeanu, N.; Vlatakis, S.; Brocchini, S.; Khaw, P.T.; Bouremel, Y. Hydrodynamics of Intravitreal Injections into Liquid Vitreous Substitutes. *Pharmaceutics* **2019**, *11*, 371. [CrossRef]
230. Azhdam, A.M.; Goldberg, R.A.; Ugradar, S. In Vivo Measurement of the Human Vitreous Chamber Volume Using Computed Tomography Imaging of 100 Eyes. *Transl. Vis. Sci. Technol.* **2020**, *9*, 2. [CrossRef]
231. Schatz, C.; Domard, A.; Viton, C.; Pichot, C. Versatile and Efficient Formation of Colloids of Biopolymer-Based Polyelectrolyte Complexes. *Biomacromolecules* **2004**, *5*, 1882–1892. [CrossRef]

APPENDIX 2.2: RESEARCH ARTICLE

European Journal of Pharmaceutics and Biopharmaceutics 192 (2023) 62–78

Contents lists available at ScienceDirect

European Journal of Pharmaceutics and Biopharmaceutics

journal homepage: www.elsevier.com/locate/ejpb

Research paper

NAD+-associated-hyaluronic acid and poly(L-lysine) polyelectrolyte complexes: An evaluation of their potential for ocular drug delivery

Saoirse Casey-Power [a,*], Camila Vardar [b], Richie Ryan [a], Gautam Behl [c], Peter McLoughlin [a], Mark E. Byrne [b,d], Laurence Fitzhenry [a]

[a] Ocular Therapeutics Research Group, Pharmaceutical and Molecular Biotechnology Research Centre, Waterford Campus, South East Technological University, Waterford X91 K0EK, Ireland
[b] Department of Biomedical Engineering, Rowan-Virtua School of Translational Biomedical Engineering & Sciences, Rowan University, 201 Mullica Hill Road, Glassboro, NJ 08028, USA
[c] EirGen Pharma, UNIT 64/64A, Westside Business Park, Old Kilmeaden Road, Co. Waterford X91 YV67, Ireland
[d] Department of Chemical Engineering, Rowan University, 201 Mullica Hill Road, Glassboro, NJ 08028, USA

ARTICLE INFO

Keywords:
Nanoparticles
Polyelectrolyte complexes
Polyelectrolyte complexation
Ocular drug delivery
NAD+
Hyaluronic acid
Physicochemical characterisation
Microfluidic release
Ex vivo permeation

ABSTRACT

This study details the formation and characterisation of a novel nicotinamide adenine dinucleotide (NAD+)-associated polymeric nanoparticle system. The development of a polyelectrolyte complex (PEC) composed of two natural polyelectrolytes, hyaluronic acid and poly(L-lysine), and an evaluation of its suitability for NAD+ ocular delivery, primarily based on its physicochemical properties and *in vitro* release profile under physiological ocular flow rates, were of key focus. Following optimisation of formulation method conditions such as complexation pH, mode of addition, and charge ratio, the PEC was successfully formulated under mild formulation conditions via polyelectrolyte complexation. With a size of 235.1 ± 19.0 nm, a PDI value of 0.214 ± 0.140, and a zeta potential value of – 38.0 ± 1.1 mV, the chosen PEC, loaded with 430 μg of NAD+ per mg of PEC, exhibited non-Fickian, sustained release at physiological flowrates of 10.9 ± 0.2 mg of NAD+ over 14 h. PECs containing up to 200 μM of NAD+ did not induce any significant cytotoxic effects on an immortalised human corneal epithelial cell line. Using fluorescent labeling, the NAD+-associated PECs demonstrated retention within the corneal epithelium layer of a porcine model up to 6 h post incubation under physiological conditions. A study of the physicochemical behaviour of the PECs, in terms of size, zeta potential and NAD+ complexation in response to environmental stimuli,highlighted the dynamic nature of the PEC matrix and its dependence on both pH and ionic condition. Considering the successful formation of reproducible NAD+-associated PECs with suitable characteristics for ocular drug delivery via an inexpensive formulation method, they provide a promising platform for NAD+ ocular delivery with a strong potential to improve ocular health.

1. Introduction

The complexity and restrictive nature of the human eye, primarily attributed to the presence of numerous anatomical and physiological barriers, poses a significant challenge for effective ocular drug delivery [1]. Nanomaterial-based formulations have gained significant traction in ophthalmic research in recent years as they provide a platform for overcoming such barriers due to their submicron size and tuneable functionality. In comparison to free therapeutic molecules, nanoparticles typically exhibit a more sustained therapeutic release profile, a

Abbreviations: %AE, association efficiency; CD44, cluster determinant 44; DAPI, 2-(4-amidinophenyl)-1H -indole-6-carboxamidine; DLS, dynamic light scattering; EDX, energy dispersive x-ray spectroscopy; FITC, fluorescein isothiocyanate; FT-IR, Fourier transform-infrared spectroscopy; HA, hyaluronic acid; HCl, hydrochloric acid; HMWHA, hyaluronic acid sodium salt (MW: 200 – 500 kDa); HPLC, high-performance liquid chromatography; KBr, potassium bromide; KCl, potassium chloride; LMWHA, hyaluronic acid sodium salt (MW: 80 kDa to 100 kDa); MCR, molar charge ratio; MWCO, molecular weight cut off; NaCl, sodium chloride; NAD+, nicotinamide adenine dinucleotide; NaOH, sodium hydroxide; PBS, phosphate buffer saline; PDI, polydispersity index; PECs, polyelectrolyte complexes; PLL, ε-poly (L-lysine); SD, standard deviation; SEM, scanning electron microscopy; ZP, zeta potential.

* Corresponding author.
E-mail addresses: saoirse.casey-power@postgrad.wit.ie (S. Casey-Power), vardar89@rowan.edu (C. Vardar), richie.j.ryan@setu.ie (R. Ryan), gautam.behl@eirgen.com (G. Behl), peter.mcloughlin@setu.ie (P. McLoughlin), byrnem@rowan.edu (M.E. Byrne), laurence.fitzhenry@setu.ie (L. Fitzhenry).

https://doi.org/10.1016/j.ejpb.2023.10.004
Received 18 July 2023; Received in revised form 20 September 2023; Accepted 2 October 2023
Available online 4 October 2023
0939-6411/© 2023 The Authors. Published by Elsevier B.V. This is an open access article under the CC BY license (http://creativecommons.org/licenses/by/4.0/).

reduced risk of adverse effects, enhanced therapeutic diffusivity and permeation through ocular tissues, as well as targeted interaction with biological barriers via surface modification [2,3]. Nanoparticles synthesised from biomaterials are particularly advantageous as they exhibit both faster enzymatic degradation and high ocular clearance rates *in vivo* and decreased immunogenicity and toxicity in comparison to their more synthetic counterparts [4,5].

This research presents the development of a nanomaterial formulation formed via polyelectrolyte complexation of two polyelectrolytes: hyaluronic acid (HA) and ε-poly(L-lysine) (PLL). HA, an anionic glycosaminoglycan present in abundance in the vitreous humour and extracellular matrices, is an ideal ophthalmic excipient due to its inherent biocompatibility, cluster determinant 44 (CD44) receptor-mediated endocytosis, its ability to stimulate corneal re-epithelialisation and cell proliferation during corneal wound healing, mucoadhesive capabilities and high water retention. An extensive summary of the application of HA as both an excipient and a therapeutic in laboratory and clinical ophthalmic research has been previously detailed by our group [6]. Due to the deprotonation of the carboxylic acid group, HA possesses a negative charge at physiological pH and can therefore complex with cationic polysaccharides such as chitosan [7–9] and diethylaminoethyl dextran [10], polypeptides such as poly(arginine) [11,12] and PLL [13] and cationic therapeutic molecules such as timolol maleate [14], colistin [15] and l-arginine [16], via electrostatic interaction. PLL is an inherently antimicrobial polyaminoacid that exhibits enhanced permeation capability of the negatively charged phospholipid bilayer of cellular membranes due to the presence of a cationic α-amine group in physiological environments [17–20]. PLL and its derivatives have also been frequently investigated in ocular gene therapy to induce condensation and improve the transduction efficiency of DNA via electrostatic interaction between the α-amine group and the anionic phosphate groups of the nucleotides [21,22].

The self-assembly of HA and PLL into polyelectrolyte complex coacervates in aqueous solution is driven by both supramolecular packing of the opposing electrostatically charged moieties (carboxylate anion of HA and α-amine group of PLL) and an increase in entropy via counterion displacement from the respective polyelectrolytes [23,24]. Aside from the favourable biological and chemical attributes of the polyelectrolyte constituents themselves, polyelectrolyte complexation is a green and cost-effective formulation method as polyelectrolyte complexes (PECs) are spontaneously formed by gentle agitation under ambient conditions, without the need for large volumes of organic solvents, elevated reaction temperatures and potentially cytotoxic chemical crosslinking agents [25,26]. However, the physicochemical attributes of the respective polyelectrolytes, and the selected extrinsic formulation parameters, play a fundamental role in the formation of the resulting PECs and therefore must be carefully controlled to ensure formation of the desired complex structure [27]. For example, the extent of electroneutralisation between the respective polyelectrolytes directly impacts the extent of PEC precipitation into either discreet colloidally stable particles or insoluble gelatinous aggregates. Therefore, extrinsic parameters, such as the pH and ionic strength of the formulation medium, that control residual charge stabilisation will also affect the physiochemical behaviour of the PEC system.

The primary aim of this work was to study, for the first time, the preparation of a HA and PLL-based PEC and to assess its potential utility as a nanocarrier for nicotinamide adenine dinucleotide (NAD+) for ocular delivery. A potent biomarker of the ageing process in ocular tissues is the decline in intracellular NAD+ concentration. An imbalance in the activity of NAD+ synthesising and NAD+ consuming enzymes directly correlates to an increase in mitochondrial dysfunction, impaired cellular metabolism and respiration, excessive inflammatory cytokine function and decreased cellular longevity [28,29]. Such detrimental processes characterise the early onset pathogenesis of numerous age-related ocular diseases. Replenishment of intracellular NAD+ concentration pools via administration of both NAD+ or NAD+ precursors has shown promising efficacy against the deleterious effects of several neurodegenerative ocular diseases such as glaucoma and age-related macular degeneration [30–35]. This work could provide a starting point for the development of a biocompatible, NAD+-laden ocular drug delivery system. The PECs possessing favourable physicochemical attributes would then be subjected to further *in vitro* and *ex vivo* safety and efficacy studies.

2. Materials and methods

2.1. Materials

Hyaluronic acid sodium salt (MW: 200–500 kDa) (HMWHA), hyaluronic acid sodium salt (MW: 80-100 kDa, purity > 91%) (LMWHA), ε poly (L-lysine) HCl (MW: 3.5–4.5 kDa, purity > 98%) (PLL), and β -nicotinamide adenine dinucleotide (MW: 663.43 g/mol, purity ≥ 95%) (NAD+), were purchased from Carbosynth Ltd. (Berkshire, England). Additional quantities of both hyaluronic acid sodium salt (80 kDa to 100 kDa) and NAD+ (MW: 663.43 g/mol, purity ≥ 95%) were later purchased from Cymit Quimica (Barcelona) and VWR International (Dublin, Ireland), respectively. Spectra/Por Biotech dialysis tubing (molecular weight cut off (MWCO): 1000 kDa, 31 mm width) was purchased from Fischer Scientific Ireland (Dublin, Ireland). SLS select 50 mL sterile polypropylene centrifuge tubes and Vivaspin® Turbo 15 centrifugal filters (10 kDa MWCO) were purchased from Analab (Antrim, Northern Ireland). Disposable, 12 mm square, polystyrene cuvettes (DTS0012) and folded capillary zeta cells (DTS1070) were purchased from Particular Sciences Ltd. (Dublin, Ireland).

2.1.1. Reagents and chemicals used

High-performance liquid chromatography (HPLC) grade methanol (purity ≥ 99.9%) and potassium dihydrogen phosphate (purity > 99%) were purchased from Fischer Scientific Ireland (Dublin, Ireland) and Sigma Aldrich Ireland Ltd. (Wicklow, Ireland), respectively. D-(+)-trehalose dihydrate (purity ≥ 99%), sodium hydroxide (NaOH) (purity ≥ 97%) and hydrochloric acid (HCl) (ACS reagent grade) were also purchased from Sigma Aldrich Ireland Ltd. (Wicklow, Ireland). Phosphate buffer saline (PBS) was prepared using the following reagents: laboratory-grade sodium chloride (NaCl) (purity ≥ 99.5%), molecular biology grade potassium chloride (KCl) (purity ≥ 99.0%), and disodium hydrogen phosphate dodecahydrate (Ph Eur, BP, JP, USP) (Na_2HPO_4) (purity ≥ 99.0%), were purchased from Sigma Aldrich Ireland Ltd. (Wicklow, Ireland). IM-ocular epithelial cell medium was purchased from Innoprot (Bizkaia, Spain). Tyrpsin-EDTA (0.05%), phenol red was purchased from Thermo Fisher Scientific (Dublin, Ireland).Ultra-pure water was deionised and filtered in-house using an Evoqua ® Water Technologies purification system.

2.2. Potentiometric titration for determination of optimal complexation pH

The optimal pH for complexation was calculated based on a method adapted from the study conducted by Kaur et al. [36]. 0.1% (w/v) stock solutions of HA, PLL and NAD+ were prepared in 100 mL volumetric flasks, in duplicate. The initial pH of 20 mL aliquots of 0.1% (w/v) HA and NAD+ was adjusted to a pH of 2 whereas the initial pH of 20 mL aliquots of 0.1% (w/v) PLL was adjusted to a pH of 10 (2 pH units either above or below the pKa of the functional group of interest). Under continuous stirring at 200 rpm, the PEC reagent solutions were titrated against 20 μL aliquots of both 0.1 M NaOH and 0.1 M HCl, respectively. Changes in pH were recorded after the addition of each aliquot to the solutions. First derivative pH titration curves were plotted to determine the pKa of HA, PLL and NAD+. The pH at which 100% ionisation of the respective PEC reagents is achieved was identified using a pH-dependent fractional composition diagram. The ionised fractions of both HA, PLL and NAD+ were calculated using Eq. (1):

$$\frac{[H^+]}{[H^+] + Ka/Kb} \text{ (Protonated)} \qquad \frac{[Ka/Kb]}{[H^+] + Ka/Kb} \text{ (Deprotonated)} \tag{1}$$

where, $[H^+]$ is the hydronium ion concentration at each respective pH value and Ka/Kb is the acid or base dissociation constant of HA, PLL and NAD+ calculated using the antilog of the respective pKa and pKb values of HA, PLL and NAD +.

2.3. Preparation of blank and NAD+-associated polyelectrolyte complexes (PECs)

Solutions of HMWHA, LMWHA, and PLL were prepared in 50 mL polypropylene centrifuge tubes at final concentrations of 2 and 5% (w/v) in ultrapure water. The pH of each solution was adjusted to pH 5.5 using 0.1 M NaOH. Under continuous stirring at 200 rpm, the polyelectrolyte in default was added to the polyelectrolyte in excess via one-shot addition or dropwise addition at a constant flow rate. The pH of the resulting complexes was recorded and adjusted to pH 5.5, if necessary. Complexation was continued overnight in an ES-20 orbital shaker-incubator (Grant Instruments, Cambridge, United Kingdom), maintained at 200 rpm at a temperature of 25 °C, yielding PECs with total concentrations of 2 and 5% (w/v) and molar charge ratios of between 0.5 and 2. NAD+-associated PECs were prepared in a similar fashion to blank PECs. NAD+ loading concentrations of 50 and 100% (w/w), relative to the combined mass of both HA and PLL in each formulation, were selected for investigation. PLL and NAD+ solutions were pre-mixed prior to addition to the HA solutions. NAD+-associated PECs were prepared with total concentrations of 2% (w/v) and a molar charge ratio of 2.

Following complexation, the PECs were centrifuged at 4000 g for 50 min at 4 °C in Vivaspin® Turbo 15 centrifugal filter tubes in a SIGMA 3-18KS refrigerated bench-top centrifuge (Focus Scientific, Co. Meath, Ireland) to both isolate the sub-micron sized PECs and remove free NAD+ from the formulation. For cryoprotection, 1 mL of 1% (w/v) trehalose dihydrate solution was added for every 10 mL of the PEC and free NAD+ fractions isolated during centrifugation before freezing at −20 °C for 4 h. The resulting frozen aliquots were then lyophilised for 48 h using a Freezone 2.5 Litre Benchtop Freeze Drier (Labconco, Kansas City, MO, USA).

Fluorescein isothiocyanate (FITC) PECs (FITC-PECs) were prepared using a method adapted from Ilka et al. [37]. Briefly, 2 mg of FITC was dissolved in ultrapure water at pH 5.5 and added dropwise to PEC formulations during complexation. The resulting PECs were kept overnight protected from light before centrifugation as before to remove free FITC.

2.4. Physiochemical characterisation of PECs

2.4.1. Fourier-transform infrared spectroscopy (FT-IR)

FT-IR analysis was conducted using a Varian 660-IR & 610-IR Excalibur Series Biorad Elementec IR spectrometer (Agilent Technologies, California, USA). The resulting spectra were generated between the frequencies of 4000 cm^{-1} and 600 cm^{-1}, at a resolution of 2 cm^{-1} with a total of 32 overlay scans. Approximately 10 mg of each starting reagent or complex lyophilisate was weighed and subsequently ground with potassium bromide (KBr) in a 1:5 ratio. Sample discs were prepared by pressing the resulting powder using an Atlas™ Power 25 T pressure hydraulic press (Specac Ltd., Orpington, United Kingdom). A background spectrum was also obtained using a blank KBr disc.

2.4.2. Dynamic light scattering

Dynamic light scattering (DLS) analysis was conducted using a Malvern Zetasizer Ultra-Red analyser (Malvern Panalytical, Malvern, United Kingdom). Particle size distributions were determined via measurement of the dynamic light scattering of PEC samples diluted with Milli-Q ultrapure water. A 1 mL aliquot of each PEC sample was pipetted into a 12 mm square, disposable, polystyrene cuvette (DTS0012). Following analysis at 25 °C at a backscattering angle of 173°, the 1 mL aliquots were placed into a U-shaped folded capillary zeta cell (DTS1070) with gold-plated beryllium/copper electrodes for zeta measurements. An equilibration time of 120 s for both particle size and zeta measurement was selected, with a set temperature of 25 °C. Analyses were conducted in triplicate where appropriate.

2.4.3. Scanning electron microscopy (SEM)

PEC samples were mounted onto SEM stubs using conductive tape and sputter-coated with a thin layer of gold for approximately 2 hhours before SEM analysis using a TM4000 Plus II benchtop scanning electron microscope (Hitachi High-Tech Corporation, United Kingdom). SEM images of each centrifugation fraction were taken at various magnifications at an accelerating voltage of 15 kV using a Mix vacuum mode (Backscattering Electron Mode + Secondary Electron mode). For qualitative analysis of NAD+, SEM analysis was coupled with energy dispersive x-ray spectroscopy (EDX) using AZtecOneXplore® software. EDX analysis was used to generate elemental line profiles on the SEM images of the PECs obtained. Lines were drawn *in situ* on the SEM image, followed by irradiation of the PEC sample with the incident high-energy electron beam. The elemental composition of the area of analysis is depicted following the generation of elemental peaks from the emission of X-rays with energies that are equivalent to the difference between the higher and lower electron level binding energies of each element. The presence of NAD+ within the complexes was identified via the generation of a peak associated with phosphorus within the resulting line spectra.

2.4.4. Percentage transmittance analysis

Approximately 2 mL of PEC samples with varying molar charge ratios were placed into a quartz cuvette. The percentage transmittance of the PEC solutions was recorded by running simple reads of the solution in transmittance mode at 500 nm using a UV/Vis spectrophotometer (Cary® 50, Agilent Technologies, Ireland. A blank run using ultrapure water at pH 5.5 was run after analysis of each sample.

2.4.5. NAD+ chromatographic conditions

HPLC analysis was conducted using a reversed-phase HPLC methodology on an Agilent 1200 Series HPLC System (Agilent Technologies, California, USA), equipped with the following modules: G1312B SL binary pump, G1329B autosampler, G1316B column compartment and a G1365B multiple UV wavelength detector. Method conditions were selected based on a HPLC method developed and validated by Forrow et al. [38]. The mobile phase consisted of a 95:5 (% v/v) mixture of 20 mM potassium phosphate buffer (pH 8):HPLC grade methanol. A flow rate of 1.0 mL/min, an injection volume of 10 μL and an autosampler temperature of 35 °C were set. Each injection was conducted in triplicate. An Xterra RP C18, 5 μm (250 × 4.6 mm) column was used (Waters Technologies Ireland Ltd., Wexford, Ireland). As shown in Supplementary Fig. 1, a retention time of approximately 4.4 min was observed for NAD+ at a wavelength of 260 nm. An NAD+ standard calibration curve was generated in the range of 2–200 μg/mL, prepared via appropriate dilution of a 1000 μg/mL standard stock solution in mobile phase. A summary of the HPLC validation parameters analysed is outlined in Supplementary Table 1. The peak area of a 100 μg/mL bracketing standard was used to quantify NAD+ in subsequent runs.

2.4.6. Quantification of NAD+ loading and association efficiency

The association efficiency (%AE) of NAD+ was quantified via indirect and direct methods by measuring both the quantity of free NAD+ in the bottom fraction of the Vivaspin® Turbo 15 centrifugal filters and the quantity of PEC-associated NAD+ in the top fraction. A given mass of PEC and free NAD+ lyophilisates were weighed out and dispersed in sample diluent (mobile phase) to yield solutions with concentrations of 1% (w/v). The resulting solutions were vortexed for 30 s at 500 rpm using a Fisherbrand™ vortex mixer (Fisher Scientific Ireland, Dublin,

Ireland) to ensure a homogenous solution was prepared. 100 uL aliquots of the lyophilisate solutions were pipetted into amber HPLC vials and diluted to a final volume of 1 mL with sample diluent and analysed via reverse-phase HPLC. The loading capacity of NAD+ in the top fractions was calculated by calculating the mass of NAD+ in each fraction as a percentage of the total mass of the lyophilisate. Direct %AE was determined by calculating the mass of NAD+ in the top fraction as a percentage of the total mass of NAD+ added. Indirect NAD+ %AE was found by calculating the mass of NAD+ remaining in the top fraction, after isolation of the mass of free NAD+ in the bottom fraction, as a percentage of the total mass of NAD+ added.

2.4.7. Changes in physiochemical parameters of NAD+-associated PECs in response to environmental stimuli

Change in physicochemical size parameters: NAD+-associated PECs were dispersed in 10 mL of sample medium to yield 1 mg/mL solutions, in triplicate. 1 mL of the resulting solutions was then diluted to 10 mL in 20 mL clear, glass vials with the same media and shaken at 200 rpm at 37 °C in an ES-20 orbital shaker-incubator (Grant Instruments, Cambridge, United Kingdom). At time zero, a 1 mL aliquot was withdrawn from each glass vial and analysed via DLS analysis as described in Section 2.4.2. To maintain sink conditions, equal volumes of fresh sample media were re-added to the glass vials upon sample withdrawal.

Changes in NAD+ complexation: NAD+-associated PECs suspensions containing 15 mg of NAD+ were pipetted into pre-soaked Spectra/Por Biotech dialysis membrane tubing (MWCO – 1000 kDa). Following equilibration to 37 °C, the loaded dialysis membranes were suspended in each medium under continuous stirring at 200 rpm in a sealed, temperature-controlled Stuart® S160D incubator (Anatylica Scientific, Illinois, USA). At predetermined time points, 500 μL aliquots were withdrawn from the receptor medium, diluted to 1 mL with diluent and analysed via reverse-phase HPLC.

2.4.8. Dynamic in vitro NAD+ release

The dynamic release of NAD+ from NAD+-associated PECs was performed in a microfluidic chamber in conditions modelling that of ocular and intraocular flowrates under a set flow rate of 3 μL/min. The polydimethylsiloxane device was produced by mixing Sylgard 184 Silicone base and curing agents at a ratio of 10:1 for four minutes, and then pouring the mixture onto a glass plate within a circular mould. Needles (1.27 mm outer diameter) were placed at opposite ends of the mould to create an inlet and an outlet channel and a hemisphere on the glass plate (9.00 ± 0.10 mm radius of curvature) created a well where the nanoparticle samples could be placed. The device was then cured for 6 h at 60 °C. Dissolved gas was removed from 0.01 M PBS via ultrasonic degassing. Our microfluidic device mimics the anatomical shape of the anterior segment, with two inlets and two outlet flow lines. Each inlet line received a flow rate of 1.5 μL/min from a flow pump (KD Scientific, Inc., Model 220), for a total flow rate of 3 μL/ min into the chamber. The interior of the chamber was lined with Spectra/Por Biotech dialysis membrane tubing (MWCO − 1000 kDa) and exposed to fluid flow before 400 μL of PEC suspension, equivalent to 15 mg of NAD+, was pipetted into the chamber. Outlet flow samples were collected at predetermined time points for reverse phase HPLC analysis of NAD+ concentration. Cumulative *in vitro* NAD+ release was calculated using Eq. (2):

$$\left(\frac{M_t}{M_{inf}}\right) \text{x } 100 \quad (2)$$

Where,

M_t = Total mass of NAD+ at time (t) (Total = Mass of NAD+ in receptor medium at time (t) + cumulative mass of NAD+ removed during sample withdrawal).

M_{inf} = Mass of NAD+ released at infinite t. (Mass released at the last time point).

Both the kinetics and mechanism of *in vitro* NAD+ release were evaluated by modelling the *in vitro* microfluidic release data to three mathematical models [39–43]. The model of best fit to the cumulative NAD+ release profile was selected based on the correlation coefficient (R^2) value obtained from each of the graphs plotted. The highest degree of correlation indicates the model of best fit to the experimental data. NAD+ release in accordance with the Higuchi model was assessed by plotting the cumulative NAD+ release as a function of the square root of time, in hours. The first 60% of NAD+ release was assessed as per the Korsmeyer-Peppas kinetic model by plotting a graph of the log of cumulative NAD+ release as a function of the log of time in hours [44–46]. The Hixson-Crowell mathematical model, assessed by plotting the cube root of NAD+ remaining as a function of time, in hours, was used to assess whether a change in diameter and surface area governs NAD+ release.

2.4.9. In vitro cytotoxicity analysis

Immortalised human corneal epithelial (IMHCE) cells (P10871-IM, Innoprot, Bizkaia, Spain) were cultured in ocular epithelial cell medium, supplemented with 5% (v/v) fetal bovine serum (FBS), 1% (v/v) of epithelial cell growth supplement (EpiCGS) solution and 1% (v/v) penicillin/streptomycin solution. IMHCE cells were maintained at 37 °C in a humidified atmosphere with 5% CO_2. Cells of a passage number of 6 were used in the *in vitro* cytotoxicity studies.

The viability of IMHCE cells exposed to PEC formulations containing between 40 and 800 μM of NAD+ was assessed by means of an acid phosphatase colorimetric assay. IMHCE cells were seeded at a density of 5×10^3 cells per well into a 96-well cell culture plate. After 24 h of incubation under the aforementioned culture conditions at between 70% and 80% confluence, the culture medium was removed and replaced with 100 μL of PEC formulations containing increasing concentrations of NAD+, followed by incubation for a further 24 h. Upon removal of the PEC formulations, the IMHCE cells were washed thrice with ice cold 0.01 PBS (pH 7.4) and incubated with the *para*-nitrophenylphosphate substrate for a further 2 h. 20 μL of stop solution (1 M NaOH) was added to each well prior to analysis of the absorbance of each well at 405 nm using a BioTek Epoch®microplate reader (Agilent Technologies, Dublin, Ireland). The viability of IMHCE cells exposed to both blank PEC formulations and NAD+ alone at equivalent concentration to the NAD+-associated PEC formulations was also assessed. Percentage cytotoxicity was calculated as a percentage with the regards to the absorbance of control cells, incubated with 100 μL of culture medium as opposed to a treatment, at 405 nm. Technical replicates were conducted, with each concentration being analysed in triplicate (three wells per concentration).

2.4.10. Ex-vivo permeation via fluorescence microscopy

Nine fresh porcine eyes were collected from a local abattoir and immersed in 0.9% (w/v) saline solution maintained at 4 °C before use. Corneas were surgically excised and washed thoroughly with fresh 0.9% (w/v) saline solution prior to being clamped into Franz diffusion cells (receptor chamber: 3 mL of 0.01 M PBS (pH 7.4), average permeation area 1.3 cm^2). After equilibration for 30 min at 37 °C, 200 μL of the donor solution (FITC-PECs (n = 3), FITC solution – positive control (n = 3) and 0.01 M PBS – negative control (n = 3)) was added to the Franz diffusion cells. Following 6 h of incubation, the corneal tissues were removed, washed thrice with ice-cold 0.01 M PBS, and stained with 3 mL of 2-(4-amidinophenyl)-1H-indole-6-carboxamidine (DAPI) (0.0001% (w/v)) for 5 min. Corneal tissues were washed again with ice-cold 0.01 M PBS to remove excess DAPI stain prior to analysis using an Olympus fluorescence microscope (Olympus Life Sciences, Tokyo, Japan) at a set magnification of 20x. DAPI and FITC modes of analysis were used to analyse the extent of corneal permeation.

2.5. Statistical analysis

Statistical analysis was conducted using Minitab® 17 Statistical

Software (Penn State University, State College, PA, USA). 2-sample t-tests were used throughout to determine whether a statistically significant difference existed between the means of two sample populations when comparing the same variable (i.e. size, association efficiency etc). Ryan-Joiner normality tests and 2 Variances tests were also conducted to assess whether the experimental data was normally distributed and whether the standard deviations of two sample populations are equal to the hypothesised ratio, respectively. The generation of a p-value of <0.05 was considered statistically significant.

3. Results and discussion

3.1. Optimisation of method parameters

3.1.1. Determination of the complexation pH via potentiometric titrations

pKa values of 2.33 and 6.98 were determined from the first derivative potentiometric titration curves for the anionic carboxylate anion of HA and the α-amine group of PLL, respectively. A pKa value of 2.25 was also identified for the anionic diphosphate group linking the ribose moieties of NAD +. The respective first derivative potentiometric titration curves are depicted in Supplementary Fig. 2 (a), (b) and (c). Such pKa values were then used to plot the fractional composition diagram shown in Fig. 1, from which the percentage ionisation of HA, PLL and NAD+ as a function of pH within the range of 1 to 10 can be identified.

Based on the percentage of carboxylate (COO^-) deprotonation and NH_3^+ protonation, inter-polyelectrolyte complexation is unlikely to occur between pH values of 1 to 2 and above a pH of 9. HA and PLL are considered weak polyelectrolytes. Therefore, the pH of the formulation medium can significantly influence the charge density of the respective polyelectrolytes and subsequent complexation [10,47,48]. Within the lower pH range, the carboxylic acid groups of HA primarily exist in a neutral form (COOH – 68.1% to 95.5%) and cannot undergo electrostatic interaction. Similarly, at a pH > 9, the deprotonated state of the PLL α–amine group (NH_2) predominates (89.0 – 98.8 %), thus significantly decreasing the α–amine groups available for complexation with HA carboxylate anions.

Between pH values of 5 to 6, 99.8% to 99.9% of HA carboxylate groups are deprotonated (COO–). Similarly, 90.5% to 99.0% of the α–amine groups of PLL are protonated (NH_3^+). Complexation is likely to occur between pH values of 3 and 8. However, based on the reduction in HA carboxylic acid group deprotonation from 82.4% to 59.7% with a concurrent reduction in pH from 3 to 2.5 and a similar reduction in α–amine group protonation above a pH of 6.5, maximal complexation cannot be achieved. Therefore, due to the high percentage of ionisation and the formation of negligible quantities of both protonated HA carboxylic acid groups (0.02–0.2%) and deprotonated PLL α–amine groups (1.0-9.5%), a pH range of 5 to 6 was chosen as the optimal pH for complexation. Similar pH values of 6 and 7 have been reported for the pH adjustment of ε-poly(L-lysine) and hyaluronic acid solutions before complexation [13,49].

NAD+ is a low molecular weight molecule, possessing two phosphate functional groups with a pyrophosphate bridge and a cationic nitrogen atom within the pyridine ring of the nicotinamide moieties. Within the chosen complexation pH range, the diphosphate groups of NAD+ should primarily exist in their deprotonated state (98.9–100.0% at pH 5 to pH 6). As such, the cationic charge may be compensated by one of the anionic phosphate groups, rendering NAD+ an overall anionic species at this pH. This may have further repercussions during the complexation process, particularly if the phosphate groups of NAD+ and the carboxylate anions of HA compete for electrostatic binding to the α–amine groups of PLL.

3.1.2. Optimisation of polyelectrolyte addition: dropwise titration or one-shot addition

Two addition methods for the formation of 2% and 5% (w/v) PECs at varying charge ratios, using both HMWHA and LMWHA, were investigated as part of this study. The dropwise addition of the polyelectrolyte in default to the polyelectrolyte in excess during complexation produced

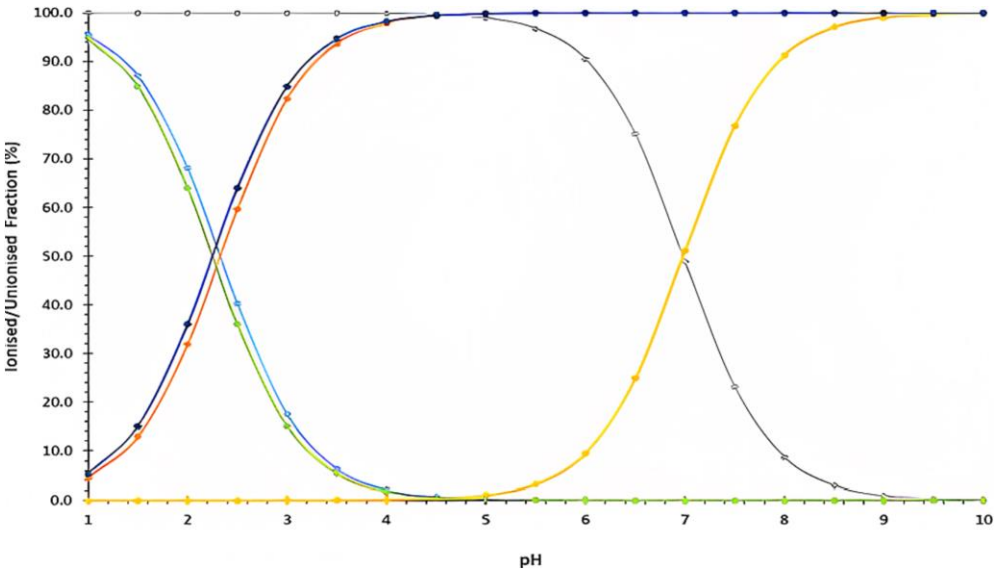

Fig. 1. Fractional composition diagram of HA, PLL and NAD+ showing the percentage ionisation of each species at each pH value from pH 1 to pH 10. (● – HA protonated fraction (COOH), ● – HA deprotonated fraction (COO^-), ● – PLL protonated fraction (NH_3^+), ● – PLL deprotonated fraction (NH_2), ● – NAD+ protonated fraction (PO_4), ● – NAD+ deprotonated fraction (PO_4^-)).

homogenous, turbid PEC dispersion. By adding all of the polyelectrolyte in default to the polyelectrolyte in excess at once, large quantities of gelatinous aggregates were formed. The rate of primary complexation is controlled by the rate of collision of the respective polyelectrolyte chains [50,51]. A one-shot addition of the polyelectrolyte solutions to one another may have resulted in instantaneous collision and subsequent neutralisation of almost all of the available charges on the respective chains, leading to a reduction in intercomplex repulsion and the formation of thermodynamically stable gel-like aggregates. Dropwise addition may allow for a more gradual formation of inter-polyelectrolyte electrostatic interactions and the establishment of intercomplex repulsive forces during secondary complex reconfiguration, thus improving overall PEC stability. Similar to our study, Bravo et al. [52] observed that the use of a dropwise titration method minimised gel aggregate formation during the formation of calf-thymus DNA and elastin-like polypeptide complexes. Gel aggregate formation was also found to be independent of HA molecular weight. However, Van Le et al. [10] observed irreversible aggregate formation during the dropwise addition of HA to diethylaminoethyl dextran and vice versa. This was attributed to the polyelectrolytes reaching a stoichiometric charge ratio during complexation before adjustment to the final charge ratio. However, this only occurred when the polyelectrolyte in excess was added to the polyelectrolyte in default, highlighting the sensitivity of this addition method to the mixing order [53].

3.2. Selection of the optimal PEC – charge ratio and turbidity analysis

Fig. 2 details the size, zeta potential (ZP) and polydispersity index (PDI) of control PECs across a range of molar charge ratios (MCR). PECs prepared with an excess cationic charge exhibited an MCR of < 1 ($(COO^-)/(NH_3^+) < 1$). Conversely, anionic PECs possessed an MCR of > 1 ($(COO^-)/(NH_3^+) > 1$).

The PECs at an MCR of 1 (PEC-CR1) immediately aggregated, as evidenced by a visual formation of gelatinous material, a highly variable and drastic increase in particle size and a polydispersity index (PDI) value of above 0.5 (PDI values - Supplementary Table 2). PECs are not thermodynamically stable and exhibit higher surface free energy in comparison to the bulk medium and without stabilisation, will tend towards aggregation to reduce the total Gibb's free energy of the system, thus resulting in macroscopic phase separation [54–57]. As expected, PECs with an MCR of < 1 exhibited a positive ZP value, attributed to the excess of PLL charge. However, such PECs also aggregated, exhibiting sizes of over 2 μm and PDI values of over 0.7. This could be attributed to the molecular weight of PLL used. As observed by Schatz et al. [53] during an evaluation of the colloidal stability of 5 kDa dextran sulphate and 16 kDa chitosan PECs, both the molecular weight and flexibility of the polyelectrolyte in excess play a pivotal role in complex stability. The molecular backbone of PLL exhibits inherently high structural flexibility [58]. When a large number of PLL chains are added to a HA chain, behaving as a host molecule in this case, PLL may adapt its configuration to favour complete-ion pairing between the α-amine and carboxylate functional groups as opposed to impacting electrostatic stabilisation to the individual PECs, which may result in increased inter-polyelectrolyte aggregation.

Exhibiting a size of 1633.3 ± 50.5 nm and ZP value of -30.37 ± 0.10 mV, the PEC with an MCR of 2 (PEC-CR2) was chosen for subsequent characterisation. Such PECs contain HA in excess, allowing the residual carboxylate anions to form an electrostatically stabilised corona surrounding the charged neutralised, stoichiometric polyelectrolyte core, thus imparting kinetic *meta*-stabilisation to the system via electrostatic repulsive forces between the surface-bound charges of PECs in close proximity [59–61]. A schematic of this type of PEC has been highlighted previously by our group [6].

As shown in Table 1, a significant decrease in size ($p \sim 0.001 \ll 0.05$) was observed following lyophilisation of PEC-CR2 with 1% (w/v) trehalose. For comparative purposes, the PEC with an MCR of 0.5 (PEC-CR0.5) was also lyophilised under equivalent conditions. However, although a decrease in size was also observed in PEC-CR0.5 after lyophilisation, this decrease was not statistically significant ($p = 0.066 > 0.05$). Furthermore, this PEC was excluded from further characterisation as its size remained over 500 nm.

Table 1
The particle size and PDI of PEC-CR0.5 and PEC-CR2, analysed before and after lyophilisation with 1% (w/v) trehalose. Data is expressed as mean ± SD (n = 3).

Condition	Before Lyophilisation		After Lyophilisation	
MCR	0.5	2	0.5	2
Size (nm)	4714.7 ± 1832.4	1633.3 ± 50.5	790.7 ± 39.7	322.7 ± 1.82
PDI	0.741 ± 0.379	0.765 ± 0.085	0.537 ± 0.040	0.300 ± 0.032

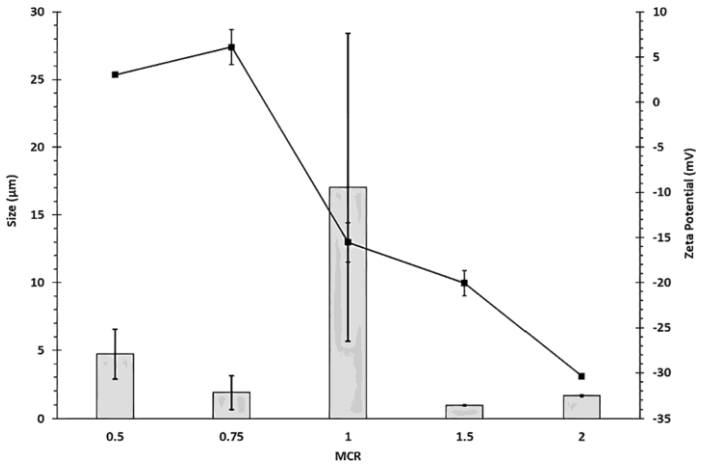

Fig. 2. The change in particle size (bars) and zeta potential (line) as a function of $(COO^-)/(NH_3^+)$ MCR. Data is expressed as mean ± standard deviation (SD) (n = 3).

Lyophilisation is typically associated with nanoparticle aggregation due to particulate damage and external mechanical stress imparted by ice crystallisation [62,63]. However, the addition of trehalose cryoprotectant can preserve hydrogen bond-mediated particle structure and stability by replacing water molecules on the surface of the particles during sublimation [64,65]. Increased hydrogen bonding may have led to further compaction of the residual HA chains within the PEC corona, thus leading to a reduction in particle size. HA itself can also behave as a cryoprotectant due to its remarkable water retention capabilities and ability to form intra and intermolecular hydrogen bonds [26]. The preservation of this "pseudo-hydrated" state during lyophilisation prevented PEC aggregation during lyophilisation, thus improving their redispersibility upon reconstitution in an aqueous medium [66]. In agreement with our study, Umerska et al. [67] and Yan et al. [68] have both reported on the improved dispersibility of HA and chitosan polyelectrolyte complexes and bovine serum albumin-loaded chitosan and tripolyphosphate nanoparticles, respectively, following lyophilisation with varying concentrations of trehalose cryoprotectant. However, neither study reported a significant decrease in particle size following lyophilisation.

The results obtained following analysis of the percentage transmittance at 500 nm of the PEC samples of varying MCR values corroborated the trends observed during DLS analysis. As depicted in Fig. 3, a sharp, significant decrease in percentage transmittance ($p \sim 0.000 \ll 0.05$) in the PEC samples with MCR values above 1 suggests the formation of PECs that remain suspended in an aqueous medium via mutual electrostatic repulsion between the residual HA carboxylate anions present on the surface of adjacent PECs. Turbidity following complexation indicates the phase separation of the individual polyelectrolytes into discreet, colloidally stable nanoparticles via electrostatic interaction [69]. PECs with MCR values equal to and<1 were optically clear and exhibited sedimentation of gelatinous aggregate material. The generation of percentage transmittance values above 70%, coupled with the DLS data obtained, supports this observation. An increase in percentage transmittance is indicative of particle aggregation and sedimentation as fewer dispersed particles are restricting the transmission of UV light through the sample. The significant decrease in percentage transmittance from 85.68 ± 0.20% to 72.78 ± 0.41% with an increase in MCR from 0.5 to 1 ($p \sim 0.000 \ll 0.05$) may be attributed to the presence of both aggregated material and small populations of PECs within PEC-CR1 which further supports the large error bars generated upon analysis of the size of PEC-CR1. Exhibiting suitable physiochemical size parameters for pharmaceutical and drug delivery applications (size: ~ 300 nm, zeta potential: > − 30 mV, PDI: < 0.25) and maximal turbidity, lyophilised PEC-CR2 was chosen for further characterisation and NAD+ loading.

3.3. Physicochemical characterisation of NAD+-associated PECs

The physicochemical characteristics of three NAD+-associated PECs, all with an MCR (NPEC-CR2), are shown in Table 2. To the best of our knowledge, there is no published data on the loading of NAD+ into a PEC nanoparticulate system. Therefore, an evaluation of the effect of NAD+ addition on the physicochemical attributes of the HA and PLL PEC was of critical importance to determine the suitability of the system for drug delivery application. Compared to the control PECs of equivalent composition in Table 1 (322.7 ± 1.82 nm), the NAD+-associated PECs reconstituted after lyophilisation were statistically smaller in size.

A similar observation was made by Mahta and coworkers, in which the addition of cationic diaminocyclohexane-platinum lead to a reduction in size in anionic HA and poly(arginine) complexes from 206 nm to 161 nm, attributed to enhanced electrostatic interaction between the individual components [12]. As it possesses charged functional groups, NAD+ is likely to form electrostatic interactions with the charged moieties of both PLL and HA. NAD+ can also readily partake in hydrogen bonding with the respective polyelectrolytes due to the presence of a large number of both partially positive hydrogen atoms and electronegative atoms on the molecular structure of the individual components. This hypothesis was further supported by comparing the sizes of NPEC-CR2-2–50 and NPEC-CR2-2–100. The significant increase in loading capacity in NPEC-CR2-2–100 ($p = 0.019 < 0.05$) may explain the decrease in particle size (194.8 ± 2.36 nm vs. 235.1 ± 19.0 nm in 50% (w/w) of NAD+ PEC). Increased interaction between a larger number of NAD+ molecules and the PLL and HA polymer chains may result in further compaction of the PEC structure. However, the increase in particle size found between NPEC-CR2-2–50 and NPEC-CR2-2–100 was statistically insignificant ($p = 0.068 > 0.05$). In agreement with our study, Sladek et al. [9] prepared anionic HA and chitosan PECs with sizes ranging from 232 ± 36 nm to 295 ± 58 nm, depending on the loading concentration of insulin. Cationic PECs prepared with HA and excess trimethyl chitosan exhibited a size of 186 ± 4.3 nm and a positive zeta potential of 15 mV [8]. Interestingly, an increase in total

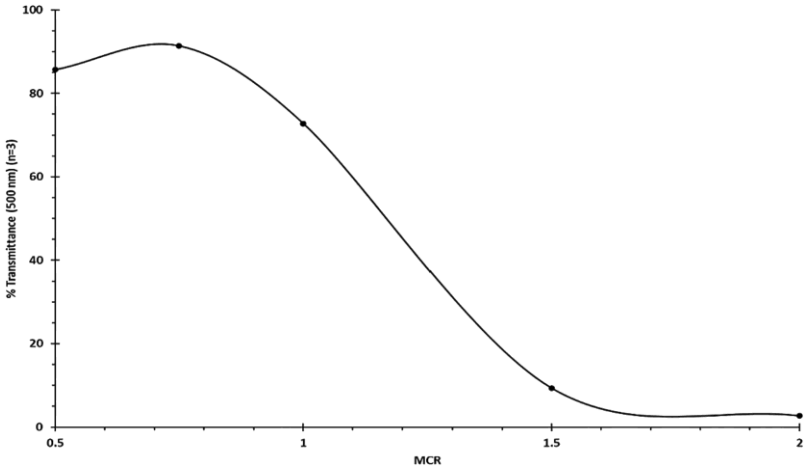

Fig. 3. The change in % transmittance as a function of $((COO^-)/(NH_3^+)$ MCR at 500 nm. Data is expressed as mean ± SD (n = 3).

Table 2
The physiochemical parameters of the NPEC-CR2 prepared. Data is expressed as mean ± SD (n = 3). (The association efficiencies reported are the results of the direct quantification of NAD+ within the PEC formulations. These values are supported by the values obtained following the indirect quantification of NAD+ (data not shown)).

Abbreviation	Concentration (% (w/v))	NAD+ Loading (% (w/w))	Size (nm)	ZP (mV)	PDI	NAD+ Association Efficiency (%)	NAD+ Loading Capacity (%)
NPEC-CR2-2-100	2	100	194.8 ± 2.4	34.9 ± 1.9	0.066 ± 0.018	22.3 ± 3.5	57.0 ± 5.9
NPEC-CR2-2-50	2	50	235.1 ± 19.0	−38.0 ± 1.1	0.214 ± 0.140	77.2 ± 9.5	42.8 ± 5.3
NPEC-CR2-5-50	5	50	267.7 ± 1.8	−31.3 ± 9.4	0.129 ± 0.045	65.4 ± 4.4	36.3 ± 4.5

concentration from 2% (w/v) to 5% (w/v) at an NAD+ loading of 50% (w/v) did not result in a statistically significant increase in particle size ($p = 0.099 > 0.05$). The increase in counterion concentration with an increase in polyelectrolyte concentration was expected to result in a reduction of the Debye length or the thickness of the electrical double layer surrounding the respective PECs.

A decrease in NAD+ loading from 100% (w/w) to 50% (w/v) led to a significant increase in NAD+ association efficiency from 22.3 ± 3.5% to 77.22 ± 9.5% ($p = 0.001 \ll 0.05$). This may be attributed to the generation of a smaller concentration gradient between areas of high and low NAD+ concentration within the formulation medium of the 50 % (w/w) sample, thus decreasing the rate of free NAD+ diffusion into the uncomplexed fraction during centrifugation. Despite an increase in total concentration from 2% (w/v) to 5% (w/v), no significant difference was found between NPEC-CR2-2-50 and NPEC-CR2-5-50 ($p = 0.125 > 0.05$).

The FT-IR spectrum of a physical mixture of HA, PLL and NAD+ in a 1:1:1 mass ratio confirmed that no significant interactions occurred between NAD+ and the respective polyelectrolyte materials in the powder form, as evidenced by the conservation of the characteristic peaks of NAD+, as shown in Fig. 4 (a). In Fig. 4 (b), the slight downward shift in the NAD+ absorption band representing the C_4-N_9-C_8-H stretching vibrations in the nicotinamide and adenine moieties from 1417 to 1413 cm^{-1} in the FT-IR spectrum may be attributed to overlap with the absorption band representing the symmetric stretching of the residual HA COO^- groups occurring at 1411 cm^{-1} [70,71]. The generation of an infrared absorption peak at 1242 cm^{-1} within the PEC FT-IR spectrum may also be attributed to the asymmetric stretching of the phosphate bridge linking the adenosine and nicotinamide moieties of NAD+ [71].

The generation of a phosphorus peak within the elemental composition profile, shown in Fig. 5, following SEM-EDX analysis suggests the presence of NAD+ within the PECs, as phosphorous is an element specific to the molecular structure of NAD +. Energy dispersive X-ray analysis was used to generate elemental line profiles on the SEM images of the PECs obtained. Lines were drawn *in situ* on the SEM image followed by irradiation of the PEC sample with the incident high-energy electron beam.

3.4. Characterisation of PEC matrix stability in response to environmental stimuli

NAD+ remained stable when stored in each sample medium at 37 °C over 7 days, indicated by a statistically equivalent % recovery of NAD+ at time zero and after 7 days under each condition (Supplementary Table 3).

As shown in Fig. 6 (a), the size of NAD+ -associated PECs stored in 0.01 M PBS (pH 7.4) was significantly larger at each time point in comparison to the time point previous. For example, an increase in size from 248 ± 84.6 nm to 429.3 ± 51.1 nm to 1340.3 ± 204.8 nm was evident between 0 and 8 and 8 to 24 h. No significant change in particle size was observed in ultrapure water over 48 h, regardless of pH, ($p = 0.336 > 0.05$ – pH 7.4 (0–48 h) and $p = 0.678 > 0.05$ – pH 5.5 (0–48 h)), whereas the PECs stored in 0.01 M PBS (pH 7.4) were also significantly larger than those stored in ultrapure water at equivalent pH at each timepoint apart from time zero. This provides an indication of PEC colloidal stability in physiological medium as PECs may tend towards aggregation via intercomplex van der Waals attractive forces when stored under physiological ionic conditions, primarily attributed to the loss in electrostatic repulsion-mediated stability via enhanced charge screening between individual PECs and ions within the medium. An immediate increase in size was also observed in the 0.01 M PBS (pH 5.5) PEC sample, as depicted in Fig. 6 (a). This suggests that the PECs may be swelling to a greater extent when placed in an ionic environment at a pH equal to the pH at which maximal complexation occurs due to preservation of the electrostatic interactions between the individual HA and PLL chains. Such intercomplex aggregation was demonstrated by Kayitmazer *et* al. [72] who observed an increase in the radius of hydration of HA and chitosan PECs with a concurrent increase in NaCl, with macroscopic flocculation of the PECs occurring at a NaCl concentration of 0.3 M. Wu et al. [73] has also reported on the destabilisation of chitosan (degree of acetylation of 4%) and HA complexes when added to 0.01 M PBS at pH 7.4. However, it was not stated in either study whether PEC destabilisation was denoted by a change in size or ZP.

To ensure adequate colloidal stability, particles should exhibit ZP values between + 30 mV and < − 30 mV. ZP values of between 60 mV and −60 mV indicate excellent stability [74]. At time zero, there was a significant decrease in ZP value upon comparison of the PECs stored in 0.01 M PBS with those stored in ultrapure water at both pH 7.4 ($p = 0.001 < 0.05$) and pH 5.5 ($p = 0.044 < 0.05$), as shown in Fig. 6 (b). Overall, the PECs in 0.01 M PBS exhibited lower ZP values at each timepoint. No significant difference was found between the ZP values of the PECs stored in both 0.01 M PBS at pH 7.4 and pH 5.5 ($p = 0.855 > 0.05 – 0$ h and $p = 0.291 > 0.05 – 48$ h) and in ultrapure water at pH 7.4 and pH 5.5 ($p = 0.187 > 0.05 – 0$ h and $p = 0.826 > 0.05 – 48$ h), over time, suggesting that the reduction in ZP is independent of changes in pH. The immediate reduction in ZP observed can be attributed to ion-mediated electrostatic charge screening between adjacent PECs. The preservation of ZP over 48 h in the PECs stored in ultrapure water at both pH 7.4 and pH 5.5 ($p = 0.087 > 0.05$ – pH 7.4 and $p = 0.467 > 0.05$ – pH 5.5) further supports this hypothesis. A similar trend was observed by Saether et al. [75] with alginate and chitosan complexes in which a reduction in ZP +/- 40 to 50 mV to +/- 15 to 25 mV occurred after the addition of NaCl to a final concentration of 0.15 M.

As depicted in Fig. 6 (c), significantly lower quantities of NAD+ remained complexed to the PECs placed in ultrapure water at both pH 7.4 and pH 5.5 in comparison to those stored in 0.01 M PBS at equivalent pH at each time point. This may be attributed to the absence of ions in ultrapure water, thus creating a steep osmotic gradient between the donor and receptor compartment that drives NAD+ decomplexation from the PEC matrix. At 4 h post storage, the mass of NAD+ complexed to the PECs maintained at pH 7.4 in 0.01 M PBS (3.90 ± 0.95 mg) was significantly lower than that complexed to those maintained at pH 5.5 under equivalent ionic conditions (6.31 ± 0.11 mg). Similarly, the mass of NAD+ retained in the PEC sample at pH 7.4 in ultrapure water

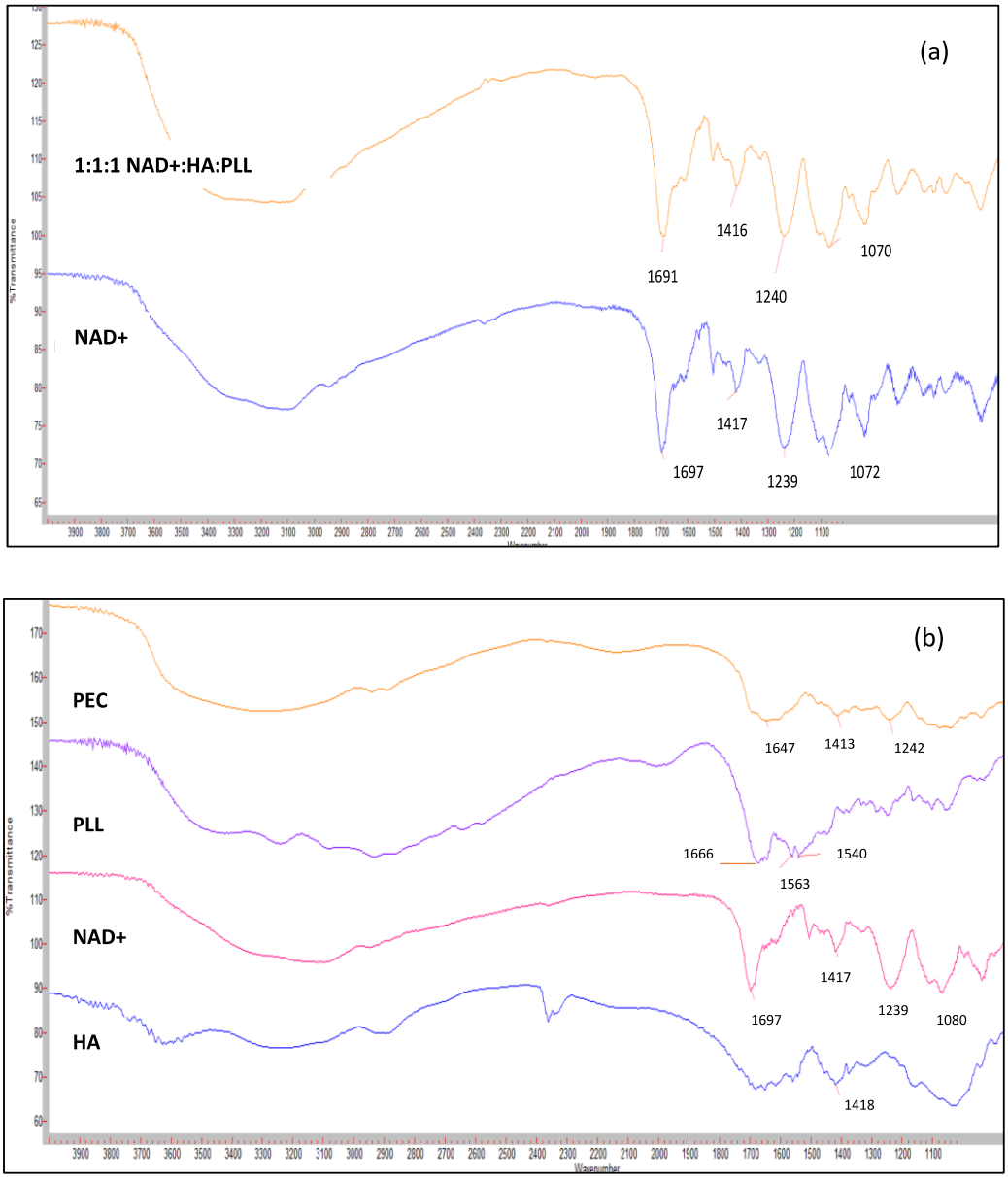

Fig. 4. FT-IR spectra generated upon analysis of (a) the physical mixture of the starting materials (HA:PLL:NAD+ → 1:1:1) in comparison to that of pure NAD+ and (b) the individual starting materials and the NPEC-CR2-2–50 (Resolution – 2 cm^{-1}. Number of overlay scans – 32).

dropped below 1 mg (0.57 ± 0.41 mg) whilst 2.42 ± 0.14 mg was retained at pH 5.5 after 4 h. This may be attributed to the loss of poly-electrolyte ionisation, particularly poly(L-lysine), with an increase in pH from 5.5 to 7.4. As depicted in the schematic in Fig. 7, the ionisation of both HA and PLL is above 95% at pH 5.5. Theoretically, complexation should be maximal at this pH, preserving the electrostatic interaction between the carboxylate anion of HA and the α–amine group of PLL and the stability of the resulting matrix. Upon swelling of the PECs when placed in 0.01 M PBS at pH 5.5, the preservation of the matrix allows for the sequential binding of NAD+ via intermolecular interaction. At pH

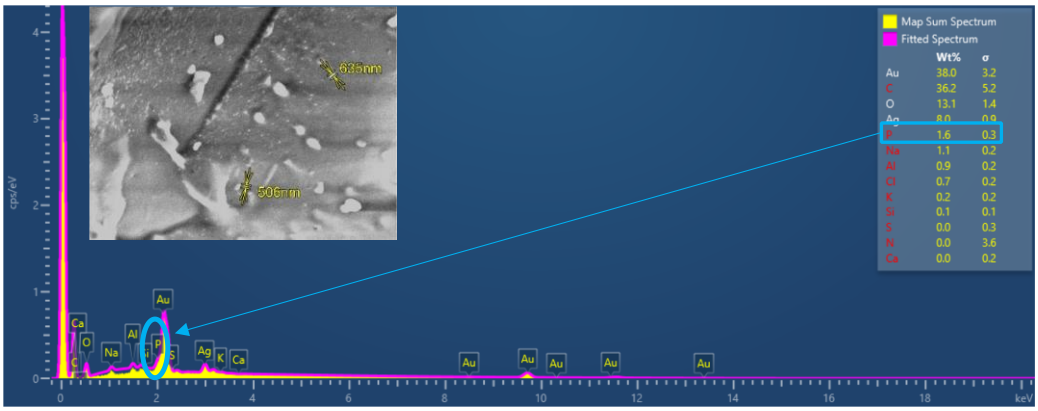

Fig. 5. EDX elemental spectrum profile of NPEC-CR2-2–50. The corresponding SEM micrograph (scale – 20 μm) (10 kV – 6.5 mm × 2.00 k) is shown in the insert. (Typical result after three individual trials).

7.4, PLL ionisation decreases from 96.8% to 23.2%, potentially resulting in electrostatic bond degradation. This loss in electrostatic interaction in the PEC matrix can result in both the freeing of anionic HA chains from the tightly bound PEC meshwork and collapse of the now charge-neutralised PLL segments via hydrophobic interactions. Such processes may limit the remaining surface area available for NAD+ complexation.

Ultimately, the data suggests that the degree of complexation between the respective polyelectrolytes, and the association of NAD+ to the established matrix, is highly dependent on both pH and ionic conditions. To ensure the successful formation of sub-micron sized PECs, such parameters must be carefully controlled during formulation. However, this study also provides a starting point for the design of tunable NAD+-associated PECs that exhibit variable physicochemical functionality in response to environmental stimuli.

3.5. *In vitro* NAD+ release under microfluidic conditions

As shown in Fig. 8, sustained release of 10.9 ± 0.2 mg of NAD+ was achieved for up to 14 h under simulated ocular volumetric flowrates, delivering over 73.0 ± 2.1% of the NAD+ payload. The release profile qualitatively exhibited sustained release, and, for the first 7 h, there was a relatively linear release at a rate of 0.9 mg/hr. Conversely, the total mass of an injected NAD+ solution was cleared from the microfluidic chamber under equivalent conditions in less than an hour. This indicated that the PEC matrices may be providing a diffusion barrier to rapid NAD+ release, potentially attributed to the diffusion of NAD+ through the nanochannels created in the PEC matrix via electrostatic interactions between the carboxylate anion and α–amine group of PLL.

The mean flowrate of tears on the ocular surface is ~ 3 μL/min and aqueous-humour flowrate is 2.78 +/-0.27 μL/min [76,77]. The microfluidic physiological flow device has previously proven to be a more effective method to correlate *in vitro* results with *in vivo* conditions [78–80]. The device more closely mimics the volume and fluid dynamics of the eye than infinite sink studies. Therefore, it can more accurately predict the *in vivo* drug release behaviour of the polyelectrolyte complexes. Under these conditions, no burst release was observed. For polyelectrolyte nanomaterial systems where there is high surface electrostatic adsorption, burst release is typically observed [13,81,82,83]. Silva et al. [83] observed an *in vitro* burst release of over 60–70% of the theoretical loading concentration of erythropoietin from HA and chitosan polyelectrolyte complexes within the first 15 min. That study was not conducted under physiological ocular flow nor was the volume of release medium stated. Therefore, it is difficult to interpret whether this burst release was indicative of PEC behaviour during release or the result of a secondary effect such as a concentration gradient. Amato et al. [13] observed that over 60% of the loaded berberine concentration was released from HA and ε-poly(L-lysine) nanogels prepared via polyelectrolyte complexation within the first 1-hour post addition to a dialysis membrane submerged in 12 mL 0.9% (w/v) saline solution. A large degree of variation in *in vitro* berberine release was also observed, suggesting that the rate of berberine diffusion through the polyelectrolyte matrix was limited and irreproducible [78]. In our system, the release duration suggests gradual diffusion through the PEC matrix and that surface desorption is not the primary governing factor of NAD+ release. As such, the release duration indicates that a once or twice-daily administered dose is possible.

3.6. *Kinetic modelling of in vitro NAD+ release*

On the basis of best-fit, *in vitro* NAD+ release under microfluidic condition was best fitted to the Higuchi mathematical model (R^2 = 0.9704) providing a good indication that the release of NAD+ from the PEC was governed by diffusion. The release exponent value, or 'n', obtained following fitting to the Korsmeyer-Peppas model (0.8441, R^2 = 0.9364), also lies between 0.45 and 1, indicating that NAD+ release was governed by anomalous or non-Fickian diffusion in which the rates of intra-polyelectrolyte solvent transport or NAD+ diffusion and polyelectrolyte relaxation are comparable [84–86]. This further corroborates the behaviour observed in the study detailed in Section 3.4. Loss of electrostatic interaction and enhanced mobility of the individual polyelectrolytes at pH 7.4 may result in a larger increase in the rate of polymer relaxation in comparison to the rate of NAD+ diffusion.

Such behaviour is typical for polymer-based nanomaterial formulations that exhibit high swelling ability or when the release of the therapeutic may be governed by a combination of release mechanisms [41,87]. Ćirić et al. [88] demonstrated that the release of escin from xanthan gum and chitosan PECs was best fit either to the Higuchi or Korsmeyer-Peppas mathematical models, depending on the escin:polymer mass ratio. Colistin release from hyaluronic acid-based PECs was also best fit to the Higuchi model, thus confirming that the rapid *in vitro* release of over 85% of the total loaded concentration of colistin from the lyophilised PECs in the first hour was governed by colistin diffusion [89]. The *in vitro* release of aceclofenac from chitosan and pectin PEC microparticles was best fit to the Korsmeyer-Peppas model but also

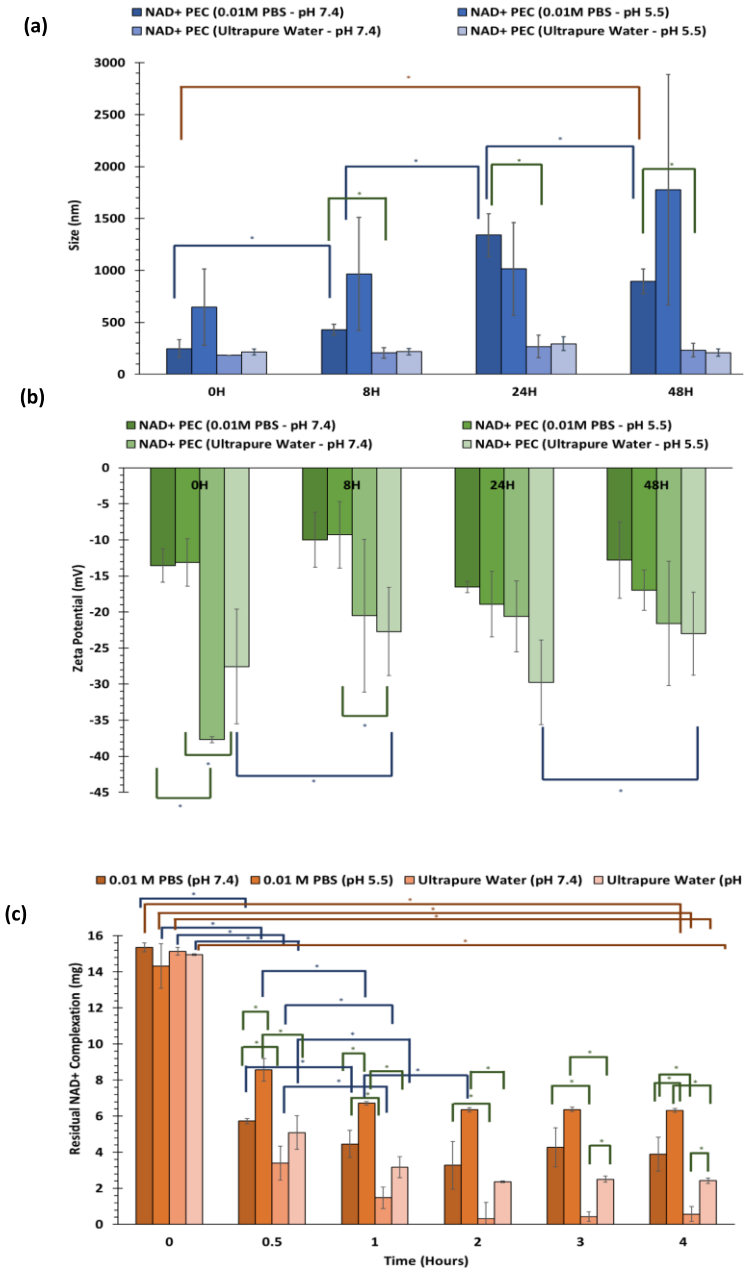

Fig. 6. The change in size (a), ZP (b) and residual NAD+ complexation (c) values for the NAD+ -associated PECs as a function of time in each of the sample media analysed. Data is expressed as mean ± SD (n = 3). (* - statistically significant at a 5% confidence interval. Colour of statistical significance bar: blue – between time points, green – between conditions and orange – from first to last time point). (For interpretation of the references to colour in this figure legend, the reader is referred to the web version of this article.)

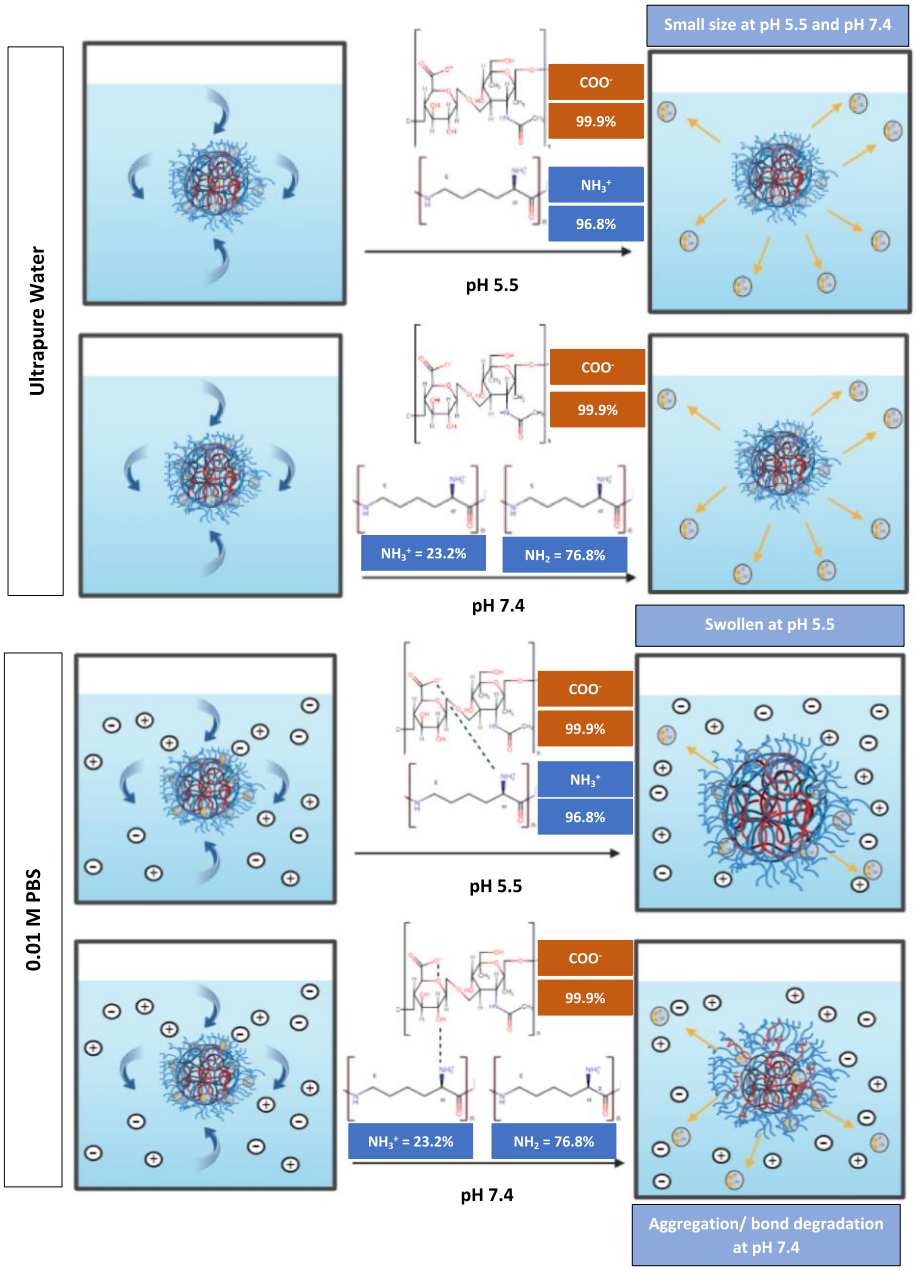

Fig. 7. A schematic detailing the effect of the change in PEC structure when placed in ionic medium at a pH of 5.5 and pH 7.4 and in ultrapure water at equivalent pH. The percentage ionisation of HA and PLL at the respective pH values is also shown.

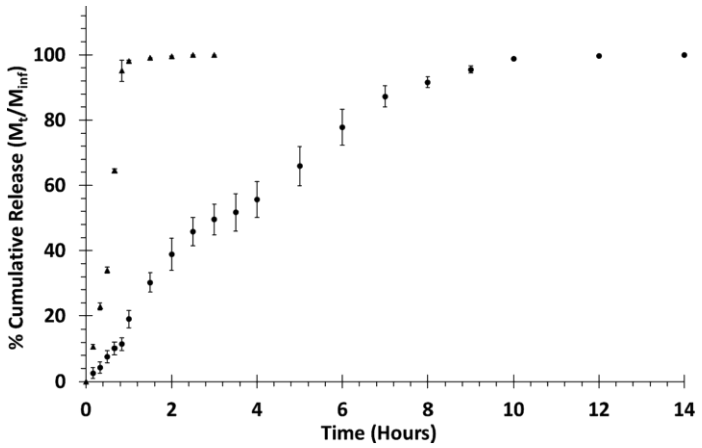

Fig. 8. Cumulative *in vitro* NAD+ release profiles from PECs (circle) and an NAD+ bolus control (triangle) in 0.01 M PBS (pH 7.4) under microfluidic conditions. (Data is expressed as mean % Mt/Minf ± SD (n = 3).

demonstrated a high degree of correlation to the Higuchi model. In agreement with our study, release was governed by anomalous diffusion, as indicated by the release exponent value [90]. Magalhaes Jr. and co-workers [91] also fit the *in vitro* release of chloroquine from PECs composed of chitosan and an anionic rhamnogalacturonoglycan polysaccharide to the Korsmeyer-Peppas model. However, this study primarily focused on an evaluation of the effect of mixing order and chitosan molecular weight on the release exponent value.

3.7. Cytotoxicity of PEC formulations in IMHCE cells

Once a suitable *in vitro* release profile was achieved, the cytotoxic

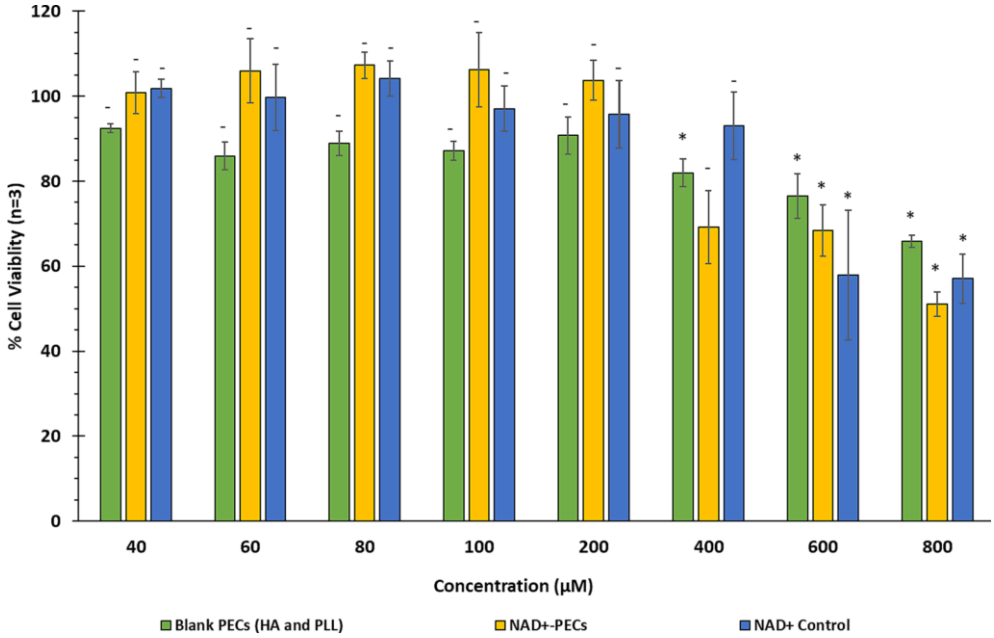

Fig. 9. Percentage cell viability of IMHCE cell lines upon exposure to NAD+, blank PEC formulations and NAD+ -associated PEC formulations of increasing concentration for 24 h. Data is expressed as mean % cell viability ± SD (n = 3). (* = statistically significant at a 5% confidence interval. - = statistically equivalent to cell viability of control = 100 ± 3.7%).

potential of NAD+, blank PEC formulations and NAD+-associated PEC (NPEC) formulations in IMHCE cells over 24 h was analysed via an acid phosphatase assay. As shown in Fig. 9, none of the treatments analysed exhibited a cytotoxic effect at an NAD+ concentration, or a concentration of PEC formulation equivalent to an NAD+ concentration of 400 μM or below. Within this concentration range, the percentage cell viabilities of the treatments analysed were statistically equivalent to that of the control IMHCE cells. However, despite being statistically equivalent to the control IMHCE cells, the high degree of variation in percentage viability of the cells incubated with the PEC formulation containing 400 μM of NAD+ (76.9 ± 14.9%) was unfavourable. This may be attributed to the PEC components themselves as a statistically significant difference was found between the percentage viability of the blank PEC formulation and the control IMHCE cells at this concentration ($p = 0.003 \ll 0.05$). Incubation of IMHCE cells with NAD+ alone at a concentration of 400 μM exhibited no cytotoxic effect (93.1 ± 7.9% - $p = 0.228 > 0.05$). This may be due to the presence of an increased concentration of PLL. Despite its inherent biocompatibility and biodegradability, PLL has also been shown to induce cytotoxic effects on human cell lines in a concentration and molecular dependant manner, attributed to its ability to accumulate on the outer cell membrane via electrostatic interaction with the negatively charged phosphate groups within the phospholipid bilayer [92–94]. As such, PEC formulations containing 200 μM of NAD+ will be utilised for future *in vitro* efficacy studies.

At concentrations above 400 μM, a statistically significant decrease in viability was observed for the IMHCE cells incubated with both NAD+ alone and NPECs (600 μM – 57.8 ± 15.3% (NAD+), 68.4 ± 6.0% (NPEC), 800 μM – 57.1 ± 5.8% (NAD+), 51.0 ± 2.9% (NPEC)). Similarly, Zhu et al. [31] exhibited a decrease in cell viability upon incubation of ARPE-19 cells with 1 mM and 20 mM of NAD +. Despite the proven efficacy of NAD+ augmentation against the deleterious effects of ageing through NAD+ precursor supplementation, an excessive intracellular concentration of NAD+ could potentially result in an imbalance in homeostatic conditions. For example, Hwang et al. [95] summarised the potential toxicity risks of nicotinamide, a by-product of NAD+ consumption via enzymatic action. Braidy et al. [96] also highlighted the potential risks of increased NAD+ supplementation, particularly regarding the accumulation of potentially toxic metabolites from increased NAD+ consumption and the increase in cellular senescence with proinflammatory senescence associated secretory phenotype.

3.8. Ex vivo permeation via fluorescence microscopy

A qualitative *ex vivo* study was conducted to assess the corneal distribution of the NPECs in a porcine model. As shown in the inverted microscopy images in Fig. 10, the fluorescein isothiocyanate (FITC)-PECs were visible within the corneal epithelium of the cornea after an incubation time of 6 h at 37 °C. Also, the positive and negative control fluorescent images are equivalent, suggesting that the FITC fluorescence observed in the FITC-PECs is due to the presence of PECs and not free FITC. Free FITC did not permeate through the corneal tissues and was effectively removed during the washing step with ice-cold 0.01 M PBS.

Due to the restriction of both paracellular and transcellular diffusion, imposed by the pore size of the tight junctional complexes joining superficial corneal epithelial cells (2–4 nm), and the lipophilic nature of the corneal epithelial multilayer, it would be expected that the transcorneal diffusion of the NPECs would be limited to the apical layer [97–99,100]. However, when analysing the *ex vivo* permeation of timolol maleate from chitosan and flax seed gum complexes of similar size (267.06 ± 8.65 nm), Mittal et al. [101] observed a significant increase in timolol maleate permeation through a goat cornea in comparison to a marketed Iotim® eye-drop formulation, attributed to the enhanced corneal retention of the complexes post-administration. Similarly, Kimna et al.[102] observed a significant increase in timolol maleate permeation through a porcine cornea upon comparison of a chitosan and alginate complex of 251 ± 96 nm in size and a timolol maleate solution. However, these results could be attributed to the permeation enhancing capabilities of chitosan via increased electrostatic interaction with sialic acid and sulphate groups in corneal mucosa and tight junction disruption as opposed to their size [103,104]. From another perspective, the NPECs may facilitate the transcorneal diffusion of NAD+ by a more indirect approach, namely by prolonging its corneal residence time. Despite the anionic surface charge of the NPECs, the NPECs may exhibit some degree of mucoadhesion to the corneal surface, due to a combination of attractive electrostatic interactions between residual HA carboxylate anions within the PEC corona and the cationic amino groups of the zwitterionic backbones of corneal bound mucin, hydrophobic interactions and van der Waals forces [105,106]. Also, HA has been proven to promote endocytosis in corneal epithelial cells in both rabbit and an organotypic human corneal epithelial models via binding to the hyaluronic acid binding domain on CD44 receptors [103,107,108]. The expression of which have been demonstrated in the corneal epithelium of both porcine models and human models under both normal and pathological conditions [109,110]. A combination of prolonged residence time and enhanced endocytosis at the apical corneal layer may be highly beneficial for targeting cellular dysfunction caused by the deleterious effects of ocular surface disorders such as dry eye disease. However, if the NPECs were intended for treatment of a target site within the posterior layers, intraocular migration through the conjunctival-scleral pathway may be more beneficial due to the increase in paracellular pore density and enhanced permeation of therapeutic

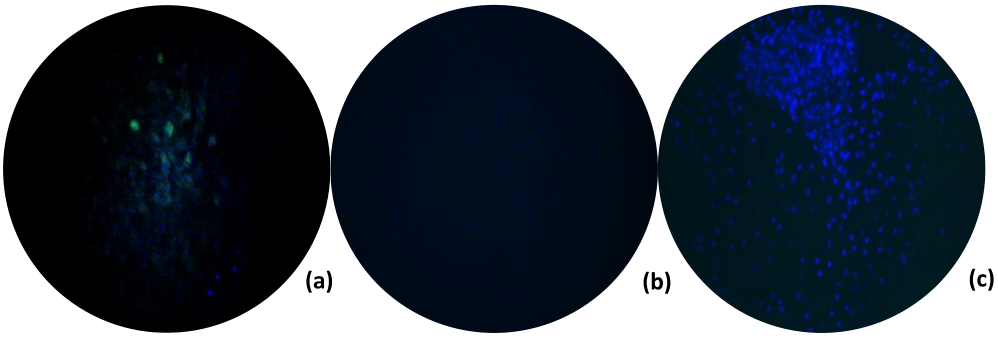

Fig. 10. Fluorescent microscopy images of (a) FITC-PECs (0.1% (w/v) FITC), (b) 0.1% (w/v) FITC solution and (c) negative control taken after incubation of porcine corneal tissues at 37 °C for 6 h. (Images taken at 20× magnification. Representative images of n = 3).

molecules with sizes of between 5 and 10 kDa [111]. The hydrophilicity and within the corona may also promote diffusion through the negatively charged collagen fibril and proteoglycan matrix within the sclera. Ultimately, the retention of the fluorescent PECs within the corneal epithelium further highlights their suitability for topical NAD+ delivery to the corneal surface and provides scope for investigating the safety and efficacy of this formulation further.

4. Conclusions

NAD+-associated HA and PLL PECs (NPECs) were successfully formulated under mild aqueous conditions via polyelectrolyte complexation for the first time. The selected PEC, with a polyelectrolyte concentration of 2% (w/v), a molar charge ratio of 2 and a percentage NAD+ loading of 42.8 ± 5.3%, was capable of extending the release of 10.9 ± 0.2 mg of NAD+ over 14 h, demonstrated under physiological ocular flow rates. The significant changes in size, zeta potential and NAD+ complexation as a function of both pH and ionic condition highlights the dependence of the physicochemical behaviour of the PEC matrix on changes in environmental condition, thus providing evidence of two formulation parameters that must be carefully controlled during PEC formulation. The NPECs were also well tolerated on an immortalised human corneal epithelial cell line and did not evoke significant cytotoxic effects at NAD+ loading concentrations of up to and including 200 μM. The accumulation of fluorescent NPECs within the corneal epithelium layer of an ex vivo porcine model suggests that they may have a specific use as a treatment for corneal surface disorders.

Ultimately, the results obtained support the hypothesis that this nanoformulation is suitable for use as a system for NAD+ ocular delivery, intended for once or twice-daily topical administration. Further characterisation primarily focused on *in vitro* cell internalisation and quantitative *ex vivo* permeation, is required to obtain a well-rounded evaluation of the PECs as an ocular drug delivery system. However, it is expected to have significant clinical promise and efficacy against the deleterious effects of several neurodegenerative ocular diseases leading to overall better ocular health.

Funding

This work was supported by the South East Technological University (SETU) PhD Scholarship Programme (Formerly WIT Co-fund PhD Scholarship Programme 2019 - WIT 2019 Call 1 CoFund).

Declaration of Competing Interest

The authors declare that they have no known competing financial interests or personal relationships that could have appeared to influence the work reported in this paper.

Data availability

The authors do not have permission to share data.

Acknowledgements

The authors acknowledge Dawn Meats Grannagh, Waterford, Ireland, for their continued help and support in the organisation and collection of porcine eyes used in the conducted *ex vivo* studies.

Appendix A. Supplementary material

Supplementary data to this article can be found online at https://doi.org/10.1016/j.ejpb.2023.10.004.

References

[1] S. Gorantla, V.K. Rapalli, T. Waghule, P.P. Singh, S.K. Dubey, R.N. Saha, G. Singhvi, Nanocarriers for Ocular Drug Delivery: Current Status and Translational Opportunity, RSC Adv. 10 (46) (2020) 27835–27855, https://doi.org/10.1039/d0ra04971a.
[2] N. Omerović, E. Vranić, Application of Nanoparticles in Ocular Drug Delivery Systems, Health Technol. (Berl) 10 (1) (2020) 61–78, https://doi.org/10.1007/s12553-019-00381-w.
[3] V. Harish, D. Tewari, M. Gaur, A.B. Yadav, S. Swaroop, M. Bechelany, A. Barhoum, Review on Nanoparticles and Nanostructured Materials: Bioimaging, Biosensing, Drug Delivery, Tissue Engineering, Antimicrobial, and Agro-Food Applications, Nanomaterials 12 (3) (2022), https://doi.org/10.3390/nano12030457.
[4] A. Plucinski, Z. Lyu, B.V.K.J. Schmidt, Polysaccharide Nanoparticles: From Fabrication to Applications, J. Mater. Chem. B 9 (35) (2021) 7030–7062, https://doi.org/10.1039/d1tb00628b.
[5] A. Zielinska, F. Carreiró, A.M. Oliveira, A. Neves, B. Pires, N. Venkatesh, A. Durazzo, M. Lucarini, P. Eder, A.M. Silva, et al., Polymeric Nanoparticles: Production, Characterization, Toxicology and Ecotoxicology, Molecules 25 (16) (2020) 3731, https://doi.org/10.3390/molecules25163731.
[6] S. Casey-Power, R. Ryan, G. Behl, P. McLoughlin, M.E. Byrne, L. Fitzhenry, Hyaluronic Acid: Its Versatile Use in Ocular Drug Delivery with a Specific Focus on Hyaluronic Acid-Based Polyelectrolyte Complexes, Pharmaceutics 14 (7) (2022) 1–41, https://doi.org/10.3390/pharmaceutics14071479.
[7] B. Silva, L.M. Gonçalves, B.S. Braz, E. Delgado, Chitosan and Hyaluronic Acid Nanoparticles as Vehicles of Epoetin Beta for Subconjunctival Ocular Delivery, Mar. Drugs 20 (2) (2022) 151, https://doi.org/10.3390/md20020151.
[8] F. Chaharband, N. Daftarian, M.R. Kanavi, R. Varshochian, M. Hajiramezanali, P. Norouzi, E. Arefian, F. Atyabi, R. Dinarvand, Trimethyl Chitosan-Hyaluronic Acid Nano-Polyplexes for Intravitreal VEGFR-2 SiRNA Delivery: Formulation and in Vivo Efficacy Evaluation, Nanomed. Nanotechnol. Biol. Med. 26 (102181) (2020), https://doi.org/10.1016/j.nano.2020.102181.
[9] S. Sladek, F. McCartney, M. Eskander, D.J. Dunne, M.J. Santos-Martinez, F. Benetti, L. Tajber, D.J. Brayden, An Enteric-Coated Polyelectrolyte Nanocomplex Delivers Insulin in Rat Intestinal Instillations When Combined with a Permeation Enhancer, Pharmaceutics 12 (3) (2020), https://doi.org/10.3390/pharmaceutics12030259.
[10] H. Van Le, V. Dulong, L. Picton, D. Le Cerf, Polyelectrolyte Complexes of Hyaluronic Acid and Diethylaminoethyl Dextran: Formation, Stability and Hydrophobicity, Colloids Surfaces A Physicochem. Eng. Asp. 629 (September) (2021), 127485, https://doi.org/10.1016/j.colsurfa.2021.127485.
[11] M.G. Villamizar-Sarmiento, I. Moreno-Villoslada, S. Martínez, A. Giacaman, V. Miranda, A. Vidal, S.L. Orellana, M. Concha, F. Pavicic, J.G. Lisoni, et al., Ionic Nanocomplexes of Hyaluronic Acid and Polyarginine to Form Solid Materials: A Green Methodology to Obtain Sponges with Biomedical Potential, Nanomaterials 9 (7) (2019), https://doi.org/10.3390/nano9070944.
[12] K. Matha, G. Lollo, G. Taurino, R. Respaud, I. Marigo, M. Shariati, O. Bussolati, A. Vermeulen, K. Remaut, J.P. Benoit, Bioinspired Hyaluronic Acid and Polyarginine Nanoparticles for DACHPt Delivery, Eur. J. Pharm. Biopharm. 150 (February) (2020) 1–13, https://doi.org/10.1016/j.ejpb.2020.02.008.
[13] G. Amato, M.A. Grimaudo, C. Alvarez-Lorenzo, A. Concheiro, C. Carbone, A. Bonaccorso, G. Puglisi, T. Musumeci, Hyaluronan/Poly-L-Lysine/Berberine Nanogels for Impaired Wound Healing, Pharmaceutics 13 (1) (2020) 34, https://doi.org/10.3390/pharmaceutics13010034.
[14] F.D. Battistini, L.I. Tártara, C. Boiero, M.L. Guzmán, L.C. Luciani-Giaccobbe, S. D. Palma, D.A. Allemandi, R.H. Manzo, M.E. Olivera, The Role of Hyaluronan as a Drug Carrier to Enhance the Bioavailability of Extended Release Ophthalmic Formulations. Hyaluronan-Timolol Ionic Complexes as a Model Case, Eur. J. Pharm. Sci. 105 (2017) 188–194, https://doi.org/10.1016/j.ejps.2017.05.020.
[15] N.V. Dubashynskaya, S.V. Raik, Y.A. Dubrovskii, E.S. Shcherbakova, E. V. Demyanova, A.Y. Shasherina, Y.A. Anufrikov, D.N. Poshina, A.V. Dobrodumov, Y.A. Skorik, Hyaluronan/Colistin Polyelectrolyte Complexes: Promising Antiinfective Drug Delivery Systems, Int. J. Biol. Macromol. 187 (July) (2021) 157–165, https://doi.org/10.1016/j.ijbiomac.2021.07.114.
[16] N.R. Kale, D. Dutta, W. Carstens, S. Mallik, M. Quadir, Functional Applications of Polyarginine-Hyaluronic Acid-Based Electrostatic Complexes, Bioelectricity 2 (2) (2020) 158–166, https://doi.org/10.1089/bioe.2020.0011.
[17] X.S. Chen, K.F. Wang, G.C. Zheng, Y. Gao, Z.G. Mao, Preparation, Characterization and Antimicrobial Activity of ε-Poly-L-Lysine with Short Chain Length Produced from Glycerol by Streptomyces Albulus, Process Biochem. 68 (February) (2018) 22–29, https://doi.org/10.1016/j.procbio.2018.03.001.
[18] J.S. Heo, H.O. Kim, S.Y. Song, D.H. Lew, Y. Choi, S. Kim, Poly-L-Lysine Prevents Senescence and Augments Growth in Culturing Mesenchymal Stem Cells Ex Vivo, Biomed Res. Int. 2016 (2016) 1–13, https://doi.org/10.1155/2016/8196078.
[19] H. Sasaki, K. Karasawa, K. Hironaka, K. Tahara, Y. Tozuka, H. Takeuchi, Retinal Drug Delivery Using Eyedrop Preparations of Poly-l-Lysine-Modified Liposomes, Eur. J. Pharm. Biopharm. 83 (3) (2013) 364–369, https://doi.org/10.1016/j.ejpb.2012.10.014.
[20] M. Hyldgaard, T. Mygind, B.S. Vad, M. Stenvang, D.E. Otzen, R.L. Meyer, The Antimicrobial Mechanism of Action of Epsilon-Poly-L-Lysine, Appl. Environ. Microbiol. 80 (24) (2014) 7758–7770, https://doi.org/10.1128/AEM.02204-14.
[21] S. Maiti, S. Jana, B. Laha, *Cationic Polyelectrolyte–Biopolymer Complex Hydrogel Particles for Drug Delivery*; Elsevier Inc., 2018. https://doi.org/10.1016/b978-0-12-813627-0.00006-5.

[22] B. Tian, E. Bilsbury, S. Doherty, S. Teebagy, E. Wood, W. Su, G. Gao, H. Lin, Ocular Drug Delivery: Advancements and Innovations, *Pharmaceutics* 14 (9) (2022), https://doi.org/10.3390/pharmaceutics14091931.

[23] S. Shah, A. Eyler, S. Tabandeh, L. Leon, Electrostatically Driven Self-Assembled Nanoparticles and Coatings, in: *Nanoparticles for Biomedical Applications*; Chung, E. J., Rinaldi, L., Leon, C., Eds.; Elsevier, 2020; pp 349–370. https://doi.org/10.1016/B978-0-12-816662-8.00020-5.

[24] M. Siyawamwaya, Y.E. Choonara, D. Bijukumar, P. Kumar, L.C. Du Toit, V. Pillay, A Review: Overview of Novel Polyelectrolyte Complexes as Prospective Drug Bioavailability Enhancers, Int. J. Polym. Mater. Polym. Biomater. 64 (18) (2015) 955–968, https://doi.org/10.1080/00914037.2015.1038816.

[25] D. Wu, L. Zhu, Y. Li, X. Zhang, S. Xu, G. Yang, T. Delair, Chitosan-Based Colloidal Polyelectrolyte Complexes for Drug Delivery: A Review, Carbohydr. Polym. 238 (March) (2020), https://doi.org/10.1016/j.carbpol.2020.116126.

[26] H. Van Le, D. Le Cerf, Colloidal Polyelectrolyte Complexes from Hyaluronic Acid: Preparation and Biomedical Applications. *Small* **2022**, *18*, 1–26. https://doi.org/10.1002/smll.202204283.

[27] E.S. Dragan, M.V. Dinu, Polysaccharides Constructed Hydrogels as Vehicles for Proteins and Peptides. A Review, *Carbohydr. Polym.* 225 (May) (2019), 115210, https://doi.org/10.1016/j.carbpol.2019.115210.

[28] E. Verdin, NAD+ in Aging, Metabolism, and Neurodegeneration. *Science (1979)* **2015**, *350* (6265), 1208–1213. https://doi.org/10.1126/science.aac4854.

[29] L. Hosseini, M.S. Vafaee, J. Mahmoudi, R. Badalzadeh, Nicotinamide Adenine Dinucleotide Emerges as a Therapeutic Target in Aging and Ischemic Conditions, Biogerontology 6 (2019), https://doi.org/10.1007/s10522-019-09805-6.

[30] G. Cimaglia, M. Votruba, J.E. Morgan, H. Andr, P.A. Williams, Supplementation for Glaucoma and Age-Related Macular Degeneration, Nutrients 12 (9) (2020) 2871, https://doi.org/10.3390/nu12092871.

[31] Y. Zhu, K.K. Zhao, Y. Tong, Y.L. Zhou, Y.X. Wang, P.Q. Zhao, Z.Y. Wang, Exogenous NAD+ Decreases Oxidative Stress and Protects H2O2-Treated RPE Cells against Necrotic Death through the up-Regulation of Autophagy, Sci. Rep. 6 (January) (2016) 1–12, https://doi.org/10.1038/srep26322.

[32] P.A. Williams, J.M. Harder, B.H. Cardozo, N.E. Foxworth, S.W.M. John, Nicotinamide Treatment Robustly Protects from Inherited Mouse Glaucoma, Commun. Integr. Biol. 11 (1) (2018), https://doi.org/10.1080/19420889.2017.1356956.

[33] J.S. Saini, B. Corneo, J.D. Miller, T.R. Kiehl, Q. Wang, N.C. Boles, T.A. Blenkinsop, J.H. Stern, S. Temple, Nicotinamide Ameliorates Disease Phenotypes in a Human IPSC Model of Age-Related Macular Degeneration, Cell Stem Cell 20 (5) (2017) 635–647, https://doi.org/10.1016/J.STEM.2016.12.015.

[34] N.E. de Picciotto, L.B. Gano, L.C. Johnson, C.R. Martens, A.L. Sindler, K.F. Mills, S. ichiro Imai, D.R. Seals, Nicotinamide Mononucleotide Supplementation Reverses Vascular Dysfunction and Oxidative Stress with Aging in Mice. Aging Cell 15 (3) (2016) 522–530. https://doi.org/10.1111/acel.12461.

[35] K.F. Mills, S. Yoshida, L.R. Stein, A. Grozio, S. Kubota, Y. Sasaki, P. Redpath, M. E. Migaud, R.S. Apte, K. Uchida, et al., Long-Term Administration of Nicotinamide Mononucleotide Mitigates Age-Associated Physiological Decline in Mice, Cell Metab 24 (6) (2017) 795–806, https://doi.org/10.1016/j.cmet.2016.09.013.

[36] J. Kaur, G. Kaur, Optimization of PH Conditions and Characterization of Polyelectrolyte Complexes between Gellan Gum and Cationic Guar Gum, Polym. Adv. Technol. 29 (12) (2018) 3035–3048, https://doi.org/10.1002/pat.4424.

[37] R. Ilka, M. Mohseni, M. Kianirad, M. Naseripour, K. Ashtari, B. Mehravi, Nanogel-Based Natural Polymers as Smart Carriers for the Controlled Delivery of Timolol Maleate through the Cornea for Glaucoma, Int. J. Biol. Macromol. 109 (2018) 955–962, https://doi.org/10.1016/j.ijbiomac.2017.11.090.

[38] N.J. Forrow, G.A. Shabir, Development and Validation of a HPLC Method for NAD: Application to Stability Studies in Buffered Solutions and Dry Test Strips, J. Liq. Chromatogr. Relat. Technol. 32 (19) (2009) 2805–2821, https://doi.org/10.1080/10826070903288680.

[39] S. Bohrey, V. Chourasiya, A. Pandey, Polymeric Nanoparticles Containing Diazepam: Preparation, Optimization, Characterization, in-Vitro Drug Release and Release Kinetic Study, Nano Converg 3 (1) (2016) 3–9, https://doi.org/10.1186/s40580-016-0061-2.

[40] G.H. Son, B.J. Lee, C.W. Cho, Mechanisms of Drug Release from Advanced Drug Formulations Such as Polymeric-Based Drug-Delivery Systems and Lipid Nanoparticles, J. Pharm. Investig. 47 (4) (2017) 287–296, https://doi.org/10.1007/s40005-017-0320-1.

[41] L. Ahmed, R. Atif, T.S. Eldeen, I. Yahya, A. Omara, M. Eltayeb, Study the Using of Nanoparticles as Drug Delivery System Based on Mathematical Models for Controlled Release, Int. J. Latest Technol. Eng., Manage. Appl. Sci. 8 (5) (2019) 52–56.

[42] J. Bhasarkar, D. Bal, Kinetic Investigation of a Controlled Drug Delivery System Based on Alginate Scaffold with Embedded Voids, J. Appl. Biomater. Funct. Mater. 17 (2) (2019), https://doi.org/10.1177/2280800018817462.

[43] S.M. Sreedharan, R. Singh, Ciprofloxacin Functionalized Biogenic Gold Nanoflowers as Nanoantibiotics against Pathogenic Bacterial Strains, Int. J. Nanomed. 14 (2019) 9905–9916, https://doi.org/10.2147/IJN.S224488.

[44] S. Dash, P.N. Murthy, L. Nath, P. Chowdhury, Kinetic Modeling on Drug Release from Controlled Drug Delivery Systems, Acta Pol. Pharm. 67 (3) (2010) 217–223.

[45] C. Mircioiu, V. Voicu, V. Anuta, A. Tudose, C. Celia, D. Paolino, M. Fresta, R. Sandulovici, I. Mircioiu, Mathematical Modeling of Release Kinetics from Supramolecular Drug Delivery Systems, Pharmaceutics (2019) 11 (3), https://doi.org/10.3390/pharmaceutics11030140.

[46] D. Wójcik-Pastuszka, J. Krzak, B. Macikowski, R. Berkowski, B. Osí Nski, W. Musiał, Evaluation of the Release Kinetics of a Pharmacologically Active Substance from Model Intra-Articular Implants Replacing the Cruciate Ligaments of the Knee, Materials 12 (8) (2019) 1202, https://doi.org/10.3390/ma12081202.

[47] C.C.M. Sproncken, B. Gumí-Audenis, S. Foroutanparsa, J.R. Magana, I.K. Voets, Controlling the Formation of Polyelectrolyte Complex Nanoparticles Using Programmable PH Reactions, Macromolecules 56 (1) (2023) 226–233, https://doi.org/10.1021/acs.macromol.2c01431.

[48] Z. Folchman-Wagner, J. Zaro, W.C. Shen, Characterization of Polyelectrolyte Complex Formation between Anionic and Cationic Poly(Amino Acids) and Their Potential Applications in PH-Dependent Drug Delivery. Molecules 22 (7) (2017) https://doi.org/10.3390/molecules22071089.

[49] M.A. Grimaudo, G. Amato, C. Carbone, P. Diaz-Rodriguez, T. Musumeci, A. Concheiro, C. Alvarez-Lorenzo, G. Puglisi, Micelle-Nanogel Platform for Ferulic Acid Ocular Delivery, Int. J. Pharm. 576 (2020) 1–9, https://doi.org/10.1016/j.ijpharm.2019.118986.

[50] E. Tsuchida, Formation of Polyelectrolyte Complexes and Their Structures, J. Macromol. Sci. Part A 31 (1) (1994) 1–15, https://doi.org/10.1080/10601329409349713.

[51] S. Lankalapalli, V.R.M. Kolapalli, Polyelectrolyte Complexes: A Review of Their Applicability in Drug Delivery Technology, Indian J. Pharm. Sci. 71 (5) (2009) 481–487, https://doi.org/10.4103/0250-474X.58165.

[52] L.M. Bravo-anaya, B. Garbay, J.L.E. Nando-rodríguez, F.C. Ramos, E. Ibarboure, K. Bathany, Nucleic Acids Complexation with Cationic Elastin-like Polypeptides : Stoichiometry and Stability of Nano-Assemblies, J. Colloid Interface Sci. 557 (2019) 777–792, https://doi.org/10.1016/j.jcis.2019.09.054.

[53] C. Schatz, A. Domard, C. Viton, C. Pichot, Versatile and Efficient Formation of Colloids of Biopolymer-Based Polyelectrolyte Complexes, Biomacromolecules 5 (5) (2004) 1882–1892, https://doi.org/10.1021/bm049786+.

[54] C.G. Otoni, M.V.A. Queirós, J.B. Sabadini, O.J. Rojas, W. Loh, Charge Matters: Electrostatic Complexation As a Green Approach to Assemble Advanced Functional Materials, ACS Omega 5 (3) (2020) 1296–1304, https://doi.org/10.1021/acsomega.9b03690.

[55] J. van der Gucht, E. Spruijt, M. Lemmers, M.A. Cohen Stuart, Polyelectrolyte Complexes: Bulk Phases and Colloidal Systems. J. Colloid Interface Sci. 361 (2) (2011) 407–422. https://doi.org/10.1016/j.jcis.2011.05.080.

[56] E.R. Leite, C. Ribeiro, Basic Principles: Thermodynamics and Colloidal Chemistry, in: Crystallization and Growth of Colloidal Nanocrystals, Springer Verlag:, New York, 2012, pp. 7–17, https://doi.org/10.1007/978-1-4614-1308-0_2.

[57] A.F. Thünemann, M. Müller, H. Dautzenberg, J.-F. Joanny, H. Löwen, Polyelectrolytes with Defined Molecular Architecture II, in: Adv Polym Sci, Vol. 166, Springer, Berlin Heidelberg, 2004, pp. 113–171, https://doi.org/10.1007/b11350.

[58] M. Zheng, M. Pan, W. Zhang, H. Lin, S. Wu, C. Lu, S. Tang, D. Liu, J. Cai, Poly(α-L-Lysine)-Based Nanomaterials for Versatile Biomedical Applications: Current Advances and Perspectives, Bioact. Mater. 6 (7) (2021) 1878–1909, https://doi.org/10.1016/j.bioactmat.2020.12.001.

[59] A. Golchoobi, A. Khosravi, H. Modarress, A. Ahmadzadeh, Effect of Charge, Size and Temperature on Stability of Charged Colloidal Nano Particles, Chinese J. Chem. Phys. 25 (5) (2012) 617–624, https://doi.org/10.1088/1674-0068/25/05/617-624.

[60] A.E. Marras, M. Ting, K.C. Stevens, M.V. Tirrell, Advances in the Structural Design of Polyelectrolyte Complex Micelles, J. Phys. Chem. B 125 (26) (2021) 7076–7089, https://doi.org/10.1021/acs.jpcb.1c01258.

[61] Y. Zhang, E. Yildirim, H.S. Antila, L.D. Valenzuela, M. Sammalkorpi, J. L. Lutkenhaus, The Influence of Ionic Strength and Mixing Ratio on the Colloidal Stability of PDAC/PSS Polyelectrolyte Complexes, Soft Matter 11 (37) (2015) 7392–7401, https://doi.org/10.1039/c5sm01184a.

[62] P.V. Date, A. Samad, P.V. Devarajan, Freeze Thaw: A Simple Approach for Prediction of Optimal Cryoprotectant for Freeze Drying, AAPS PharmSciTech 11 (1) (2010) 304–313, https://doi.org/10.1208/s12249-010-9382-3.

[63] M. Mohammady, Y. mohammadi, G. Yousefi, Freeze-Drying of Pharmaceutical and Nutraceutical Nanoparticles: The Effects of Formulation and Technique Parameters on Nanoparticles Characteristics. J. Pharm. Sci. 109 (11) (2020) 3235–3247. https://doi.org/10.1016/j.xphs.2020.07.015.

[64] A.D. Elbein, Y.T. Pan, I. Pastuszak, D. Carroll, New Insights on Trehalose: A Multifunctional Molecule, Glycobiology 13 (4) (2003) 17–27, https://doi.org/10.1093/glycob/cwg047.

[65] S. Siddhanta, I. Barman, C. Narayana, Revealing the Trehalose Mediated Inhibition of Protein Aggregation through Lysozyme-Silver Nanoparticle Interaction, Soft Matter 11 (37) (2015) 7241–7249, https://doi.org/10.1039/c5sm01896j.

[66] A. Rampino, M. Borgogna, P. Blasi, B. Bellich, A. Cesàro, Chitosan Nanoparticles: Preparation, Size Evolution and Stability, Int. J. Pharm. 455 (1–2) (2013) 219–228, https://doi.org/10.1016/j.ijpharm.2013.07.034.

[67] A. Umerska, K.J. Paluch, M.J. Santos-Martinez, O.I. Corrigan, C. Medina, L. Tajber, Freeze Drying of Polyelectrolyte Complex Nanoparticles: Effect of Nanoparticle Composition and Cryoprotectant Selection, Int. J. Pharm. 552 (1–2) (2018) 27–38, https://doi.org/10.1016/j.ijpharm.2018.09.035.

[68] Q. Yan, J. Weng, X. Wu, W. Wang, Q. Yang, F. Guo, D. Wu, Y. Song, F. Chen, G. Yang, Characteristics, Cryoprotection Evaluation and in Vitro Release of BSA-Loaded Chitosan Nanoparticles, Mar. Drugs 18 (6) (2020), https://doi.org/10.3390/md18060315.

[69] A. Strand, L. Vähäsalo, A. Ketola, K. Salminen, E. Retulainen, A. Sundberg, In-Situ Analysis of Polyelectrolyte Complexes by Flow Cytometry, Cellul. 25 (7) (2018) 3781–3795, https://doi.org/10.1007/s10570-018-1832-1.

[70] S.A. de Oliveira, B.C. da Silva, I.C. Riegel-Vidotti, A. Urbano, P.C. de Sousa Faria-Tischer, C.A. Tischer, Production and Characterization of Bacterial Cellulose Membranes with Hyaluronic Acid from Chicken Comb, Int. J. Biol. Macromol. 97 (January) (2017) 642–653, https://doi.org/10.1016/j.ijbiomac.2017.01.077.
[71] L. Li, Y. Xie, Y. Wang, X. Yang, R. Fu, R. Fang, Colloids and Surfaces B : Biointerfaces Study on Nicotinamide Adenine Dinucleotide Adsorbed at Nano-Boehmite / Water and Nano-Corundum / Water Interfaces. 102 (2013) 398–404. https://doi.org/10.1016/j.colsurfb.2012.07.029.
[72] A.B. Kayitmazer, A.F. Koksal, E. Kilic Iyilik, Complex Coacervation of Hyaluronic Acid and Chitosan: Effects of PH, Ionic Strength, Charge Density, Chain Length and the Charge Ratio, Soft Matter 11 (44) (2015) 8605–8612, https://doi.org/10.1039/c5sm01829c.
[73] D. Wu, T. Delair, Stabilization of Chitosan/Hyaluronan Colloidal Polyelectrolyte Complexes in Physiological Conditions, Carbohydr. Polym. 119 (2015) 149–158, https://doi.org/10.1016/j.carbpol.2014.11.042.
[74] S. Honary, F. Zahir, Effect of Zeta Potential on the Properties of Nano-Drug Delivery Systems - A Review (Part 2), Trop. J. Pharm. Res. 12 (2) (2013) 265–273, https://doi.org/10.4314/tjpr.v12i2.20.
[75] H.V. Sæther, H.K. Holme, G. Maurstad, O. Smidsrød, B.T. Stokke, Polyelectrolyte Complex Formation Using Alginate and Chitosan, Carbohydr. Polym. 74 (4) (2008) 813–821, https://doi.org/10.1016/j.carbpol.2008.04.048.
[76] R.D. Schoenwald, Ocular Pharmacokinetics and Pharmacodynamics. In *Ophthalmic Drug Delivery Systems*; Mitra, A. K., Ed.; Marcel Dekker Inc.: New York, 2003; pp 135–181. https://doi.org/10.4324/9781003113423.
[77] G. Emmanuel, S.J. Comia, M. Lat-Luna, M.B. Agulto, Fluorophotometric Measurements of Aqueous-Humor Flow in Filipino Eyes, Philippine Academy of Ophthalmol. 32 (2) (2007) 56–59.
[78] M. Ali, S. Horikawa, S. Venkatesh, J. Saha, J.W. Hong, M.E. Byrne, Zero-Order Therapeutic Release from Imprinted Hydrogel Contact Lenses within in Vitro Physiological Ocular Tear Flow, J. Control. Release 124 (3) (2007) 154–162, https://doi.org/10.1016/j.jconrel.2007.09.006.
[79] A. Tieppo, A.C. Boggs, P. Pourjavad, M.E. Byrne, Analysis of Release Kinetics of Ocular Therapeutics from Drug Releasing Contact Lenses: Best Methods and Practices to Advance the Field, Cont. Lens Anterior Eye 37 (4) (2014) 305–313, https://doi.org/10.1016/j.clae.2014.04.005.
[80] A.F.R. Pimenta, A. Valente, J.M.C. Pereira, J.C.F. Pereira, H.P. Filipe, J.L.G. Mata, R. Colaço, B. Saramago, A.P. Serro, Simulation of the Hydrodynamic Conditions of the Eye to Better Reproduce the Drug Release from Hydrogel Contact Lenses: Experiments and Modeling, Drug Deliv. Transl. Res. 6 (6) (2016) 755–762, https://doi.org/10.1007/s13346-016-0303-1.
[81] A. Umerska, K.J. Paluch, M.J.S. Martínez, O.I. Corrigan, C. Medina, L. Tajber, Self-Assembled Hyaluronate/Protamine Polyelectrolyte Nanoplexes: Synthesis, Stability, Biocompatibility and Potential Use as Peptide Carriers, J. Biomed. Nanotechnol. 10 (12) (2014) 3658–3673, https://doi.org/10.1166/jbn.2014.1878.
[82] W. Xiong, L. Li, Y. Wang, Y. Yu, S. Wang, Y. Gao, Y. Liang, G. Zhang, W. Pan, X. Yang, Design and Evaluation of a Novel Potential Carrier for a Hydrophilic Antitumor Drug: Auricularia Auricular Polysaccharide-Chitosan Nanoparticles as a Delivery System for Doxorubicin Hydrochloride, Int. J. Pharm. 511 (1) (2016) 267–275, https://doi.org/10.1016/j.ijpharm.2016.07.026.
[83] B. Silva, J. Marto, B.S. Braz, E. Delgado, A.J. Almeida, L. Gonçalves, New Nanoparticles for Topical Ocular Delivery of Erythropoietin, Int. J. Pharm. 576 (2020) 1–11, https://doi.org/10.1016/j.ijpharm.2020.119020.
[84] Y. Fu, W.J. Kao, Drug Release Kinetics and Transport Mechanisms of Non-Degradable and Degradable Polymeric Delivery Systems, Expert Opin. Drug Deliv. 7 (4) (2011) 429–444, https://doi.org/10.1517/17425241003602259.
[85] M.L. Brusch, Mathematical Models of Drug Release. In *Strategies to Modify the Drug Release from Pharmaceutical Systems*; Marcos Luciano Bruschi, Ed.; Woodhead Publishing Ltd, 2015; pp 63–86. https://doi.org/10.1016/b978-0-08-100092-2.00005-9.
[86] P.L. Ritger, N.A. Peppas, A Simple Equation for Description of Solute Release I. Fickian and Non-Fickian Release from Non-Swellable Devices in the Form of Slabs, Spheres, Cylinders or Discs, J. Control. Release 5 (1987) 23–26, https://doi.org/10.1016/S0168-3659(03)00195-0.
[87] J.N. Putro, V.B. Lunardi, F.E. Soetaredjo, M. Yuliana, S.P. Santoso, I.G. Wenten, S. Ismadji, A Review of Gum Hydrocolloid Polyelectrolyte Complexes (Pec) for Biomedical Applications: Their Properties and Drug Delivery Studies, Processes 9 (10) (2021), https://doi.org/10.3390/pr9101796.
[88] A. Ćirić, J.M. Budinčić, Đ. Medarević, V. Dobričić, M. Rmandić, T. Barudžija, A. Malenović, L. Petrović, L. Djekic, Evaluation of Chitosan/Xanthan Gum Polyelectrolyte Complexes Potential for PH-Dependent Oral Delivery of Escin, Int. J. Biol. Macromol. 221 (2022) 48–60, https://doi.org/10.1016/J.IJBIOMAC.2022.08.190.
[89] N.V. Dubashynskaya, S.V. Raik, Y.A. Dubrovskii, E.V. Demyanova, E. S. Shcherbakova, D.N. Poshina, A.Y. Shasherina, Y.A. Anufrikov, Y.A. Skorik, Hyaluronan/Diethylaminoethyl Chitosan Polyelectrolyte Complexes as Carriers for Improved Colistin Delivery, Int. J. Mol. Sci. 22 (16) (2021), https://doi.org/10.3390/ijms22168381.
[90] S. Jana, A. Banerjee, A. Gandhi, Preparation and Characterization of Chitosan Based Polyelectrolyte Complex as a Carrier of Aceclofenac, Journal of PharmaSciTech 3 (2) (2014) 68–71.
[91] G.A. Magalhães, E. Moura Neto, V.G. Sombra, A.R. Richter, C.M.W.S. Abreu, J.P. A. Feitosa, H.C.B. Paula, F.M. Goycoolea, R.C.M. de Paula, Chitosan/Sterculia Striata Polysaccharides Nanocomplex as a Potential Chloroquine Drug Release Device, Int. J. Biol. Macromol. 88 (2016) 244–253, https://doi.org/10.1016/j.ijbiomac.2016.03.070.
[92] E. Alinejad-Mofrad, B. Malaekeh-Nikouei,L. Gholami, SH. Mousavi, HR. Sadeghnia, M. Mohajeri, M. Darroudi, RK. Oskuee, Evaluation and Comparison of Cytotoxicity , Genotoxicity , and Apoptotic Effects of Poly- L -Lysine / Plasmid DNA Micro- and Nanoparticles, Human Exp Toxicol. 38 (8) (2019) 983-991. https://doi.org/10.1177/0960327119846924.
[93] S. Chen, S. Huang, Y. Li, C. Zhou, Recent Advances in Epsilon-Poly-L-Lysine and L-Lysine-Based Dendrimer Synthesis, Modification, and Biomedical Applications, Front Chem. 9 (March) (2021) 1–14, https://doi.org/10.3389/fchem.2021.659304.
[94] P. Symonds, J.C. Murray, A.C. Hunter, G. Debska, A. Szewczyk, S.M. Moghimi, Low and High Molecular Weight Poly(L-Lysine)s/Poly(L-Lysine)-DNA Complexes Initiate Mitochondrial-Mediated Apoptosis Differently, FEBS Lett. 579 (27) (2005) 6191–6198, https://doi.org/10.1016/j.febslet.2005.09.092.
[95] E.S. Hwang, S.B. Song, Possible Adverse Effects of High-Dose Nicotinamide: Mechanisms and Safety Assessment, Biomolecules 10 (687) (2020) 1–21, https://doi.org/10.3390/biom10050687.
[96] N. Braidy, Y. Liu, NAD+ Therapy in Age-Related Degenerative Disorders: A Benefit/ Risk Analysis, Exp. Gerontol. 132 (110831) (2020), https://doi.org/10.1016/j.exger.2020.110831.
[97] D. Khiev, Z.A. Mohamed, R. Vichare, R. Paulson, S. Bhatia, S. Mohapatra, G. P. Lobo, M. Valapala, N. Kerur, C.L. Passaglia, et al., Emerging Nano-Formulations and Nanomedicines Applications for Ocular Drug Delivery, Nanomaterials 11 (1) (2021) 1–19, https://doi.org/10.3390/nano11010173.
[98] P.M. Campos, R. Petrilli, R.F.V. Lopez, The Prominence of the Dosage Form Design to Treat Ocular Diseases, Int. J. Pharm. 586 (March) (2020), 119577, https://doi.org/10.1016/j.ijpharm.2020.119577.
[99] G. Begum, T. Leigh, E. Courtie, R. Moakes, G. Butt, Z. Ahmed, S. Rauz, A. Logan, R.J. Blanch, Rapid Assessment of Ocular Drug Delivery in a Novel Ex Vivo Corneal Model, Sci. Rep. 10 (1) (2020) 1–12, https://doi.org/10.1038/s41598-020-68254-1.
[100] K.M. Hämäläinen, K. Kananen, S. Auriola, K. Kontturi, A. Urtti, Characterization of Paracellular and Aqueous Penetration Routes in Cornea, Conjunctiva, and Sclera, Invest. Ophthalmol. Vis. Sci. 38 (3) (1997) 627–634.
[101] N. Mittal, G. Kaur, Investigations on Polymeric Nanoparticles for Ocular Delivery, Adv. Polym. Tech. 2019 (2019), https://doi.org/10.1155/2019/1316249.
[102] C. Kimna, B. Winkeljann, J. Hoffmeister, O. Lieleg, Biopolymer-Based Nanoparticles with Tunable Mucoadhesivity Efficiently Deliver Therapeutics across the Corneal Barrier, Mater. Sci. Eng. C 2021 (121) (September 2020), 111890, https://doi.org/10.1016/j.msec.2021.111890.
[103] M.A. Kalam, Development of Chitosan Nanoparticles Coated with Hyaluronic Acid for Topical Ocular Delivery of Dexamethasone, Int. J. Biol. Macromol. 89 (2016) 127–136, https://doi.org/10.1016/J.IJBIOMAC.2016.04.070.
[104] T. Yeh, L. Hsu, M.T. Tseng, P. Lee, K. Sonjae, Y. Ho, H. Sung, Mechanism and Consequence of Chitosan-Mediated Reversible Epithelial Tight Junction Opening, Biomaterials 32 (26) (2011) 6164–6173, https://doi.org/10.1016/j.biomaterials.2011.03.056.
[105] A. Graça, L.M. Gonçalves, S. Raposo, H.M. Ribeiro, J. Marto, Useful in Vitro Techniques to Evaluate the Mucoadhesive Properties of Hyaluronic Acid-Based Ocular Delivery Systems, Pharmaceutics (2018) 10 (3), https://doi.org/10.3390/pharmaceutics10030110.
[106] C. Guarise, L. Acquasaliente, G. Pasut, M. Pavan, M. Soato, G. Garofolin, R. Beninatto, E. Giacomel, E. Sartori, D. Galesso, The Role of High Molecular Weight Hyaluronic Acid in Mucoadhesion on an Ocular Surface Model, J. Mech. Behvior Biomed. Materials 143 (2023), 105908.
[107] M. de la Fuente, B. Seijo, M.J. Alonso, Bioadhesive Hyaluronan-Chitosan Nanoparticles Can Transport Genes across the Ocular Mucosa and Transfect Ocular Tissue, Gene Ther. 15 (9) (2008) 668–676, https://doi.org/10.1038/gt.2008.16.
[108] D. Liu, Y. Lian, Q. Fang, L. Liu, J. Zhang, J. Li, Hyaluronic-Acid-Modified Lipid-Polymer Hybrid Nanoparticles as an Efficient Ocular Delivery Platform for Moxifloxacin Hydrochloride, Int. J. Biol. Macromol. 116 (2018) 1026–1036, https://doi.org/10.1016/j.ijbiomac.2018.05.113.
[109] S.N. Zhu, B. Nolle, G. Duncker, Expression of Adhesion Molecule CD44 on Human Corneas, Br. J. Ophthalmol. 81 (1) (1997) 80–84, https://doi.org/10.1136/bjo.81.1.80.
[110] N. Polisetti, G. Martin, H.R. Cristina Schmitz, U. Schlötzer-Schrehardt, G. Schlunck, T. Reinhard, Characterization of Porcine Ocular Surface Epithelial Microenvironment, Int. J. Mol. Sci. 24 (8) (2023), https://doi.org/10.3390/ijms24087543.
[111] S. Boddu, H. Gupta, S. Patel, Drug Delivery to the Back of the Eye Following Topical Administration: An Update on Research and Patenting Activity, Recent Pat. Drug Deliv. Formul. 8 (1) (2014) 27–36, https://doi.org/10.2174/1872211308666140130093301.

APPENDIX 2.3: ARVO POSTER PRSENTATION

AN EVALUATION OF HYALURONIC ACID AND POLY(L-LYSINE) POLYELECTROLYTE COMPLEXES FOR INTRAOCULAR NICOTINAMIDE ADENINE DINUCLEOTIDE (NAD+) DELIVERY

Saoirse Casey-Power [1], Camila Vardar [2], Richie Ryan [1], Gautam Behl [1], Peter McLoughlin [1], Mark Byrne [2] and Laurence Fitzhenry [1]
[1] Ocular Therapeutics Research Group, Pharmaceutical and Molecular Biotechnology Research Centre, South East Technological University, Waterford, Ireland.
[2] Biomimetic & Biohybrid Materials, Biomedical Devices & Drug Delivery Laboratories, Department of Biomedical Engineering, Rowan-Virtua School of Translational Biomedical Engineering & Sciences, Rowan University, 201 Mullica Hill Road, Glassboro, NJ 08028, USA.

PRESENTATION NUMBER 2620

SETU Ollscoil Teicneolaíochta an Oirdheiscirt / South East Technological University

INTRODUCTION

474 MILLION — Cases of moderate to severe visual impairment by 2050 [1]

Aging is the primary risk factor

At a cellular level
Pathogeneses of ocular diseases are similar [2-3].
- Decline in intracellular NAD+ pools

Disadvantages of current treatments [4-5].
- Invasive
- High frequency of administration
- Low ocular bioavailability
- Adverse effects

RESEARCH OBJECTIVE

To evaluate whether a hyaluronic acid (HA) and poly(L-lysine) (PLL) polyelectrolyte complex (PECs) nanoparticle system exhibits suitable physicochemical characteristics for effective ocular NAD+ delivery.

HYPOTHESIS

The PECs will behave as a depot, delivering NAD+ to minimise age-related cellular dysfunction and damage before or at the early onset of ocular disease.

METHODOLOGY

Formulation of NAD+-associated HA and PLL PECs via polyelectrolyte complexation in aqueous medium.

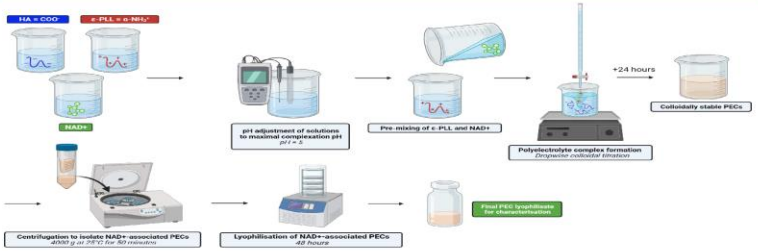

Figure 1: Schematic diagram of the formulation and work-up of NAD+-associated HA and PLL PECs.

Optimisation and characterisation of NAD+-associated HA and PLL PECs.

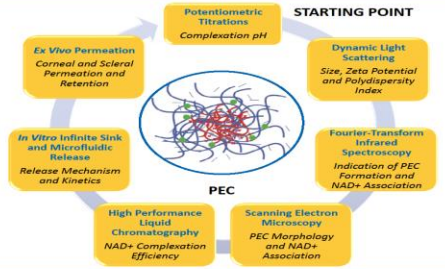

KEY RESULTS AND DISCUSSION

pH 5.5	2	235 nm	77.2%	11.5 mg	429 nm	14 hours	112.1 ug/cm³	495.7 ug/cm³
Maximal complexation between COO^- (HA) and NH_3^+ (PLL).	Optimal charge ratio (COO^-/ NH_3^+) for non-stoichiometric PEC formation.	Size of PECs formed after lyophilisation with cryoprotectant.	Percentage of NAD+ successfully complexed to the PECs.	Mass of NAD+ released after 8 hours until infinite sink conditions.	Size of PECs after storage in 0.01 M PBS (pH 7.4) for 8 hours.	Extended release of NAD+ under physiological ocular flow rates.	Mass of NAD+ permeated per cm³ of porcine cornea over 8 hours.	Mass of NAD+ permeated per cm³ of porcine sclera over 8 hours.

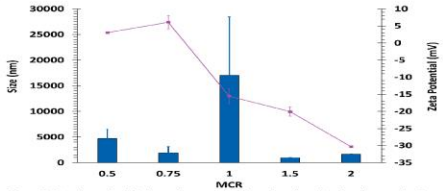

Figure 2: The change in PEC size and zeta potential as a function of molar charge ratio. Data is expressed as mean ± SD (n = 3).

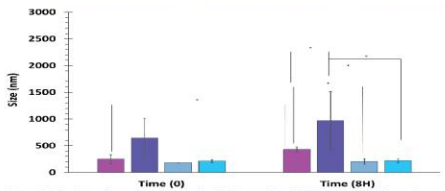

Figure 3: The size values recorded for the NAD+-associated PECs in each of the release media analysed over the *in vitro* release period. 0.01 M PBS (pH 7.4), 0.01 M PBS (pH 5.5), ultrapure water (pH 7.4) and ultrapure water (pH 5.5). Data is expressed as mean ± SD (n = 3). (* - statistically significant at a 5% confidence interval).

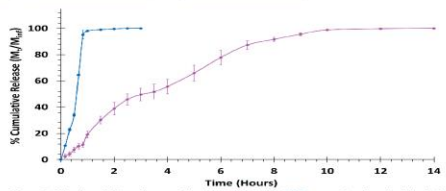

Figure 4: % *In vitro* NAD+ release profiles from PECs and a NAD+ control under physiological microfluidic conditions (flow rate = ~ 3 µL/min) over a 14 hour period. Data is expressed as mean % cumulative release (M_t/M_{inf}) ± SD (n = 3).

CONCLUSIONS

- Successful formulation of colloidally stable NAD+-associated PECs with suitable physiochemical size and % complexation efficiency parameters.
- Sustained release of NAD+ under physiological ocular conditions for up to 14 hours – suitable release profile for once-daily topical application.
- Enhanced *ex vivo* scleral permeation in comparison to corneal permeation – hydrophilicity of PEC formulation.
- Significant increase in size ($p = 0.006 > 0.05$) in physiological buffer solution over infinite sink release period.

FUTURE WORK

- Cell uptake study in porcine ocular tissues via fluorescent microscopy (observe extent of PEC cell internalisation – determine if increase in size is a limiting factor for corneal permeation).
- Further characterisation of NAD+-associated PECs via isothermal titration calorimetry and transmission electron microscopy.
- *In vitro* cell viability and NAD+ efficacy study in a hydrogen peroxide-mediated cell damage model via cell counting kit-8 (CCK-8) assay.

REFERENCES

[1] The International Agency for the Prevention of Blindness, "Projected Change in Vision Loss 2020 to 2050", 2020. [Online]. [Accessed: 06-Jan-2021].
[2] Liguori I., *et al.*, "Oxidative stress, aging, and diseases," Clin. Interv. Aging, vol. 13, pp. 757–772, 2018.
[3] Verdin, E., "NAD+ in aging, metabolism, and neurodegeneration," Science, vol. 350, no. 6265, pp. 1208–1213, 2015.
[4] Nayak, K. and Misra, M., "A review on recent drug delivery systems for posterior segment of eye," Biomed. Pharmacother., vol. 107, pp. 1564–1582, 2018.
[5] Gote, V., *et al.*, "Ocular Drug Delivery: Present Innovations and Future Challenges," J. Pharmacol. Exp. Ther., vol. 370, pp. 602–624, 2019.

DISCLOSURE: NONE

Curious about HA-based polyelectrolyte complex systems?
Check out our review paper published in the Pharmaceutics Special Issue "Innovative Technologies to Treat Diseases of the Back of the Eye"

ACKNOWLEDGEMENTS

This work was funded by the SETU PhD Scholarship Programme.

SETU | TRC | PMBrc Pharmaceutical & Molecular Biotechnology Research Centre

CONTACT

Saoirse Casey-Power
saoirse.casey-power@postgrad.wit.ie
https://www.linkedin.com/in/saoirse-casey-power/
@IsMiseSaoirse
https://research.wit.ie/en/persons/saoirse-casey-power